HSU

THE MAJOR CAUSE OF EARTHQUAKE DISASTERS : SHEAR BANDINGS

Bridges Damaged in the 921 Jiji Earthquake

Shear Banding Table Test Results

NOT FOR SALE

THE MAJOR CAUSE OF EARTHQUAKE DISASTERS: SHEAR BANDINGS

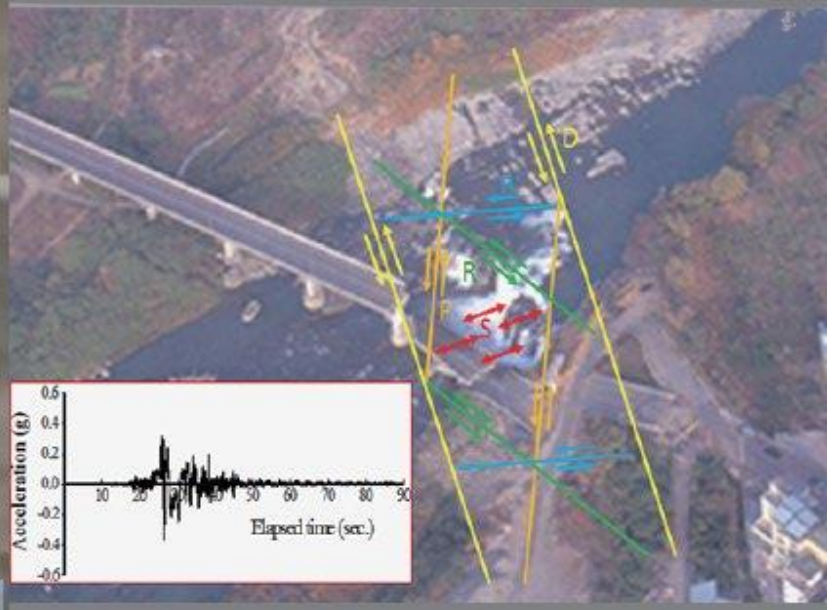

Edited by Tse-Shan Hsu

THE MAJOR CAUSE OF EARTHQUAKE DISASTERS: SHEAR BANDINGS

Edited by

Tse-Shan Hsu

Institute of Mitigation for Earthquake

Shear Banding Disasters

Taichung, Taiwan

The Procedure for Shear Banding, Highly Concentrated Excess Pore Water Pressure and Vibration to be Induced in a Tectonic Earthquake

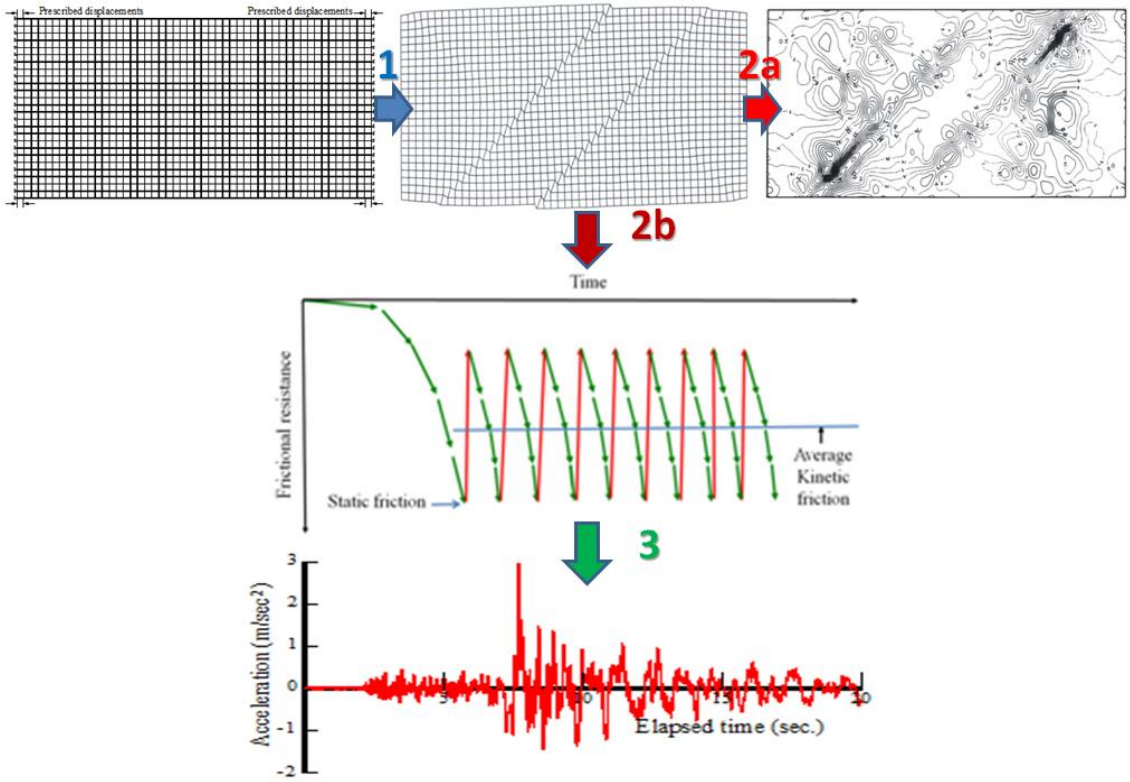

Step 1: Shear bandings induced by lateral compression
Step 2a: Highly concentrated excess pore water pressures induced by shear bandings
Step 2b: Stick-slip-… induced by shear bandings
Step 3: Vibration induced by stick-slip-.....

Contents

Chapter 1

Capturing Shear Bandings

T.-S. Hsu

1.1 Introduction

It is generally observed that geotechnical failures start within a zone of strain concentration, and then propagate along the weakest strain softening plane. Movements and strength of geological materials are therefore closely related. This is true especially when failures are associated with strain softening of materials. Under such condition, a variation of strength is generally found with the increase in the movements.

In traditional soil mechanics, limit analyses and one dimensional consolidation theory are used in stability analyses and settlement computations respectively. It has been pointed out by Parry and Wroth (1981) that these two types of calculations are completely divorced from each other; it has been traditional to consider soil strength and soil movements as totally unrelated quantities.

The advent of electronic computers, the development of numerical methods, and the establishment of constitutive relationship have made it possible to relate soil strength and soil movements in a complete structure analysis. This is the contribution of the numerical methods developed in last fifty years. However, it was mentioned by Prevost and Hughes (1981) that many of these solutions are deficient in not converging toward a limit load when such a limit exists or in not exhibiting localization of deformation phenomena when such localizations should occur. The reasons for the above deficiencies may be: (1) strain hardening or elasto-perfect plastic material models are used, and (2) the material models are constrained by the Drucker's postulate, therefore, strain softening is not allowed in a load step. It may be pointed out that, if a true failure pattern is not captured, a good agreement between the predicted and the actual stress-strain relationship is not necessarily a good prediction, because in many cases it may be caused by compensating errors in the individual steps or operations, such as sampling, testing, and analysis (Hvorslev, 1969). Materials therefore should exhibit

different strengths for different type of movements due to different failure patterns.

In view of the above deficiencies, it is then necessary to extend the engineering solutions to make up for the deficiencies and to carry out an analysis for strain softening materials. Such extension forms the major work of this book.

It may be noted that the phenomenon of localizations of deformations and formation of shear bands has long been observed in real life. Analytical investigations related to the onset of shear band have been performed by Hadamard (1903), Thomas (1961), and Hill (1962). Quantitative determinations of the localization of plastic deformation were initiated with the work of Rudnicki and Rice (1975), and Rice (1977). It was after 1980 that shear bands became visible in a deformed mesh by using finite element methods. Prevost and Hughes (1981) demonstrated that localization could be captured in finite element analysis for strain softening materials. Needleman and Tvergaard (1983) investigated several constitutive relationships which can lead to instability in the form of shear bands and demonstrated that these instabilities do appear in finite element computations in the form of highly localized zones of shear deformations. Prevost (1984) extended the analyses for frictional materials having non-associative flow rules.

Figure 1.1 shows that a shear band was induced by the 921 Jiji earthquake in Nantou, Taiwan. Figure 1.2 presents simulation results of the shear band produced by some investigators. It is clearly vivid that only the shear band produced by the author is quite similar to the real one; the other shear bands which were provided by Prevost and Hughes (1981), de Borst (1988), and Shuttle and Smith (1988) are all different from the real one. This fact indicates that it is not easy to perform a shear band simulation by using finite element method. The most difficult part is that both the material constitutive model and the numerical scheme have to be able to capture localizations of deformations.

For a tectonic plate which is laterally compressed continuously, once the shear band in the deformed mesh from finite element analysis is similar to the real one, the distributions of strain energy density (details in Figure 1.3), velocity vectors (details in Figure 1.4) and excess pore water pressure (details in Figure 1.5) in the plate can be plotted a step further in order to identify whether shear bands and soil liquefactions have happened.

圖 1.1. A shear band induced by the 921Jiji earthquake

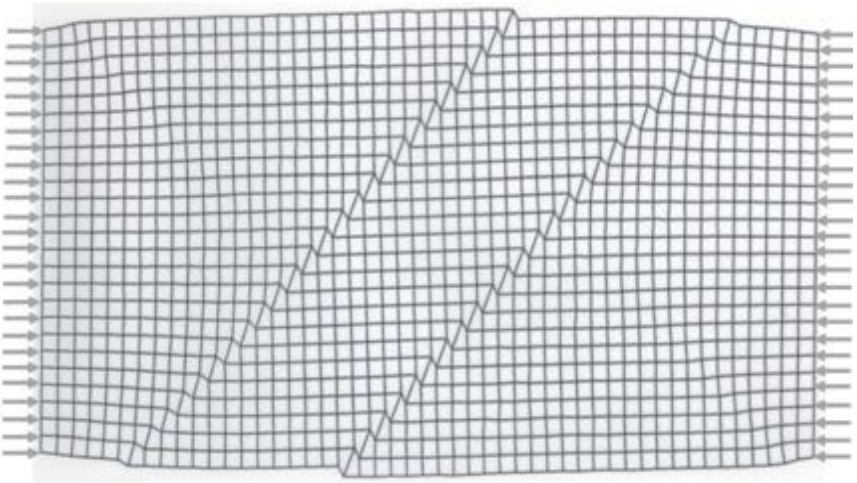

(a) The authors

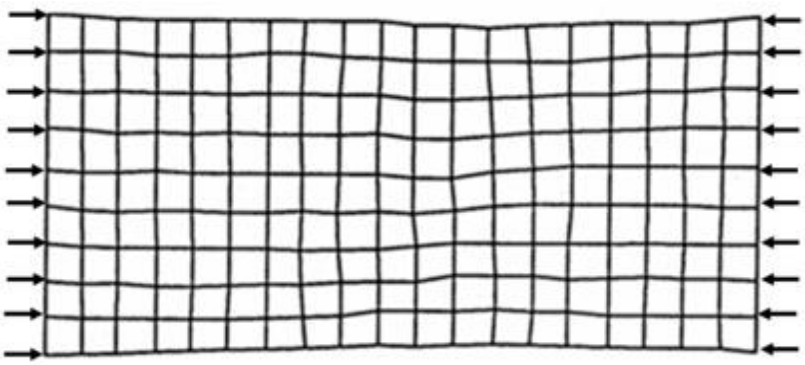

(b) Prevost and Hughes (1981)

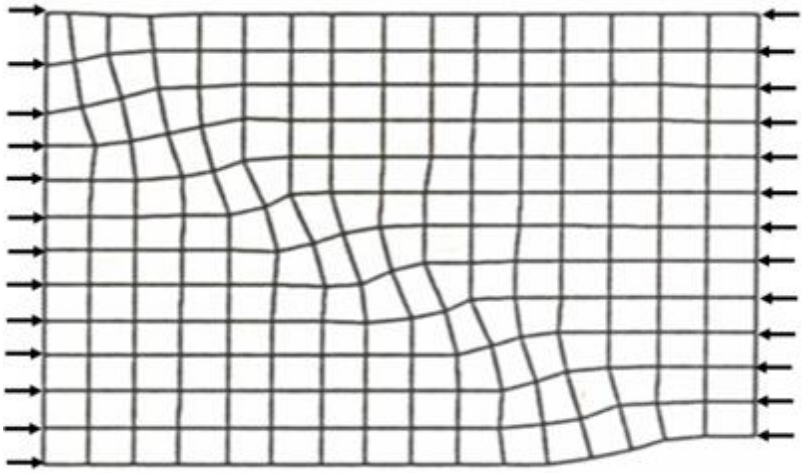

(c) de Borst (1988)

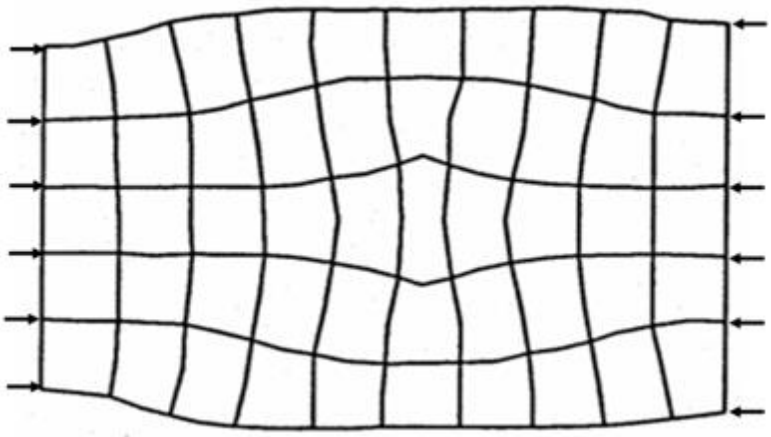

(d) Shuttle and Smith (1988)

Figure 1.2. Results of shear band simulation obtained by different researchers

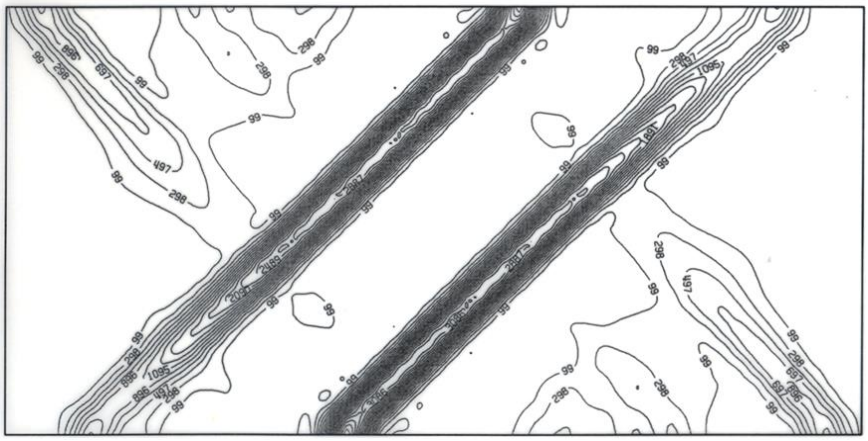

Figure 1.3. Distribution of Strain energy density

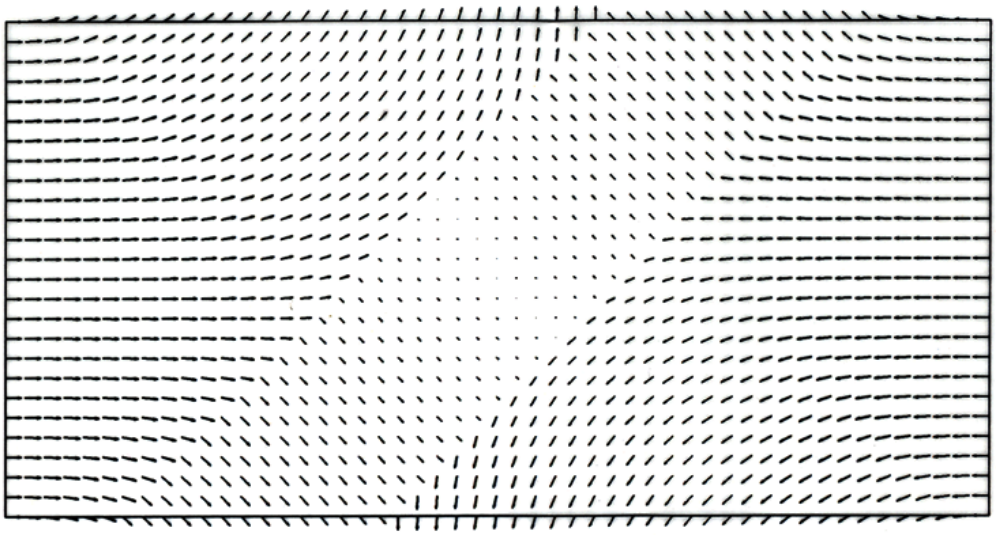

Figure 1.4. Distribution of velocity vectors

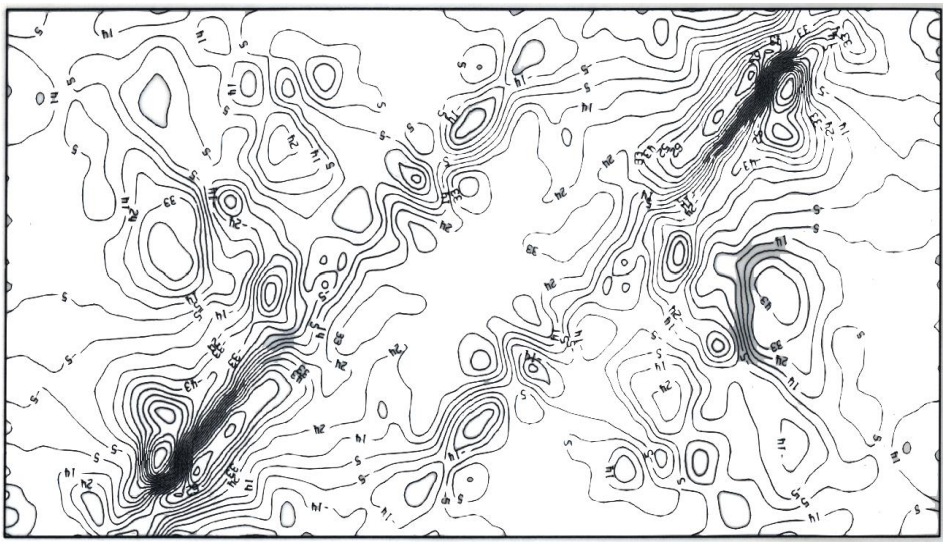

Figure 1.5. Distribution of excess pore water pressure

In a tectonic earthquake, when shear banding occurs in a soil or rock stratum, Figure 1.6 shows that when the foundations on the left and the right hand side of the building located in the hanging wall and foot wall separately, even if the building is very seismic vibration-resistant, yet the building will be damaged unavoidably by shear banding. However, when the foundations of the building are all located in the foot wall, there is no influence of shear bandings on the building. Thus, even if the building only fulfill the building earthquake-resistant design specifications of 1970s', such a building can still be remain stable in a tectonic earthquake.

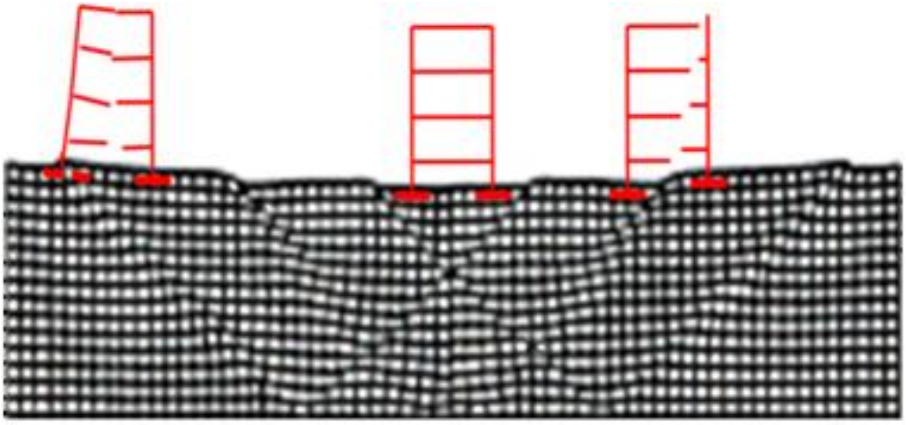

Figure 1.6. The mechanism of building collapse in a tectonic earthquake

It is to be stressed that although a building fulfills all the requirements of the current building earthquake-resistant design specifications, the building can still be damaged by shear bandings just because their effect is not included in the so called “earthquake-resistant” design.

Figure 1.7 is shown more clearly vivid that the ground vibrations and the highly concentrated phenomenon of excess pore water pressure are caused by shear bandings in a tectonic earthquake. Where shear banding energy is found to be greater than 90% of the total tectonic earthquake’s energy; and ground vibration energy is only less than 10% of the total tectonic earthquake’s energy. This is the major reason for most of the earthquake disasters to happen in the shear banding zones.

It is known to all of us that the seismic vibration-resistant forces for the upper structure components kept on increasing after earthquake disasters had happened in the past. However, it will not help to reduce the occurrence of earthquake disasters. In the future, only after including the shear banding effect into the new building earthquake-resistant design specifications can the tectonic earthquake disasters be reduced significantly.

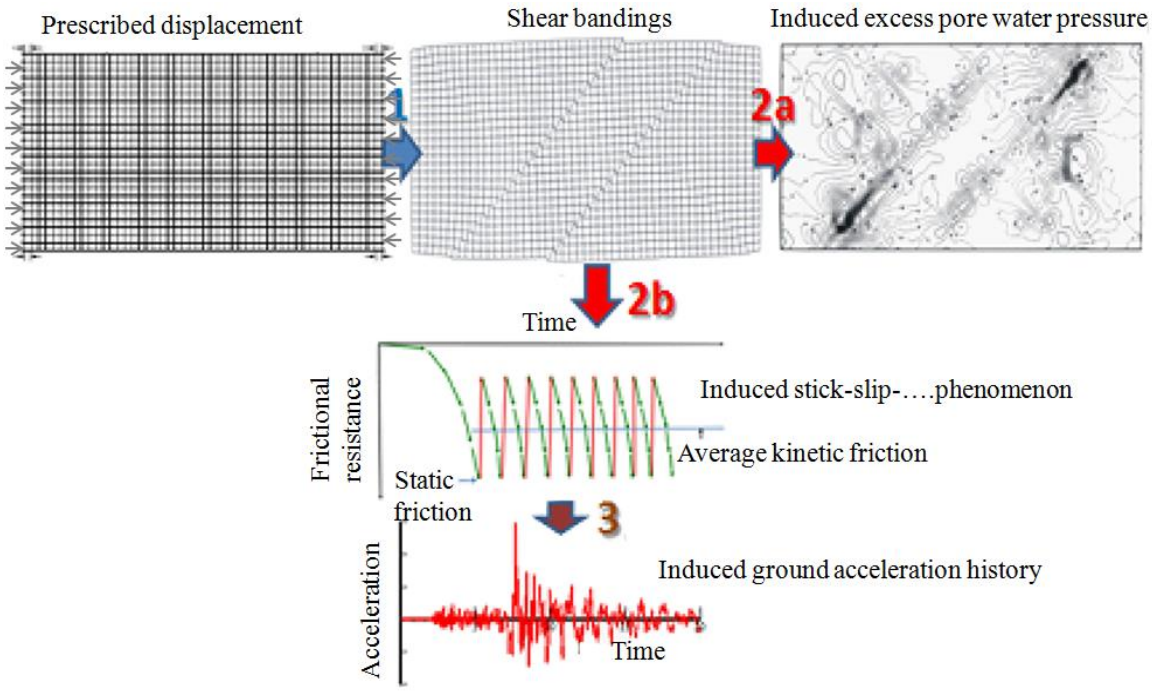

Legend： 1. Local shear banding is induced in a tectonic plate by lateral compression.

2a. Highly concentrated excess pore water pressure is induced in the shear band.

2b. When shear banding occurs, stick-slip-…phenomenon appears repeatedly.

3. Acceleration time history for the ground vibration is induced by stick-slip-…phenomen.

Figure 1.7. A flow chart for the ground vibration and the highly concentrated pore water pressure to be induced by shear banding

1.2 Finite Element Analysis of Localization in Plasticity

It is generally noticed that when ductile solids such as rocks, overly consolidated clays, granular materials, polymers, and structural metals are deformed sufficiently far into the plastic range, a smoothly and continuously varying deformation pattern gives way to highly localized deformations in the form of shear bands (Rice, 1977). Such a phenomenon can be understood as the instability in the macroscopic constitutive description of inelastic deformation of the material. Specifically, instability is understood in the sense that the constitutive relations may allow the homogeneous deformation of an initially uniform material to lead to a bifurcation point, at which nonuniform deformation can be incipient in a planar band under conditions of continuing equilibrium and continuing homogeneous deformation outside the zone of localization (Rudnicki and Rice, 1975). This chapter will discuss sequentially the background of localization, the constitutive formulation, the

analysis of bifurcation, the condition of stability, and the uniqueness of the incremental finite element solutions for strain softening materials.

1.2.1 Background of Localization

When a material is considered as rate and time independent, a quasi-static and isothermal field equation can be used to model its behavior. The analytical framework for analyzing the onset of shear band formation started with the work of Hadamard (1903) for elastic solids. The plastic flow and fracture in solids was investigated by Thomas (1961). In 1962, a general theoretical work for localizations was given by Hill, who investigated them in connection with the special case of a stationary acceleration wave in elasto-plastic solids. The above three works are the earliest and the most important works of localization in plasticity. The basic theories developed in these works were later used by most of the investigators. In 1970, Berg proposed an explanation for the inception of rupture in ductile materials owing to the nucleation and progressive growth of microscopic voids. In 1975, Rudnicki and Rice modeled the behavior of brittle rock masses under compressive principal stresses. Rice gave a formulation for localization in connection with shear band formulation in over-consolidated clay soils in 1977. By using finite element methods, shear bands were shown in deformed meshes by Tvergaard et al. (1981) for a plane strain tensile test; by Peirce et al. (1981) for ductile single crystals; by Larsson et al. (1981) for an internally pressured aluminum alloy tube; by Triantafyllidis et al. (1982) for a plane strain plate strip subjected to pure bending; and, by Needleman and Tvergaard (1983) for deeply cracked center crack panel specimens and edge crack bend specimens. For geological materials shear bands were obtained by Prevost and Hughes (1981) for a plane strain tensile test of a plate and for footings and slopes under loading conditions with associated flow rule; by Prevost (1984) for the same problems as those done by Prevost and Hughes (1982) but with the non-associated flow rule; by Vermeer and De Borst (1984) for soils, concrete and rock with non-associated flow rule; and, by De Borst and Vermeer for a footing under strip loading with both associate and non-associate flow rules.

Besides the above analytical and quantitative determinations, laboratory tests related to the localized shearing have been done by Chang and Asaro (1980) for aluminum-copper single crystals, by Anand and Spitzig (1980) for

the aged steel; and, by Larsson et al. (1981) for an internally pressurized aluminum alloy tube. Laboratory tests for geological material also have been conducted by Lambe and Whiteman (1972) for retaining structures under active and passive failure conditions; by Drescher (1972) for a granular material by using two-dimensional photo-elastic techniques; by Hallbauer et al. (1973) for quartzite specimens in stiff triaxial compression tests under different stress levels; by Blair-Fish and Bransby (1973) for the flow pattern in a Mass-flow Bunker; by Oda and Konishi (1974) for granular material in simple shear; by Drescher (2015) for granular materials in the investigation of flow rules; by Mandl (1966) for the crystal faults over arch of uniform curvature simulated in a shear box; and, by Vermeer and De Borst (1984) for the ground anchor in the investigation of failure mechanism involving shear bands.

The literature study reveals that many methods have been proposed for analyzing and explaining the behavior of structural metals, such as single-crystal plasticity of Taylor and Elam (1923, 1925); continuum model of a ductile porous material of Rudnicki and Rice (1975); and, J_2 corner theory of Christoffersen and Hutchinson (1979), etc. In analyzing the elasto-plastic boundary-value problems, Prevost and Hughes (1981) mentioned that if localization phenomena are to be captured by the numerical solutions, the use of elasto-plastic material stiffness is more helpful than any other algorithmically convenient stiffness to form the global stiffness. Despite development of many sophisticated soil models, an ‘elasto-plastic strain softening material model’ based on the extended Von-Mises yield criterion is proposed and utilized in this research.

1.2.2 Formulation of Constitutive Equations

Since the elasto-plastic strain softening constitutive equation will be extensively utilized in this research, a review of constitutive equations related to this area only is herewith presented. The three main contributions in this area are due to Nayak and Zienkiewicz (1972), Yamada et al. (1968), and Zienkiewicz (1977). A discussion of each contribution follows:

Nayak and Zienkiewicz's Formulation. The assumed yield function is

$$F\left(\underline{\sigma}, \underline{\varepsilon}^{p}, \kappa\right) = 0 \qquad (1.1)$$

where

$\underline{\sigma}$ = the stress vector;

$\underline{\varepsilon}^p$ = the plastic strain vector;

κ = the instantaneous size of the yield surface.

The assumed plastic potential is

$$g\left(\underline{\sigma}, \underline{\varepsilon}^p, \kappa\right) = 0 \tag{1.2}$$

The flow rule is

$$d\underline{\varepsilon}^p = \lambda \frac{\partial g}{\partial \underline{\sigma}} = \lambda \frac{\partial F}{\partial \underline{\sigma}} \tag{1.3}$$

where λ is an arbitrary nonnegative value.

Differentiating Equation 1.1 leads to

$$\begin{aligned} dF &= \left(\frac{\partial F}{\partial \underline{\sigma}}\right)^T d\underline{\sigma} + \left(\frac{\partial F}{\partial \underline{\varepsilon}^p}\right)^T d\underline{\varepsilon}^p + \frac{\partial F}{\partial \kappa} d\kappa \\ &= \left(\frac{\partial F}{\partial \underline{\sigma}}\right)^T d\underline{\sigma} - H\lambda \\ &= 0 \end{aligned} \tag{1.4}$$

where H is the hardening parameter and it is

$$H = \frac{-1}{\lambda}\left[\left(\frac{\partial F}{\partial \underline{\varepsilon}^p}\right)^T d\underline{\varepsilon}^p + \frac{\partial F}{\partial \kappa} d\kappa\right] \tag{1.5}$$

The incremental stress vector is

$$d\underline{\sigma} = \underline{\underline{D}}^e\left(d\underline{\varepsilon} - d\underline{\varepsilon}^p\right) = \underline{\underline{D}}^e\left(d\underline{\varepsilon} - \lambda \frac{\partial g}{\partial \underline{\sigma}}\right) \tag{1.6}$$

Substituting Equation 1.6 into 1.4 leads to

$$\lambda = \frac{\left(\frac{\partial F}{\partial \underline{\sigma}}\right)^T \underline{\underline{D}}^e d\underline{\varepsilon}}{H + \left(\frac{\partial F}{\partial \underline{\sigma}}\right)^T \underline{\underline{D}}^e \frac{\partial g}{\partial \underline{\sigma}}} \tag{1.7}$$

Then the stress-strain matrix is obtained as follows:

$$\begin{aligned} \underline{\underline{D}}^{ep} &= \underline{\underline{D}}^e - \underline{\underline{D}}^p \\ &= \underline{\underline{D}}^e - \underline{\underline{D}}^e \frac{\partial g}{\partial \underline{\sigma}} \left(\frac{\partial F}{\partial \underline{\sigma}}\right)^T \underline{\underline{D}}^e \left[H + \left(\frac{\partial F}{\partial \underline{\sigma}}\right)^T \underline{\underline{D}}^e \frac{\partial g}{\partial \underline{\sigma}} \right]^{-1} \end{aligned} \tag{1.8}$$

Yamada's Formulation. The assumed yield function is

$$F = \underline{\sigma} - A\left(\underline{\varepsilon}^p\right) \tag{1.9}$$

where

$\underline{\sigma}$ = the equivalent deviatoric stress = $\sqrt{3} J_{2D}^{1/2}$;

$\underline{\varepsilon}^p$ = the equivalent plastic strain = $\int d\underline{\varepsilon}^p$;

J_{2D} = the second invariant of deviatoric stress;

$$d\underline{\varepsilon}^p = \frac{1}{\sqrt{3}} \left[2(d\varepsilon_{11}^p)^2 + 2(d\varepsilon_{22}^p)^2 + 2(d\varepsilon_{33}^p)^2 + (d\varepsilon_{12}^p)^2 + (d\varepsilon_{23}^p)^2 + (d\varepsilon_{31}^p)^2 \right]^{1/2} \tag{1.10}$$

The flow rule is

$$d\underline{\varepsilon}^p = \lambda \frac{\partial F}{\partial \underline{\sigma}} \tag{1.11}$$

Substituting Equation 1.11 into 1.10 gives

$$d\underline{\varepsilon}^p = \lambda \tag{1.12}$$

The derivative of the yield function is

$$dF = d\underline{\sigma} - \frac{\partial F}{\partial \underline{\varepsilon}^p} d\underline{\varepsilon}^p = 0 \tag{1.13}$$

The hardening parameter, H, is therefore equal to

$$H = \frac{1}{\lambda} \frac{\partial A}{\partial \underline{\varepsilon}^p} d\underline{\varepsilon}^p = \frac{\partial A}{\partial \underline{\varepsilon}^p} = \frac{\partial \underline{\sigma}}{\partial \underline{\varepsilon}^p} \tag{1.14}$$

The stress-strain matrix is

$$\begin{aligned} \underline{\underline{D}}^{ep} &= \underline{\underline{D}}^{e} - \underline{\underline{D}}^{p} \\ &= \underline{\underline{D}}^{e} - \underline{\underline{D}}^{e} \left(\frac{\partial F}{\partial \underline{\sigma}} \right)^T \frac{\partial F}{\partial \underline{\sigma}} \underline{\underline{D}}^{e} \left[H + \left(\frac{\partial F}{\partial \underline{\sigma}} \right)^T \underline{\underline{D}}^{e} \frac{\partial F}{\partial \underline{\sigma}} \right]^{-1} \end{aligned} \tag{1.15}$$

where

$\underline{\underline{D}}^{ep}$ = the elasto-plastic stress-strain matrix;

$\underline{\underline{D}}^{e}$ = the elastic stress-strain matrix;

$\underline{\underline{D}}^{p}$ = the plastic stress-strain matrix.

For plane strain condition:

$$\underline{\underline{D}}^{e} = \frac{E}{(1+\nu)(1-2\nu)} \begin{bmatrix} 1-\nu & \nu & 0 \\ \nu & 1-\nu & 0 \\ 0 & 0 & \dfrac{1-2\nu}{2} \end{bmatrix} \tag{1.16}$$

$$\underline{\underline{D}}^{p} = \frac{1}{P} \begin{bmatrix} S_1 S_1 & S_1 S_2 & S_1 S_3 \\ S_2 S_1 & S_2 S_2 & S_2 S_3 \\ S_3 S_1 & S_3 S_2 & S_3 S_3 \end{bmatrix} \tag{1.17}$$

where

E = the Young's modulus;

ν = the Poisson's ratio;

$P = \left(\frac{4}{3} \right)^{-2} G \left(1 + \frac{H}{3G} \right)$;

$S_1 = \sigma_{11} - (\sigma_{11} + \sigma_{22} + \sigma_{33})/3;$

$S_2 = \sigma_{22} - (\sigma_{11} + \sigma_{22} + \sigma_{33})/3;$

$S_3 = \sigma_{33} - (\sigma_{11} + \sigma_{22} + \sigma_{33})/3;$

G = the shear modulus.

Zienkiewicz's Formulation. The assumed yield function is

$$F(\underline{\sigma}, \kappa) = 0 \tag{1.18}$$

Differentiating Equation 1.18 leads to

$$dF = \left(\frac{\partial F}{\partial \underline{\sigma}}\right)^T d\underline{\sigma} + \frac{\partial F}{\partial \kappa} d\kappa = 0 \tag{1.19}$$

Let the hardening parameter, H be equal to

$$H = \frac{-1}{\lambda} \frac{\partial F}{\partial \underline{\sigma}} d\underline{\sigma} \tag{1.20}$$

Substitution of Equation 1.20 into Equation 1.19 leads to

$$dF = \left(\frac{\partial F}{\partial \underline{\sigma}}\right)^T d\underline{\sigma} - H\lambda = 0 \tag{1.21}$$

The flow rule is

$$d\underline{\varepsilon}^p = \lambda \frac{\partial F}{\partial \underline{\sigma}} \tag{1.22}$$

Then

$$d\kappa = \underline{\sigma}^T d\underline{\varepsilon}^p = \lambda \underline{\sigma}^T \frac{\partial F}{\partial \underline{\sigma}} \tag{1.23}$$

Substitution of Equation 1.23 into Equation 1.20 leads to

$$H = -\frac{\partial F}{\partial \kappa} \underline{\sigma}^T \frac{\partial F}{\partial \underline{\sigma}} \tag{1.24}$$

The incremental stress vector is

$$d\underline{\sigma} = \underline{\underline{D}}^e\left(d\underline{\varepsilon} - d\underline{\varepsilon}^p\right) = \underline{\underline{D}}^e\left(d\underline{\varepsilon} - \lambda\frac{\partial F}{\partial \underline{\sigma}}\right) = 0 \tag{1.25}$$

Substituting Equation 1.25 into 1.21 gives

$$\lambda = \frac{\left(\frac{\partial F}{\partial \underline{\sigma}}\right)^T \underline{\underline{D}}^e d\underline{\varepsilon}}{H + \left(\frac{\partial F}{\partial \underline{\sigma}}\right)^T \underline{\underline{D}}^e \frac{\partial F}{\partial \underline{\sigma}}} \tag{1.26}$$

Then the stress-strain matrix is obtained as follows:

$$\begin{aligned} \underline{\underline{D}}^{ep} &= \underline{\underline{D}}^e - \underline{\underline{D}}^p \\ &= \underline{\underline{D}}^e - \underline{\underline{D}}^e\left(\frac{\partial F}{\partial \underline{\sigma}}\right)^T \frac{\partial F}{\partial \underline{\sigma}} \underline{\underline{D}}^e \left[H + \left(\frac{\partial F}{\partial \underline{\sigma}}\right)^T \underline{\underline{D}}^e \frac{\partial F}{\partial \underline{\sigma}}\right]^{-1} \end{aligned} \tag{1.27}$$

The Proposed Elasto-Plastic Constitutive Equation. In 1985, Molenkamp (1985) expressed the physical meaning of the stiffness ratio, H/2G, as equal to the ratio of the elastic incremental deviatoric strain to the plastic incremental deviatoric strain if the partial derivatives of the

yield surface, F = 0, are normalized with $\partial F/\partial \underline{S}$ which is the partial derivative of the yield surface with respect to the deviator stress, $\underline{S}$. In engineering, often a quantity called octahedral shear strain, γ_{oct}, is used. Because the deviatoric strain is proportional to the octahedral shear strain, the stiffness ratio and the plastic octahedral shear strain, γ_{oct}^p, are therefore closely related. Thus it makes more sense to use the stiffness ratio and the plastic octahedral shear strain to update the size of the yield surface. The proposed yield function, F, is then expressed as follows:

$$F = J_{2D}^{1/2} - \left(\kappa + H\,\gamma_{oct}^{P}\right) = 0 \tag{1.28}$$

where

J_{2D} = the second invariant of deviatoric stress;

κ = the size of the initial yield surface;

γ_{oct}^{p} = the plastic octahedral shear strain;

H = the strain hardening parameter.

Differentiating Equation 1.28 leads to

$$dF = \left(\frac{\partial F}{\partial \underline{\sigma}}\right)^{T} d\underline{\sigma} + \left(\frac{\partial F}{\partial \gamma_{oct}^{p}}\right)^{T} d\gamma_{oct}^{p} = \left(\frac{\partial F}{\partial \underline{\sigma}}\right)^{T} d\underline{\sigma} - H\,d\gamma_{oct}^{p} = 0 \tag{1.29}$$

where

$d\underline{\sigma}$ = the incremental stress vector;

$d\gamma_{oct}^{p}$ = the incremental plastic octahedral shear strain;

The plastic incremental octahedral shear strain can be found as follows:

$$\begin{aligned}\left(d\gamma_{oct}^{p}\right)^{2} = \frac{1}{9}\left[(d\varepsilon_{11}^{p} - d\varepsilon_{22}^{p})^{2} + (d\varepsilon_{22}^{p} - d\varepsilon_{33}^{p})^{2} + (d\varepsilon_{33}^{p} - d\varepsilon_{11}^{p})^{2}\right] \\ + \frac{2}{3}\left[(d\varepsilon_{12}^{p})^{2} + (d\varepsilon_{23}^{p})^{2} + (d\varepsilon_{31}^{p})^{2}\right]\end{aligned} \tag{1.30}$$

The flow rule is:

$$d\underline{\varepsilon}^{p} = \lambda \frac{\partial F}{\partial \underline{\sigma}} = \lambda\left(\frac{1}{2} J_{2D}^{-1/2} \underline{S}\right) \tag{1.31}$$

Substitution of Equation 1.31 into Equation 1.30 leads to:

$$\begin{aligned}\left(d\gamma_{oct}^{p}\right)^2 &= \frac{1}{9}\left(\frac{\lambda}{2}J_{2D}^{-1/2}\right)^2\left[(S_{11}-S_{22})^2+(S_{22}-S_{33})^2+(S_{33}-S_{11})^2\right] \\ &\quad+\frac{2}{3}\left(\frac{\lambda}{2}J_{2D}^{-1/2}\right)^2\left[(S_{12})^2+(S_{23})^2+(S_{31})^2\right] \\ &= \frac{1}{6}\left(\lambda J_{2D}^{-1/2}\right)^2\left\{\left[\frac{1}{6}(\sigma_{11}-\sigma_{22})^2+(\sigma_{22}-\sigma_{33})^2+(\sigma_{33}-\sigma_{11})^2\right]\right. \\ &\quad\left.+\left[{\tau_{12}}^2+{\tau_{23}}^2+{\tau_{31}}^2\right]\right\} \\ &= \frac{1}{6}\left(\lambda^2 J_{2D}^{-1}\right)\{J_{2D}\} \\ &= \frac{\lambda^2}{6}\end{aligned} \tag{1.32}$$

Therefore

$$d\gamma_{oct}^{p} = \frac{\lambda}{\sqrt{6}} \tag{1.33}$$

Substitution of Equation 1.33 into Equation 1.29 leads to:

$$dF = \left(\frac{\partial F}{\partial \underline{\sigma}}\right)^T d\underline{\sigma} - \frac{1}{\sqrt{6}}H\lambda = 0$$

(1.34)

The incremental stress vector is

$$d\underline{\sigma} = \underline{\underline{D}}^e\left(d\underline{\varepsilon} - d\underline{\varepsilon}^p\right) = \underline{\underline{D}}^e\left(d\underline{\varepsilon} - \lambda\frac{\partial F}{\partial \underline{\sigma}}\right) \tag{1.35}$$

Substituting Equation 1.35 into 1.34 leads to

$$\lambda = \frac{\left(\frac{\partial F}{\partial \underline{\sigma}}\right)^T \underline{\underline{D}}^e d\underline{\varepsilon}}{\frac{1}{\sqrt{6}}H + \left(\frac{\partial F}{\partial \underline{\sigma}}\right)^T \underline{\underline{D}}^e \frac{\partial F}{\partial \underline{\sigma}}} \tag{1.36}$$

The stress-strain matrix is therefore can be obtained as follows:

$$\begin{aligned}\underline{\underline{D}}^{ep} &= \underline{\underline{D}}^{e} - \underline{\underline{D}}^{p} \\ &= \underline{\underline{D}}^{e} - \underline{\underline{D}}^{e}\left(\frac{\partial F}{\partial \underline{\sigma}}\right)^{T}\frac{\partial F}{\partial \underline{\sigma}}\underline{\underline{D}}^{e}\left[\frac{1}{\sqrt{6}}H + \left(\frac{\partial F}{\partial \underline{\sigma}}\right)^{T}\underline{\underline{D}}^{e}\frac{\partial F}{\partial \underline{\sigma}}\right]^{-1}\end{aligned} \tag{1.37}$$

Using bulk modulus of water B_w and volumetric strain $\delta_{ij}d\varepsilon_{ij}$, the excess pore water pressure increment du_e is calculated as follows:

$$du_e = B_w \delta_{ij}\varepsilon_{ij} \tag{1.38}$$

where δ_{ij} is the Kronecker delta. For plane strain condition, if the incremental stress and the incremental strain vectors are

$$d\underline{\sigma} = \{d\sigma_{11}\ d\sigma_{22}\ d\tau_{12}\ d\sigma_{33}\}^{T} \tag{1.39}$$

$$d\underline{\varepsilon} = \{d\varepsilon_{11}\ d\varepsilon_{22}\ d\gamma_{12}\}^{T} \tag{1.40}$$

respectively, the stress-strain matrix is therefore shown as follows:

$$\underline{\underline{D}}^{e} = \frac{E}{(1+\nu)(1-2\nu)}\begin{bmatrix} 1-\nu & \nu & 0 \\ \nu & 1-\nu & 0 \\ 0 & 0 & \frac{1-2\nu}{2} \\ \nu & \nu & 0 \end{bmatrix} \tag{1.41}$$

$$\underline{\underline{D}}^{p} = \frac{1}{1+\frac{H}{2G}\left(\frac{2}{\sqrt{6}}\right)}\begin{bmatrix} H_1H_1 & H_1H_2 & H_1H_3 \\ H_2H_1 & H_2H_2 & H_2H_3 \\ H_3H_1 & H_3H_2 & H_3H_3 \\ H_4H_1 & H_4H_2 & H_4H_3 \end{bmatrix} \tag{1.42}$$

where

$$H_1 = J_{2D}^{-1/2}S_{11} = J_{2D}^{-1/2}\left(\sigma_{11} - \frac{\sigma_{11}+\sigma_{22}+\sigma_{33}}{3}\right);$$

$$H_2 = J_{2D}^{-1/2}S_{22} = J_{2D}^{-1/2}\left(\sigma_{22} - \frac{\sigma_{11}+\sigma_{22}+\sigma_{33}}{3}\right);$$

$$H_3 = J_{2D}^{-1/2}S_{12} = J_{2D}^{-1/2}\left(\tau_{12}\right);$$

$$H_4 = J_{2D}^{-1/2} S_{33} = J_{2D}^{-1/2} \left(\sigma_{33} - \frac{\sigma_{11} + \sigma_{22} + \sigma_{33}}{3} \right);$$

1.2.3 Analysis of Conditions for Bifurcation

The term bifurcation is synonym of non-uniqueness of a quasi-static response of a structure under prescribed small incremental forces or displacements. Hill (1958) formulated a rigorous theory of bifurcation and stability in solids obeying normality. Mandel (1966) discussed the mechanical stability conditions of a soil element and Drucker's postulate, where Drucker's postulate was proven to be a sufficient stability condition but not a necessary condition. These two theories have been applied to different engineering problems concerning uniqueness and stability such as necking in bars and sheets, bulging in shells and buckling of long columns. The bifurcation phenomena in the plane strain tension test have been treated in detail by Hill and Hutchinson (1975). Such phenomena were extended to the plane compression test by Young (1976). Rice (1977), and Needleman and Rice (1978) discussed that the critical strain at which a shear band bifurcation is predicted turns out to be sensitive to subtle details of the constitutive description. Tvergaard et al. (1981) addressed that the slight degree of compressibility included in the constitutive formulation has little effect on the bifurcation predictions. Hill's theory of bifurcation and stability was later generalized to include a non-associated flow rule by Raniecki and Bruhns (1981). Petryk and Thermann (1985) showed that the exclusion condition of Hill (1958, 1959, 1962) rules out not only a first- but also a second-order bifurcation.

According to Rice (1977), and Asaro and Rice (1977), for the stress rate $\dot{\sigma}_{ij}$ and the velocity gradient field $v_{k,l}$, if the constitutive rate relation is imagined to have the form:

$$\dot{\sigma}_{ij} = C_{ijkl} v_{k.l} \tag{1.42}$$

and if the same set of constitutive coefficient C_{ijkl} apply both inside and outside the band at incipient localization, the critical condition for localization on a plane of normal n_i is first met when

$$\det\left(n_i \cdot C_{ijkl} \cdot n_l\right) = 0$$

(1.43)

The above condition has been simplified by Bardet and Mortazavi (1987) for a plane strain plate subjected to uniform prescribed displacements where in the Von Mises material model was used. The simplified equation obtained by Bardet and Mortazavi is:

$$(\beta+1)t^4 - 2t^2 + \beta + 1 = 0$$

(1.44)

where

$t = n_1/n_2 = \tan(\alpha)$;

α = the orientation of the shear band;

β = H/2G.

The orientation of the shear band can be determined as follows:

$$\alpha = \tan^{-1}\left[\pm\sqrt{\frac{1\pm\sqrt{-\beta(2+\beta)}}{1+\beta}}\right] \qquad (1.45)$$

In conformity with the notation for systems of partial differential equations, elliptic (E), parabolic (P), or hyperbolic (H) regimes can be identified depending upon whether there are no, two, or four real values of the orientations of shear bands, α. Thus

E: $\beta > 0$, or $\beta < -1$ (Bifurcation excluded);

P: $\beta = 0$, or $\beta = -1$; (1.46)

H: $\beta < 0$, or $\beta > -1$.

For H/2G equal to zero, the orientation of the shear band is ± 45 degrees. For H/2G equal to -0.05, the orientation of the shear band is ± 40.39 degrees, or ± 49.61 degrees.

1.2.4 Incremental Plastic Strain Energy and Damage Energy

For strain softening materials, two kinds of energy--the incremental plastic strain energy and damage energy--are dissipating during a load step in

strain softening range. The incremental plastic energy of an element for a particular load step is equal to the shaded area below the stress-strain curve shown in Figure 1.8 times the volume of the element. And the incremental damage energy of an element for a particular load step is equal to the shaded above the stress-strain curve shown in Figure 1.8 times the volume of the element.

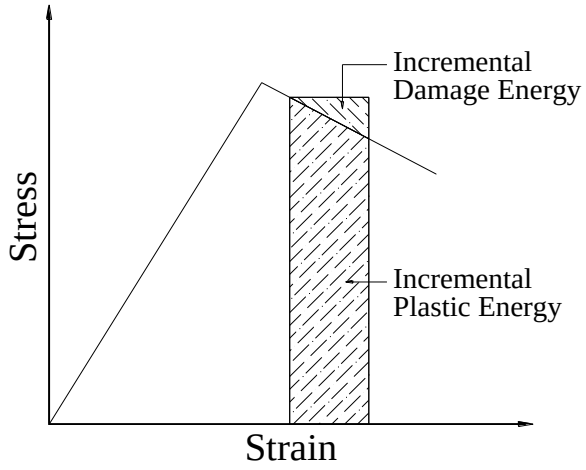

Figure 1.8. Schematic diagram of the incremental damage energy and the incremental plastic energy

1.2.5 The Criterion for the Stability of the Solution in Incremental Finite Element Analyses Which Include Strain Softening Material Behavior

Based on the physical behavior of materials, it is generally accepted that if the total external incremental applied energy is positive, the total induced internal incremental strain energy has to be positive. On the other hand, if the total external incremental applied energy is negative, the total induced internal incremental strain energy must also be negative. Any numerical solution has to obey such a law; otherwise the solutions will be unstable. The above criterion has been used in this research for determining the condition of stability of the incremental solutions.

In a variational approach, the total potential energy π_p is used in static elastic analyses. It can be deduced that the total incremental potential energy, $d\pi_p$ should be used in the derivation of the equation of equilibrium for the incremental load condition. The total incremental potential energy is:

$d\pi_p$ = (Total Incremental Potential Energy due to Total Existing Loads and the Corresponding Induced Internal Stresses) + (Total Incremental

Potential Energy due to the External Load Increments and the Corresponding Induced Internal Stress Increments)

$$= \left(\int_V \underline{\sigma}^T d\underline{\varepsilon}\, dV - \sum d\underline{u}^T \underline{F} \right) + \left(\frac{1}{2} \int_V d\underline{\sigma}^T d\underline{\varepsilon}\, dV - \sum d\underline{u}^T d\underline{F} \right) \qquad (1.47)$$

where

$\underline{\sigma}$ = the existing stress vector;

$d\underline{\sigma}$ = the incremental stress vector;

$d\underline{\varepsilon}$ = the incremental strain vector;

$d\underline{u}$ = the incremental displacement vector;

$\underline{F}$ = the existing force vector;

$d\underline{F}$ = the incremental force vector.

Since the structure is supposed to be in equilibrium under a set of existing forces, it can be concluded that the first part on the right hand side of Equation 1.47 will vanish for the existing forces, i.e. the existing forces will contribute no incremental potential energy. However the incremental forces which include body force, surface tractions, and applied concentrated forces will produce some incremental potential energy. Therefore, the total incremental potential energy becomes:

$$d\pi_p = \frac{1}{2}\int_V d\underline{\sigma}^T d\underline{\varepsilon}\, dV - \sum d\underline{u}^T d\underline{F} \tag{1.48}$$

In the finite element approximation, Equation 1.48 can be expressed as follows:

$$d\pi_p = \frac{1}{2}\int_V d\underline{u}^T \underline{\underline{B}}^T \underline{\underline{D}}\,\underline{\underline{B}}\, d\underline{u}\, dV - \sum d\underline{u}^T d\underline{F} \tag{1.49}$$

where

$\underline{\underline{B}}$ = the strain-displacement matrix;

The global stiffness matrix $\underline{\underline{K}}$ is:

$$\underline{\underline{K}} = \int_V \underline{\underline{B}}^T \underline{\underline{D}}\,\underline{\underline{B}}\, dV \tag{1.50}$$

Substitution of Equation 1.50 into 1.49 leads to:

$$d\pi_p = \frac{1}{2} d\underline{u}^T \underline{\underline{K}}\, d\underline{u} - d\underline{u}^T d\underline{F} \tag{1.51}$$

It is seen from Equation 1.51 that for the condition of prescribed displacements, since all of the forces are induced, both terms on the right side of Equation 1.51 always have the same sign. It means the condition of stability for the incremental solutions for the prescribed displacement case is guaranteed. When the forces are prescribed and if the total external incremental energy is positive, the stability for the incremental solutions is guaranteed only when the global stiffness matrix is positive definite. When the global stiffness matrix is negative definite, the instability condition of the solutions will occur.

1.2.6 Loading, Neutral Loading and Unloading

It may be pointed out that the loading conditions (see Equation 1.52) used for strain hardening materials cannot be used for strain softening materials.

$$\begin{aligned}
&\left(\frac{\partial F}{\partial \underline{\sigma}}\right)^T : d\underline{\sigma} > 0 \qquad \text{(loading)} \\
&\left(\frac{\partial F}{\partial \underline{\sigma}}\right)^T : d\underline{\sigma} = 0 \qquad \text{(Neutral loading)} \\
&\left(\frac{\partial F}{\partial \underline{\sigma}}\right)^T : d\underline{\sigma} < 0 \qquad \text{(unloading)}
\end{aligned} \tag{1.52}$$

The conditions for loading, neutral loading, and unloading for strain softening materials can be incorporated by multiplying a hardening-softening parameter, HS, with the terms on the left hand side of Equation 1.52. HS equal to -1 is used only for materials under the strain softening condition; otherwise 1 will be used. The equation incorporating softening can then be written as follows:

$$
\begin{aligned}
&(HS)\left(\frac{\partial F}{\partial \underline{\sigma}}\right)^{T} : d\underline{\sigma} > 0 \qquad \text{(loading)} \\
&(HS)\left(\frac{\partial F}{\partial \underline{\sigma}}\right)^{T} : d\underline{\sigma} = 0 \qquad \text{(Neutral loading)} \\
&(HS)\left(\frac{\partial F}{\partial \underline{\sigma}}\right)^{T} : d\underline{\sigma} < 0 \qquad \text{(unloading)}
\end{aligned}
\tag{1.53}
$$

1.2.7 The Uniqueness of the Incremental Solutions

For strain hardening material the Drucker's postulate is the required condition for the uniqueness of the solution. For handling the strain softening material, the incorporated procedure outlined above must be used; otherwise the Drucker's postulate will be violated. This means that the incremental solution can be unique even with the negative net work performed by the external agency. It has been argued that two solutions can be obtained if there are more than one minimum of the total incremental potential energy as shown in Figure 1.9.

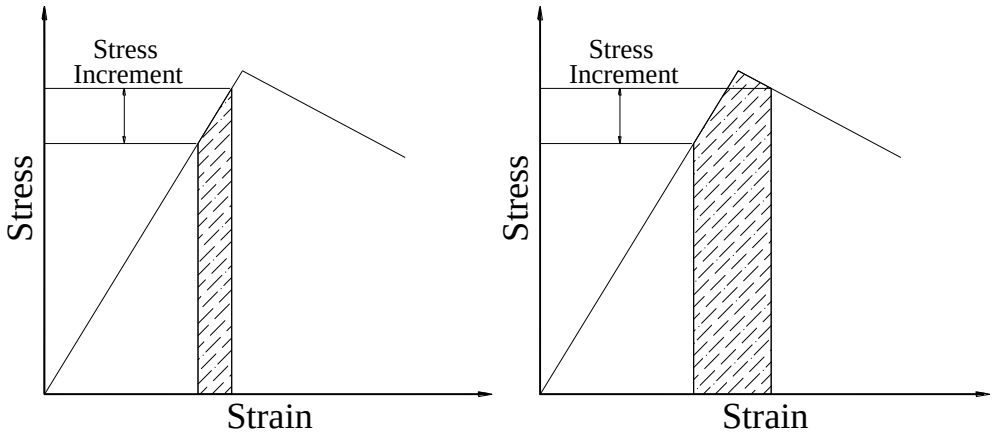

(1) Without Damage Energy (2) With Damage Energy

Figure 1.9. Two solutions for two minimum total incremental potential energies for a loading step

However, as explained in Figure 1.10, there is only one minimum total incremental potential energy. This is so because the average of the stress-strain matrix for the existing stresses ($\underline{\sigma}$) and the existing stresses

plus the stress increments ($\underline{\sigma} + d\underline{\sigma}$) is used to form the global stiffness matrix. As shown in Figure 1.10, only one of the four conditions will be used; hence only one minimum total incremental potential energy will exist.

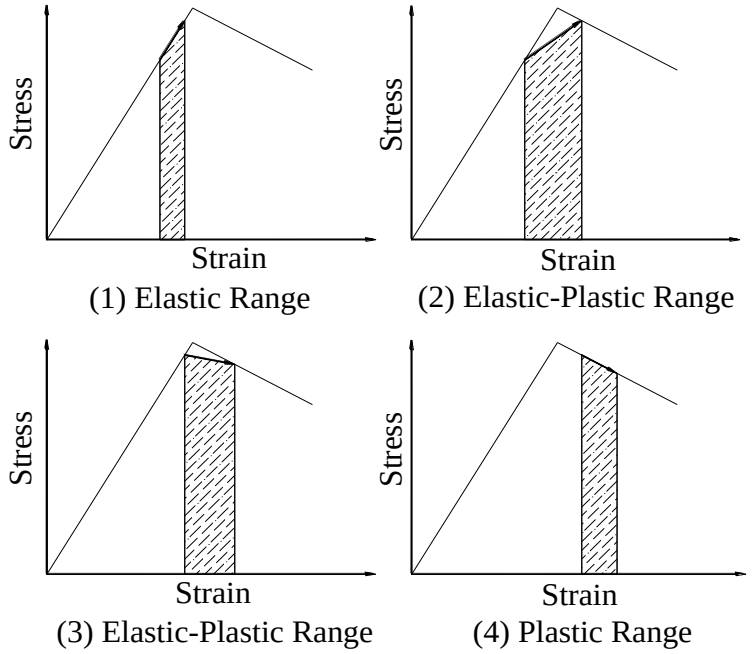

Figure 1.10. Four possible conditions in a loading step when averaging scheme is used to form the stress-strain matrix

The uniqueness of the incremental finite element solutions can be obtained by using a procedure similar to that used in the finite element textbook of Bathe (1982). The difference being that in the textbook it is used only for elastic behavior. For uniqueness, two sets of solutions--$d\underline{u}_1$ and $d\underline{u}_2$--are assumed to satisfy the condition of equilibrium at the same time. Because the condition of equilibrium is derived by minimizing of the total incremental potential energy, both $d\underline{u}_1$ and $d\underline{u}_2$ should provide the same minimum total incremental potential energy. Substituting $d\underline{u}_1$ and $d\underline{u}_2$ into Equation 1.49 and minimizing the total incremental potential energy with respect to du$ and du$, one will get:

$$\underline{\underline{K}} d\underline{u}_1 = d\underline{F} \tag{1.54}$$

$$\underline{\underline{K}} d\underline{u}_2 = d\underline{F} \tag{1.55}$$

Equations (1.54) and (1.55) can be combined as follows:

$$\underline{\underline{K}}\left(d\underline{u}_1 - d\underline{u}_2\right) = \underline{0} \tag{1.56}$$

Therefore, one of the following two conditions has to be true.

$$\left|K\right| = 0 \tag{1.57}$$

or

$$d\underline{u}_1 = d\underline{u}_2 \tag{1.58}$$

For a material with strain softening behavior, stiffness matrix could be singular. In case where the stiffness matrix is singular, displacements rather than forces can be prescribed to produce a non-singular stiffness matrix.

1.3 Guidelines for Optimization of Finite Element Solutions and the Feasibility of Mesh Optimization in Localization Analyses

Shephard (1979) defined that optimization of finite element solutions as an algorithmic procedure for the generation of a finite element discretization that yields the required accuracy for the minimum amount of effort. There are two fundamental approaches--analytical and topological--for the optimization of finite element solutions. The analytical methodology includes the nodal coordinates as unknowns in the equation of the potential energy and therefore poses two difficulties--(1) high nonlinearity of the equations, and (2) nonlinear constraints of the nodal coordinates--making the solution tedious and time consuming. The topological investigation based on the optimal mesh configurations has resulted in guidelines which enable the analyst to lay out a grid configuration that provides a mesh topology with characteristics similar to that of an optimum mesh for his specific problem (Turcke, 1974). The effort required for the analytical investigation is relatively great and the analyst could obtain the same accuracy at less expense by using topological investigation with finer mesh. In the last ten years, many researches have been involved in the topological investigation. Criteria for mesh optimization have been proposed by Oliveria (1973), Turcke and McNeice (1974), Shephard, Gallagher, and Abel (1979), and Turcke (1974). Guideline for mesh optimizations have also been done by

Turcke and McNeice (1974). A definite way to evaluate the quality of the 'optimum' finite element solutions from any proposed method is not available in the literature. Thus different investigators using different methods obtain different 'optimum' meshes.

1.3.1 Scope of Study in This Section

In view of the problem, the condition for the optimum finite element solutions will be proposed. A new term named 'degree of freedom density (DOFD)' will be defined, and used to define the above proposed condition. By using the DOFD and the strain energy density (SED) contours, new guidelines are proposed. To evaluate the proposed guidelines, a square plate loaded at the four corners will be used in this study. Then the results will be compared with those from three other methods.

It is to be noted that the study of mesh optimization so far is limited to the elastic condition. For a localization analysis associated with work softening, it is believed that much more has to be known before the optimization scheme can be applied. Therefore, the feasibility of the mesh optimization in localization analyses will be examined in the second part of this chapter. In the following a brief literature review will be presented.

1.3.2 Review of Literature

Analytical Investigation. Although the mathematical concept will not be used in this study, this approach is helpful, especially in finite element analyses. Therefore, some of the mathematical concepts will still be reviewed.

As noted by Turcke and McNeice (1974), the equation of the total potential energy can be expressed as follows:

$$\pi_p = \int_V \frac{1}{2} \underline{u}^T \underline{\underline{B}}^T \underline{\underline{D}}\,\underline{\underline{B}}\,\underline{u}\, dV - \int_V \underline{X}^T \underline{u}\, dV - \int_{S_t} \underline{P}^T \underline{u}\, dS_t \qquad (1.59)$$

in which

$\underline{u}$ = the displacement vector;

$\underline{\underline{B}}$ = the displacement-strain matrix;

$\underline{\underline{D}}$ = the stress-strain matrix;

$\underline{X}$ = the body force density vector;

$\underline{P}$ = the surface traction vector;

S_t = a boundary over which the surface tractions are specified.

Since the displacement-strain matrix, $\underline{\underline{B}}$, is obtained by performing the appropriate differentiation on the element shape function, which is a function of the nodal coordinates, x_j, the total potential energy is then viewed as function of both the nodal displacements, u_i, and the nodal coordinates.

$$\pi_p = \sum_{e=1}^{NUMEL} \pi_p^e \left(u_i, x_j \right) \tag{1.60}$$

in which

NUMEL = the total number of elements;
i = 1, 2, 3, ..., n;
j = 1, 2, 3, ..., m;
n = the number of unrestrained nodal displacements;
m = the number of unconstrained nodal coordinates.

For a stationary condition, the following equations must be satisfied:

$$\frac{\partial \pi_p}{\partial u_i} = 0 \tag{1.61}$$

$$\frac{\partial \pi_p}{\partial x_j} = 0 \tag{1.62}$$

Equation (1.61) leads to the equations of equilibrium:

$$\underline{\underline{K}}\,\underline{u} - \underline{F} = \underline{0} \tag{1.63}$$

where $\underline{F}$ is the global load vector, and $\underline{\underline{K}}$ is the global stiffness matrix.

Equation (1.62) leads to the following nonlinear equations:

$$\frac{1}{2}\underline{u}^T \frac{\partial \underline{\underline{K}}}{\partial x_j} - \frac{\partial \underline{F}}{\partial x_j}\underline{u}^T = \underline{0} \tag{1.64}$$

Neglecting the second term of Equation (1.64), as proposed by Melosh and Marcal (1977), causes incorrect results. The global load vector is the sum of concentrated loads, body forces, surface tractions, and the loads due to temperature change. It is necessary to have certain volume and surface integrals to obtain body forces and surface tractions respectively. These integrals involve the element shape functions. Therefore, the global load vector is a function of nodal coordinates. The second term of Equation (1.64) should not be neglected except in cases, where there are no body forces and surface tractions. A sufficient condition for the solutions of Equations (1.63) and (1.64) to be a minimum is that $\delta^2 \pi_p > 0$. This condition is true if all of the principle minors of the Hessian matrix are positive (Turcke and McNeice, 1974). The Hessian matrix is defined as follows:

$$\begin{bmatrix} \dfrac{\partial^2 \pi_p}{\partial x_K \partial x_l} & \dfrac{\partial^2 \pi_p}{\partial x_K \partial u_l} \\ \dfrac{\partial^2 \pi_p}{\partial u_K \partial x_l} & \dfrac{\partial^2 \pi_p}{\partial u_K \partial u_l} \end{bmatrix} \tag{1.65}$$

It is to be noted that $\partial^2 \pi_p / \partial u_K \partial u_l$ is the stiffness matrix, $\underline{\underline{K}}$. Therefore, for given coordinates, conditions necessary to be satisfied to optimize a mesh are the same as those for unique solutions.

Topological Investigation. Two types of topological investigation are reviewed: (a) contouring method, and (b) mesh optimization based on guidelines of Turcke and McNeice (1974).

a. Contouring Method.

Contours for a particular solution parameter of current step are used in the contouring method (Turcke, 1974) to design a new mesh for the next step.

The advantage of this method is that the new mesh is totally independent of the old mesh. Thus one can put more degrees of freedom (DOF) in the regions where the particular solution parameter varies more rapidly. However, it is hard to redistribute the degrees of freedom quantitatively because there are no specific guidelines to follow.

b. Mesh Optimization Based on Guidelines of Turcke and McNeice.

In 1974, Turcke and McNeice (1974) proposed guidelines for mesh optimization to supplement the contouring method. The guidelines are demonstrated by using the square plate loaded at four corners.

1. By using the initial uniform mesh shown in Figure 1.11, the variations of the strain energy density along some particular paths are plotted as those shown in Figures 1.12, and 1.13.

2. To obtain a new mesh, the number of the contours, N, has to be decided first. Then it requires a series of N+1 straight lines to approximate the curves in Figures 1.12 and 1.13.

3. By conducting the above procedures, the intersections of the line segments provide nodal points on the specific paths in the plate. Those intersections of line segments also suggest approximately where the isoenergetics should be drawn, as shown in Figure 1.14.

4. Starting in the high strain energy gradient region, appropriate nodes are decided to place on the highest valued isoenergetic contour. More nodes could have been placed along this contour, but this would have resulted in more degrees of freedom than that of the current mesh.

5. After the elements within the highest contour level and the plate boundary were established, subsequent elements are then placed to emanate from this region between successive isoenergetic lines along trajectories normal to the isoenergetics.

6. The new mesh configuration will then be obtained as that shown in Figure 1.15.

The advantage of this method is that it is easy to follow. The disadvantage of this method is that it is really hard to judge whether or not the series of N+1 straight lines have captured the features of doing mesh optimization.

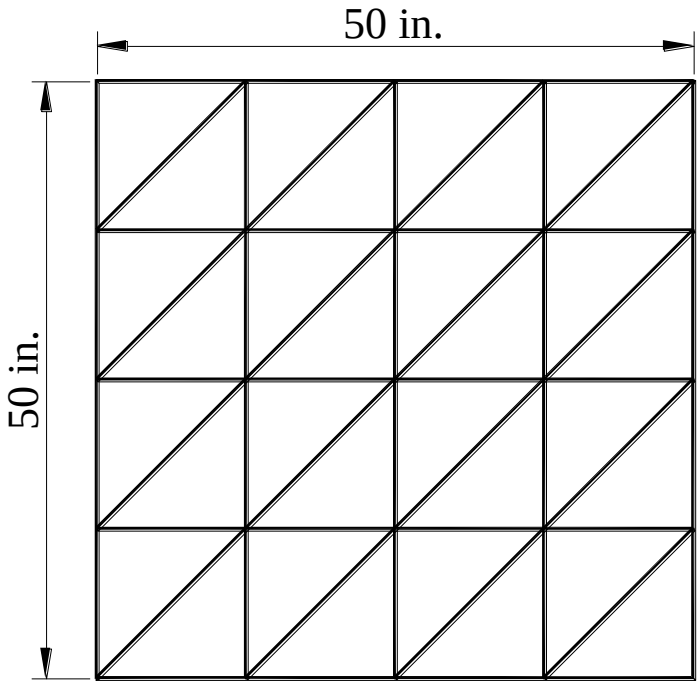

Figure 1.11. Unifor mesh (Fom Turcke and McNeice, 1974)

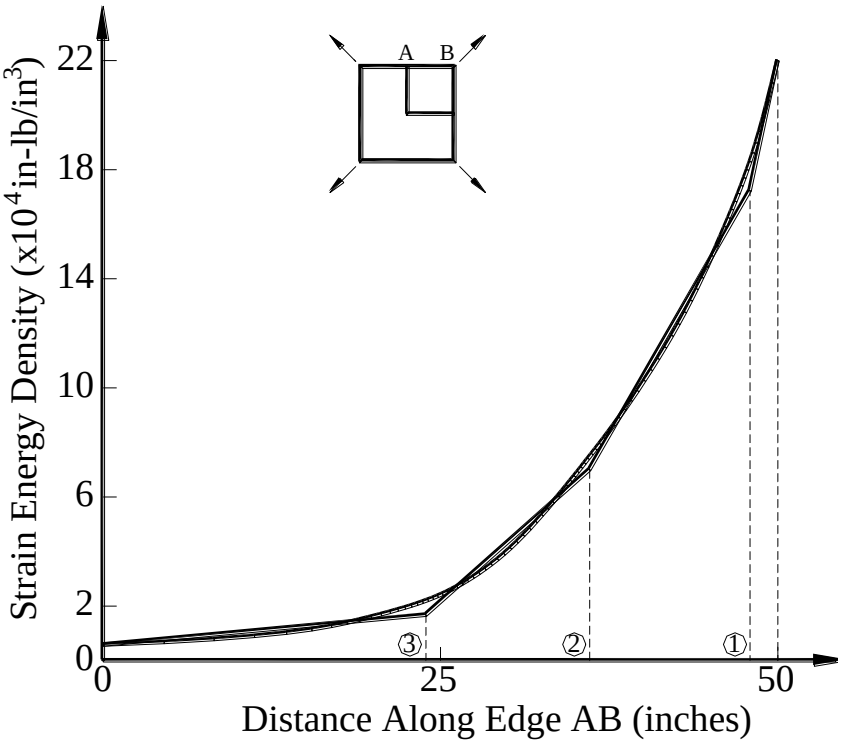

Figure 1.12. Strain energy density along edge AB (From Turcke and McNeice, 1974)

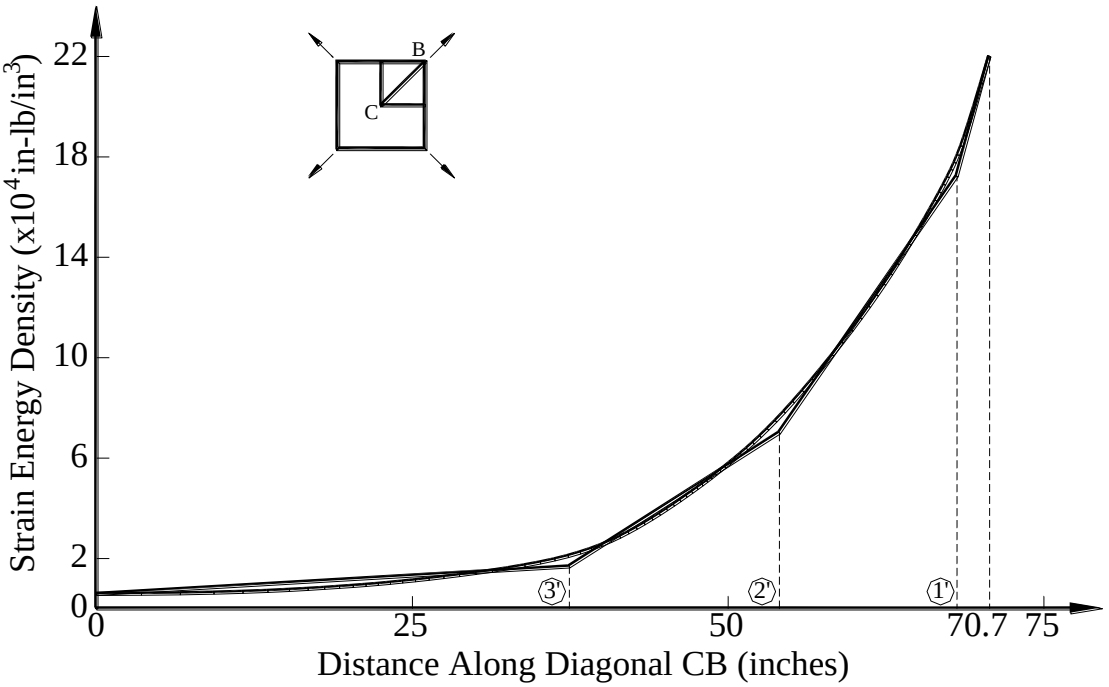

Figure 1.13. Strain energy density along diagonal CB (From Turcke and McNeice, 1974)

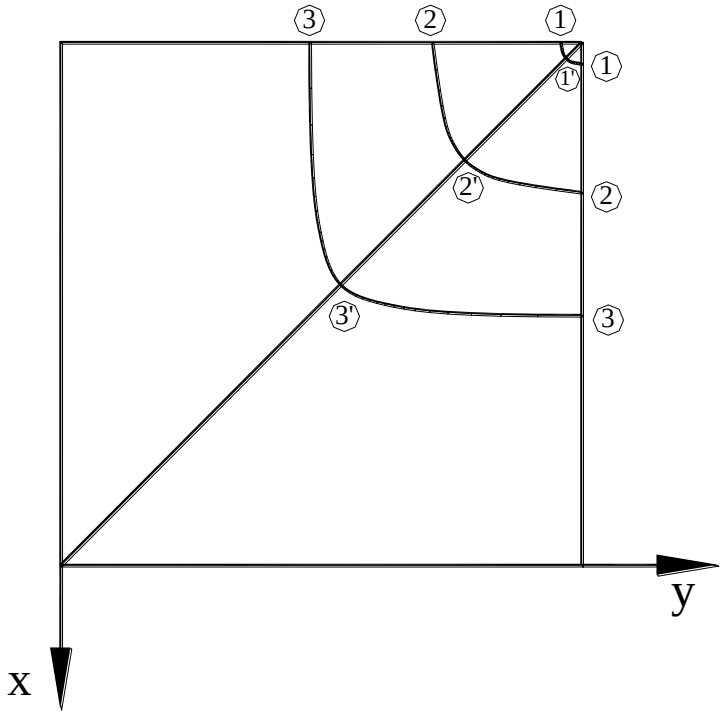

Figure 1.14. Location of strain energy density contours (From Turcke and McNeice, 1974)

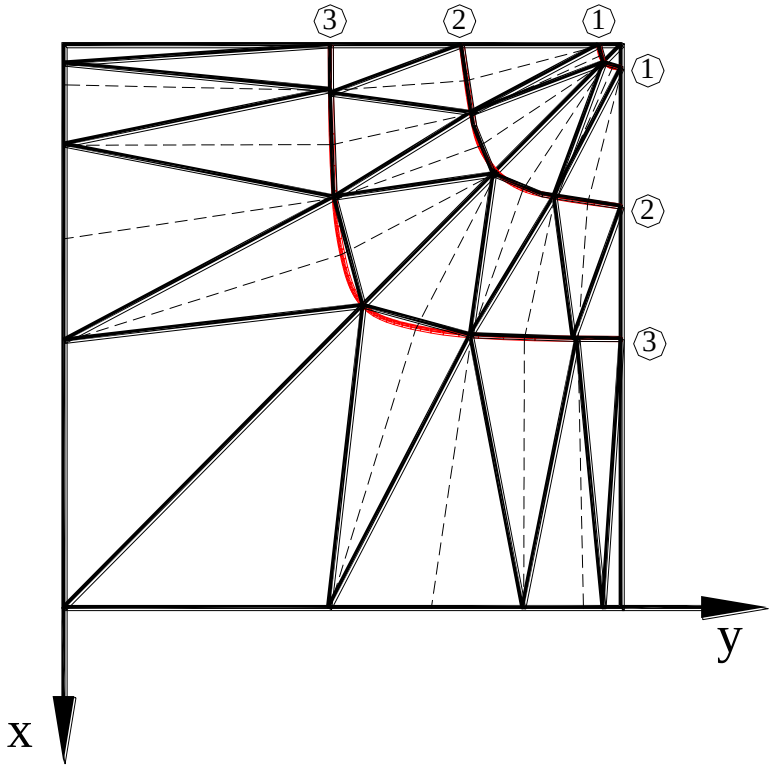

Figure 1.15. Optimum mesh produced by using guidelines (From Turcke and McNeice, 1974)

1.3.3 Proposed Guidelines

First, the DOFD will be defined. Second, the condition for the optimum finite element solutions will be proposed. Finally, based on the above two, the new guidelines for mesh optimization will be proposed.

Degree of Freedom Density (DOFD). The degree of freedom density is equal to the ratio of the total degrees of freedom, within a defined area, divided by that area. For a simple problem as that shown in Figure 1.16.a, the areas 1, 2, etc., can be used as defined areas in determining the degree of freedom density. For any other sophisticated problems as that shown in Figure 1.16.b, a moving circle or a moving square with a constant area can be used as the defined area. By placing the center of the moving circle or the moving square on the top of each nodal point, the total number of degrees of freedom covered by the moving circle or the moving square can be determined and the degree of freedom density can be obtained. If the nodal point is near the boundaries of the mesh, only the area within the mesh, which is covered by the moving circle or the moving square has to be used.

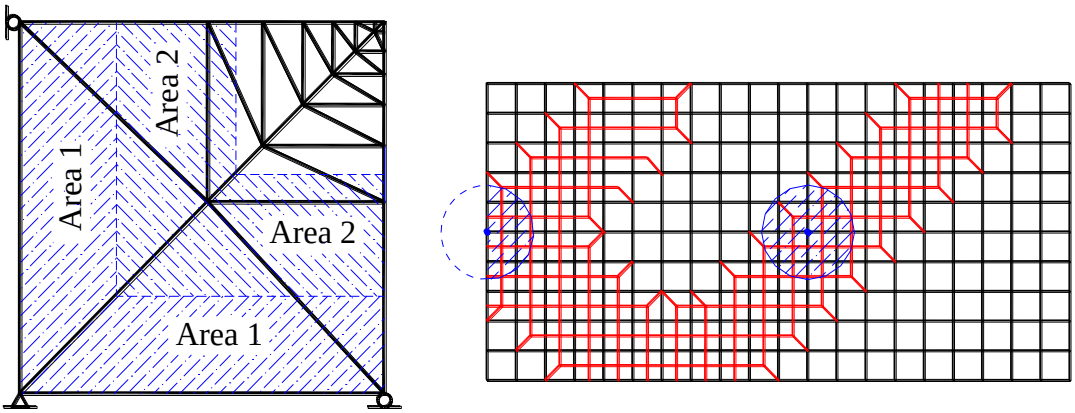

a. The Defined Area in a Simple Mesh b. The Defined Area in a Complicted Mesh

Figure 1.16. Definition of the area used in the determination of the degree of freedom density

Condition for the Optimal Finite Element Solutions. If the variational approach is used in finite element methods, the resulting total strain energy is generally less than the exact solution for a prescribed force condition. Since the exact total strain energy cannot be calculated for a complicated problem, the quality of the finite element solutions is difficult to establish. By comparing the total strain energies obtained from different methods of mesh optimization (Shephard, Gallagher, and Abel, 1979), it may be noted that the mesh with the highest total strain energy was founder of necessarily to be the optimum one. By comparing the total strain energy of a very fine mesh (Turcke and McNeice, 1974), it is relatively easy to differentiate solutions between an optimized mesh and a very fine mesh. Since the purpose of optimizing a mesh is to obtain the best possible accuracy with minimum effort, solutions obtained from extremely fine mesh (in the study of mesh optimization) essentially do the overkill.

In view of the above problems, obviously it is very important to establish a condition based on some solution parameters obtained from the current step to check the quality of the solutions. The condition for the optimum finite element solutions will then be proposed as follows:

If the variations of the strain energy density and the degree of freedom density along any selected path in a mesh are plotted together, the condition for the optimum finite element solutions is obtained when the strain energy density curve coincides with the degree of freedom density curve.

Optimization of Finite Element Solutions. Based on the above two proposed concepts, new guidelines are proposed. They are as follow:

1. For a given problem, the basic engineering judgment can be used, thereby more degrees of freedom will be placed at places where stress concentrations are supposed to occur; otherwise a uniform initial mesh can be used.

2. Using the solutions from a proposed mesh, it is easy to plot the variations of the strain energy density and the degree of freedom density along some selected paths in the mesh.

3. By examining the difference between the strain energy density curve and the degree of freedom density curve, an analyst will be able to judge the quality of the finite element solutions.

4. By examining the strain energy density curve and the degree of freedom density curve, or by tracing the variation of the total strain energy with the change in the length ratio of each two successive segments along any selected path, the analyst shall be able to find the optimum finite element solution. If the conditions for the optimum finite element solutions have been satisfied, further iteration can be stopped after this particular step.

5. If it is necessary to have other iteration, the length ratio between each two successive segments along any selected path has to be changed. Before changing the length ratio, the number of the segments, N, for each selected path has to be first decided. The thumb rule for determining the number of segments is that the more segments that can be used, the better solutions will be. The length ratio can be determined by examining the variation of the gradient of the strain energy density because the variation of degree of freedom density has to be made similar to the variation of the strain energy density. The selected path is then divided proportionally into N segments. The locations of the nodal points along the selected path can then be determined.

6. By using the new nodal points, a new mesh can be drawn.

7. By repeating the procedures from 2 to 7, the analyst is able to get near optimal solutions in a few iterations.

1.3.4 Numerical Experiments

The problem analyzed in this section is the square plate, which has been used by some other investigators, with diagonal loads at four corners. Due to axis-symmetry, only a quarter of the plate will be analyzed. The material properties used for this particular problem are:

Young's Modulus = 10000000 psi
Poisson's ratio = 0
Thickness = 1.0 in.
Length = 100 in.
Load = 25000000 lbs

The 'optimum' meshes obtained from different methods in the literature will be examined first. Then by following the new proposed guidelines, a mesh with the characteristics very close to that of the optimal finite element condition can be obtained. Finally a comparison among all of the obtained results will be presented in this section.

Turcke and McNeice's Guidelines. The optimum mesh obtained from Turcke and McNeice's guidelines is shown in Figure 1.15. The total strain energy was found to be equal to $1.1299 \times 10^8 lb - in$. The maximum displacements in both x and y direction are equal to 6.392 inches. The variations of the strain energy density and the degree of freedom density along edge AB and diagonal CB are shown in Figure 1.17 and Figure 1.18 respectively. From Figures 1.17 and 1.18 it is seen that much more degrees of freedom are needed in the region of high strain energy density gradient. This makes the quality of the solutions very poor.

Turcke's Mathematical Programming Technique. The optimum mesh obtained from Turcke's mathematical programming technique is shown in Figure 1.19. The total strain energy is found to be equal to $1.1756 \times 10^8 lb - in$. The maximum displacements in both x and y directions are equal to 6.649 inches. The variations of the strain energy density and the degree of freedom density along edge AB and diagonal CB are shown in Figure 1.20 and Figure 1.21 respectively. From Figures 1.20 and 1.21 it is seen that the degree of freedom density curves are below the strain energy density curves, indicating that degrees of freedom are unfulfilled everywhere. Although these curves fit better in the region of high strain energy density gradient, as compared with those in the above case, the solutions are only slightly improved. Therefore,

the quality of the solutions is still poor.

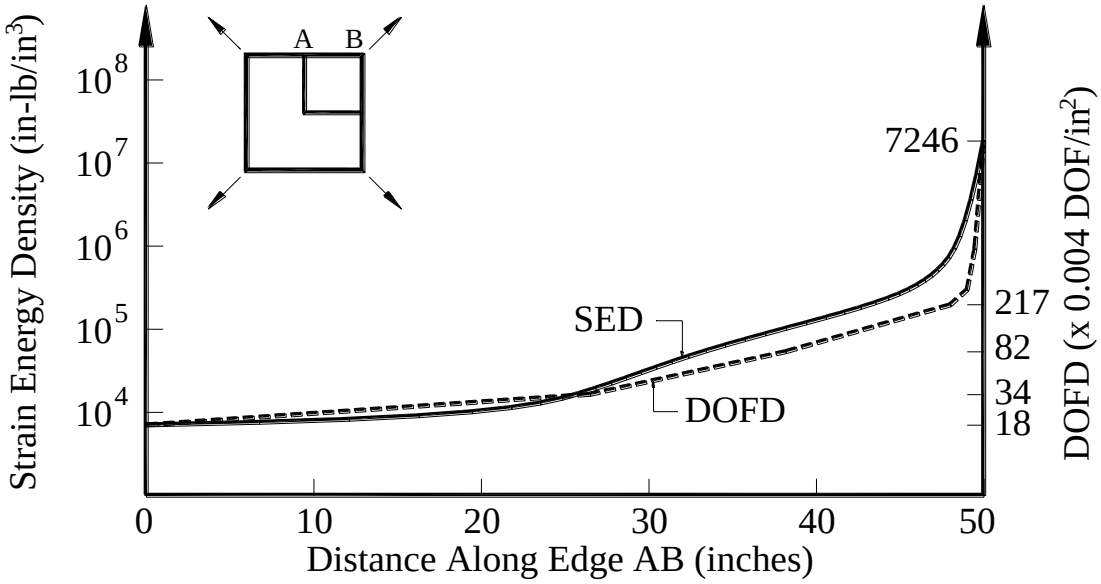

Figure 1.17. Strain energy density and degree of freedom density along edge AB

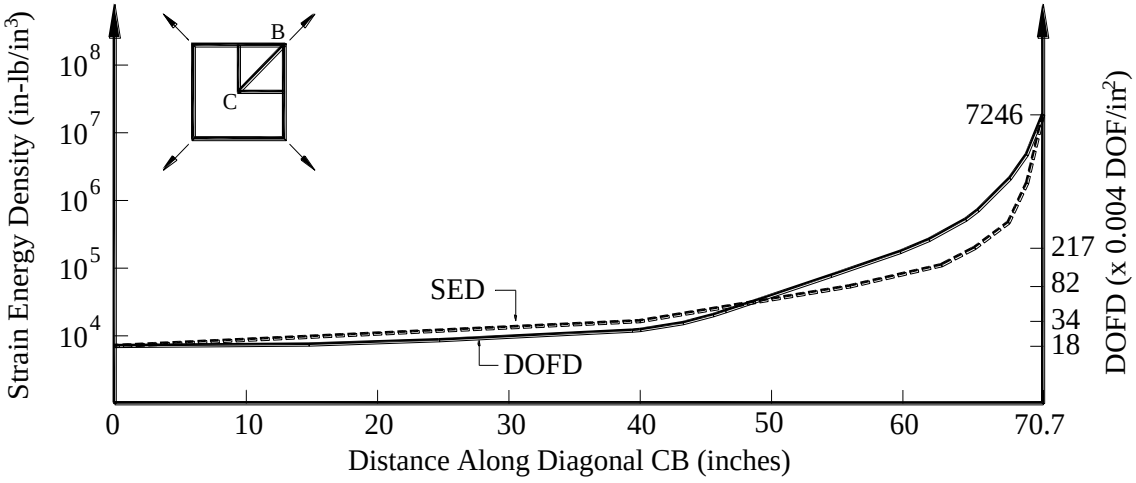

Figure 1.18. Strain energy density and degree of freedom density along diagonal CB

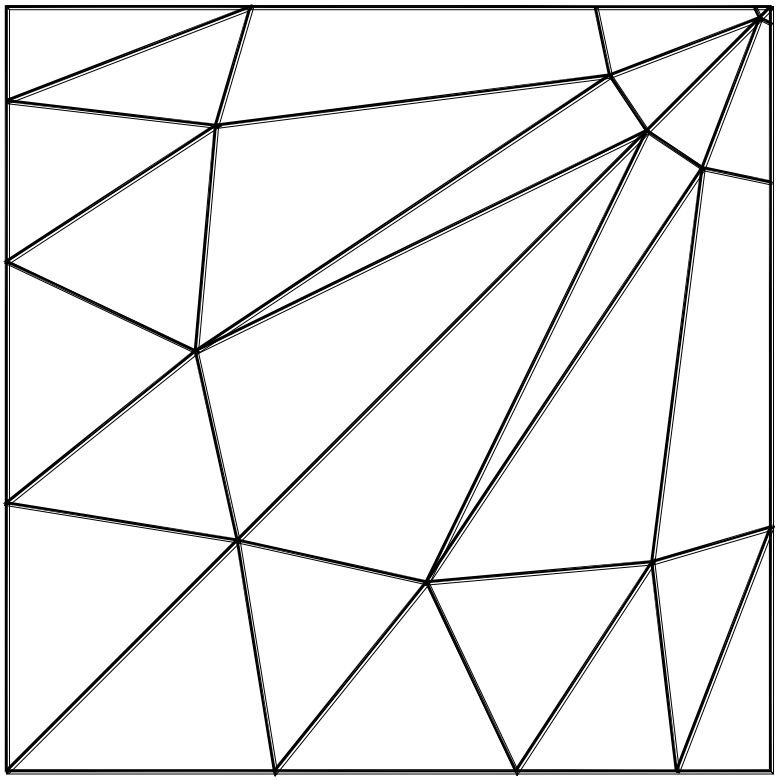

Figure 1.19. Optimum mesh produced by using mathematical programming technique (From Turcke, 1979)

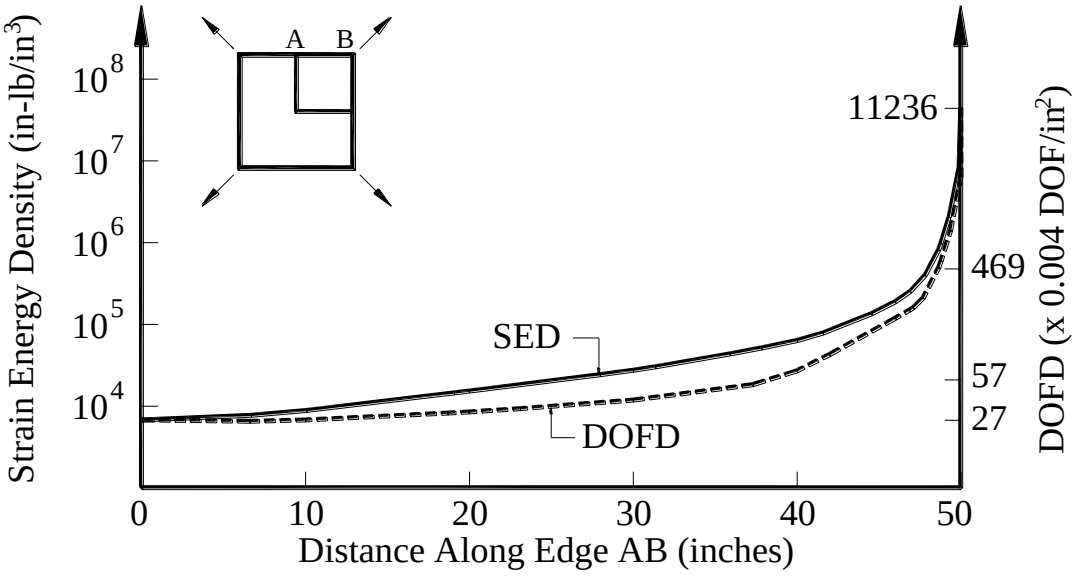

Figure 1.20. Strain energy density and degree of freedom density along edge AB

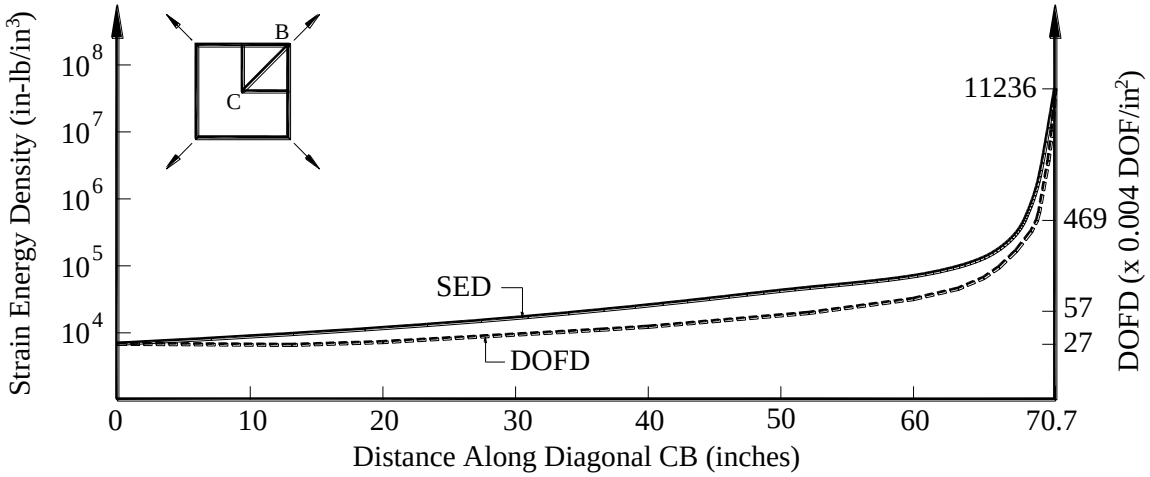

Figure 1.21. Strain energy density and degree of freedom density along diagonal CB

Shephard's Contouring Method. The optimum mesh obtained from Shephard's contouring method is shown in Figure 1.22. The total strain energy is found to be equal to $1.2671 \times 10^8 lb - in$. The maximum displacements in both x and y directions are 7.167 inches. The variations of the strain energy density and the degree of freedom density along edge AB and diagonal CB are shown in Figure 1.23 and Figure 1.24 respectively. From Figures 1.23 and 1.24 it is seen that, except in the region of high strain energy density gradient, the degree of freedom density curves are above the strain energy density curves. This makes the solutions of Shephard's contouring method better than those of the above two methods. However, those curves in the region of high strain energy density gradient are not matching very well. Therefore, the quality of the solutions may not be good enough.

New Proposed Guidelines by the Author. The uniform mesh shown in Figure 1.11 will be examined. The variations of the strain energy density and the degree of freedom density along the edge AB and diagonal CB are shown in Figure 1.25 and Figure 1.26 respectively. It is seen from Figures 1.25 and 1.26 that the quality of the solutions is extremely poor because the degree of freedom density curves and the strain energy density curves are divergent in the region of high strain energy density gradient. This also means that the mesh with length ratio equal to 1 gives very poor solutions. The length ratio is defined by the ratio of the length on the lower strain energy density side

divided by that on the higher strain energy density side. By varying the length ratio, the solutions corresponding to the new mesh can then be obtained. Then by plotting the total strain energy versus the length ratio of segments along the selected path as that shown in Figure 1.27, the maximum strain energy is found to be $2.35328 \times 10^8 lb - in$ and the corresponding length ratio is 3.5826. The lengths of the segments along the selective paths AB and CB are listed in Table 1.1. The optimum mesh based on the proposed guidelines can then be drawn as that shown in Figure 1.28. The variations of the strain energy density and the degree of freedom density along edge AB and diagonal CB are shown in Figures 1.29 and 1.30 respectively. From Figure 1.29 it is seen that the degree of freedom density curve matches the strain energy density curve very well. From Figure 1.30 it is seen that the degree of freedom density curve agrees with the strain energy density curve very well in the region of high strain energy density gradient. Although the fit is not as well in low strain energy density region, the influence may not be significant; therefore, the quality of the solutions will be reasonably good.

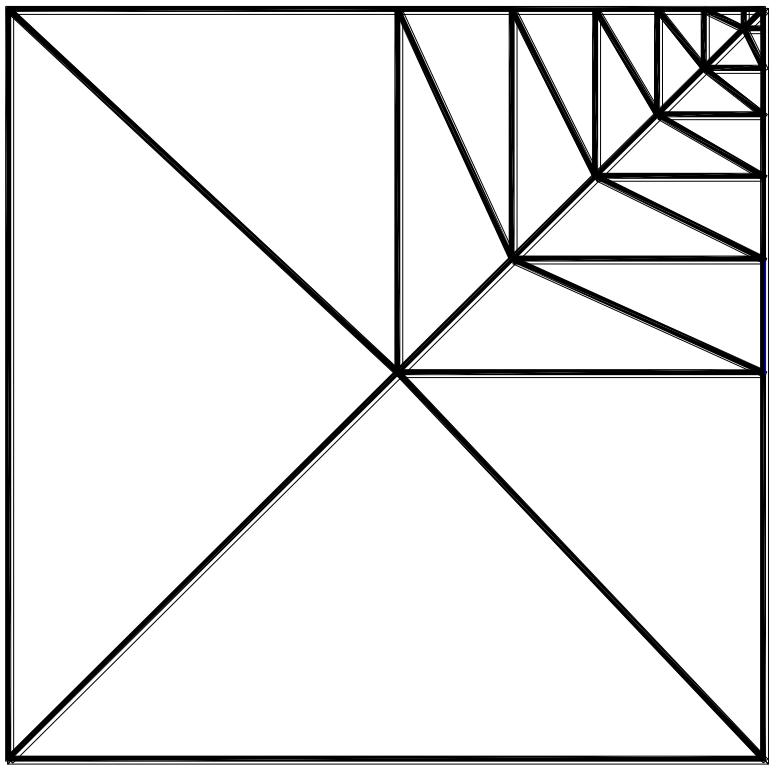

Figure 1.22. Optimum mesh produced by using contouring method (From Shephard, 1979)

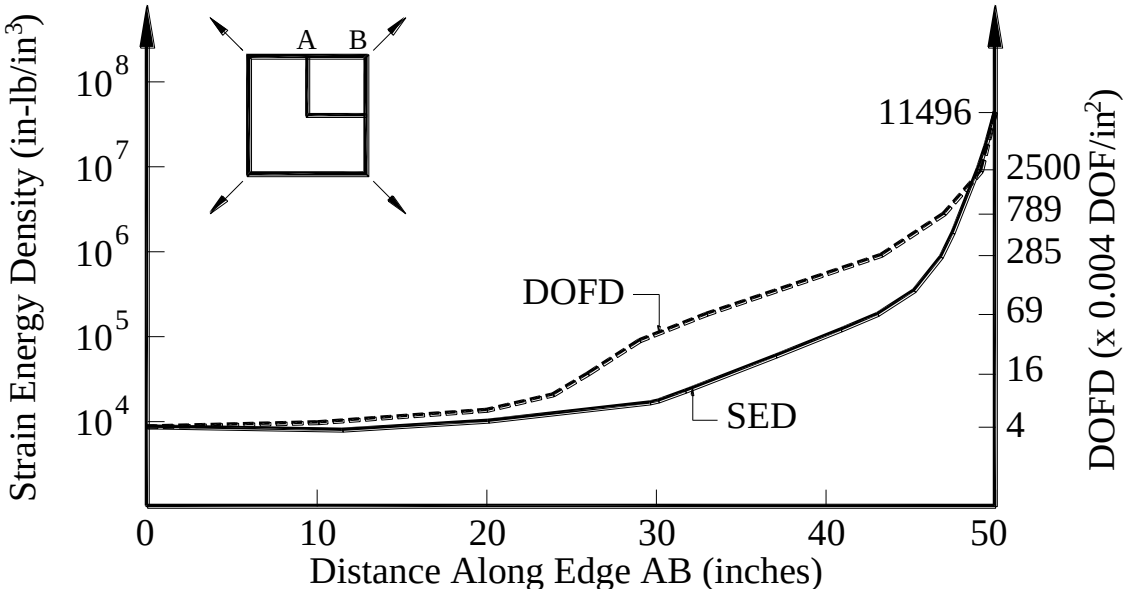

Figure 1.23. Strain energy density and degree of freedom density along edge AB

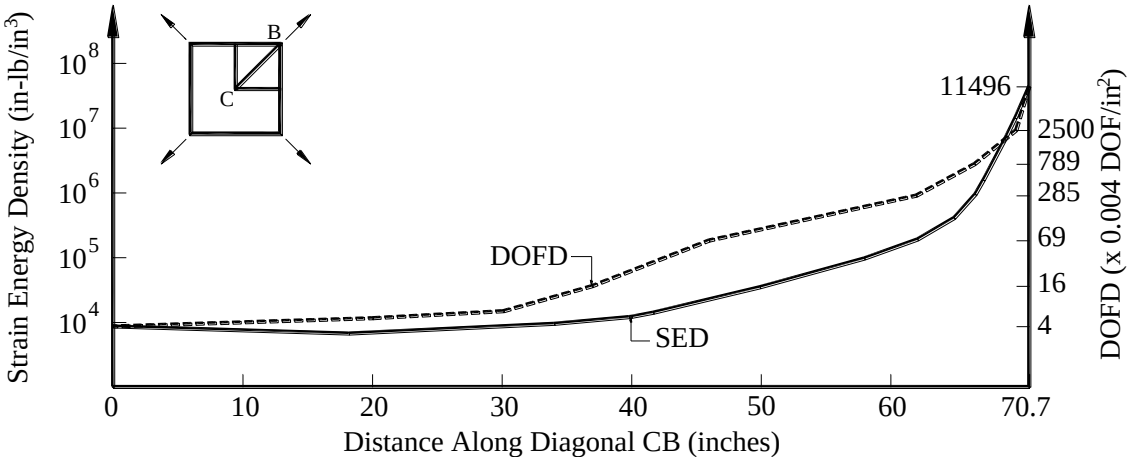

Figure 1.24. Strain energy density and degree of freedom density along diagonal CB

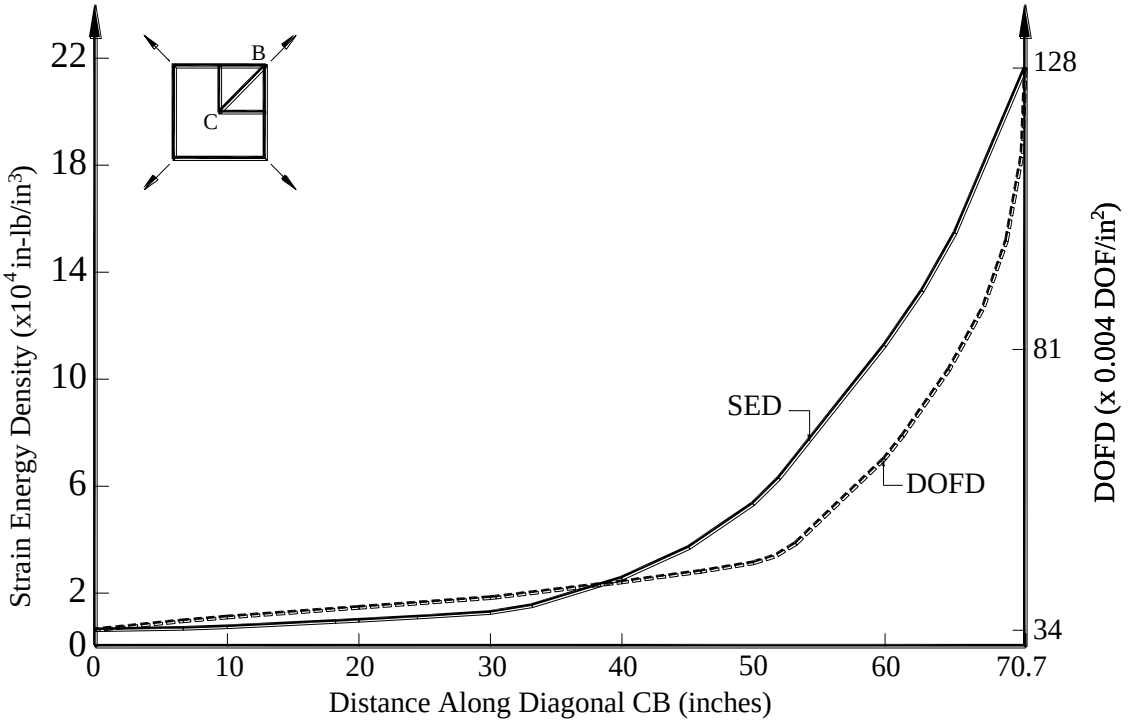

Figure 1.25. Strain energy density and degree of freedom density along edge AB

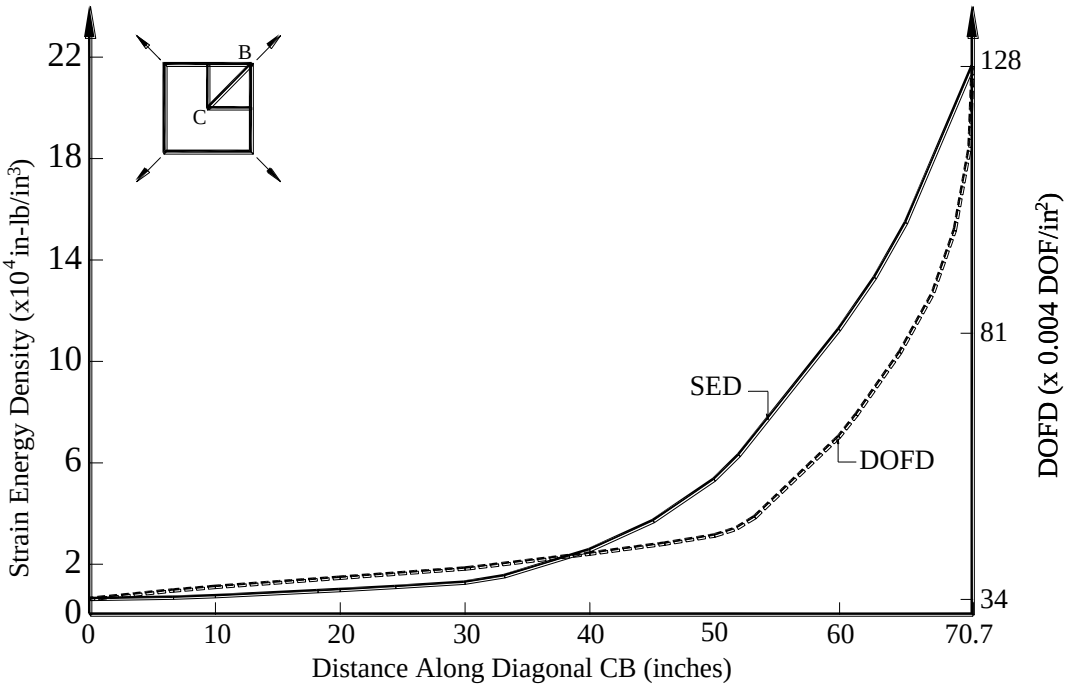

Figure 1.26. Strain energy density and degree of freedom density along diagonal CB

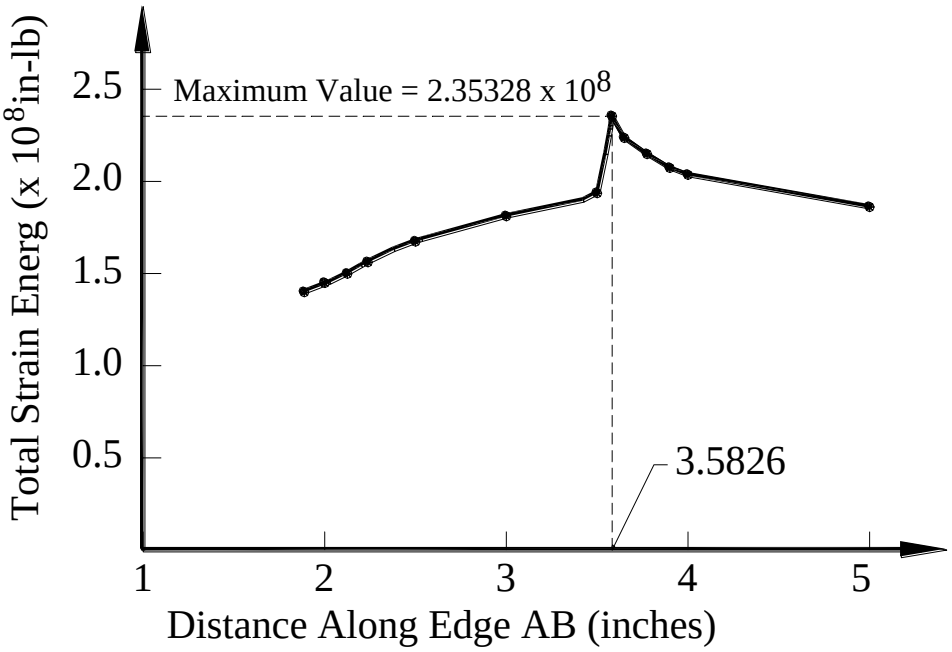

Figure 1.27. The relationship between total strain energy and length ratio

Table 1.1. The length of segments along edge AB and diagonal CB

The Length of Segments along Edge AB	The Length of Segments along Diagonal CB
36.0484	50.9801
10.0621	14.2300
2.8086	3.9720
0.7839	1.1086
0.2189	0.3096
0.0610	0.0863
0.0171	0.0242

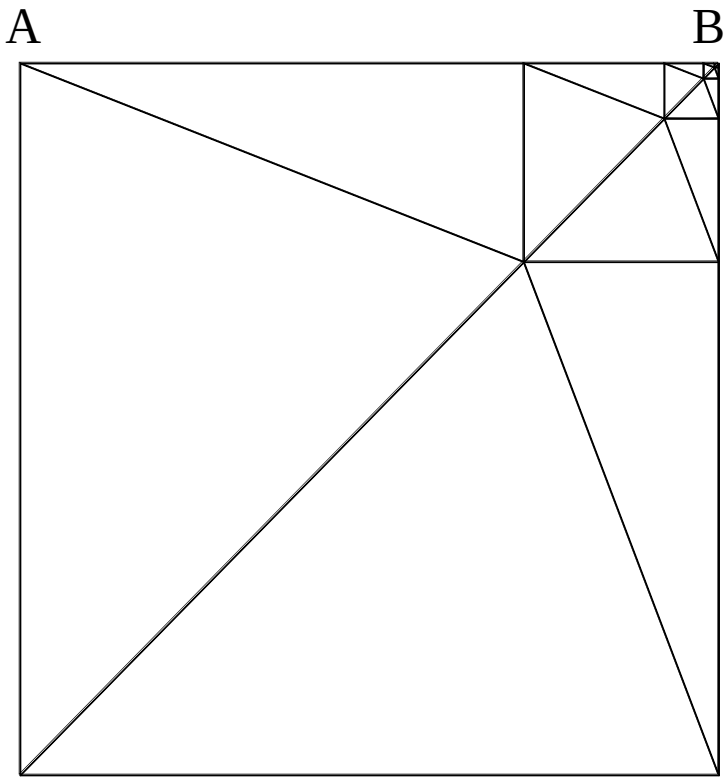

Figure 1.28. Optimum mesh produced by using the proposed guidelines

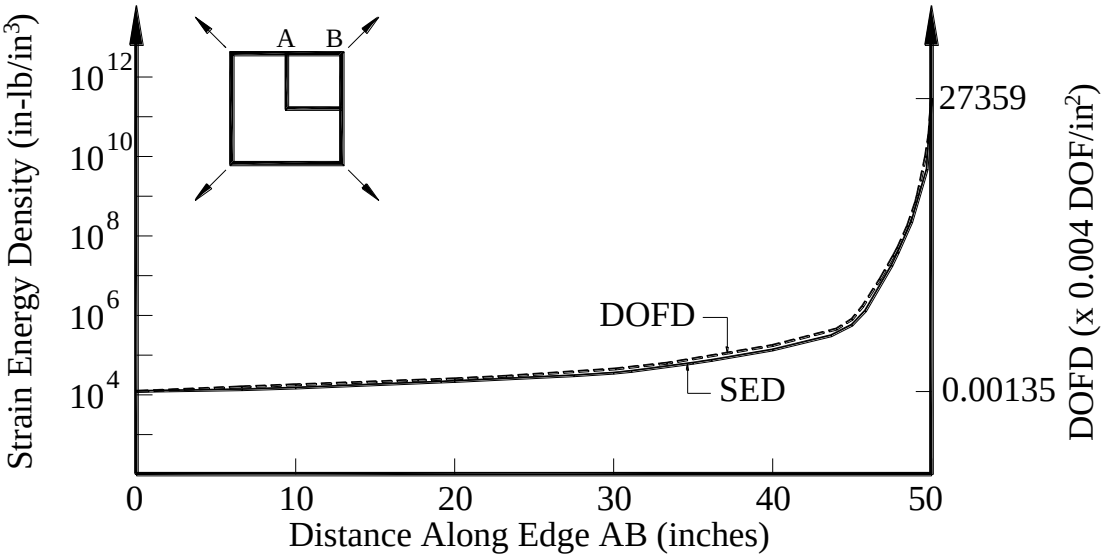

Figure 1.29. Strain energy density and degree of freedom density along edge AB

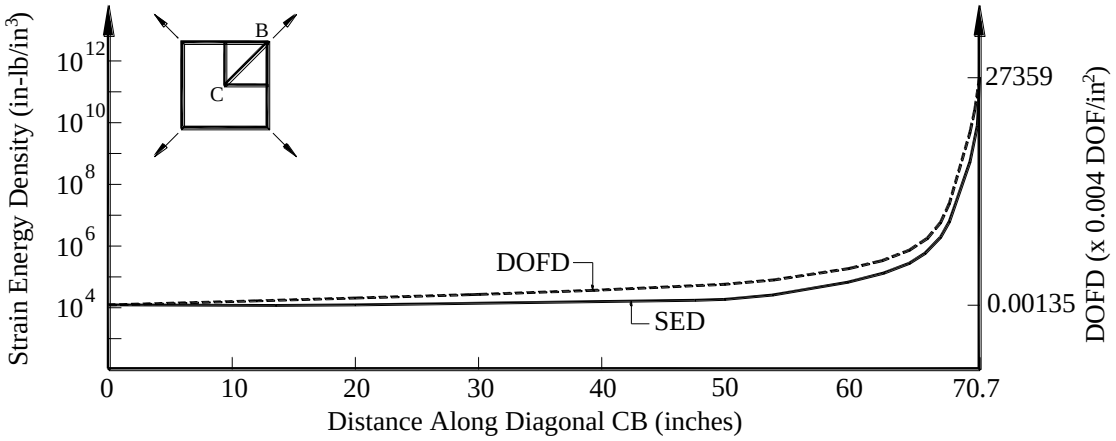

Figure 1.30. Strain energy density and degree of freedom density along diagonal CB

Comparison of the Results. The total strain energies and the maximum displacements for different optimum meshes obtained from different methods are presented in Table 1.2. The table shows that the total strain energies for the optimum meshes from Turcke and McNeice's guidelines, Turcke's mathematical programming technique, and Shephard's contouring method are only about 48.0%, 50.0%, and 53.8% of that obtained from the proposed guidelines respectively. The maximum displacements in both x and y direction shown in Table 1.2 indicate that there is a similar trend to that for the total strain energy mentioned above.

Two conclusions can therefore be drawn as follows: (1) If the variation of the degree of freedom density is the same as the variation of the strain energy density along any selected path in a mesh, the condition for the optimum finite element solutions is obtained. Such condition may never be achieved, but its usefulness in examining the quality of the finite element solutions is proved. (2) Numerical results reveal that the proposed guidelines, which are based on the proposed condition for the optimum finite element solutions, can lead an analyst to obtain much better solutions because the guidelines can reasonably accurately capture the characteristics of the mesh optimization.

Table 1.2. Comparison of the total strain energies and the maximum displacements for different optimum meshes from different methods

Method	Total Strain Energy, $(\times 10^8 lb/in)$	Maximum Displacement in x Direction, in Inches	Maximum Displacement In y Direction, In Inches
Author's Guidelines	2.3533 (100%)*	11.050 (100%)	11.050 (100%)
Turcke and McNeice's Guidelines	1.1299 (48.0%)	6.393 (57.8%)	6.393 (57.8%)
Turcke's Mathematical Programing Technique	1.1756 (50.0%)	6.649 (60.2%)	6.649 (60.2%)
Contouring Method of Shephard et al.	1.2671 (53.8%)	7.167 (64.9%)	7.167 (64.9%)

1.3.5 The Feasibility of Mesh Optimization in Localization Analyses

From the studies of shear bands in uniform strained solids, Yamamoto (1978), Hutchinson and Tvergaard (1981), and Saje et al. (1980) showed that the strains grow very large inside the bands without noticeably affecting the strains in the neighboring material. In a finite element approximation of a displacement field, solutions can only be described with reasonably accuracy if the band interfaces follow along element boundaries (Needleman and Tvergaard, (1983). Therefore having a central node in a quadrilateral element is helpful to resolve bands of highly localized straining, and to reduce the influences of the aspect ratio and the orientation of elements. Such an element is therefore used in this research. An example is presented.

Investigators like Needleman and Tvergaard (1983) have observed that even when the mesh is not optimally designed, localization has been captured in a number of computations but with a certain delay as compared to the case using a well-designed mesh. For the plate problem studied in this research, the theoretical solutions for the orientation of the shear bands have been indicated in the bifurcation analysis of Chapter II. The results indicate that the orientations of the shear bands are all close to 45 degrees for cases; H/2G equal to zero and -0.05. To obtain shear banding in a numerical solution close to 45 degrees, it will be better to use a square or close to

square rectangle so that shear banding along the diagonal can be achieved (with the five-node element used in this research). Therefore square or rectangle elements have been used in this research. The selection of such similar elements at the initial stage in all investigations will also enable us to note the effect of change of various variables on the solution.

While the behavior of localization in finite element analysis is detailed in next chapter, one specific example is selected here to show the difficulties of optimization. For a 2" x 4" plate loaded at both ends, where the movement in the direction perpendicular to the loading is constrained, the uniform 12 x 24 mesh shown in Figure 1.31.a is used to analyze the behavior of a quarter of the plate under uniform prescribed loading conditions. Material properties used are: (1) the initial size of yield surface, 500 psf, (2) the Young's modulus, 0.49, and (3) the hardening parameter, H/2G, equal to -0.05. The behavior of localization under different load steps is shown in Figures 1.31.b to 1.31.f. The velocity vector and the strain energy density contours corresponding to each load step are shown in Figures 1.32 and 1.33 respectively. The variation of the strain energy density along the diagonal AB for each load step is shown in Figure 1.34. The above results reveal that the localizations initiate from the constrained ends. The localization will be changing its location with the increase in the number of the load steps. Such a phenomenon is clearly shown in Figures 1.31, 1.32 and 1.33, in which highly localized deformations are different from step to step. This makes the optimization scheme impractical to be applied to localization analyses. The reason being that it is impossible to know the location of the highly localized deformation before the load is applied. However, the location of the highly localized deformations for the next load step should be known in order to optimize the mesh. Chapter IV of this dissertation will elaborate a another important point, which can be summarized as follows: "A selective refinement can force the localizations along some artificial paths, which are located immediately next to the refined region. This means that the redistribution of the degrees of freedom may force the big element to become too brittle when the stresses are in strain softening range."

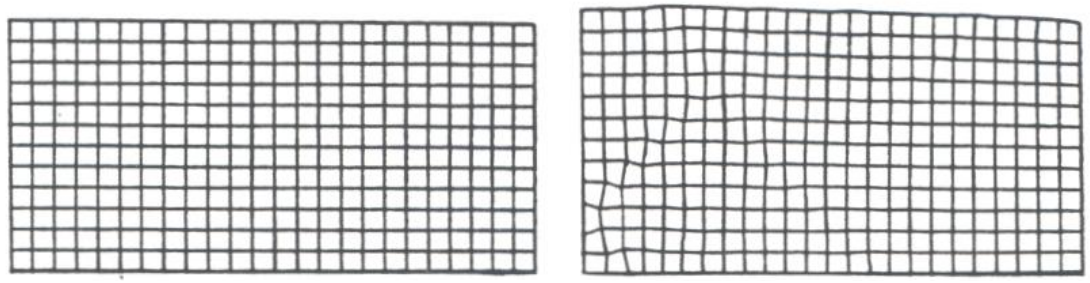

a. Initial mesh

d. The third load step

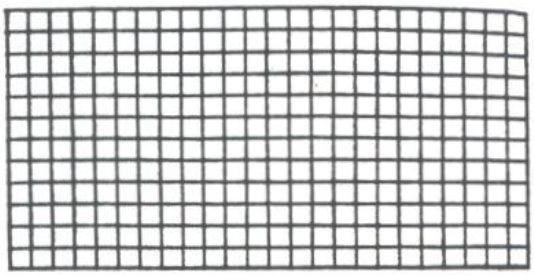

b. The first load step

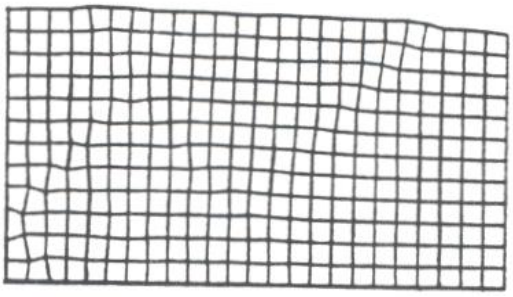

e. The fourth load step

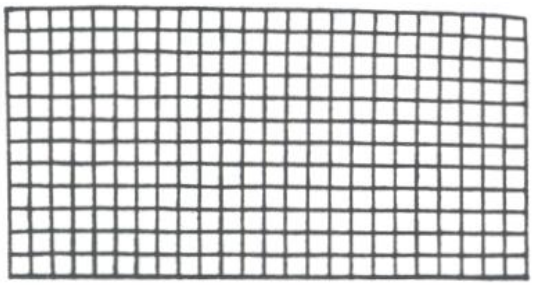

c. The second load step

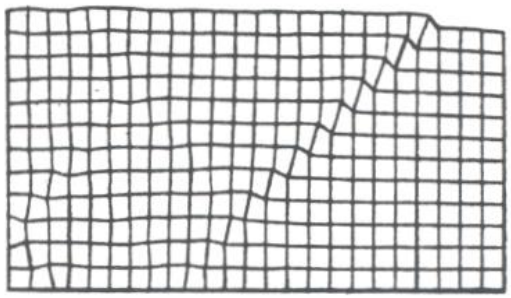

f. The fifth load step

Figure 1.31. The behavior of localization under different load steps in a quarter of the plate

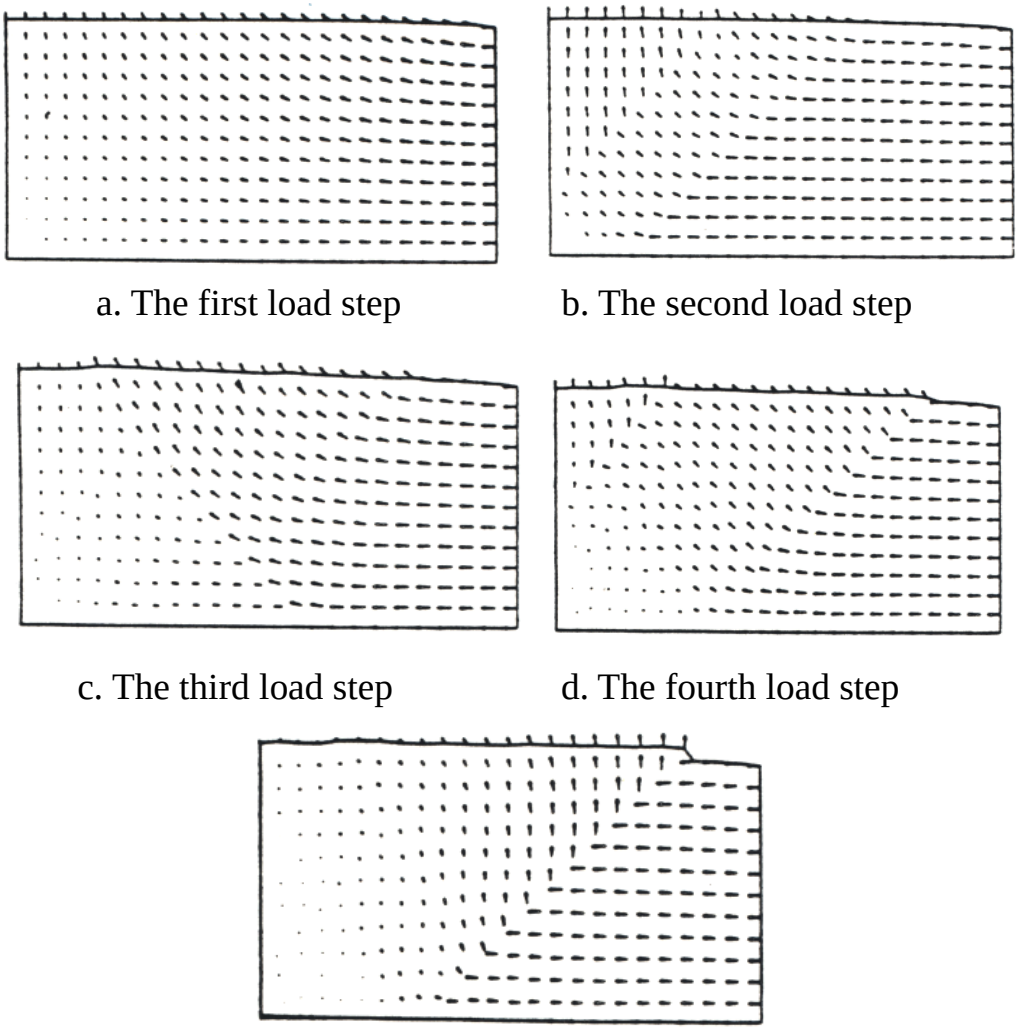

a. The first load step

b. The second load step

c. The third load step

d. The fourth load step

e. The fifth load step

Figure 1.32. Velocity vectors (H/2G=-0.05, and 3 substeps used)

a. The first load step b. The second load step

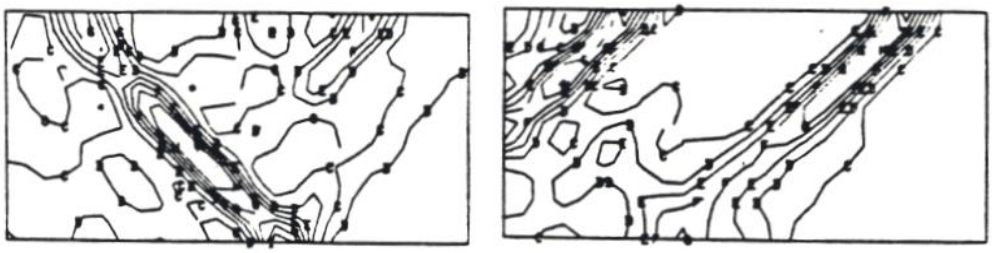

c. The third load step d. The fourth load step

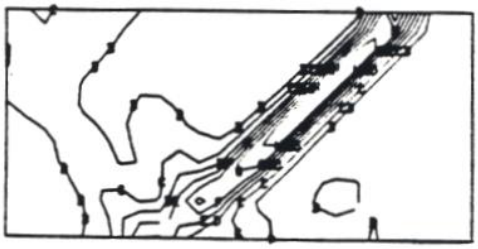

e. The fifth load step

Figure 1.33. Strain energy density contours (H/2G=-0.05, and 3 substeps used)

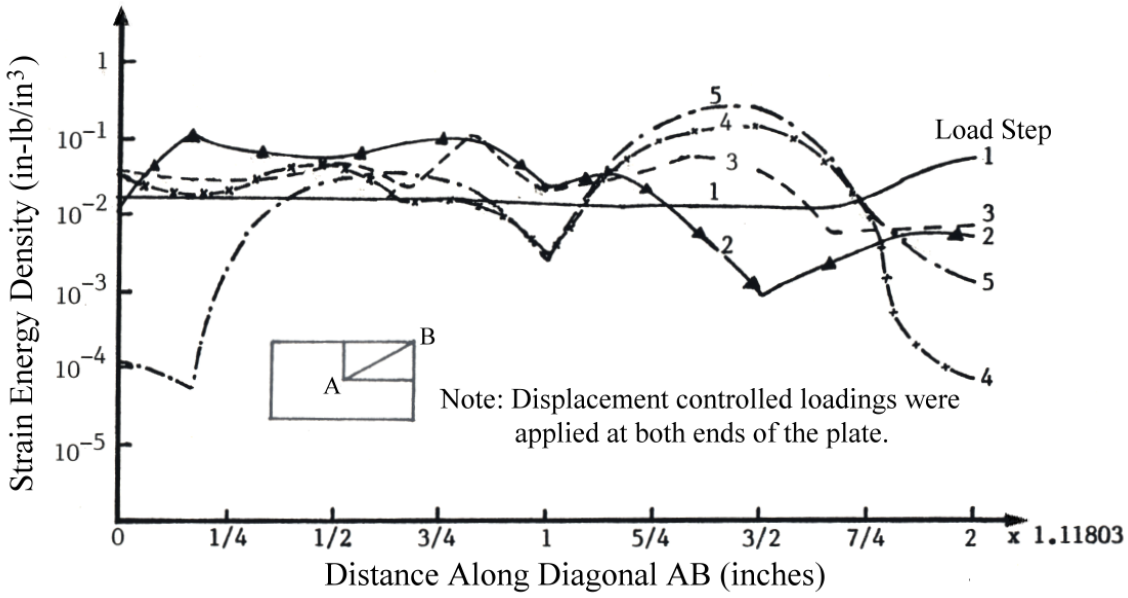

Figure 1.34. Distribution of strain energy density along diagonal AB for different load steps

It may therefore be concluded that it can be technically impossible to optimize a mesh in localization analyses. The difficulties in optimizations arise due to the following two factors: (1) No knowledge for the location of the highly localized deformation is available before the load is applied. (2) Mesh refinement based on previous load step may lead the localization toward an erroneous and undesirable path. The literature study did not reveal any proposed method for solving the first difficulty listed above. However, the second difficulty has been treated by Bazant et al. (1984) by proposing the non-local formulation to limit localization in order to reduce mesh sensitivity. Bazant (1984) also proposed an alternative procedure for limiting localization, in which a higher-order spatial derivative was introduced into the governing equations. Both these approaches are limited in one-dimensional cases only. For two or three dimensional cases, more efforts are needed to produce realistic solutions, which is beyond the scope of this research.

Because of the above mentioned difficulties in mesh optimizations for strain softening materials, further study of mesh optimizations was pursued in this research.

1.4 The Behavior of Localization in Finite Element Analyses

The behavior of localization in finite element analyses has been studied by a number of investigators. It was mentioned earlier in this dissertation that for a plate problem the localization behavior is sensitive to the initial inhomogeneity assigned within a plate. Using weak elements within a mesh (Prevost and Hughes, (1981) or varying the stiffness across a mesh (Needleman and Tvergaard, (1983) would give rise to localization of deformation but also made the results sensitive to the details of the property variations. Thus the contribution of mesh design will be limited because the inhomogeneity is also modeled and embedded in the mesh. To produce inhomogeneous conditions while keeping material properties constant, a plate under plane strain conditions loaded at both ends by applying uniform prescribed displacements is shown in Figure 1.35. Displacements at the loaded ends of the plate in y direction are constrained ends of the plate. The material properties are assumed to be constant within each element and shown in Figure 1.36, where κ is the size of the yield surface, E is the Young's modulus, G is the shear modulus, ν is the Poisson's ratio, and H is the hardening parameter. For the problem described above, a sufficient stress concentration is induced to initiate localization of deformation even with uniform material properties. Such stress concentration is shown in Figure 1.37 in which typical strain energy density contours for the initial elastic loading are plotted.

For the plate problem analyzed in this study, the uniform prescribed displacements were applied incrementally. The sequence for the application of the uniform prescribed displacements in the main load steps are 0.045 inch, 0.025 inch, 0.025 inch, 0.025 inch, 0.025 inch, and 0.025 inch respectively. Each main load step can be further subdivided into several substeps of load. Only the results of the last substep in each main load step will be presented.

For positive uniform prescribed displacements, the numerical experiment is similar to a unconfined tension test. On the other hand, an unconfined compression test can be simulated when negative uniform prescribed displacements are applied. Within the elastic range, a value of the Poisson's ratio equal to 0.3 will be used in tension simulations, and that equal to 0.49 will be used in compression simulations to examine the behavior of

soft clays under the undrained conditions. Since the extended Von-Mises yield criterion is used, there will be no plastic volume change for both types of simulations when stresses are beyond elastic range.

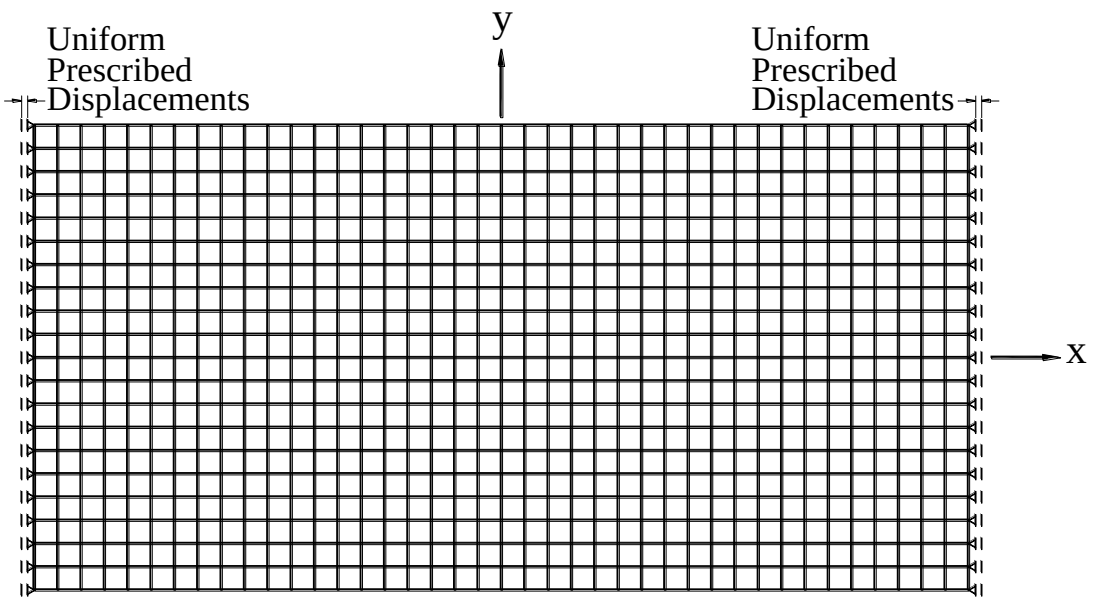

Figure 1.35. Boundary conditions of the plate and the uniform prescribed displacements

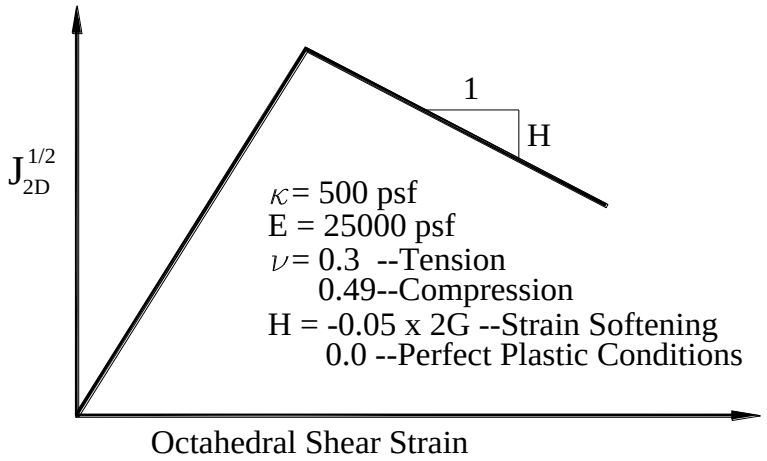

Figure 1.36. Material properties for the 2" x 4" plate

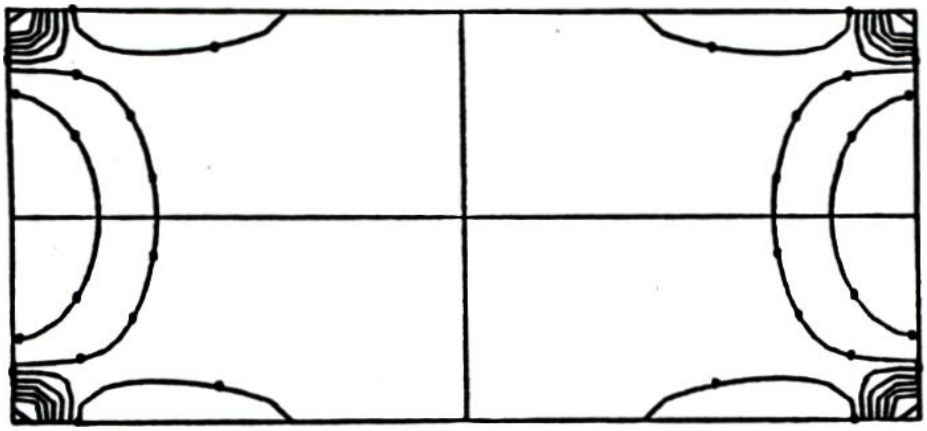

Figure 1.37. Typical srain eergy dnsity cntours for
the frst lad sep

In this chapter, results of different patterns of localizations for both tension and compression simulation are presented. A non-dimensional hardening parameter, which is equal to the ratio of hardening parameter divided by the shear modulus, H/2G, will be used. Two conditions will be examined in each simulation; (1) H/2G less than zero, and (2) H/2G equal to zero. The name for each pattern of localizations will be based on the number, and the shape of shear bands obtained.

Summations of all the results of the numerical experiments for the plate problem are shown in Table 1.3 and 1.4 first. The details of the behavior of localization are then discussed.

1.4.1 Behaviour of Localization in Tension Simulation

Experiments with H/2G Less Than Zero. Five experiments are studied in this section. The details of the mesh are as follows. A 30 x 60 uniform mesh is used in the first and the second experiments. A 24 x 52 non-uniform mesh is used in the third and the fourth experiments. In the third experiment, initially there are two rows and two columns of half-size elements at the outer edge of the plate and near the point 'D' respectively in Figure 1.38. Similar half-size elements are near the centerlines of the plate for the fourth experiment. For the fifth experiment, a 24 x 48 uniform mesh is used.

Table 1.3. A Summation of different patterns of shear bands for tension simulations ($E = 25000\ psf$, $\nu = 0.3$, $\kappa = 500\ psf$)

Hardening Parameter, H	Initial Mesh	Number of Substep	Pattern of Shear Bands	Angle of Shear Bands with Respect to the Horizontal, degree
-0.05	30x60	2	3I	38.5
-0.05	30x60	3	4I	39.5
-0.05	24x52*	3	2S	48.1
-0.05	24x52**	3	2V2X	43.0
-0.05	24x48	3	4V4R	44.0
0.0	20x40	3	X	40.0
0.0	20x40***	3	X	41.2
0.0	24x48	3	X	39.5
0.0	24x52*	3	X	40.6

*: Half-size elements are at the outer edge of the plate.

**: Half-size elements are near the centers of the plate.

***: A refined mesh is used.

Table 1.4. A summation of different patterns of shear bands for compression simulations ($E = 25000\ psf$, $\nu = 0.49$, $\kappa = 500\ psf$)

Hardening Parameter, H	Initial Mesh	Number of Substep	Pattern of Shear Bands	Angle of Shear Bands with Respect to the Horizontal, degree
-0.05	30x60	3	4I	46.5
-0.05	24x48	3	2X2V4R	45.7
-0.05	20x40	3	4I’	48.4
-0.05	20x40	8	2I	44.1
-0.05	20x40	5	3I	45.1
-0.05	20x40	10	2X	48.3
0.0	20x40	3	X	45.9
0.0	24x48	3	X	45.2
0.0	24x52**	3	X	45.4
0.0	20x40***	3	X	45.9

**: Half-size elements are near the centers of the plate.

***: A refined mesh is used.

The first experiment provided a pattern of localizations called 3I pattern. From Figure 1.38 it is seen that the 3I pattern is formed by two sets of three I-shape shear bands. The number of loading substeps used for this pattern is two. From Figure 1.38.d it is seen that 3I pattern is formed initially with 2I pattern--two sets of two I-shape shear bands. Then the third I-shape shear band joins each set of shear bands (see Figure 1.38.f). The 2I pattern is formed perhaps due to the influence of the constrained ends. The appearance of the third set of shear bands may be caused by the propagation of the localized deformations near the center of the plate. Totally there are sixteen blocks in the plate formed by the 3I pattern. The angle of the shear bands with respect to the horizontal is found to be 38.5 degrees in Figure 1.38.f.

The second experiment resulted in a pattern of localizations called 4I pattern. The number of loading substeps used for this pattern is three. From Figure 1.39 it is seen that the 4I pattern is formed by two sets of four I-shape shear bands, which are not fully developed. The feature of this pattern is the formation of a big diamond made up of nine small diamonds at the center portion of the plate. The shear bands near the edge of the big diamond are formed perhaps due to the influence of the constrained ends. The rest of them are formed perhaps due to the propagation of the localized deformations near the center of the plate. The angle of the shear bands with respect to the horizontal is found to be 39.5 degrees Figure 1.39.e.

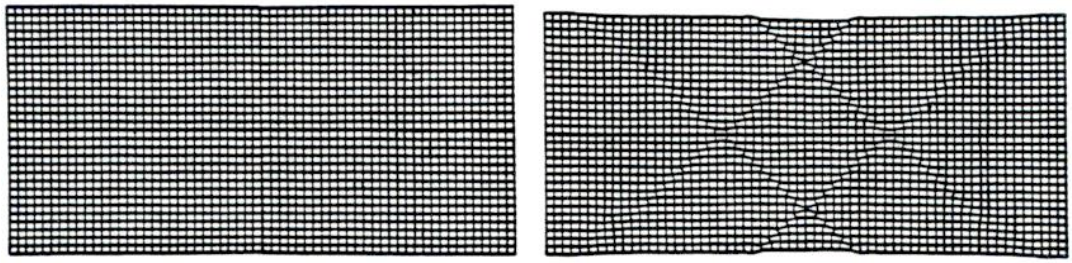

a. Initial mesh (30 x 60)

d. The third load step

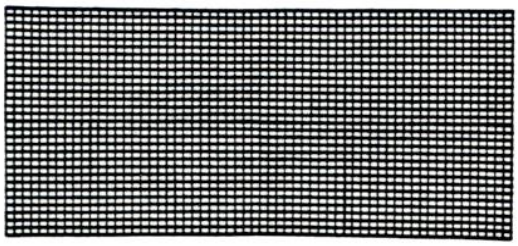

b. The first load step

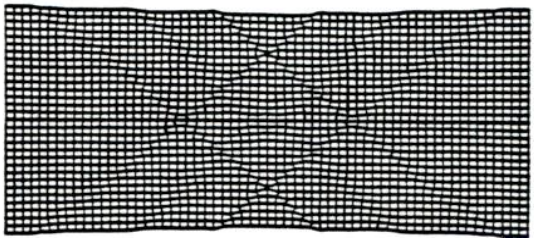

e. The fourth load step

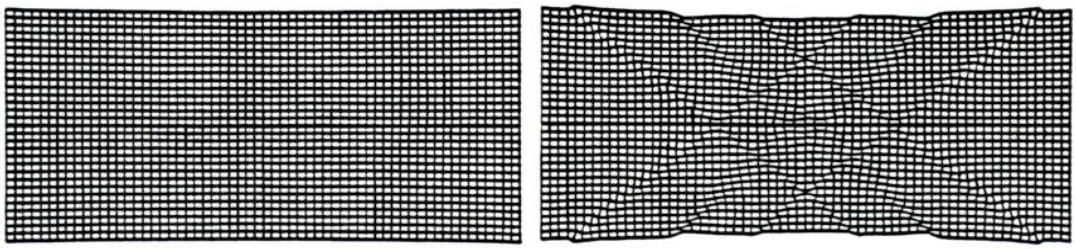

c. The second load step f. The fifth load step

Figure 1.38. The 3I pattern of localization of deformation in the unconfined tension simulation
(H/2G = -0.05, number of substeps = 2)

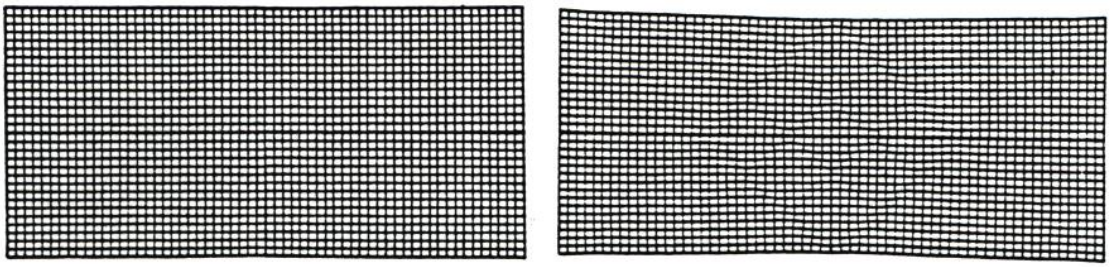

a. Initial mesh (30 x 60) d. The third load step

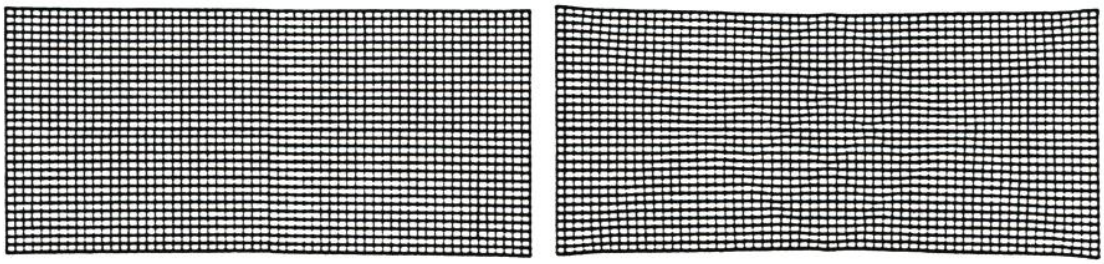

b. The first load step e. The fourth load step

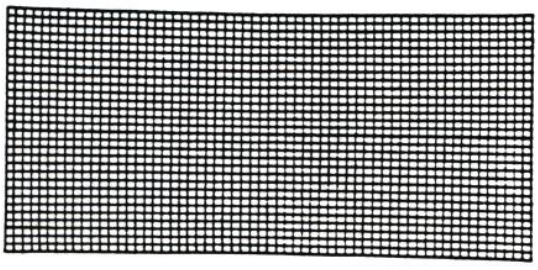

c. The Second Load Step

Figure 1.39. The 4I pattern of localization of deformation in the unconfined tension simulation
(H/2G = -0.05, number of substeps = 3)

The third experiment provided a pattern of localization of deformation is called 2S pattern. The number of loading substeps used for this pattern is three. From Figure 1.40 it is seen that the 2S pattern is formed by two sets of two S-shape shear bands. The 2S pattern can also be considered as the combination of two V-shape shear bands near the ends and two X-shape shear bands at the center portion of the plate. Two X-shape shear bands have formed one diamond and two triangles. From Figures 1.40.e to 1.40.g it is seen that more disturbances can be found in these two triangles if the central diamond is further expanded. The V-shape shear bands formed, may be caused by the influence of the constrained ends. The X-shape shear bands formed, may be due to the propagation of the localized deformations near the center of the plate. Figure 1.40.g reveals that the tendency for the formation of the V-shape shear bands and the X-shape shear bands may be equally strong. Therefore, the wavy outline of the plate may be caused by the interaction between these two types of shear bands. Totally there are nine blocks in the plate formed by 2S pattern. Except those shear bands, which coincide with the centerline of the plate, the angle of the shear bands with respect to the horizontal is found to be 48.1 degrees in Figure 1.40.g.

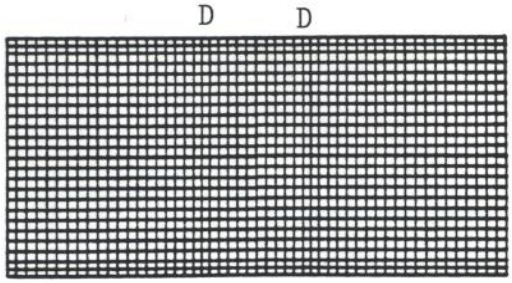

a. Initial mesh (24 x 52)

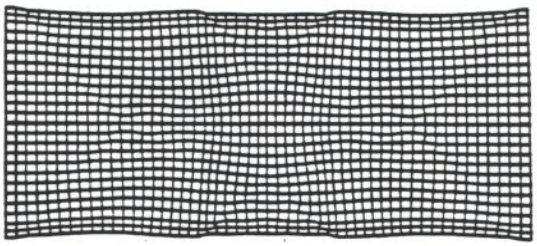

e. The fourth load step

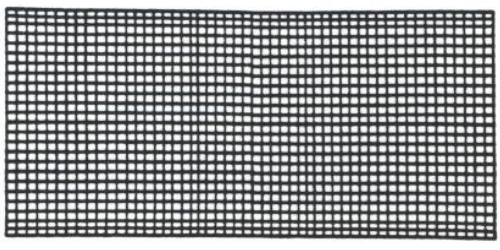

b. The first load step

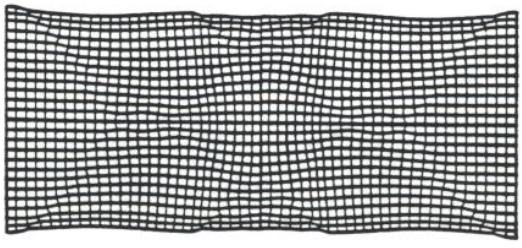

f. The fifth load step

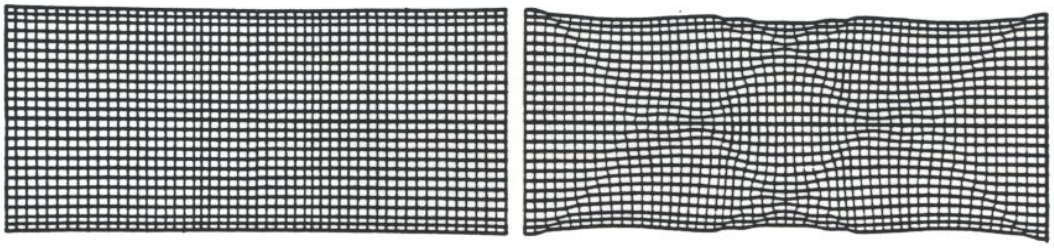

c. The second load step g. The sixth load step

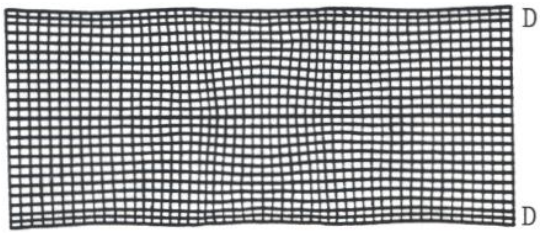

d. The third load step

Figure 1.40. The 2S pattern of localization of deformation in the unconfined tension simulation
(H/2G = -0.05, number of substeps =3)

The fourth experiment produced a pattern of localizations called 2V2X pattern. The number of loading substeps used for this pattern is three. From Figure 1.41 it is seen that the 2V2X pattern is formed by two V-shape shear bands near the ends of the plate and two X-shape shear bands near the center of the plate. The feature of this pattern is that the V-shape shear bands are extremely clear, but the X-shape shear bands are not as clear. From Figures 1.40, and 1.41 it is seen that both 2S pattern and 2V2X pattern are similar. However, the outline of the plate for the 2V2X pattern is less wavy than that of the 2S pattern. Therefore, it may be deduced that very limited interaction exists between those two types of shear bands in the 2V2X pattern. Totally there are nine blocks in the plate formed by the 2V2X pattern. The angle of the shear bands with respect to the horizontal is found to be 43.0 degrees in Figure 1.41.g.

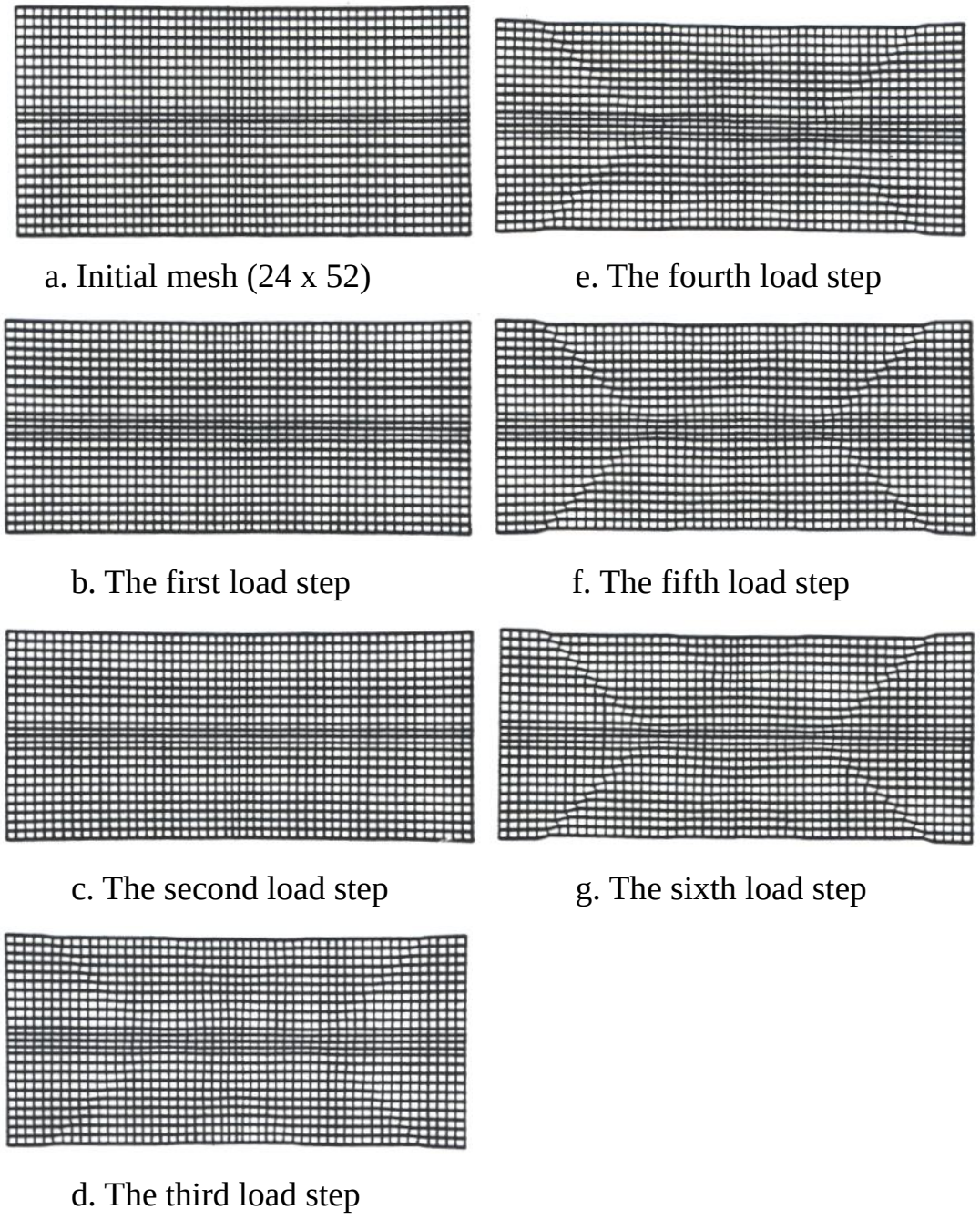

a. Initial mesh (24 x 52)

b. The first load step

c. The second load step

d. The third load step

e. The fourth load step

f. The fifth load step

g. The sixth load step

Figure 1.41. The 2V2X pattern of the localization of deformation in the unconfined tension simulation
(H/2G = -0.05, number of substeps = 3)

The fifth experiment gave a pattern of localizations called 4V4R pattern. The number of loading substeps used for this pattern is three. From Figure 1.42 it is seen that the 4V4R pattern is formed initially by two V-shape shear bands near the ends of the plate (see Figure 1.42.d). Then the other two V-shape shear bands join together with the two original V-shape shear bands

(see Figure 1.42.e). From Figure 1.42.f it is seen that there are four reflective shear bands near the central edge of the plate, and these shear bands may be caused by the interaction of the V-shape shear bands and the localized deformations near the center of the plate. Due to the reflective shear bands, the center portion of the plate is expanded in the fifth load step. The angle of the shear bands with respect to the horizontal is found to be 39.8 degrees in Figure 1.42.f.

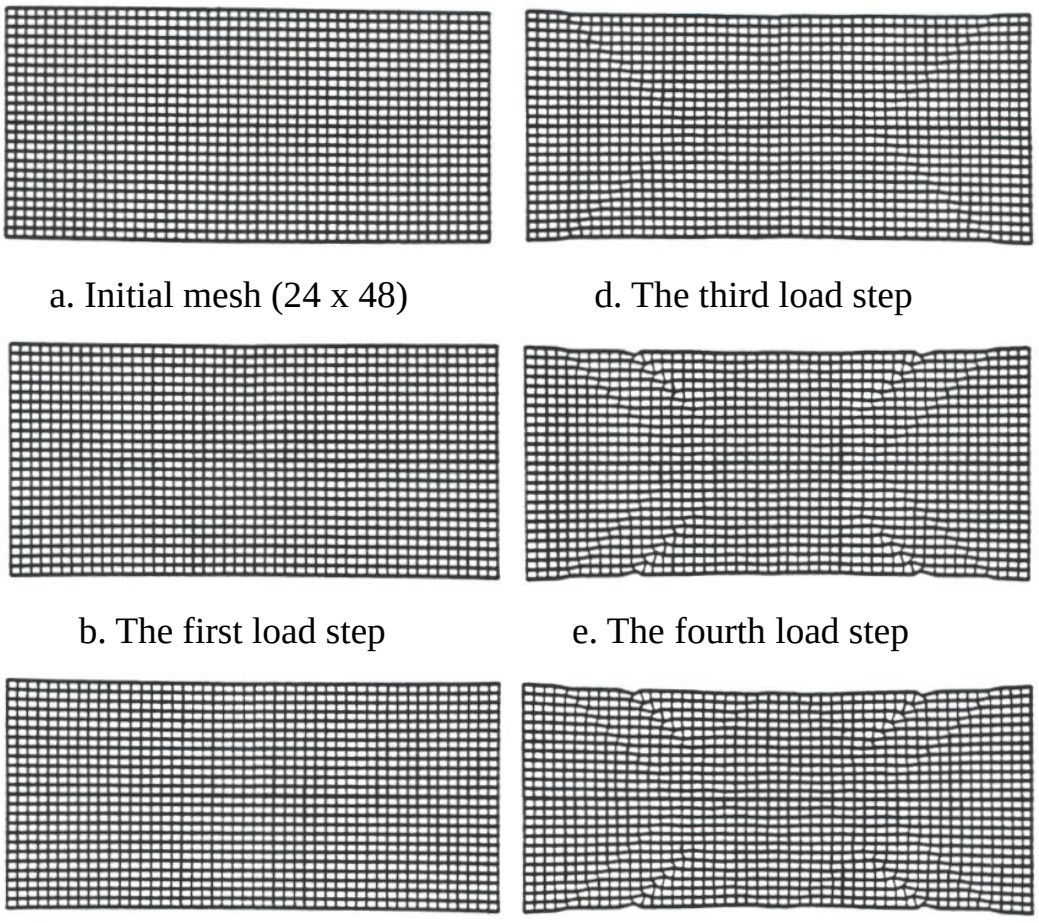

a. Initial mesh (24 x 48)

d. The third load step

b. The first load step

e. The fourth load step

c. The second load step

f. The fifth load step

Figure 1.42. The 4V4R pattern of localization of deformation in the unconfined tension simulation
(H/2G = -0.05, number of substeps = 3)

Experiments with H/2G Equal to Zero. Totally four experiments are studied in this section; the first experiment with 20 x 40 uniform mesh, the second experiment with 20 x 40 refined mesh, the third experiment with 20 x 48 uniform mesh and the fourth experiment with 24 x 52 non-uniform mesh.

The 20 x 40 refined mesh is formulated such that more degrees of freedom are allowed in the area where strain energy density gradient is higher. In the 24 x 52 non-uniform mesh, two rows, and two columns of half-size elements are located at the outer edge of the plate, and near the point 'D' shown in Figure 1.4.12 respectively. For all the experiments studied under this condition, the number of loading substeps used is three. From Figures 1.43 to 1.46, it is seen that the X pattern is the only pattern of localizations found in these experiments. The angle of the shear bands with respect to the horizontal is found to be 40.0 degrees in Figure 1.4.43.g; 41.2 degrees in Figure 1.4.44.g; 39.5 degrees in 1.4.45.f; and 40.6 degrees in Figure 1.4.46.g. The results from the 20 x 40 refined mesh reveal that the selective refinement of a mesh does not improve the formation of the localization in this experiment. Furthermore, this experiment produced observable localizations in a deformed mesh only when the stresses are far beyond the elastic range. Such phenomenon indicates that the intensity of the localized deformations is increased slowly in each load step. It is also found that the localizations do not further propagate after the X-shape shear band was formed. Therefore, it may be concluded that the behavior of localization under this condition is totally different from those which are obtained from the condition of H/2G less than zero. However, localization of deformation is not sensitive either to the details of mesh design or to the selective refinement of a mesh under this condition.

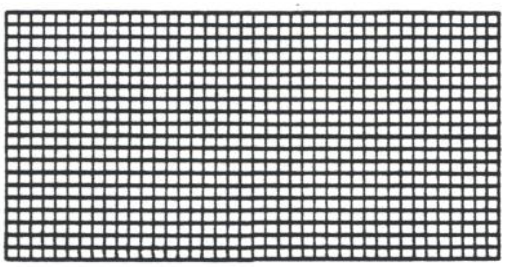

a. Initial mesh (20 x 40)

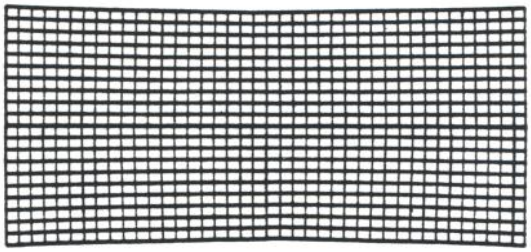

. The fourth load step

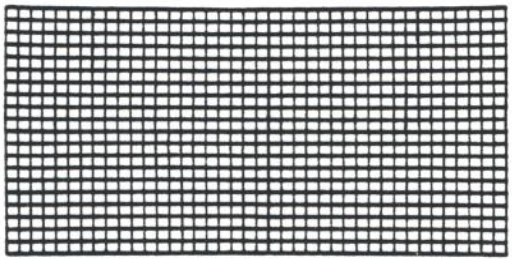

b. The first load step

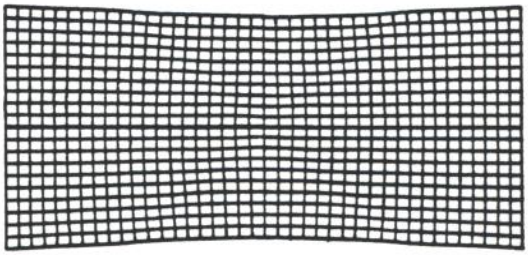

f. The fifth load step

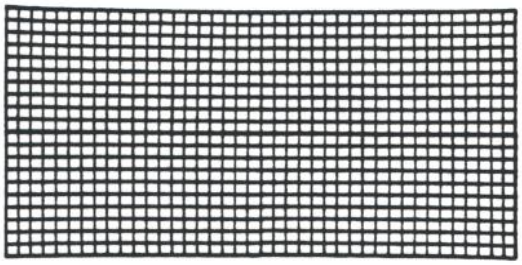

c. The second load step

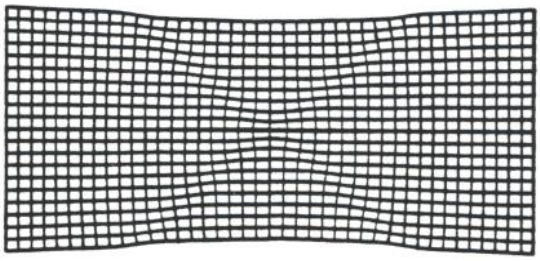

g. The sixth load step

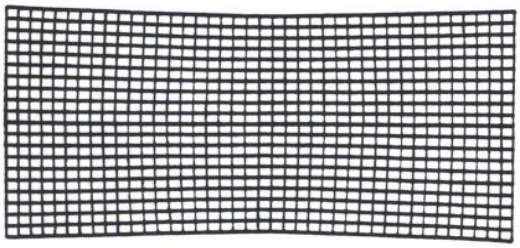

d. The third load step

Figure 1.43. The X pattern of localization of deformation in the unconfined tension simulation
(H/2G = 0.0, number of substeps = 3)

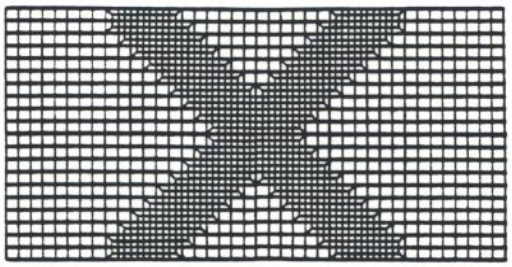

a. Initial Mesh

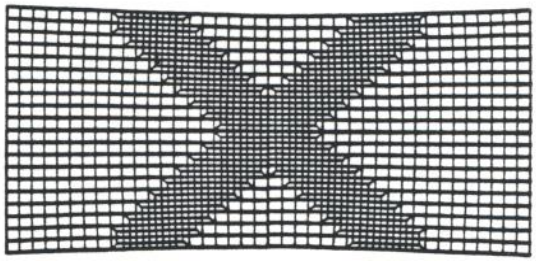

e. The Fourth Load Step

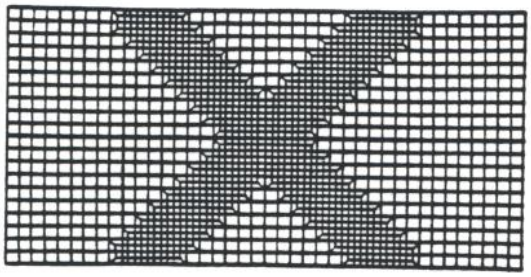

b. The first load step

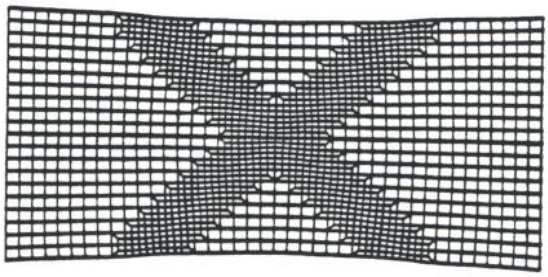

f. The fifth load step

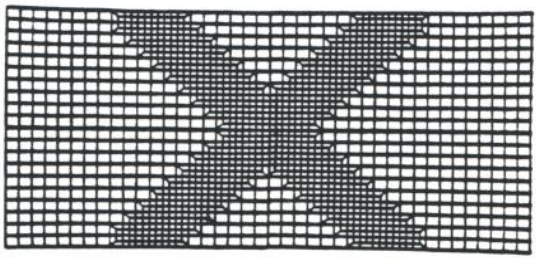

c. The second load step

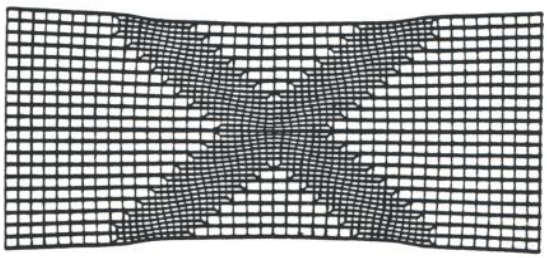

g. The sixth load step

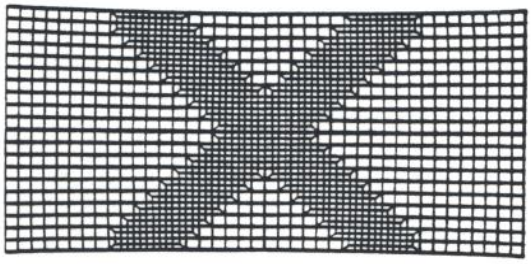

d. The third load step

Figure1.44. The X pattern of localization of deformation in the unconfined tension simulation
(H/2G = 0.0, number of substeps = 3)

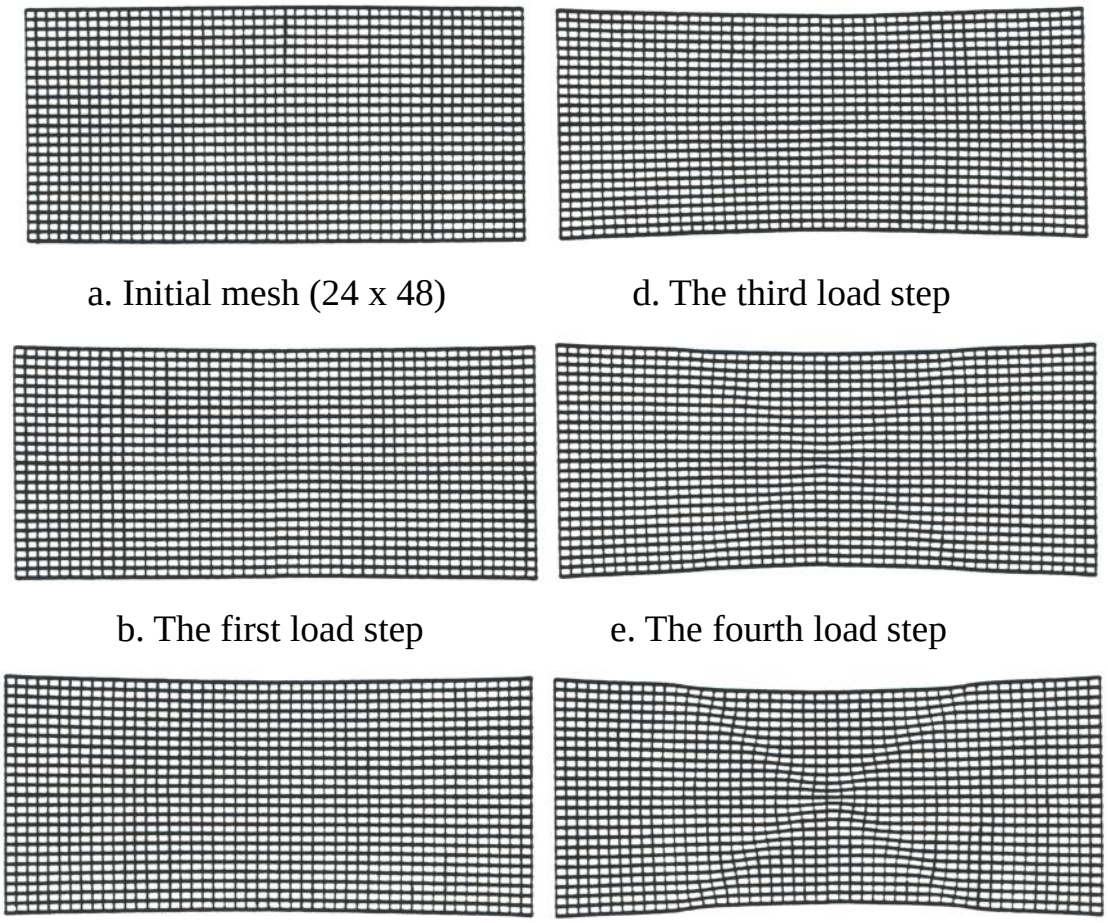

a. Initial mesh (24 x 48)

b. The first load step

c. The second load step

d. The third load step

e. The fourth load step

f. The fifth load step

Figure 1.45. The X pattern of localization of deformation in the unconfined tension simulation
(H/2G = 0.0, number of substeps = 3)

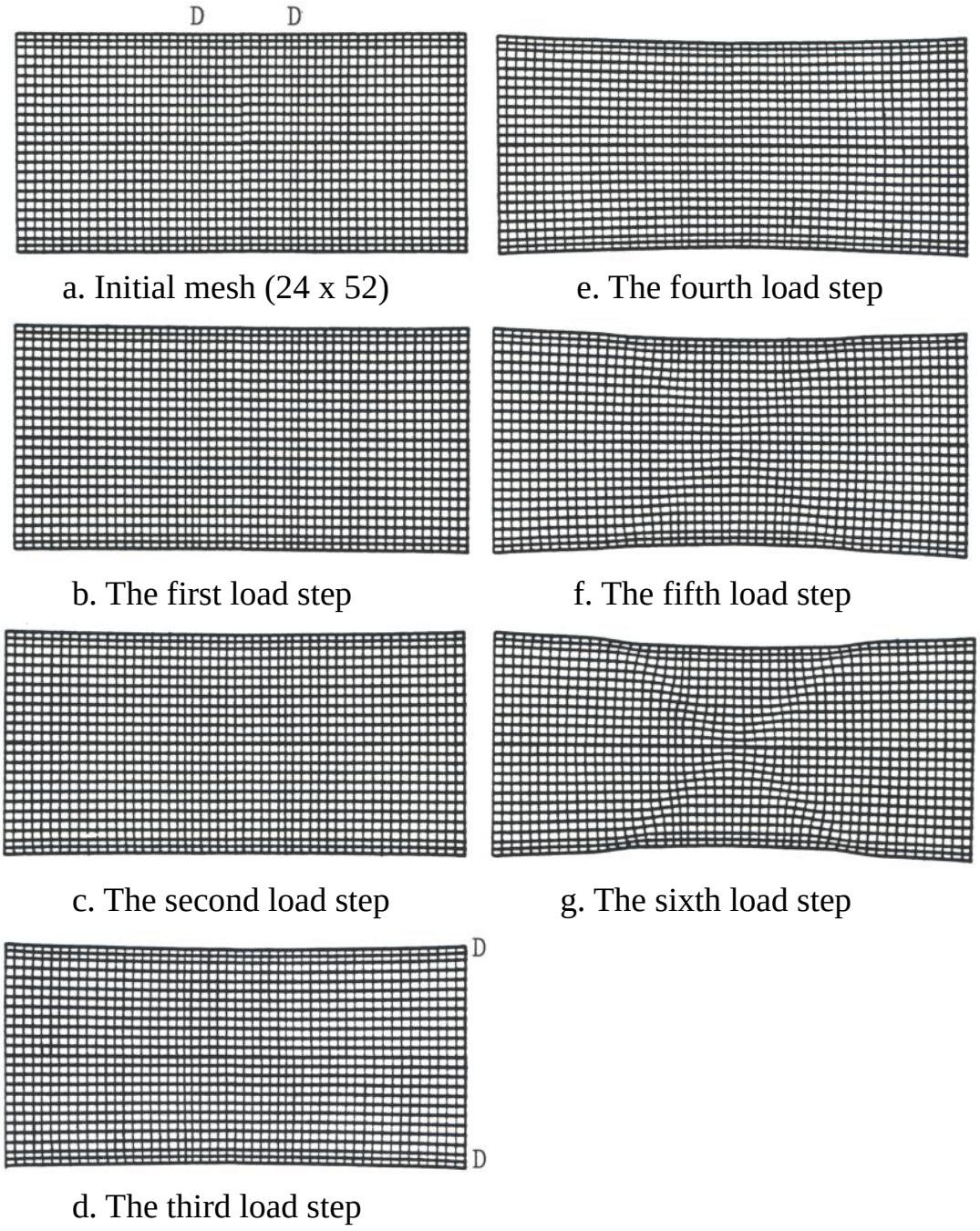

a. Initial mesh (24 x 52)

b. The first load step

c. The second load step

d. The third load step

e. The fourth load step

f. The fifth load step

g. The sixth load step

Figure 1.46. The X pattern of localization of deformation in the unconfined tension simulation
(H/2G = 0.0, number of substeps = 3)

1.4.2 Behaviour of Localization in Compression Simulation

Experiments with H/2G Less Than Zero. Six experiments produced six patterns of localizations in these attemps. The first experiment started with a 30 x 60 uniform mesh while a 24 x 48 uniform mesh is used in the second experiment. A 20 x 40 uniform mesh is used in all other trials.

The first experiment gave a pattern of localizations called 4I pattern. The number of loading substeps used for this pattern is three. From Figure 1.47 it is seen that the 4I pattern of localizations is formed by two sets of four I-shape shear bands. It may be caused by the propagation of the localized deformations near the center of the plate that two V-shape shear bands are found near the center of the plate (see Figure 1.47.b). Besides the influence of the propagation of localization initiated from the center of the plate, the constrained ends also have some influence. Figure 1.47.d explicitly shows the influence of the constrained ends becoming more significant with the increase in the number of load steps. Therefore, in addition to the first two V-shape shear bands near the center of the plate, there are two other V-shape shear bands near the constrained ends. From Figure 1.47.f it is seen that shear bands are all fully developed. It is to be pointed out that a big X-shape shear band is formed in Figure 1.47.g because of the decrease in the distance between those two V-shape shear bands near the center of the plate. Such phenomenon is caused by the expansion of the V-shape shear bands. Perhaps the formation of the X-shape shear bands causes the shear bands, which is between the first two V-shape shear bands, to come closer to the X-shape shear bands. The combination of all the above processes makes the central portion of the plate become significantly distorted. Local bulges are found at both ends of each shear band (see Figure 1.47.g) causing the outline of the plate to become very wavy. Totally there are twenty three blocks in the plate formed by the 4I pattern. The angle of the shear bands with respect to the horizontal is found to be 46.5 degrees in Figure 1.47.g.

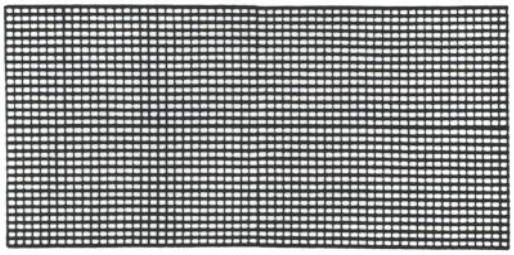

a. Initial mesh (30 x 60)

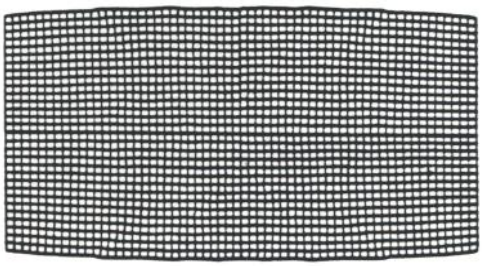

e. The fourth load step

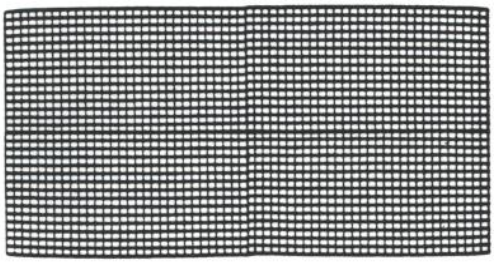

b. The first load step

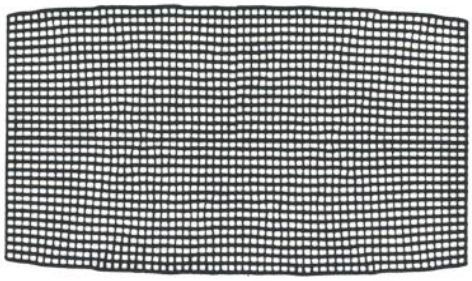

f. The fifth load step

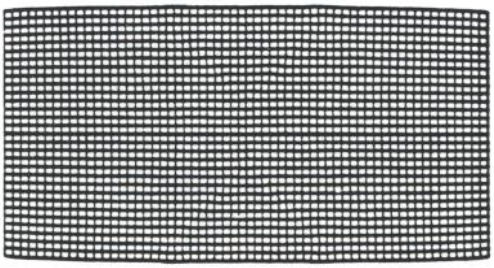

c. The second load step

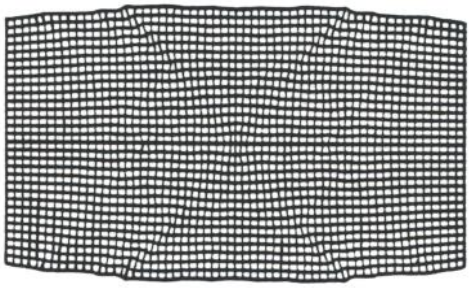

g. The sixth load step

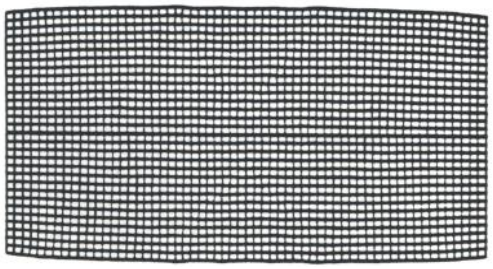

d. The third load step

Figure 1.47. The 4I pattern of localization of deformation in the unconfined compression simulation
(H/2G = -0.05, number of substeps = 3)

The second experiment gave a pattern of localization of deformation called 2X2V4R pattern. The number of loading substeps used for this pattern is three. From Figure 1.48.f, it is seen that the 2V2X4R pattern is formed by two V-shape shear bands, two X-shape shear bands, and four reflective shear bands. Although the localized deformations are initiated from the constrained ends, a shear band may be created from the propagation of the localized deformations near the center of the plate (see Figure 1.48.e). Two V-shape shear bands near the center of the plate are therefore formed under this condition. It is quite clear that these two V-shape shear bands are developed most explicitly amongst all three types of shear bands. Four reflective shear bands have been formed and can be seen quite clearly in Figure 1.48.e. It may be noted that the influence of the constrained ends is relatively small up to this load step. From Figure 1.48.f it is seen that the intensity of the X-shape shear bands is increased while the other two types of shear bands remain almost the same as before. This means that the influence of the constrained ends becomes significant only after the number of the load steps becomes large enough in this case. The angle of the shear bands with respect to the horizontal is found to be 45.7 degrees in Figure 1.48.f.

The third experiment provided a pattern of localization of deformation called 4I' pattern. The number of loading substeps used for this pattern is three. From Figure 1.49 it is seen that the 4I' pattern of localizations is formed by two sets of four partially developed I-shape shear bands. The whole pattern looks like a big hexagon with a diamond in its center. In Figure 1.49.f, the central diamond is formed probably because of the propagation of localized deformations near the center of the plate. The shear bands near the constrained ends are different from any others obtained in this research. Such shear bands seem to be initiated from some locations on the edges of the plate. The reason for their formation is not clearly known, but they could be created by the reflection of the propagating of the localized deformations near the center of the plate. Therefore, two inversed V-shape shear bands rather than the 'regular' V-shape shear bands are obtained near the constrained ends. The angle of the shear bands with respect to the horizontal is found to be 48.4 degrees in Figure 1.49.f.

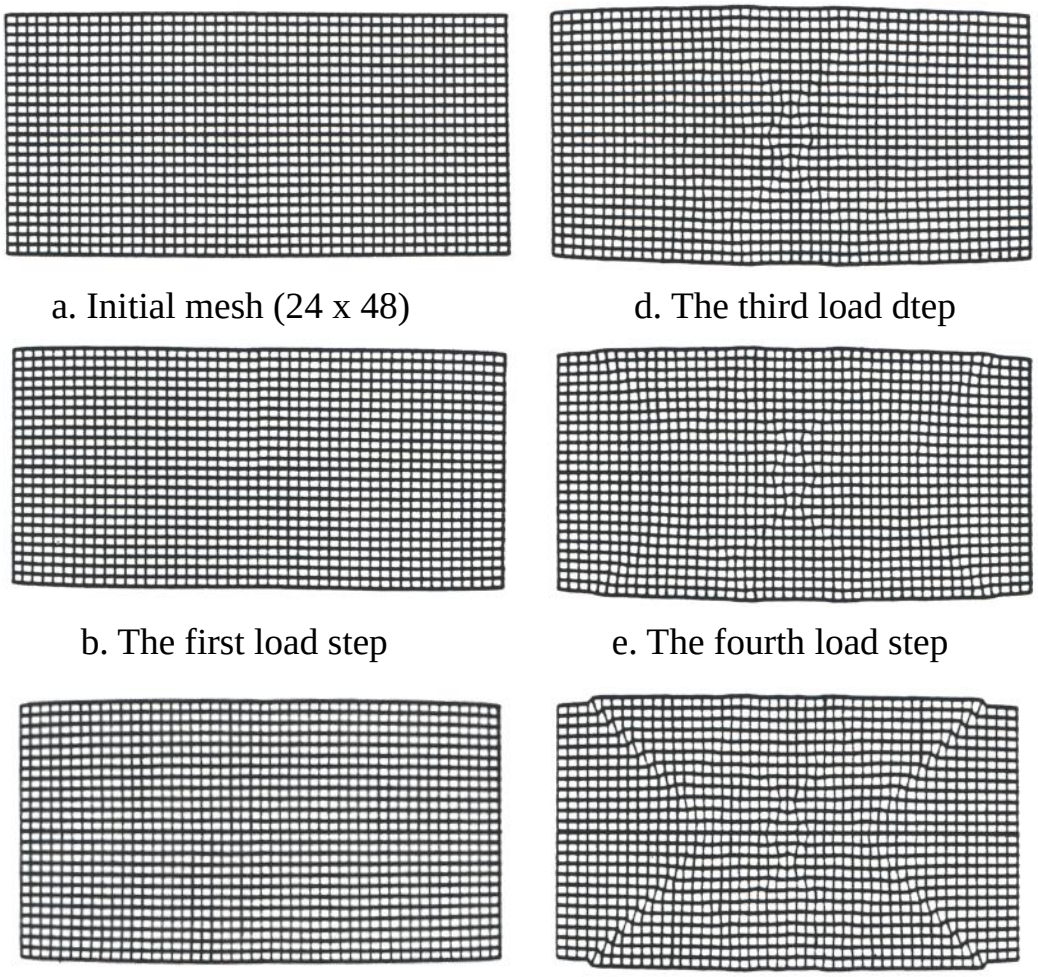

a. Initial mesh (24 x 48)

d. The third load dtep

b. The first load step

e. The fourth load step

c. The second load step

f. The fifth load step

Figure 1.48. The 2X2V4R pattern of localization of deformation in the unconfined compression simulation
(H/2G = -0.05, number of substeps = 3)

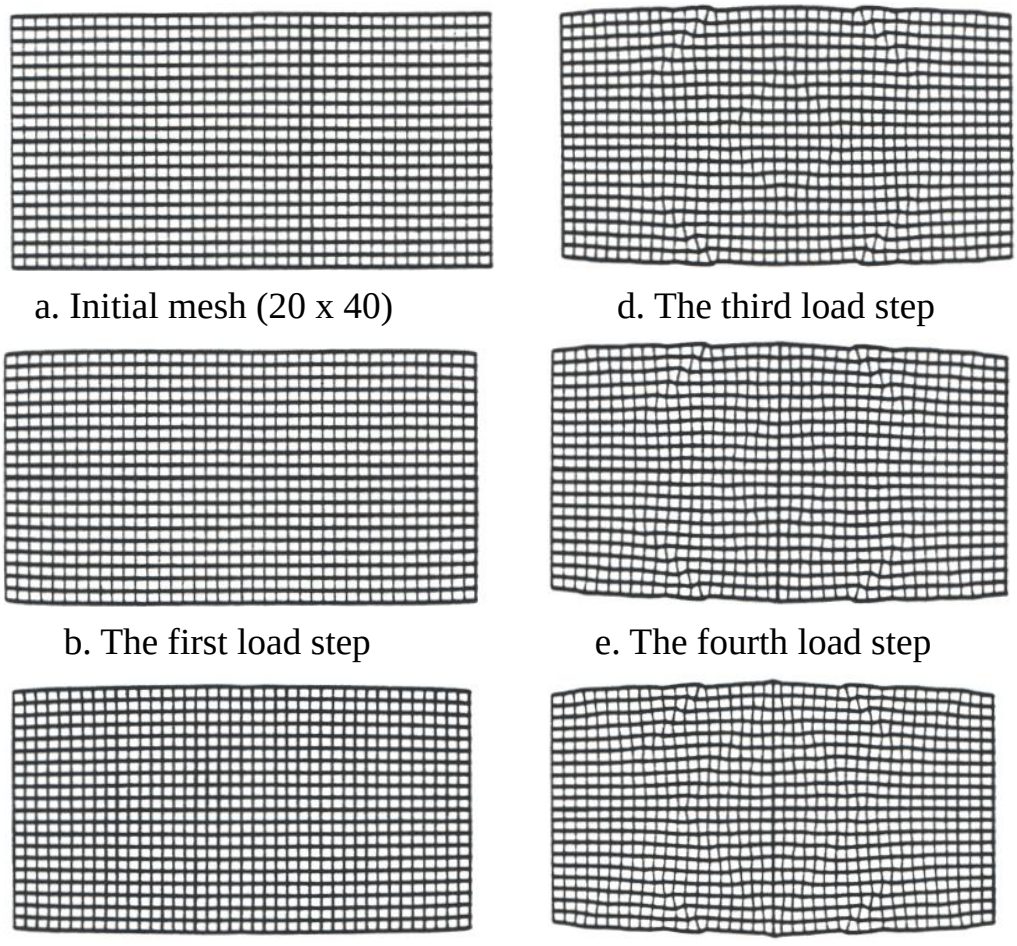

a. Initial mesh (20 x 40)
d. The third load step
b. The first load step
e. The fourth load step
c. The second load step
f. The fifth load step

Figure 1.49. The 4I' pattern of localization of deformation in the unconfined compression simulation (H/2G = -0.05, number of substeps = 3)

The fourth experiment gave a pattern of localizations called 2I pattern. The number of loading substeps used for this pattern is eight. From Figure 1.50 it is seen that the 2I pattern is formed by two sets of two fully developed I-shape shear bands. Totally there are nine blocks in the plate formed by this pattern. Two triangles near the central edge of the plate are almost diminished in this particular case. It is noted that, even in the sixth load step, the center of the plate has very limited deformation. Therefore, the formation of all the shear bands in this case may be caused by the influence of the constrained ends only. The angle of the shear bands with respect to the horizontal is found to be 44.1 degrees in Figure 1.50.e.

The fifth experiment produced a pattern of localizations called 3I pattern. The number of loading substeps used for this pattern is five. From Figure 1.51 it is seen that the 3I pattern is formed by two sets of three I-shape shear bands. It is to be noted that 3I pattern is formed gradually. From Figure 1.51.d it is seen that a 2I pattern is formed first in the third load step. Then the 3I pattern is formed in the fourth load step (see Figure 1.50.e). Totally there are sixteen blocks in the plate formed by the 3I pattern. The angle of the shear bands with respect to the horizontal is found to be 45.1 degrees in Figure 1.51.e.

The sixth experiment provided a pattern of localizations called 2X pattern. The number of loading substeps used for this pattern is 10. From Figure 1.52 it is seen that the 2X pattern is formed by two X-shape shear bands near the center of the plate. Perhaps the shear bands in this pattern are caused by the propagation of the localized deformations near the center of the plate. From Figure 1.52.c it is seen that two X-shape shear bands near the center of the plate have been formed. These two X-shape shear bands form a central diamond and two triangles. From Figure 1.52.d it is revealed that the intensity of the shear bands is increased with the increase in the number of load steps. However, these shear bands do not further propagate to form other types of shear bands. The angle of the shear bands with respect to the horizontal is found to be 48.3 degrees in Figure 1.52.d.

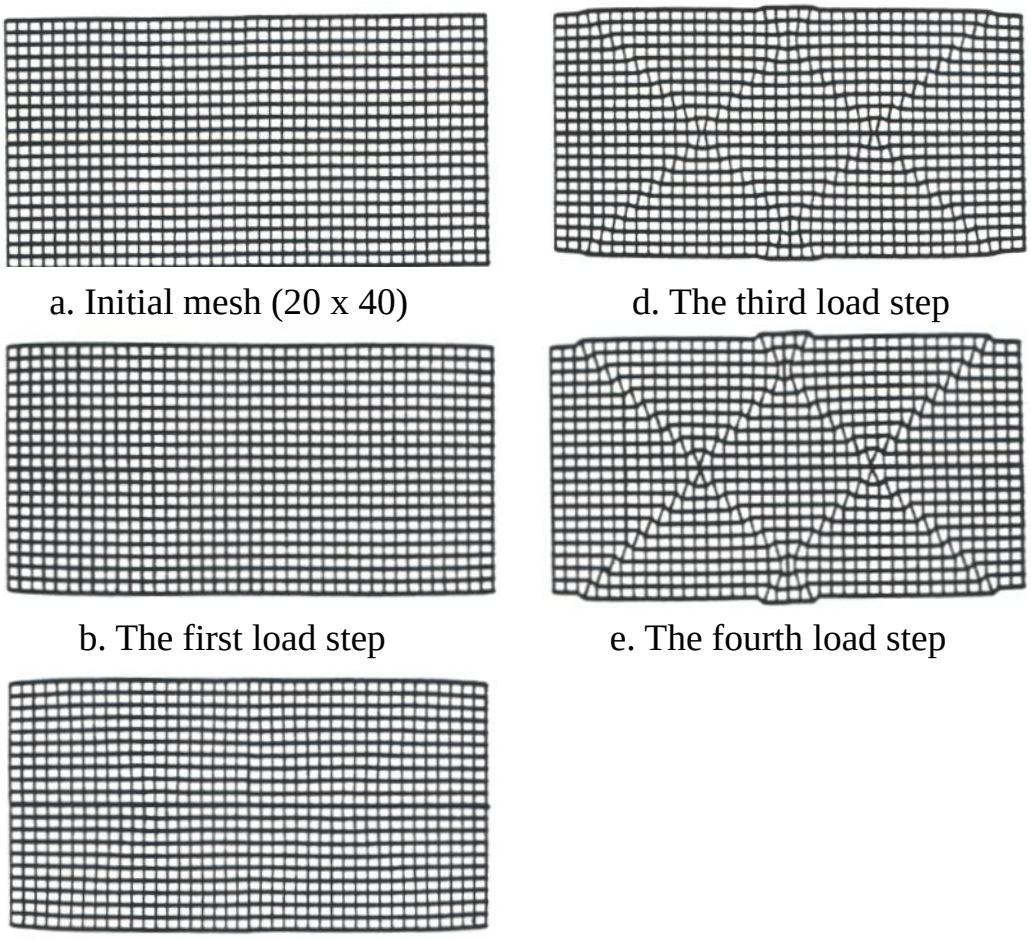

a. Initial mesh (20 x 40)

b. The first load step

c. The second load step

d. The third load step

e. The fourth load step

Figure 1.50. The 2I pattern of localization of deformation in the unconfined compression simulation (H/2G = -0.05, number of substeps = 8)

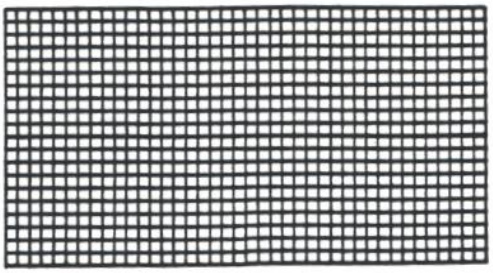

a. Initial mesh (20 x 40)

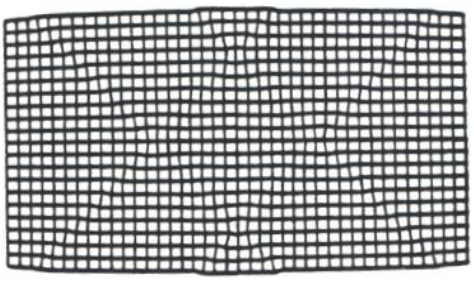

d. The third load step

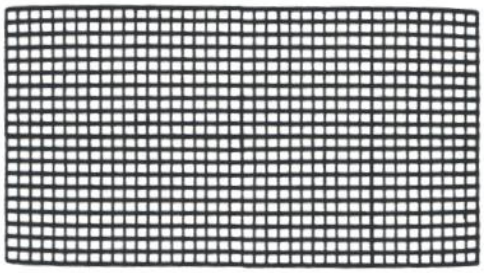

b. The first load step

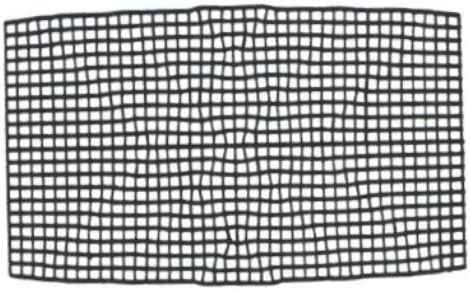

e. The fourth load step

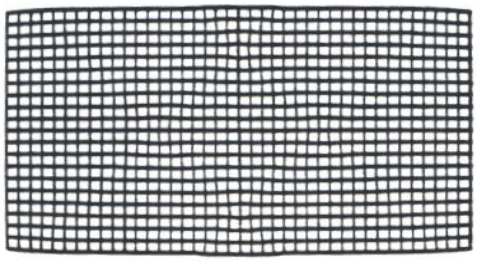

c. The second load step

Figure 1.51. The 3I pattern of localization of deformation in the unconfined compression simulation (H/2G = -0.05, number of substeps = 5)

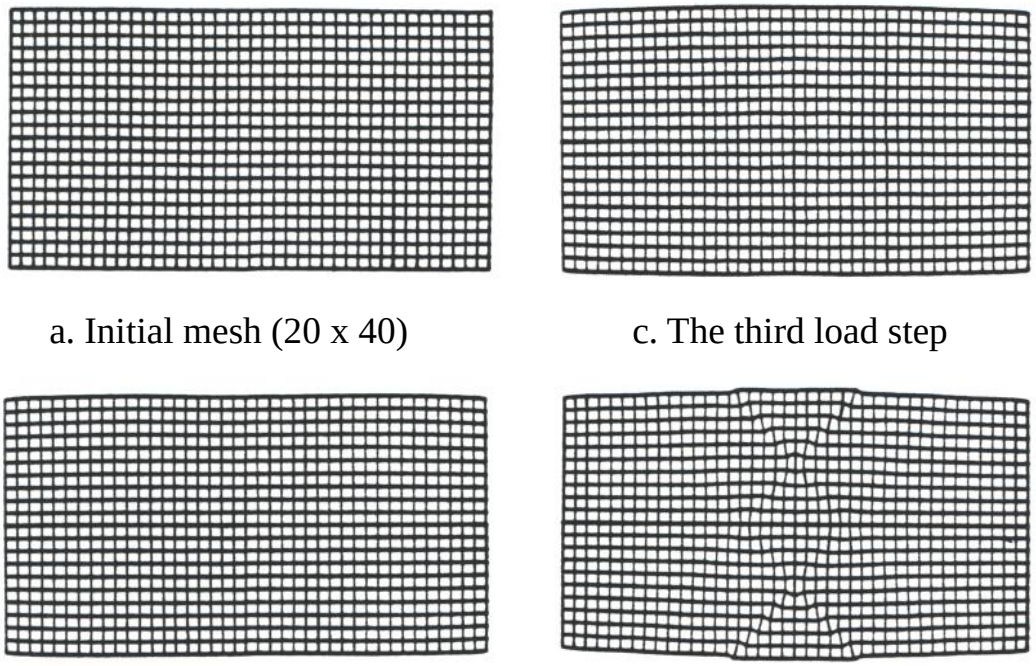

a. Initial mesh (20 x 40) c. The third load step

b. The first load step d. The fourth load step

Figure 1.52. The 2X pattern of localization of deformation in the unconfined compression simulation (H/2G = -0.05, number of substeps = 10)

Experiments with H/2G Equal to Zero. It is generally observed that the behavior of the localization under this condition is similar to that obtained from the tension simulation. The only difference is that, instead of necking, a non-uniform bulging near the center of the plate generally causes the localizations in the compression simulation. There are four cases to be studied in this section. These are: the 20 x 40 uniform mesh, the 24 x 48 uniform mesh, the 24 x 52 non-uniform mesh, and the 20 x 40 refined mesh. For all of the cases studied under this condition, the number of substep used is 3. From Figures 1.53 to 1.56 it is seen that the mesh keep on bulging at the center portion of the plate when the number of load steps is increased. It is to be noted that the X-shape shear band can be seen clearly in a deformed mesh only after the fourth load step. It means that the localizations under this condition is clearly formed only after the stresses are deep into the plastic range. This clearly indicates that the intensity of the localized deformations is increased slowly with the increase in the number of the load steps. The

results from the 20 x 40 refined mesh show that the selective refinement of a mesh does not improve the formation of the localization. It is to be pointed out that localizations do not further propagate to form other types of shear bands. The angle of the shear bands with respect to the horizontal is found to be 45.9 degrees in Figure 1.53.f, 45.2 degrees in Figure 1.54.f, 45.4 degrees in Figure 1.55.f, and 45.9 degrees in Figure 1.56.f.

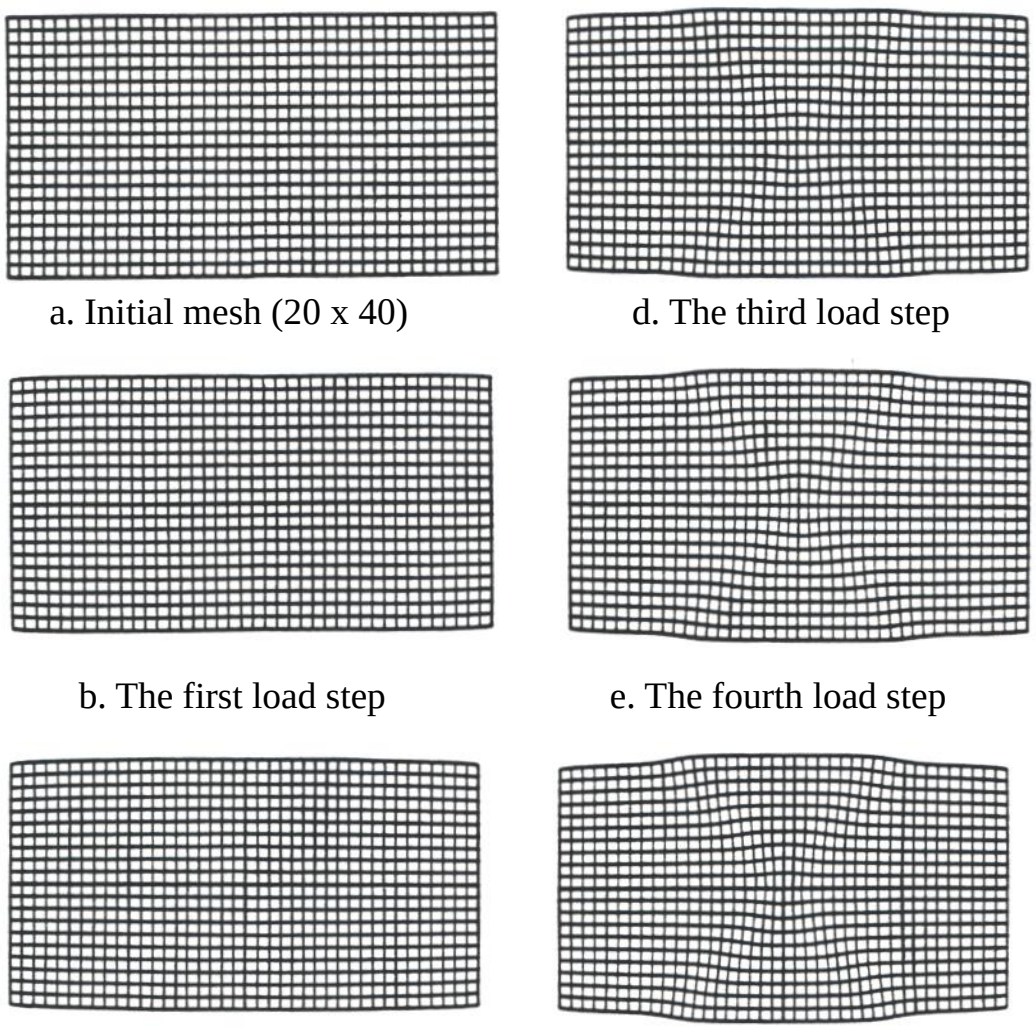

a. Initial mesh (20 x 40)

b. The first load step

c. The second load step

d. The third load step

e. The fourth load step

f. The fifth load step

Figure 1.53. The X pattern of localization of deformation in the unconfined compression simulation (H/2G = 0.0, number of substeps = 3)

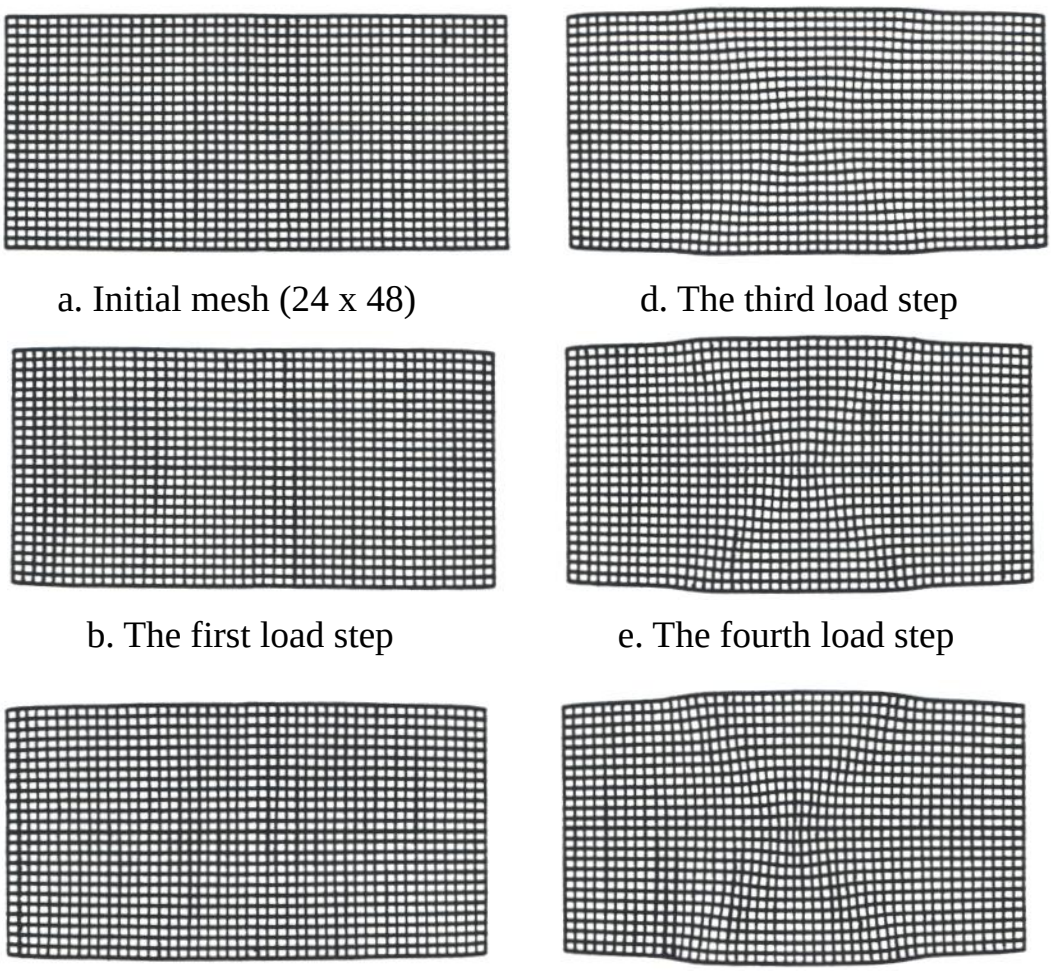

a. Initial mesh (24 x 48)

d. The third load step

b. The first load step

e. The fourth load step

c. The second load step

f. The fifth load step

Figure 1.54. The X pattern of localization of deformation
in the unconfined compression simulation
(H/2G = 0.0, number of substeps = 3)

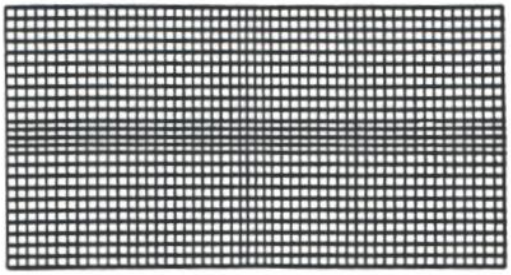

a. Initial mesh (24 x 52)

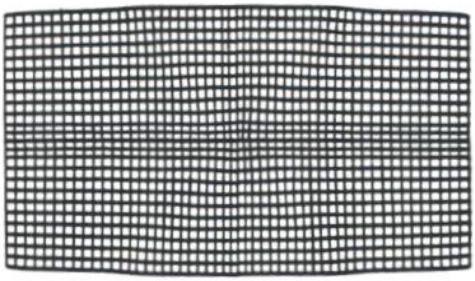

d. The third load step

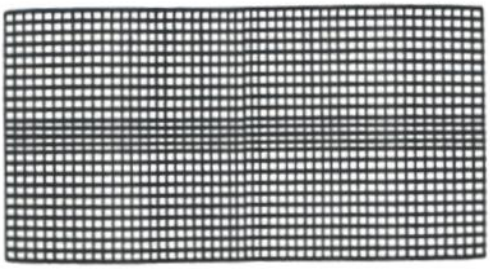

b. The first load step

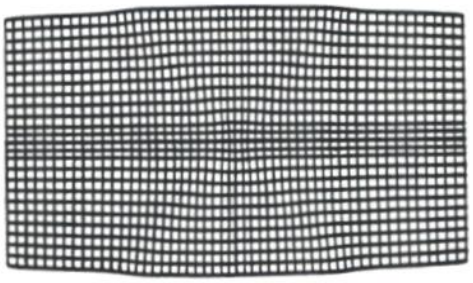

e. The fourth load dtep

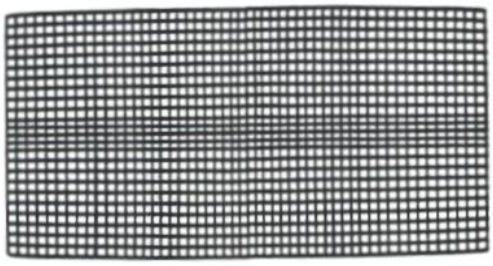

c. The second load step

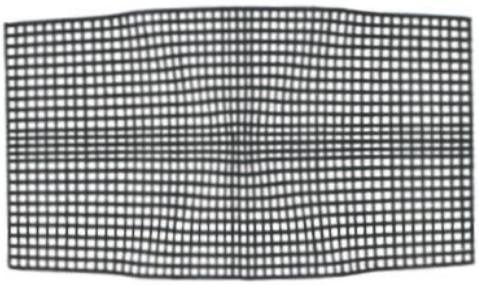

f. The fifth load step

Figure 1.55. The X pattern of localization of deformation in the unconfined compression simulation (H/2G = 0.0, number of substeps = 3)

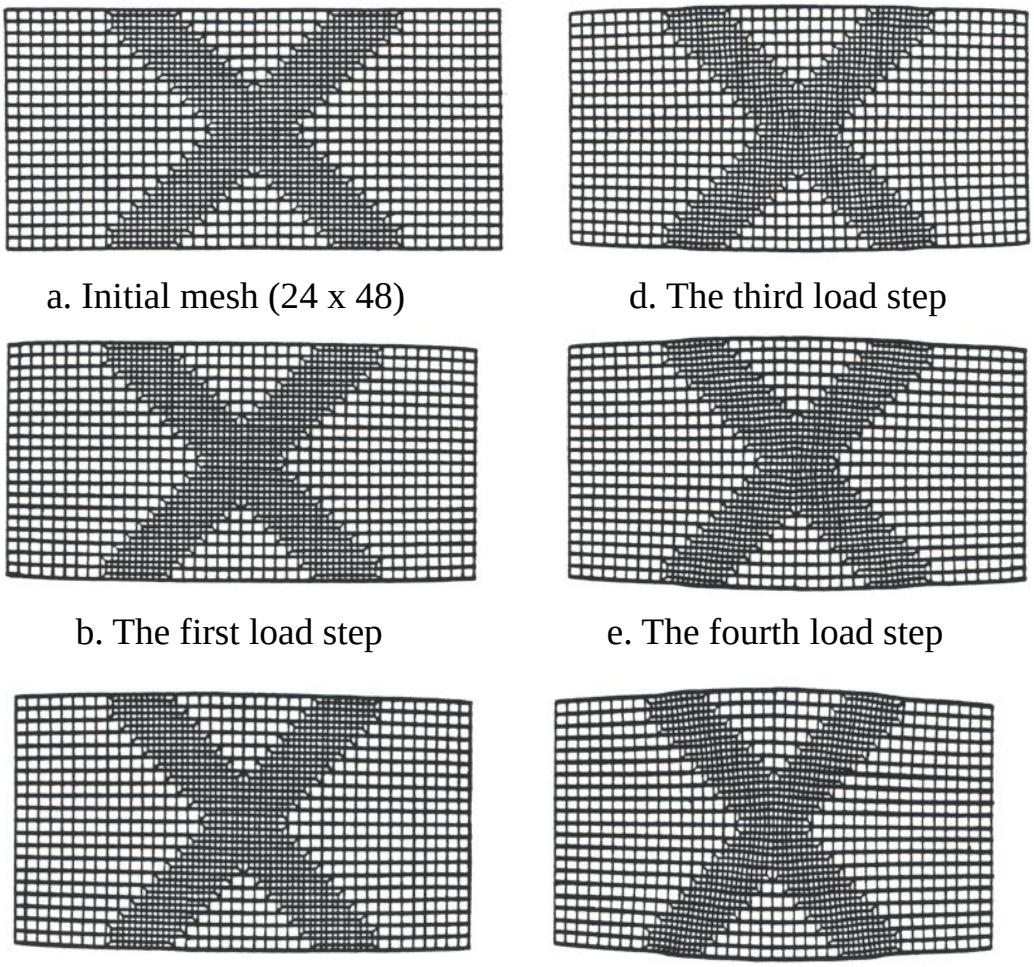

a. Initial mesh (24 x 48)

b. The first load step

c. The second load step

d. The third load step

e. The fourth load step

f. The fifth load step

Figure 1.56. The X pattern of localization of deformation in the unconfined compression simulation (H/2G = 0.0, number of substeps = 3)

1.4.3 Some Factors Influencing the Behavior of Localization

The pattern of localization, which is served as a reference in this chapter, is shown in Figure 1.57. In Figure 1.57.a the deformed mesh is shown to illustrate the pattern of shear bands. Figure 1.57.b shows the velocity vectors for the corresponding localization step. From inspection of these figures it can be seen that the quarter plate develops into a four-piece mechanism separated by groups of elements aligned along line segments ab, bc, and cd which are shown in Figure 1.57.c. It is noted that there appears to be no direct relationship between strain energy density contours for the elastic loading (see Figure 1.36) and the location of the shear bands. An optimum mesh for the initial elastic loading would be far from optimum for the localization condition.

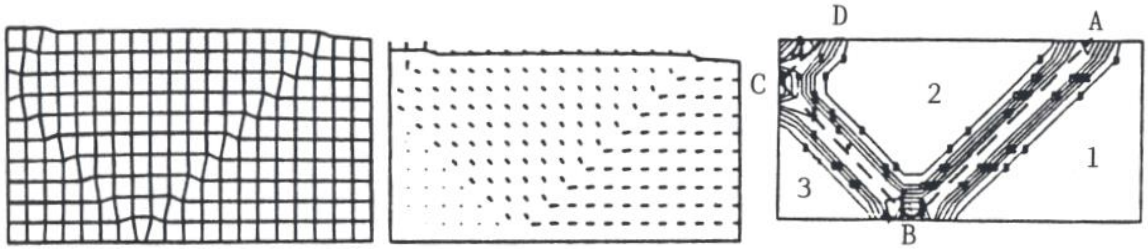

a. Deformed mesh b. Velocity vectors c. SED contours

Figure 1.57. Reference of Localization Pattern in Plate Problem

Influence of Mesh Refinement. Figure 1.58 compares results for mesh refinements consisting of uniform square elements in arrays of 10 x 20, 12 x 24, and 15 x 30 respectively. In all cases shown, the load step has been broken into three substeps. It can be seen that the coarse 10 x 20 mesh produces the clearest pattern of localization displaying the complete formation of the localization pattern shown in Figure 1.57. The finer meshes tended to display a less well develop pattern with neither of the fine meshes breaking into the complete four-piece mechanism.

It is well known that, for a displacement formulation, the finite element approximation is always stiffer than the actual structure and that a structure made up of course elements is stiffer than one with fine elements when elastic material properties are used. From Figure 1.58, numerical results

reveal that a coarse element tends to behave like more brittle materials in strain softening range. Therefore, it can be deduced that the finite element discretization makes a coarse mesh become hard to deform in elastic range but easier to deform in strain softening range. The above phenomenon clearly indicates that too fine a mesh cannot have the clearest pattern of localization of deformation for a particular load step. On the other hand, since a shear band is generally found in a narrow zone, too coarse a mesh may generally be not as good to simulate a shear band. Therefore, the best course to be adopted is to use a uniform mesh of 'medium' size for shear band formation.

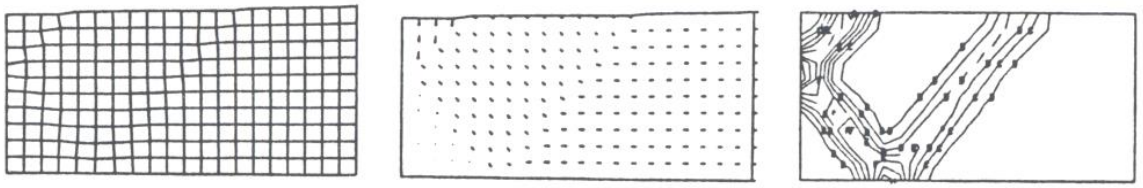

a. 10 x 20 mesh

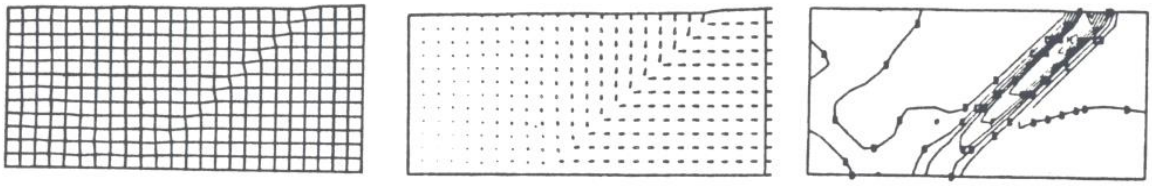

b. 12 x 24 mesh

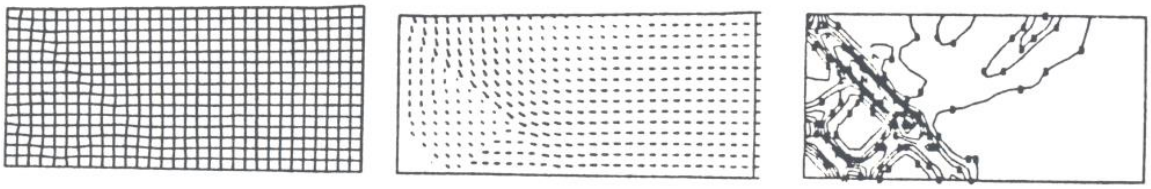

c. 15 x 30 mesh

Figure 1.58. Performance at different refinement levels

(3 Substeps used)

Mesh refinement can be done by placing more nodal degrees of freedom in elements instead of reducing the size of the elements. Such problem has been examined by Sengupta and Saxena (1987) for a plate of the same material properties as used in this research, however, an elastic visco-plastic formulation was adopted. The results for the four-node, the eight-node, and nine-node elements are reproduced and showed in Figure 1.59, 1.60, and 1.61 respectively. It is to be noted that the localization is much less sensitive to this type of mesh refinement. But as Sengupta and Saxena concluded, the most pronounced localization is obtained from the mesh with four-node elements. This clearly indicates that mesh refinement by providing more degrees of freedom in elements is just doing overkill. This phenomenon is similar to the one obtained previously for the mesh refinement by reducing the size of the elements. If such result is true, then the method proposed by Bazant (1984) as that mentioned in Chapter III will not be effective in localization analyses for the plate problem.

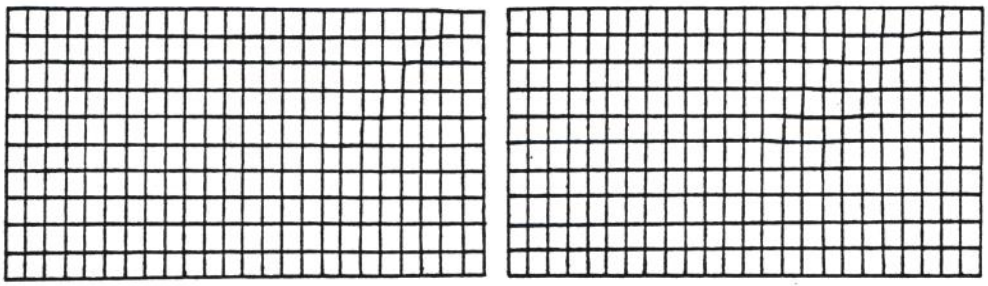

1*

2

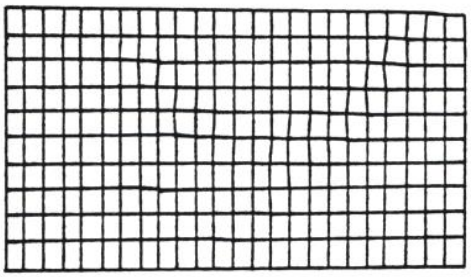

3

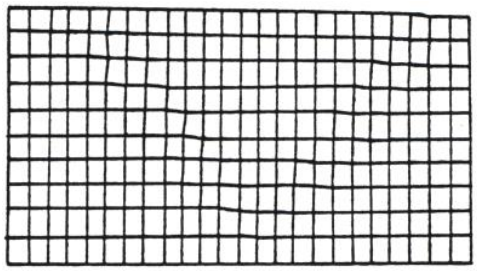

4

*: Number of the Load Step

Figure 1.59. Localization of deformation of the plate for the four-node element (From Sengupta and Saxena, 1987)

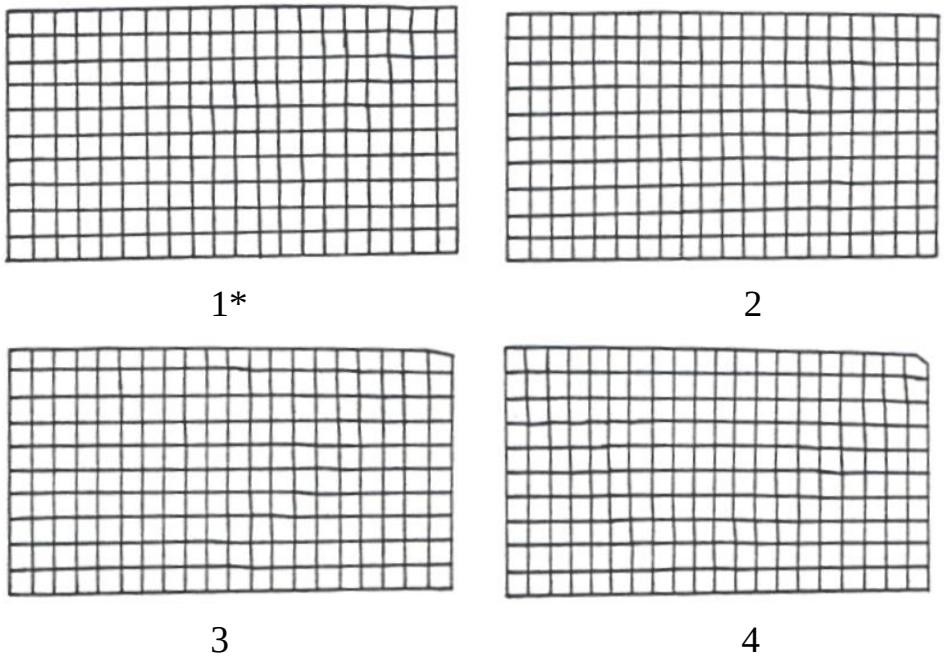

*: Number of the load step

Figure 1.60. Localization of deformation of the plate for the eight-node element (From Sengupta and Saxena, 1987)

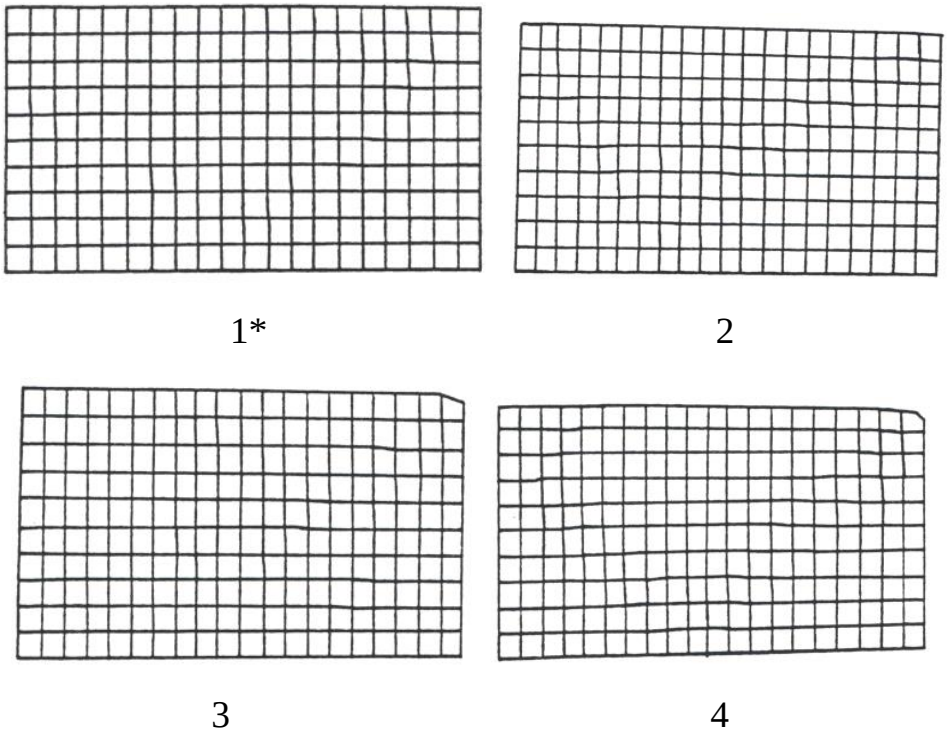

*: Number of the load step

Figure 1.61. Localization of deformation of the plate for the nine-node element (From Sengupta and Saxena, 1987)

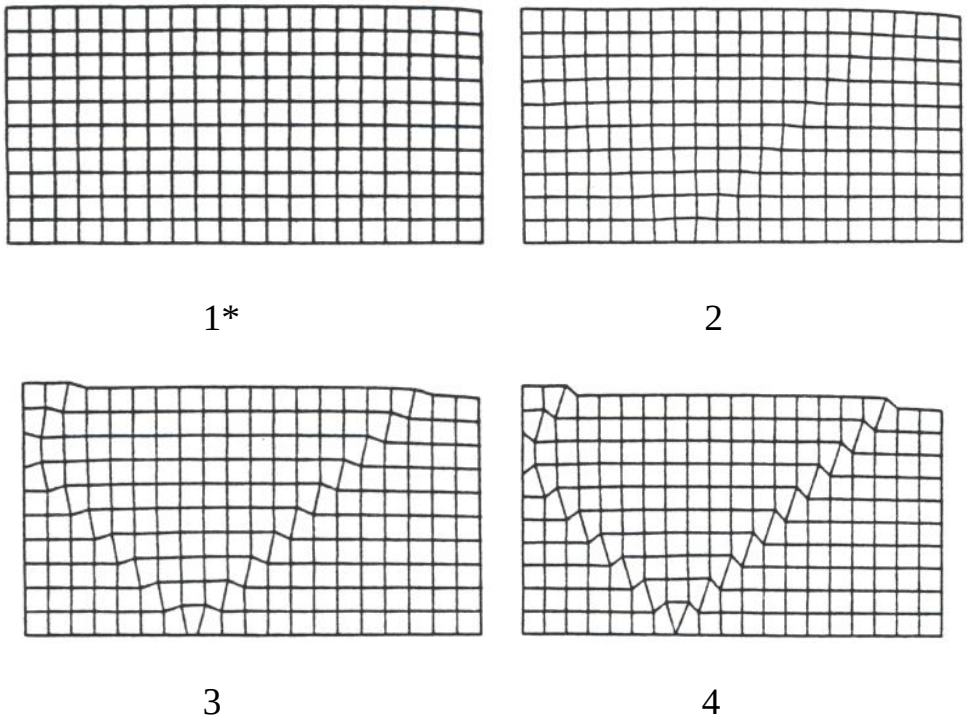

*: Number of the load step

Figure 1.62. Localization of deformation of the plate for the five-node element

The results of the same problem from this research are shown in Figure 1.63. In which the quadrilateral element with a central node is used. As compared with Figures 1.60, 1.61 and 1.62, it is found that the localization is much more pronounced in Figure 1.63. It may therefore deduced that the quadrilateral element made up of four triangular sub-elements; formed by the two diagonals of the quadrilateral, may be the best element to be used in the localization analysis. The reasons for such kind of element to become significant in localization analyses are

(1) A grid which consists of such kind of elements can accommodate isochoric deformations (Nagtegaal et al., 1974). Such a feature is important since the plastic strain rate is volume preserving in many of the constitutive relations used in localization analyses (Needleman and Tvergaard, 1983).

(2) For each quadrilateral, static condensation is employed to eliminate the nodal degrees of freedom associated with the central node. This

allows the overall solution time not to exceed that for four-node element.

(3) It can resolve bands of highly localized straining (Needleman and Tvergaard, 1983).

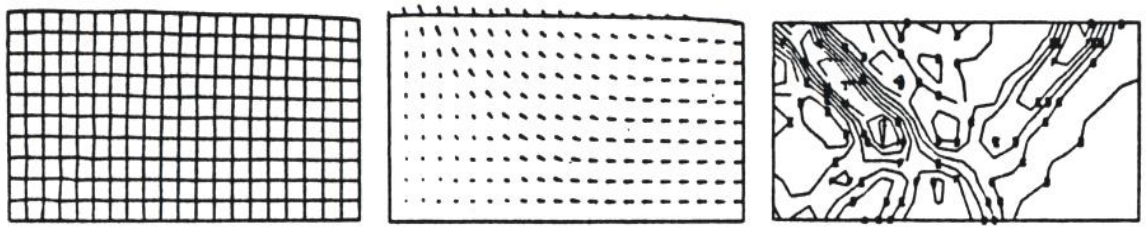

a. 3 Substeps of load increment

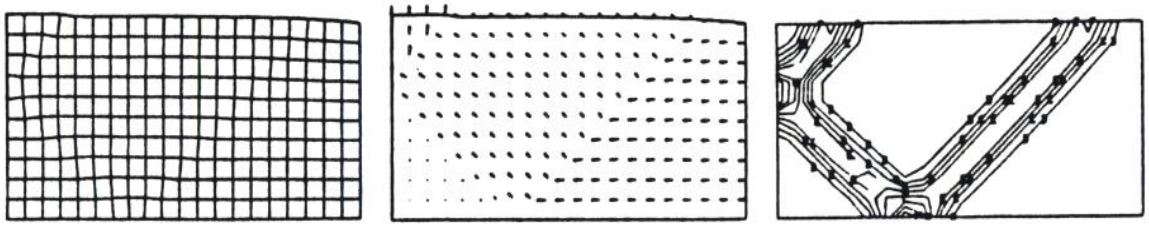

b. 5 Substeps of load increment

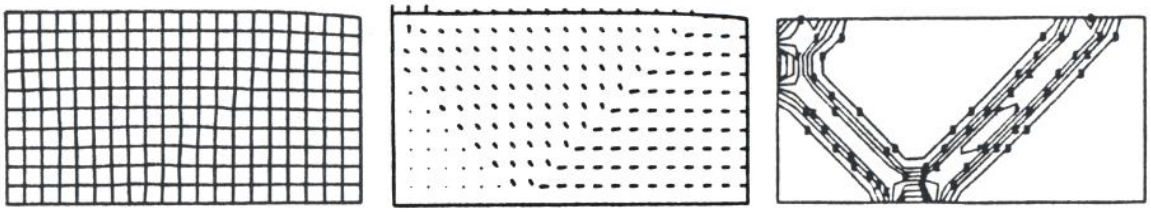

c. 8 Substeps of Load Increment

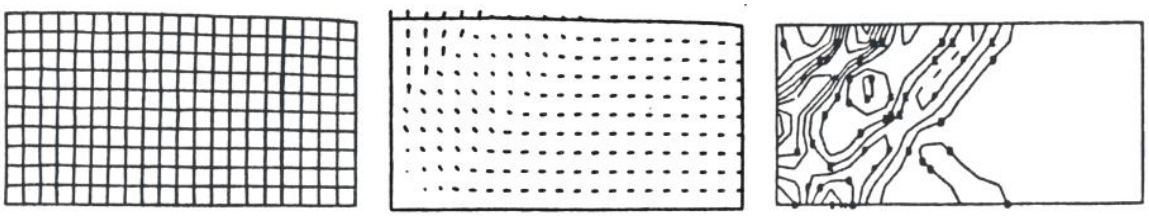

d. 10 Substeps of load increment

Figure 1.63. Performance using different substep sizes of load increment

Influence of Substep Size of Load Increment. Results of the 10 x 20 mesh using 3, 5, 8, and 10 substeps of load increment are compared in Figure 1.64. It is seen that localizations are clearly developed when 5 and 8 substeps are used; but they are not clearly developed when 3 and 10 substeps

are used. Although the four-piece mechanism in Figures 1.64.b and 1.64.c looks like equally developed, but the maximum strain energy density is 0.1616 psi in Figure 1.64.b and 0.1086 psi in Figure 1.64.c. Therefore it is clear that the four-piece mechanism is developed better when using 5 substeps than when using 8 substeps. The deformed mesh of Figures 1.64.b and 1.64.c also supports this conclusion. From the above observation it may be deduced that there is an optimum substep size of load increment which is between 4 and 7 substeps in this particular case.

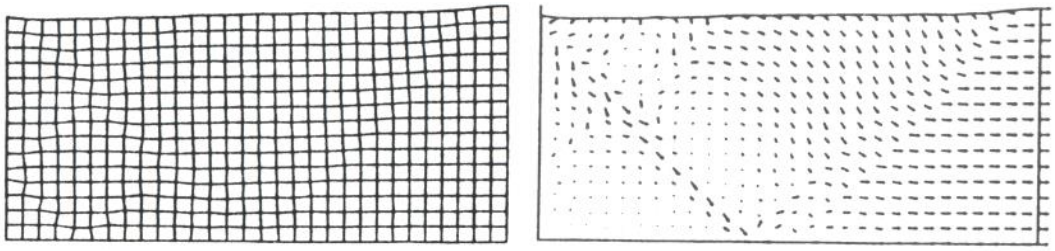

a. Stable solution for the fourth load step (10 substeps used)

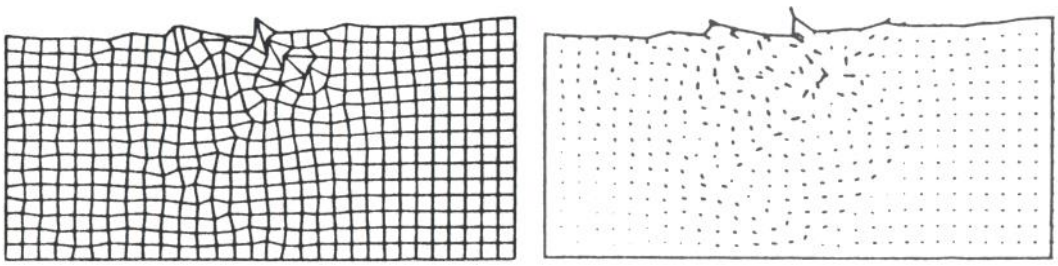

b. Near critical solution for the fifth load step (10 substeps used)

Figure 1.64. A near critical condition of the incremental finite element solutions in localization analyses

Based on the incremental finite element scheme, it is pointed out that smaller load increments normally give better solutions. However, the physical meaning of the change of the substep size of load increment is the change of the load rate (related to wave propagation). The propagation of localizations can be caused by the propagation of the plastic wave due to the incremental damage energy; where the incremental damage energy due to strain softening depends on the rate of the load. The smaller the rate of load application, the larger the length of the plastic wave will be. If the length of a plastic wave is equal to the length of the elements, a critical condition will occur. Such critical condition has been obtained several times during this research and one of the examples is shown in Figure 1.65. Therefore, based on the physical meaning of the substep size of load increment, it may be

pointed out that too small a load increment may lead to a critical condition. A substep size of load increment cannot be either too large or too small. However, there exists an optimum step which in this research had been obtained only by trial and error.

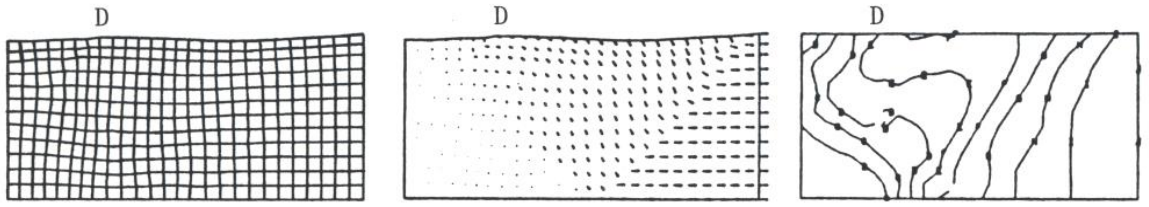

The third load step

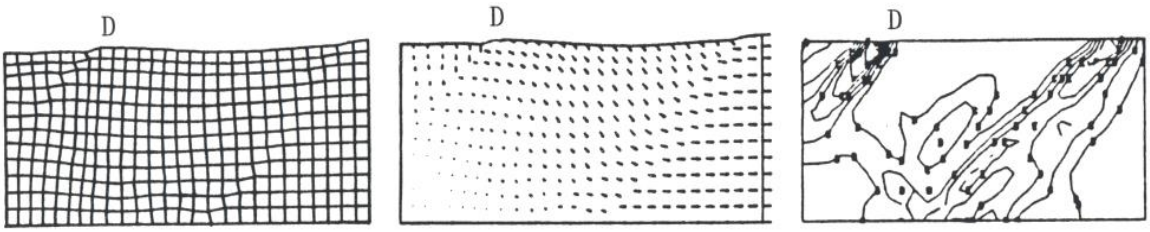

The fourth load step

a. Half-size elements at outer edge of the plate

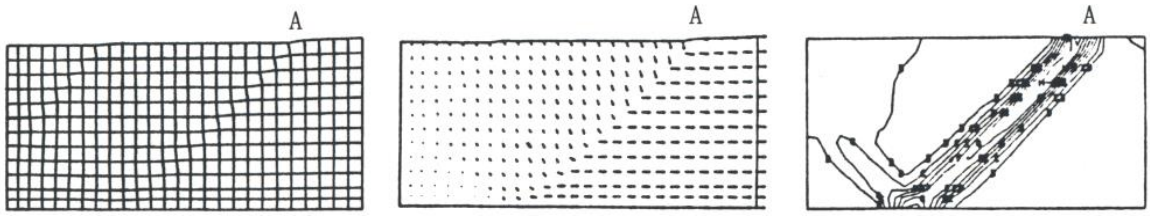

The third load step

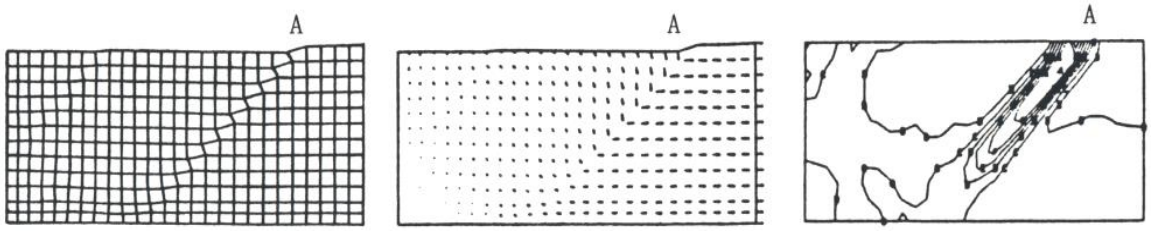

The fourth load step

b. Half-size elements near the centerlines of the plate

Figure 1.65. Performance using different mesh details (3 substeps used)

Influence of Mesh Details. Two nearly identical meshes are compared in Figure 1.66. The mesh in Figure 1.66.a has two rows of half-size elements at the outer edge of the plate and two columns of half-size elements near the point 'D' in Figure 1.66.a. The mesh in Figure 1.66.b has two rows and two columns of half-size elements near the centerlines of the plate. It was generally observed that shear bands propagated from a source point--'D' in Figure 1.66.a and 'A' in Figure 1.66.b--located at the plate boundary. Segments cd and ab are fully developed in Figures 1.66.a and 1.66.b respectively. Therefore with the same amount of prescribed deformation, the mesh with half-size elements near the centerlines of the plate exhibits more detrimental behavior (i.e. more deformation in a region). The strain energy density contours suggest that the presence of the half-size elements retards the development of localization. Above results reveal again that coarse elements tend to exhibit more 'brittle' behavior than small elements. This provides a clue for the small elements to have a tendency to retard the development of localization.

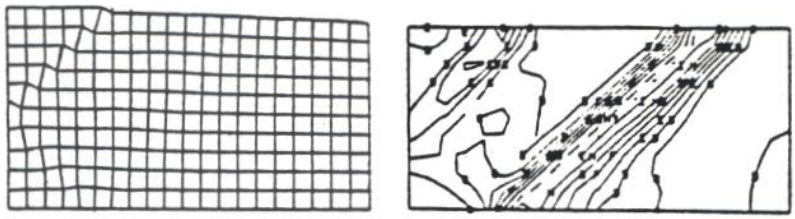

a. Unrefined mesh

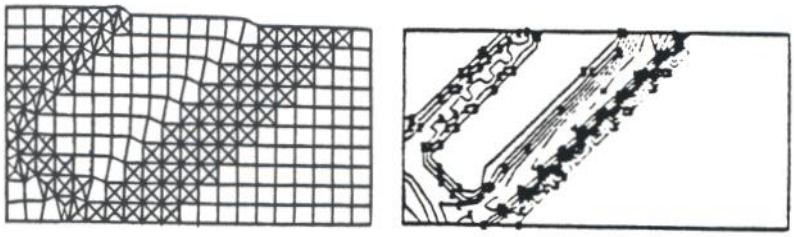

b. Refinement along path observed in Figure 5.9.a

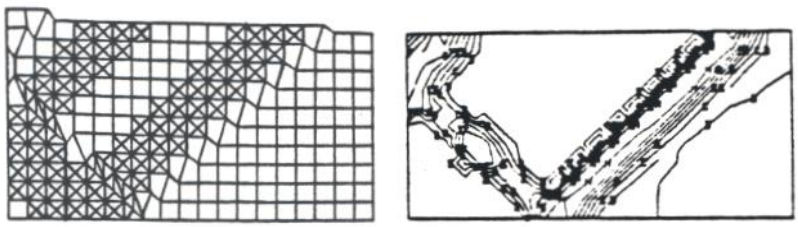

c. Refinement along path observed in Figure 5.9.b

Figure 1.66. Influence of selective refinement along shear band path (10 substeps used)

Influence of Selective Refinement. The sequence in Figure 1.67 illustrates an attempt to selectively refine the mesh to better capture the localization. It was assumed that by placing a greater number of degrees of freedom in the path of the propagation shear band the large strain gradients associated with the banding could be represented better. The result, shown in Figure 1.67.b, was to move the band from its original path to the group of elements immediately next to the refined region. Again, moving the refined region to the 'improved' prediction of the shear band location moves the band to the adjacent group of coarse elements.

It is important to recognize that the refinement shown in Figure 1.67 does not constitute an optimized mesh. The selective refinement makes the refined elements behave like less brittle materials than the unrefined elements. From Figures 1.67.b and 1.67.c it is seen that shear bands in the whole plate always follow a path with the maximum dissipative energy.

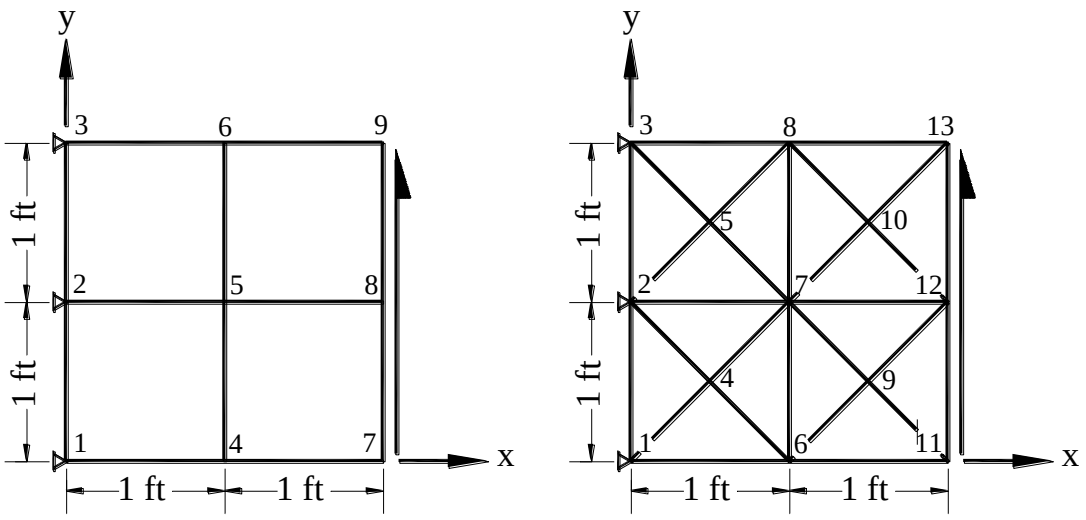

a. Quadrilateral elements b. Triangular elements

Figure 1.67. Two different types of elements in finite element methods

From a relatively simple problem shown in Figure 1.68 and Table 1.5 it is seen that to refine a coarse quadrilateral element into four triangular elements seems to retard the development of plastic strain. The reason is that even the elastic deformation for a refined mesh is smaller than that of the coarser (unrefined) mesh. This may be yet another reason for the movement of the location of the localizations.

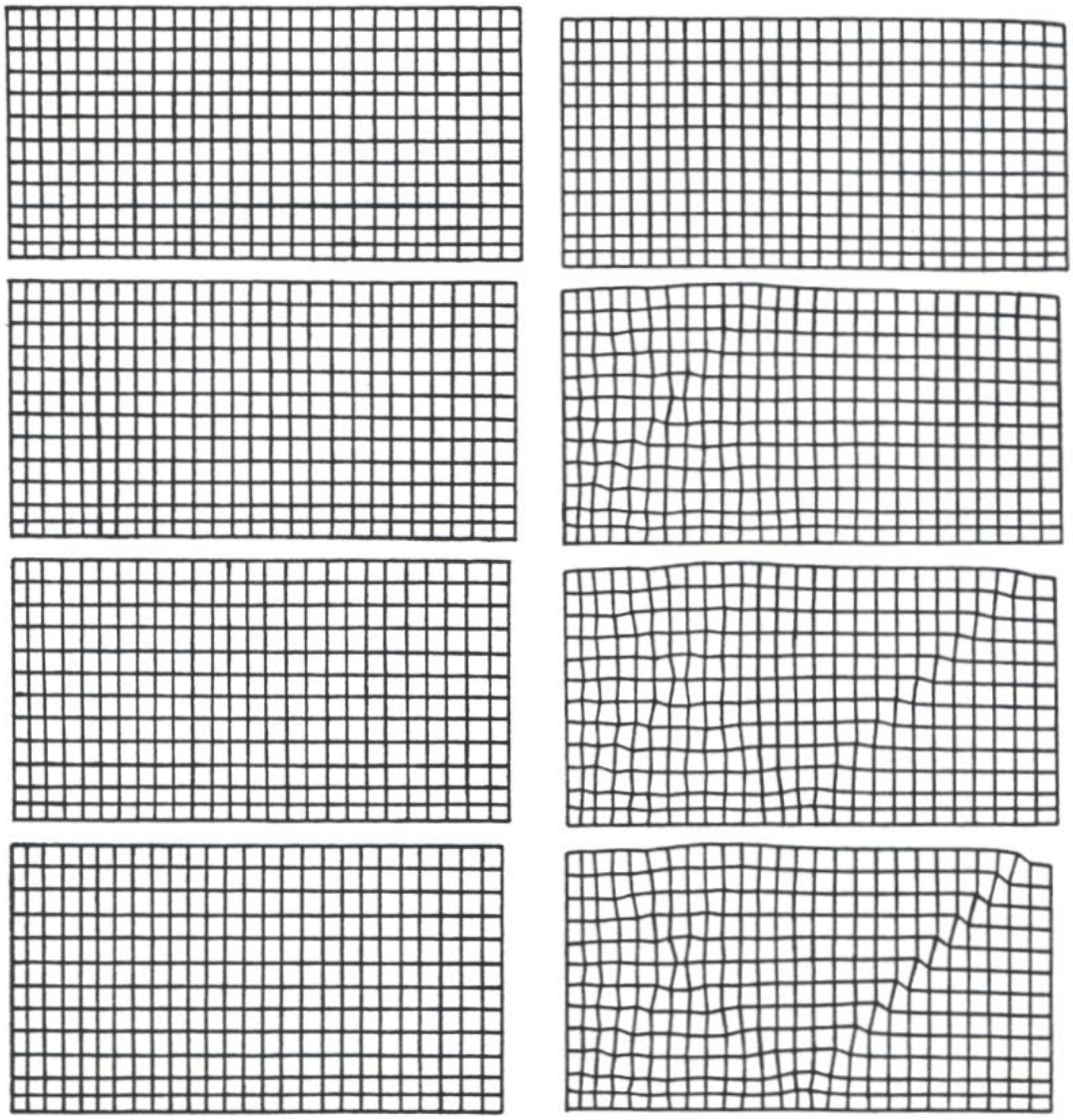

a. Free ends b. Fixed ends

Figure 1.68. Influence of boundary conditions and material properties (Uniform material with H/2G = -0.05 used)

Table 1.5. Finite element solutions for different types of elements in Figure 1.67 ($E = 100000\ psf$, $\nu = 0.49$, the pressure applied is 3000psf)

Node* Number	x Displ., (ft)	Y Displ., (ft)	Node@ Number	x Displ., (ft)	y Displ., (ft)
1	0.00000	0.00000	1	0.00000	0.00000
2	0.00000	0.00000	2	0.00000	0.00000
3	0.00000	0.00000	3	0.00000	0.00000
4	0.06086	0.14684	4	0.00214	0.04518
5	0.00000	0.09282	5	-0.00214	0.04518
6	-0.06086	0.14684	6	0.05010	0.13606
7	0.10943	0.29147	7	0.00000	0.09285
8	0.00000	0.29729	8	-0.05010	0.13606
9	-0.10943	0.29147	9	0.04627	0.18463
			10	-0.04627	0.18463
			11	0.09411	0.27631
			12	0.00000	0.27561
			13	-0.09411	0.27631

* Quadrilateral elements in Figure 1.67.

@ Triangular Elements in Figure 1.67.

From the above it is to be concluded that a selective refinement could force a localization of deformation along an artificial path. Therefore, if a coarse mesh is made up of quadrilateral elements, it is suggested that a selective refinement as that shown in Figure 1.67 be avoided in a simulation of localizations.

1.4.4 Influence of Boundary Conditions and Material Properties

Uniform Material. When a uniform material is used for a plate problem, it is seen that if displacement in y direction is not restrained at the loaded ends (free ends), a uniform pattern of stress and strain will be obtained. Even if the stresses are far beyond the elastic range, no shear band is formed under such conditions (see Figure 1.69.a). On the other hand, if the displacement in y direction is restrained at the loaded ends (fixed ends), a

sufficient stress concentration near the loaded ends initiates localized deformations, and shear bands are therefore developed (see Figure 1.69.b).

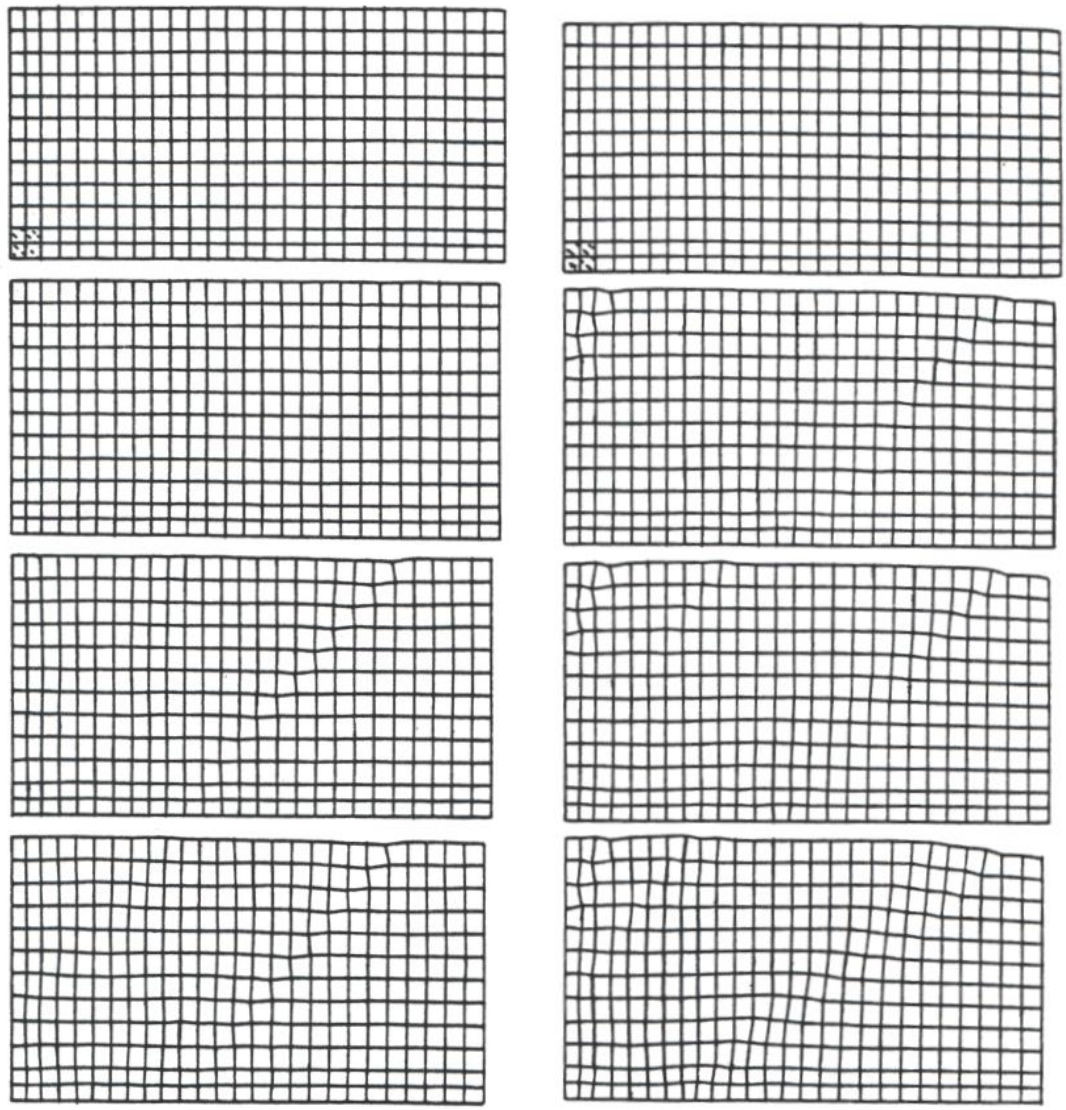

a. Free ends b. Fixed ends

Figure 1.69. Influence of boundary conditions and material properties (Nonuniform material with H/2G = -0.333 for the four center elements, and -0.05 for the rest of them)

Non-uniform Material. If a more brittle material is used at the center of the plate, from Figure 1.70 it is seen that shear bands are obtained for both free end and fixed end conditions. It means that the localized deformations caused by the non-uniform material are strong enough for the development of localizations. However, the localized deformations, which are caused by a combination of the conditions of non-uniform material and fixed ends, are more vivid in the first few load steps, and the difference becomes smaller with the increase in the load step (see Figure 1.70).

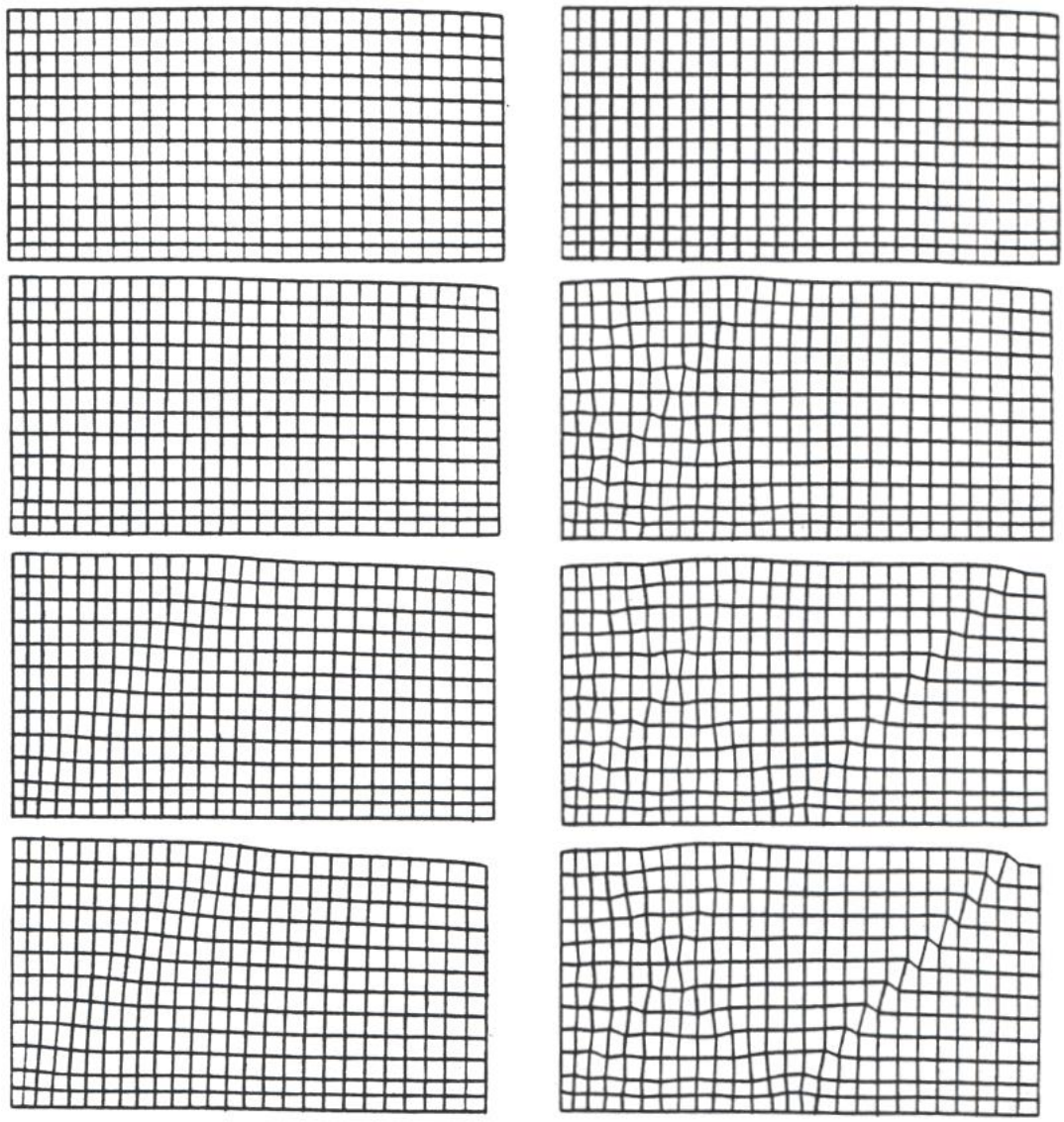

a. Free ends b. Fixed ends

Figure 1.70. Performance using different hardening parameters (Fixed ends used)

In conclusion it can be said that when uniform material properties are used for a plate problem, boundary conditions have great influence on the occurrence of the shear bands. On the other hand, when non-uniform material properties are used, the influence of the boundary conditions, such as localized deformations caused by the constraint of the loaded end in a plate, is limited to the vividness of the shear bands. Since shear bands can be obtained by using either non-uniform material properties or constrained boundary conditions, it is then concluded that a non-uniform material condition is not a sufficient condition for shear bands to occur.

Influence of the Hardening Parameter. From Figure 1.71.a it is seen that when hardening parameter is zero, shear bands are formed slowly with the increase in the prescribed deformation. These shear bands are formed due to continuous bulging (or continuous necking in tension condition) of the plate at its center portion by the loss of the ellipticity only. Therefore only one set of the shear bands is obtained.

From Figure 1.71.b it is seen that when the hardening parameter is less than zero, shear bands are formed immediately after the stresses are beyond elastic range. The formation of the shear bands associated with the damage energy due to strain softening makes it possible to have multiple sets of shear bands. The occurrence of the multiple sets of shear bands gives a way to increase the total incremental damage energy due to strain softening in a loading step. Thus it helps the total incremental potential energy to reach a minimum.

It is concluded that the pattern of shear band for a case with hardening parameter equal to zero is totally different from that of a case with hardening parameter less than zero. The former is caused by the loss of ellipticity while the later is caused by both the loss of ellipticity and the damage energy due to strain softening.

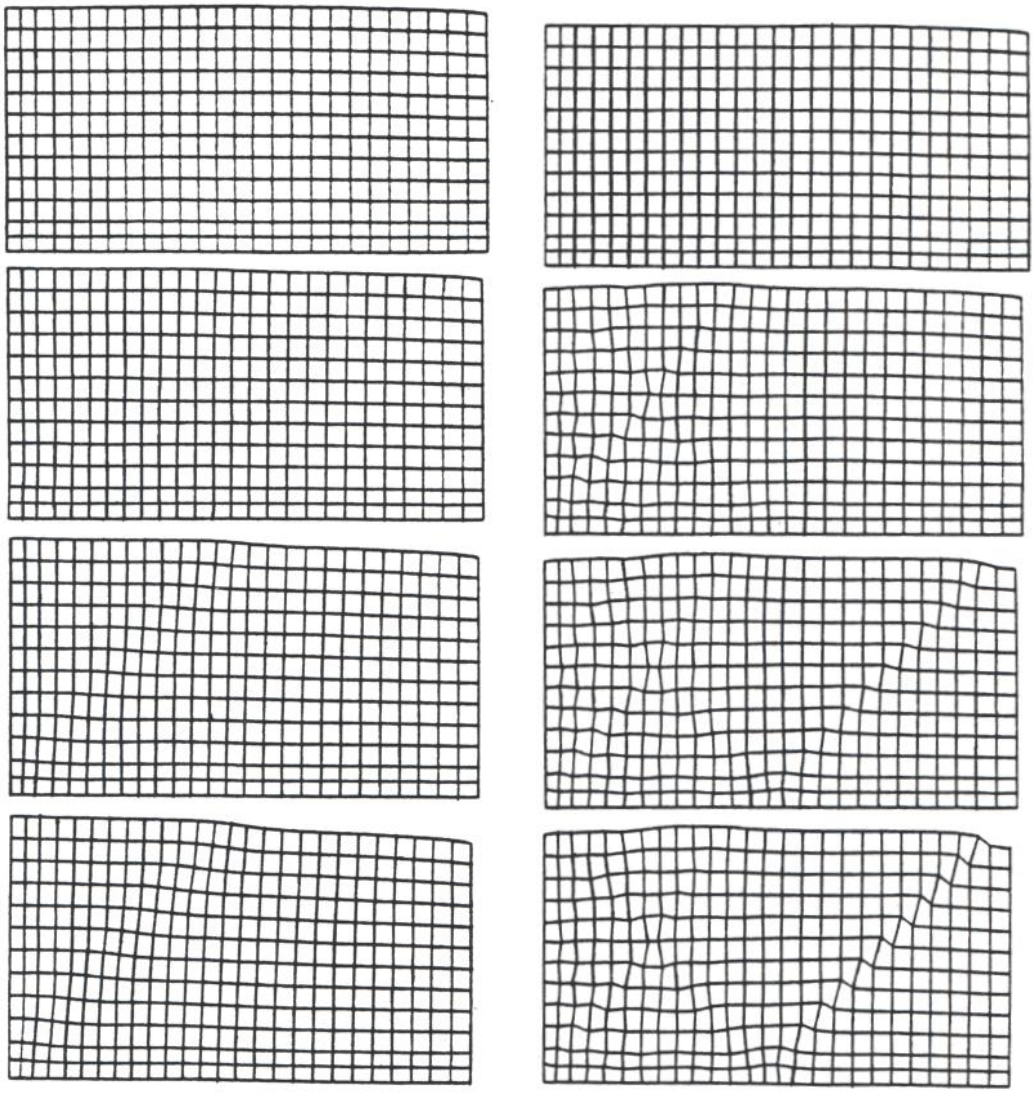

a. Free ends b. Fixed ends

Figure 1.71. Performance using different hardening parameters (Fixed ends used)

Influence of the Geometry. The influencing of the geometry of a element used in finite element methods has been illustrated in Figure 1.67. The results reveal that a quadrilateral element is more flexible to deform than a triangular element.

The change of the geometry of a structure, e.g. increasing the slope of an embankment, reducing the size of a footing, or varying the shape of a dam, certainly will change the intensity of non-uniform stresses. It is therefore deduced that the change of the geometry of a structure has great influence on the behavior of localization.

Influence of Loading Type. In 1981, Prevost and Hughes (1981) initiated a localized deformation from a homogeneous state by applying a non-uniform load at a corner of a plate. It is clearly indicated that non-uniform load can trigger a localization of deformation alone. Unfortunately most of soil structures, e.g. a slope under its body force, a footing under eccentric column load, and a dam under operating condition, are all suffering non-uniform loads. Since an inhomogeneous state exists in most of structures, it may be deduced that shear bands could form when the strength of foundation soils is lower than the stress applied.

Influence of Poisson's ratio. It can be seen from the figures in the study of the behavior of localization in the previous section of this chapter that shear bands may be formed a step earlier if the Poisson's ratio is very close to 0.5. Therefore shear bands can be obtained relatively easier in undrained condition than in drained condition. In Table 1.3 and 1.4, it also shows that the Poisson's ratio has certain influence on the orientation of the shear band. This clearly indicates that the compressibility of the material in elastic range has something to do with the instability condition of a material.

1.4.5 Some Factors Influencing the Orientation of Shear Bands

The theoretical solutions for the orientation of shear bands can be obtained from the bifurcation analysis in Chapter II. By comparing the theoretical results with those listed in Table 1.3 and 1.4, it is found that the mesh design, the number of loading substeps, and the compressibility of the material have certain influence on the orientation of the shear bands. More controlled numerical experiments are needed to identify the specific influence from each individual factor. However, it is seen from the cases of H/2G equal to zero, and the Poisson's ratios equal to 0.3 and 0.49 that the mesh design seems to have limited influence, but the compressibility of the material has certain influence on the orientation of the shear bands. This has been discussed previously in this chapter. If H/2G is equal to -0.05, for the same mesh and the same Poisson's ratio, there is a tendency for the influence of the number of loading substeps to become more significant when the number of loading substeps is increased from 3 to 8. Meanwhile the appearence of the half-size element at the edge of the element does show certain influence on the orientation of the shear bands in the case of H/2G equal to -0.05.

The behavior of localization in finite element analyses presented in this chapter gives a way to understand the failure mechanisms of structures. An investigation of failure mechanisms will be performed
in the following chapter.

1.5 An Investigation of Failure Mechanisms

Failure mechanisms have great influence on the stress-strain-strength behaviors of soils. If the failure mechanism is not captured in a numerical analysis, even a good agreement between the predicted and the actual stress-stain relationship does not necessarily mean good prediction, because it may happen due to compensating errors in individual steps or operations such as sampling, testing, and analysis (Hvorsev, 1969). This chapter evaluates the failure mechanisms in different laboratory tests, and then studies the mechanisms of localization.

1.5.1 Failure Mechanisms in Unconfined Compression Tests

Sample Preparations and Test Conditions. Two samples are compacted by using two-end compaction mold, and then saturated in a triaxial cell. The first sample, which is trimmed from a cylindrical sample, is tested under plane strain condition. The dimensions of the first sample are two inches in width, four inches in height, and one inch in thickness. The second sample is tested under axis-symmetric conditions. The dimensions of the second sample are 2.8-inch in diameter and 5.6-inch in height. Both the samples are made of kaolinite with moisture content of 38.4%, dry unit weight 82.4pcf, and degree of saturation being 100%. During the test, uniform vertical displacements are applied as a load. The rate of the load application is one percent of the vertical strain per minute. To constrain the horizontal displacements of the sample at both ends, 'Rubber Cement' glue is used. The failure mechanisms are studied through pictures of the deformed samples at different stress levels taken during the tests.

Performance of a Test under Plane Strain Conditions. The performance of the unconfined compression test under plane strain condition is shown in Figure 1.72. The stress-strain relationship from the test is shown in Figure 1.73. The initial conditions of the sample are shown in Figure 1.72.1. In Figure 1.72.6 one may observe a big diagonal shear band and

some other small shear bands near the bottom of the specimen. The diagonal shear band initiates as two parallel bands due to eccentric forces and then are forced to join each other with the increase of load as shown in Figure 1.72.3. The inclination of the shear bands is subjected to change. From Figures 1.72.3 to 1.72.6 it is seen that the variation of the angle is from 48 degrees to 53 degrees with respect to the horizontal. A theoretical bifurcation analysis will provide a value of the angle of the shear bands to be 40.39 degrees or 49.61 degrees with respect to the horizontal for H/2G equal to -0.05. It is therefore deduced that the difference between the test result and the theoretical values for the angle of shear bands is not too large. Such small difference could be attributed to frictional dilatancy of the material. Other shear bands near the bottom of the sample (see Figure 1.72.4) indicate that the inverse V-shape shear bands (also shown in Figure 1.49) can occur in the real life. From Figures 1.72 and 1.73, it may be noted that shear bands can be observed right after the stress is beyond the peak stress, and that shear bands are formed gradually. The shear bands tend to become more symmetric with the increase in the vertical displacement. The deformed meshes and the stress-strain curve of the sample indicate that the wavy post-peak stress-strain curve may be caused by the appearance of the second diagonal shear band.

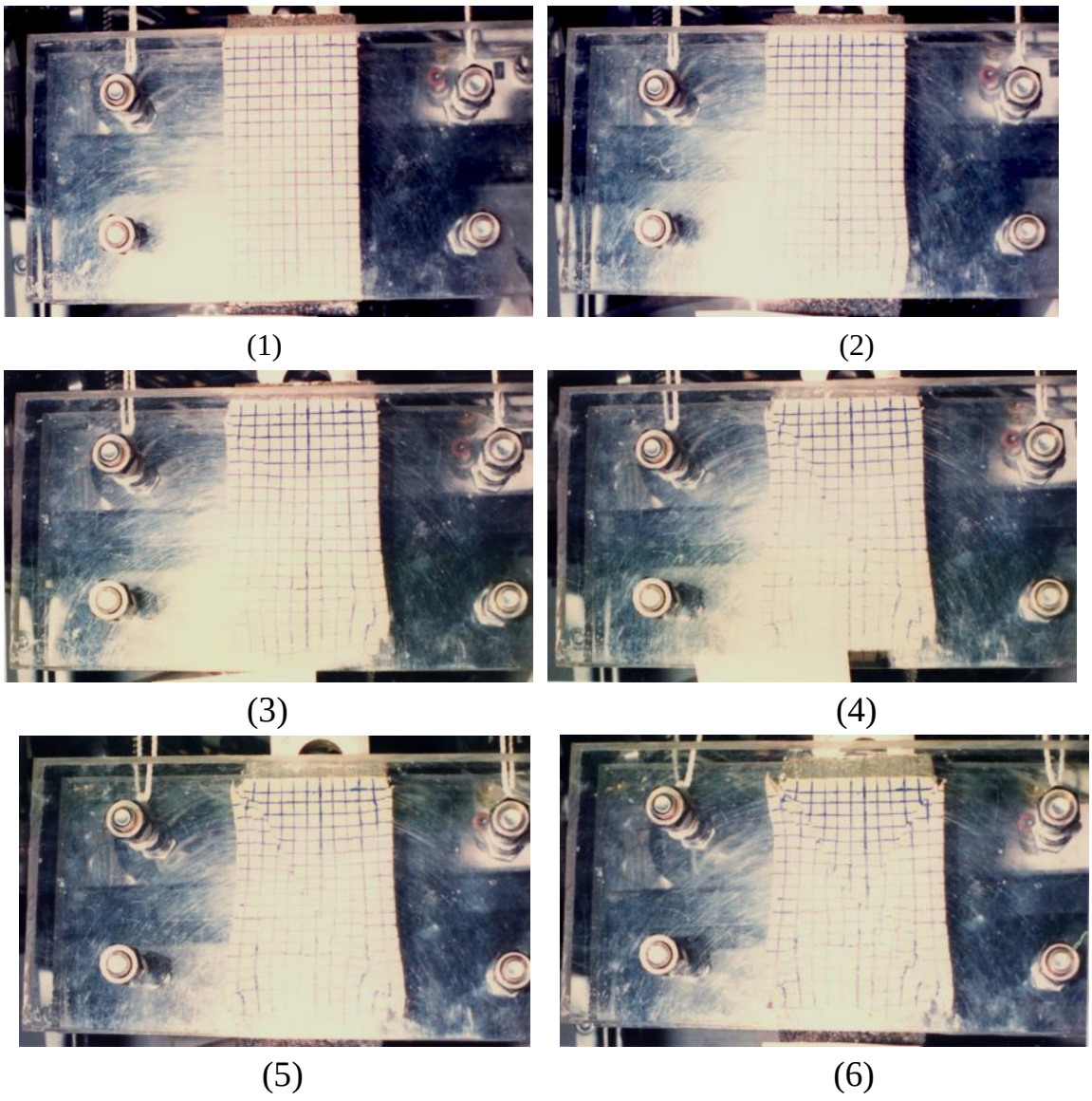

Figure 1.72. Performance of the unconfined compression test under plane strain conditions

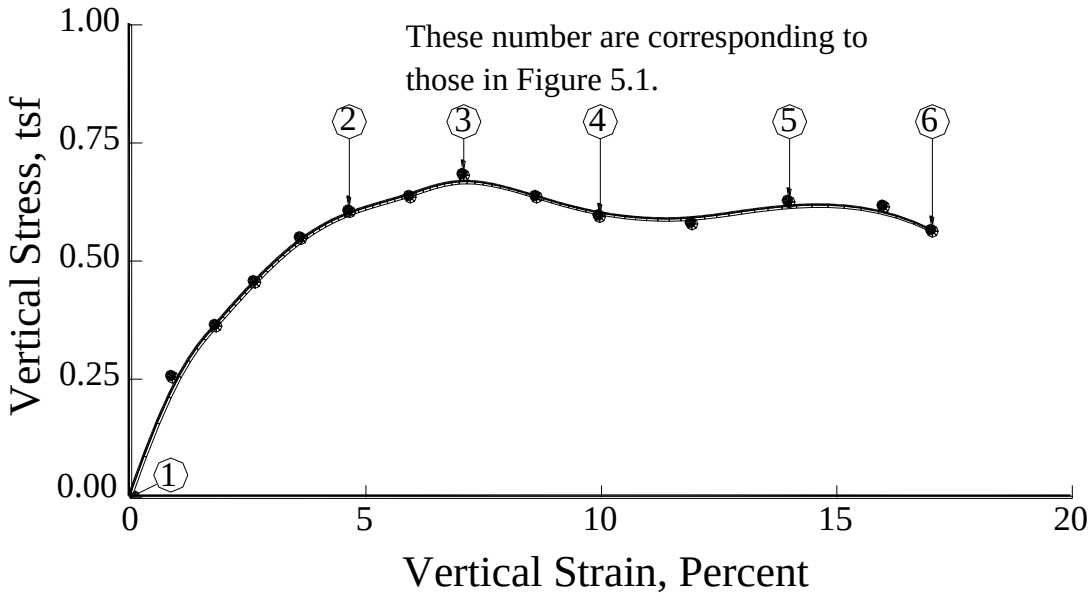

Figure 1.73. Stress-strain relationship of the specimen from unconfined compression test under plane strain conditions

The occurrence of shear bands therefore exhibits the strain softening behavior of the sample.

Performance of a Test under Axis-symmetric Conditions. To evaluate the hardening parameter (H) and initial size of yield surface (κ), a unconfined compression test under axis-symmetric conditions was performed as shown in Figure 1.74. From Figure 1.74 it is seen that the sample keeps on bulging at one end with an increase in vertical displacement. The same figure also exhibits two sets of shear bands when the stress is far beyond the peak stress.This means that shear bands are easier to be captured and observed in plane strain conditions than in axis-symmetric conditions, as also noted by Rudnicki and Rice (1975), and Rice (1977).

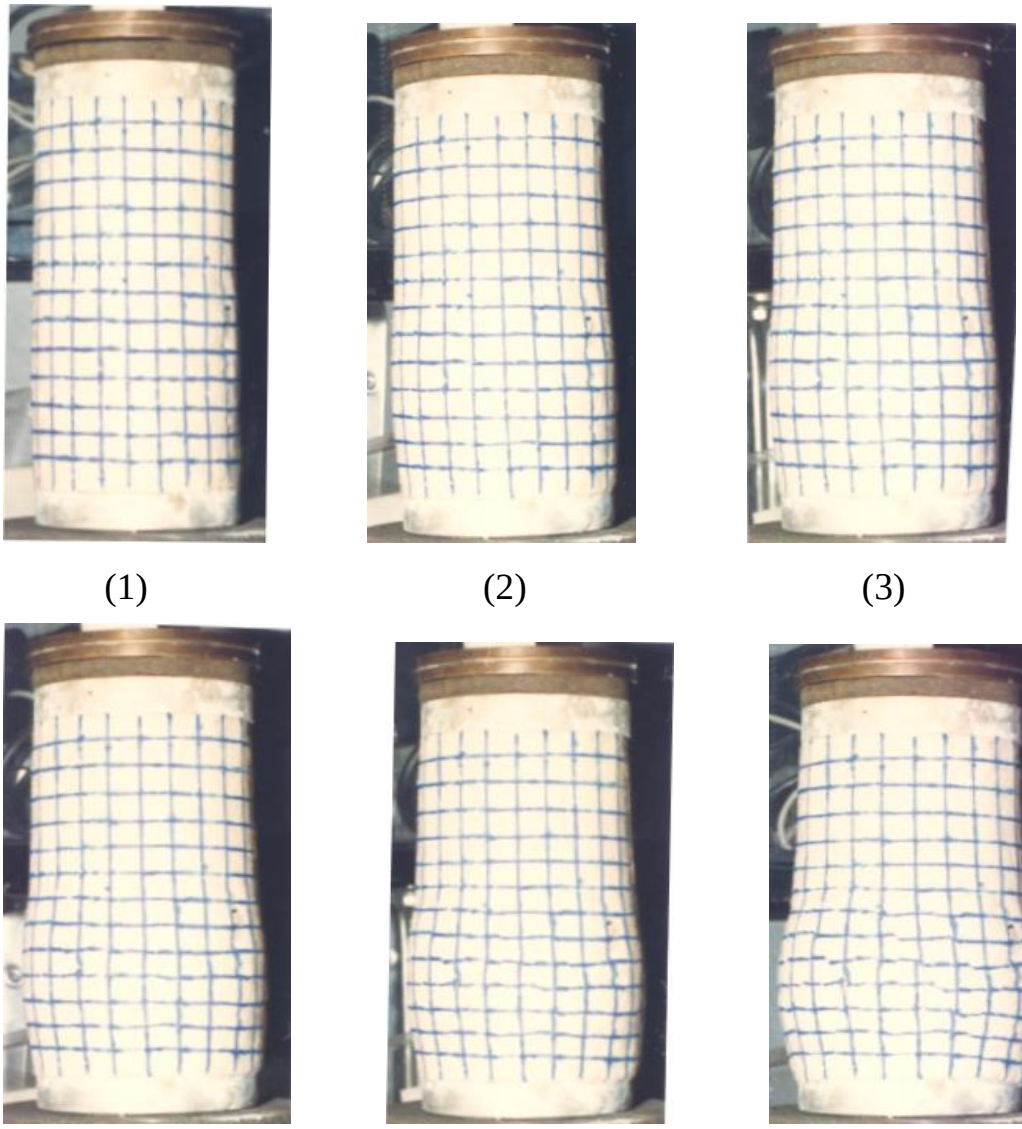

(1) (2) (3)

(4) (5) (6)

Figure 1.74. Performance of the unconfined compression test under axis-symmetry conditions

There are two stress-strain curves shown in Figure 1.75 for this particular test. One is based on the assumption of uniform deformation, thereby the deformed cross section area, A, can be calculated as follows:

$$A = \frac{A_0}{1-\varepsilon_v} \tag{1.5.1}$$

where A_0 is the initial cross section area; the vertical strain. And the other is based on the maximum bulged area obtained for each stress levels. Since the unbulged zone remains nearly undeformed, the stresses in the bulged zone should be less than those in the unbulged zone. The reading for the proving ring shown in Figure 1.76 under a specific load step is supposed to represent the vertical stress acting on the weakest plane. Thus it can be deduced that, using the assumption of uniform deformation, the post-peak stress-strain relationship may not be representative. Although the difference of the maximum stresses for both cases is about five percent only, it can be as large as thirty percent when the strain is greater than twenty percent.

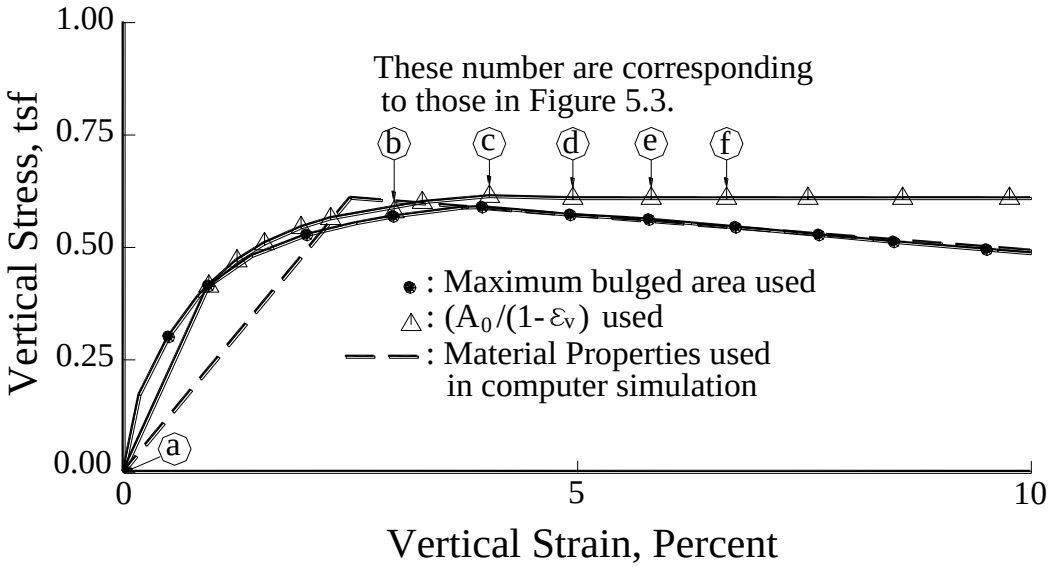

Figure 1.75. Stress-strain relationship of the specimen from unconfined compression test under axis-symmetry conditions

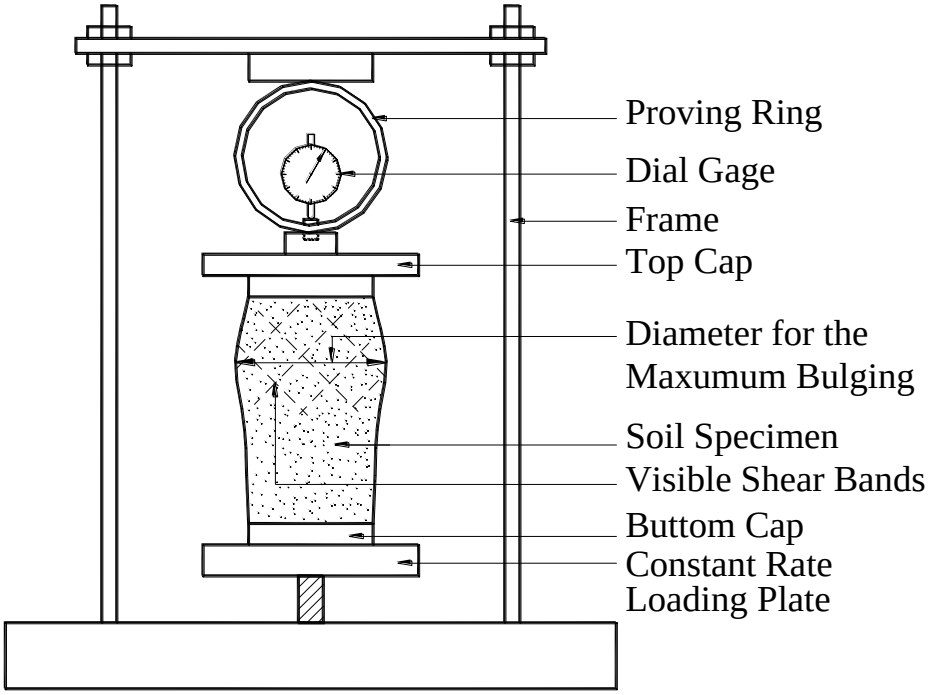

Figure 1.76. Schematic diagram of the unconfined compression test

It may therefore be concluded that the post-peak stress-strain relationship for a sample with the bulging failure mechanism is sensitive to the interpretation. In most textbooks of soil testing, uniform deformation is assumed. Under such assumption, it may be easy to obtain the stress-strain relationship for the sample. However, the stress in post-peak range is overly estimated; especially when the strain is large enough. Thus a true strain softening behavior sometimes will be interpreted as a strain hardening behavior. Since the area of the weakest plane is hard to be determined, it is suggested that the maximum bulged area can be used to obtain a better post-peak stress-strain relationship.

A Numerical Simulation under Plane Strain Conditions. Adopting the above mentioned formulation of the material behavior and the following material properties obtained from the axis-symmetric unconfined compression test, a numerical simulation is performed. The material properties are: (1) the cohesion, 600psf, (2) the Young's modulus, 25000psf, (3) the Poisson's ratio, 0.49, and (4) the hardening parameter, H/2G, equal to -0.05. The numerical simulation is presented in Figures 1.77 and 1.78. From Figure 1.77 the angle of the shear bands of 44.3 degrees with respect to the horizontal is clearly obtainable. Figure 1.77 also reveals that the shear bands

are visible when the stresses are beyond the elastic range. Since the localization behavior similar to experimental observations is duplicated, the value of the adopted hardening parameter (H/2G = -0.05) may be close to the real behavior.

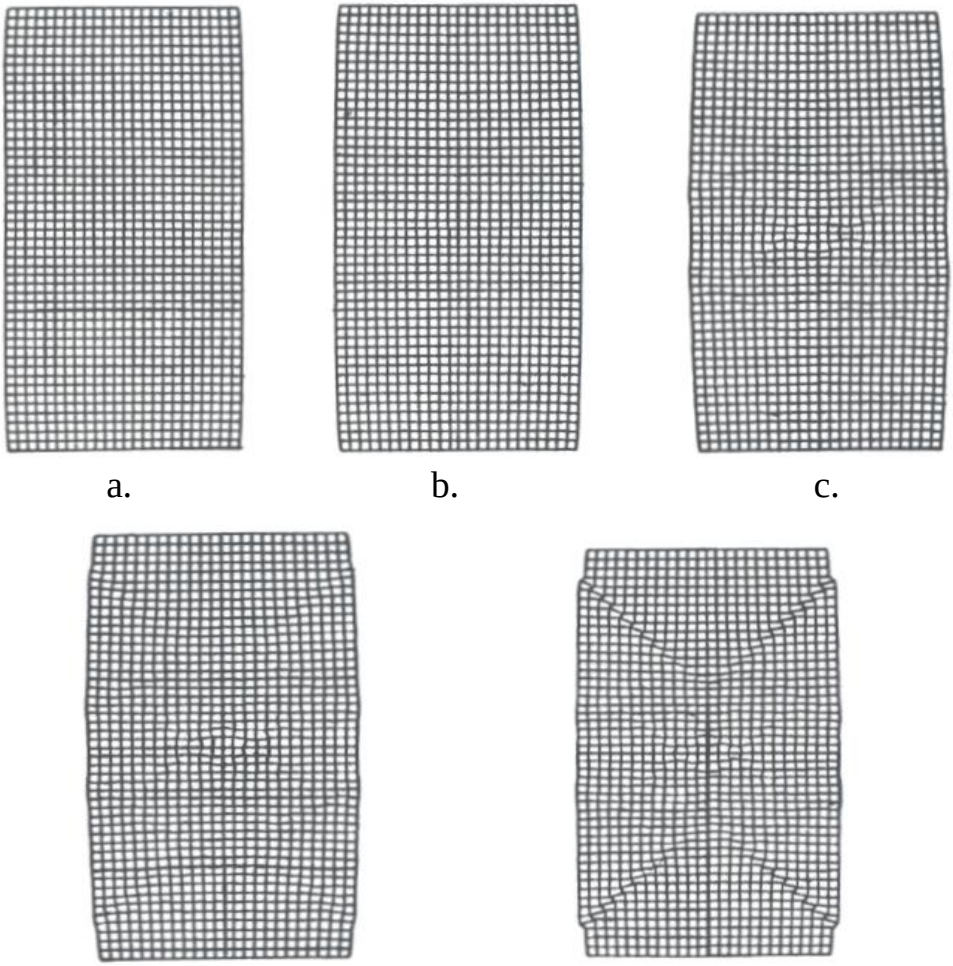

Figure 1.77. Performance of numerical simulation of the unconfined compression test under plane strain condition

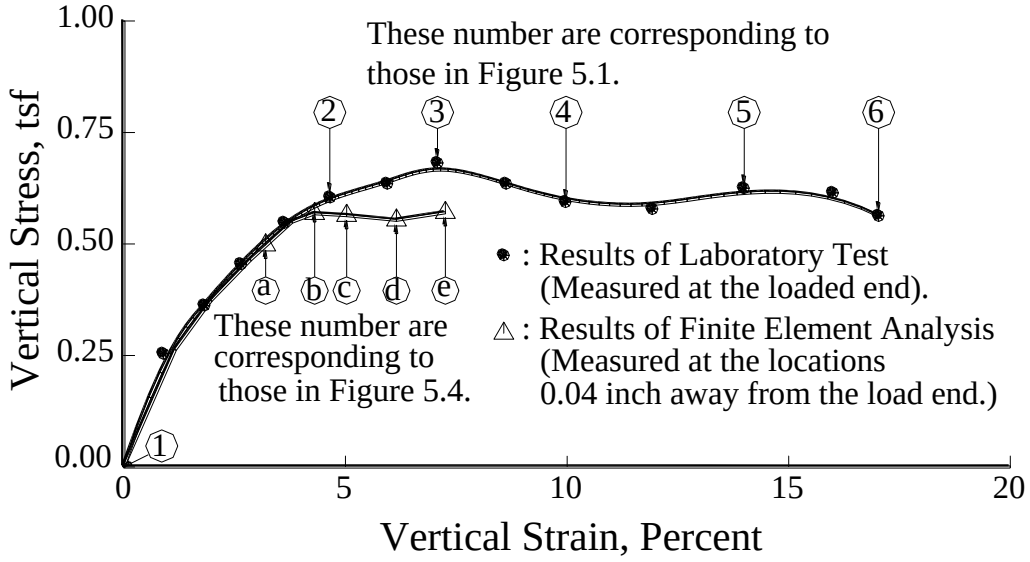

Figure 1.78. A comparison of the results of laboratory test and numerical simulation for the unconfined compression test under plane strain conditions

1.5.2 Failure Mechanisms in Laboratory Triaxial Tests

Some laboratory triaxial tests for the Pepper shale from the site of Waco dam slide were conducted at Fort Worth, U. S. Army Engineer District. Samples were obtained by using a 6-inch inside-diameter double-tube core barrel. To study the influence of anisotropy, test specimens have been prepared with different orientations with respect to the horizontal of the core samples. In Figure 1.79, it is seen that specimens whose orientations are 45 degrees and 60 degrees with respect to the horizontal of the core samples were tested. In the following of this section, samples whose orientations are 45 degrees and 60 degrees with respect to the horizontal of the core samples will be designated by S45 and S60 respectively. The dimensions of the specimens were 1.5 inches in diameter and 3 inches in height. Overall three sets of the unconsolidaed undrained tests were conducted. Each set consisted of four specimens. The samples obtained had two conditions--with, or without visible joints prior to testing. The first set of samples used was with 60 degrees orientation (S60) without visible joints prior to testing. The second set of samples used were with 45 degrees orientation (S45) without visible joints prior to testing and the third set used were also S45 with visible joints prior to testing. The confining pressures for different specimens in

each set are 1.5tst, 3.0tsf, 6.0tsf, and 12.0 tsf respectively. All other details of the test can be obtained from the report by Stroman (1984).

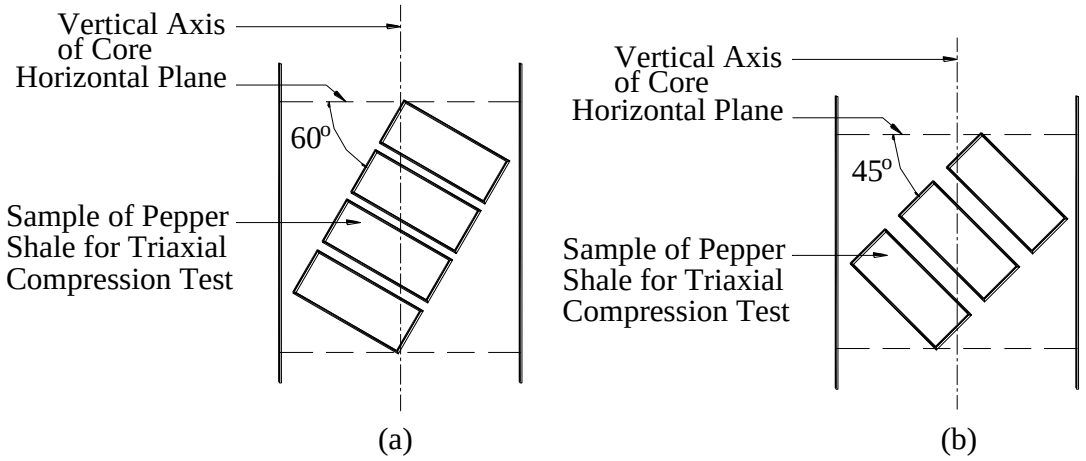

Figure 1.79. Orientation of test specimens with respect to the core sample (From Stroman, 1984)

The test results of the first and the second set are shown in Figures 1.80 and 1.81 respectively. It may be observed that the angle of a failure plane has great influence on the U.U. strength of the pepper shale. The test results of the third set are shown in Figure 1.5.82. Due to the visible joint existing before tests, the failure patterns and the stress-strain curves shown in Figure 1.82 are totally different from those shown in Figures 1.80 and 1.81 where visible joint did not exist. Figure 1.82 shows that a stress-strain curve with two peaks is obtained if the visible joint is active. The first peak of the stress-strain curve (shown as A in Figure 1.82) is believed to be created by shearing along the visible joint. This can be confirmed by comparing the residual strength of sample 'd' and the first peak strength of other samples in Figure 1.82. The second peak of the stress-strain curve is believed to be obtained by shearing along the weakest plane within the undisturbed zone. A summation of all the triaxial test results is shown in Table 1.6. Table 1.6 indicates that samples S60 are stronger than S45, and samples without visible joint are stronger than those with visible joint. Also it can be deduced from the results of the first two sets of tests that the weakest plane of pepper shale is the horizontal plane in the field.

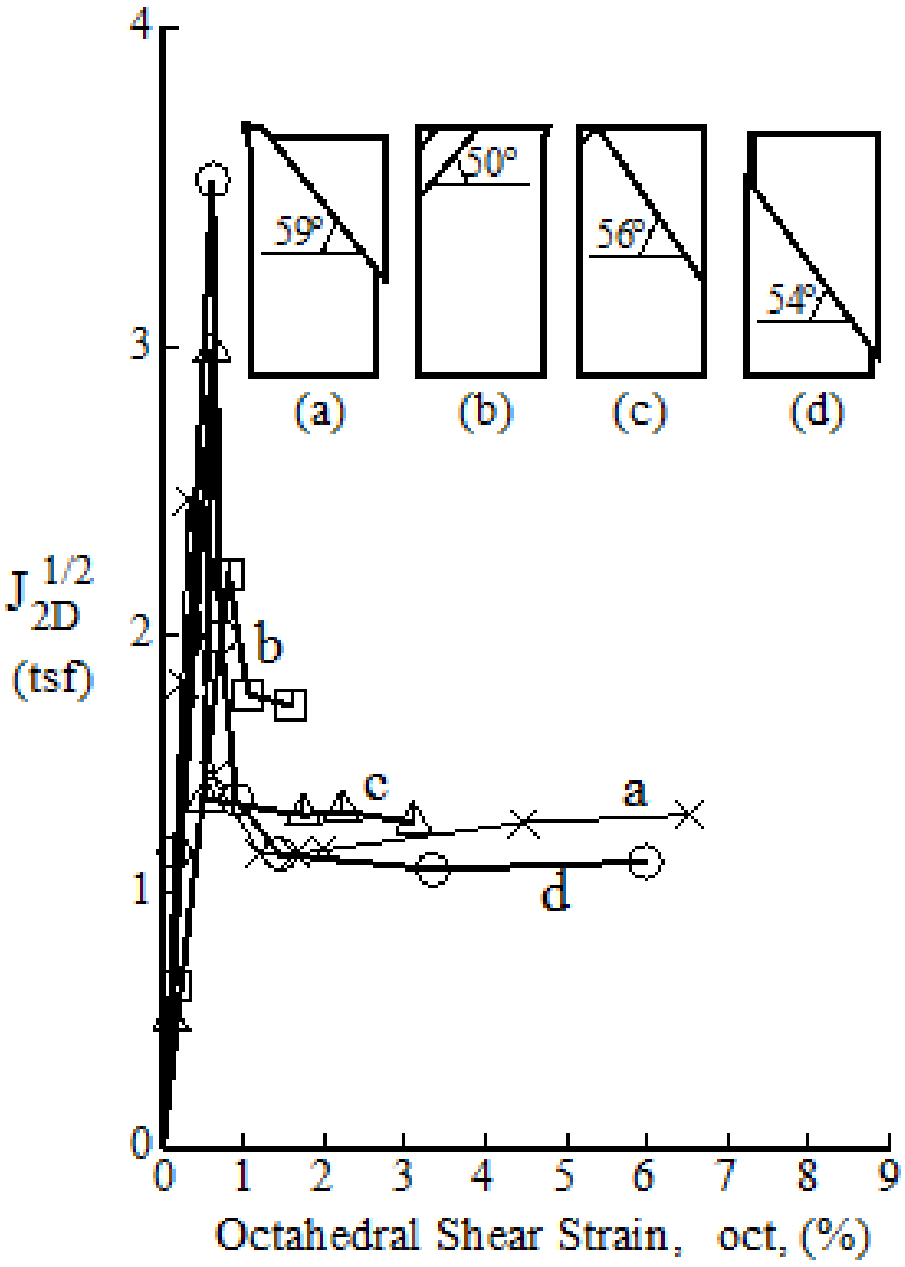

Figure 1.80. Results of unconsolidated undrained triaxial tests (The orientation of test specimens with respect to the core sample is 60 degrees as that shown in Figure 1.79.a.)

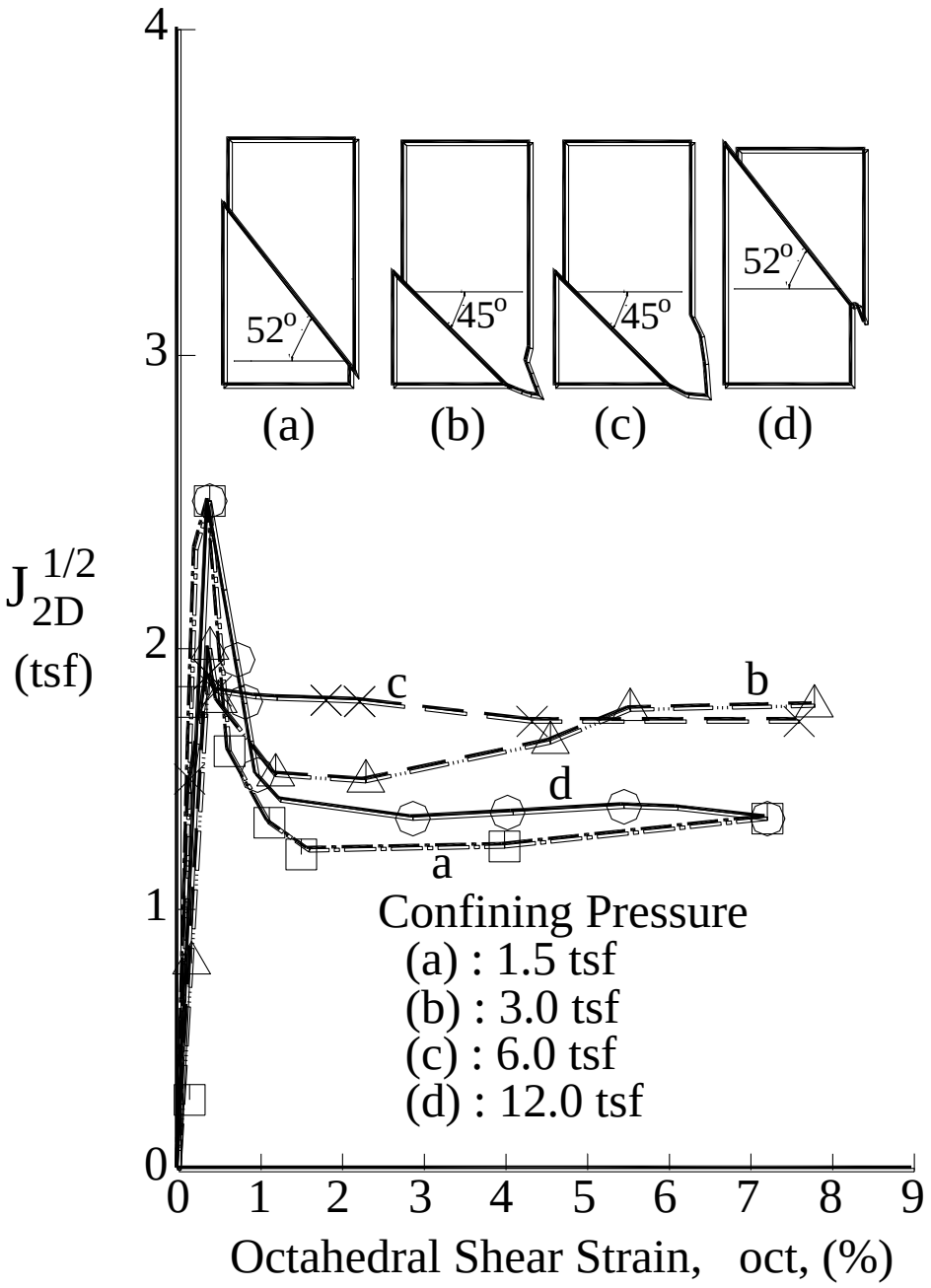

Figure 1.81. Results of unconsolidated undrained triaxial tests (The orientation of test specimens with respect to the core sample is 45 degrees as that shown in Figure 1.79.b)

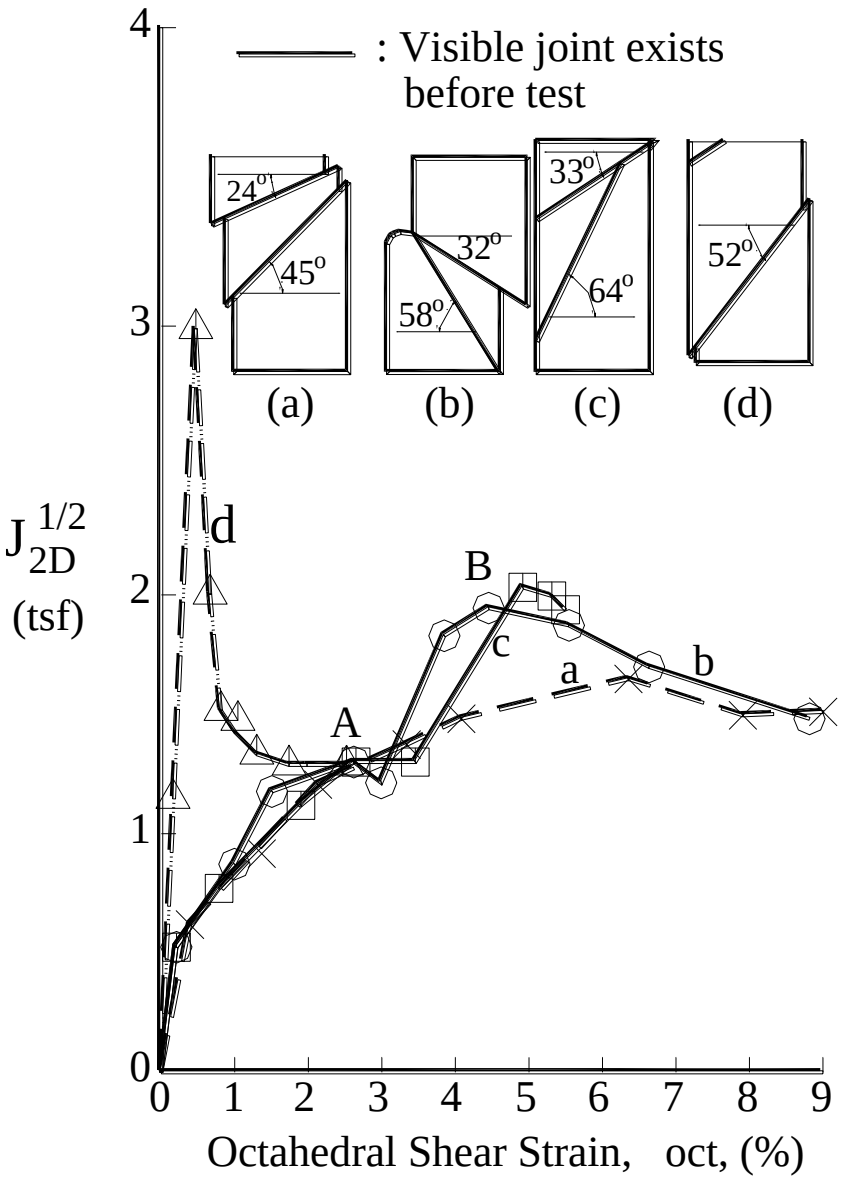

Figure 1.82. Results of unconsolidated undrained triaxial tests (The orientation of test specimens with respect to the core sample is 45 degrees as that shown in Figure 1.79.b)

Table 1.6. Summation of the unconsolidated undrained triaxial test results (From Stroman and Feese, 1984)

Orientation of Specimen with Respect to the Horizontal of Core Sample	Angle of the Failure Surface wth respect to the Horizontal of the Specimen, in degrees	Angle of the Visible Joint with respect to the Horizontal of the Specimen, in degrees	Peak Strength, in tsf	Residual Strength, in tsf
60 degrees, without Visible Joint	59	---	2.5	1.2
	50	---	2.2	1.8
	56	---	3.0	1.3
	54	---	3.6	1.1
45 degrees, without Visible Joint	52	---	2.5	1.2
	45	---	2.0	1.7
	45	---	2.0	1.8
	52	---	2.5	1.3
45 degrees, with Visible Joint	45	24	---	1.3
	58	32	1.8	1.2
	64	33	1.9	1.3
	52	52	3.0	1.3

1.5.3 Failure Mechanisms in Laboratory Direct Shear Tests

Many direct shear tests for the shales from the site of the Waco dam slide have been completed at Fort Worth, U. S. Army Engineer District. It was mentioned by Stroman and Feese (1984) that the specimens were 3.0 inch square and 1.0 inch in thickness. Test specimens were trimmed into cutters and then placed directly into shear box, inundated with tap water, and consolidated under 1.5-tsf normal stress for at least 16 hours. The normal stress was then increased to the full desired levels, and the specimen was permitted to consolidate for an additional 24 hours. The shear box is split horizontally at mid-plane which coincides with the plane in the test specimen along which force is applied. At the start of tests the upper box was raised to a position of 0.05 inch above the lower box. The two halves of the shear box containing the test specimen remained in contact along lips having a width of

0.1 inch. Undrained tests were performed under different normal stress with the shear rate around 0.006 inch/minute. The normal stresses used are 1.5tsf, 3.0tsf, 6.0tsf, 12.0tsf, and 18.0tsf. A test was discontinued when failure occurred; failure being defined by a continuing drop in shear resistance or when the shear resistance remained constant for a long period of time. From Figure 1.83 it is seen that there are 6 different patterns of shear band obtained from the direct shear tests for the shale near Waco dam slide. Since six different patterns exist, a numerical analysis of direct shear test was conducted to investigate reasons for such divergent patterns.

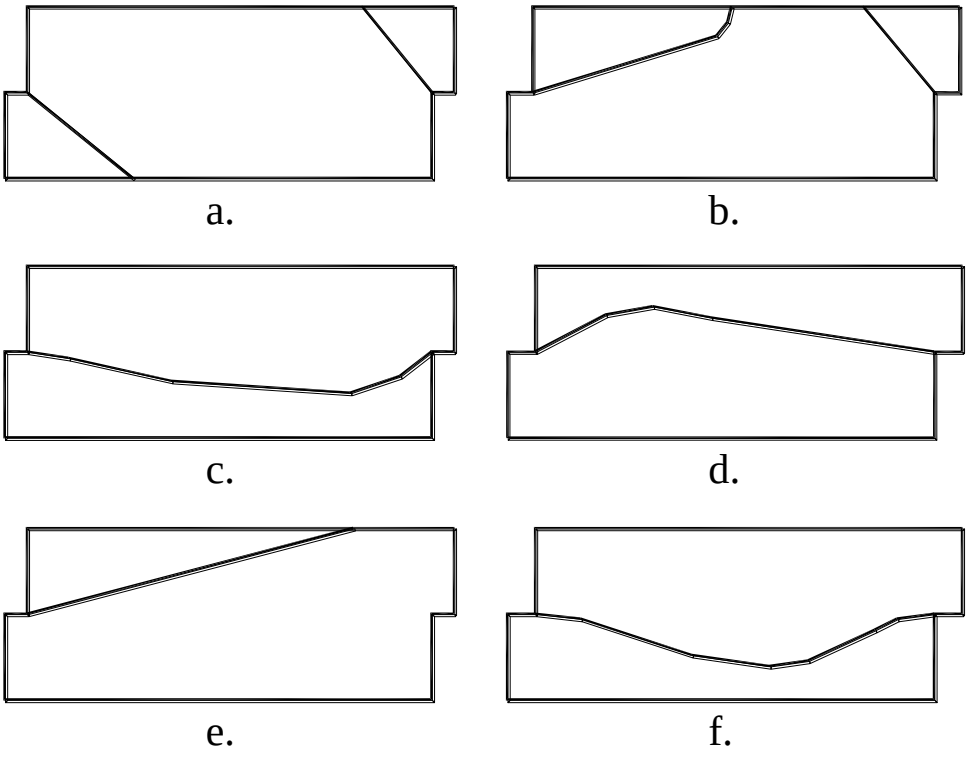

Figure 1.83. Failure patterns of direct shear tests for the shales near Waco dam (From Stroman and Feese, 1984)

1.5.4 Failure Mechanisms in Numerical Simulations of Direct Shear Test

The Details of the Numerical Simulation. The numerical simulation of direct shear test was performed by using the initial finite element mesh formed by quadrilateral elements and interface elements (see Figure 1.84). It may be noted that the mesh used in a numerical simulation has a slightly different configuration from that of a actual test. The mesh depicts the

conditions shown in Figure 1.85.b instead of Figure 1.85.a. In Figure 1.85.b the top plate including the porous stone is not inside the upper shear box which in the actual apparatus it is inside (see Figure 1.85.a). The top plate has two significant functions. First it distributes normal force uniformly on the top of a test specimen, and secondly it transmits shear stress across either ends. In a real test, the top plate moves along with the upper shear box. In a square shear box, the third direction (which is perpendicular to the paper of Figure 1.85.a) is restrained by the shear box, therefore, the plane strain numerical simulation is valid. It was observed during the tests that the upper shear box was tilting when the shear force was applied (Peters, 1986). The above phenomenon indicates that the upper shear box can be lifted at the end where the shear force is applied. To simulate such phenomenon, the vertical movement of the upper shear box will be restrained only at that end which is farther from where the shear force is applied (see Figure 1.84). A prescribed uniform horizontal displacement is then applied to the upper shear box. Since the top plate is supposed to move horizontally along with the upper shear box, the prescribed uniform horizontal displacement is applied to the top plate as well. As shown in Figure 1.84, the rollers which are used to constrain the horizontal displacements are also used to prescribe the uniform horizontal displacement. The solid bars are used to indicate the interface elements. Since very limited tensile strength exists in the interface between soils and the metal, the interface elements should be assumed not to contain any tensile strength. However, due to the computational limitation, 1psf is assigned for the tensile strength of interface elements. The shear strength assumed for the interface elements between soil and the side wall of the shear box is 500psf. The influence of the teeth on the top plate causes a good adherence between the top plate and soil. Therefore, residual shear strength of the specimen is used for those interface elements between soil and the top plate. Evaluating Table 1.6, the following material properties were selected and used in the simulation of direct shear test.

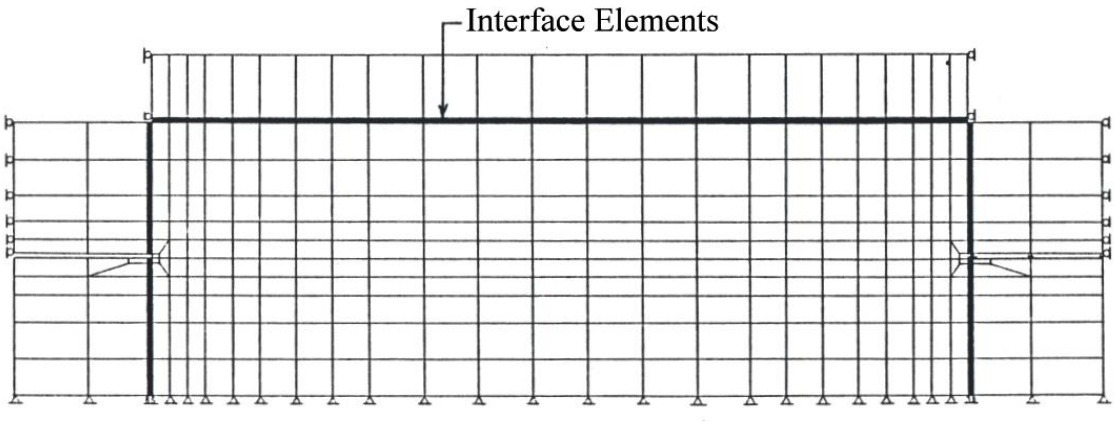

Figure 1.84. Initial mesh for the simulation of direct shear tests

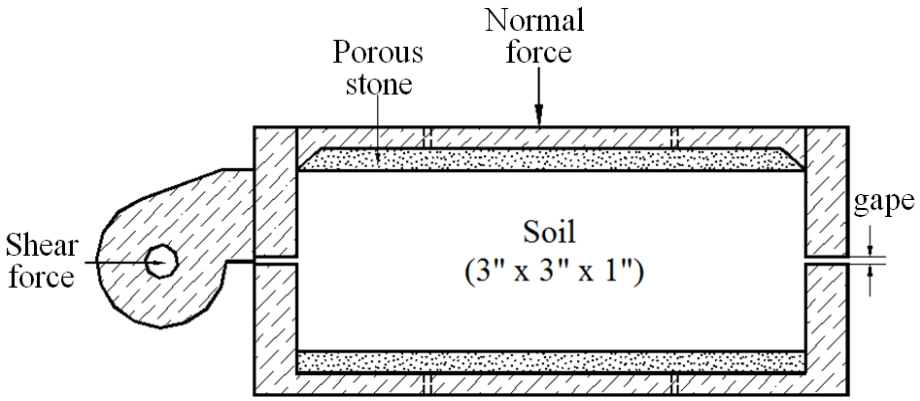

(a) Profile of actual direct shear test

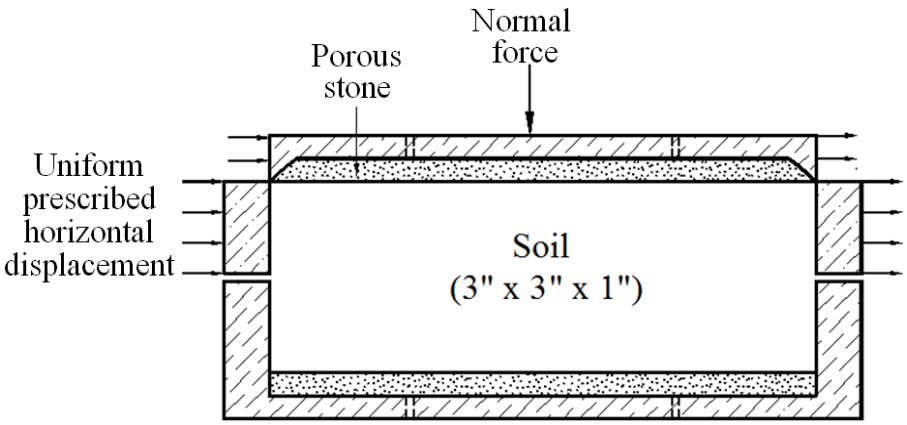

(b) Numerical simulation profile of direct shear test

Figure 1.85. Profile of direct shear test specimen

Hardening Parameter (H/2G) = -0.3;
Initial Size of Yield Surface (κ) = 2.4tsf;
Young's Modulus (E) = 480tsf;

Sensitivity (Peak $J_{2D}^{1/2}$ /Residual $J_{2D}^{1/2}$) = 2.0;

Poison's ratio (ν) = 0.49;
Normal stress = 1.5tsf.

Using the above values for the proposed material model, numerical experiments were conducted. The numerical scheme adopted does not allow a sudden jump from the elastic range to residual stress range. Therefore the hardening parameter used is obtained after several trials, and it is less than the value (-0.75) obtained from the triaxial compression test (which is -0.75). In the following of this chapter SG will be used to denote the size of the gap between the upper and the lower shear box. There are two reasons for varying SG. First, in a real direct shear test, usually the gap was set randomly in between 0.025 inch and 0.050 inch. Although it was specified by Lambe (1951) that the size of the gap should be 0.025 inch, very few experiments do measure it before running a direct shear test. Secondly, the size of the gap definitely has some influence on the failure pattern of a specimen; especially for shales which are very stiff materials. SG values used in this investigation are 0.025 inch, 0.030 inch, 0.034 inch, and 0.038 inch. The results corresponding to each SG value are shown in Figures 1.86, 1.87, 1.88, and 1.89 respectively.

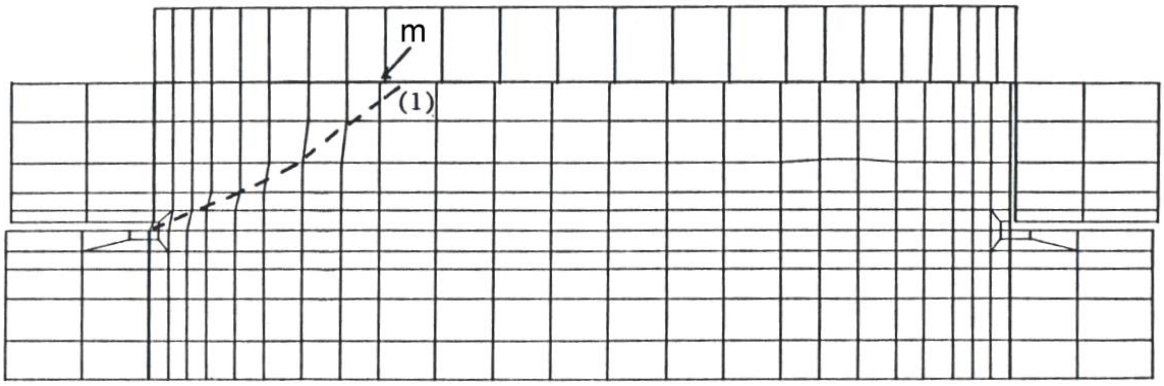

a. Total incremental prescribed horizontal displacement is 0.0122 inch

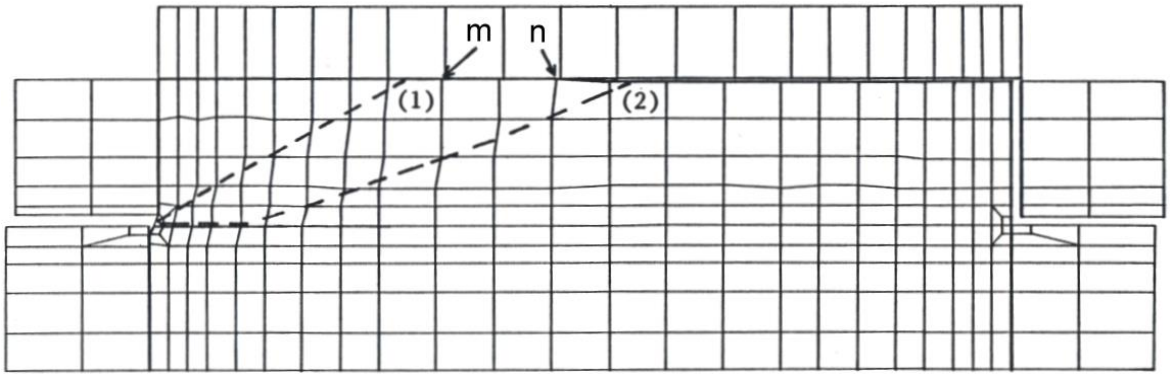

b. Total incremental prescribed horizontal displacement is 0.0322 inch

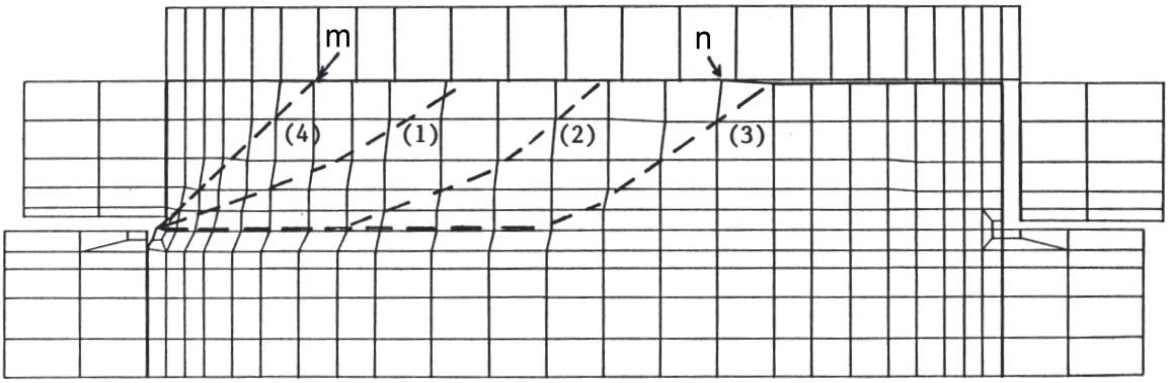

c. Total incremental prescribed horizontal displacement is 0.0722 inch

Figure 1.86. Numerical simulation of direct shear test

(Size of the gape = 0.025 inch)

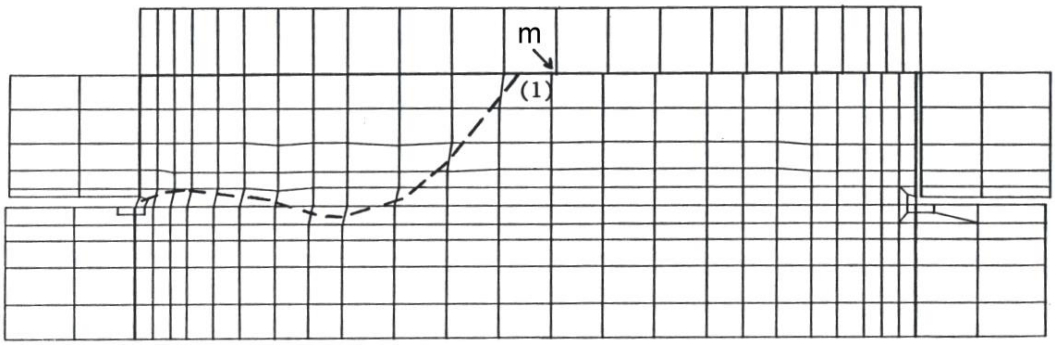

a. Total incremental prescribed horizontal displacement is 0.0222 inch

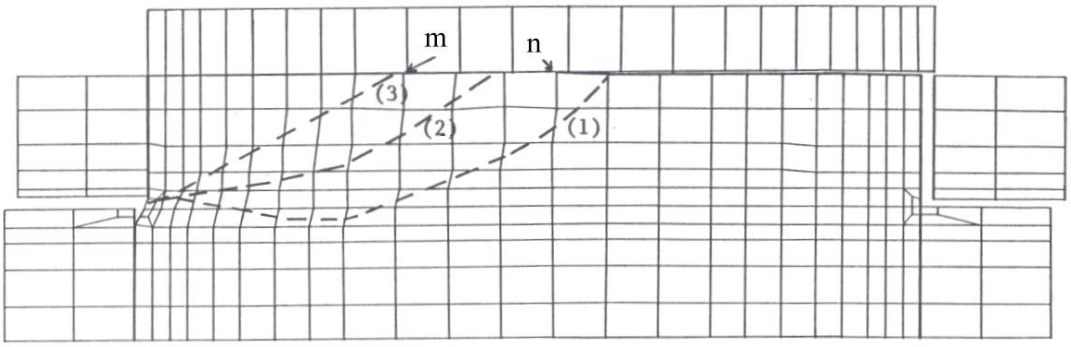

b. Total incremental prescribed horizontal displacement is 0.0522 inch

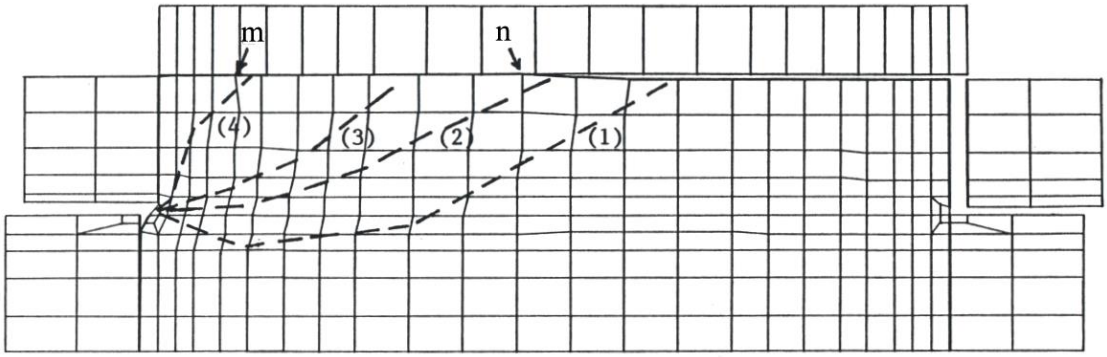

c. Total incremental prescribed horizontal displacement is 0.0722 inch

Figure 1.87. Numerical simulation of direct shear test

(Size of the gape = 0.030 inch)

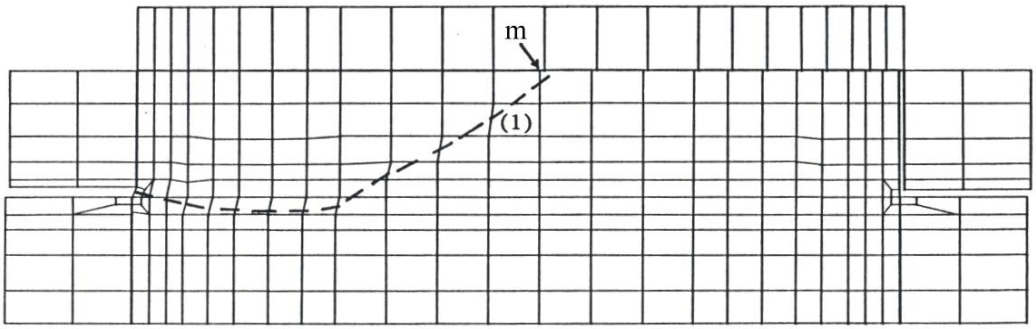

a. Total incremental prescribed horizontal displacement is 0.0222 inch

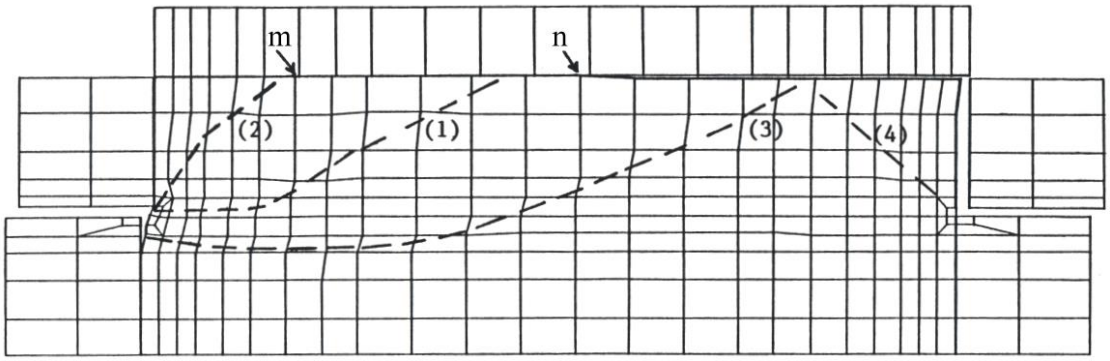

b. Total incremental prescribed horizontal displacement is 0.0422 inch

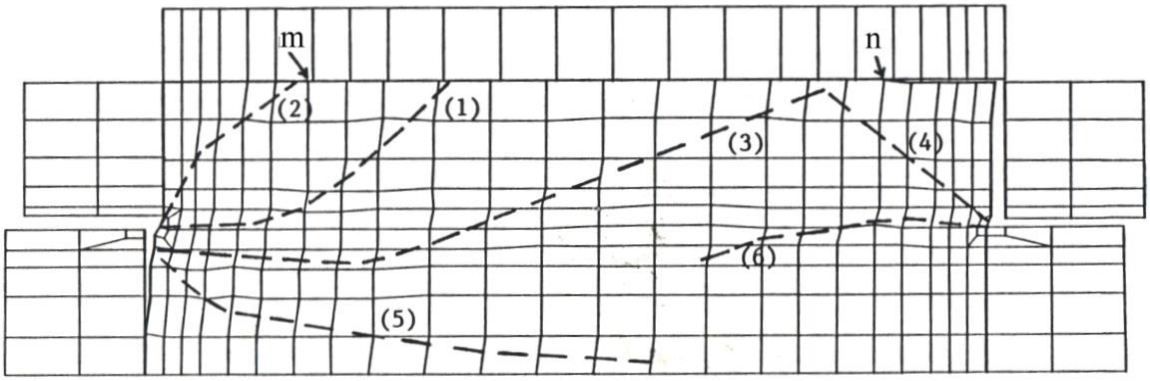

c. Total incremental prescribed horizontal displacement is 0.0722 inch

Figure 1.88. Numerical simulation of direct shear test

(Size of the gape = 0.034 inch)

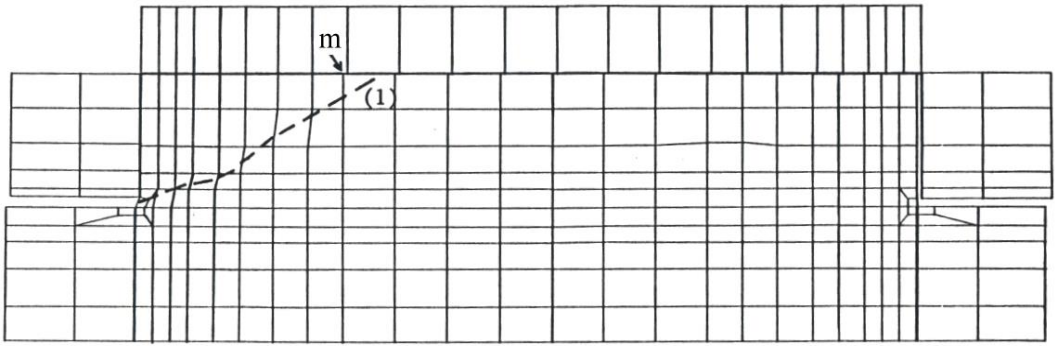

a. Total incremental prescribed horizontal displacement is 0.0122 inch

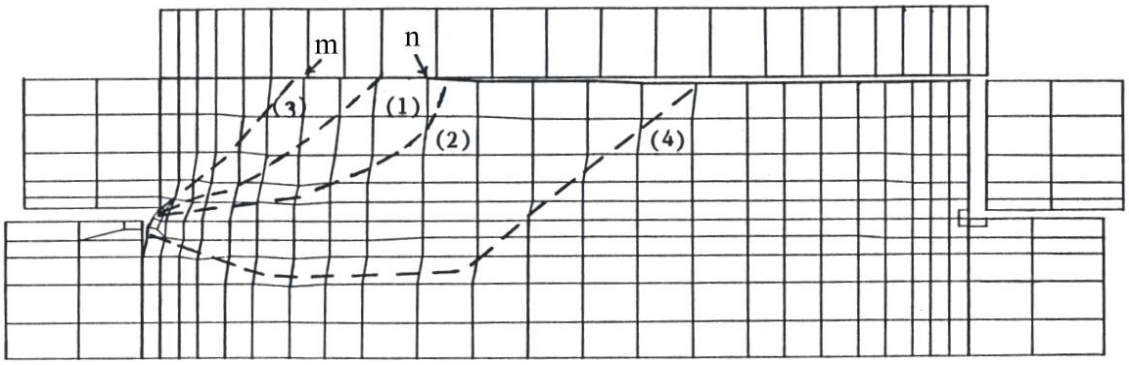

b. Total incremental prescribed horizontal displacement is 0.0722 inch

Figure 1.89. Numerical simulation of direct shear test

(Size of the gape = 0.038 inch)

Discussions. From Figure 1.86 to 1.89, it is observed that significant relative movement occurs along the interface elements between the top plate and the specimen when the interface elements yield. Such phenomenon may have caused the first shear band to occur at the upper left hand side of the specimen. If the nodal point m denotes the last nodal point for the above relative movement to occur, it is observed that the first shear band normally is connected to the nodal point m (see Figures 1.86.a, 1.87.a, 1.88.a, and 1.89.a). It is also observed that the location of the nodal point m varies with the change in SG, all other conditions remain the same. The location of the first shear band influences the internal deformation of the specimen. It causes the internal deformation localized in the upper left hand side of the specimen with a clear boundary defined by the first shear band. Such kind of localized deformation forces the top plate to move up, and therefore tensile stress may be obtained in some of the interface elements. Since only a very small tensile strength is allowed in the interface elements, tensile stress

exceeds the strength causing a gap between the top plate and the specimen (see Figures 1.86.b, 1.87.b, 1.88.b, and 1.89.b). From Figures 1.86.b, 1.86.c, 1.87.b, 1.87.c, 1.88.b, 1.88.c, and 1.89.b it is seen that the propagation of the relative movement along the interface elements is influenced by the location of the first shear band or the initial nodal point m. In other words, SG does have great influence on the behavior of the shear band in direct shear tests.

It is interesting to see the behaviors of shear band for different SG values. If the nodal point n is used to denote the last nodal point for the gap between the top plate and the specimen to occur, it is seen that the second shear band in a specimen normally is connected to the nodal point n (see Figures 1.86.b, 1.87.b, and 1.89.b). In case the initial nodal point m and the nodal point n have almost the same location (see Figures 1.88.a, 1.88.b), the first shear band will remain at its location and will also automatically be connected to the nodal point n. It is observed that there is a tendency for the shear bands to go deeper to the specimen when SG is increased from 0.025 inch to 0.034 inch (see Figures 1.86.c, 1.87.c, and 1.88.c). On the other hand, there is a tendency for the shear bands to go to shallower when SG is increased from 0.034 inch to 0.038 inch (see Figures 1.87.c, and 1.88.b). It is seen that displacements are not visible at the upper right hand side of the specimen when SG are equal to 0.025 inch, 0.030 inch, and 0.038 inch. Under this condition, it is observed that localizations are formed at the left hand side of the specimen only (see Figures 1.86.c, 1.87.c, and 1.88.b). Displacements are visible at the upper right hand side of the specimen when SG is equal to 0.034 inch. From Figure 1.88.c it is found that shear bands exist at both side of the specimen. Therefore under the test conditions mentioned in the previous section of this chapter, that an optimum SG value for direct shear tests under certain specific conditions may exist. From the observation of the pattern of shear bands in numerical simulation it is believed that the optimum SG for the specimen in this study could be 0.034 inch.

In the following of this section, the terms shallow shear band and a deep shear band will be defined and used. A shallow shear band is defined when most of the shear band exists within the upper shear box, while a deep shear band is defined when the shear band penetrates deep to the lower shear box. Some other details of the numerical results have to be pointed out as follows: First of all, the gap between the top plate and the specimen will be widened if a shallow shear band is formed. On the other hand, such gap has a

tendency to close if a deep shear band is formed. Secondly, in Figure 1.90, the stress-strain relationship for a real direct shear test is drawn together with those results from numerical experiments. It is seen that the first peak of stress-strain curve is obtained when the first shear band is formed. When any other shear band is acting together with the first shear band, the second peak of the stress-strain curve will then be obtained. Such phenomenon is confirmed by the results from the triaxial tests for the upper pepper shale with a visible joint existing before tests (see Figure 1.82).

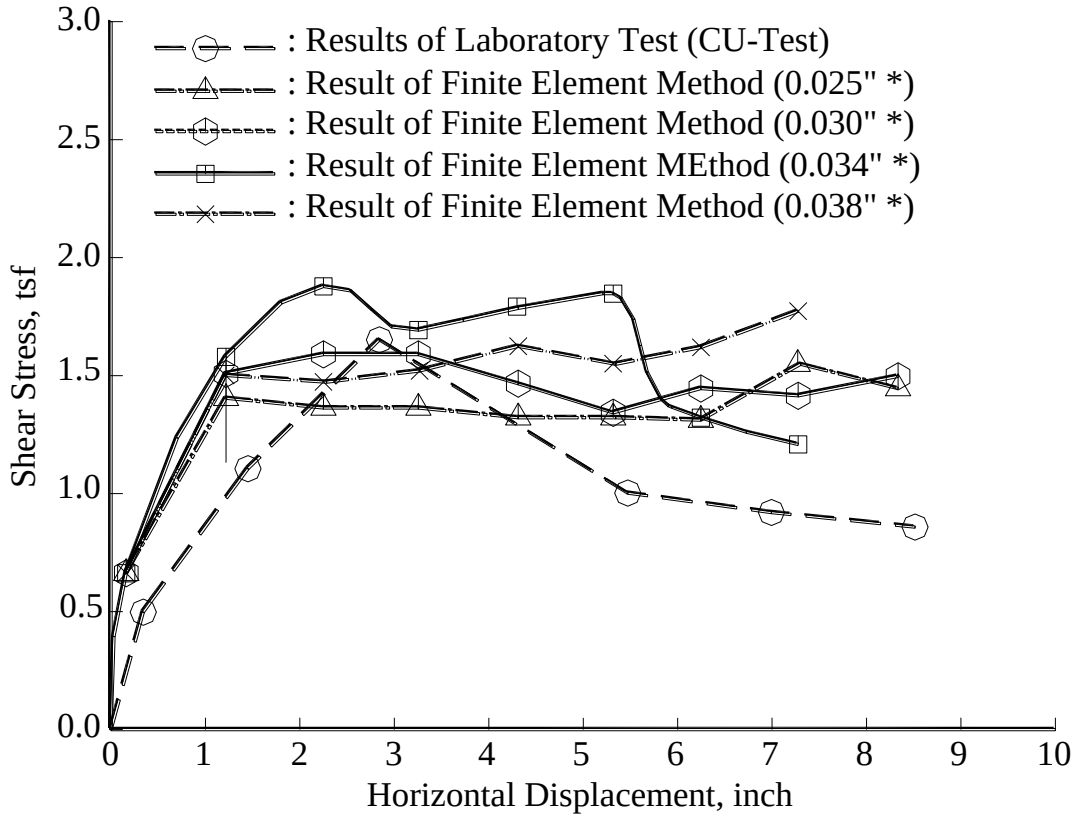

Figure 1.90. A comparison of direct shear test results

Thirdly, the swelling pressure for the pepper shale obtained by Stroman and Feese (1984) is about 1.6 tsf. The 1.5-tsf normal stress seems not enough to overcome the swelling pressure, and therefore expansion of the specimen might have occurred before running the test. This may be the reason for the real test specimen to become softer than those of numerical experiments. Fourthly, the fourth shear band together with the fifth one in Figure 1.88.c are similar to those shown in Figure 1.91 which were obtained by Hvorslev (1961).

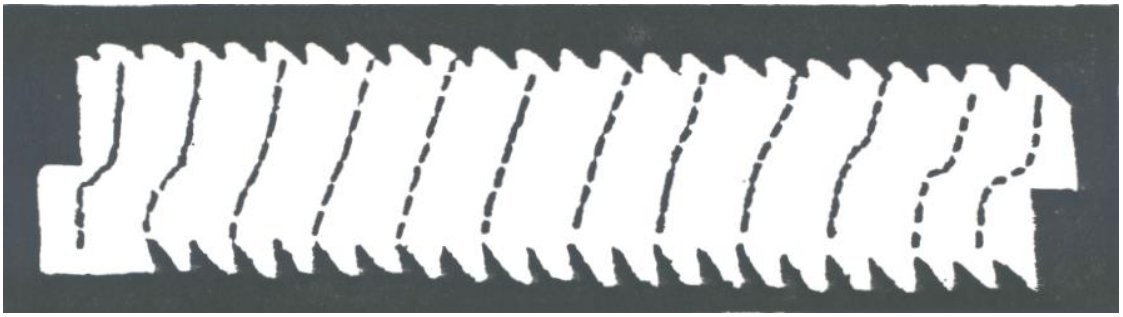

a. Horizontal displacement is 4.0 mm

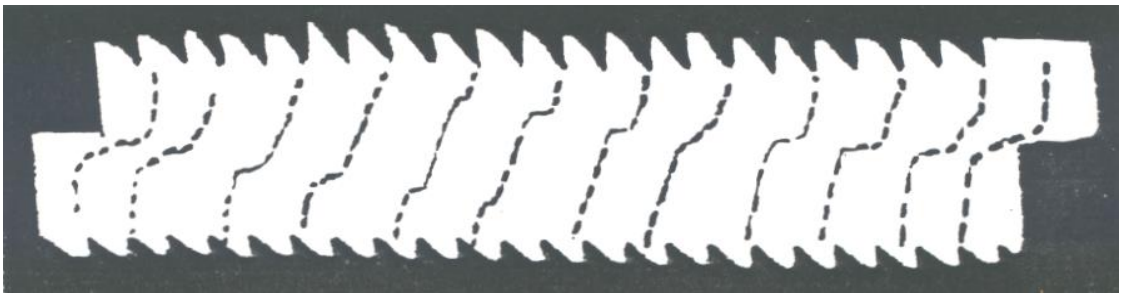

b. Horizontal displacement is 8.5 mm

Figure 1.91. Internal deformations in direct shear tests

(Hvorslev, 1961)

The above two shear bands are similar to those shown in Figure 1.83.a too. The first shear band together with the fourth one in Figure 1.88.c is similar to the pattern of the shear band shown in Figure 1.83.b. The third shear band shown in Figure 1.88.c is similar to that shown in Figure 1.83.e. Therefore, the numerical experiments can capture the shear bands for the pepper shale in direct shear tests. Finally, a change in the normal stress or in the shear strength of the interface elements between the top plate and the specimen should have some influences on the behavior of localization. An extensive study of these two factors is beyond the scope of this research. However a totally different pattern of shear band is obtained when SG value is equal to 0.025 inch, normal stress is equal to 3.0tsf, and the shear strength of the interface elements between the top plate and specimen is equal to 2.4 tsf (see Figure 1.92). The pattern of shear band shown in Figure 1.92 is quite similar to that shown in Figure 1.83.f. Therefore, it is believed that those patterns of shear band shown in Figures 1.83.c, and 1.83.d are possible to be captured in numerical simulations if those three factors--SG, normal stress, and shear strength of the interface elements--are changed.

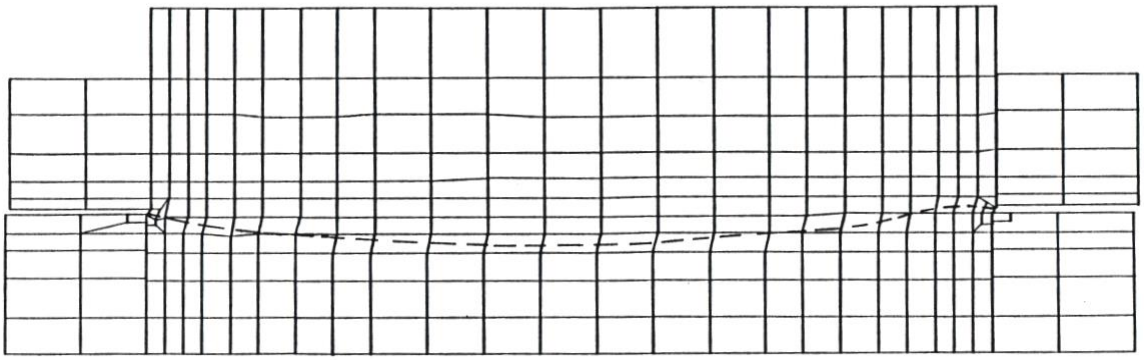

Figure 1.92. Numerical simulation of direct shear test
(Size of gape = 0.025 inch, doubled normal stress
and shear strength of the interface elements)

1.5.5 Mechanisms of Localization

In 1976, Rice (1977) addressed the mechanisms of localization by describing the ingredients necessary to the physical process for the formation of localizations. Such mechanisms of localization are mainly based on the deformations caused by slip. However, it was clearly shown in crystal plasticity (Gilman, 1969; Hull, 1965) that 'twinning', which is shown in Figure 1.5.22, is the other mechanism of localization. Therefore, a scheme, which is mainly based on the influence of slip only, may need to have a lower hardening parameter to obtain localizations. Using the procedure suggested by Molenkamp (1985), a critical hardening parameter equal to -0.37 is obtained for the constitutive equation used in this study. This parameter is lower than used in direct shear simulation, however, it was clearly shown in Chapter IV that hardening parameter, which is equal to -0.05, is low enough to obtain shear bands.

Based on the results of the continuous process for the formation of localizations, the mechanisms of localization will be presented by using the internal velocity vectors. The internal velocity vectors demonstrate the mechanisms of localization visibly, and perhaps easily comprehensible. Also it may be pointed out that 'twinning' and 'slip' may be active simultaneously in the plate shown in Chapter IV. This may be the reason for the shear band to occur with a hardening parameter as high as -0.05.

Discussion. It is clearly shown in Figures 1.93, and 1.94 that the bifurcation from homogeneous state into a highly localized deformation can lead to the occurrence of a shear band. The velocity vectors show that there are two different types of mechanism of localization. These are: (1) a sudden change of the size of the velocity vectors (see Figure 1.95.b and Figure 1.96.a), and (2) a sudden change of the direction of the velocity vectors (see Figure 1.95.c Figure 1.96.b). The necessary conditions for causing the change of either the size or the direction of the velocity vectors are: (1) the loss of ellipticity, and (2) the damage energy due to strain softening. Since localizations will not be obtained in a uniform stress and strain field, the above conditions are not sufficient conditions for localizations to occur. Therefore, a bifurcation from homogeneous state is required for the formation of localizations. The initiation of a bifurcation from homogeneous state is mainly dependent upon the material properties, the geometry, the boundary conditions, the loading type, etc. used in a numerical experiment. From Figure 1.63.b it is seen that the mechanisms of localization may also depend upon the location of a localization of deformation.

It has been shown by Rice (1977) that localizations can only occur when the hardening parameter, H, is equal to or less than zero when associate flow rule is used. The discussions that follow will therefore be limited to the cases with H equal to or less than zero.

From Figures 1.93 and 1.94 it is seen that the intensity of localization is less strong for the case with H equal to zero than that for the case with H less than zero. In other words, the change of the size or the direction of the velocity vectors will not be significant if the loss of ellipticity is the only condition available. Therefore, the damage energy due to strain softening works like a catalyst which accelerates the development of a localization of deformation.

As Tvergaard et al. (1981) noted, it is not surprising that numerical studies carried out within the theoretical framework by Hadamard (1903), Thomas (1961), and Hill (1962) have given no indication of shear band formation. The reason for the above (given by Tvergaard et al., 1981) is that the classical elasto-plastic solid with a smooth yield surface is quite resistant to the localization of deformation into a shear band. Therefore, the damage energy is one of the principal factors to reduce the resistance to the formation of a shear band. However, the exact contribution of loss of ellipticity, damage energy and their coupling, if any, needs further study.

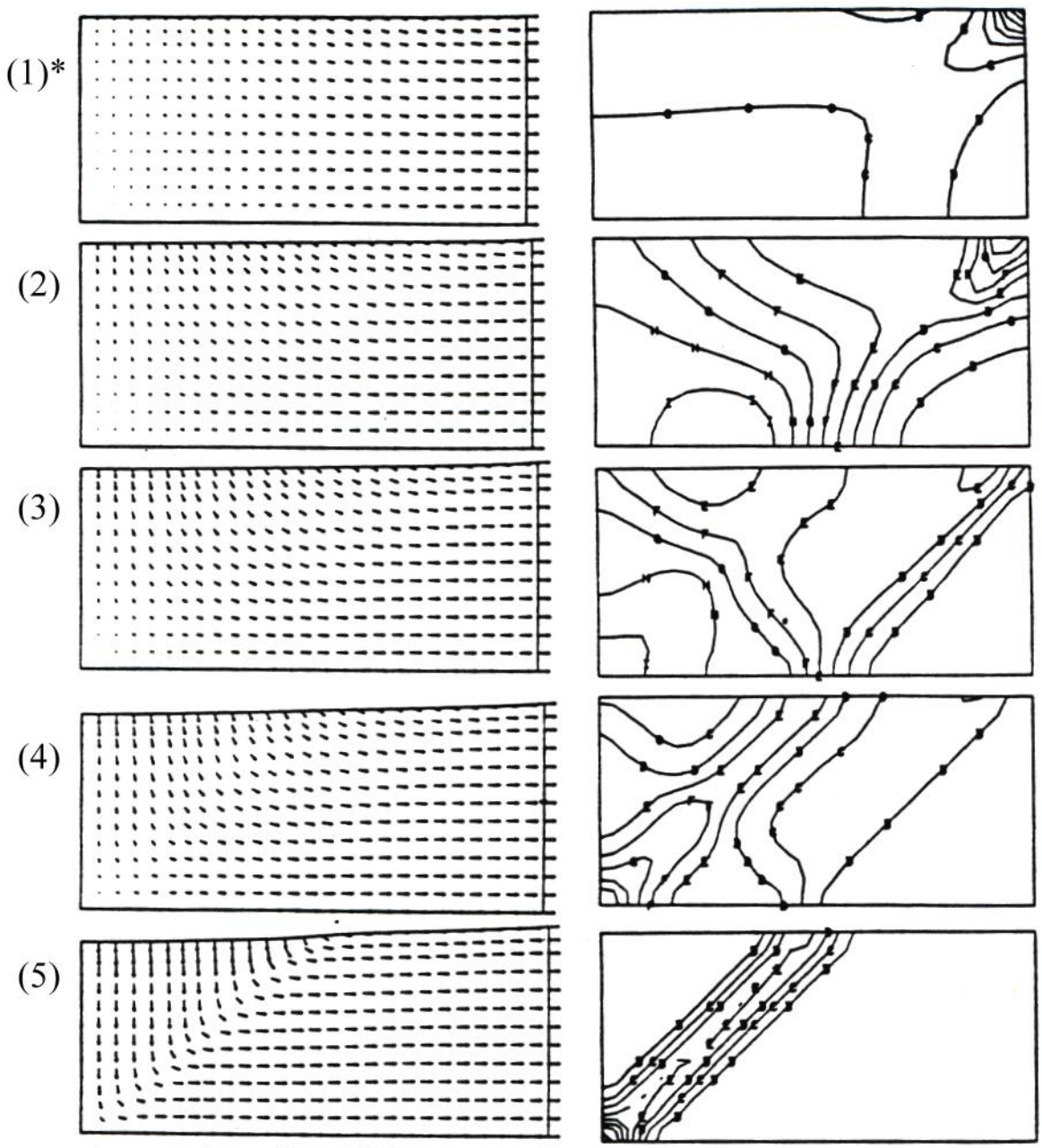

Figure 1.93. Continuous process of the formation of localizations

(Hardening parameter equal to zero)

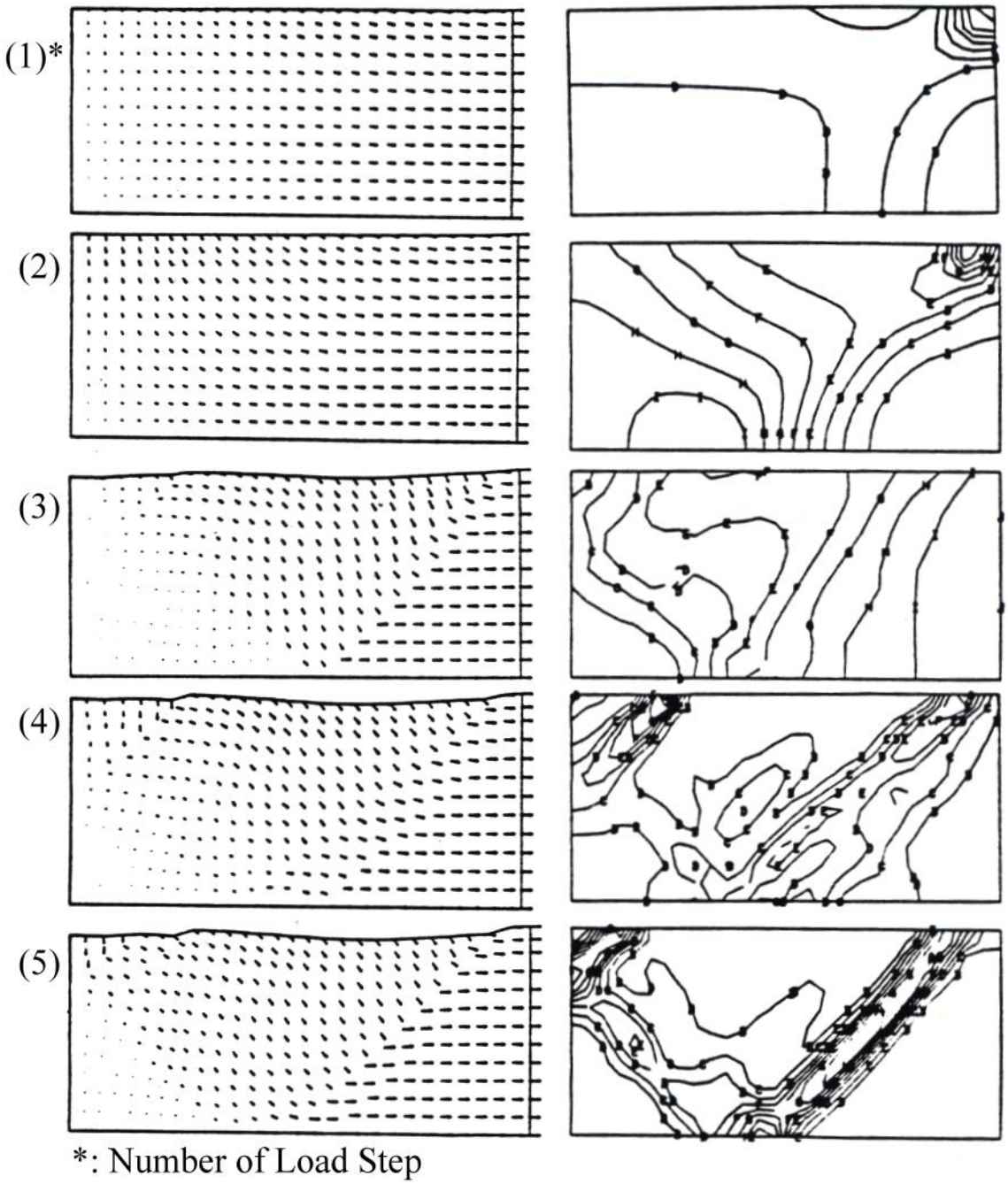

Figure 1.94. Continuous process of the formation of localizations

(Hardening parameter less than zero)

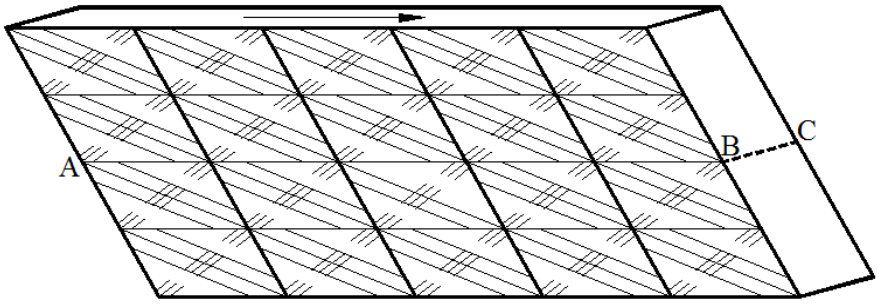

(a) Undeformed crystal

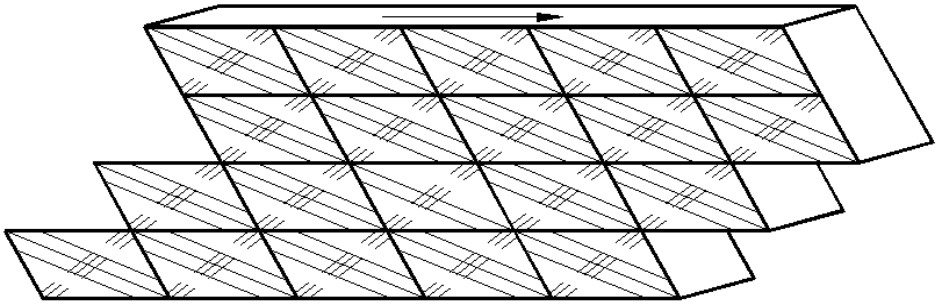

(b) Deformed crystal due to slip

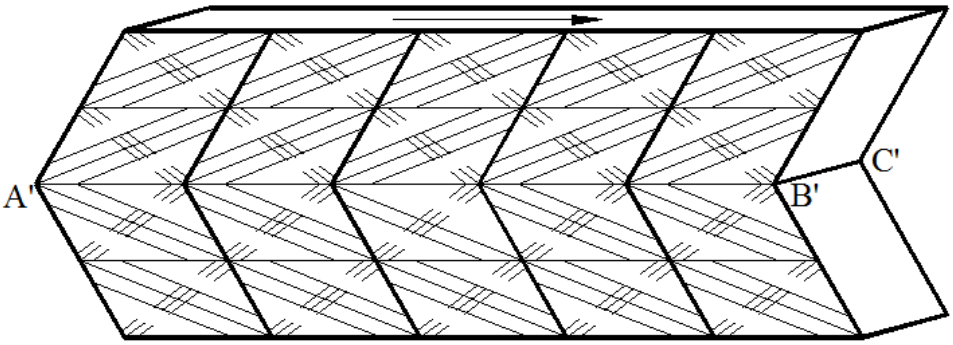

(c) Deformed crystal due to twinning

Figure 1.95. Behaviors of slip and twinning in crystal plasticity

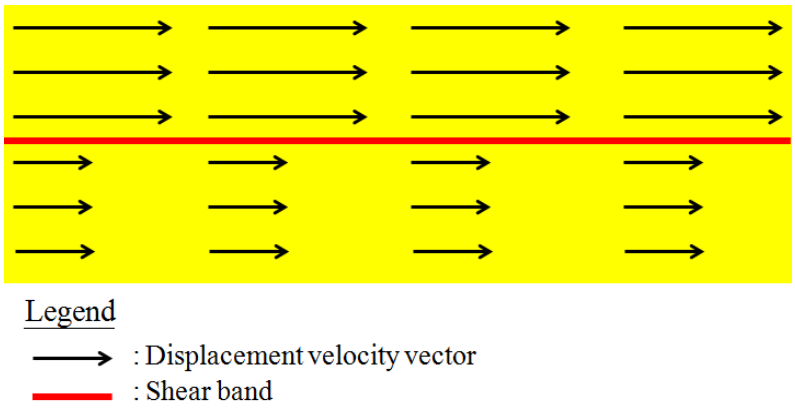

(a) A sudden change of the size of the velocity vectors

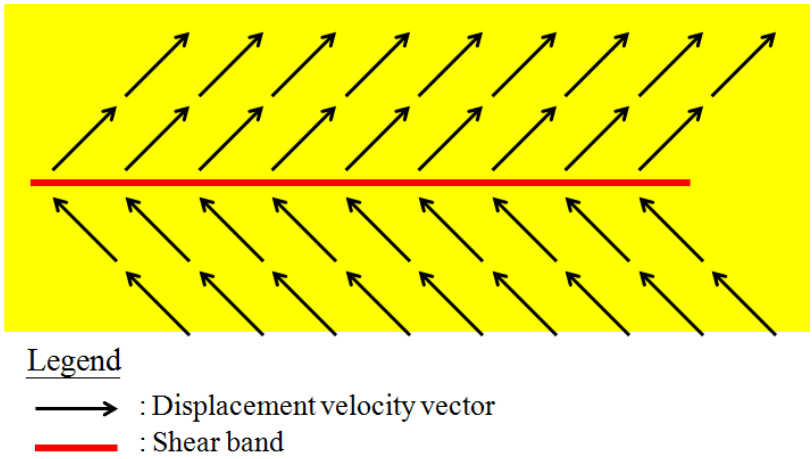

(b) A sudden change of the direction of the velocity vectors

Figure 1.96. Mechanisms of localization of deformation

1.6 Summary of the Main Points

1. Localization of deformation was relatively pronounced in a uniform but relatively coarse mesh. Further mesh refinement either by reducing the size of the element or by increasing the number of nodes in an element generally was found equivalent to over-killing for strain softening materials.
2. Very small or very big load increments were found to give less vivid pattern of localization. An optimum sub-step size of load increment, perhaps, exists but such a step size will vary from problem to problem.

3. Selective refinement along known zones of shear banding was tried but it was found that it could force the shear band to move immediately next to the refined region.
4. For uniform materials, boundary conditions have great influence on the formation of the shear bands. Boundary conditions were less important for the formation of shear bands when non-uniform materials were used.
5. Shear banding could occur only for materials with hardening parameter equal to or less than zero; however for elastic perfect plastic materials only one set of shear bands was observed, while for strain softening materials multiple sets of shear bands were obtained.
6. The initiation of localized deformation from homogeneous state generally was the onset of a shear band. Non-uniform geometry or non-uniform loading conditions could easily trigger a localized deformation form homogeneous state.
7. Poisson's ratio was directly related to the compressibility of the material. It was observed that shear bands may propagate relatively easy in a material with a higher value of Poisson's ratio.
8. The size of the gap between the upper and lower shear box has a major influence on the pattern of initiation of localization.
9. The post-peak stress-strain relationship in an unconfined compression test needs a nontraditional interpretation when portion of the sample bulges; and conventional uniform deformation assumption may lead to incorrect behavior.
10. Localization of deformation could be initiated by both a sudden change of the size and the direction of velocity vectors. Such mechanisms were found similar to those exhibited in sliding and twinning in crystal plasticity.

Chapter 2

Building Disasters Caused by Shear Bandings

T.-S. Hsu, C.-C. Ho, M.-C. Ke and C.-Y. Su

2.1 Introduction

The China Earthquake Disaster Prevention Center (2017) states that earthquakes can be divided into a total of five different types, namely, tectonic earthquakes, volcanic earthquakes, collapse earthquakes, induced earthquakes, and artificial earthquakes. Of which, tectonic earthquakes are most prevalent, accounting for about 90% of the total number of earthquakes around the world. Their destructive power is also the strongest. All earthquakes that cause major disasters are tectonic earthquakes.

The properties of tectonic plates vary with changes in temperature, Sibson et al. (1975) pointed out that when the temperature is less than 250℃, the tectonic plate is brittle; when the temperature is between 250℃ and 350℃, the tectonic plate gradually changes from brittle to plastic; and when the temperature is greater than 350℃, the tectonic plate is plastic (details in Figure 2.1).

Because there are several different tectonic plates on earth, each tectonic plate floating on the hot magma has a tendency to move, so under the situation of mutual interaction between the tectonic plates, lateral compression or lateral extension phenomena may exist. Once the shear strain goes deep into the plastic range, Drucker (1950), Hill (1962), Mandel (1960), Rudnicki and Rice (1975), Rice (1976), and Valanis (1989) consider that localization of deformations will appear due to the loss of ellipticity, and further induce shear bands as shown in Figure 2.2.

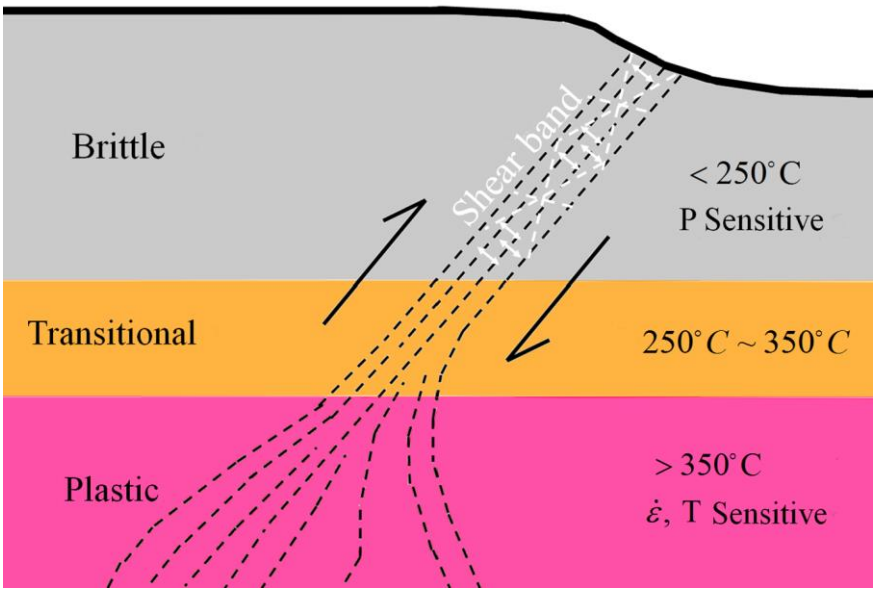

Figure 2.1. The formation of a shear band (redrawn from Sibson et al., 1975)

Figure 2.2. Shear bands appearing in Zhushan of Taiwan during the 921 Jiji earthquake

During shear banding, both sides of a shear band will induce repeated stick-slip phenomenon as shown in Figure 2.3. When the sticking action continues to raise the friction resistance up to the maximum value of static friction resistance, the sticking phenomenon will then change to slipping. At this point of time, the friction resistance changes from static friction to kinetic friction. While when the slipping action continues until the sticking

reappears, the friction resistance will drop to the minimum value of kinetic friction resistance, thereafter the static friction resistance will increase again.

When the stick-slip phenomenon repeatedly appears in shear bandings, once the state changes from sticking to slipping, the plates on both sides of the shear band will accelerate; and when the state changes from slipping to sticking, the plates on both sides of the shear band will decelerate. Therefore, while shear banding, the ground acceleration time-history curve, as shown in Figure 2.4, can be recorded by the seismometer.

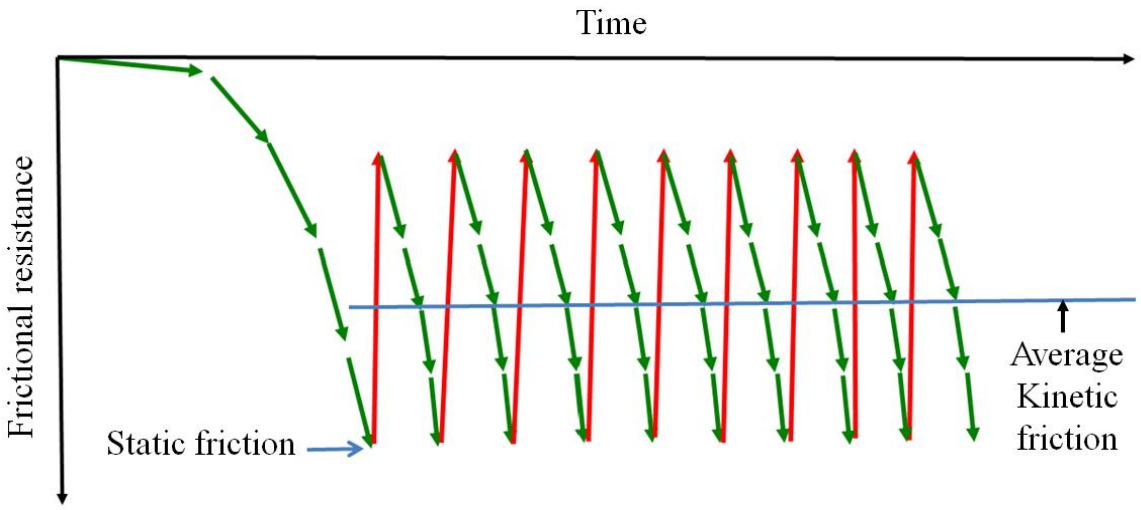

Figure 2.3. Stick-slip phenomenon in shear bandings (redrawn from Lambe and Whitman, 1969)

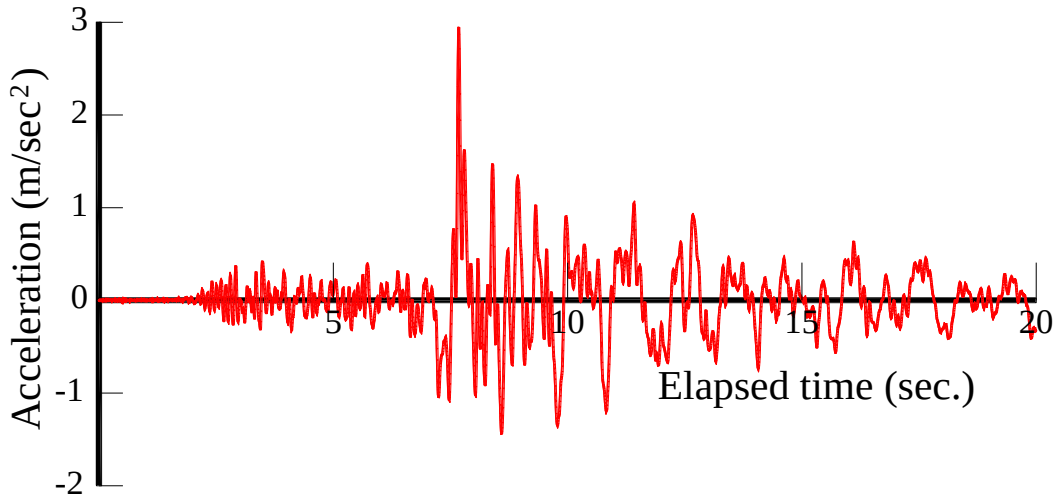

Figure 2.4. Acceleration time-history of ground vibration

In view of the above, in a tectonic earthquake, shear banding only exists locally, while seismic vibration exists throughout the entire plate. During the 921 Jiji earthquake, a tectonic earthquake, when the Dongshih-Dynasty building and the Xiangyang-Yongzhao building were collapsed, all other buildings that were in closely proximity to these two collapsed buildings remained stable (details in Figure 2.5); so it was revealed that the collapse to buildings in a tectonic earthquake only occurred locally. Wu (2010) used satellite imagery and a displacement velocity vector distribution map to show that the collapse to these two buildings is closely related to the local shear bandings. However, during the amendments to seismic design specifications of buildings, the reason for these collapsed buildings considered is limited to their insufficient resistance to the horizontal seismic vibration, thereby only amending the horizontal seismic vibration resistance of the upper structural components including columns, beams, slabs and shear walls, etc.

After 1999, the horizontal seismic vibration resistance provided in the seismic design specification of buildings has been greatly enhanced based on the magnitude of M_L = 7.3 in the 921 Jiji earthquake. However, Figure 2.6 shows that the building subjected to alteration work in accordance with the latest seismic design specification of buildings still appears to be seriously damaged during the 0206 Meinong earthquake in 2016 with a magnitude of M_L = 6.4; and other old buildings in close proximity to this building remained stable during the same earthquake.

Thus we can see the current seismic design specifications of buildings, although the resistance to horizontal seismic vibration has been elevated to the seismic standard for the magnitude of M_L = 7.3, cannot ensure prevention from tilting damage in the Meinong tectonic earthquake with a magnitude of M_L = 6.4.

Since the expertise of scholars and experts relevant to the seismic design of buildings is in structure dynamics and the earthquake type is classified as geotechnical earthquake engineering, in the development or amendment of the seismic design specifications of buildings, the sole focus is on the seismic vibration effects in relation to structural dynamics, but neglects the shear banding effects. Also, as the primary effect of a tectonic earthquake is the local shear banding, rather than the all-around vibration,

the current seismic design specifications of buildings essentially do not meet the requirement of tectonic earthquakes.

(a) The Dongshih-Dynasty building

(b) The Xiangyang-Yongzhao building

Figure 2.5 Buildings with local collapse in the 921 Jiji earthquake (Wu, 2010)

(a) Before the tilting damage (Google Earth, 2016)

(b) After the tilting damage

Figure 2.6 Tilting damage on a re-designed and altered building in the Meinong earthquake

As far as we know, currently no countries worldwide include the primary effect of tectonic earthquakes into the seismic design specifications of buildings, and thus the derived seismic design only focuses on the horizontal vibration resistances of components of upper structure for meeting the seismic design specifications of buildings and the requirements of shaking table validation tests. As a result, during shear banding, design specifications are still unable to ensure the prevention of collapse to buildings.

In 2014, Taiwan had the outbreak of evil oil event. By engineering ethics, it was revealed that the reason why evil oil can be sold in public is because the food specifications have not included its fatal factors into the specifications; thereby evil oil also can pass the relevant tests and be placed on the shelves “legally” for open sale.

In view of the above-mentioned issue, in order to avoid a similar problem and prevent earthquake-resistant buildings from becoming “evil” earthquake-resistant buildings, during the development or the amendment of specifications, the government should include the fatal factors into the specifications. Therefore, the development or the amendment of the seismic design specifications of buildings should focus mainly on the discussion of fatal factors. Only including the fatal factors into the specifications can then ensure that the building is able to remain stable under conditions where the earthquake magnitude is smaller than the designated earthquake magnitude.

Next, after the 921 Jiji earthquake, the Kuangfu Junior High School in Taichung was kept as an earthquake memorial museum for shear banding, ground uplift, and school building collapse, thereby preserving the historical facts of the earthquake, as well as providing students and social public earthquake teaching materials. In 2001, the school was renamed as the 921 Earthquake Education Park. Although the conceptual intention of establishing the 921 Earthquake Education Park is good, the relevant explanation does not contain the fatal factors, and thus it is difficult to achieve the education function for tectonic earthquakes. Taking the Kuangfu Junior High School building as example, the local collapse is depicted in Figure 2.7. The actual mechanism for such a local collapse is shown in Figure 2.7.c as to be caused by shear bandings in a tectonic earthquake. However, under the guidance of the instructor of the park, currently almost

all students, teachers, or people in the community, who have come here to visit, consider that the local collapse to the school building is mainly due to excessive seismic vibration. It is to be stressed that this kind of discourse will be make it difficult for people to understand, why there are school buildings that still remain stable under the same earthquake within the school district.

In view of the above, correctly stipulating or amending the seismic design specifications of buildings and correctly executing the earthquake education are both required to incorporate fatal factors into the specifications and seismic textbooks, so that the buildings can remain stable during tectonic earthquakes with magnitudes less than the design magnitude.

(a) Front view

(b) Rear view (Peggy, 2013)

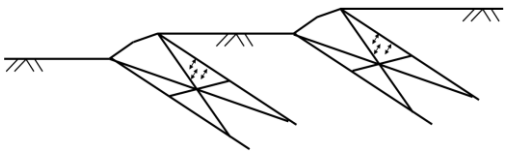

(i) The terrain of the slope

(ii) Leveling with digging and filling balance

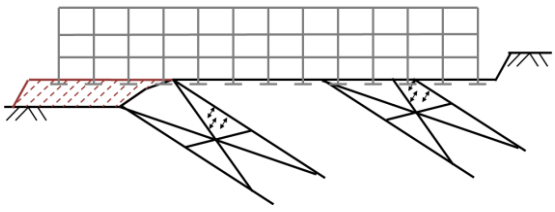

(iii) End of building construction

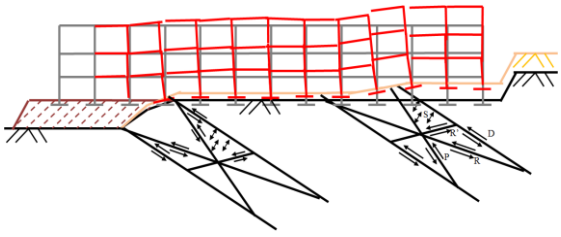

(iv) Local collapse of a building by caused by shear bandings

(c) Schematic diagrams of construction process and local collapse mechanism in a tectonic earthquake

Figure 2.7 Local collapse of Kuangfu Junior High School Building in the 921 Jiji earthquake

2.1 Literature Review

2.1.1 Current Seismic Design Specifications of Buildings

This section describes the seismic design specifications of buildings (Construction and Planning Agency, Ministry of the Interior, 2011); hereby the provisions related to the seismic design of buildings are excerpted as the following:

Stable Ground. During an earthquake, in the case that the ground is stable, the provisions related to seismic design of buildings are as follows:

1. **Static analysis method**

When a building of regular shape does not need to be subjected to dynamic analysis, the seismic force can be calculated in accordance with the provisions of the static analysis method, and the structural analysis can be conducted via the static method. The seismic force can be assumed to act individually and separately on the tops of the two principal axial directions of the building. A building consists of upper and lower parts; the rigidity of the lower part is large and the rigidity of the upper part is very small. When these two parts are taken into consideration separately, both are parts of a regular shaped building. The average floor stiffness of lower parts must be at least 10 times higher than the average floor stiffness of the upper part. In the case that the basic vibration period of the entire building is not 1.1 times greater than the basic vibration period obtained by viewing the bottom ends of structural columns in the upper part as the fixed ends, at this point in time, the seismic forces of both the upper and the lower structures can be calculated separately. In this case the factors to be considered include the minimum horizontal resistance required by the design, the horizontal spectral acceleration coefficients at short period and a 1-second period for the seismic zone of a general site, the horizontal spectral acceleration coefficients at short period and a 1-second period for a site near the fault region, the horizontal spectral acceleration coefficients at short period and a 1-second period for a site near the fault region, the site design and maximum considered horizontal spectral acceleration coefficients, the occupancy importance factor, the initial yielding seismic force amplification multiple and structural system seismic force reduction factors, the design seismic forces for moderate to

small earthquakes and maximum considered earthquake, the vertical distribution of seismic force, as well as the design horizontal seismic force for the underground parts of the building, etc. The simulation related to the structure in static analysis should reflect the actual situation as much as possible. Therefore, it is necessary to strive to have accuracy in the simulation, mass distribution, and construction materials' sectional properties of geometric shapes, as well as the simulation of the interaction between soils and the foundation structure.

2. Dynamic analysis method

Under the following circumstances, the buildings shall be designed by dynamic analysis: (1) Buildings in which their height is equal to or more than 50 meters or above of 15 floors; (2) Buildings whose height exceeds 20 meters or above of 5 floors, and their stiffness, weight configuration, or façade geometric shape is irregular; or its planar torsion is irregular; (3) Buildings whose height exceeds 5 floors or 20 meters, and not whole height possess the same type of structural system. The factors that need to be taken into consideration in the dynamic analysis method contain the design horizontal acceleration response spectral coefficients, the adjustment of resistance, the multi vibration mode response spectral superposition method, the time-history analysis method, the dynamic torsion, the design seismic force for the underground part of the building, the spacing of interlayer relative lateral displacement with the building, the checking of ultimate story shear strength, as well as the vertical earthquake effect, etc. The simulation of the related building structure in the dynamic analysis should reflect the actual situation as much as possible. Therefore, the simulation, mass distribution, construction materials' sectional properties of geometric shapes, as well as simulation of the interaction between soils and foundation structure should all strive to be accurate.

Unstable Ground. During an earthquake, in the case that the ground is unstable, the provisions related to seismic design of buildings are as follows :

1. Those very soft and weak soil layers will lead to a significant drop in soil strength during an earthquake. That is, there is a clay soil layer or silt soil layer within 3 meters depth of the ground surface depth; deduced by using a uniaxial compression test or an on-site test, the soil layer with an uniaxial compression strength below 0.2kgf/cm^2 is regarded as a very soft and weak soil layer in seismic design.

2. Alluvial saturated sandy soil layer will produce soil liquefaction or fluidization during an earthquake. That is, focusing on the saturated sandy soil layer of alluvium, the JRA simplified empirical method for highway bridges should be used to determine the liquefaction potential. When the liquefaction resistance safety factor of F_L is less than 1.0, it is determined that this soil layer may be liquefied. The soil liquefaction determining method can be performed in accordance with the provisions of "Building technical regulations, Volume of Building Structures, Structural Design Specifications of Foundations" by the Ministry of the Interior. The site should be checked separately for the possibility of liquefaction occurrence during moderate and small earthquakes (when the ground surface horizontal acceleration for a general site and near-fault worksite is $A = [0.42S_{DS}/4.2]g$, or the ground surface horizontal acceleration for the Taipei Basin is $A = [0.4S_{DS}/3.5]g$); during a design earthquake (when the ground surface horizontal acceleration is $A = 0.4S_{DS}g$), and during the maximum considered earthquake (when the ground surface horizontal acceleration is $A = 0.4S_{MS}g$).

3. When it is determined that there could be a very soft and weak soil layer or soil liquefaction, the soil parameters used in seismic design should be reduced in accordance with the provisions. During moderate and small earthquakes, the site shall not have the possibility of liquefaction. During the design earthquake and the maximum considered earthquake, although the soil liquefaction occurrence is permissible, the building should adopt appropriate foundation form and the safety should be checked. When the seismic design is conducted, the soil layer should also be taken into consideration so that an unstable situation will not be generated, and more stringent results are adopted as the basis of seismic design. For example, when calculating the basic vibration period, the soil parameters do not need be reduced.

Installing Seismometers. The competent building authority shall depend on the requests of the competent authority of seismological reports, or research institute for seismology, or building research institution to require the building owner to coordinate and set aside appropriate space during the construction of a building design for the competent authority for seismological reports, or research institute for seismology, or building research institution to set up seismic recorders; and safeguard the recorders during the use of the building. After an earthquake, the records are to be collected by the competent authority for seismological reports, or research institute for seismology, or building research institution for reference and checking.

2.1.2 History of Seismic Design Specification of Buildings

In 1945, the Ministry of the Interior began to publish building technical regulations. The content contains relevant guidelines for the planning, design and construction of building projects.

In 1945, although the Ministry of the Interior published the building technical regulations, the building technical regulations have no provision for the design seismic force, and also no related provision for seismic zoning and seismic design of construction materials. When an engineer is designing a building, the minimum horizontal seismic force provided is mainly in accordance with the seismic intensity method of Japan, whereby the minimum horizontal seismic force required for earthquake-resistance is $V = KW$ (National Center for Research on Earthquake Engineering NCREE, 2017).

In 1974, the Ministry of the Interior set the minimum horizontal seismic force required for earthquake-resistance as $V = ZKCW$ (National Center for Research on Earthquake Engineering NCREE, 2017; Ye and Lee, 2005) and divided Taiwan into different seismic zones in accordance with the occurrence probability, magnitude, and seismic intensity of earthquake. The design seismic force coefficients for each seismic zone are shown in Figure 2.8. Whereby, for a strong seismic zone, $Z = 1.25$; for a moderate seismic zone, $Z = 1.0$; for a light seismic zone, $Z = 0.75$. As for the reinforced concrete structure, there had been regulations on the toughness design at this stage.

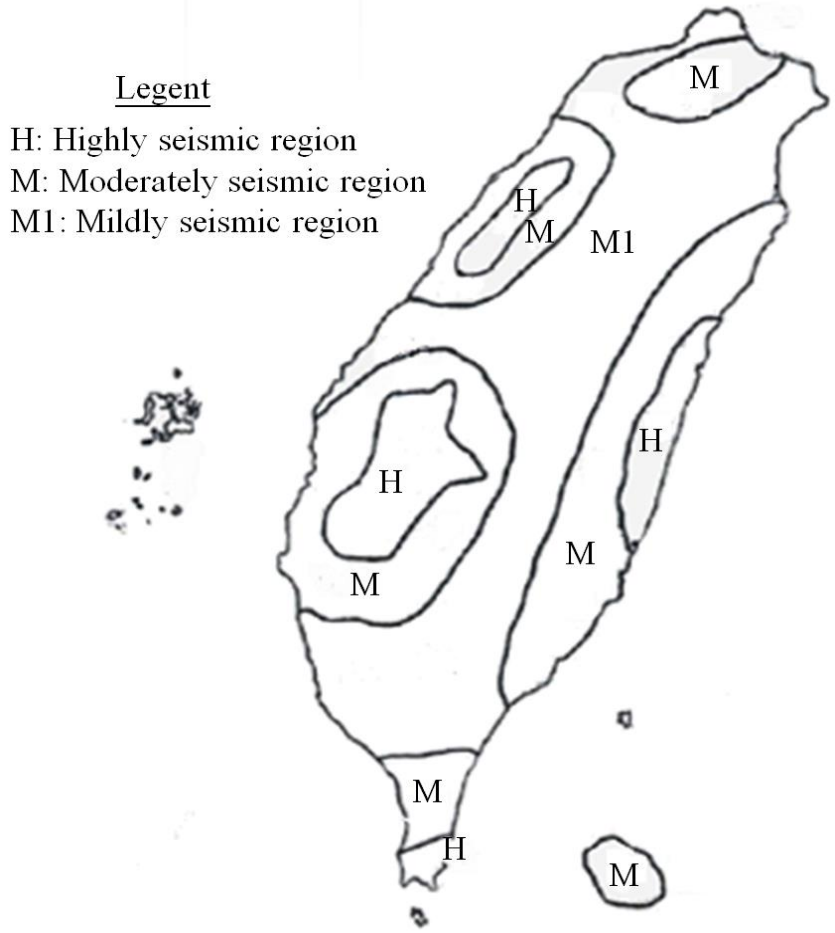

Figure 2.8. Division of the seismic zones of Taiwan in 1974 (National Center for Research on Earthquake Engineering NCREE, 2017)

In 1982, the Ministry of the Interior amended the Z of the strong seismic zone to 1.0, the Z of the moderate seismic zone to 0.8, and the Z of the weak seismic zone to 0.6; as well as developing different importance levels for different building purposes as *I*. Hence, the minimum horizontal seismic force required for seismic resistance was amended to $V = ZKCIW$ (National Center for Research on Earthquake Engineering NCREE, 2014; Ye and Lee, 2005). During this one period, in view of the severe catastrophes generated by basin effects of the 1985 Mexico earthquake and 1986 Hualien offshore earthquake, the basin effects were updated in 1989; and the Taipei Basin was classified as a special seismic zone and the seismic force coefficient of Taipei Basin was amended as *C* (National Center for Research on Earthquake Engineering NCREE, 2017).

In 1997, the Ministry of the Interior divided the regulations and specifications to simplify the clauses in the regulations. In view of the soil liquefaction disaster of 1995 Japan's Great Hanshin Earthquake, the soil liquefaction evaluation method was updated into the seismic design specifications of buildings; while the site type and vertical seismic force also began to be taken into consideration, whereby the minimum design seismic force was amended as $V = ZICW/(1.4\alpha_y F_u)$. Moreover, the seismic zone was re-modified into Earthquake Zone 1A, Earthquake Zone 1B, Earthquake Zone 2, and Earthquake Zone 3, as shown in Figure 2.9; the construction details of reinforced concrete were strictly specified (National Center for Research on Earthquake Engineering NCREE, 2017; Ye and Lee, 2005).

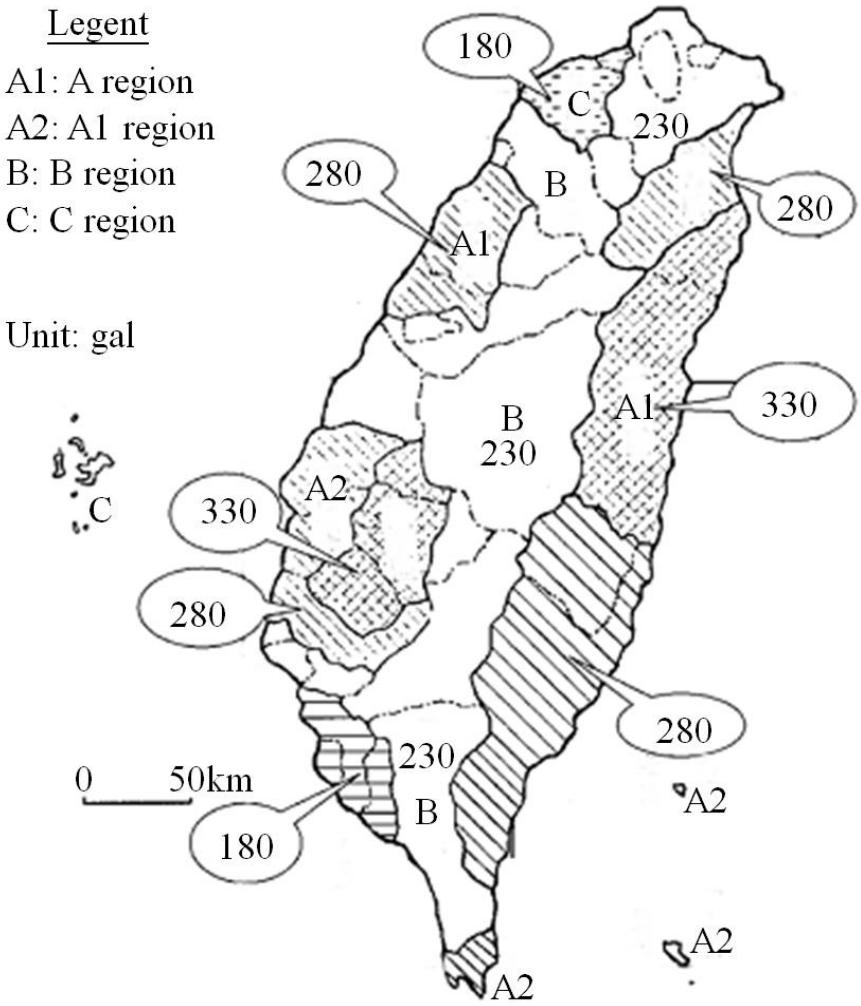

Figure 2.9. Seismic zone division of Taiwan in 1997 (Construction Department of the Interior Ministry, 2000)

In 1999, in accordance with the Central Geological Survey under the Ministry of Economic Affairs, the Chelungpu Fault was amended as the first type of active fault after the 921 Jiji earthquake. The Ministry of Interior amended the normalized work-site-dependent acceleration response spectral coefficient in the seismic design specifications of buildings and adjusted the vertical seismic force; while the division of seismic zones was again amended as Earthquake Zone A and Earthquake Zone B (details in Figure 2.10).

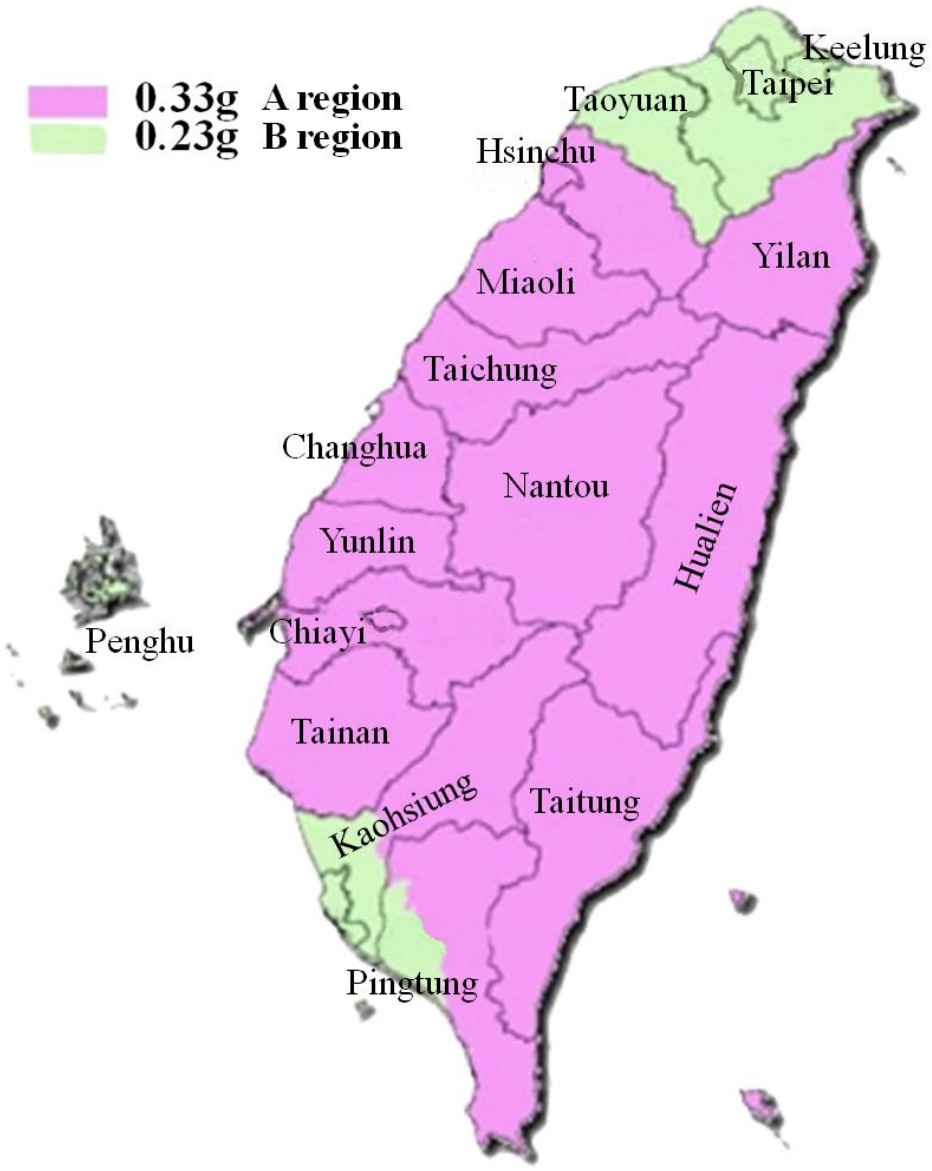

Figure 2.10. Seismic zone division of Taiwan in 1999 (National Center for Research on Earthquake Engineering NCREE, 2017)

In 2005, the Ministry of the Interior re-adjusted the seismic zones (details in Figure 2.11); and in accordance with the near-fault effect of the 921 Jiji earthquake, the design seismic force for near-fault buildings was updated.

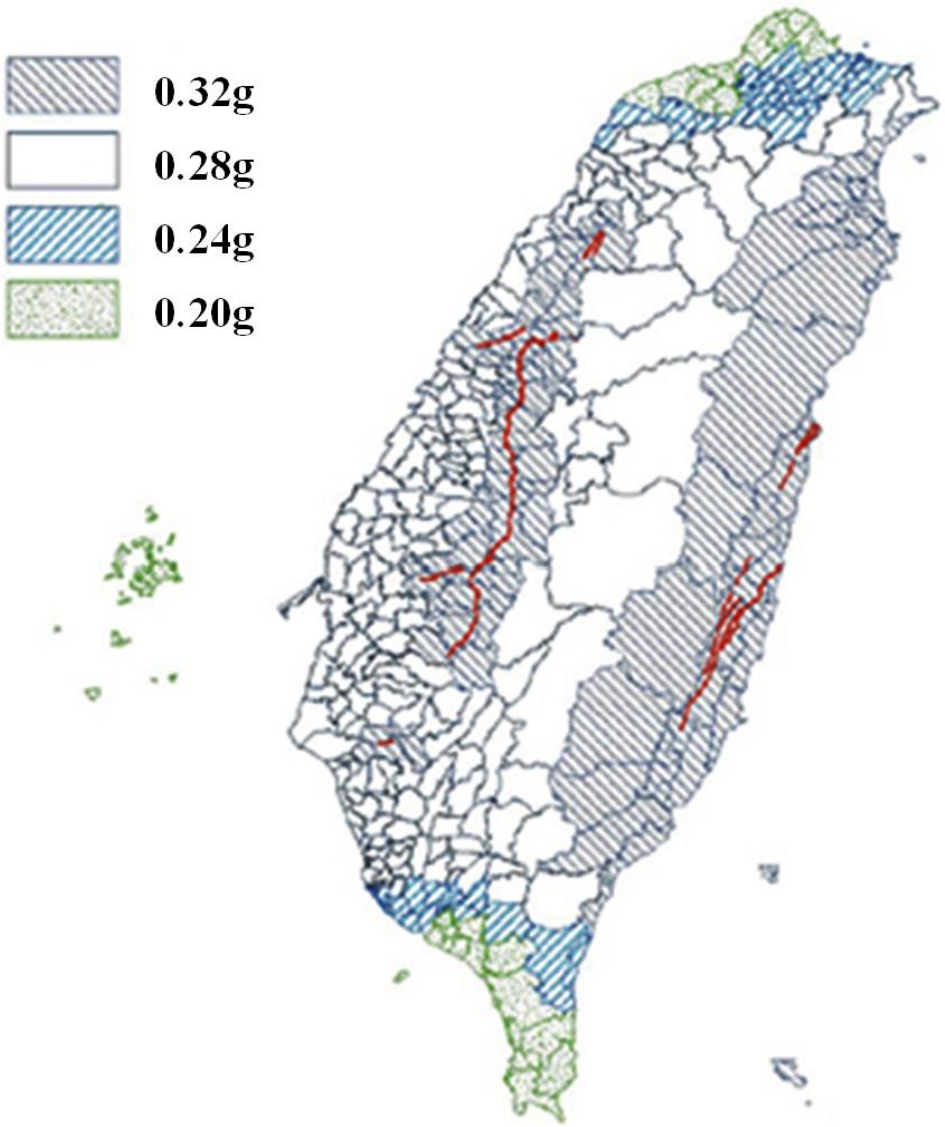

Figure 2.11. Seismic zone division of Taiwan in 2005 (National Center for Research on Earthquake Engineering NCREE, 2017)

In 2011, the Ministry of the Interior again amended the seismic design regulations of buildings for structural systems and toughness capacity, site classification criteria, CU value of calculated period's upper limit coefficient, microzonation for design earthquakes in Taipei Basin, spacing requirements

between buildings, seismic isolation building design, and ground surface horizontal acceleration for the determination of soil liquefaction potential, etc.

2.1.3 Seismic Reinforcement of School Buildings after the 921 Jiji Earthquake

Table 2.1 shows the tabulated statistics for the number of school buildings constructed and the percentage taking up the total school buildings in different years within the central region of Taiwan, as provided by Shyh-Jiann Hwang from the National Center for Research on Earthquake Engineering in 2014. From Table 2.1 we can see that the total number of elementary and junior high school buildings in the central region of Taiwan is 5058. Before 1974, there were 986 buildings constructed, 19.49% of the total school buildings. The seismic design of these school buildings is mainly based on the Japanese seismic intensity method, whereby the minimum horizontal seismic force is $V = KW$. During the period from 1974 to 1982, there were 1,131 buildings constructed, 22.36% of the total school buildings. The minimum horizontal seismic forces adopted in the seismic design of these buildings are $V = ZKCW$; whereby the design seismic force coefficients for each seismic zone are shown in Figure 2.7. For the strong seismic zone, $Z = 1.25$; for the moderate seismic zone, $Z = 1.0$; for the light seismic zone, $Z = 0.75$. During the period from 1982 to 1989, there were 1,279 buildings constructed, 25.29% of the total school buildings; during the period from 1989 to 1997, there were 1,372 buildings constructed, 27.13% of the total school buildings; during the period from 1997 to 1999, there were 290 buildings constructed, 5.73% of the total school buildings. For the school buildings constructed from 1982 to 1999, the minimum horizontal seismic force adopted in the seismic design is $V = ZKCIW$; whereby for the strong seismic zone, Z = 1.0; for the moderate seismic zone, Z = 0.8; for the weak seismic zone, Z = 0.6; and I is the importance level of occupancy for different buildings.

During the 921 Jiji earthquake, there were 656 elementary and junior high school buildings that collapsed or were severely damaged in the central region of Taiwan, accounting for 12.97% of the total school buildings. The funding for post-disaster reconstruction was about NT$ 40 billion (Hwang, 2014), which is equivalent to the total amount of construction funding for

elementary and junior high schools for 10 years. Since 2009, the Ministry of Education entrusted the National Center for Research on Earthquake Engineering to engage in the structural seismic reinforcement for junior high and elementary school buildings.

Evaluation and Design Basis of Seismic Reinforcement. On November 27, 2008, the Executive Yuan promulgated the scheme for implementing seismic capacity evaluation and reinforcement of buildings (Construction and Planning Agency, Ministry of the Interior, 2008). In 2009, the National Center for Research on Earthquake Engineering presented the Technology handbook for seismic evaluation and reinforcement of school buildings (Hsiao, et al., 2009), thereby promoting the seismic evaluation and reinforcement of school building structures.

The seismic reinforcement of school building structures is based on the performance design method (Hsiao, et al., 2009). The school building structures are divided into two types as general school building and emergency evacuation school building. The design is carried out for 475-year return-period ground surface acceleration in order to ensure that the degree of damage to school buildings is only considered moderate or mild range, thereby the life safety of teachers and students in major future earthquakes can be ensured.

Table 2.1. Number of school buildings constructed and percentage of the total school buildings in different years within the central region of Taiwan (Hwang, 2014)

	Number of the constructed buildings	Percentage as regard to all number of the constructed buildings
Before 1974	986	19.49%
1974~1982	1,131	22.36%
1982~1989	1,279	25.29%
1989~1997	1,372	27.13%
1997~1999	290	5.73%

Lateral Pushover Analysis. When executing the seismic evaluation method presented by the National Center for Research on Earthquake Engineering, it is required to first carry out lateral pushover analysis, in order to understand the magnitude of lateral acting force that can be resisted by the school building and the amount of non-linear displacement (Hsiao, et al., 2009).

The lateral pushover analysis is conducted under a specific vertical ratio; whereby the lateral acting force is applied under the displacement control method and it is applied to each floor of the school building until the school building is pushed over.

The lateral pushover analysis mainly uses structural analysis software, such as ETABS, MIDAS, and PISA3D to analyze the relationship between the total horizontal force of floor earthquake, V (a.k.a. base shear force), and the lateral displacement of the rooftop, Δ, thereby obtaining the V-Δ relationship curve, as shown in Figure 2.12. This V-Δ relationship curve is also known as the capacity curve.

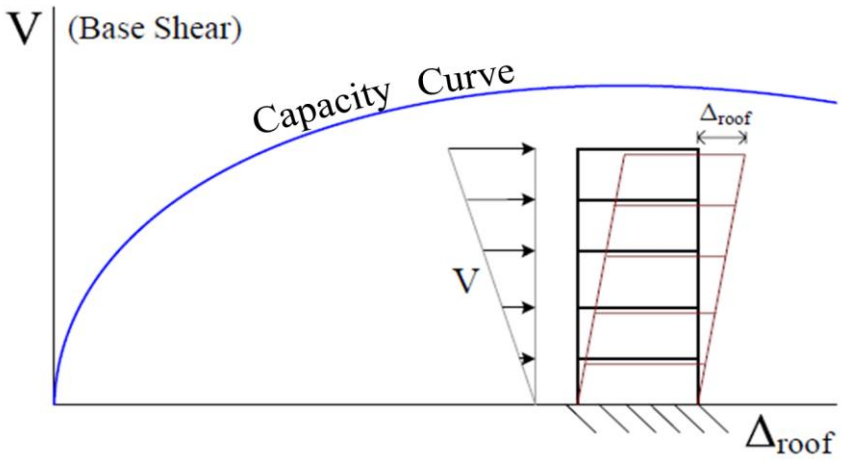

Figure 2.12. Capacity curve of lateral pushover in a structural building (Hwang, 2014)

Under the action of external force, the National Center for Research on Earthquake Engineering uses the hyperbolic column deformation mechanism, as shown in Figure 2.13, to evaluate the corresponding nonlinear hinge parameters of structural components, as well as simulate the applied force behavior of brick walls with equivalent bracings, and also simultaneously simulate the applied force behavior of RC walls with columns of equivalent width.

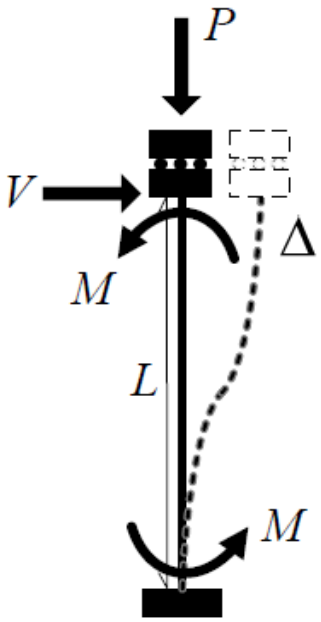

Figure 2.13. Applied force and deformation mechanisms of the hyperbolic column (Hwang, 2014)

When the capacity curve is known, and then taking the ATC-40 capacity spectrum method of United State as basis, supplemented with the damping ratio correction coefficient as provided in the seismic design specifications by the Ministry of the Interior, as well as the period and damping ratio of any function point on the capacity curve line, the capacity curve can be converted into the capacity curve of the equivalent single degree of freedom system. Finally, after deriving the seismic performance curve of a school building and the ground surface acceleration corresponding to the target performance point, supplemented by the different performance levels of operational, immediate occupancy, life safety and collapse prevention, we can evaluate whether the seismic capacity of this school building is sufficient.

The National Center for Research on Earthquake Engineering has conducted lateral pushover analysis under the established structural analysis model, focusing on the old buildings of four schools, Sincheng Junior High School in Hualien, Kouhu Elementary School in Yunlin, Ruipu Elementary School in Taoyuany, and Guanmiao Elementary School in Tainan. The detailed displacements of structural analysis models obtained from the analysis are shown in Figure 2.14.

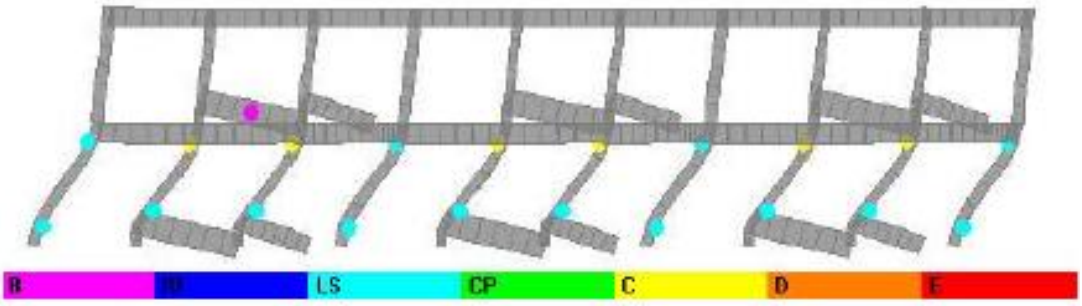

(a) Sincheng Junior High School in Hualien

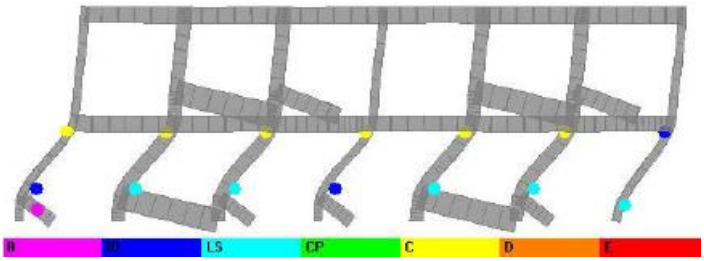

(b) Kouhu Elementary School in Yunlin

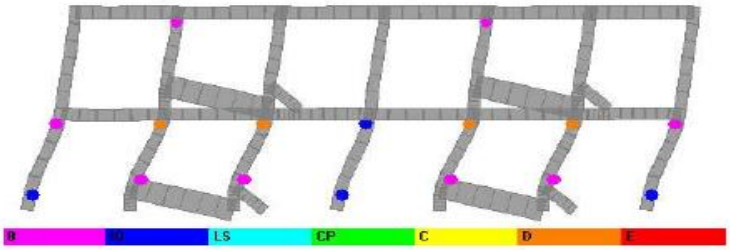

(c) Ruipu Elementary School in Taoyuan

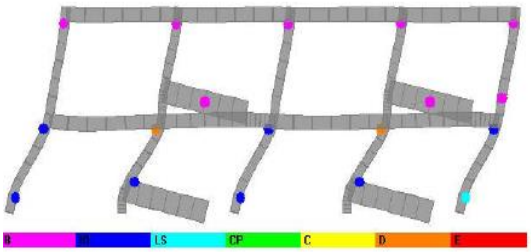

(d) Guanmiao Elementary School in Tainan

Figure 2.14. Displacements of structural analysis models obtained by the lateral pushover analysis (Hwang, 2009)

Lateral Pushover Test. The National Center for Research on Earthquake Engineering has also conducted lateral pushover test for actual structures, focusing on the old buildings of four schools, Sincheng Junior High School in Hualien, Kouhu Elementary School in Yunlin, Ruipu Elementary School in Taoyuan, and Guanmiao Elementary School in Tainan. The displacement diagrams of actual structures obtained from the tests are shown in Figure 2.15.

(Left) Before the test (Right) After the test

(a) Sincheng Junior High School in Hualien

(Left) Before the test (Right) After the test

(b) Kouhu Elementary School in Yunlin

(Left) Before the test (Right) After the test

(c) Ruipu Elementary School in Taoyuan

(Left) Before the test (Right) After the test

(d) Guanmiao Elementary School in Tainan

Figure 2.15. Displacements of actual structures obtained from the lateral pushover test (Hwang, 2009)

Seismic Reinforcement Methods for School Buildings. The school building reinforcement methods provided by the National Center for Research on Earthquake Engineering include RC jacketing reinforcement, RC wing wall reinforcement, RC shear wall reinforcement, and other methods. Hsu et al. (2015) also have proposed the composite column reinforcement method. These methods are described as follows:

1. RC jacketing reinforcement method

The detailed design diagram of the RC jacketing reinforcement method is shown in Figure 2.16. The RC jacketing reinforcement method can improve the bearing capacity, stiffness and shear resistance strength, flexural resistance strength, axial force resistance strength, and toughness of the column after reinforcing, thereby it is classified as a reinforcement method that increases the strength and toughness. Figure 2.17 shows the practical application of the RC jacketing reinforcement method.

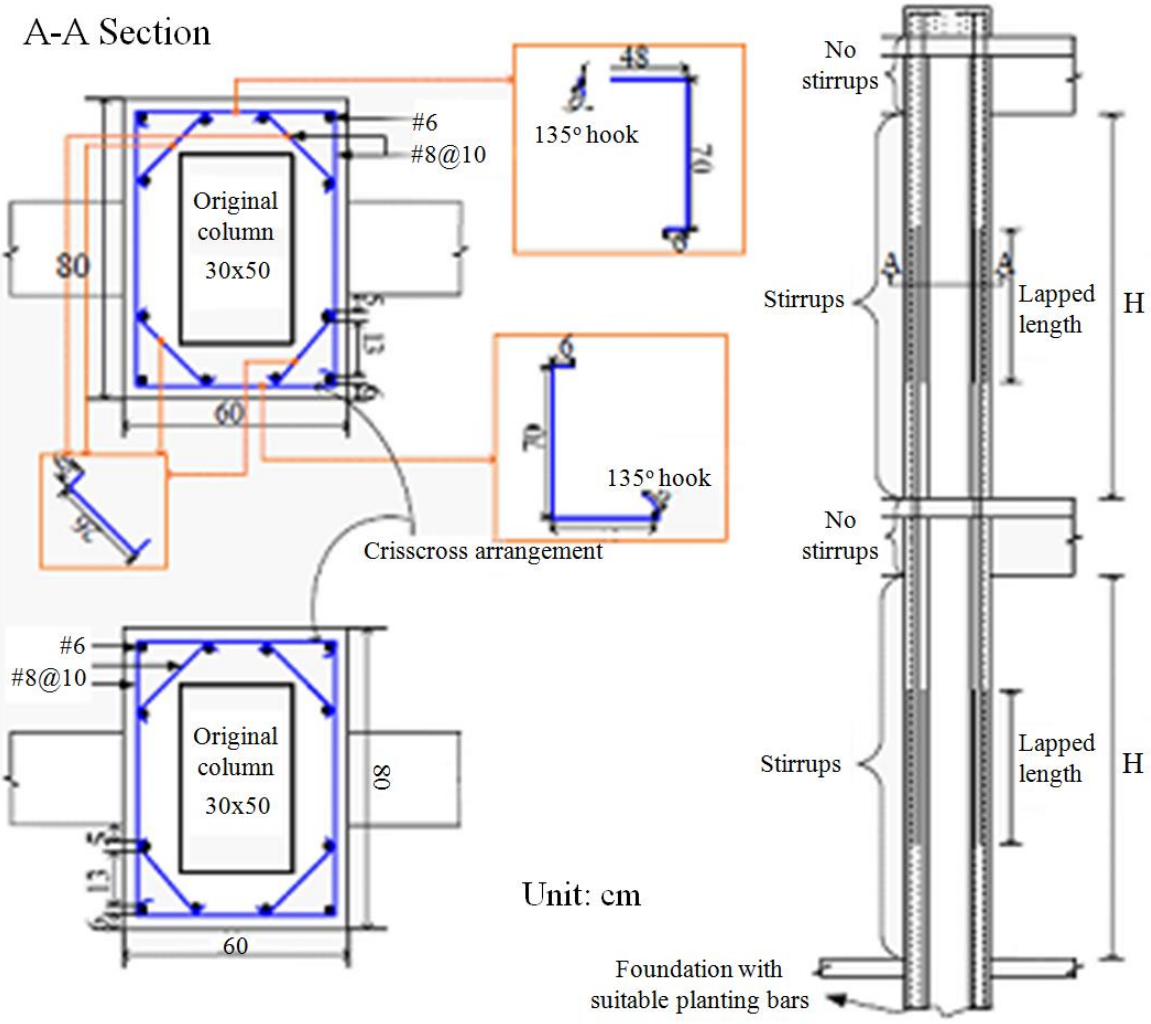

Figure 2.16. Design of RC jacketing reinforcement method (Chung, et al., 2009)

(a) Rebar assembly

(b) After completion

Figure 2.17. Practical application of RC jacketing reinforcement method (Ren-Mei General Affairs Office, 2015)

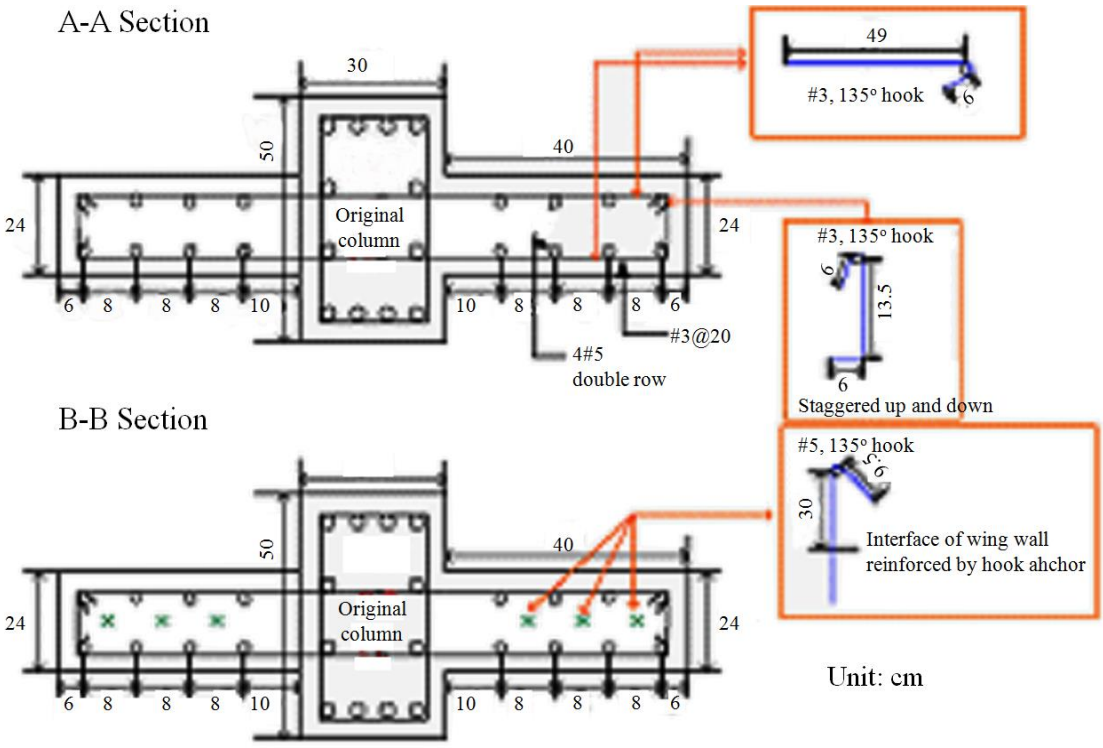

(a) Sectional views of A-A and B-B

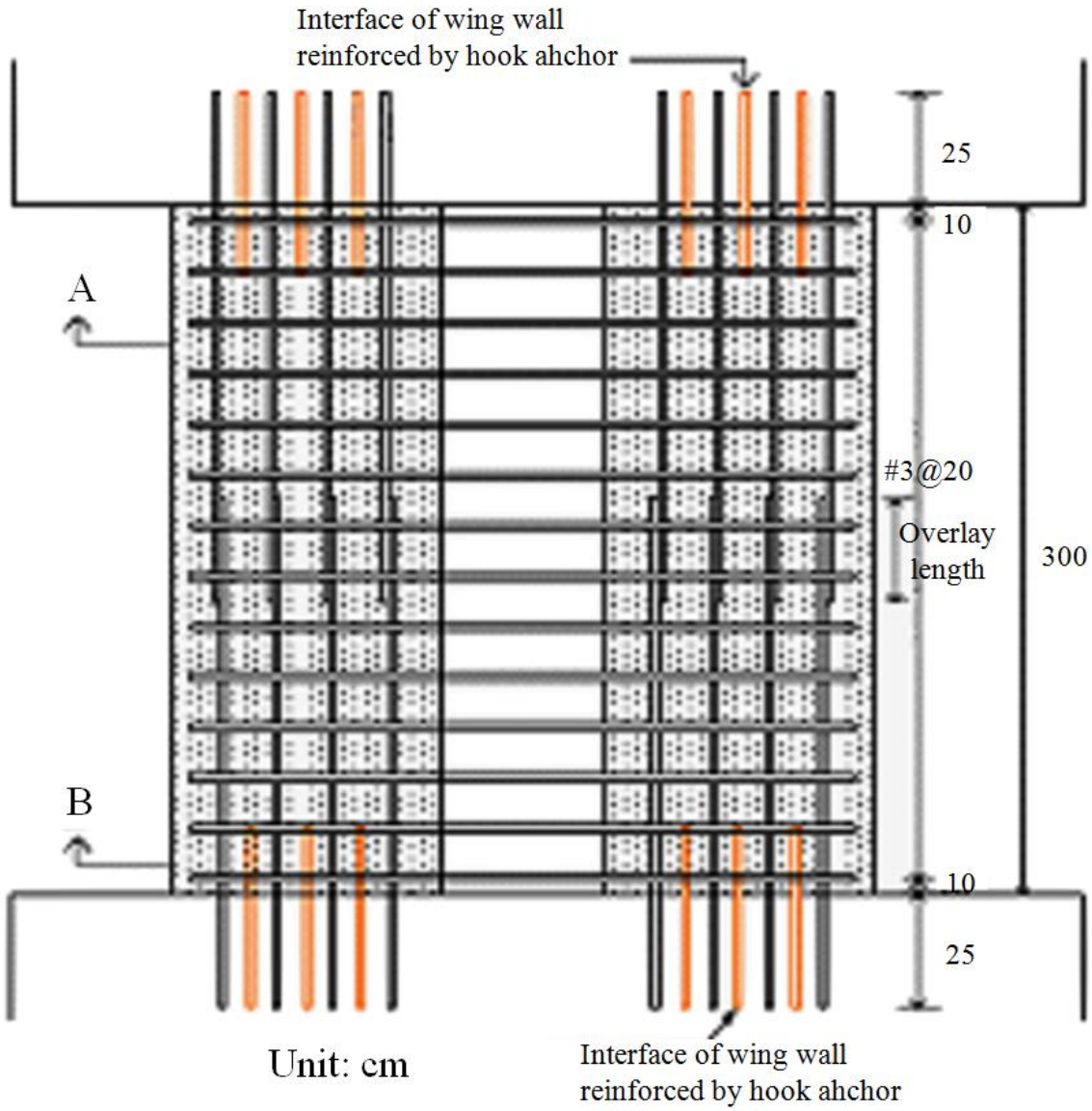

(b) Vertical plan view

Figure 2.18. Design of the RC wing wall reinforcement method (Chung, et al., 2009)

2. RC wing wall reinforcement method

The detailed design diagram of the RC wing wall reinforcement method is shown in Figure 2.18. The RC wing wall reinforcement method adds a RC wing wall in the weak direction of the structure. Its purpose is to enhance the overall structural strength. Figure 2.19 shows the practical application of this method.

(a) Rebar assembly (Ting-Wei Hsu, 2011)

(b) After completion

Figure 2.19. Practical application of the RC wing wall reinforcement method

3. RC shear wall reinforcement method

The detailed design diagram of the shear wall reinforcement method is shown in Figure 2.20. The shear wall reinforcement method can improve the strength of the overall structure resisting the horizontal force of earthquake; at the same time, it can eliminate the damage to soft and weak layers, reducing the structural torsion effect caused by the plane eccentricity. Figure 2.21 shows the practical application of the shear wall reinforcement method.

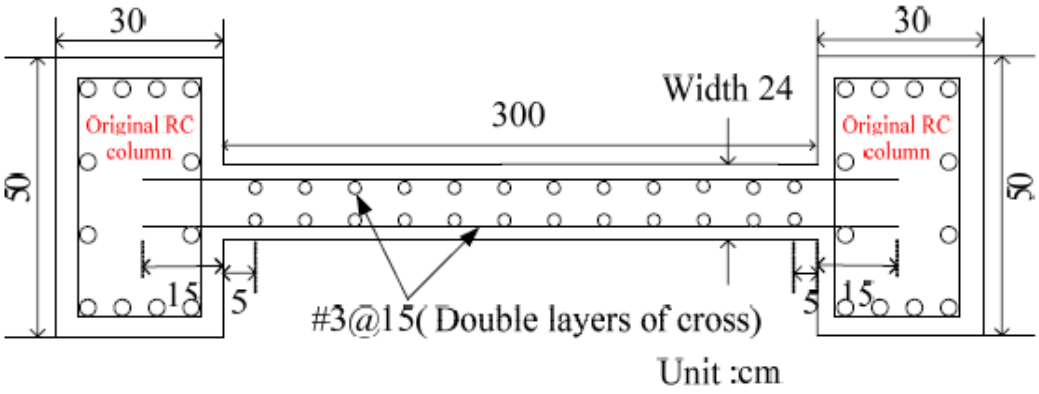

Figure 2.20. The RC shear wall reinforcement method (Chung, 2009)

(a) Rebar assembly

(National Center for Research on Earthquake Engineering NCREE, 2014)

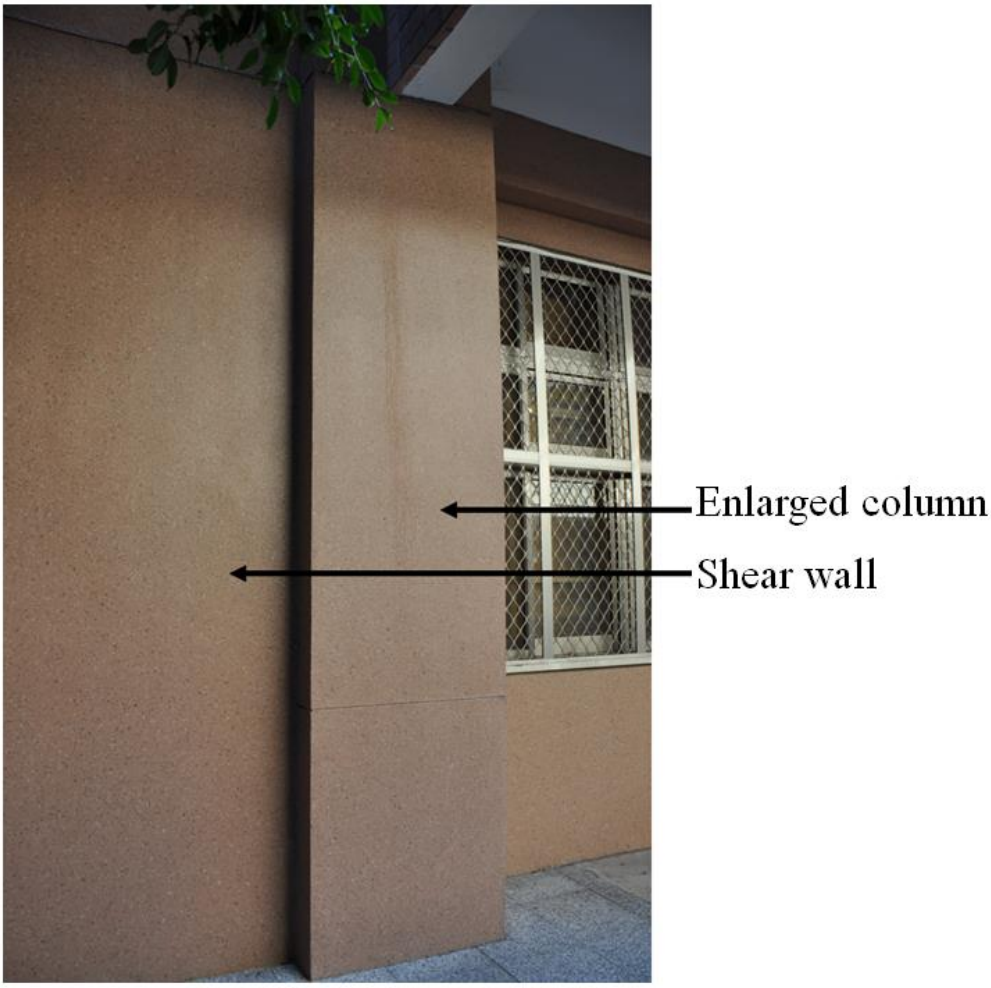

(b) After completion

Figure 2.21. Practical application of the shear wall reinforcement method

4. Composite column reinforcement method

The detailed design diagram of the composite column reinforcement method is shown in Figure 2.22, whereby steel sheet is used to wrap the original column body, and the steel sheet is tied with HILTI; while the interface of steel sheet and the original column body is bonded using epoxy resin. This one composite column reinforcement method can increase the axial force resistance, bending moment resistance, shear resistance of the column, and the toughness of overall structure. Figure 2.23 shows the practical application of the composite column reinforcement method.

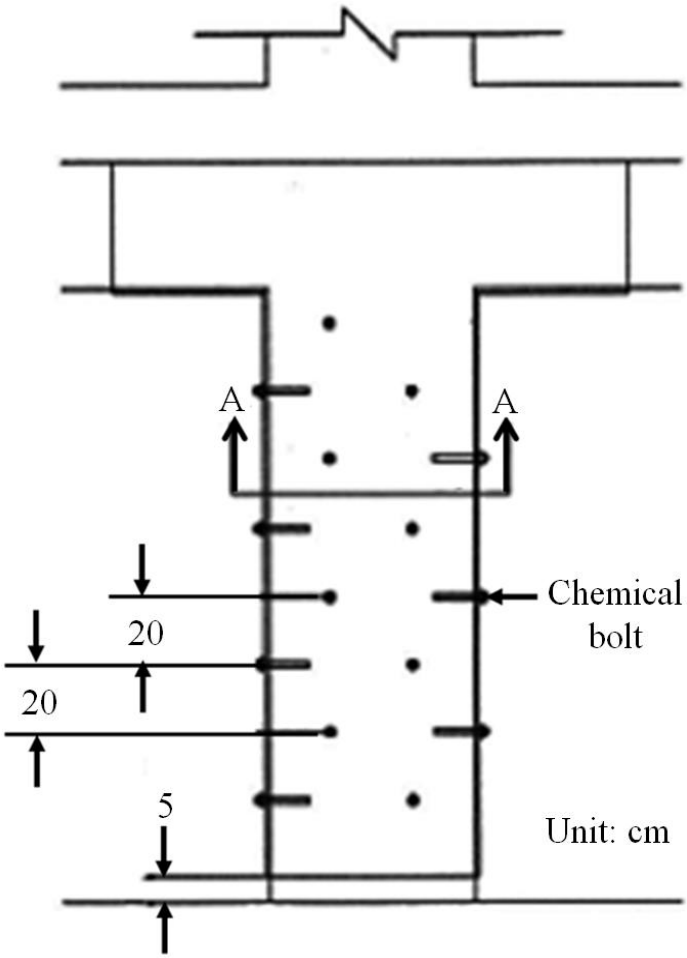

(a) side view

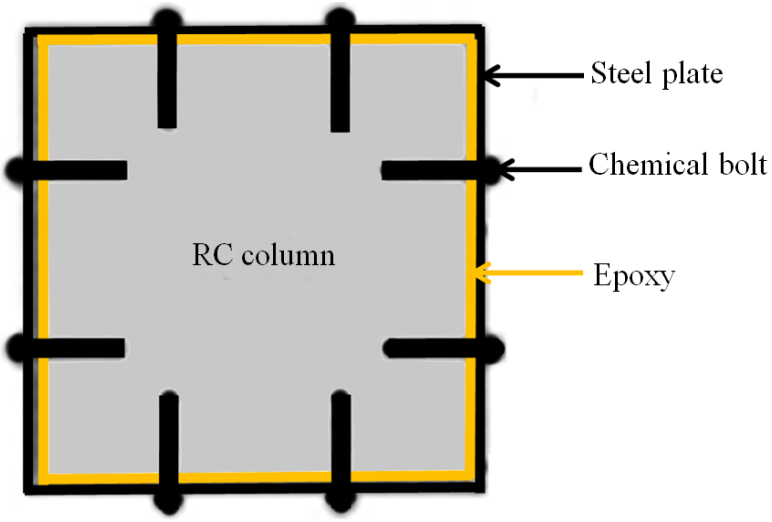

(b) cross section

Figure 2.22. Design of the composite column reinforcement method (Hsu et al., 2015)

(a) Removing the paint layer

(b) Wrapping with steel sheet

Figure 2.23. Practical application of the composite column reinforcement method (Hsu et al., 2015)

5. Foundation reinforcement method

Figure 2.24 and Figure 2.25 show the column foundation reinforcement methods. From Figure 2.24, it is found that the technicians added one section of foundation reinforcement steel bars next to the original column and surrounding the original ground beam. From Figure 2.25, it is learnt that in addition to the addition of one section of the foundation reinforcement steel bars next to the original column and surrounding the ground beam, technicians implanted another section of foundation reinforcement steel bars into the original column and the original ground beam.

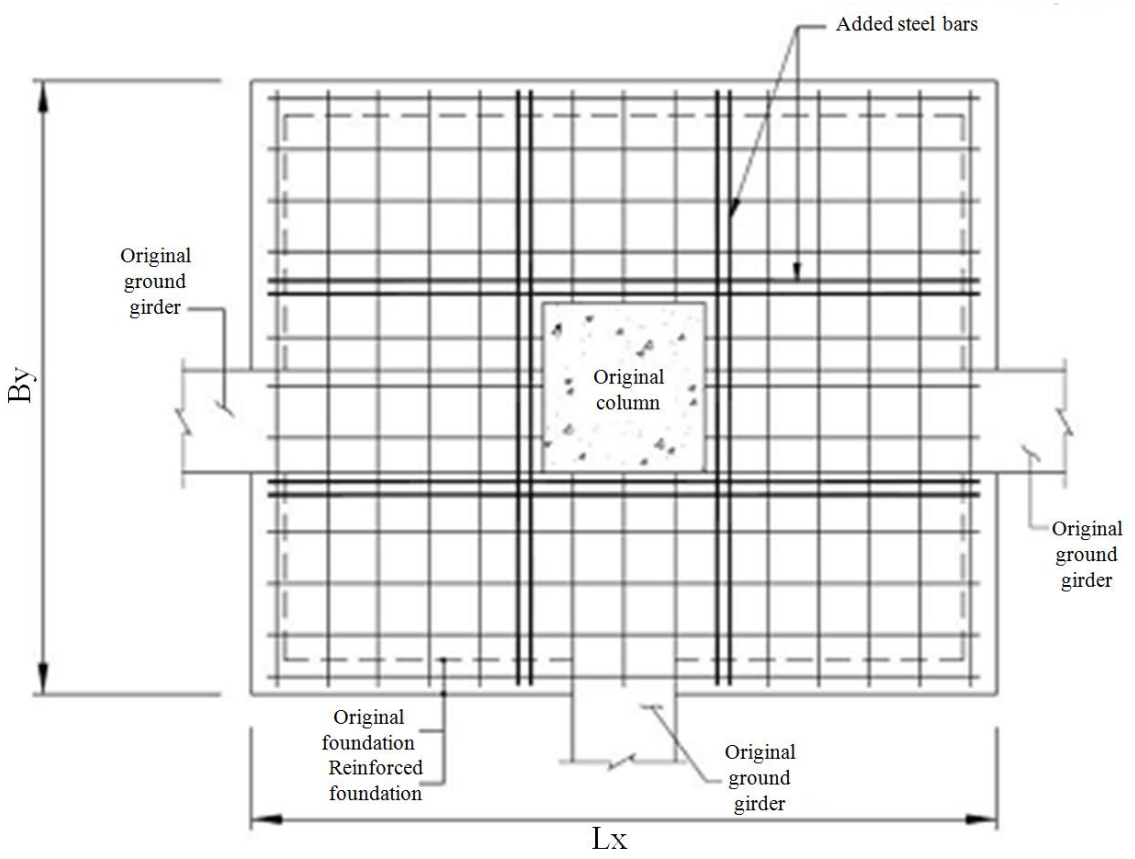

(a) Rebar arrangement drawing

(b) Rebar assembly

Figure 2.24. First method of column foundation reinforcement (Chen, 2015)

Figure 2.25. Second method of column foundation reinforcement (Chen, 2015)

Figure 2.26 shows the design diagram of the RC shear wall foundation reinforcement method. From Figure 2.26, it can be seen that the RC shear wall foundation reinforcement directly positions the RC foundation with a larger area beneath the RC shear wall and both sides of the columns as well as above the foundation of the original column.

2.2 Tectonic Earthquake Effects and Their Impacts

2.2.1 Tectonic Earthquake Effects

Table 2.2 shows the primary effect and secondary effect of tectonic earthquakes, volcanic earthquakes, collapse earthquakes, induced earthquakes, and artificial earthquakes. From Table 2.2, it can be seen that the tectonic earthquake effect is different from the effects of the other four earthquakes. The primary effect of a tectonic earthquake is shear banding while the secondary effect is seismic vibration. The only effect of the other four earthquakes is seismic vibration.

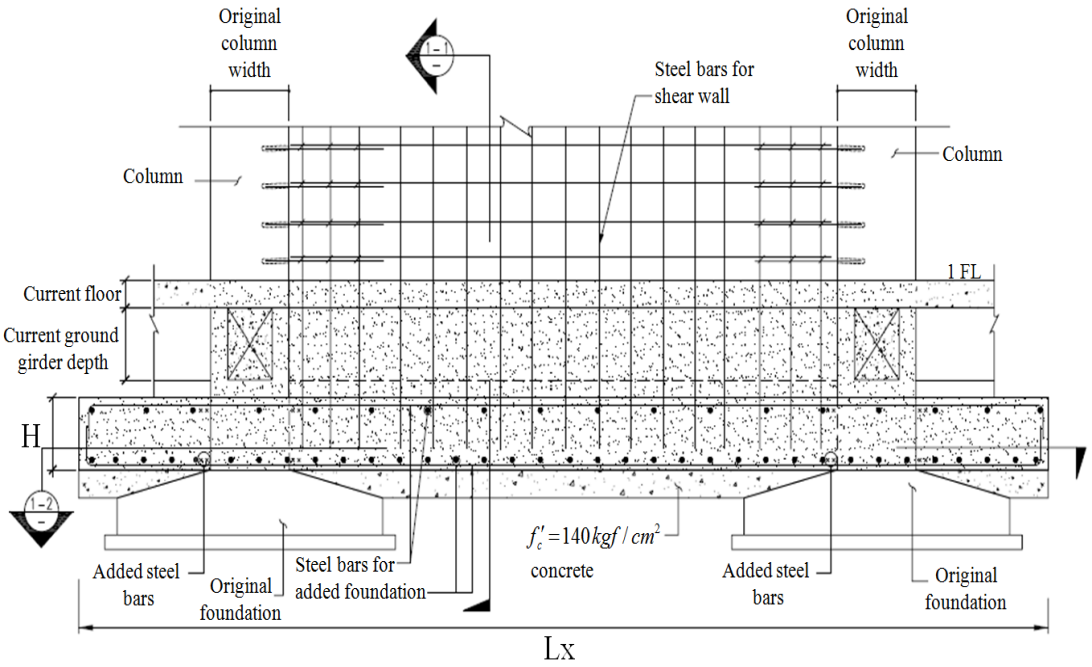

(a) Newly-added foundation of shear wall

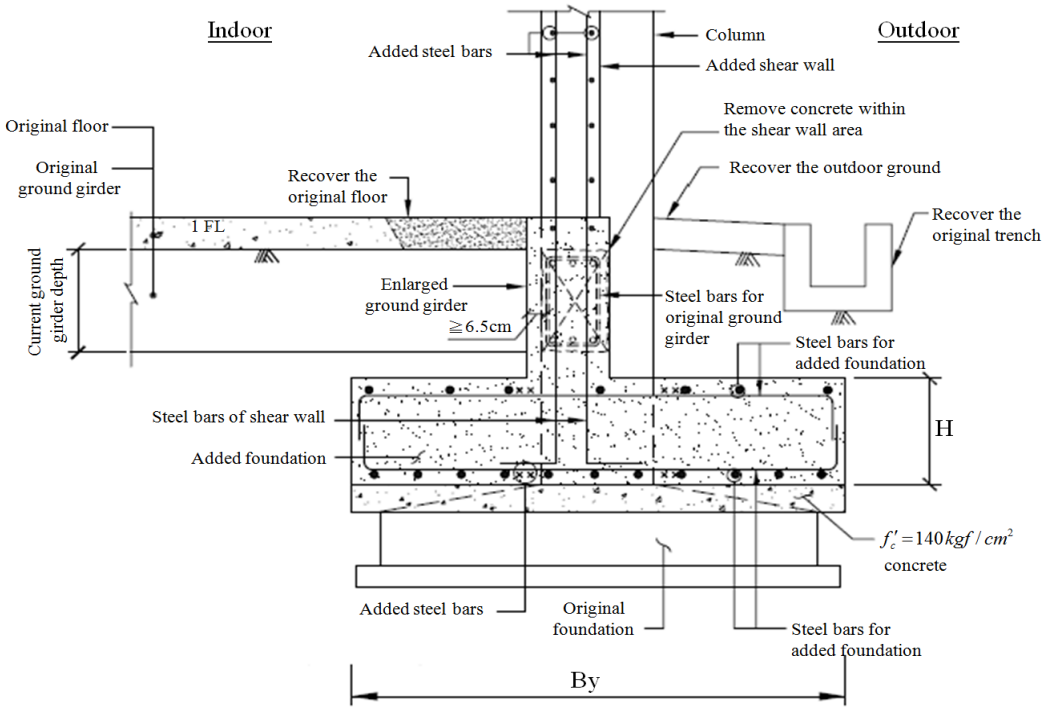

(b) Detailed view of Section 1-1 (shear wall and ground beam without dislocation)

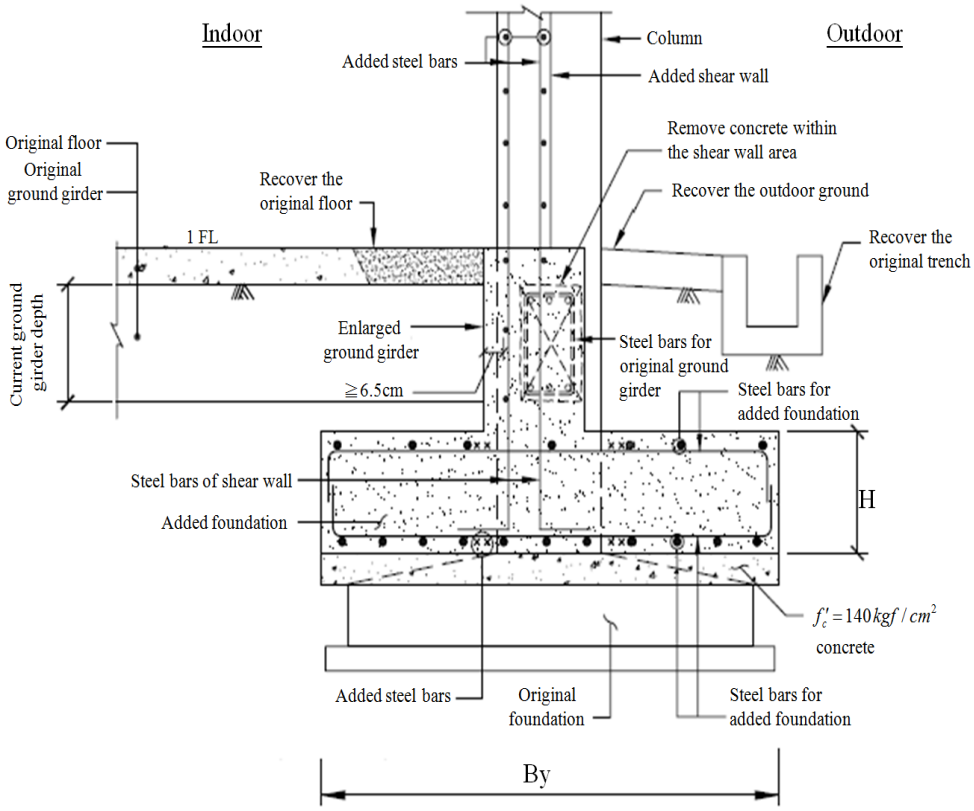

(c) Detailed view of Section 1-1 (shear wall and ground beam with dislocation)

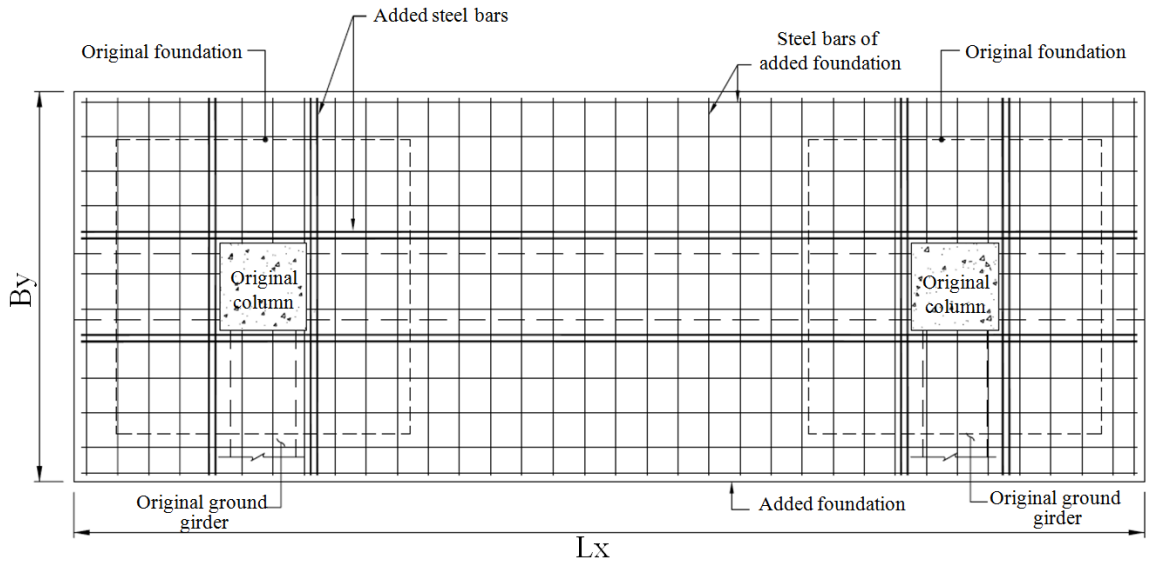

(d) Detailed view of Section 1-2

Figure 2.26. Design of the shear wall foundation reinforcement method (National Center for Research on Earthquake Engineering NCREE, 2017)

Table 2.2. Primary and secondary effects of all types of earthquakes

	Major effect	Minor effect
Tectonic earthquake	Shear banding	Seismic vibration
Volcanic earthquake	Seismic vibration	---
Collapse earthquake	Seismic vibration	---
Induced earthquake	Seismic vibration	---
Artificial earthquake	Seismic vibration	---

As both the scope and the volume covered by tectonic earthquake are far greater than the other four kinds of earthquakes, large-scale earthquakes with strong destructive power are caused by tectonic earthquakes.

Generally speaking, both shear banding effect and seismic vibration effect will have impacts on buildings. However, because of the huge energy release during a tectonic earthquake, more than 90% of the energy acts from the shear banding, and only less than 10% acts from the seismic vibration, so the collapse in the majority of the buildings is mostly and mainly caused by the shear banding effect.

2.2.2 Impacts of Tectonic Earthquake on Building Foundation

The primary effect of tectonic earthquakes is shear banding, the secondary effect is seismic vibration; therefore the impact of tectonic earthquake on the building foundation can be divided into the impact of shear banding and the impact of seismic vibration.

Impact of Shear Banding on Building Foundation. When tectonic plates are faulting, once the fault surface is extended towards the foundation soil, uplifting (or subsiding) phenomenon of the fault surface appears on one side of foundation relative to the other side of foundation, the original foundation with the same elevation will have the phenomenon of different elevations because of the presence of shear banding in the foundation soil. When parts of the foundation as well as its columns and beams above are being uplifted (or subsided), these uplifted (or subsided) foundations, columns, and beams will be subjected to excessively uneven stretches and distortional deformation, leading to fracture damage. This is the main cause of the collapse of a building during a tectonic earthquake (details in Figure 2.27).

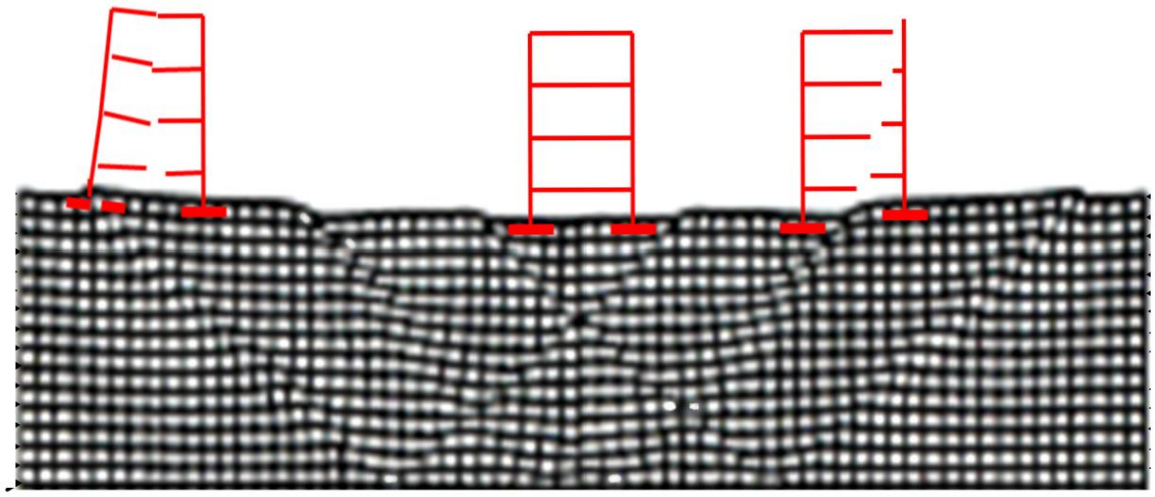

(a) Schematic diagram

(b) A real case

Figure 2.27. Building collapsed by shear banding

Next, during a tectonic earthquake, when shear bandings occur, groups of shear textures with different strikes will develop simultaneously within the overall width a shear band; and these shear textures include the principal deformation shear, thrust shear, Riedel shear, conjugate Riedel shear, and compression texture (Tchalenko, 1968), etc. Whereby, the maximum overall shear band width can be counted in kilometers, while the minimum overall shear band width can be counted in millimeters. Therefore, as shown in Figure 2.7, the building of Kuangfu Junior High School also will collapse under all types of shear textures induced by shear banding.

Impact of Seismic Vibration on Building Foundations. During a tectonic earthquake, when the foundation uplifting (or subsiding) phenomenon caused by tectonic plate faulting is under control, accompanied by the seismic vibration under the action of seismic acceleration, with the increase of the seismic acceleration coefficients (k_h and k_v), the shear failure plane corresponding to the ultimate bearing capacity of foundation exhibits the shallowing phenomenon.

For granular soil, the degree of shallowing in the shear failure plane corresponding to ultimate bearing capacity of the foundation will increase with the decrease in internal friction angle, ϕ. Under the condition of identical relative density, the residual internal friction angle of gravels with larger particle size, ϕ_r, is larger than the residual internal friction angle of sandy soil or silty soil with small particle size, so the ultimate bearing capacity of the foundation positioned in the sandy soil layer or silt soil layer will drop greatly due to the severe shallowing in the shear failure surface during the tectonic earthquake.

In the seismic design of buildings, structure-related professional engineers in the past conducted all static analysis and dynamic analysis using the simplified structural analysis model as shown in Figure 2.28. Subsequently, they reused the axial force and bending moments received at the bottom of columns established as the fixed end to test whether the safety factor of underlying soil bearing capacity below each column is greater than the value as required in the specifications; whereby the soil bearing capacity of the foundation mostly comes from the geological drilling report signed and verified by a geotechnical professional engineers.

Since the bearing capacity corresponding to the N value of the standard penetration test for each soil layer in the geological drilling report actually does not change with the foundation shape, the foundation width and the embedment depth, it also does not decrease drastically with the increase in seismic acceleration coefficients (k_h and k_v). Therefore, when the structure-related technicians use the soil bearing capacity attached to the geological drilling report to check the safety factor of the foundation's bearing capacity, it is practically impossible to check if the results of the safety factor of the foundation's bearing capacity do not comply with the provided specifications for any building that will be damaged due to tilting during the earthquake.

Currently, the structure-related professional engineers are in charge of both the seismic analysis and design of buildings; the geotechnical professional engineer is only responsible for providing the usual soil elasticity coefficient and foundation's bearing capacity. Under these division of labor circumstances, the bottoms of all building columns will move and

rotate due to the seismic vibration, and the overall building will undergo shear failure of the foundation soil caused by the situation where the safety factor of seismic bearing capacity for foundation is less than 1.0 (details in Fig. 2.29), thereby vertical sinking, lateral movements, or rotations emerge in the bottoms of columns, and the building is therefore severely damaged by tilting (Fig. 2.30).

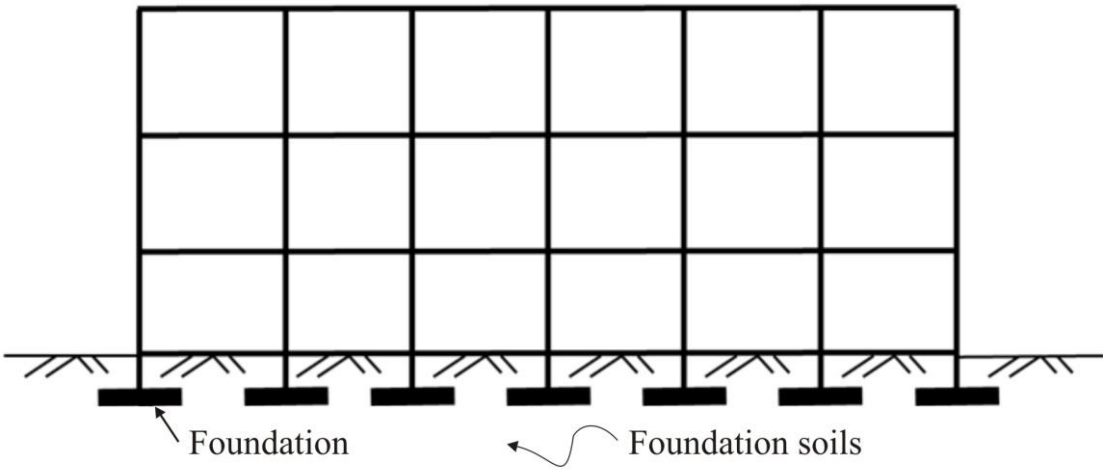

(a) Schematic diagram of the actual building

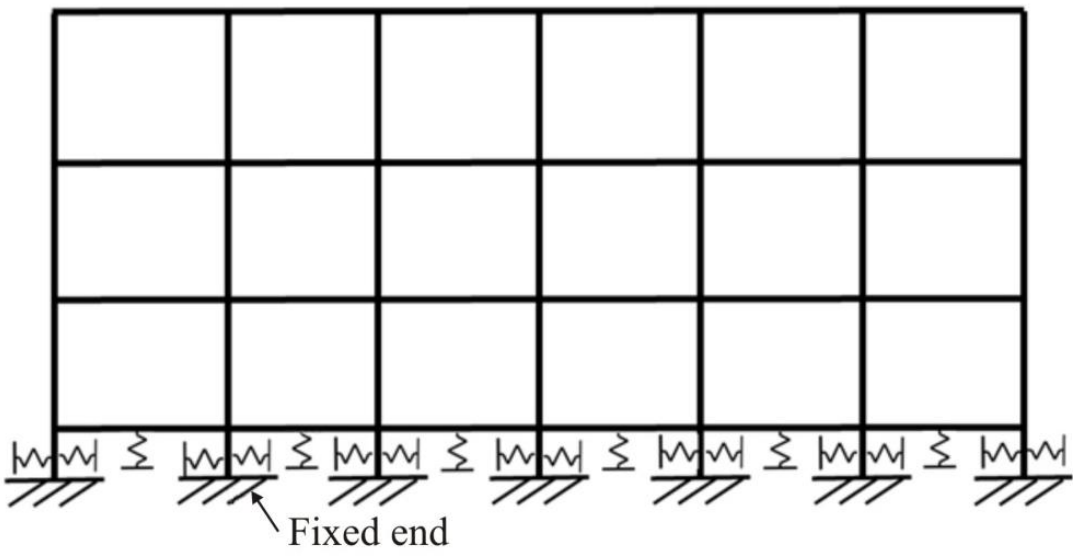

(b) Simplified structural analysis model

Figure 2.28. Comparison of the actual building and simplified structural analysis model

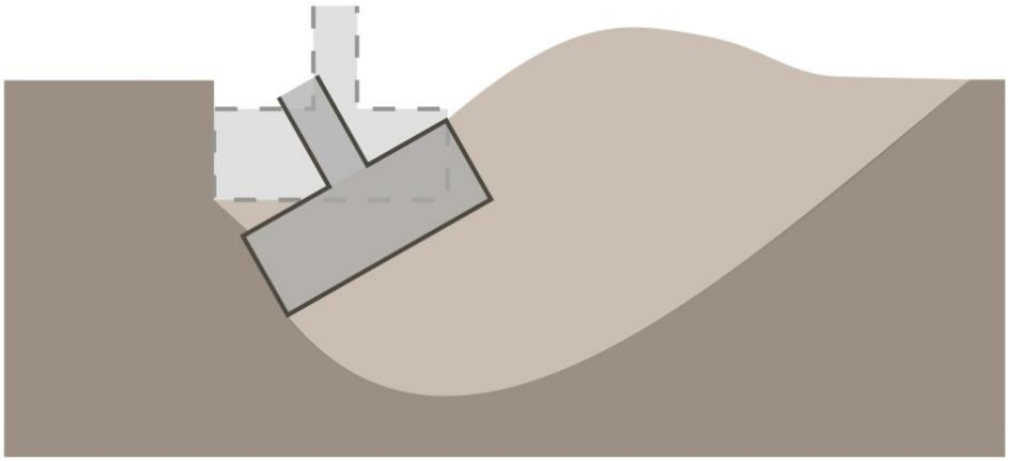

(a) general shear failure

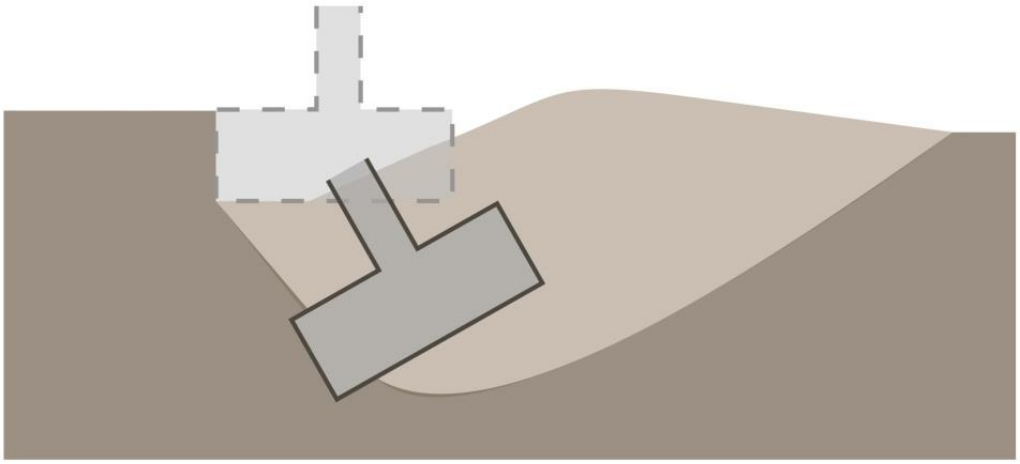

(b) local shear failure

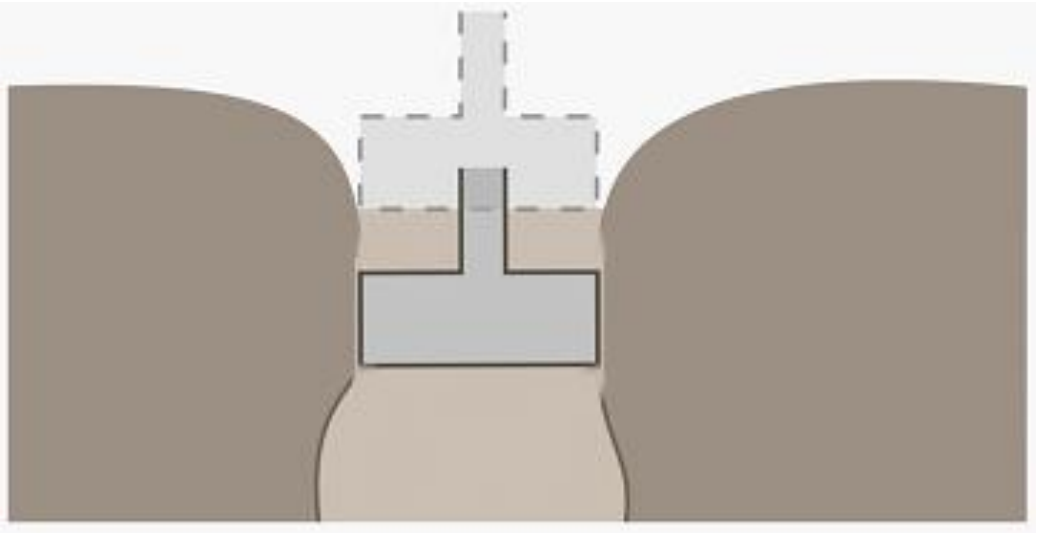

(c) punching shear failure

Figure 2.29. Different types of shear failure in foundation soils

(a) Local tilting of a civil house (New Tang Dynasty, 2016)

(b) Local tilting of King's Town Bank

Figure 2.30. Buildings tilted by insufficient of bearing capacity of foundation during the 2016 Meinong earthquake

2.2.3 Applicability of the Current Specifications

When an earthquake-resistant design specification allows the structural analysis model to be simplified to the absence of the foundation, it is necessary to strictly require that the foundation will not include shear bandings or will not induce shear failure in the seismic vibration due to insufficient bearing capacity, thereby assuring both the amount of movement and the amount of rotation at the bottoms of columns are so small as to the extent to be negligible, so that the actual conditions at the bottom of the columns do not deviate from the conditions at the fixed end as assigned.

After the 921 Jiji earthquake, it was found through the destruction of buildings in the disaster zone that even though the collapse of buildings were induced because the shear banding causes foundations to be locally uplifting (or locally subsiding), or the building sinking or damage due to tilting was induced because the seismic vibration causes the shear failure of foundation soil; the structure-related technicians still generally consider that the damage of buildings is mainly due to a lack of vibration resistance on the upper structural components. Thus, during the amendment to the seismic design specifications of buildings, the upgrades for the horizontal vibration resistance of upper structural components were focused on and the impact of the foundation's uplifting (or subsiding) and the foundation soil's shear failure on the overall building were ignored completely.

Considering the current seismic design specifications of buildings issued by the Ministry of the Interior (2011), both the static analysis and dynamic analysis related to stable grounds require structural simulations to reflect the actual situation as much as possible. In other words, all the simulations, mass distributions, geometric shapes, and the construction material properties, as well as the simulation of the soil-structure foundation interaction should be accurate. While for the seismic design of buildings related to unstable ground, the specifications also separately define the extremely soft soil layer and the saturated sandy soil layer of alluvium of soil liquefaction or fluidization, set down reduction on the soil parameters used in seismic design for the extremely soft soil layer, and state clearly that the site shall not have liquefaction potential during moderate and small earthquakes; and during a design earthquake and the maximum considered earthquake, although the occurrence of soil liquefaction is allowed, the

specifications again stipulate that the building should be of appropriate adopted foundation, form, and its safety should be tested after liquefaction. In other words, in the seismic design, it is necessary to avoid unstable soil layers that compromise the safety of the building, thus it is stipulated to require adopting more conservative soil parameters as the basis for seismic design.

In the current seismic design specifications of buildings, when considering unstable ground, the Ministry of the Interior not only sets down the provisions above, but also provides a self-checklist for soil liquefaction. It is considered that as long as any one of the following five factors has been conformed to, there is no risk that the building will be under the threat of soil liquefaction. These five factors include:

1. The building foundation is positioned on a non-liquefied ground layer, such as clay soil layer, pebble and gravel layer, bedrock, etc.
2. The building is designed in accordance with the amendment of the seismic design specification of buildings on December 29, 1999.
3. The building has more than 3 floors of underground basement.
4. The building foundation type uses a pile foundation.
5. The building foundation is a raft or slab foundation, and the building height is not more than 3 floors.

Based on the above-mentioned self-checklist of soil liquefaction provided by Ministry of the Interior, when the structure-related technicians are conducting the seismic design of buildings, they all generally consider that after implementing the following methods, the building can be exempted from the impact of soil liquefaction:

1. When the high liquefaction potential zone is positioned between the foundation and the non-sandy soil layer, the loose sandy soil of this high liquefaction potential zone shall be replaced with cemented sands.
2. When the bottom of the foundation is in a high liquefaction potential zone, ground improvement of a certain depth shall be conducted using the grouting method.
3. After passing through the shallow soil layer that will induce liquefaction, the foundation piles shall penetrate into the hard bed rock.
4. After the foundation piles or continuous walls pass through the shallow

soil layer that will induce liquefaction, although not penetrating into the hard bedrock, the bearing capacity of foundation piles or continuous walls positioned in the non-sandy soil layer is sufficient to bear the weight of the building.

Currently, since the structure-related technicians are responsible for the structural analysis and design of buildings, when structure-related technicians deal with the bearing capacity of foundations, they all refer only to the geotechnical drilling reports provided by the geotechnical technician. Whereby, the bearing capacity of each soil layer is derived by converting the N value obtained in accordance with the on-site standard penetration test (SPT), therefore it cannot be applied arbitrarily into foundations of different size, shape, and embedment depth; in particular the shear failure surface of foundations will experience shallowing with an increase of horizontal vibration acceleration during the earthquake, the ultimate bearing capacity of a foundation will therefore be reduced. Under the circumstance that the safety factor of seismic bearing capacity is insufficient, the foundation will move or rotate, thereby causing building damage due to tilting.

As for the soft clay soil layer or the loose sandy soil layer below groundwater level, its lack of seismic bearing capacity will induce local shear failure or punching shear failure of the foundation. As for the aforementioned two types of foundation shear failures, the failure mechanisms are completely different from the soil liquefaction mechanism, but yet it is easy to confuse.

Because the foundation shear failure mechanism is completely different from the soil liquefaction mechanism, after close inspection of the soil liquefaction checklist provided by the Ministry of the Interior (2016), it can be found that the method for suppressing the soil liquefaction adopted by technicians based on this type of self-checklist can in fact only enhance the foundation bearing capacity, and it does not help to eliminate the problems caused by soil liquefaction induced by shear banding.

2.3 The Current Seismic Reinforcement Methods of Buildings

Since the current seismic reinforcement methods of buildings adopt the lateral pushover analysis method, whereby the adopted structural analysis

model ignores internal columns of the basement, columns and side walls surrounding the basement, soils supporting the columns and side walls surrounding the basement as well as soils supporting the foundation thereby the model only contains columns, beams, slabs, and walls of each floor above ground level, and the bottoms of all columns are established as fixed ends. In other words, the applicable conditions of this type of lateral pushover analysis model are limited to seismic vibration, and are not applicable for shear banding. Therefore, although the Ministry of Education has spent a huge amount of funds to complete the seismic reinforcement of school buildings, the seismic reinforcement conditions for these school buildings do not include the impact of shear bandings.

In the lateral pushover test for the seismic reinforcement of school buildings, although the actual test is being carried out, the lateral pushover test conditions do not include the shear bandings. In other words, the lateral pushover test conditions do not include the column being uplifted (or subsided), or the loosening of foundation soils under dislocations of shear textures. Therefore, the entire pushover test process is limited to conduct the simulation test for seismic vibration without relative movement or rotation for the bottom ends of columns. Thus, although the lateral pushover test is full-scale and the test funds are impressive, the test results do not include the impact of shear bandings, nor do they consider the impact of the possible shear textures included in the foundation soil.

The reinforcement method of school buildings as developed from the lateral pushover analysis results, includes the RC jacketing reinforcement method, RC wing wall reinforcement method, RC shear wall reinforcement method, and composite column reinforcement method.

Although it is claimed that the aim of all reinforcement methods is to enhance the seismic capacity of the overall structure of the school building, as these reinforcement methods of school buildings one-sidedly focus on the upgrade for the resistance of upper components to seismic vibration; and does not yet focus on reinforcement for the foundation uplifting (or subsiding) under shear bandings, or the shear textures possibly included in the foundation soil.

An in-depth understanding of the shear wall reinforcement method finds that this reinforcement method only implants the vertical steel bars into the beam without passing through the beam. So, for concrete walls surrounded by two adjacent columns and two beams, although there are double-layer and bidirectional steel bars, as the vertical steel bars for this type of concrete wall in each floor are discontinuous, its function is not the same as the shear wall. Generally speaking, the shear wall can undertake a large portion of seismic force transmitted from the foundation, but under the situation of discontinuous vertical steel bars, this type of reinforced concrete wall after reinforcement in fact cannot undertake a large portion of seismic force transmitted from the foundation.

Finally, referring to all the methods for the reinforcement of school buildings, since the majority of the participating designers are experts in structural engineering, the foundation after reinforcement cannot effectively play its proper and correct function. Referring to Figures 2.24 to 2.26, the shortcomings of foundation reinforcement design include: (1) In the reinforcement of a column foundation, after the foundation steel bars cover one part of original ground beam, the proper and correct structural behavior of ground beams with a foundation has been destroyed; (2) After reinforcement, the column foundation with a larger area should be positioned beneath the original foundation with a smaller area, but the fact is the opposite, so the increment in bearing capacity of column foundation after reinforcement is not as anticipated; (3) Under the situation of reinforcement the foundation steel bars that cover the original ground beam, the original beam will block the reinforced foundation from sinking, thereby the reinforced foundation cannot exhibit the proper and correct bearing capacity, and the original ground beam may also be cleaved by the reinforced foundation with excessive applied force; (4) The dowel bar for a column foundation should be extended from the bending of a column’s vertical steel bars into the foundation, so implanting horizontal steel bars to reinforce the foundation is not correct; (5) The dowel bar for shear wall foundations should be extended from the bending of continuous vertical steel bars in the walls of each floor into the foundation; extending from the bending of non-continuous vertical steel bars in the walls of each floor in fact cannot transmit the seismic force upwardly.

2.3.1 For Building Foundations under the Shear Banding Effect

Under shear banding, when the hanging wall is uplifted and the footwall has yet to be lifted (details in Figure 2.7), no matter how the upper structural components, such as columns, beams, slabs, and shear walls undergo seismic isolation, seismic mitigation, or seismic reinforcement, the damage due to tilting of all buildings cannot be avoided.

Learning from this, how to prevent the shear banding from extending into the range surrounding the shear failure plane corresponding to the ultimate bearing capacity of foundation is intrinsically the first step for disaster mitigation of tectonic earthquakes. In this step, in order to eliminate the propagation of shear bandings, the foundation soil can be replaced by layering and zoning with block bodies or long-stripe bodies formed of geotextiles wrapped in boulders, cobbles, gravels, and sands. As these types of block bodies or long-stripe bodies need to be laid out in a number of layers, the design shear banding can then be eliminated; it can be confirmed through validation test by a shear banding table. In other words, a certain number of layers of these types of block bodies or long-stripe bodies can be placed underneath the range surrounding the shear failure surface corresponding to the bearing capacity of the foundation, thereby ensuring that the seismic bearing capacity of the foundation is not impacted by shear bandings.

2.3.2 For Building Foundations under the Seismic Vibration Effect Only

During a tectonic earthquake, after ensuring that the foundation is not under the impact of shear banding, in the case that the foundation soil will induce shear textures, such as propelling shear of P, Riedel shear of R, conjugate Riedel shear of R’ and compressive structures of S, due to the lateral sliding of a foundation during seismic vibration, the shear failure surface corresponding to the ultimate bearing capacity of a foundation will thus be subject to a drastic decrease in the seismic bearing capacity. Under this circumstance, taking the school building shown in Figure 2.7 as an example, the adopted soils’ physical properties and shear strength parameters are shown in Table 2.3.

Table 2.3. The adopted soil properties and strength parameters

Wet unit weight γ_{wet}, kN/m^3	18.2
Peak cohesion c_p, kPa	3.2
Residual cohesion c_r, kPa	0
Peak angle of internal friction ϕ_p, degree	32
Residual angle of internal friction ϕ_r, degree	29

For the foundation width B = 2m and the embedment depth D_f = 1.5m, when the hanging wall contains shear textures, the residual cohesion, c_r and the residual internal friction angle, ϕ_r are chosen; and when the footwall does not contain shear textures, the peak cohesion, c_p, and the peak internal friction angle, ϕ_p are chosen.

The peak ground acceleration (PGA) from TCU065 Station for the 921 Jiji earthquake are to be used. The horizontal east-west PGA is 0.79g; the horizontal north-south PGA is 0.57g; and the vertical PGA is 0.26g.

Based on the horizontal PGA of 0.79g and the vertical PGA of 0.26g, with respect to the corresponding relationship between PGA and the seismic acceleration coefficient as shown in Table 2.4 and provided by the Water Resources Agency under the Ministry of Economic Affairs. The horizontal seismic acceleration coefficient, k_h, can be further obtained as 0.237; and the vertical seismic acceleration coefficient, k_v, can be further obtained as 0.119. Based on various different load combinations, the design bearing capacity, q_{design}, selected for use is 300kN/m^2.

Table 2.4. Corresponding relationship between PGA and the seismic acceleration coefficient (Ministry of Economic Affairs, 2008)

PGA	k_h
<0.12g	0.10
0.12g~0.18g	0.10~0.12
0.18g~0.50g	0.12~0.16
0.50g~0.80g	0.16~0.24
>0.80g	0.24
Note: $k_v = k_h \times R$, $R \geq 0.5$.	

For a square foundation, Equation 1 can be used to calculate the seismic ultimate bearing capacity of foundation, $q_{ult,E}$:

$$q_{ult,E} = c\,N_{cs} s_c e_c + qN_{qs} s_q e_q + \frac{1}{2} B\gamma N_{\gamma s}\, s_\gamma e_\gamma \tag{2.1}$$

Whereby, c is the cohesion; q is the overburden pressure above the bottom surface of the foundation; γ is the unit weight of soil; N_{cs}, N_{qs}, and $N_{\gamma s}$ are the bearing capacity parameters of soil for a long-stripe foundation, provided by Meyerhof (Meyerhof, 1951); s_c, s_q, and s_γ are shape correction factors, provide by Hansen (1970); and the seismic correction factors of e_c, e_q, and e_γ, provided by Budhu and Al-Karni (1993), are calculated as:

$$e_c = exp\left(-4.3k_h^{1+D}\right) \tag{2.2}$$

$$e_q = (1-k_v)\exp\left[-\left(\frac{5.3k_h^{1.2}}{1-k_v}\right)\right] \tag{2.3}$$

$$e_\gamma = (1-\frac{2}{3}k_v)\exp\left[-\left(\frac{9k_h^{1.1}}{1-k_v}\right)\right] \tag{2.4}$$

In the three equations above, $D = C/(\gamma H)$; where H is the depth of the sliding failure surface from the ground surface. When the foundation embedment depth of D_f is known, H can be calculated as follows:

$$H = D_f + \frac{0.5B}{\cos\left(\frac{\pi}{4} + \frac{\phi}{2}\right)} \exp\left(\frac{\pi}{2} \tan\phi\right) \tag{2.5}$$

When the foundations are positioned on the hanging wall and footwall respectively, Table 2.5 shows the seismic bearing capacity safety factors for the foundations obtained from analysis.

Table 2.5. Analysis results of the safety factors of seismic bearing capacity for foundations located on the hanging wall and footwall

Location of Foundations	Analysis Conditions	c (kPa)	ϕ	k_h	k_v	q_{ult} (kPa)	FS_E
Foot wall	Without shear bandings	3.2	32^o	0.237	0.1185	384	1.28
Hanging wall	With shear bandings	0.0	29^o	0.237	0.1185	201	0.67

From Table 2.5, when the foundation is positioned on the footwall, as the foundation soil in a tectonic earthquake does not contain the shear crack structures, the safety factor of the seismic bearing capacity of the foundation obtained from analysis is $FS_E = 1.28 > 1.2$. This analysis result meets the provisions in the design specifications of building foundations (Construction and Planning Agency, Ministry of the Interior, 2016).

When the foundation is positioned on the hanging wall, as the foundation soil contains the shear textures in a tectonic earthquake, the safety factor of the seismic bearing capacity of the foundation obtained from the analysis is $FS_E = 0.67 << 1.2$. Therefore, the foundation will have shear failure during a tectonic earthquake, which may be the cause of severe

damage for school buildings positioned on the hanging wall in the earthquake.

As indicated from the case analysis above, as long as the soil in the tectonic earthquake does not contain the shear textures, the shear strength parameters of soil will not change from those of the peak strength to those of the residual strength, the tilting damage of the building may be avoided under the situation that the safety factor of the seismic bearing capacity of the foundation is still larger than 1.2. However, once the soil contains shear textures in a tectonic earthquake, the shear strength parameters of soil will change from those of the peak strength to those of the residual strength and the building may be damaged due to tilting in the situation where the safety factor of the seismic bearing capacity for the foundation is smaller than 1.0.

Even under the situation where shear bandings have not caused impacts on the foundation, foundation soil will still contain shear textures when the lateral movement of foundation is large enough. Therefore, after the depth of H is calculated by using Equation 2.5, the foundation soil is suggested to be replaced with graded gravel in a range of H depths under the ground surface. Thereafter, the foundation can be free from shear failure under seismic vibration.

2.4 Validation Test for the Disaster Mitigation Methods

Based on the requirements of validation tests on tectonic earthquake disaster mitigation, this section will first introduce the validation test method of earthquake disaster mitigation under shear banding, and then introduce the validation test method of earthquake disaster mitigation under seismic vibration.

Currently, the National Center for Research on Earthquake Engineering has only developed the shaking table validation test. This type of validation test fixes the bottoms of the upper structural 1^{st} floor columns of a building model on a thick and solid steel block close to rigidity, and the acceleration time-history curves recorded in large earthquakes are imported into the upper structure. Since this type of validation test completely ignores the seismic forces that should be distributed to the soils laterally supporting the columns around the basement and the external RC walls, therefore when the

earthquake-resistant design buildings guided by shaking type of test model were damaged by shear bandings in previous earthquakes, the main cause was the unstable foundation soil generated by shear bandings. Therefore, the validation tests in this chapter will only be limited to validation tests related to the instability of foundation soils.

2.4.1 Validation Test Under the Shear Banding Effect

The shear banding table shown in Figure 2.31 can be used to execute the validation test under the shear banding effect.

Figure 2.31. The first shear banding table available in the world

First, the footwall and the hanging wall of the shear banding table are adjusted, so that the table surface is leveled (details in Figure 2.32). Subsequently, the selected geotechnical synthetic blocks, sand-and-gravel graded mixed materials, model foundation, and columns are arranged sequentially on the table. Following this, the footwall is fixed and the hanging wall with special design is activated, so that the tilted hanging wall is uplifted continuously to a prescribed height; afterwards, it is checked whether the shear banding amount of hanging wall relative to the footwall is continuously eliminated to zero in the range of the selected geotechnical synthetic blocks. If the aforementioned scenario is true, the selected

geotechnical synthetic blocks and the arrangement depth will have passed the validation test of shear banding table; otherwise, it is necessary to change the configuration of the selected geotechnical synthetic blocks or arrangement depth until the validation test is passed.

2.4.2 Validation Test Under the Seismic Vibration Effect

After a product that passes the validation test of shear banding table is arranged beneath the shear failure plane corresponding to the ultimate bearing capacity of the foundation, the shear banding effect in a design tectonic earthquake can then be eliminated, so that the foundation soil within the depth range of the shear failure corresponding to the ultimate bearing capacity of the foundation only bears the seismic vibration effect.

Large-scale Direct Shear Test Apparatus. In a tectonic earthquake, when the foundation soil is only subjected to the seismic vibration effect, the depth for shear failure plane corresponding to the ultimate bearing capacity of the foundation will exhibit shallowing phenomenon (details in Figure 2.33); such that the ultimate bearing capacity of foundation decreases with the increase of seismic acceleration and the decrease of the foundation soil's angle of internal friction, ϕ.

Under a design tectonic earthquake, when the acceleration coefficients, k_h and k_v, are known, the required angle of internal friction ϕ for foundation soil can be evaluated through the calculation equation of the foundation's seismic bearing capacity. Following that, through a large-scale direct shear test apparatus, it can then be confirmed whether the choice of the sand-and-gravel graded mixed materials comply with the requirements of seismic vibration design.

Figure 2.34 shows a large-scale direct shear test apparatus developed by the author; whereby the cross-sectional area of the shear box is 30.5cm x 30.5cm; the maximum height of the upper box is 15cm; and the maximum height of the lower box is 20cm.

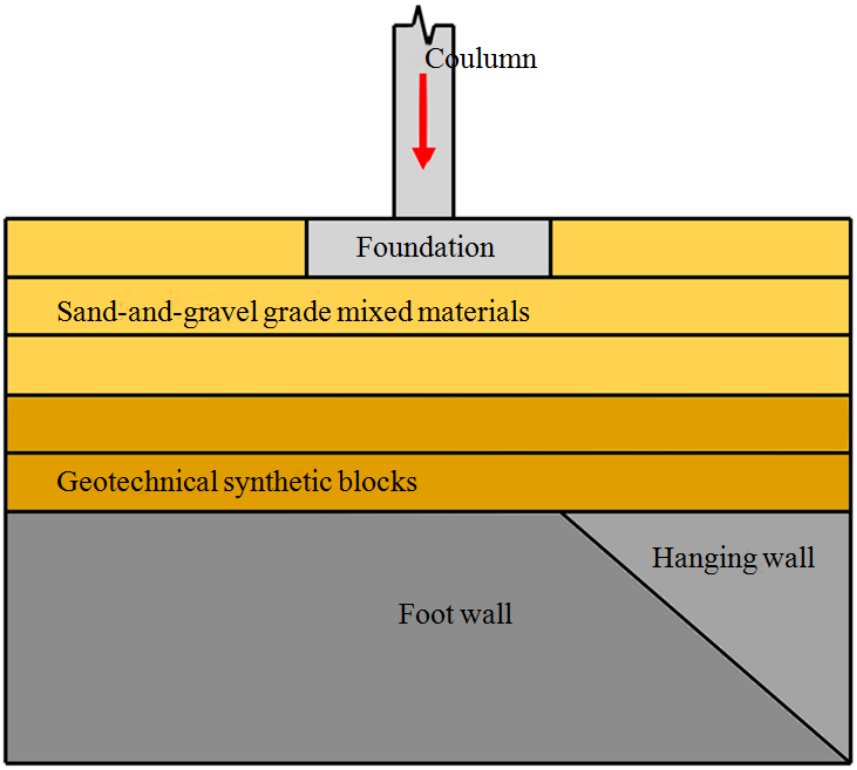

(a) Before the test

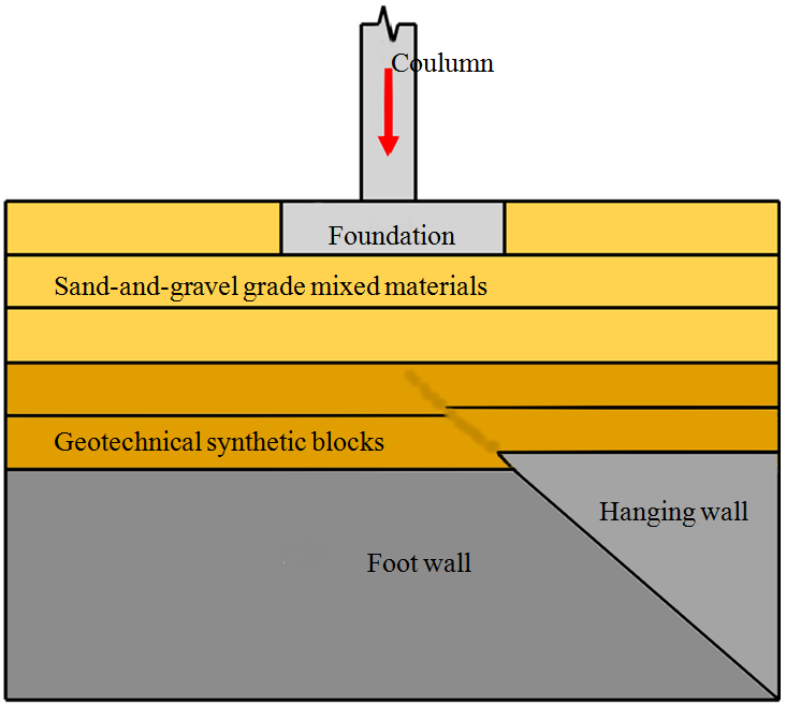

(b) After the test

Figure 2.32. Schematic diagrams of shear banding table for validation test

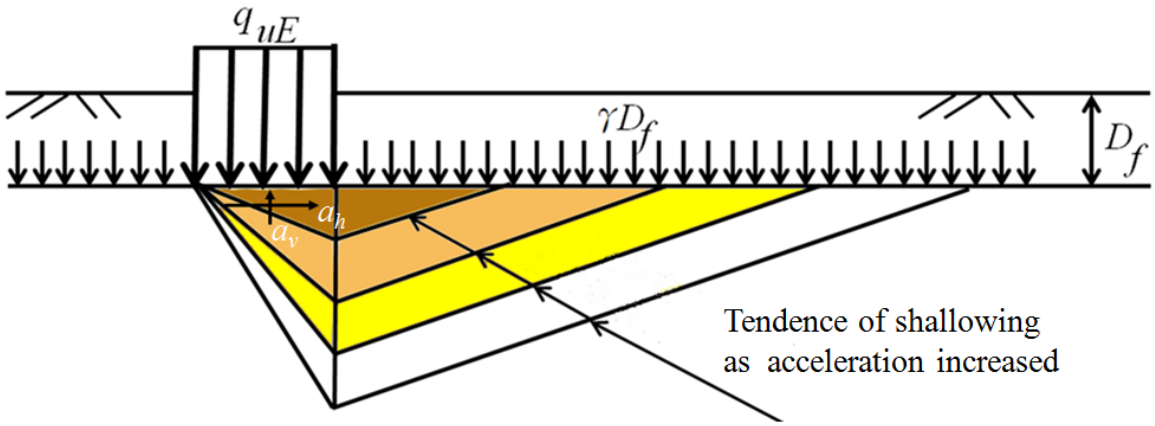

Figure 2.33. The shallowing phenomenon of the ultimate bearing capacity range for a foundation under the seismic vibration effect

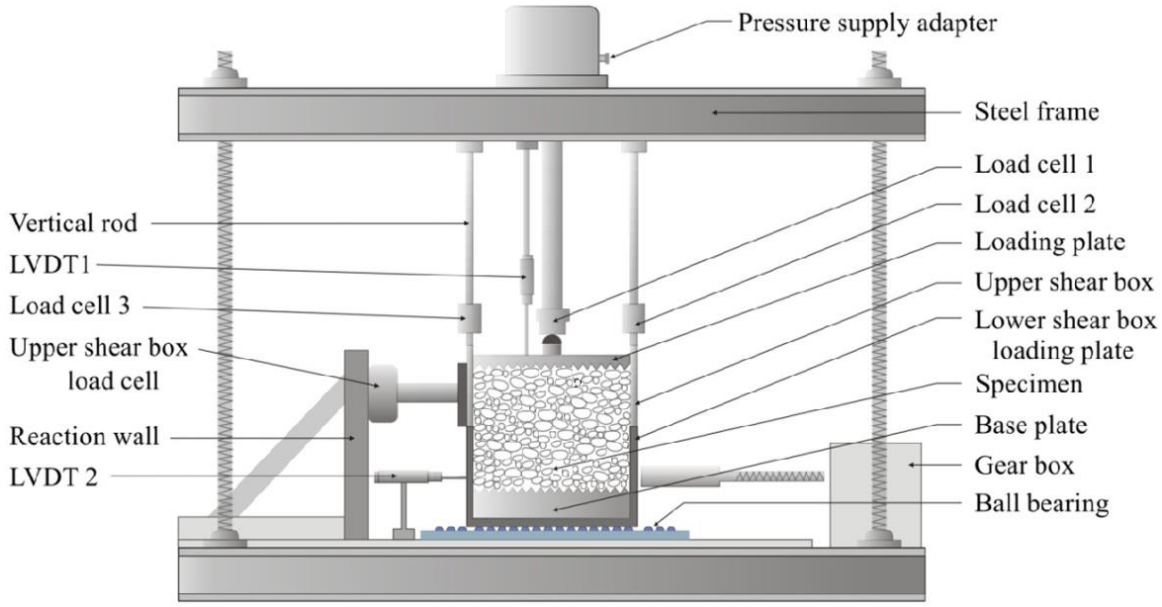

Figure 2.34. Schematic diagram of a large-scale direct shear test apparatus

As the cross-sectional area of the direct shear box is 30.5cm x 30.5cm, based on the reliability of the test results, by choosing the ratio value of direct shear box side length over the maximum particle size of a sample that is equal to 5~12, therefore the maximum particle size of the chosen gravel-graded mixed material in the test is 6.1~2.54cm. As this direct shear test apparatus shown in Figure 2.34 can be used to conduct a direct shear test

to the left by pushing or to the right by pulling, when the sample and measuring instrument both are properly installed, a vertical force can be applied on the loading sheet by a hydraulic pump and a force-applying rod until the value displayed in Force Gauge 1 reaches the pre-set vertical force. Next, by resetting the readings of Force Gauge 2, Force Gauge 3, LVDT 1, and LVDT 2 to zero, the horizontal displacement rate is controlled through a drive rod and transmission, and then the lower box of the shear box above the steel ball bearing is controlled via a control valve to move it to the left or to the right, so as to conduct the direct shear test by pushing or pulling.

Since in the process of applying shear force, the upper box of the shear box will be lifted upwardly, in order to suppress this lifting amount to a tiny value, a set of vertical rods and force gauges is additionally installed on both the left and right sides of the upper box of the shear box respectively; and these two force gauges will display the vertical force additionally generated in the test. Therefore in the process of applying horizontal displacement, the actual acting vertical force is the sum of vertical forces shown from Force Gauge 1 to Force Gauge 3 in Figure 2.34 as $\sum_{n-1}^{3} V_n$, and the horizontal force of T is the value displayed by the force gauge of the upper box of the shear box in which the gauge is installed above the reaction wall. Therefore, under a specific horizontal displacement, the induced angle of internal friction as ϕ_i for test soil sample can be calculated as follows:

$$\phi_i = \tan^{-1}\left(T \Big/ \sum_{n-1}^{3} V_n \right) \qquad \text{(Eqn. 5.1)}$$

The Selected Test Procedure. A selected test procedure for the large-scale direct shear test is addressed as follows:

Step 1: Perform the first push-shear test, whereby the horizontal displacement is from 0 mm to 36 mm and the resulting test curve is numbered as 1.

Step 2: Perform the first pull-shear test, whereby the horizontal displacement is from 36mm to -36mm, and the resulting test curve is numbered as 2.

Step 3: Perform the second push-shear test; whereby the horizontal displacement is from -36 mm to 36 mm and the resulting test curve is numbered as 3.

Step 4: Perform the second pull-shear test; whereby the horizontal displacement is from 36 mm to -36 mm and the resulting test curve is numbered as 4.

Step 5: Perform a third push-shear test; whereby the horizontal displacement is from -36 mm to 36 mm and the resulting test curve is numbered as 5.

Typical Test Results. When using a large direct shear test equipment to conduct the test, Figure 2.35 to Figure 2.37 show the typical test results of gravel-graded mixed materials; whereby the normal stress is not a fixed value, but it varies with the changes in horizontal displacement; and under the situation that the lifting amount of upper box is a small amount, the test results tend to be reasonable and reliable.

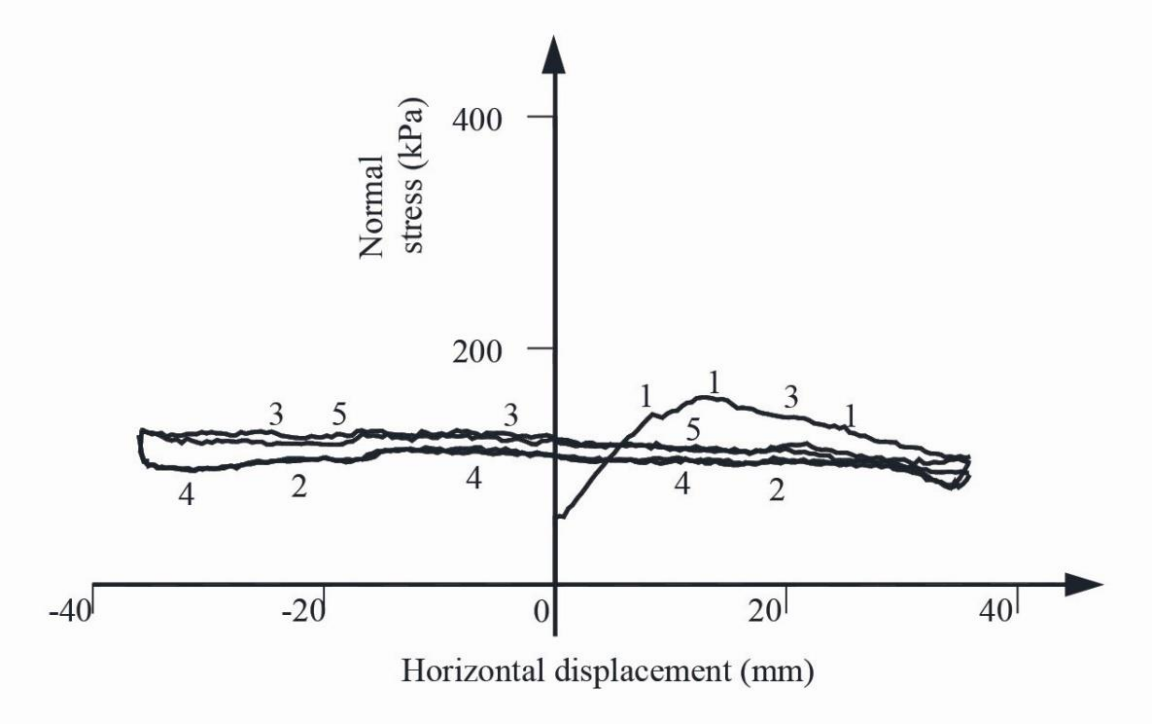

Figure 2.35. Relationship curves of normal stress in the direct shear test with respect to changes in horizontal displacement

Definitions of Peak and Residual Angles of Internal Friction. For a series of push- and pull-direct shear test, the peak and the residual angle of internal friction are defined as follows:

1. Peak angle of internal friction, ϕ_p:
   In the curve 1, the maximum value of ϕ_i is defined as the peak angle of internal friction.
2. Residual angle of internal friction from the push-shear test, $\phi_{r,push}$:
   In the curves 3 and 5, within the range where the horizontal displacement is larger than 32mm, the minimum value of ϕ_i is defined as the residual angle of internal friction from the push-shear test, $\phi_{r,push}$.
3. Residual angle of internal friction from the pull-shear test, $\phi_{r,pull}$:
   In the curves 2 and 4, within the range where the horizontal displacement is smaller than -32mm, the minimum value of ϕ_i is defined as the residual angle of internal friction from the pull-shear test, $\phi_{r,pull}$.
4. Adopted residual angle of internal friction:

$$\phi_r = \text{Min}\,(\phi_{r,push},\ \phi_{r,pull}) \qquad \text{(Eqn. 5.2)}$$

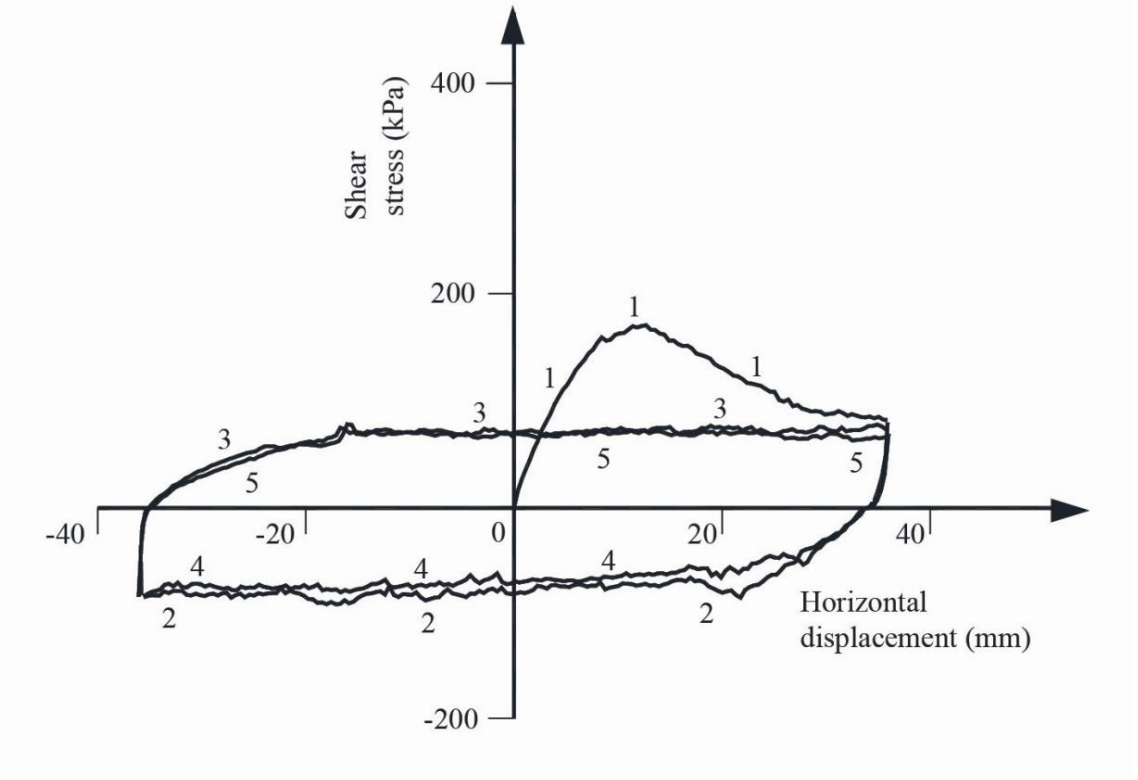

Figure 2.36. Relationship curves of shear stress in the direct shear test with respect to changes in horizontal displacement

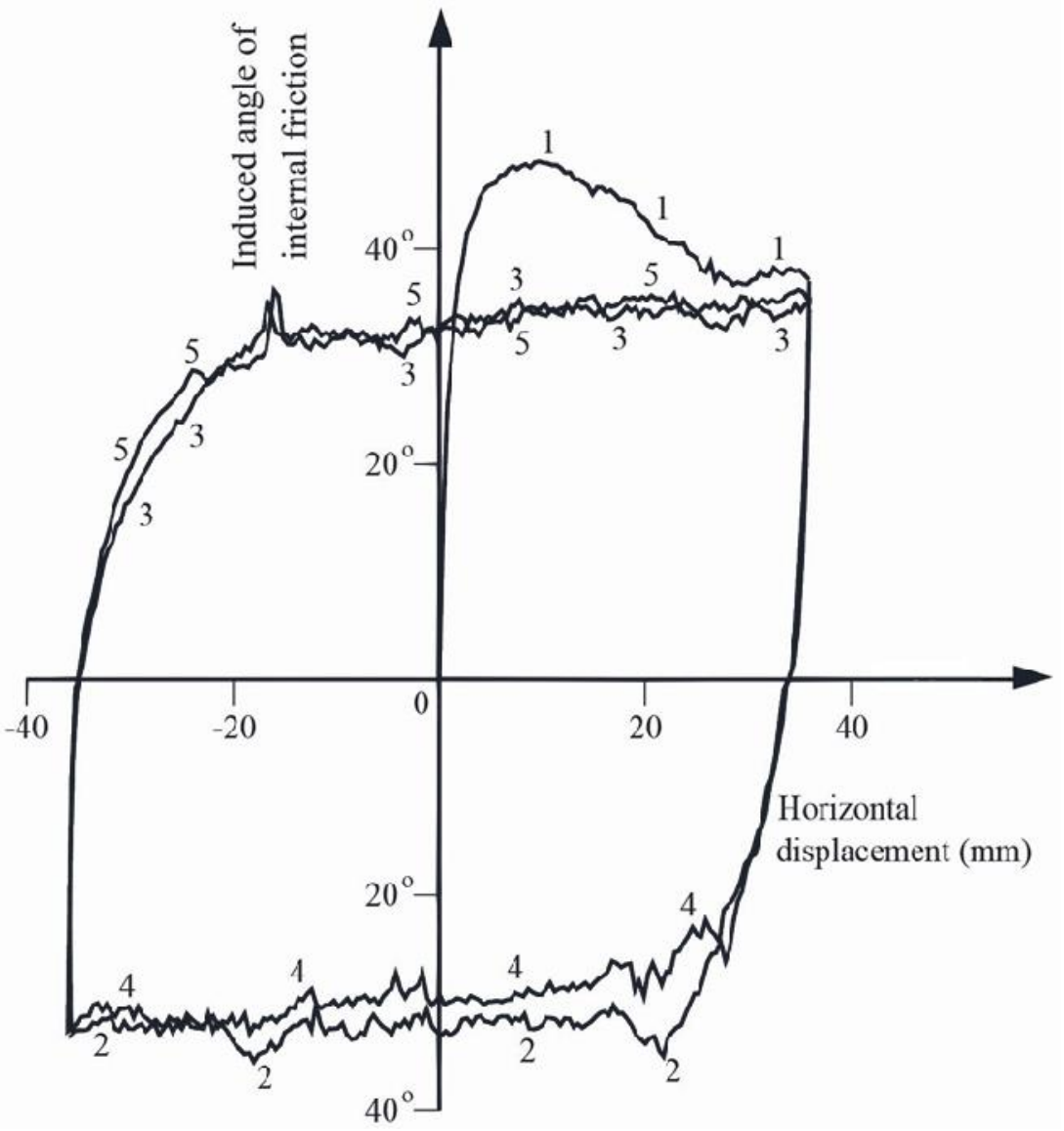

Figure 2.37. Relationship curves of the angle of internal friction induced in the direct shear test with respect to changes in horizontal shear displacement

Sand-and-gravel graded mixed materials. Figure 2.38 shows the particle size distribution curves for the three different chosen gravel-graded materials of S1, S2, and S3. Table 2.6 shows the physical properties and soil classifications for these three different gravel-graded materials. Table 2.6 also shows that the gravel content of S1 is the highest and the gravel content of S3 is the lowest; the uniform coefficient of S1 is the lowest and that of S3 is the highest.

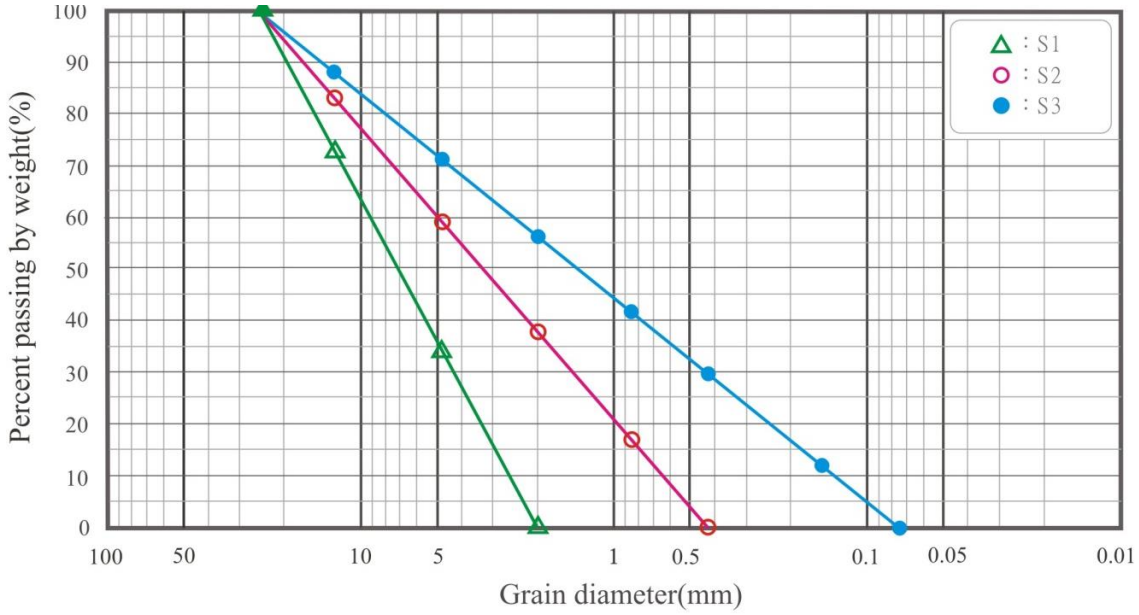

Figure 2.38. Particle size distribution curves for three different sand-and-gravel graded mixed materials

Table 2.6. Physical properties for three different sand-and gravel graded mixed materials

	Specimen S1	Specimen S2	Specimen S3
Dry unit weight, kN/m^3	17.65	17.75	18.33
Gravel content, %	65.96	40.99	28.78
Sand content, %	34.04	59.01	71.22
Coefficient of uniformity, C_u	3.56	7.73	18.9

Large Direct Shear Test Results. Table 2.7 shows the large-scale direct shear test results for three different sand-and-gravel graded mixed materials; whereby the peak angles of internal friction for S1, S2, and S3 are 48.1^o, 42.7^o, and 38.8^o respectively; and their residual angles of internal friction are 30.0^o, 33.2^o, and 34.5^o respectively.

Table 2.7. Peak and residual angles of internal friction from large-scale direct shear tests

Specimen	ϕ_p	$\phi_{r,push}$	$\phi_{r,pull}$	ϕ_r
S1	48.1°	33.4°	30.0°	30.0°
S2	42.7°	33.4°	33.2°	33.2°
S3	38.8°	34.5°	35.4°	34.5°

Validation of the Applicability of Three Different Materials. For the foundation on the hanging wall, because the impact of shear bandings is included, it is necessary to adopt the residual angle of internal friction from the test (details in Table 2.7) in the seismic bearing capacity analysis of foundation.

Table 5.3 shows the safety factor of seismic bearing capacity for foundations obtained from analysis, FS_E, when the three chosen sand-and-gravel graded mixed materials are used as foundation soils. It is clearly vivid from Table 2.8, except that the safety factor of seismic bearing capacity for S3 is FS_E > 1.2, both the FS_E for the remaining two sand-and-gravel graded mixed materials are smaller than 1.2, thereby validating that only S3 is a suitable foundation soil material.

Table 2.8. The calculated safety factor for seismic bearing capacity of foundation embedded in hanging wall

Type of Foundation Soil	Residual Angle of Internal Friction, ϕ_r	$q_{ult,E}$	FS_E
S1	30.0^o	214kPa	0.71
S2	33.2^o	333kPa	1.1
S3	34.5^o	415kPa	1.4

2.5 Professional Consideration of the Current Building Earthquake-Resistant Design Specification and the Basis of Disaster Identification

2.5.1 The Fatal Problem for the Current Building Earthquake-Resistant Design Specification

First, learning from the introduction of this chapter, of the five types of earthquakes, tectonic earthquakes are the most prevalent and have also the strongest destructive power. Next, also learning from the introduction of this chapter,, the primary effect of a tectonic earthquake is the local shear banding; the secondary effect is the all-around seismic vibration. However until now, both the development and amendment of the building earthquake-resistant design specification have only focused on the seismic vibration, so although countries around the world are committed to developing seismic isolation, seismic mitigation, and earthquake-resistant technology for buildings, the application scopes of all of these technologies are only limited to the resistance of upper components, such as columns, beams, slabs, and walls to the seismic vibration effect. Under this situation, the upper components of a building, including columns, beams, slabs, and walls, after seismic design comply with the provisions in such design specifications, and under the situation that the bottoms of columns in 1st floor are all fixed.

However, in a tectonic earthquake, once parts of the foundation of a building are uplifted (or subsided) along with the bottoms of columns in the 1st floor due to shear banding, or due to the dislocation of shear textures in foundation soil induced due to sliding of foundation in seismic vibration. Then, part of column bottoms will move or rotate because of the shear failure of a foundation, thereby deviating from the fixed end conditions as established, the overall building is also therefore damaged due to shear banding or dislocation of shear textures in foundation soil.

Taking the Weiguan building as an example, regardless of how the structural technician constructs the structural analysis model during the earthquake-resistant design, (but for the structural analysis model provided by the Tainan Civil Engineering Technician Association (TNCE) that participated the identification on disaster causes after the collapse of

Weiguan building in the Meinong earthquake, 2016), Figure 2.39 reveals that the structural analysis model of the overall structure contains only the columns, beams, slabs, and walls of each floors above the ground surface, and the bottoms of all columns in the 1st floor are established as the fixed ends.

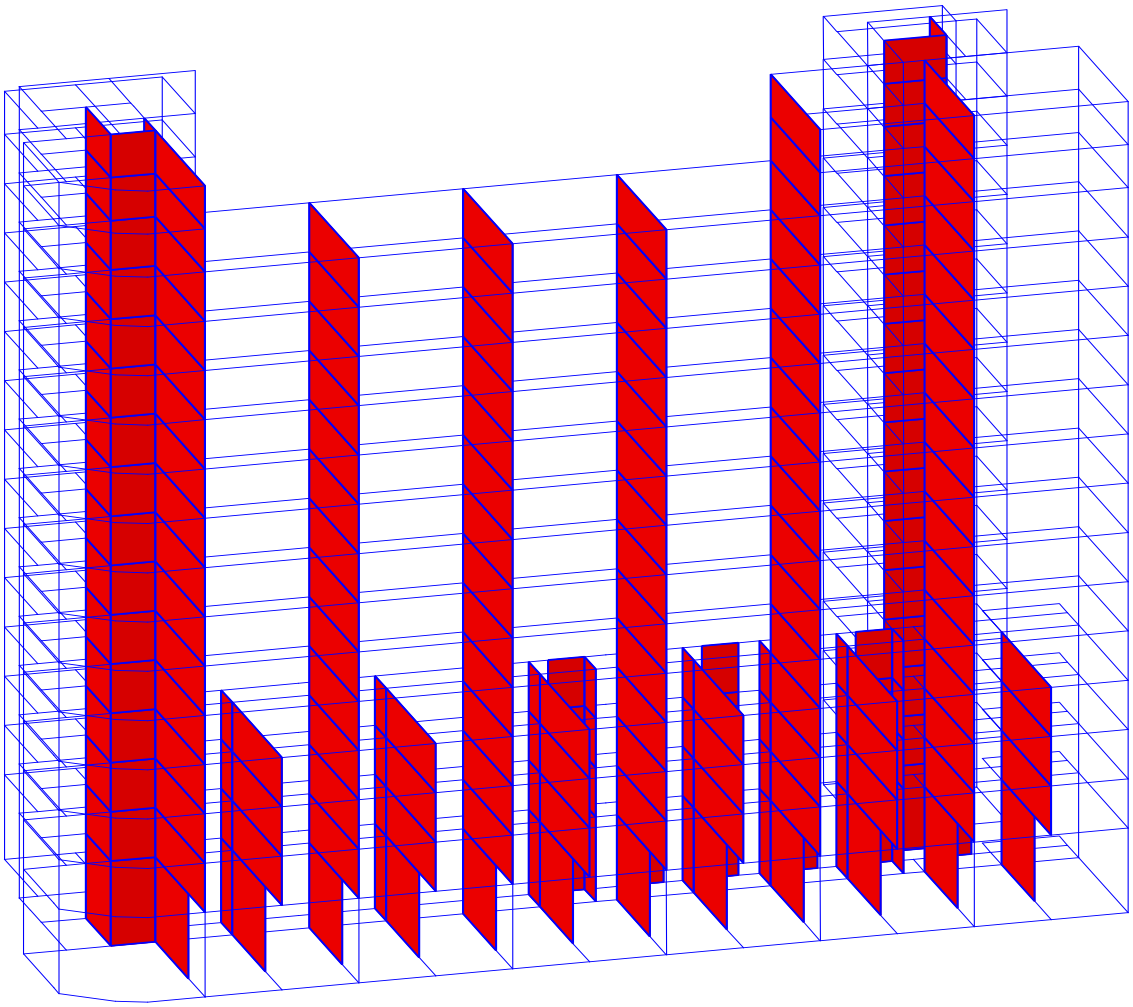

(a) Based on the original design map

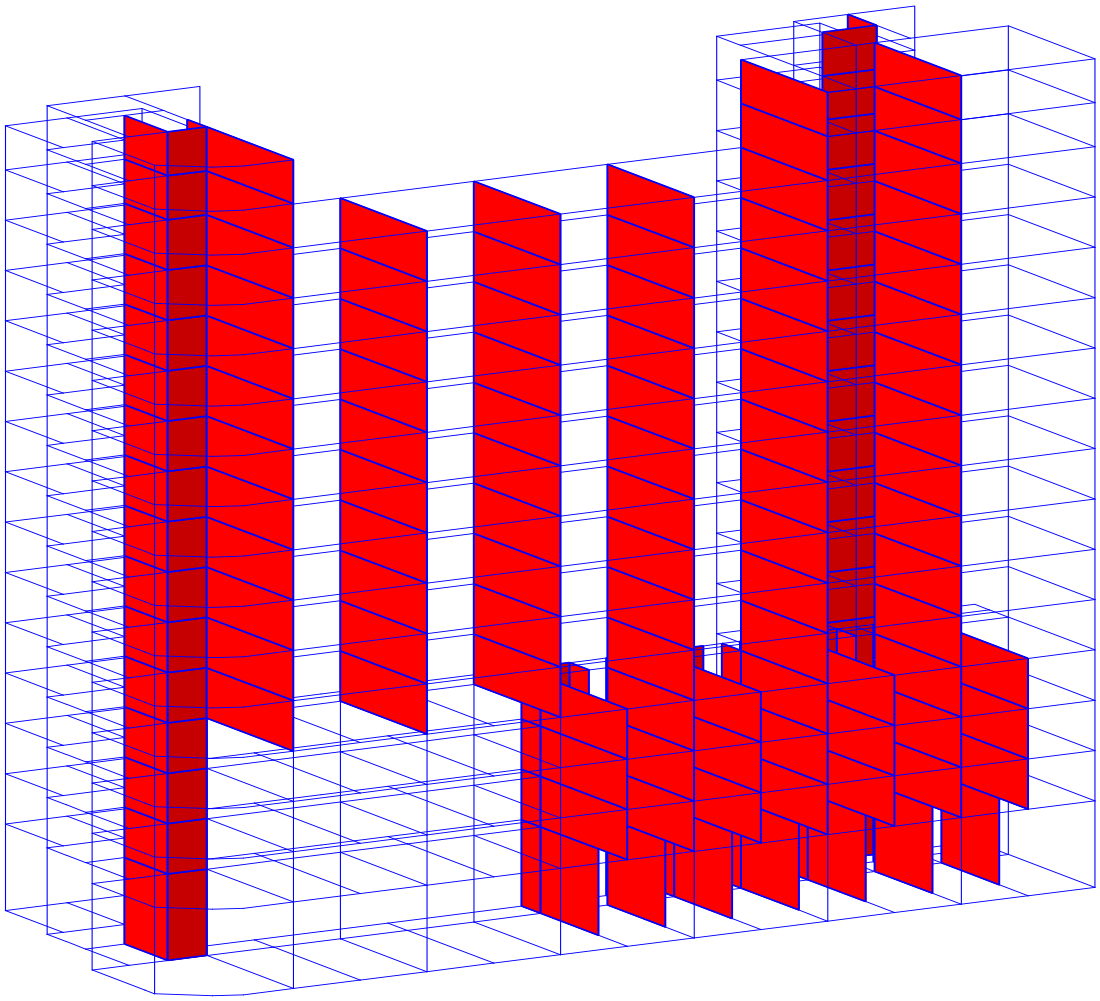

(b) Based on the completion map

Figure 2.39 TNCE's structural analysis model of Weiguan building (Shih, 2016)

As indicated from Figure 2.39, currently in static or dynamic analysis, the structural analysis model adopted by technicians participating in the structural dynamic analysis, under the situation of ignoring the internal columns of the basement, side walls of the basement, soils supporting columns and side walls surrounding the basement foundation, as well as soils supporting the foundation, the simulation analysis for the building structure under the actions of various external forces has in fact not been able to reflect the actual situation as much as possible. Thus, regardless of the simulation for geometric shapes, or also the mass distribution, construction materials' sectional properties, or simulation on the interaction between soils and foundations, all of these have not been accurate, thereby not meeting the actual requirements for the in-situ conditions.

Next, in the structural analysis model as shown in Figure 2.39, when the bottoms of all columns in the 1st floor are established as fixed ends, this means that the bottoms of all columns in the 1st floor are positioned on a rigid body. In other words, the bottoms of all columns in the 1st floor are established to be without any relative movement or any rotation.

However, in an actual building, under the action of various external forces, due to the existence of lower components such as basements and foundations, the bottoms of columns in the 1st floor have certain amount of relative movement and rotation. And such an amount of relative movement and rotation will change according to the different rigidity for different soils supporting the foundations and side walls surrounding the basement. Especially under the situation that the soils supporting the side walls surrounding the basement suddenly undergo a local disappearance, the amount of movement and the amount of rotation for bottoms of the columns in the 1st floor will thus increase substantially; following this, some beam-column joints for the column bottoms in the 1st floor will therefore be ruptured.

For an actual building, in addition to the building's upper structural analysis model as shown in Figure 2.39, there are internal columns of the basement, side walls of basement, soils supporting side walls surrounding the basement, foundations, as well as the soils supporting the foundation. In the dynamic analysis by entering the seismic acceleration time-history, the seismic forces are transmitted upwardly from the foundation. As the side walls surrounding the basement can be taken as the shear wall, a large portion of the seismic force will be transmitted to the columns and side walls surrounding the basement, only a small portion of the seismic force is transmitted to the internal columns of the basement. This is the reason why the internal columns of the basement can maintain stability during an earthquake without the support of partition walls. In addition, under the situation that the soils can effectively support the side walls surrounding the basement, large portions of seismic force in the columns and side walls surrounding the basement will be transmitted to the soils; thus only a small portion of the seismic force is transmitted upwardly. This is the reason that the beam-column joints at the bottom of a 6-meter high ceiling 1st floor did not rupture in the 2010 Jiaxian earthquake, thereby the Weiguan building

could remain stable. However, once the soils supporting side walls surrounding the basement disappear locally, massive seismic force from the side walls surrounding the basement within this one local range will all be transmitted upwardly, part of the beam-column joints at the bottom of the 6-meter 1st floor will be ruptured under excessive relative movement and rotation, thereby the overall building is tilted, and collapsed.

As seismic vibration is only a secondary effect of tectonic earthquakes, the provisions for the horizontal seismic vibration forces are not the same in all of the current building earthquake-resistant design specifications for countries around the world. Only speaking for Taiwan, the provisions for the horizontal seismic vibration forces are also not the same in the building earthquake-resistant design specifications at different periods of time. Taking the Language Building of Feng-Chia University as an example (Hsu, 2016), when earthquake-resistant designs are conducted in accordance with the 1999 edition and the 1974 edition of the building earthquake-resistant design specifications individually, the horizontal seismic vibration force required in the 1999 edition is about twice as high as that of the 1974 edition. However, up to now, the Language Building of Feng-Chia University has not been damaged simply because the horizontal seismic vibration force provided in the original earthquake-resistant design is biasedly low. The Construction and Planning Agency under Ministry of the Interior also did not request that Feng-Chia University must demolish or strengthen the Language Building after 1999 as it does not comply with the requirements in the 1999 edition of the building earthquake-resistant design specification.

On the contrary, the main structure of the building has been completely renovated, as shown in Figure 2.5, although its seismic design is in accordance with the 1999 edition of the building earthquake-resistant design specification, it was expected to remain stable in earthquakes with a magnitude of ML = 7.3, but it was tilting damaged in the Meinong earthquake of ML = 6.4.

Learning from this, when the stipulation or amendment of the building earthquake-resistant design specification only focuses on the upgrade of the horizontal seismic vibration force of an earthquake, it is in fact unable to ensure that the building will be not tilting damaged or collapsed in a tectonic earthquake.

2.5.2 The Fatal Problem for the Disaster Identification

Since the primary effect of tectonic earthquake is shear banding and the secondary effect is seismic vibration, the tilting, and collapse of a building in tectonic earthquakes caused by shear banding should have much higher relevance than that of seismic vibration.

However, once the identification of the tilting, and collapse of buildings in tectonic earthquakes is based on the current building earthquake-resistant design specification (Construction and Planning Agency, Ministry of the Interior, 2015) or the relevant provisions of CNS560 steel deformed and plain bars for concrete reinforcement (Bureau of Standards, Metrology & Inspection, Ministry of Economic Affairs, 2014), the current building technical regulations provide specifications only on the tectonic earthquake's secondary effects (seismic vibration), and completely ignore the impact of tectonic earthquake's primary effect (shear banding), thereby the regulations cannot identify the cause of fatality.

The Weiguan Building was completed in 1994. It had remained stable during the Jiaxian Tectonic Earthquake with a magnitude scale of M_L = 6.4 in 2010, but was collapsed during the Meinong Tectonic Earthquake with a magnitude scale of M_L = 6.4 in 2016.

Since the completion of the Weiguan building, geological drilling, estimation of overall building weight, horizontal seismic vibration force provided in design, strength of steel bars, number of steel bars, concrete strength, sectional size of columns and beams, configuration direction of columns and beams, number of stirrups for beam-column joints, construction quality, partition wall, height of 1st floor, and sectional configuration of the entire building have become established conditions. Even though these established conditions do not comply with the building earthquake-resistant design specification or the relevant provisions of CNS560 steel deformed and plain bars for concrete reinforcement, just as described in the Identification report of cause identification on the collapse of Weiguan building (Tainan Civil Engineering Technician Association, 2016), it cannot be inferred that these established conditions are the reasons for collapse to the Weiguan building during the Meinong earthquake in 2016 with magnitude scale of M_L=6.4, because the Weiguan building had not collapsed or been damaged during the Jiaxian earthquake with the same magnitude in 2010.

Next, even though there are missing structural elements in the design or the construction of the items mentioned above, because these missing structural elements are not directly related to the tectonic earthquake's primary effect (shear banding), it is not possible to identify the fatal reason for the collapse and damage of Weiguan building.

Finally, how can we identify the fatal reasons for the collapse and damage of Weiguan building during the Meinong earthquake? The answer to this question is only through the comparisons of the different on-site conditions that appeared before and after the two tectonic earthquakes of the same magnitude as $M_L = 6.4$.

Figure 2.40 shows the monitor record images of Weiguan building before and after the collapse and damage. Figure 2.40 proves that before the collapse of Weiguan building, a pipe burst phenomenon appeared in the tap water supply trunk pipe with a diameter of 2m embedded under the Yongda Road adjacent to the intersection of Yongda Road and Guoguang 5^{th} Street, and water-jetting phenomenon existed due to the bursting of this tap water supply trunk pipe.

After the pipe burst phenomenon in the tap water supply trunk pipe occurred as shown in Figure 2.40b and Figure2.40c, as there were 2m high earth fills above the tap water supply trunk pipe, a hole of 4m depth suddenly appeared on Yongda Road. Because of the sudden appearance of the 4m-deep hole, the constrained conditions of the side walls surrounding the basement of the Weiguan Building were therefore partially disappeared.

Since the soil layer beneath the Yongda Road is a silty alluvium layer, this silty alluvium layer still retained considerably high shear force resistance strength in a dry state, which caused Block G behind the Block I to recline on the ground surface of Yongda Road after the collapse and damage of the Weiguan building (details in Figure 2.41). In addition, the shear resistance strength of this type of silty alluvium layer drops significantly in a saturated state, which caused Block H behind Block A to fall into the ground 2.5m deep after the collapse of the Weiguan building.

(a) Car passing by the Weiguan building before the pipe burst

(b) Before the collapse and damage of Weiguan building after the pipe burst

(c) Water-jetting position marked by red circle on the image

Figure 2.40 Water-jetting phenomenon after a pipe burst in tap water supply trunk pipe (Sanlih E-Television News, 2016),

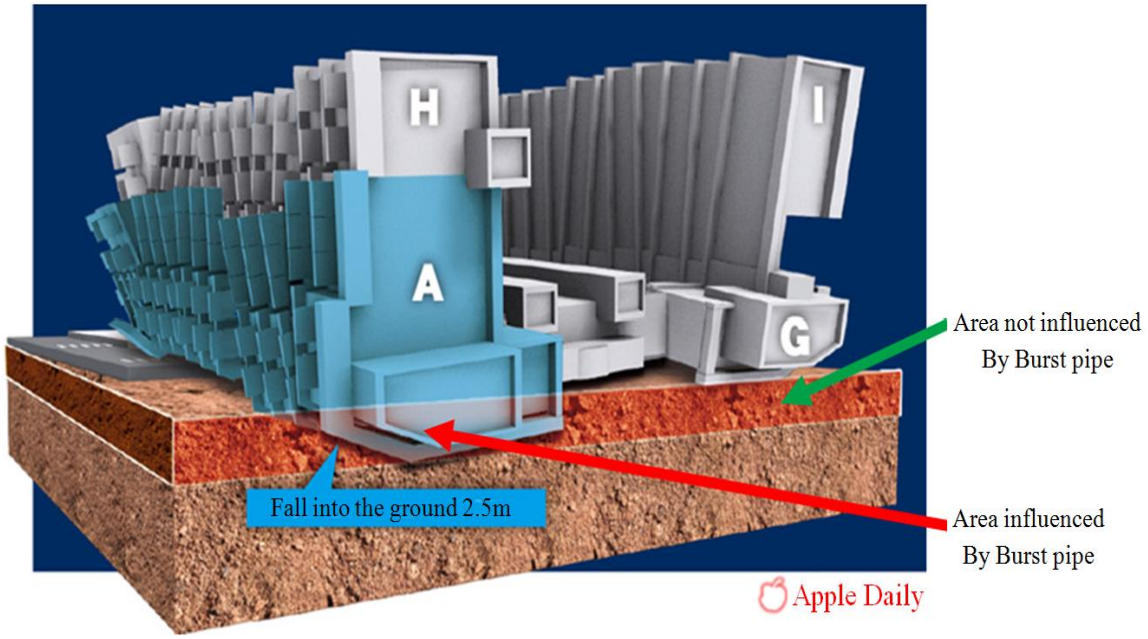

Figure 2.41 Structural model of the Weiguan building after the collapse (Apple Daily, 2016)

The fact that Block A and Block H subsided 2.5m below the ground surface as shown in Figure 2.41 proves that the pipe bursts in the tap water supply trunk pipe and the water-jetting phenomenon appearing after the pipe burst did indeed cause the local softening of silty alluvium layer near the gap after the pipe burst in the tap water supply trunk pipe. And the local softening phenomenon of this type of alluvial layer also caused the degree of distorted damage for the subsidence of Block A and Block H 2.5m below the ground surface after collapse to be more severe than the degree of distorted damage for the collapse of Block G and Block I (details in Figure 2.42).

Figure 2.42 Weiguan building after the collapse (Liberty Times Net, 2016)

When the soils supporting the surrounding side walls in the basement of Block A of the Weiguan building at one side of Yongda Road lost lateral support after the burst in the tap water supply trunk pipeline, the soils again were drastically softened after water soaking. As a result, the bottoms of all columns in the 1st floor of Block A at one side of Yongda Road deviate from the fixed end conditions as established in the structural analysis model shown in Figure 2.39, thereby inducing the aforementioned rupture of beam-column joints for the bottoms of columns in the 1st floor.

As for the cause of damage to the large-scale water supply pipeline, Liu (2007) and Hsu et al. (2015) pointed out that the peak ground acceleration (PGA) was not the main cause of the large-scale water supply pipeline damage during the earthquake; the main reason was the shear banding. Learning from this, the bursting of the tap water supply trunk pipeline that appeared on the Yongda Road adjacent to the intersection of Yongda Road and Guoguang 5th Street, as shown Figure 6.2, is actually mainly caused by shear banding.

2.5.3 A Proper Procedure for the Identification of Building Disaster Happened in a Tectonic Earthquake

Because tectonic earthquakes are most prevalent and their destructive power is also the strongest, all earthquakes that cause major disasters are tectonic earthquakes. A proper procedure for the identification of building disaster happened in a tectonic earthquake is listed as follows:

Step 1: Make sure that the earthquake is tectonic earthquake.

Step 2: Adopt satellite images, GPS velocity vectors, or in-situ topography features to find the locations of shear bands.

Step 3: If shear banding is located under the foundation of the building, the reason for causing the disaster is directly related to such a shear banding.

Step 4: If shear banding is located near the building, the reason for causing the disaster can be found only after conducting a structure dynamic analysis for a structure model of the whole building which is subject to the effects of both shear banding and seismic vibration.

Step 5: If the building disaster did not happened in the previous tectonic earthquake, the reason for causing the disaster can be found only after finding the different conditions for causing and not causing the disaster in these two tectonic earthquakes.

An Application Example. Taking the Weiguan building as an example, the procedure listed above is used as follows:

Step 1: The collapse of Weiguan building was happened in the Meinong earthquake, and such an earthquake has been proved by Central Weather Bureau in Taiwan to be a tectonic earthquake.

Step 2: The GPS velocity vectors shown in Figure 2.43 indicate that shear banding did happen near the Weiguan building. The phenomenon for a pipe burst shown in Figure 2.40 is the other evidence for shear banding near the Weiguan building. However, such a shear banding phenomenon did not happen in the 2010 Jiaxian earthquake.

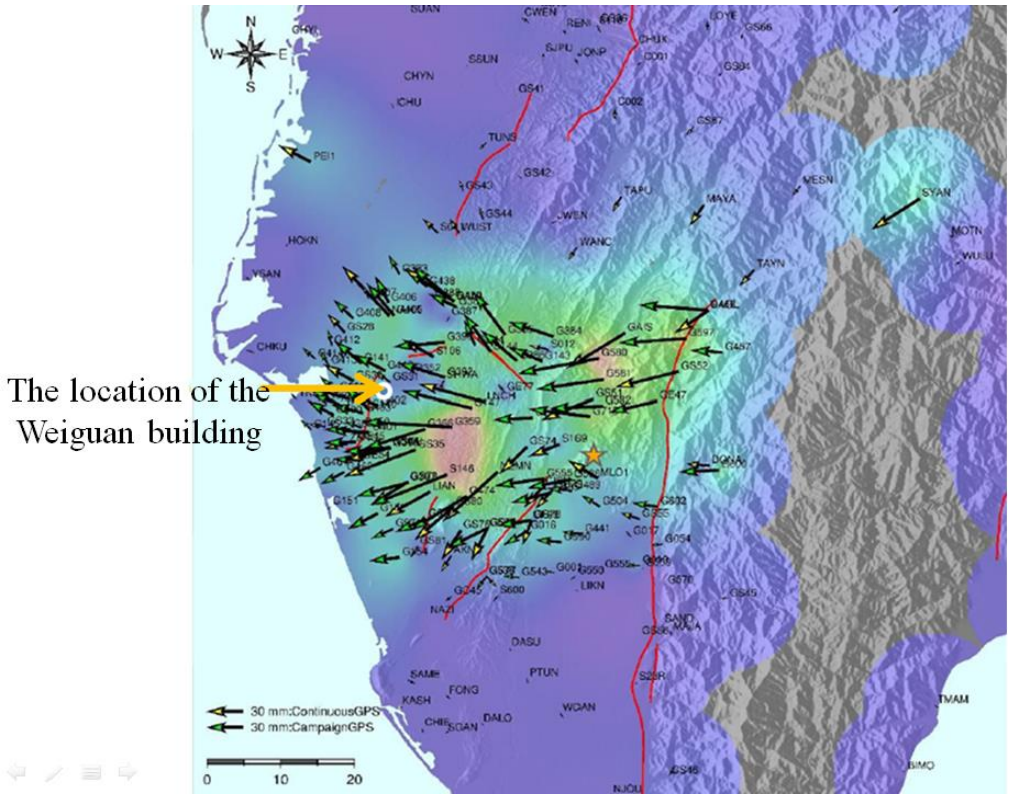

Figure 2.43 The GPS velocity vectors mainly produced by the Meinong earthquake (Central Geological Survey, 2016)

Steps 3 to 5: Since shear banding near the Weiguan building didn't occur in the 2010 Jiaxian earthquake, but did occur in the 2016 Meinong earthquake, a structure dynamic analysis for a structure model of the whole building which is subject to the seismic vibration effects with or without the shear banding effect is conducted as follows:

A structure model of the whole building. A structure model of the whole building including all elements of both the upper and the lower structures is used as that shown in Figure 2.44.

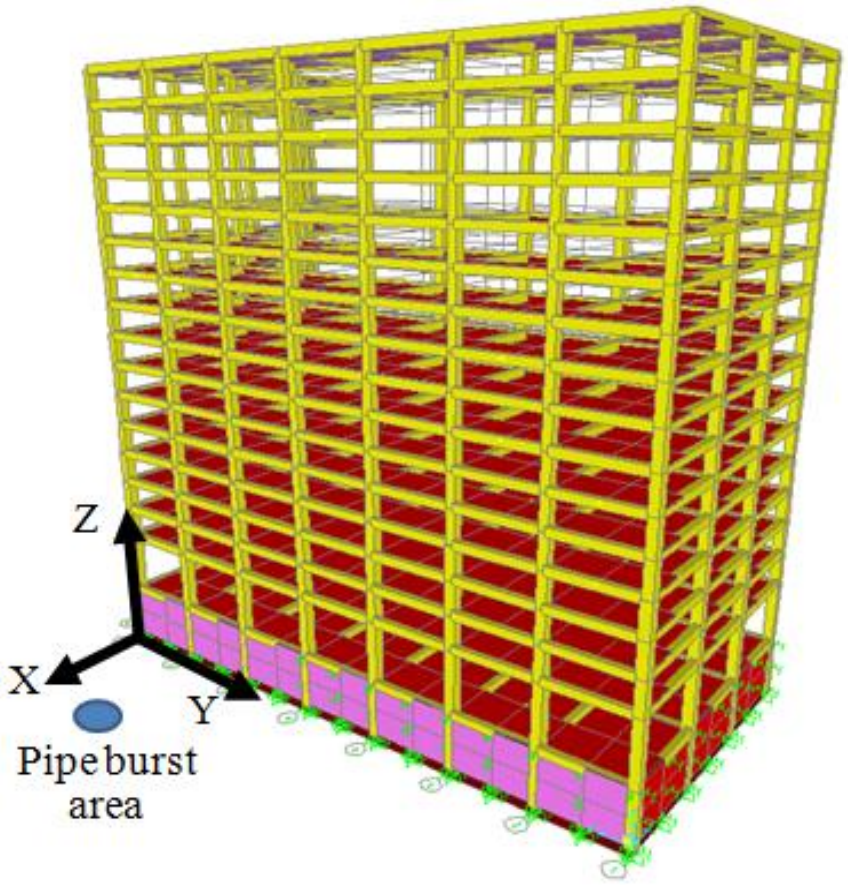

Figure 2.44. The structure model used in dynamic analyses

Conditions for the structure model. It is to be mentioned that perfect joint connections between each two elements are utilized to exclude the minor reasons for causing disaster. The cross sections and material properties used in the analyses are similar to those adopted by the original designer. The side walls surrounding the basement are constrained by springs with their elasticity modulus determined by values of N form the standard penetration tests. When the pipe burst phenomenon shown in Figure 2.40 is to be considered (or not to be considered), the springs for the side walls near the pipe burst area are to be removed (or not to be removed) such that the effect of shear banding can be determined numerically. Loading conditions including both static loads and seismic vibration forces; the static loads include life load 200kgf/m^2 and dead load 150kgf/m^2 in besides body forces of the structure elements; and the seismic vibration forces are generated by the acceleration history taken from Station No. CHY063 as shown in Figure 2.45.

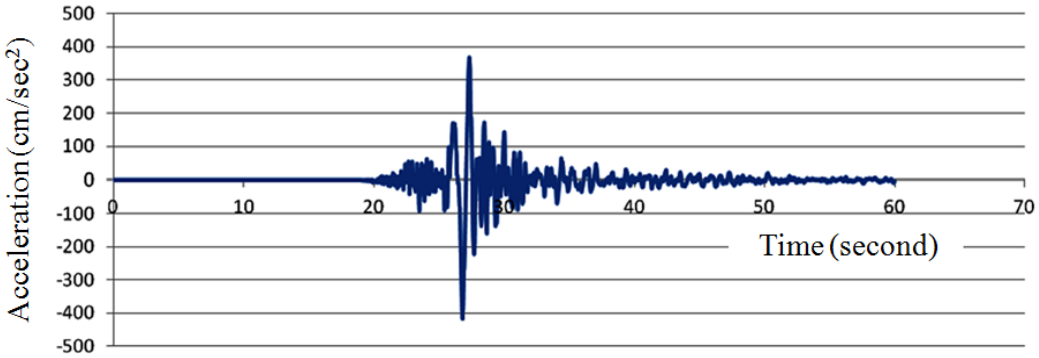

(a) X-direction

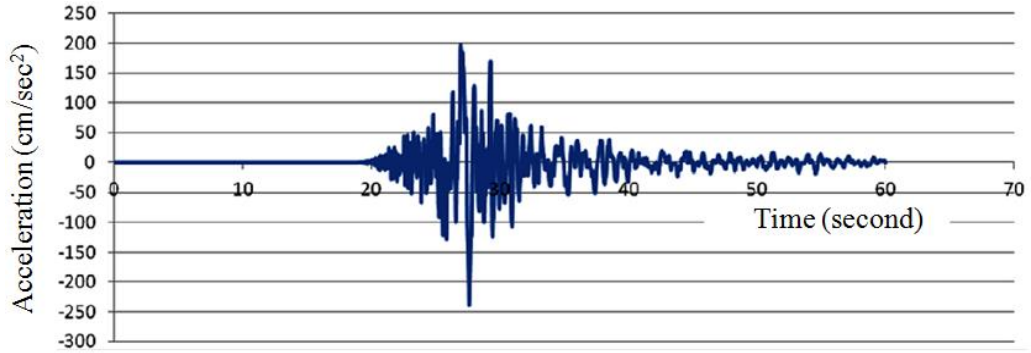

(b) Y-direction

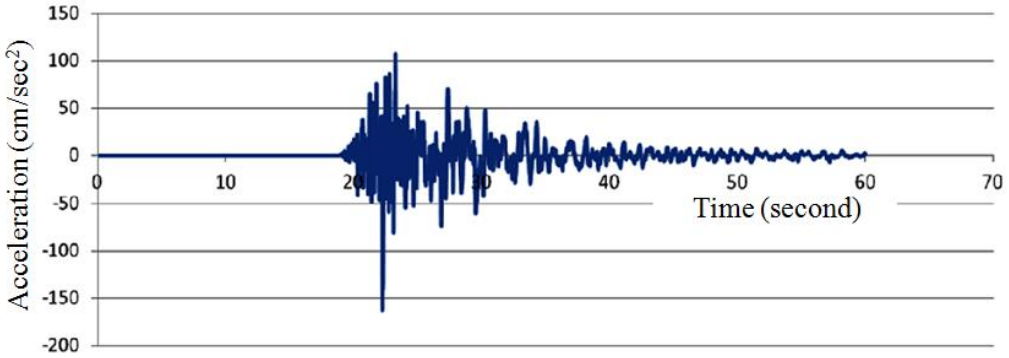

(a) Z-direction

Figure 2.45. The acceleration history adopted in the analyses (Central Weather Bureau, 2016)

Numerical results for the structure model. Because the major concerned for the Weiguan building's disaster is that the whole building to tilt initially toward the X-direction around the bottom joints of the 1st floor, numerically results are to be shown for the four nodes shown in Figure 2.46.

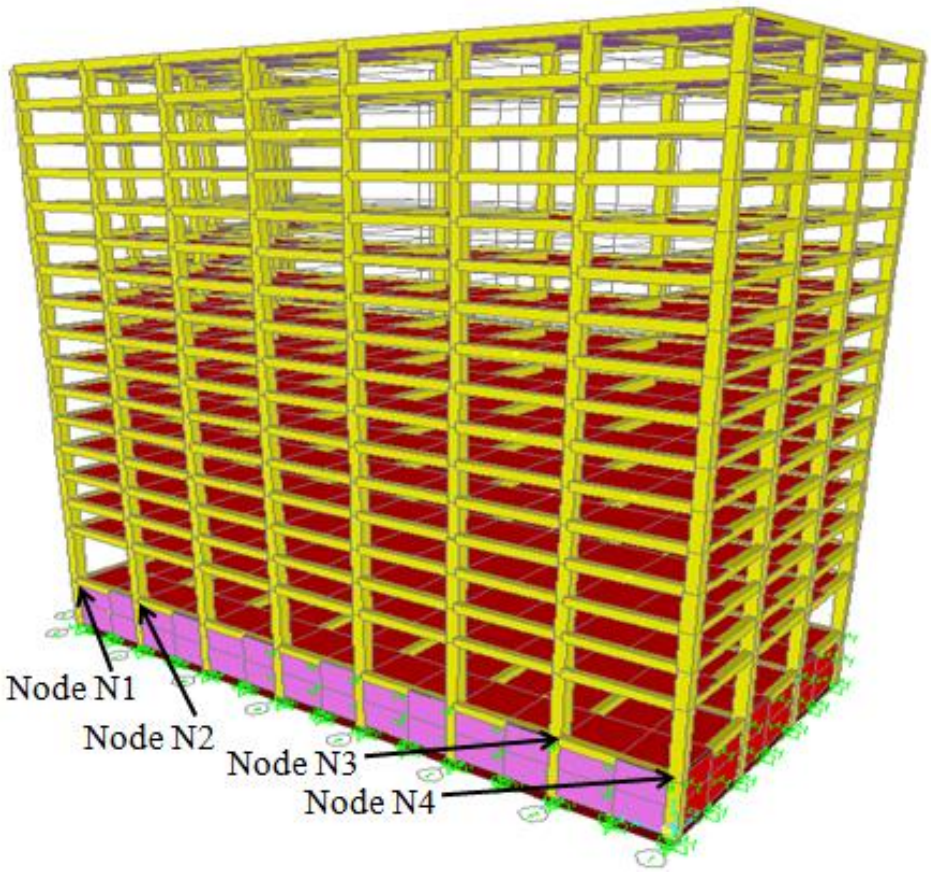

Figure 2.46. The four major concerned nodes shown in the structure model

The maximum displacements for the four joints shown in Figure 2.46 from structure dynamic analyses with and without shear banding effect are shown in Table 2.8, where case 1 does include shear banding effect and case 2 doesn't.

Table 2.8. Numerical results for structure models with and without shear banding effect

Node number	The maximum displacement appeared in a tectonic earthquake (cm)							
	X-direction component		Y-direction component		Z-direction component		The whole vector	
	Case 1	Case 2	Case 1	Case 2	Case 1	Case 2	Case 1	Case 2
N1	13.85	7.09	9.08	3.96	12.21	7.98	20.57	11.38
N2	9.15	4.44	9.01	4.11	8.92	5.50	15.63	8.34
N3	4.99	4.45	7.37	4.12	5.44	5.61	10.43	8.26
N4	8.12	7.09	7.00	3.96	7.73	8.02	13.21	11.41

Note: Case 1 does include the shear banding effect;

Case 2 doesn't include the shear banding effect.

Discussion. Since there was no disaster happened in the 2010 Jiaxian earthquake, the results of case 2 are therefore to be thought as safety values of displacements. Whether the results of case 1 can be thought as safety values will depend on the fractions F_{12} calculated by dividing the displacements of case 1 by those of case 2. The resulting fractions F_{12} are shown in Table 2.8. It can be found from Figure 2.8 that the shear banding effect is very significant for Nodes N1 and N2; and is less significant for Nodes N3 and N4.

Table 2.8. The calculated values of fractions F_{12}

Node number	X-direction component	Y-direction component	Z-direction component	The whole vector
N1	1.95	2.29	1.53	1.81
N2	2.06	2.19	1.62	1.87
N3	1.12	1.79	0.97	1.26
N4	1.15	1.77	0.96	1.16

It is the author's opinion that only a value of F_{12} for the whole displacement vector less than 1.1 can still maintain the building structure under stable conditions. However the values of F_{12} for the whole displacement vectors of Node 1 to Node 4 shown in Figure 2.46 are all greater than 1.1. The worst conditions happen at the nodes N2 and N1, where the shear banding effect makes the values of F_{12} greater than 1.8. It is

therefore believed that tilting of the Weiguan building along X-direction started from the side having great influence of shear banding due to pipe burst shown in Figure 2.44. Then it was quickly propagated to the other side.

2.6 Summary of the Main Points

1. In the past, the Ministry of Education completed the seismic reinforcement of school building structures after the 921 Jiji earthquake. Despite adopting lateral pushover analysis and the lateral pushover test, the structural model, analysis methods, and test methods are all only based on seismic vibration.

2. After the 0206 Meinong earthquake in 2016, it was found that the buildings that experienced local damage are relatively newer, and there are many older buildings that continue to remain stable in close proximity to the damaged buildings, thus the building earthquake- resistant design specifications cannot only focus on seismic vibration.

3. Localized deformations are derived from shear bandings, so the local damage of buildings during tectonic earthquakes has high relevance for the local shear bandings, and low relevance for the all-around seismic vibrations. Under this premise, the building earthquake-resistant design specifications and the CNS both have low relevance for shear bandings, so when using the building earthquake-resistant design specifications and the CNS to identify the disaster cause for the local building damage after a tectonic earthquake, the resulting disaster cause always does not match with the actual disaster one.

4. If the stipulation or amendment of the building earthquake-resistant specifications is only based on disaster causes of the seismic vibrations, regardless of how the seismic horizontal vibration force is being enhanced, the building will still be damaged by shear bandings under a tectonic earthquake.

5. In response to the needs of tectonic earthquakes, it is necessary to first understand the shear textures in a total shear band width. Regions where shear bandings exist should be designated as non-construction sites in urban plans. In regions where shear bandings appear, it is necessary to first use special methods eliminating the propagation of shear bandings to

ensure the safety of the foundations in a tectonic earthquake; subsequently, ensuring that “soils for shear failure extension depth range corresponding to the ultimate bearing capacity of foundation" can enable the safety factor of the bearing capacity of foundations under the action of seismic vibrations to meet the relevant provisions of the specifications.

6. Shaking table can conduct validation tests of seismic vibrations only, but the main cause for collapse (or damage) of buildings in tectonic earthquakes is shear bandings. Therefore, a shear banding table (details in Figures 2.47 and 2.48) and a large scale direct shear test equipment have been proposed to perform the validation tests for the chosen materials of ground modification, in order to ensure that the foundation can maintain stability in a design tectonic earthquake.

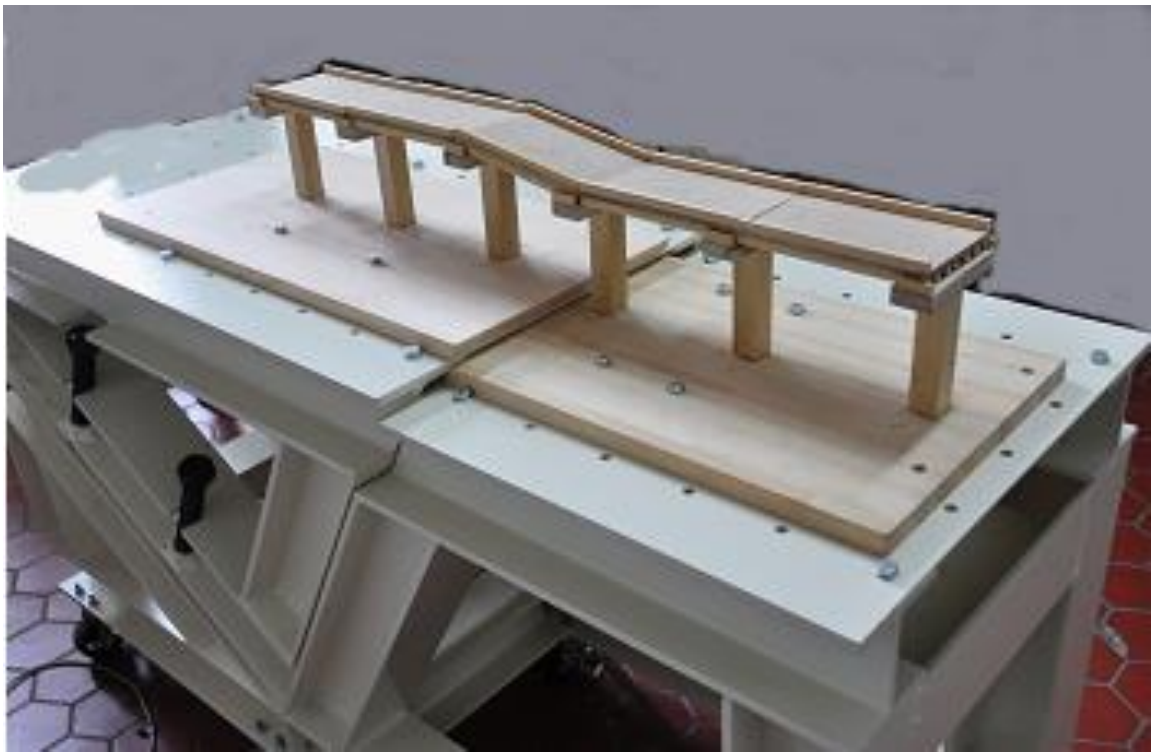

(a) Induced by shear banding table test

(b) Induced by the 921 Jiji tectonic earthquake (the Wu-shi Bridge)

Figure 2.47. Bridge tilted by shear bandings

(a) Induced by shear banding table test

(b) Induced by the 921 Jiji earthquake (the Shih-wei Bridge, Taiwan)

(c) Induced by the 1964 Niigata tectonic earthquake

(the Showa bridge, Japan; Wikipedia, 2017)

Figure 2.48. Bridge collapsed by shear bandings

Chapter 3

Piping Failures Caused by Shear Bandings

T.-S. Hsu and S.-E. Chiu

3.1 Introduction

The construction of Renyitan Reservoir was completed in 1986, and the spillway on the ridge of the southwest side (Figure 3.1) is backfilled from the valley shown in Figure 3.2. The local image is shown in Figure 3.3.

Figure 3.1 Plan view of Renyitan Reservoir and spillway (Google Earth, 2017)

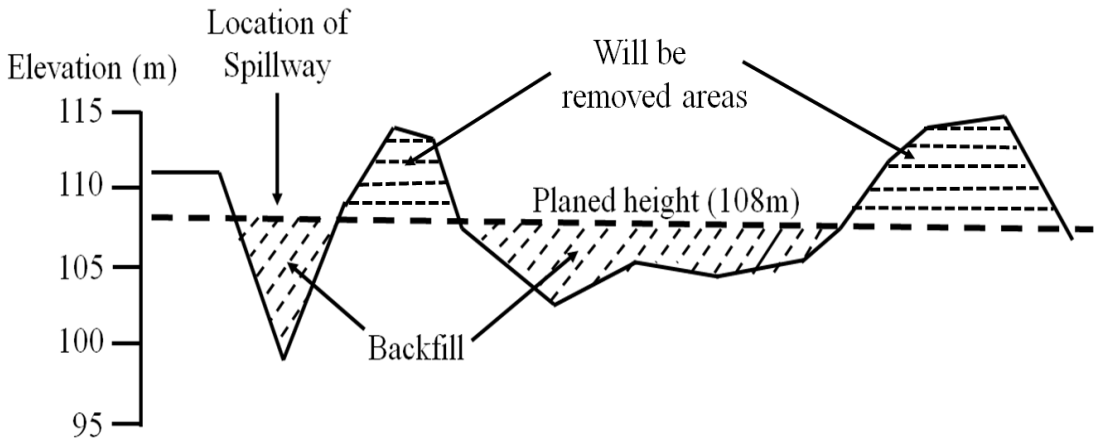

Figure 3.2 Section plan of Renyitan Reservoir spillway and adjacent area

Figure 3.3 Local image of Renyitan Reservoir spillway

The piping failure of Renyitan Reservoir spillway occurred on 2nd of September 2013. Since then the government agency has continued to entrust academic institutions and consultants to perform seepage analysis, groundwater level observation, ground penetrating radar detection, and local testing of the leakage source, however they have been unable to identify the exact cause of piping failure. Therefore, further study is very important for the repair work of the spillway floor after piping failure.

Taiwan is located on the edge of the Eurasian plateau. Under the continuous compression of the Philippine Sea plate, the Eurasian continental plate undergoes localization of deformations due to the loss of ellipticity after the shear strain is deep into the plastic range, and further causes shear banding.

Similar to shear banding in metal, river patterns and curved surfaces can be revealed by fractography. Similarly, for the shear banding of a tectonic plate, when shear banding (red line) appears at the appropriate depth of the tectonic plate (Figure 3.4), the river patterns (green and blue lines) and curved surfaces will also appear; these river patterns and curved surfaces create the ups and downs of the mountains as shown in Figure 3.5.

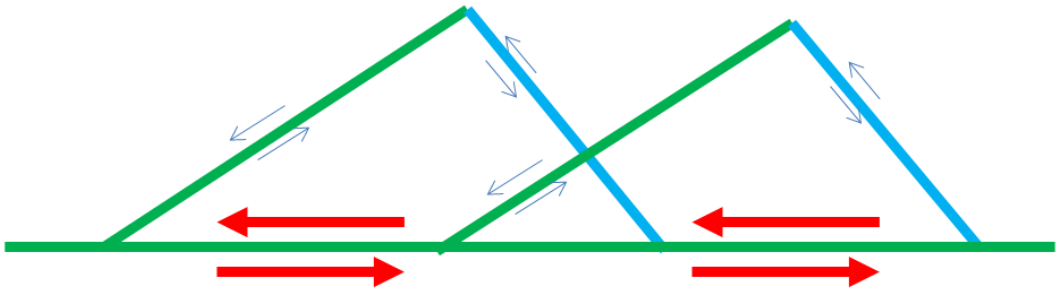

Figure 3.4 River patterns and curved surfaces caused by shear banding

Figure 3.5 Mountains on both sides of Gouhou Dam of China's Qinghai Province (Google Earth, 2017)

Figure 3.6 is drawn by adopting the river patterns and curved surfaces in Figure 3.4 and Figure 3.5. Figure 3.6 shows that the dam between the mountains is inevitably influenced by shear banding in the adjacent areas.

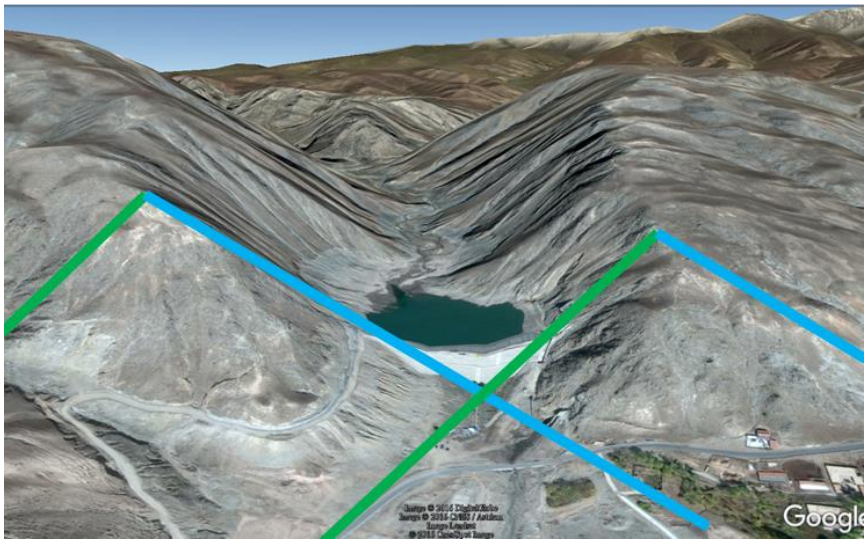

Figure 3.6 Shear textures of the dam in the adjacent areas
(The background map is from Google Earth, 2017)

Figure 3.5 and Figure 3.6 show the Gouhou Dam in Qinghai Province of China after the reconstruction work had finished. The reason for reconstruction is the piping failure of the original dam (Figure 3.7).

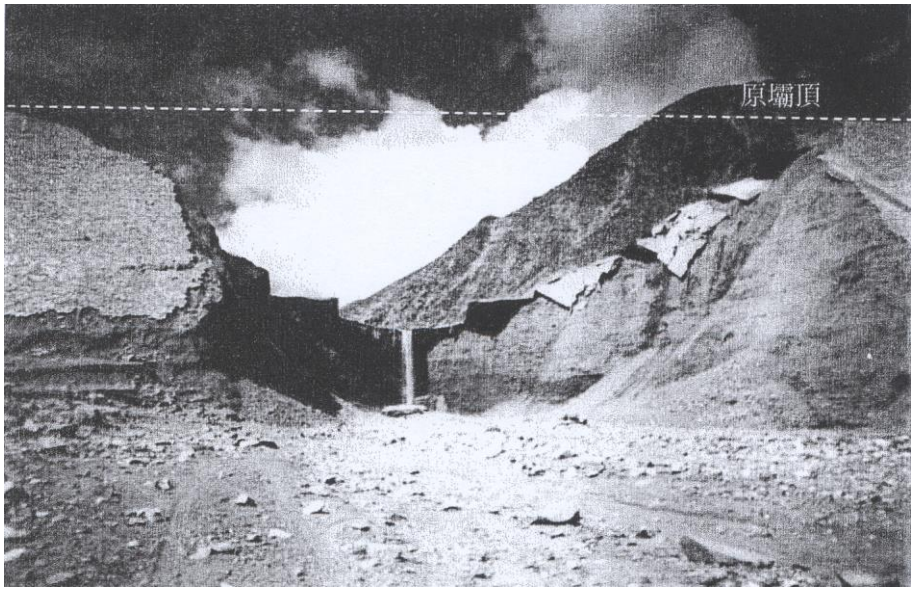

Figure 3.7 Gouhou Dam after dam break (Sinotech Foundation for Research and Development of Engineering Sciences and Technologies, 2008)

Generally, safety assessment is carried out prior to dam design, and safety assessment contains dam dynamic analysis. In the past, when the design engineer carried out the dam dynamic analysis, the shear bands and shear textures in the adjacent area of the dam was completely neglected. Only the closest fault to the dam was chosen as the design fault based on a government report, therefore the dam can be damaged due to shear banding. Take Gouhou Dam as an example, through the investigation after the piping failure it was found that there were dozens of shear bands below the dam (Figure 3.8), and there are still some shear bands criss cross the residual piping holes (Figure 3.9).

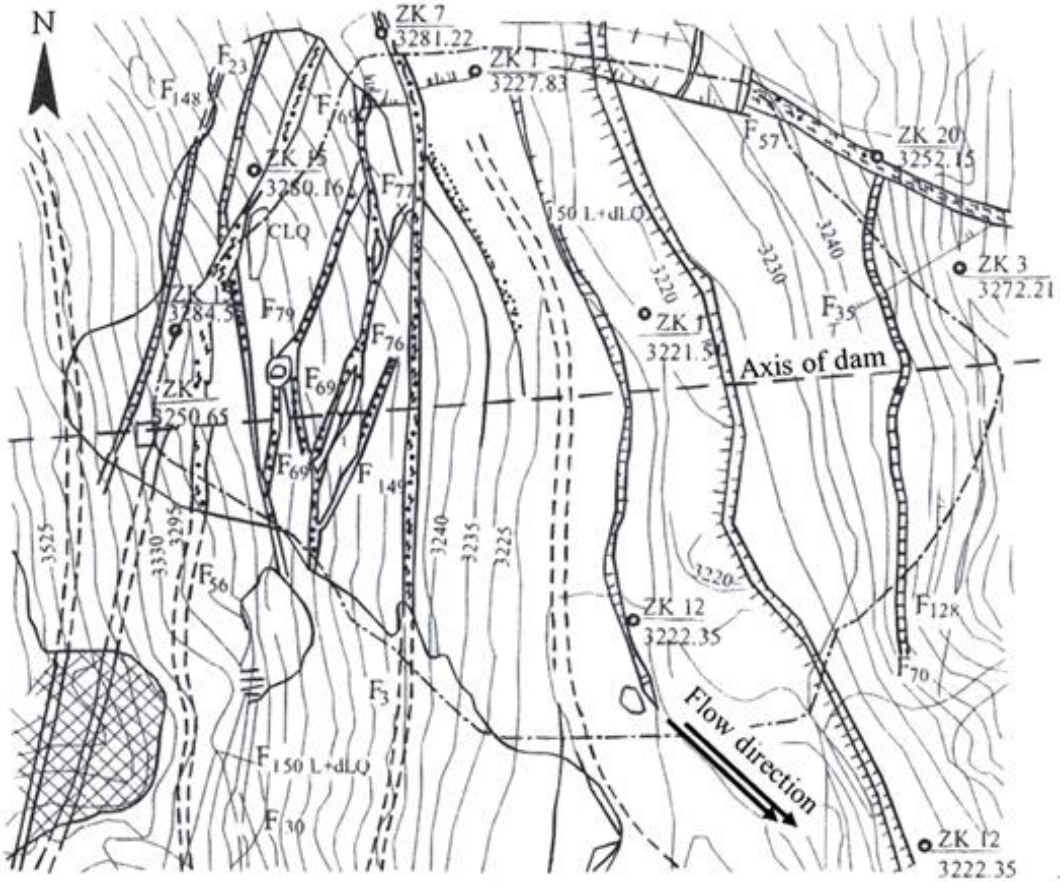

(a) Plan

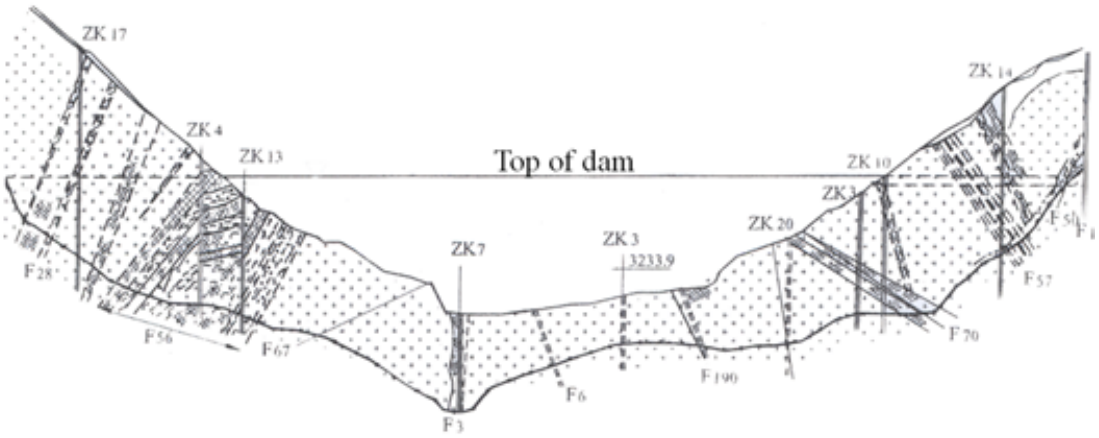

(b) Sectional Plan

Figure 3.8 Shear bands below the dam (Sinotech Foundation for Research and Development of Engineering Sciences and Technologies, 2008)

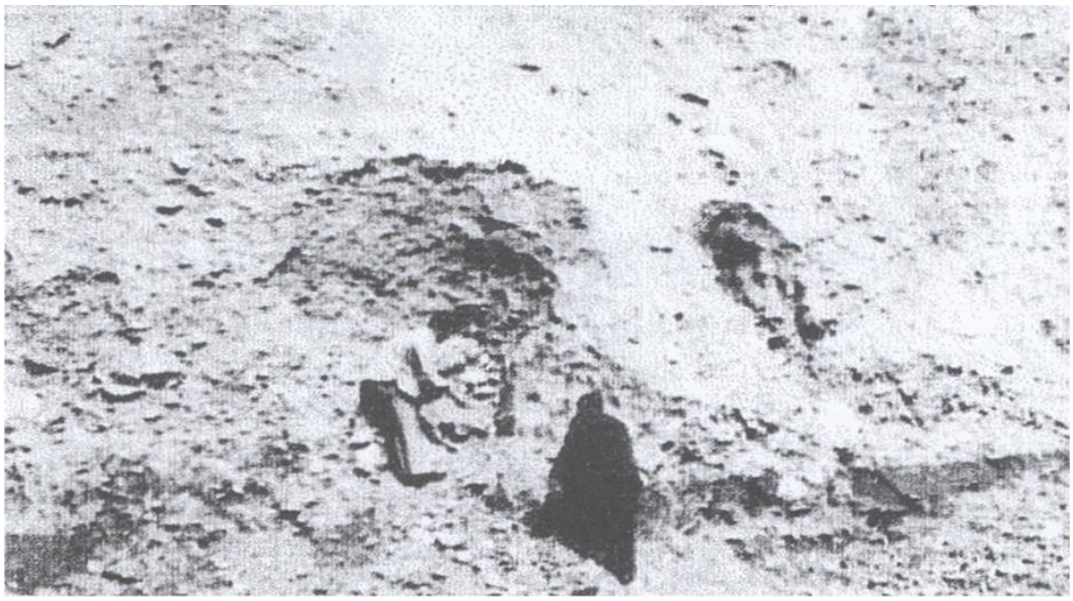

Figure 3.9 Residual piping holes in the dam (Sinotech Foundation for Research and Development of Engineering Sciences and Technologies, 2008)

Although the investigation after the dam damage was very detailed, the reconstruction process was still lacking the concept of a shear band. Therefore even after the reconstruction the dam is still affected by shear banding, and the dam due to abnormal water leakage continues to maintain the wetting phenomenon as shown in Figure 3.10.

Figure 3.10 Water leakage in the downstream of Gouhou Dam
(Google Earth, 2017)

It can be seen that the shear band model of the adjacent area should be constructed prior to the safety assessment of the dam, and the shear bands can be identified by using the GPS velocity vector distribution map, so as to locate the corresponding pipe-shaped discharge tunnel causing potential piping failure, and thus effectively prevent the occurrence of piping failure.

Based on the above, in this chapter Renyitan Reservoir spillway is taken as an example. Firstly, the shear band model existing in the adjacent area of the spillway is constructed. Secondly, the effects of the shear banding in the 1022 Chiayi Earthquake on the broken spillway and dislocation and deformation of Renyitan Reservoir spillway is used as supplementary data to confirm that the water can flow into the shear banding soils below the bottom plate of the spillway through the break zone. Finally, the possibility of piping failure is assessed by the bottom critical velocity of the particles required for piping failure, and the exact cause of piping failure is further suggested.

3.2 Literature Review

3.2.1 Piping Failure Defined by Terzaghi and Peck

Terzaghi and Peck (1967) defined piping failure as follows: “Many dams on soil foundations have failed by the apparently sudden formation of a pipe-shaped discharge tunnel located between the soil and the foundation. As the stored water rushed out of the reservoir into the outlet passage, the width and depth of the passage increased rapidly until the structure, deprived of its foundation, collapsed and broke into fragments that were carried away by the torrent. An event of this type is known as a failure by piping.”

3.2.2 Literatures Related to Shear Bands

Definition of Fault and Shear Band. Ikeda Toshio et al (2000) defined a fault as follows: "There are some discontinuities in the destruction of rocks and bedrocks. When the relative misalignment along the discontinuities reaches a certain degree, it becomes a fault." It can be concluded that a shear band is a discontinuous surface caused by the destruction of the rocks and bedrocks, while a fault is a shear band that reaches a certain degree of relative misalignment.

Shear Textures within the Overall Shear Band width. Tchalenko (1968) pointed out that shear textures within an overall shear band width include principal displacement shear, thrust shear, Riedel shear, conjugate Riedel shear, and compression texture (details in Figure 3.1).

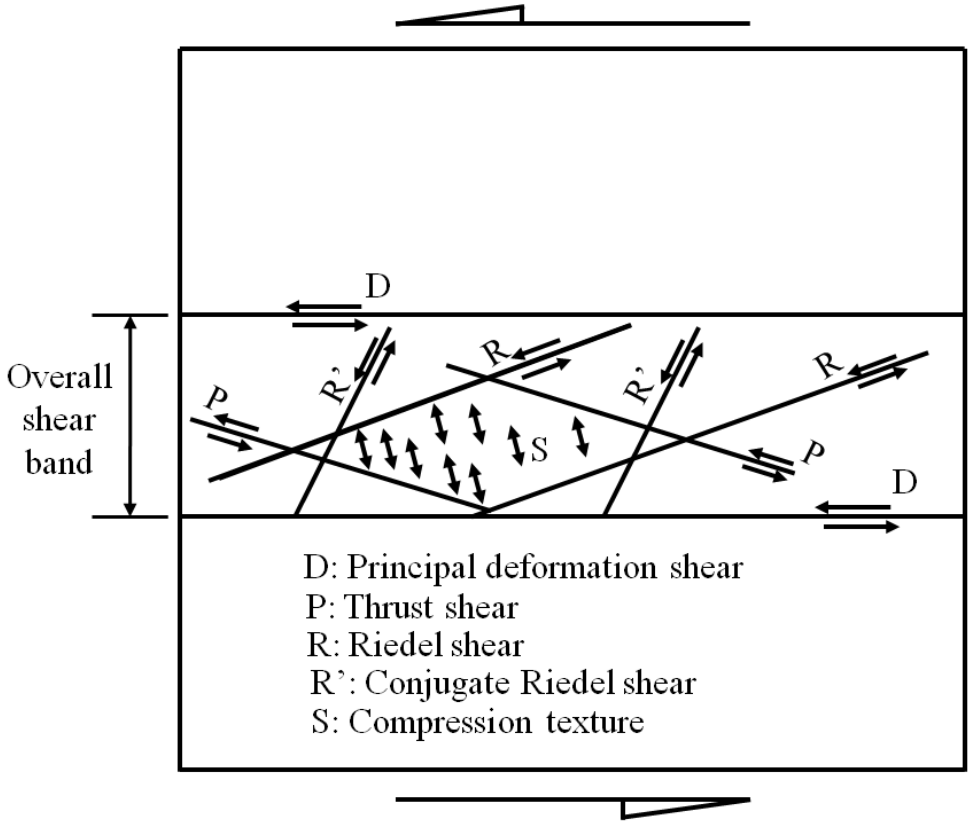

Figure 3.1 Various shear textures in the overall shear band

(redraw from Tchalenko, 1968)

3.2.3 Shear Banding Landform Features

The tectonic plates will retain some features due to shear banding. Vertical banding will produce a high and low differential terrain, and horizontal shear banding will produce a horizontal displacement terrain. The above-mentioned shear banding landform features are also called displaced landform features (Earle, 2004; Lin, 1988; Toshio Ikeda et al., 2000).

The shear banding landform is obvious in the initial phase of the dislocation, and later on due to erosion or alluvial effect, it tends to be not so obvious.

Figure 3.2 shows various shear banding landform features. These features include: (1) tectonic depression including fault valley, fault sag, graben, fault trench, fault saddle, and fault angle basin, etc.; (2) tectonic scarp including fault scarp, flexure scarp, fault scarplet, reverse scarplet, and triangular facet, etc.; (3) fault scarp, a part of which has lineament and the other part becomes river erosion scarp due to the erosion by river; (4)

tectonic bulge including horst, fault slice ridge, pressure ridge, mound, and fault-block mountain, etc.; (5) laterally offset including offset stream, offset of river terrace, and shutter ridge, etc.

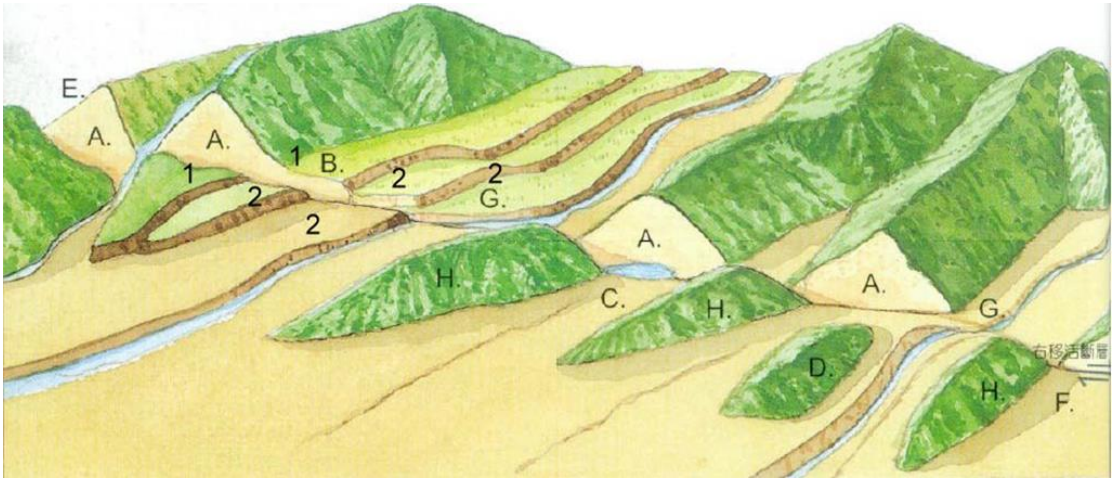

Legend: (A) triangular facet, (B) low fault scarp, (C) fault sag, (D) bulge, (E) fault saddle, (F) horst, (G) beheaded stream, (H) shutterridge, (1-1') offset of piedmont line, (2-2') offset of terrace

Figure 3.2. Features of the displaced landform (Cai and Yang, 2004)

3.2.4 Critical Conditions for Piping Failures

For a concrete gravity dam built on a riverbed, after impoundment a part of the reservoir water will flow down to the downstream of the dam.

By using flow nets, the hydraulic gradient i for a certain critical point at the toe of a dam where seepage water exits can be determined. If the hydraulic gradient i is equal to or greater than the critical one i_c, soil particles will be lost after the float, and then cause piping failure as shown in Figure 3.3.

(a) The undermining phenomenon at the toe of a dam

(b) Pipe-shaped discharge tunnel formed under a dam

Figure 3.3. Piping failure for a concrete gravity dam (McCarthy, 2007)

For granular soils including silt, sand, gravel, cobble and boulder, the critical hydraulic gradient, $i_c = (G_s\text{-}1)/(1+e)$, where G_s is the specific gravity, and e is the void ratio. Therefore, when G_s equals 3.65, for compact soil with e=0.3, it can be calculated that the critical hydraulic gradient i_c is 1.26；while for loose soil with e=1.0, it can be calculated that the critical hydraulic gradient i_c is 0.82.

Generally speaking, when the water level rises after constructing an embankment earth dam on an impermeable layer, Figure 3.4 shows that on the phreatic line, the head loss between every two equipotential lines are equal. Therefore at the outlet of the downstream slope of the dam, due to the sudden drop in the distance between the equipotential lines, local water leakage occurs when $i \geqq i_c$ (Figure 3.5a). When the local water leakage continues to increase, it is likely to cause piping failure (Figure 3.5b).

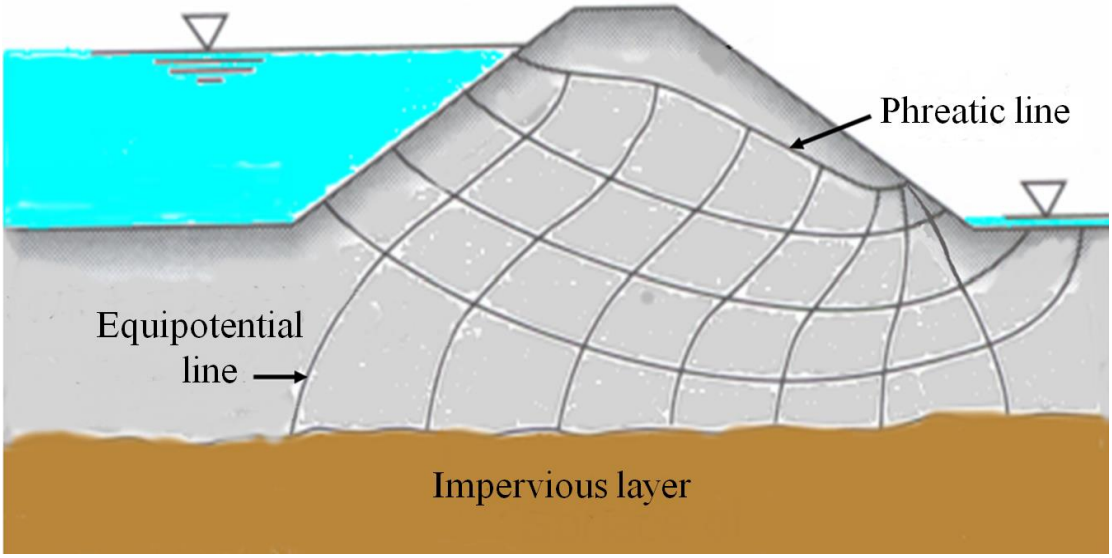

Figure 3.4. Schematic diagram of a flow net for an earth dam

(Reproduced from McCarthy, 2007)

(a) Continuous leaking

(b) Dam body soils were carried away by the torrent

Figure 3.5. Piping failure of Teton Dam (Wikipedia, 2016)

For particles that are in the water, when the "upward buoyancy" acting on the bottom of the particle is greater than the "downward effective stress", the particle will float in the water, and then flow with the water.

When the shear band extends into the dam, it is easy to evolve into a pipe-shaped discharge tunnel due to the high rupture degree in the overlapping area of shear bands in different directions. When the pipe-shaped discharge tunnel becomes the channel of the reservoir water, in the case where the pipe-shaped discharge tunnel slope β, the particle size D, the specific gravity G_s and the pore ratio e are known, the theoretical formula proposed by Hsu et al. (2014) can be used to calculate the bottom critical flow rate v_{bc} required for piping failure:

$$v_{bc}=\sqrt{\frac{2g(G_s-1)}{1+e}}\cdot\sqrt{D}\cdot\cos\beta \tag{3.1}$$

When the pipe-shaped discharge tunnel slope β is 0°, the test curve proposed by Graham et al. (1998) as shown in Figure 3.6 can also be used to calculate the bottom critical flow rate v_{bc} corresponding to the particle size D, where $v_{bc}=0.155D^{1/2}$ applies to boulders with 30.48cm < D, pebbles with 7.62cm < $D \leqq$ 30.48cm, and gravels with 4.76mm < $D \leqq$ 7.62cm; while $v_{bc}=0.197D^{4/9}$ applies to sands with 0.074mm < $D \leqq$ 4.76mm, and silts with 0.005mm < $D \leqq$ 0.074mm.

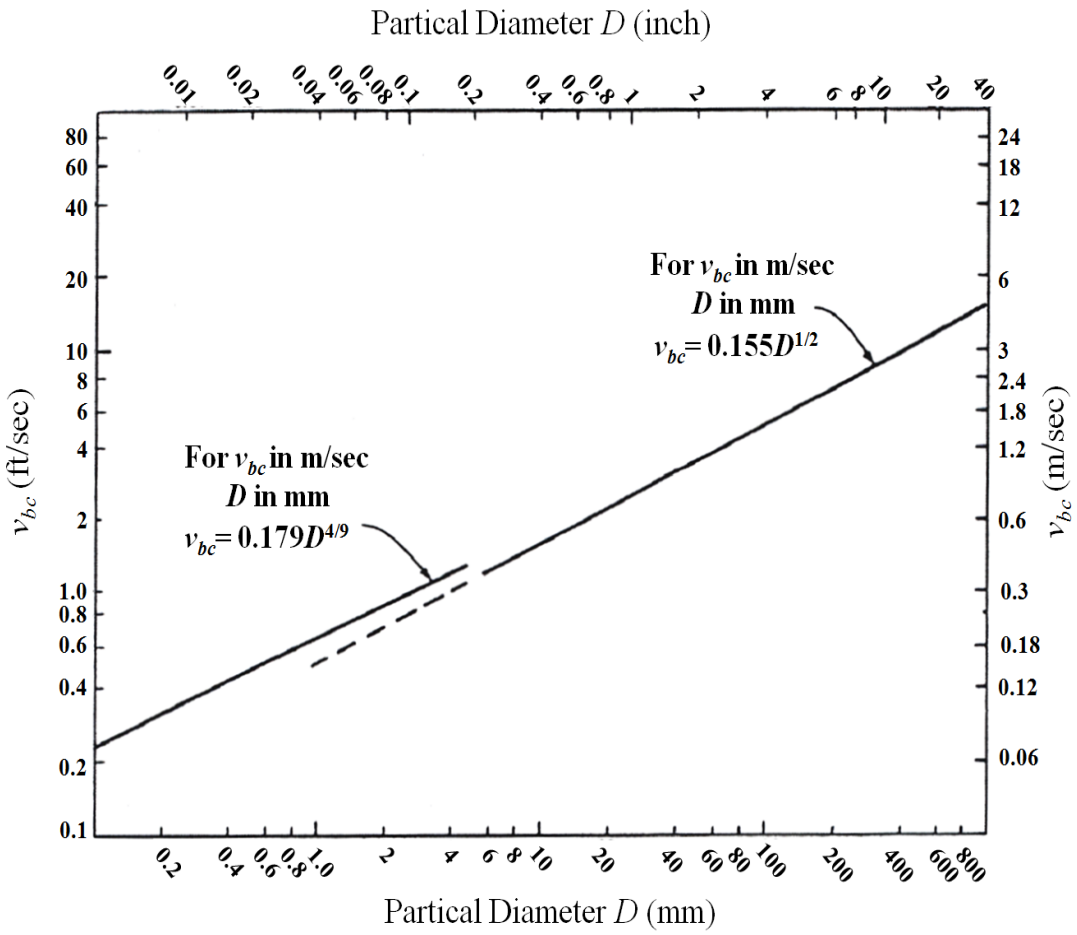

Figure 3.6. The relationship between particle diameter *D and* v_{bc} (Graham, et al., 1998)

When $\beta = 0^\circ$, e = 0.35, G_s=2.65, and *D* =4.76mm, 7.62cm, 30.48cm, or 1.0m, by using Eq. 2.1 proposed by Hsu et al. (2014) the v_{bc} equals 0.338m/sec, 1.352m/sec, 2.704m/sec, or 4.897m/sec, respectively; while by using the test curve proposed by Graham et al. as shown in Figure 3.6, v_{bc} equals 0.338m/sec, 1.353m/sec, 2.706m/sec, or 4.902m/sec, respectively. By comparing the obtained v_{bc} using different methods as mentioned above, it is known that when $\beta = 0^\circ$, the theoretical analysis results of Equation 3.1 are almost identical to the test results by Graham et al.

3.2.5 The Water Leakage and the Leakage Prevention Project of A-kung-tien Reservoir

Basic Information of the Dam Body. Figure 3.7 shows that A-kung-tien Reservoir is located at the junction of Yanchao District, Gangshan District, and Tianliao District of Kaohsiung City. The reservoir water is collected from Wanglai River and Zhuoshui River at the upper stream of A-kung-tien River.

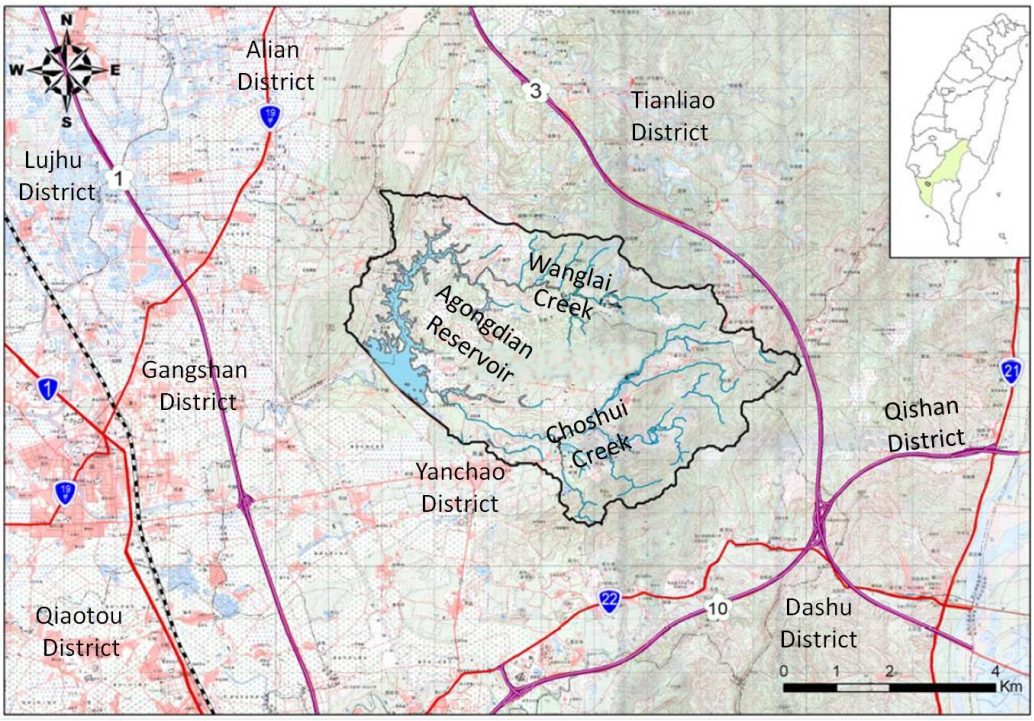

Figure 3.7. Location map of A-kung-tien Reservoir (Southern District Water Resources Bureau, 2016)

The construction of the dam body of A-kung-tien Reservoir was completed in August 1953. Figure 3.8 shows that the crest elevation is 42 meters, the maximum dam height is 31 meters, the crest length is 2380 meters, the crest width is 8 meters, the catchment area is 31.87 square kilometers, the maximum water level is 37 meters, the maximum possible water level is 40 meters, the full water level area is 410 hectares, the total storage capacity is 45 million cubic meters, the planned effective water storage capacity is 20.45 million cubic meters, and the designed flooding capacity of the spillway is 81 cubic meters/second (Southern District Water Resources Bureau, 2016).

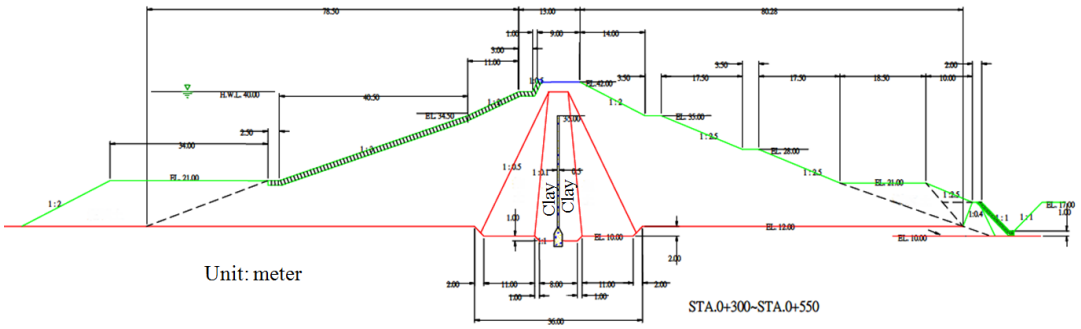

(a) Main dam

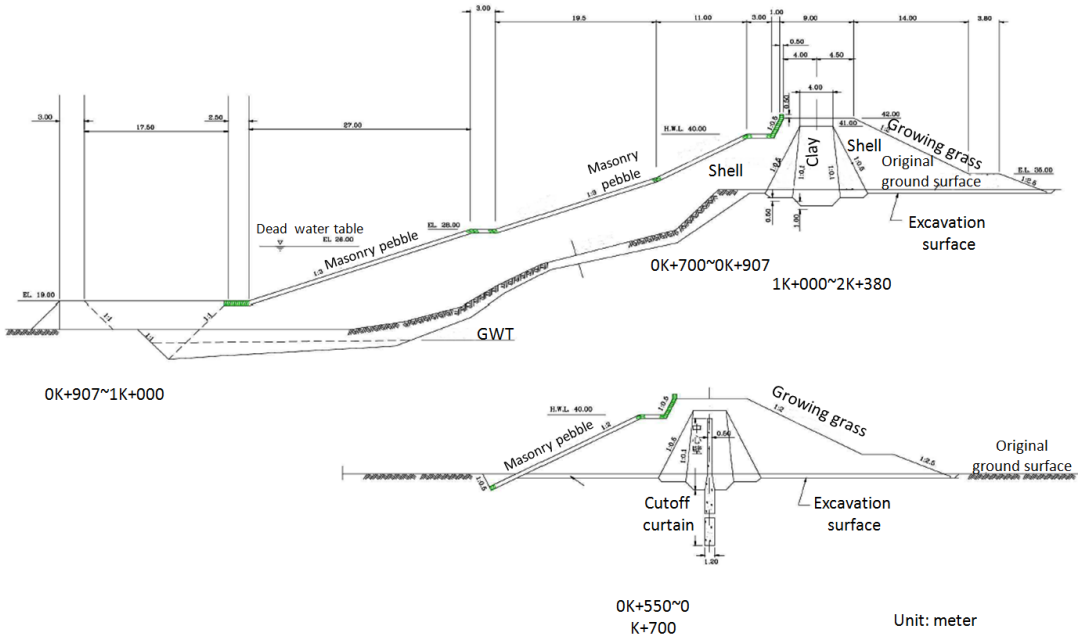

(b) Left auxiliary dam

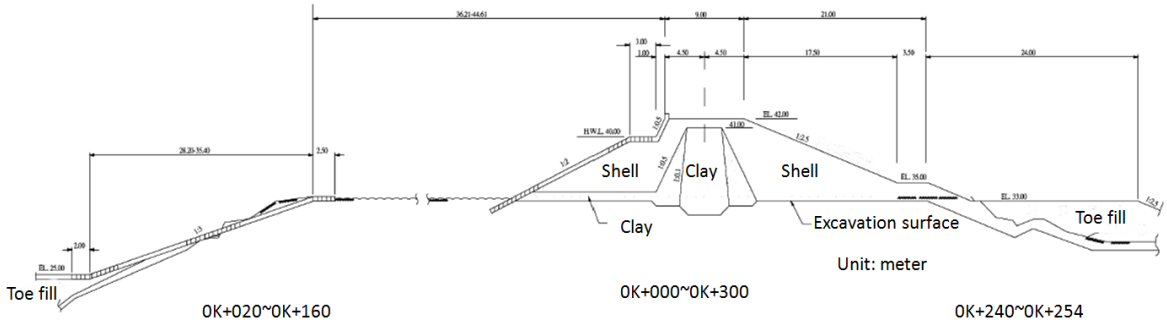

(c) Right auxiliary dam

Figure 3.8. Sectional view of the dam body of A-kung-tien Reservoir (Southern District Water Resources Bureau, 2016)

The water storage area of A-kung-tien Reservoir is rich in gray mudstone, and easy to flow into the reservoir area with the flood after water softening. The current effective reservoir capacity is 16.47 million cubic meters (Southern District Water Resources Bureau, 2016).

Dam Body Leakage History. There has been water leakage continuously occurring in A-kung-tien Reservoir since 1989. Most of the exits of leakage paths are located downstream between 0k+450m to 0k+900m, with a distance from the dam axis of between 160m to 250m (Figure 3.9).

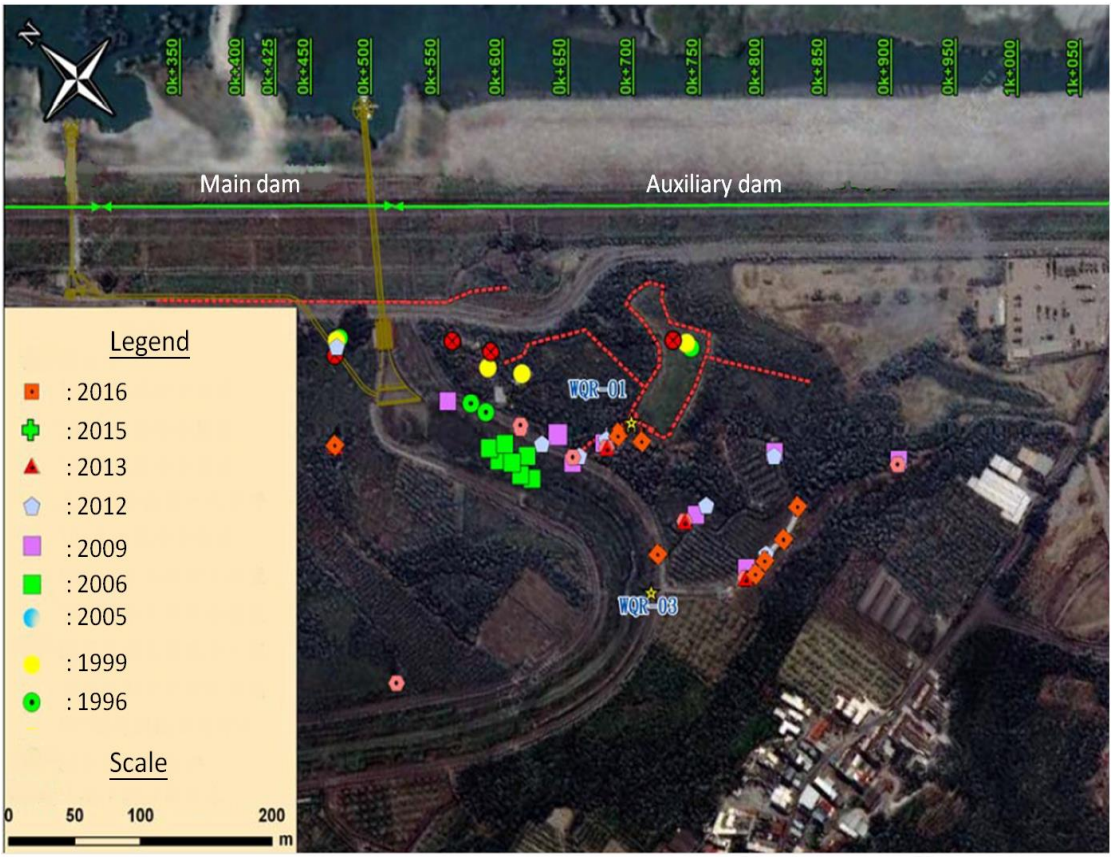

Figure 3.9. Distribution map of the exits of leakage path of A-kung-tien Reservoir over the years (Southern District Water Resources Bureau, 2016)

Leakage Path Investigation.

1. Monitoring well

Figure 3.10 shows the layout of the five monitoring wells. Taking the 0k + 280 section as an example, Figure 3.11 shows that by monitoring the total water head distribution map, it can be estimated that the flow path of the leakage is the reservoir water flowing along the bottom of the silt layer and the sand layer to the leakage exit.

Figure 3.10 Sectional view of the five monitoring wells of A-kung-tien Reservoir (Southern District Water Resources Bureau, 2016)

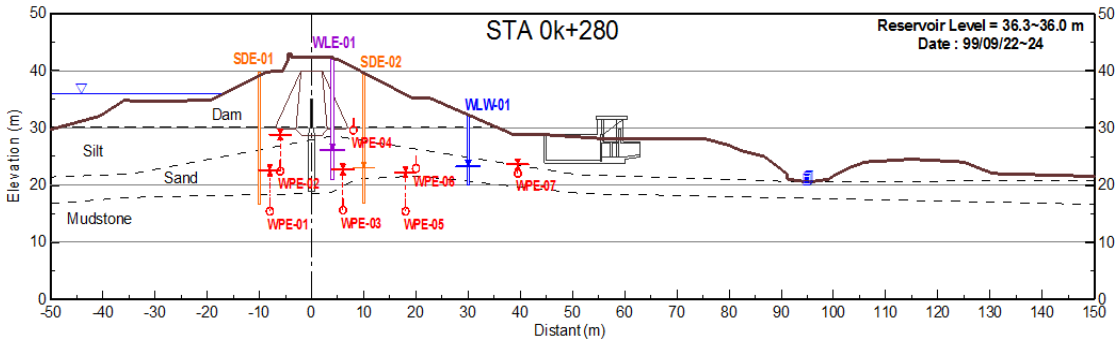

Figure 3.11. Total water head distribution map of A-kung-tien Reservoir estimated by the 0k+280 cross-section monitoring well (Southern District Water Resources Bureau, 2016)

2. Water pressure gauge

By using a water pressure gauge to monitor the pore water pressure of the 0k+280 section, then converting the pore water pressure to the total water head, the relationship between total water head distribution of the 0k+280 section and the rainfall is shown in Figure 3.12 (Southern District Water Resources Bureau, 2016).

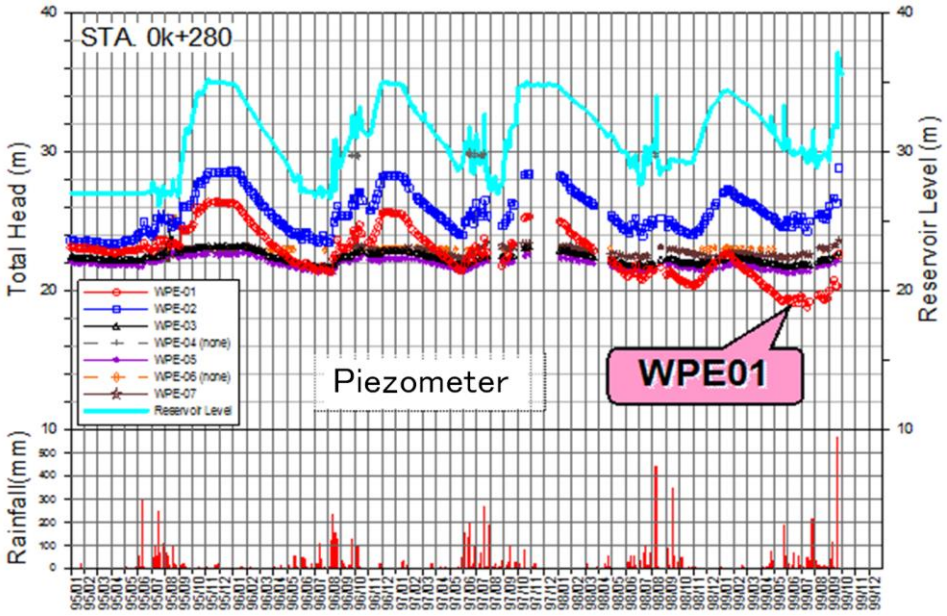

Figure 3.12. Relationship between the total water head distribution of A-kung-tien Reservoir and the rainfall (Southern District Water Resources Bureau, 2016)

It is shown in Figure 3.12 that there is no significant time difference between the total head and the change of the water level upstream of the curtain wall; therefore, it is assumed that the upstream area between the reservoir water and the impervious curtain wall may be in a connected state. However, there is a time difference between the total head and the change of the water level downstream of the curtain wall, therefore it is assumed that the permeable sand layer between the upstream and downstream curtain walls is in a non-connected state (Southern District Water Resources Bureau, 2016).

3. Ground resistance

The results of the ground resistance test show that the downstream leakage path of the dam covers a sand layer with a thickness of about 5 to 10 meters and a height of between EL.10 and 20m. Since the exits of every leakage path are all distributed within the old river course of A-kung-tien River, where the loose sand is exposed, this sand layer is considered to be the main path of water leakage (Southern District Water Resources Bureau, 2016).

4. Seepage analysis

Figure 3.13 shows the distribution of the total head contours based on various seepage analyzes. From Figure 3.13, it is known that the change of the water level in the sand below the bottom of the dam is small both at the highest water level and at the lowest water level (Southern District Water Resources Bureau, 2016).

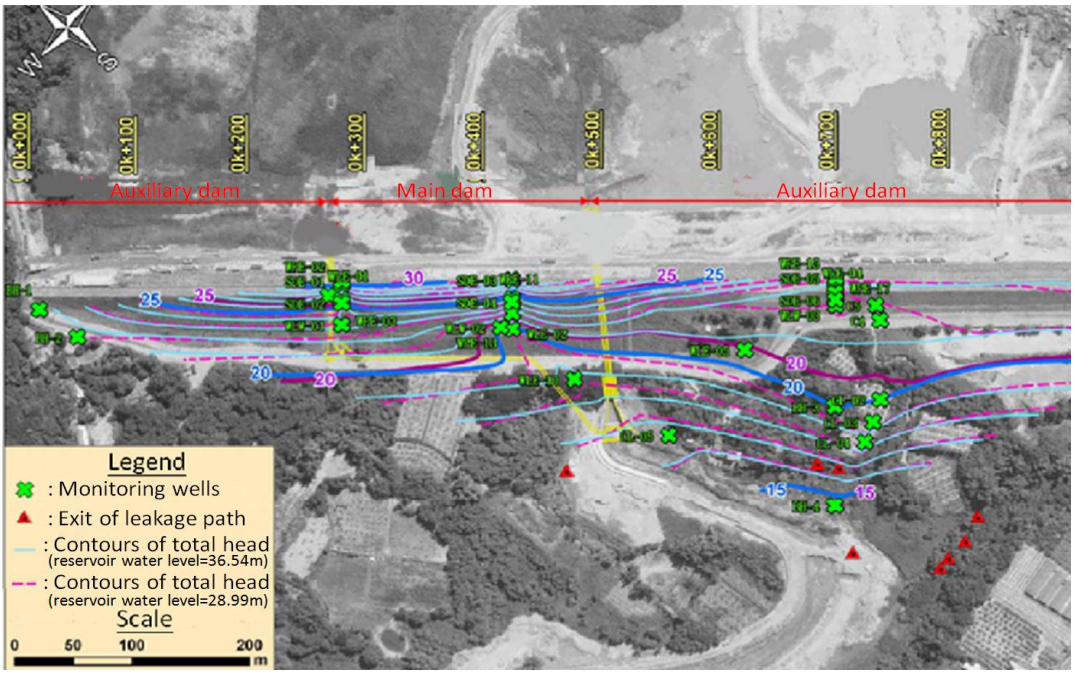

Figure 3.13 Comparison of the total head contours at the highest and the lowest water level in 2016 (Southern District Water Resources Bureau, 2016)

Since the groundwater level of the location of each leakage path is between EL.14.15m and EL.20.08m, it is deduced that the sand layer below the dam is the main path of water leakage (Southern District Water Resources Bureau, 2016).

Secondly, the hydraulic gradient is also calculated by using the water pressure and water level surface of the area covered by the leakage path. The results show that the maximum hydraulic gradient is 0.07. Since the maximum hydraulic gradient is much smaller than the critical hydraulic gradient, it can be deduced that: (1) The piping failure potential is very low; (2) Water leakage does not pose a threat to dam safety (Southern District Water Resources Bureau, 2016).

5. Isotope timing analysis

The isotopic timing analysis contains a delay analysis of the timing information of leakage path #1 and leakage path #2 compared to the sampling point. The analysis results (Southern District Water Resources Bureau, 2016) show: (1) Leakage path exit #1 has 2-3 months delay compared to the reservoir water; (2) Leakage path exit #2 has 2-4 months delay compared to sample points WLW03 and WLW04; (3) Leakage path exit #1 has a more immediate response compared to groundwater; (4) Leakage path exit #2 almost has no time delay compared to the reservoir water, stream water, and groundwater.

The Leakage Prevention Project of A-kung-tien Reservoir. Since 1989, there have been several leakage paths in the downstream slope of A-kung-tien Reservoir. In order to improve the leakage issue of the dam, toe drainage catchment systems have been set up at the outlet of each leakage path since 2005. However, this measure did not substantially improve the dam leakage.

Comprehensive Discussion.

1. The total head distribution obtained from the monitoring wells can be used to estimate the leakage path, but the reliability of the results is low. The main reason is that once the reservoir water flows along the estimated silt layer and sand layer in the bottom of the dam, the leakage path exit will be linear, rather than point-like.

2. Although the monitoring results of the water pressure gauge can be used to infer whether the upper stream and the downstream of the dam are connected, they cannot be used to deduce the leakage paths.

3. For the water leakage phenomenon shown in Figure 3.16, it is estimated that the diameter of the pipe-shaped discharge tunnel corresponding to the leakage path exit is 1 cm, the water output per second is 1 cm^3, and the average flow rate in the pipe-shaped discharge tunnel is 1.273 cm/sec. In general, the permeability coefficient of sandy soils is from $1.0x10^{-1}$ to $1.0x10^{-4}$cm/sec. If the maximum hydraulic gradient obtained in the early safety assessment of A-kung-tien Reservoir – 0.07 is true, then the average velocity of the flowing water in the pipe-shaped discharge tunnel is only $7x10^{-3}$ - $7x10^{-6}$cm/sec in this case. At such a low speed, the silt or sand will not be brought out of the water, however Figure 3.14 clearly shows that the gray-black silt and sand continue to be brought out of the water. Therefore, the assessment results based on the seepage theory do not match the real situation; therefore it is necessary to further evaluate the local leakage of the downstream slope of the dam by adopting a method in line with the actual situation.

Figure 3.14 Water leakage in the downstream slope of A-kung-tien Reservoir

4. The isotope timing analysis results can identify the connection between the leakage and the reservoir water, stream water, or groundwater, but cannot identify the actual existing leakage paths.

5. The mechanism of water leakage and seepage is completely different. Leakage will cause the loss of soil particles, and thus endanger the dam safety; seepage is the steady flow in the soil pore space, which will not harm the dam safety.

For the dam, when the reservoir water flows in the pipe-shaped discharge tunnel, the particles with small to large sizes will be brought out by the water, thus the width and height of the pipe-shaped discharge tunnel continue to increase until it causes piping failure. In fact, the pipe-shaped discharge tunnel is the overlapping zone of shear bands with different strikes, where the degree of soil rupture increases with the shear banding and the flow velocity of the water in the pipe-shaped discharge tunnel also increases with the continuous loss of the soil particles. Therefore, in the process of water leakage, once the silt and sand continue to be brought out by the water, the piping failure may occur more quickly.

It can be seen that looking for the dam leakage path, in fact is equivalent to looking for the pipe-shaped discharge tunnel. Based on the fact that the area covered by the leakage paths of A-kung-tien Reservoir was originally the old A-kung-tien River, although the height of the dam crest is the same, the height of the main dam varies with the changes in the height of the old A-kung-tien River (Figure 3.15). Also because the soil strength of the main dam is neither uniform nor even, especially in the deep groove area and at the ups and downs and turning points on both sides of the river, the shear bands extend towards the dam body, thus appears the pipe-shaped discharge tunnel.

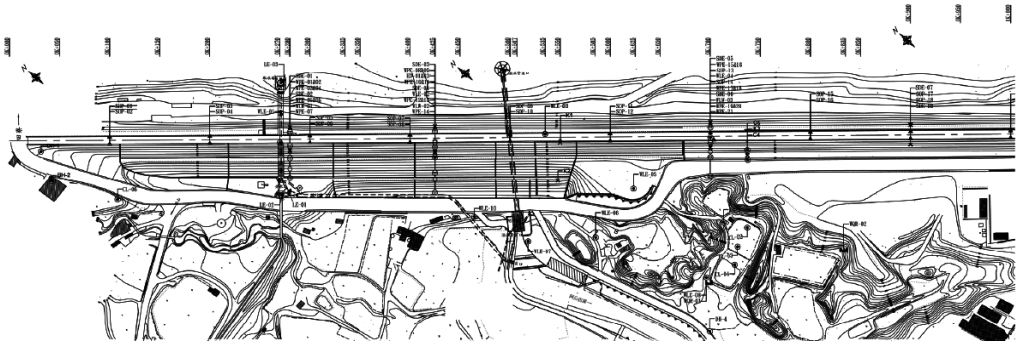

Figure 3.15 The contours of the dam of A-kung-tien Reservoir (Southern District Water Resources Bureau, 2016)

In order to assist in the search for the pipe-shaped discharge tunnels related to local water leakage, Professor Tse-Shan Hsu once provided the shear bands existing in the area covered by the leakage path exits of A-kung-tien Reservoir (Southern District Water Resources Bureau, 2016). When the shear bands are induced from the active faults on the west side of A-kung-tien Reservoir (toward N12^{o}E), Figure 3.18a shows four groups of shear bands identified by the distribution map of displacement velocity vectors, which are respectively N12^{o}E, N62^{o}E, N45^{o}W, and N87^{o}W. When the shear bands are induced from the active faults on the east side of A-kung-tien Reservoir (toward N30^{o}E), Figure 3.16b shows four groups of shear bands identified by the distribution map of displacement velocity vectors, which are respectively N30^{o}E, N70^{o}E, N22^{o}W, and N55^{o}W.

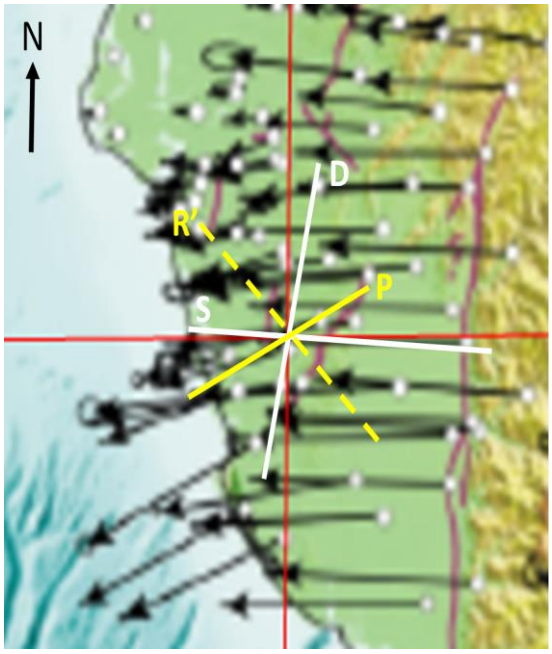

Note: The intersection of the vertical and horizontal red lines is the location of A-kung-tien Reservoir

(a) Active faults on the west side of A-kung-tien Reservoir

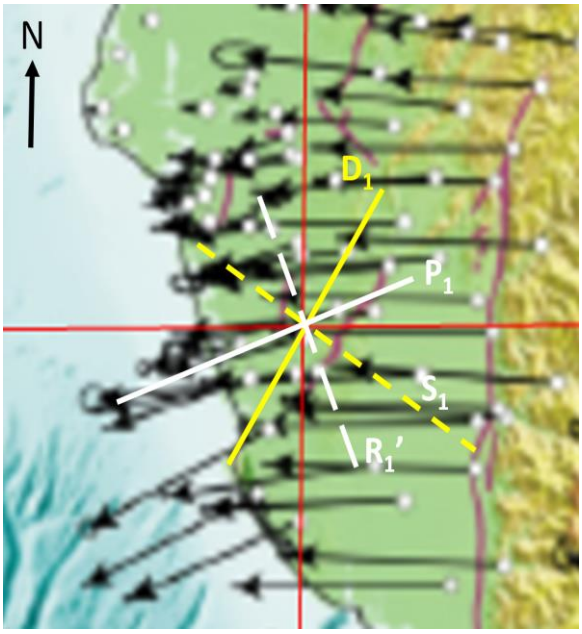

Note: The intersection of the vertical and horizontal red lines is the location of A-kung-tien Reservoir

(b) Active faults on the east side of A-kung-tien Reservoir

Figure 3.16. The shear bands identified by the distribution map of displacement velocity vectors (basemap from Google Earth, 2017, data from GPS LAB, 2007)

When the shear bands are induced from the active faults on the west side of A-kung-tien Reservoir (toward N12^{o}E), Figure 3.17a shows four groups of shear bands identified by the distribution map of displacement velocity vectors, which are respectively N12^{o}E, N62^{o}E, N10^{o}W, and N87^{o}W. When the shear bands are induced from the active faults on the east side of A-kung-tien Reservoir (toward N30^{o}E), Figure 3.17b shows four groups of shear bands identified by the distribution map of displacement velocity vectors, which are respectively N30^{o}E, N70^{o}E, N1^{o}W, and N55^{o}W.

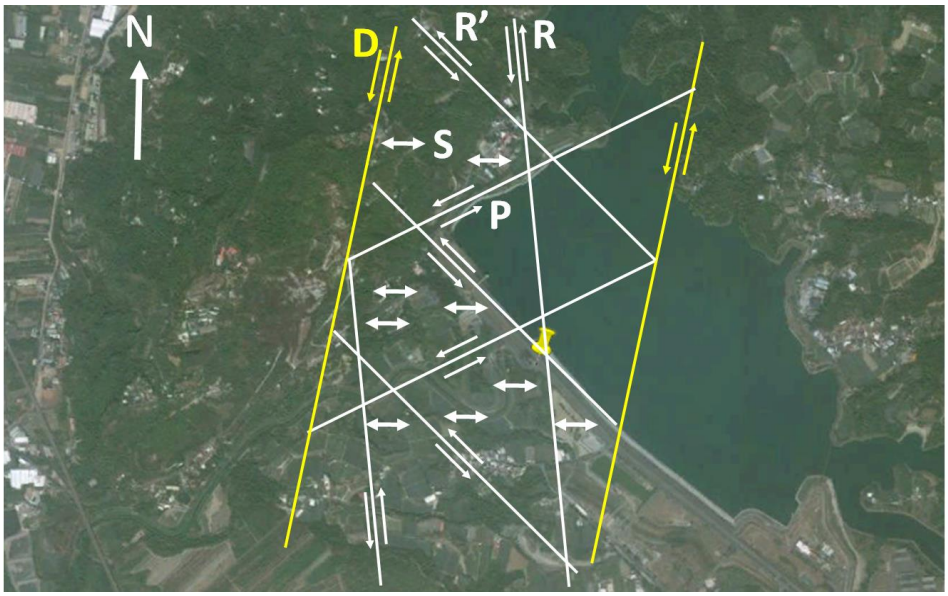

(a) Active faults on the west side of A-kung-tien Reservoir

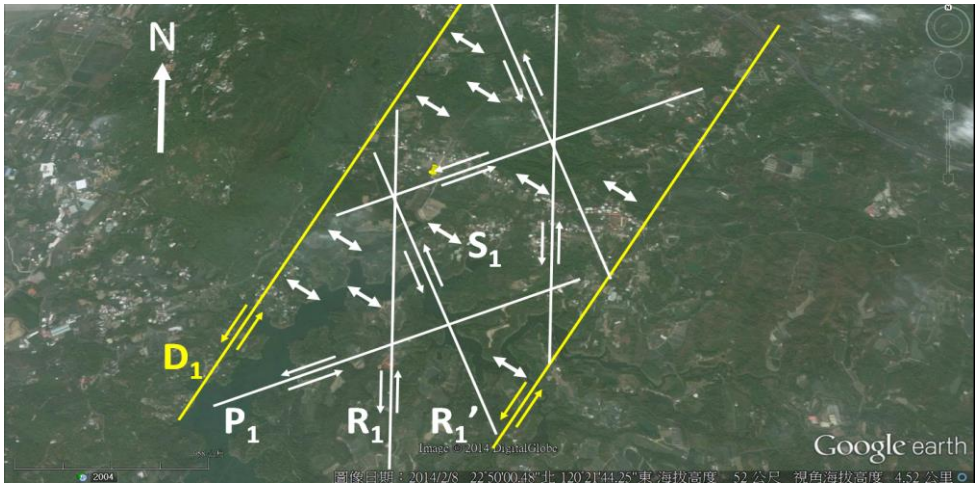

(b) Active faults on the east side of A-kung-tien Reservoir

Figure 3.17 The shear bands identified by the distribution map of displacement velocity vectors (basemap from Google Earth, 2017)

6. Figure 3.18 shows the spillway pipe of A-kung-tien, and Figure 3.19 shows the water intake pipe of A-kung-tien Reservoir.

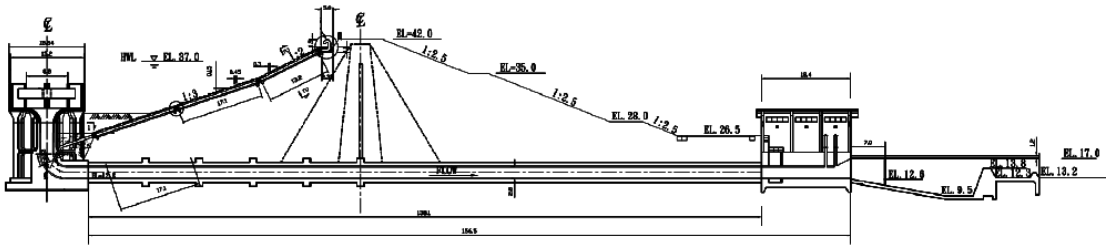

(a) Sectional view

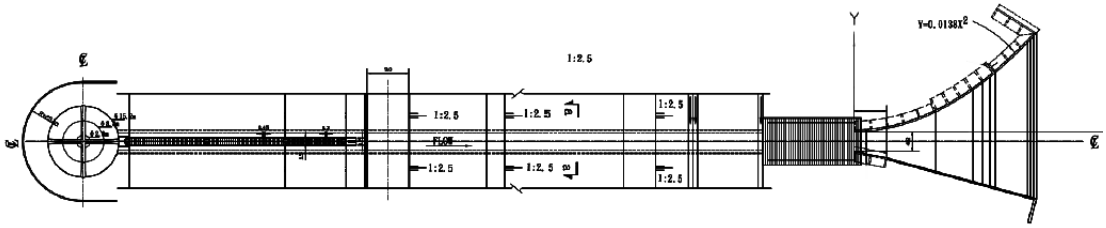

(b) Plan view

Figure 3.18 Spillway pipe of A-kung-tien Reservoir (Southern District Water Resources Bureau, 2016)

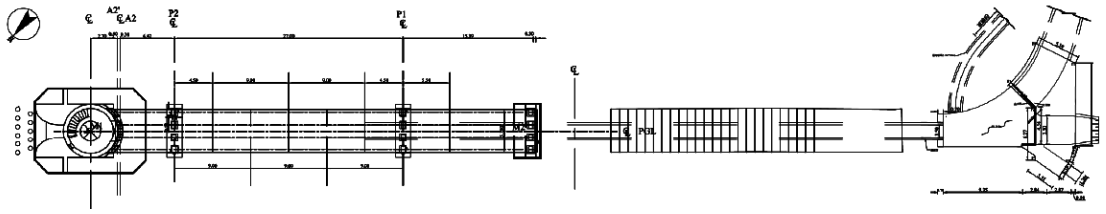

(a) Sectional view

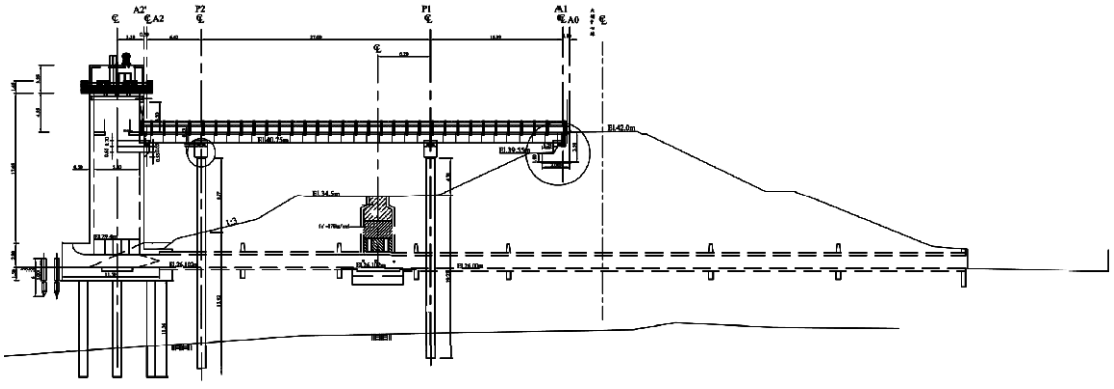

(b) Plan view

Figure 3.19 The water intake pipe, water tower, and contact bridge of A-kung-tien Reservoir (Southern District Water Resources Bureau, 2016)

For the spillway pipe or water intake pipe, when the backfill is poor, the construction quality is bad, the soil around the pipe is not compacted, the dam differences are settled, the pipe is winding and deformed, or the water level is excessive, once there is stress concentration in the soil around the pipe, hydraulic fracturing may occur around the stress concentration (Figure 3.20 and Figure 3.21).

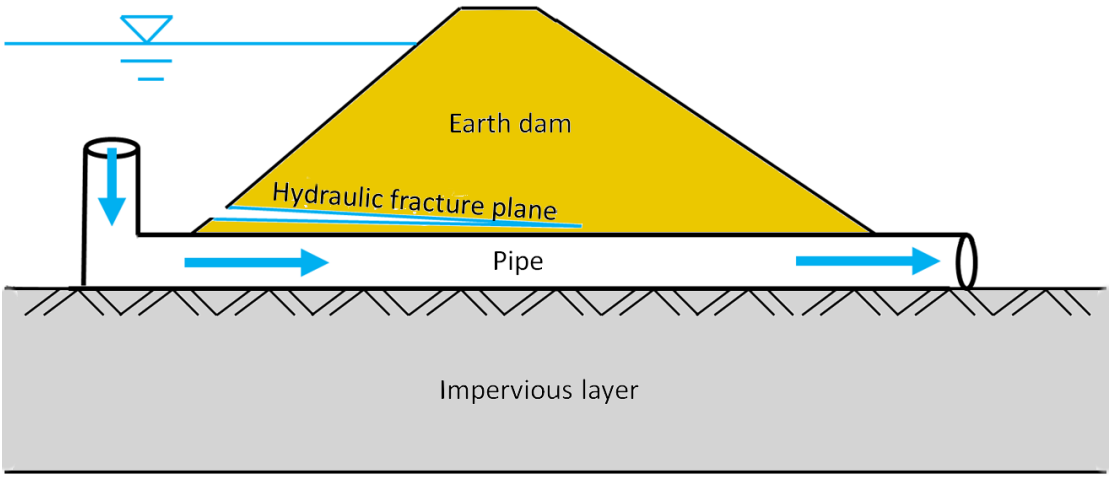

Figure 3.20 Hydraulic fracture surface above the water pipe in the dam

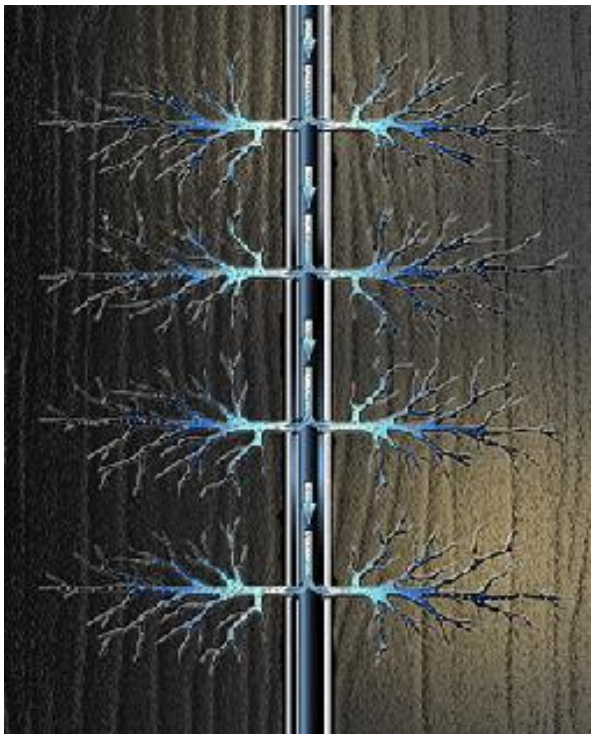

Figure 3.21 Hydraulic fracture surface induced by the notch on pressure tube side wall (Frac Focus, Chemical Disclosure Registry, 2017)

3.2.6 The Water Leakage and Leakage Prevention Project of Hsin-shan Reservoir

Basic Information of the Dam Body. Hsin-shan Reservoir is located in Keelung city. The first phase of the dam project was completed in 1980; the crest elevation was EL.75m; the water storage capacity was 4 million tons. The second phase of the dam heightening project was completed in 1998; following the second phase the crest elevation is EL.90m; the designed water storage surface elevation is EL.86m; the designed water storage capacity is 10 million tons; the main section of the dam is shown in Figure 3.22.

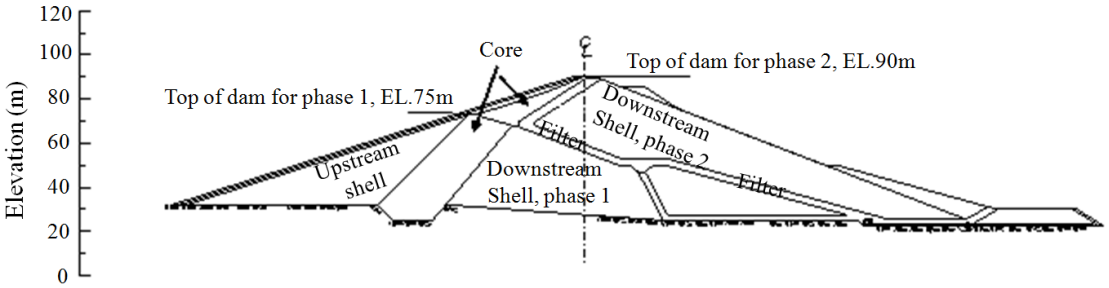

Figure 3.22. Main section of Hsin-shan Reservoir (Lin, et al., 2010)

Dam Body Leakage History. Before Hsin-shan Reservoir was heightened, water leakage had already been found in the downstream slope of the dam at an elevation of about EL.50m. At that time the scholars and experts believed that as long as the alluvium in the dam body was removed in the future reservoir heightening project, the water leakage issue could be solved.

However, after the completion of the reservoir heightening project, seven leakage paths appeared in the downstream slope of the dam (Figure 3.23).

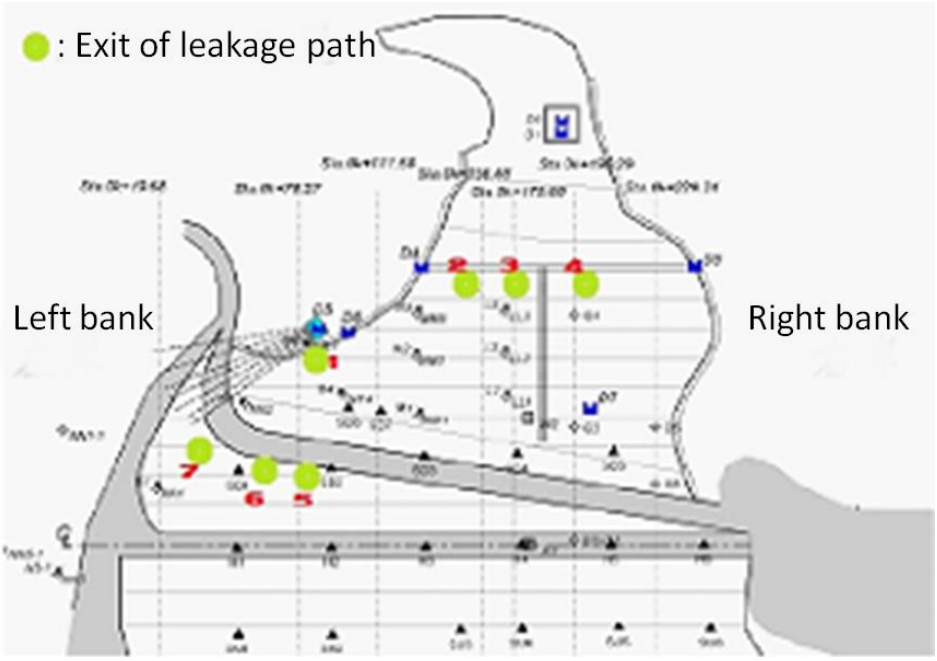

(a) Location of local leakage path exits

(b) Local leakage conditions I

(c) Local leakage conditions II

Figure 3.23 Leakage path exits of downstream slope of Hsin-shan Reservoir (Lin, et al., 2010)

Leakage Path Investigation.

1. Water quality inspection

In water quality inspection the Stiff water quality shape map method is used to analyze the water quality and difference in groundwater, in order to assess the water quality characteristics and water quality attributes (Lin, et al., 2010). The samples include the reservoir water, water leakage, and water in the water level observation well. The Stiff water quality distribution map at each sampling point is shown in Figure 3.24.

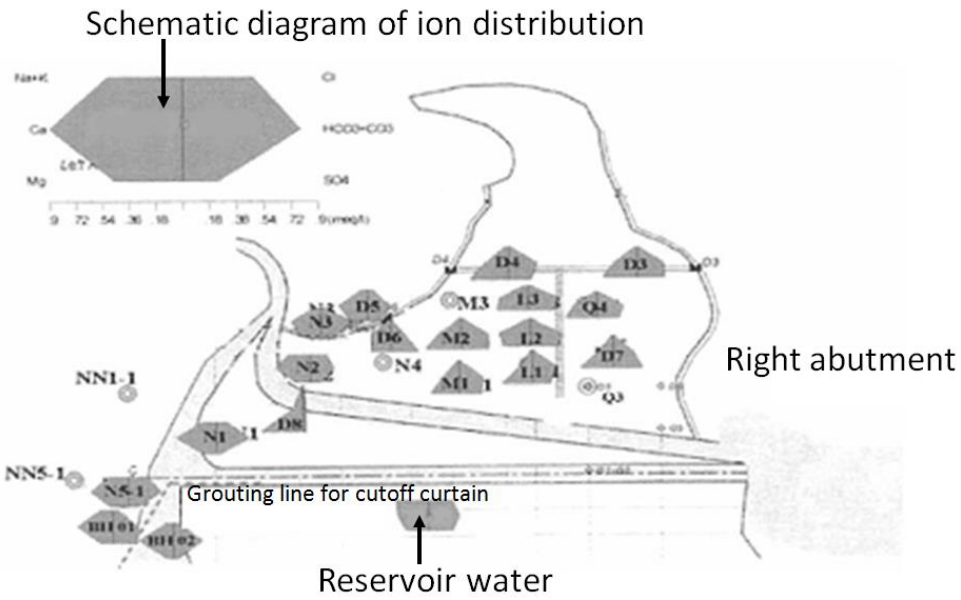

Figure 3.24. The Stiff water quality distribution map at each sampling point (Lin, et al., 2010)

For the water leaked from the shell downstream of the dam, the water quality inspection results show that: (1) the seepage path can not be determined; (2) the main leakage point D6 is not directly connected with the groundwater of the left dam.

2. Tracer test and earth resistance test

In the tracer test, non-radioactive high concentration brine was applied to two local holes, and the resistance test is carried out at the seepage location of the downstream observation well (Lin, et al., 2010).

Figure 3.25 shows the tracer test results. Due to the impact of ground rainfall, the tracer test results did not show obvious reactions. Figure 3.26 shows the results of the resistance test during the application of the tracer. It is known from Figure 3.26: (1) the testing results of the riprap layer in the downstream slope of the dam is of low resistance between 30 to 50 ohm; (2) due to the effect of the asphalt road surface, the testing results of the surface of the dam contact paths are all of high resistance between 100 to 150 ohm; (3) In the EL.80m ~ 85m range there is a region where the test results show low resistance of 20 ~ 40 ohm, suggesting that this region may be the water leakage path.

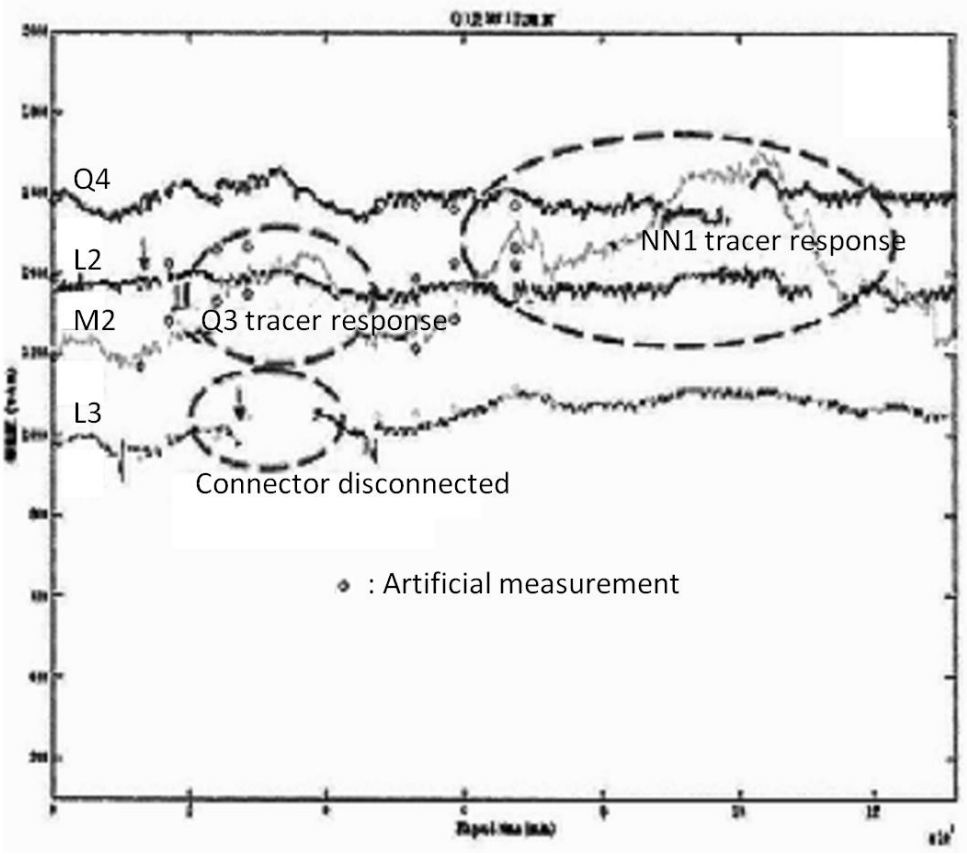

Figure 3.25. Measurement results of the tracer (Lin, et al., 2010)

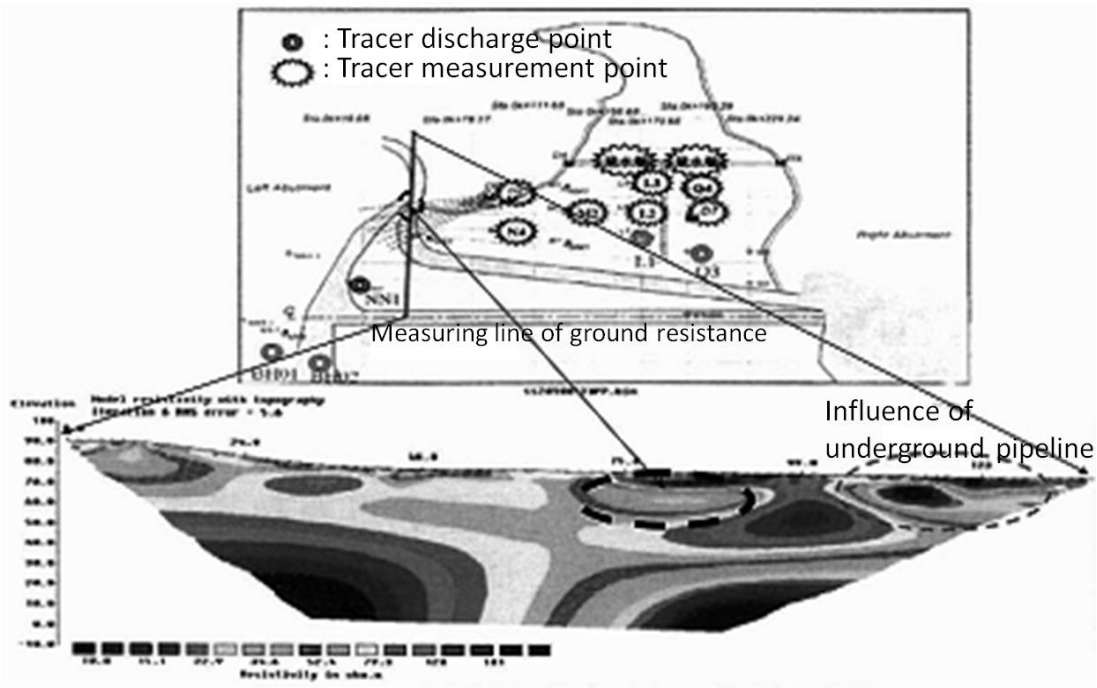

Figure 3.26. Sectional view of ground resistance before the application of tracer (Lin, et al., 2010)

Figure 3.27 shows the percentage difference in resistivity at different times (Lin, et al., 2010). It is known from Figure 3.27 that (1) the area where the resistivity has negative growth may be the seepage path of the tracer; (2) After the application of tracer, due to heavy rain, the negative growth of ground resistance may also be caused by the increase in the moisture content of the formation after rainfall; (3) In the left half of the figure, the negative growth area shows that the bottom of the shell may be the main seepage path of the tracer.

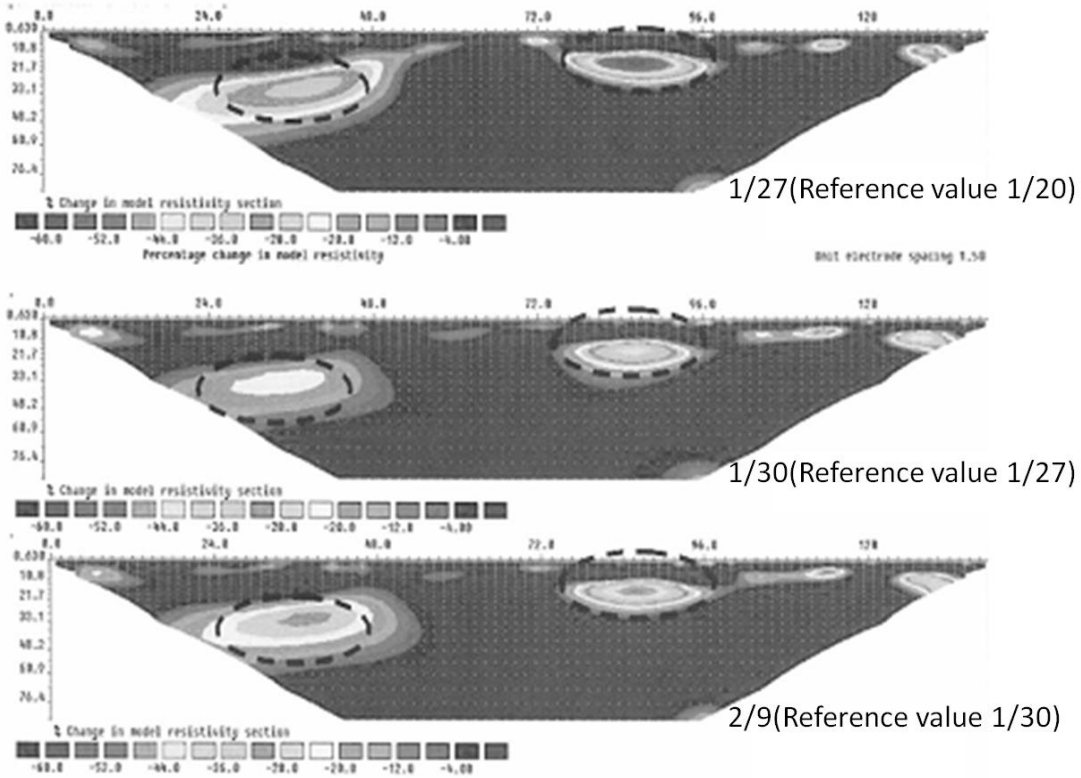

Figure 3.27. Sectional view of ground resistivity variation (Lin, et al., 2010)

3. Temperature section measurement

Temperature section measurement analyzes the possible leakage paths based on the dependence of temperature sections. The locations of temperature section measurement include the reservoir area near the dam body, BH0l drilling on the downstream side of the left ridge grouting curtain wall, and BH02 drilling on the upper stream side of the grouting curtain wall (Lin, et al., 2010).

The results show that: (1) on the temperature section of 25 ℃, the temperature and changing tendency of BH0l and BH02 drillings are similar, but with low correlation with the reservoir water; (2) on the temperature section of 28℃, although the temperatures of BH0l and BH02 drillings become similar with the change of depth, the temperature difference between the two drillings is about 0.6℃, and there is no significant correlation with the reservoir water. (3) By comparing the measurement results three days apart, it is found that the change of temperature sections of the reservoir water and BH02 drilling is not significant, while BH01 drilling changes significantly with the temperature change; (4) Because the water level of BH01 drilling in the downstream of the grouting curtain wall is higher than the water levels of the BH02 drilling in the upper stream and the reservoir water, it is presumed that BH0l drilling is affected by the upper catchment area and climate of the left ridge; however, BH02 drilling is less affected by temperature due to the barrier of the grouting curtain wall.

In order to verify the temperature section measurement results, another two temperature measurements were carried out in different seasons; the measurement periods were affected by the cold current. The results show that: (1) in terms of measurement results on different dates, the temperature of the downstream of the grouting curtain wall is obviously changed, while the temperature of the BH02 drilling in the upper stream is still relatively stable; (2) Although the temperature of the reservoir water is reduced by 5-7 ℃ in winter, the temperature of the water level observation wells do not decrease (Lin, et al., 2010).

4. Shear banding analysis

Hsu et al. (2011) , by using the distribution map of displacement velocity vectors as shown in Figure 3.28, identified that there are three shear bands in the area covered by the leakage paths of Hsin-shan Reservoir, the strikes of which are respectively N1°W (green line), N57°W (red line), N71°E (yellow line).

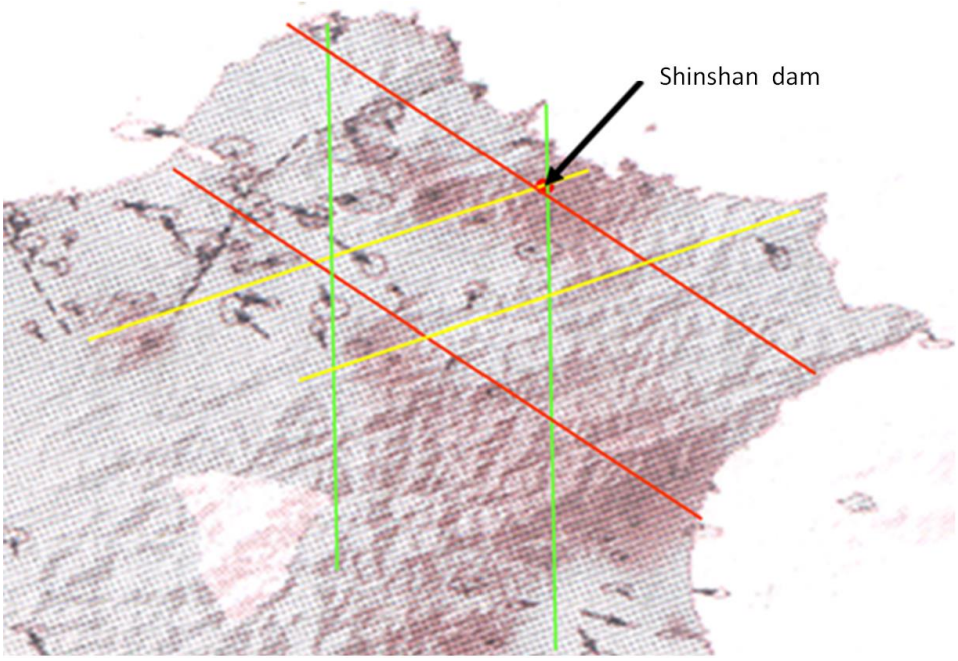

Figure 3.28. Shear bands in the area covered by the leakage points of Hsin-shan Reservoir (GPS LAB, 2007; Hsu, et al., 2011)

Hsu et al. (2011) also identified the shear bands existing in the area covered by the leakage path exits of Hsin-shan Reservoir, by using the satellite image shown in Figure 3.29. The strikes of these shear bands are the same as those shown in Figure 3.28.

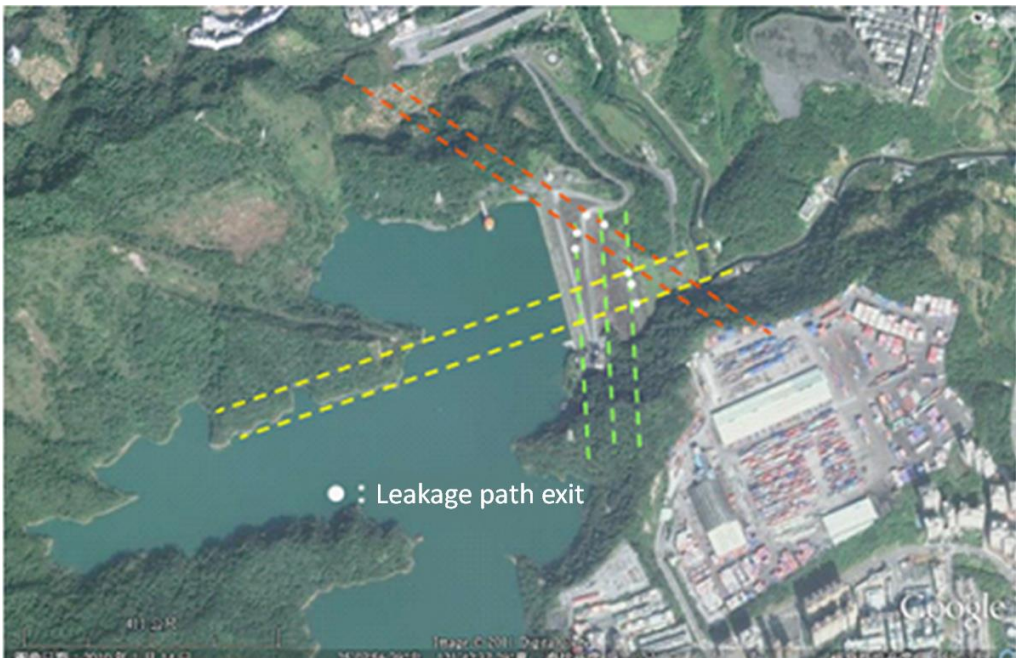

Figure 3.29 Shear bands in the area covered by the leakage path exits of Hsin-shan Reservoir (Google Earth, 2017; Hsu, et al., 2011)

Figure 3.29 shows that these local leakage pathways are highly correlated with the shear bands. In other words, the leaking water is from the pipe-shaped discharge tunnel where the reservoir water flows through the shear band.

Figure 3.29 also shows that the dam body of Hsin-shan Reservoir is located in the intersection of three deep river troughs. The formation of this special geographical environment is related to orogeny. It is known from fractography (Hull, 1999) that orogeny is derived from shear banding, and in the process of the shear banding, the river patterns shown in Figure 1.4 and the curved surfaces shown in Figure 1.5 are derived.

For Hsin-shan Reservoir, the above river patterns and curved surfaces exist on the left and right sides of the dam (see Figure 3.30). These river patterns and curved surfaces will continue to develop in the tectonic plate dislocation, and further extend into the dam body, therefore potential piping failure of the dam continues to increase.

(a) View number 1

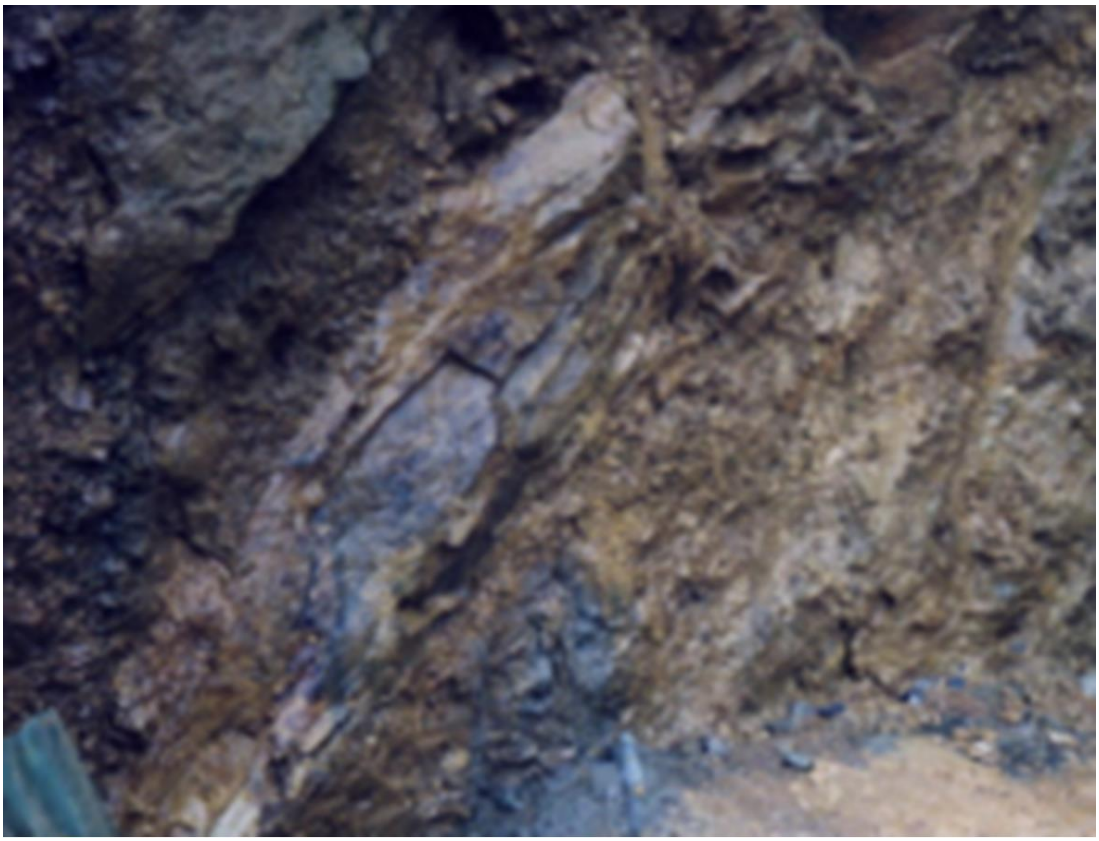

(b) View number 2

(c) View number 3

(d) View number 4

Figure 3.30. River patterns and curved surfaces on the old riverbank of Hsin-shan Reservoir

Take Gouhou Dam in Qinghai Province of China as an example, Figure 3.7 shows that the shear bands on the riverbank and in the valleys have obviously extended into the dam, thus leaving the remaining dam after piping failure with almost the same types of river patterns and curved surfaces as the old riverbank.

The Leakage Prevention Project of Hsin-shan Reservoir. For the leakage phenomenon in the downstream slope of Hsin-shan Reservoir, after the completion of the second phase of the heightening project, the curtain wall was extended up to the crest by a grouting operation, as well as extended into the left riverbank by 38m and into the right riverbank by 98m. However, in the water storage process after completion of the curtain wall project, water leakage continued to occur (Lin, et al., 2010).

In order to improve the situation, in 2002 a second grouting operation was performed on the ridge of the left dam, but after the completion of the project water leakage occurred again.

3.2.7 The Piping Failure of Teton Dam

Basic Information of Teton Dam. Teton Dam is located in Idaho, United States. Figure 3.31 shows that the bottom width of the dam is 149.35m, the top width is 701.04m, the maximum dam height is 125.6m, and the storage capacity is 355412250m^3 (Sinotech Foundation for Research and Development of Engineering Sciences and Technologies, 2008). The cross section of Teton Dam shown in Figure 3.31 contains: ① anti-seepage core, ② drainage zone, ③ miscellaneous fill zone (located at downstream of zone ②), ④ water retaining dam in the upstream during construction, ⑤ protective layer made of boulder.

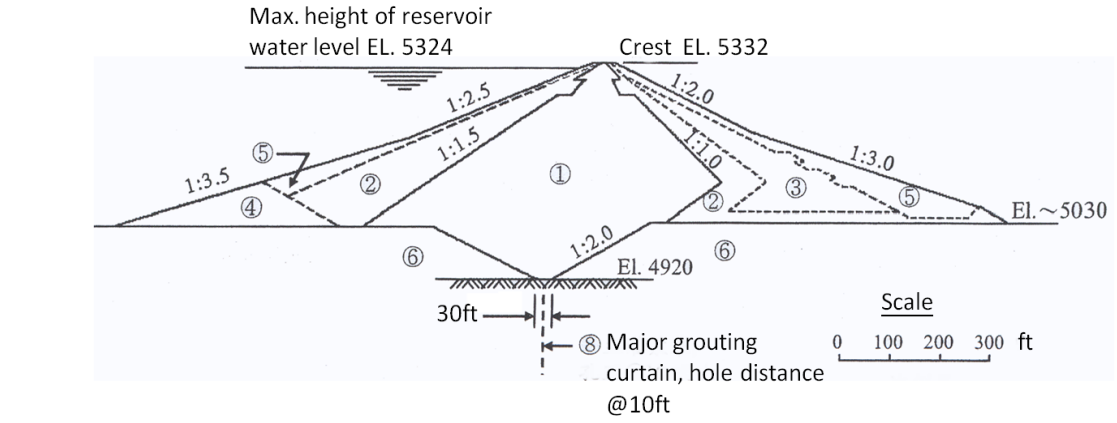

(a) On riverbed

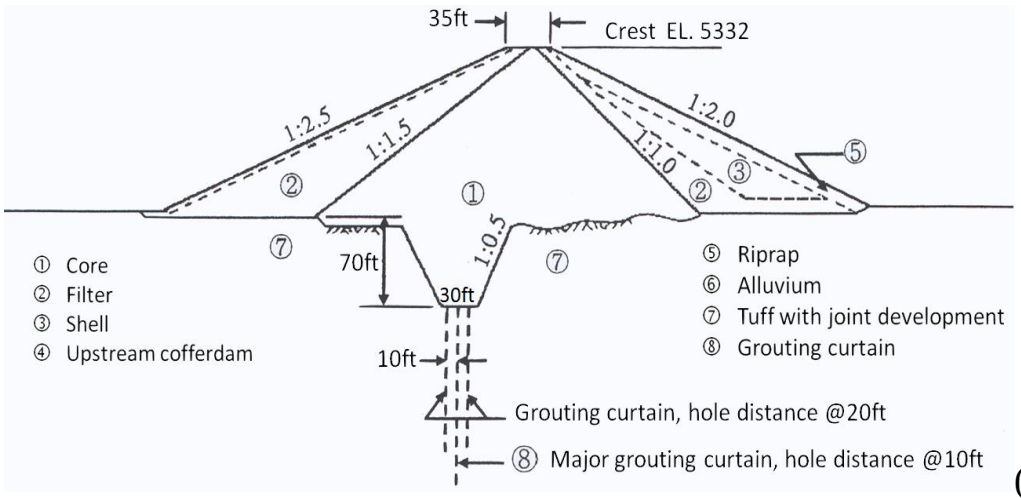

(b) (b) On both abutments

Figure 3.31. Cross section of Teton Dam (Sinotech Foundation for Research and Development of Engineering Sciences and Technologies, 2008)

Figure 3.32 shows that the geology along the dam axis can be divided into dam bedrock, riverbed alluvial layer, dam seat accumulation layer, and wind accumulation layers on both banks of the valleys.

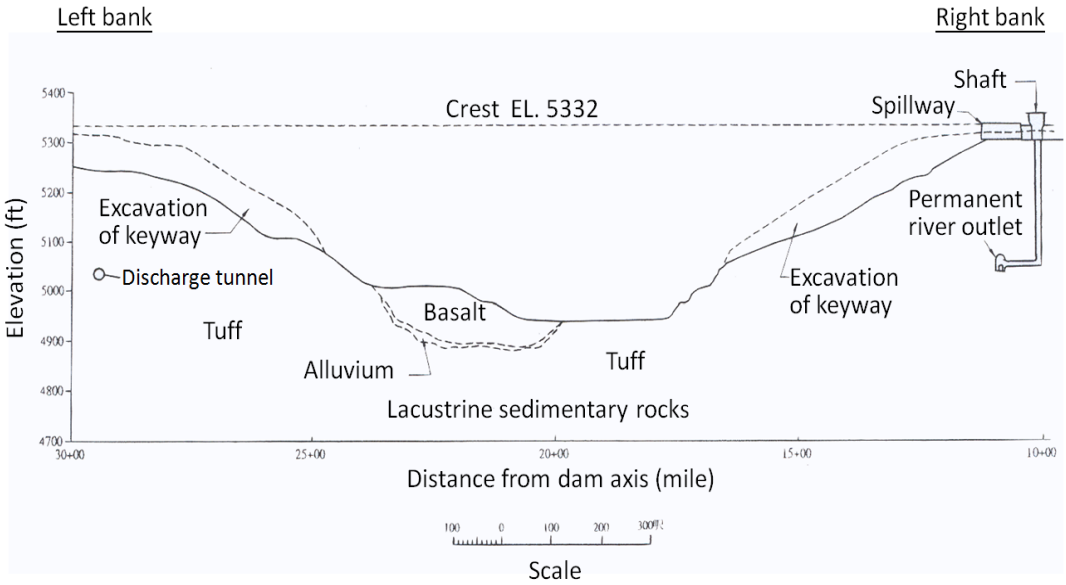

Figure 3.32. Sectional view of the geology along the dam axis of Teton Dam (Sinotech Foundation for Research and Development of Engineering Sciences and Technologies, 2008)

Disaster History. The Summary of the US Teton Dam Disaster (Sinotech Foundation for Research and Development of Engineering Sciences and Technologies, 2008) recorded that there had been no signs of water leakage on the dam before June 3rd, 1976, but on June 3rd, two leaking spots were found in the anti-seepage core at the right side slope of the dam body on the right bank of spillway outlet (See Figure 3.33). On June 4, another leakage was found in the drainage layer at the intersection of the middle portion of downstream slope of the dam body and the right bank of the valley. After that on the morning of 5 June, it was found that the leakage in the drainage layer had developed to piping (See Figure 3.33), and quickly expanded upwards in the event of a deteriorating situation, leading to burst damage (see Figure 3.5).

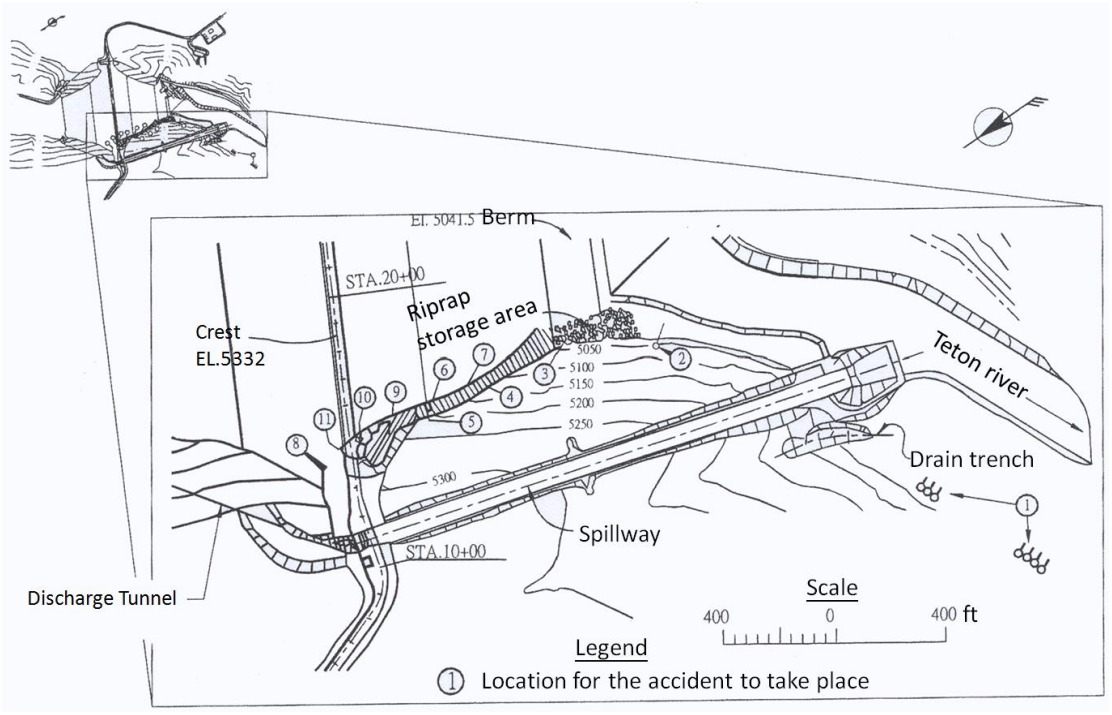

Figure 3.33 Positions of leakage path exits No. ① and No. ②
(Sinotech Foundation for Research and Development
of Engineering Sciences and Technologies, 2008)

Investigation of the Piping Failure Cause. After the piping failure of Teton Dam, the United States Interior Minister and the governor of Idaho invited nine experts to form an unofficial independent panel to conduct an investigation. At the same time, six federal organizations including the Soil and Water Conservation Bureau of the Ministry of Agriculture, the Geological Survey Bureau of the Ministry of Interior, the Bureau of Reclamation, the Army Corps of Engineers, and the Tennessee River Basin Authority, sent representatives to form an internal review team to compile the results of the investigation (Sinotech Foundation for Research and Development of Engineering Sciences and Technologies, 2008).

1. Failure Mechanism Proposed by the Independent Panel

Based on the results of various investigations the independent panel proposed the following two piping failure mechanisms:

1. Leakage path formed below the grouting cover.

2. The cracks due to hydraulic rupture or uneven settlement caused piping.

2. Failure Causes Proposed by the Internal Review Team

When the remaining left dam was excavated to near the dam foundation, a saturated thin horizontal interlayer was found in the dam body, which is called the wet soil interlayer. Figure 3.34 and Figure 3.35 show that this wet soil interlayer is almost through the core, therefore the investigation unit thought that a wet soil interlayer may also exist in the destroyed right dam body, and thus become the cause of dam collapse.

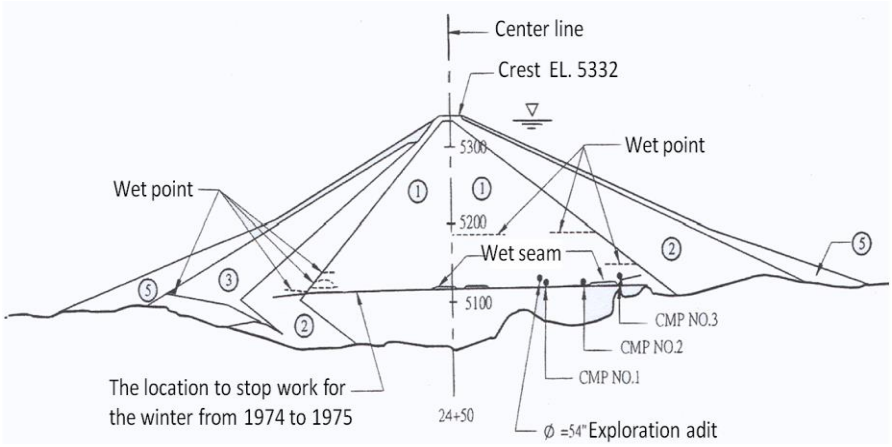

Figure 3.34. Distribution of wet soil interlayer I (Sinotech Foundation for Research and Development of Engineering Sciences and Technologies, 2008)

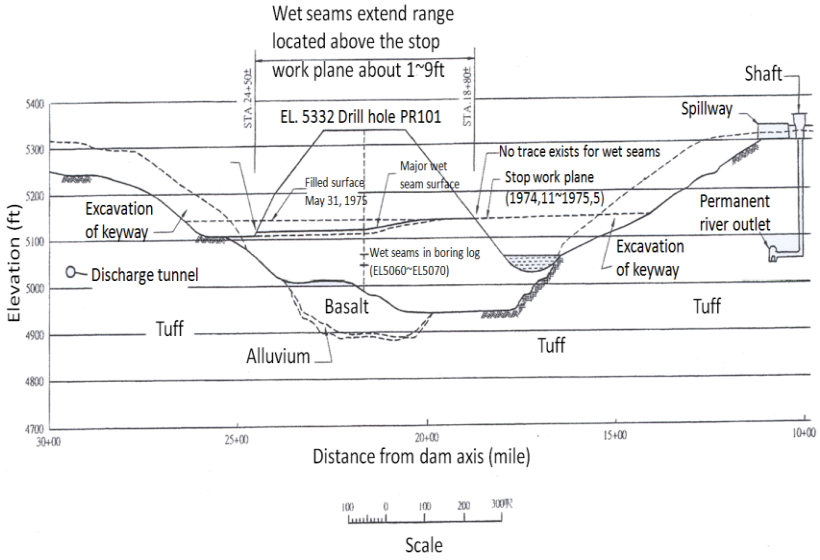

Figure 3.35. Distribution of wet soil interlayer II (Sinotech Foundation for Research and Development of Engineering Sciences and Technologies, 2008)

However, after a discussion of the causes, characteristics, location, and importance of the wet sand interlayer, and after careful comparison with the construction records, the internal review team precluded the possibility that such wet interlayers existed in the destroyed right dam (Sinotech Foundation for Research and Development of Engineering Sciences and Technologies, 2008).

Secondly, a hydraulic fracturing test was performed in the investigation after field drilling with dyed water, and excavation was carried out after the test. As a result, it was found that the hydraulic fracturing surface was mostly formed in the near vertical direction. And the hydraulic fracturing simulation test of a rock plate joint shows that the hydraulic fracture of the keyway backfill occurred at the junction of the opening adjacent to the keyway side wall, the uncompacted backfill is saturated with water, and then holes were formed by the collapse. When the water pressure of the rock plate joint was increased, the hydraulic fracture through the keyway as shown in Figure 3.36 was induced (Sinotech Foundation for Research and Development of Engineering Sciences and Technologies, 2008).

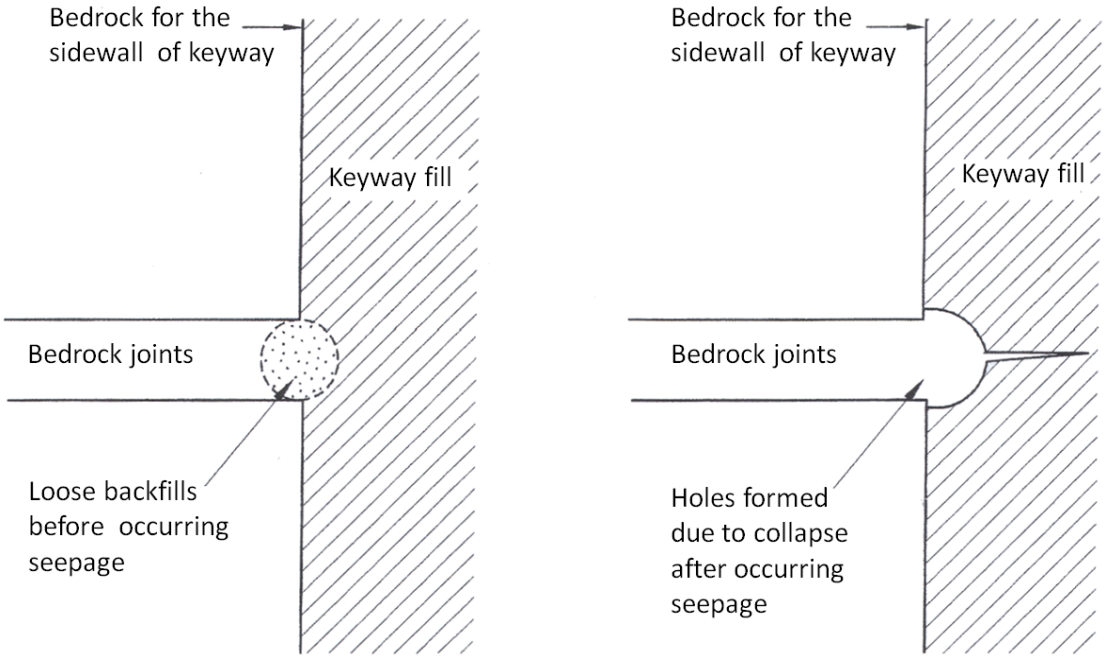

Figure 3.36 Horizontal section of the hydraulic fracture in the keyway backfill (Sinotech Foundation for Research and Development of Engineering Sciences and Technologies, 2008)

Based on the factors that the permeability of the core layer of Teton Dam was too large, the protective measures against erosion were insufficient, and the volume of water infiltrating to the core layer was much higher than estimated, etc., the internal review team concluded the following two types of possible piping failure modes for Teton Dam (Sinotech Foundation for Research and Development of Engineering Sciences and Technologies, 2008):

1. The reservoir water flew along the contact surface of the right bank of the keyway backfill with the rock plate, or flew near the top of the grouting curtain.
2. The reservoir water flew through the soil of low density and high permeability in or near the right bank keyway.

3.3 The Piping Failure of Renyitan Reservoir Spillway

3.3.1 Basic Information of Renyitan Reservoir

Geographic Location. Renyitan Reservoir is located in Fanlu Township, Chiayi, Taiwan about 2.1km east of Lantan Lake and to the north of Bazhang River (detail in Figure 3.37).

Figure 3.37. Geographic location of Renyitan Reservoir (basemap from Google Earth, 2017)

Geology and Geological Structure. The geological map of the adjacent area of Renyitan Reservoir is shown in Figure 3.38. Figure 3.38 shows that the geology of the adjacent area of Renyitan Reservoir includes the Pleistocene double layer, which is a thick interlayer of argillaceous sandstones or sand shales, and that on the left side of the dam there are six double layers exposed, which is the interlayer of siltstones, sandstones, and shales. The strata strike around the reservoir is about N10^{o}E to N5^{o}W, tilting 12^{o} to 20^{o} to the west. Because there are many thick sandstones exposed in this area, cuestas or cliffs are often formed. And in the current submerged reservoir area there are a number of narrow north-south peninsula terrain, which are hard thick sandstones (Geological Information Enquiry, Central Geological Survey of the Ministry of Economic Affairs, 2017).

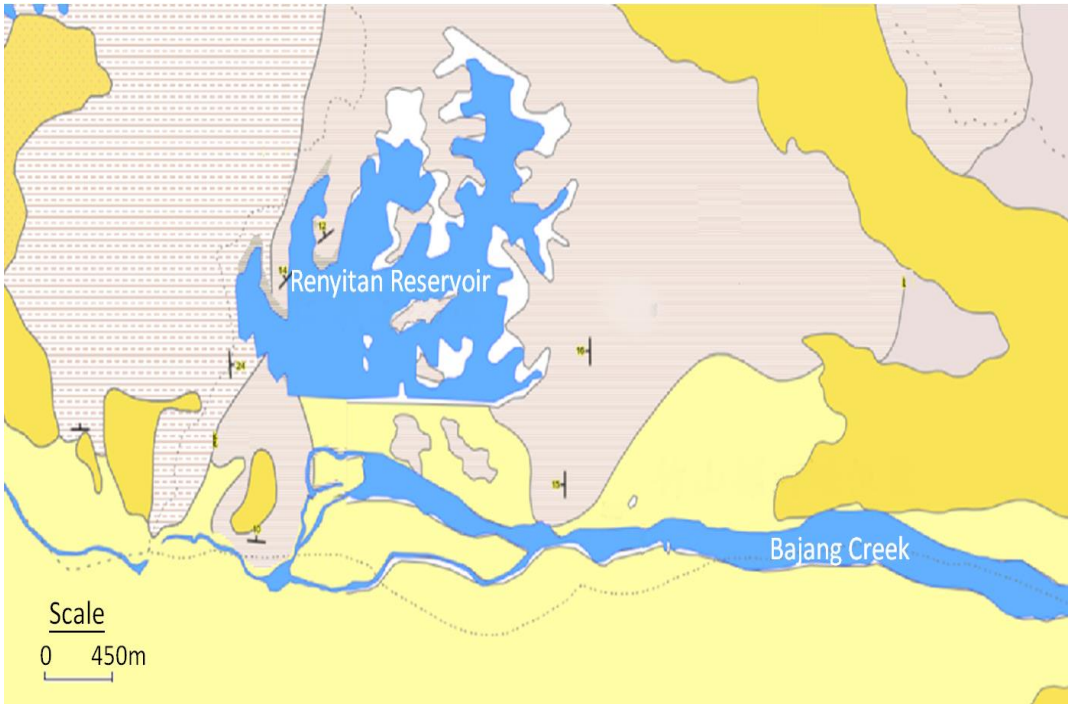

Figure 3.38. Geological map of the adjacent area of Renyitan Reservoir (Geological Information Enquiry, Central Geological Survey of the Ministry of Economic Affairs, 2017)

Figure 3.39 shows the active faults in the adjacent areas of Zhushanlan River weir, including Meishan fault, Jiu Qiong Keng fault, and Chukou fault.

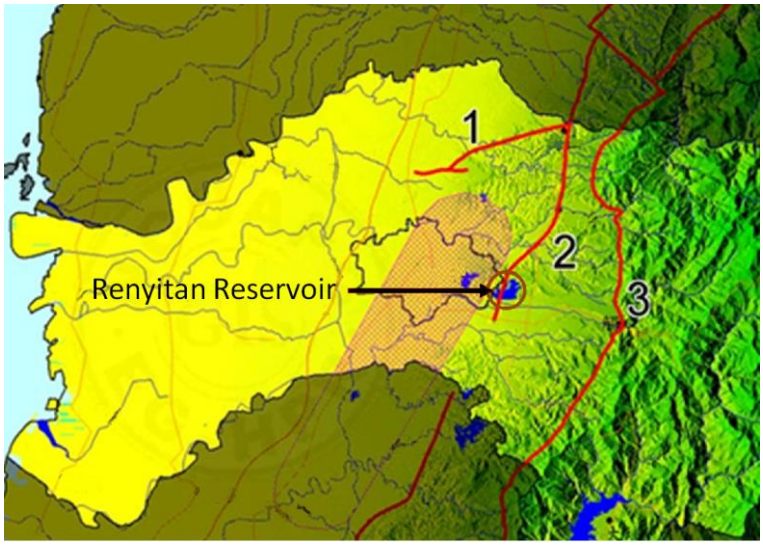

Figure 3.39. Distribution of active faults in areas adjacent to Renyitan Reservoir (Enquiry on Live Fault, Central University Institute of Geophysics and Central University Applied Geology Institute, 2017)

Meishan fault is a right shifting fault, with northeast-east direction, extending from Mei Nan Village, Meishan Township, Chiayi to the west until East Lake Village, Minxiong Township, about 13km in length. Meishan fault is zonal distributed on the earth surface, the main fault is inclined at a high angle to the south, the underground rupture zone is 450m in width, and the fault extends to the west of the pit, which may extend to the west in a latent way (Enquiry on Live Fault, Central University Institute of Geophysics and Central University Applied Geology Institute, 2017).

Jiu Xiong Keng fault is a reverse shifting fault, with north-northeast direction, starting from Hebao Mountain on the north side, extending southward to Zhuqi Southern Water Head passing through Meishan, about 17km in length. The width of the fault zone of Jiu Qiong Keng is about 850m in the section of Shi Niu Creek, which consists of several branches of faults, and the width of the fault zone is gradually reduced southward (Enquiry on Live Fault, Central University Institute of Geophysics and Central University Applied Geology Institute, 2017).

Chukou fault is a reverse shifting fault. The northern section is in the north-south direction, extending southward from Lion Village, Zhuqi Township, Chiayi to Chukou Village, Fanlu Township; the southern section is in a north-northeast direction, extending from Chukou Village to the south until Guanling Village, Baihe Township, Tainan; the combined length of the

two sections is about 28km. The northern end of Chukou fault is connected to the Dajian Mountain fault through Shuisheliao fault near Fuchienping, and the southern end of Chukou fault is connected with Lunkou fault near Guanziling. The fault width is more than 100m, and there are many fault structures and folds in the fault zone (Enquiry on Live Fault, Central University Institute of Geophysics and Central University Applied Geology Institute, 2017).

The Seismic Conditions. Figure 3.40 shows the distribution of the annual number of felt earthquakes, based on the felt earthquake data of earthquakes with epicenter in Taiwan from 1999 to 2013, published by the Central Meteorological Bureau's Global Information Network (Collection of Seismic Activities, Central Meteorological Bureau Glo- bal Information Network, 2017).

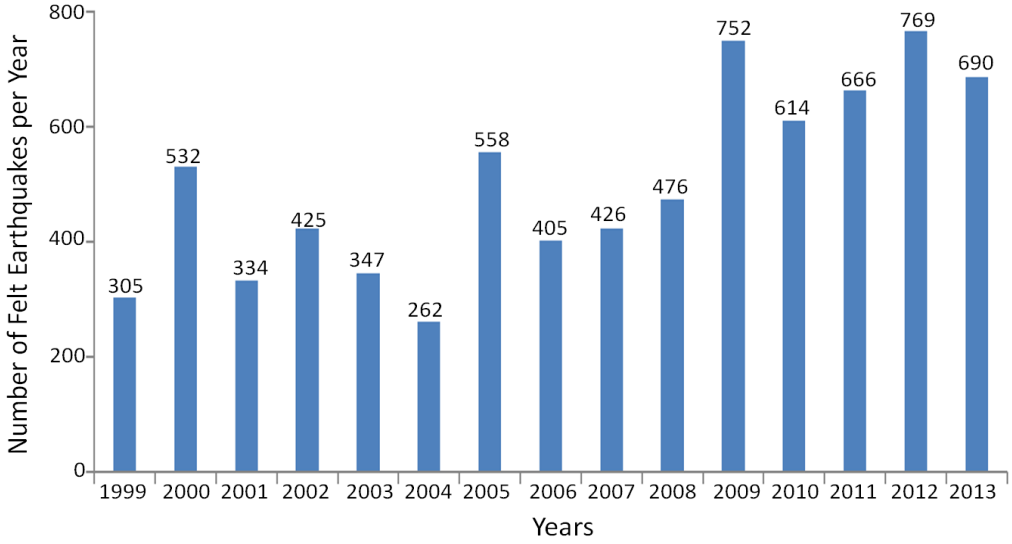

Figure 3.40. Distribution of the number of felt earthquakes per year from 1999 to 2013 (data from Collection of Seismic Activities, Central Meteorological Bureau Glo- bal Information Network, 2017)

Figure 3.40 shows that during the period from 1999 to 2013, the number of felt earthquakes that occurred in the following years exceeded 500: including 532 times in 2000, 558 in 2005, 752 in 2009, 614 in 2010, 666 in 2011, 769 in 2012, and 690 in 2013.

Figure 3.41 shows the distribution of the annual number of felt earthquakes, based on the felt earthquake data of earthquakes with epicenter in Chiayi from 1999 to 2013, published by the Central Meteorological Bureau's Global Information Network (Collection of Seismic Activities,

Central Meteorological Bureau Glo- bal Information Network, 2017). According to Figure 3.41, from R.O.C. 88 to R.O.C. 102, the number of felt earthquakes with epicenter in Chiayi was largest in year 1999, which was 65 times, followed by 33 times in year 2000 and 2011.

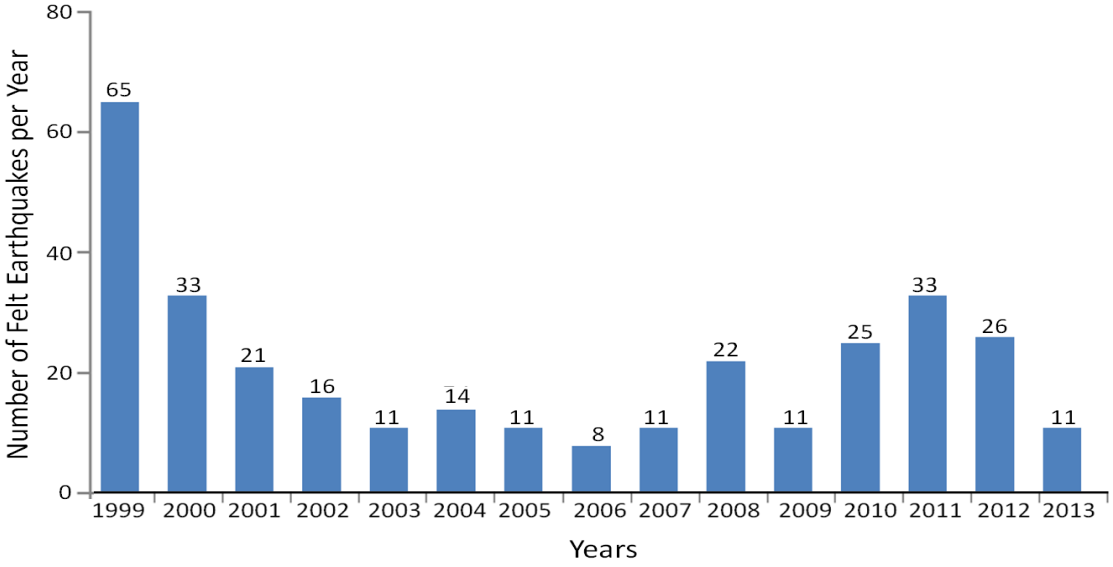

Figure 3.41. Distribution of the number of felt earthquakes per year with epicenter in Chiayi (data from Collection of Seismic Activities, Central Meteorological Bureau Glo- bal Information Network, 2017)

Figure 3.42 shows the distribution of the annual number of felt earthquakes, based on the felt earthquake data of earthquakes with epicenter in Chiayi from 1999 to 2013, published by the Central Meteorological Bureau's Global Information Network (Collection of Seismic Activities, Central Meteorological Bureau Glo- bal Information Network, 2017). According to Figure 3.6, among the felt earthquakes with epicenter in Chiayi from year 1999 to 2013, the largest magnitude occurred in 1999 with M_L=6.4, followed by year 2010 with M_L=6.1.

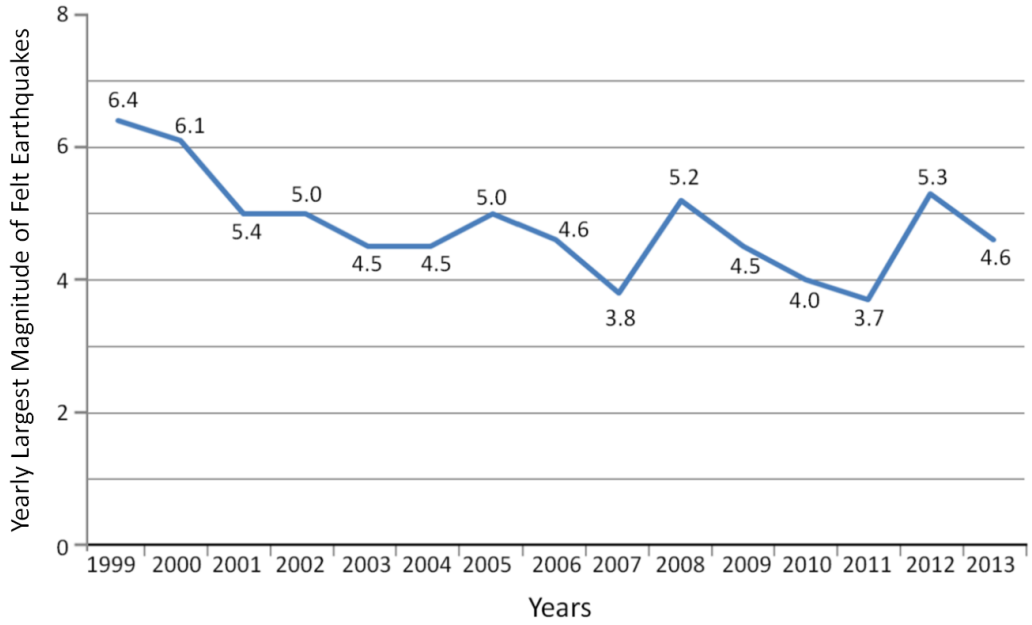

Figure 3.42 Distribution of the yearly largest magnitude of felt earthquakes with epicenter in Chiayi (data from Collection of Seismic Activities, Central Meteorological Bureau Glo- bal Information Network, 2017)

3.3 The Damage to the Spillway and the Side Wall Foundation of Renyitan Reservoir Spillway

The peak ground acceleration (PGA) recorded in the 1022 Chiayi earthquake in 1999 was 1.01g, by the strong motion seismograph (see Figure 3.43) laid on the southeast side of the west ridge of the right bank of Renyitan Dam (ZTE Engineering Consultants Co. Ltd., 2008).

Since the left bank of the spillway (detail in Figure 3.43) and the strong motion seismograph were both on the west ridge, and the spillway is only 215m away from the strong motion seismograph, so the PGA of the dam body of Renyitan Reservoir in the 1022 Chiayi earthquake should also be considerable.

Figure 3.43 Locations of the strong motion seismograph and Renyitan Reservoir spillway (background map from Google Earth, 2017)

Although the PGA of Renyitan Reservoir in the 1022 Chiayi earthquake was considerable, Figure 3.44 shows that the peak ground displacement of various stations in Chiayi was only about 2cm. Although it has been illustrated by Figure 3.45 in the second safety assessment report of Renyitan Reservoir (ZTE Engineering Consultants Co. Ltd., 2008), the 1022 Chiayi earthquake had not seriously affected Renyitan Reservoir spillway, but it has caused the spillway bottom plate cracks, side wall dislocation, extrusion cracks of the side wall foundation plate, and extrusion cracks of the spillway bottom plate and side wall foundation plate, etc.

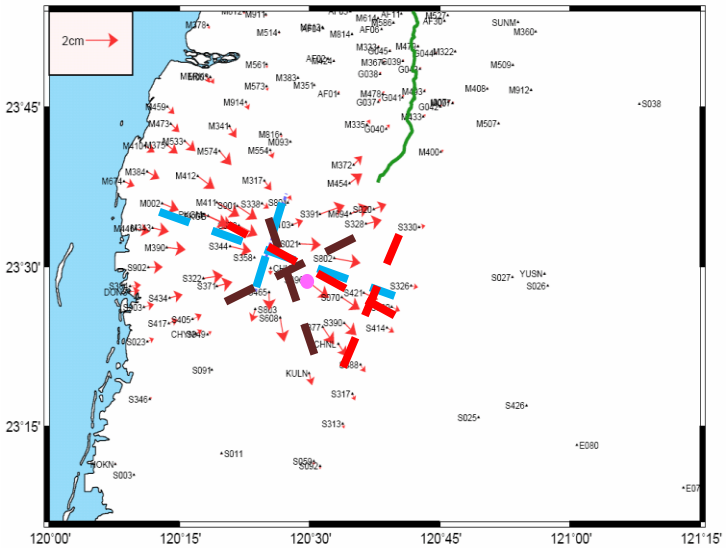

Figure 3.44 The horizontal displacement velocity vectors of various stations in Chiayi (background map from Wang, 2007)

(a) The whole picture of spillway bottom plate cracks, side wall dislocation, and side wall foundation plate cracks

(b) Groundwater seepage after the spillway bottom plate rupture

(c) Groundwater seepage after the extrusion cracks of spillway bottom plate and side wall foundation plate, as well as between the side wall foundation plates

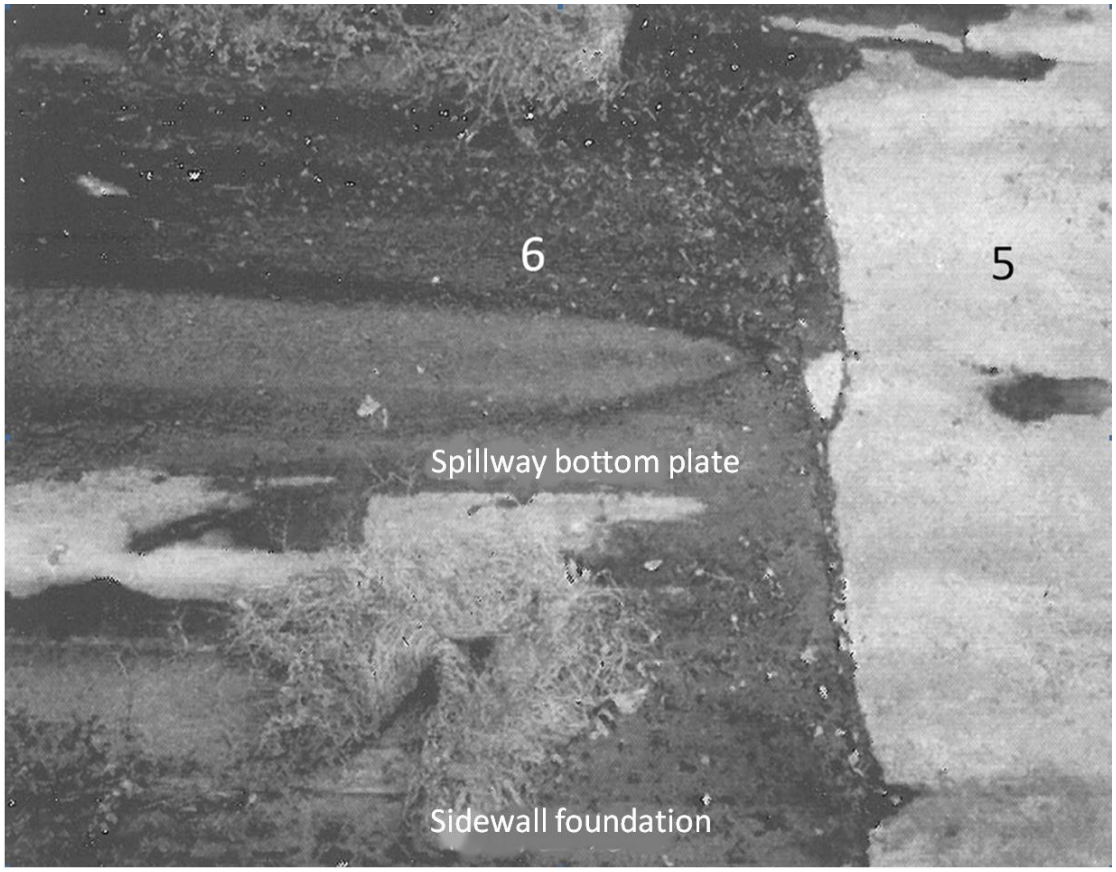

(d) Large amount of groundwater seepage from various expansion joints

Figure 3.45 Damage of Renyitan Reservoir spillway after the 1022 Chiayi earthquake1022 (ZTE Engineering Consultants Co. Ltd., 2008)

Although simple repair of the above-mentioned rupture phenomenon has been completed after the 1022 Chiayi earthquake, the problems that may arise from the abnormal water leakages induced by the various cracks as shown in Figure 3.44b, Figure 3.44c, and Figure 3.44d were ignored during the simple repair process.

During the heavy rain period after the Typhoon Kong-rey in 2013, the water level of Renyitan Reservoir was quickly raised to full water level (EL.105m), and the reservoir water continued to be discharged from the spillway (Taiwan Waterworks Fifth District Management Office, 2013). During the discharge period, the spillway had the following damage:

1. Substantial increase in the rupture of the 5th bottom plate (see Figure 3.46)

2. Damage of the 6th bottom plate (see Figure 3.47 and 3.48)

3. Large amount of water and soil particles flew from below the 5th and 6th bottom plates (see Figure 3.49)
4. Big holes appeared on the top of the left side wall of the 3rd bottom plate (see Figure 3.50)

Figure 3.46. The 5th bottom plate and adjacent bottom plates of the spillway

Figure 3.47. The 6th bottom plate and adjacent bottom plates of the spillway

Figure 3.48. The damage to the 6th bottom plate and side wall foundation plate of the spillway

Figure 3.49. Large amount of water and soil particles flew from below the 5th and 6th bottom plates

Figure 3.50. Big holes appeared on the top of the left side wall of the 3rd bottom plate

Secondly, according to the ground penetrating radar test results shown in Figure 3.51, there are suspected holes existing from the top to bottom of the spillway, in: (1) under the bottom of the 2nd side wall foundation plate; (2) below the center line of the 2nd bottom plate; (3) under the toe of the 2nd and 3rd side wall foundation plates on the left bank of the spillway; (4) below the 3rd and 4th bottom plates of the spillway; (5) below the toe of the 4th side wall foundation plate on the right bank of the spillway; (6) below the 5th bottom plate of the spillway; (7) under the toe of the 5th side wall foundation plate on the left and right banks of the spillway.

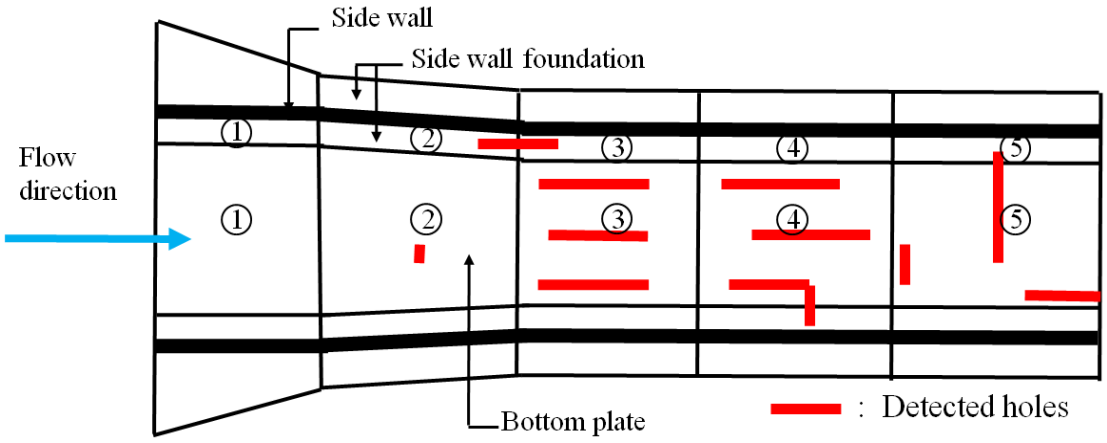

Figure 3.51. Ground penetrating radar test results (Taiwan Waterworks Fifth District Management Office, 2013)

3.4 The Shear Band Model Required for the Piping Failure of Renyitan Reservoir Spillway

3.4.1 The Existing Shear Bands or Shear Textures

Identification of Shear Bands by Distribution of Displacement Velocity Vectors. Figure 3.44 shows the distribution of the horizontal displacement velocity vectors in the adjacent area of Renyitan Reservoir in the 1022 Chiayi earthquake. Combined with the definition of shear band, we can identify in Figure 3.44 that there are two groups of brown twinning-type shear bands mutually conjugated in the directions of N66^{o}E and N21^{o}W, two groups of blue twinning-type shear bands mutually conjugated in the directions of N20^{o}E and N72^{o}W, and two groups of red slip-type shear bands mutually conjugated in the directions of N25^{o}E and N64^{o}W.

Identification of Shear Bands or Shear Textures by Images. For the adjacent area of Renyitan Reservoir, shear banding will leave some deformation terrain characteristics in the field. Therefore by using the terrain features shown in the satellite image in Figure 3.52, it can be identified that there are two groups of red shear textures mutually conjugated on the strikes of N25°E and N64°W, two groups of blue shear textures mutually conjugated on the strikes of N20°E and N72°W, and two groups of white shear textures mutually conjugated on the strikes of N66°E and N21°W.

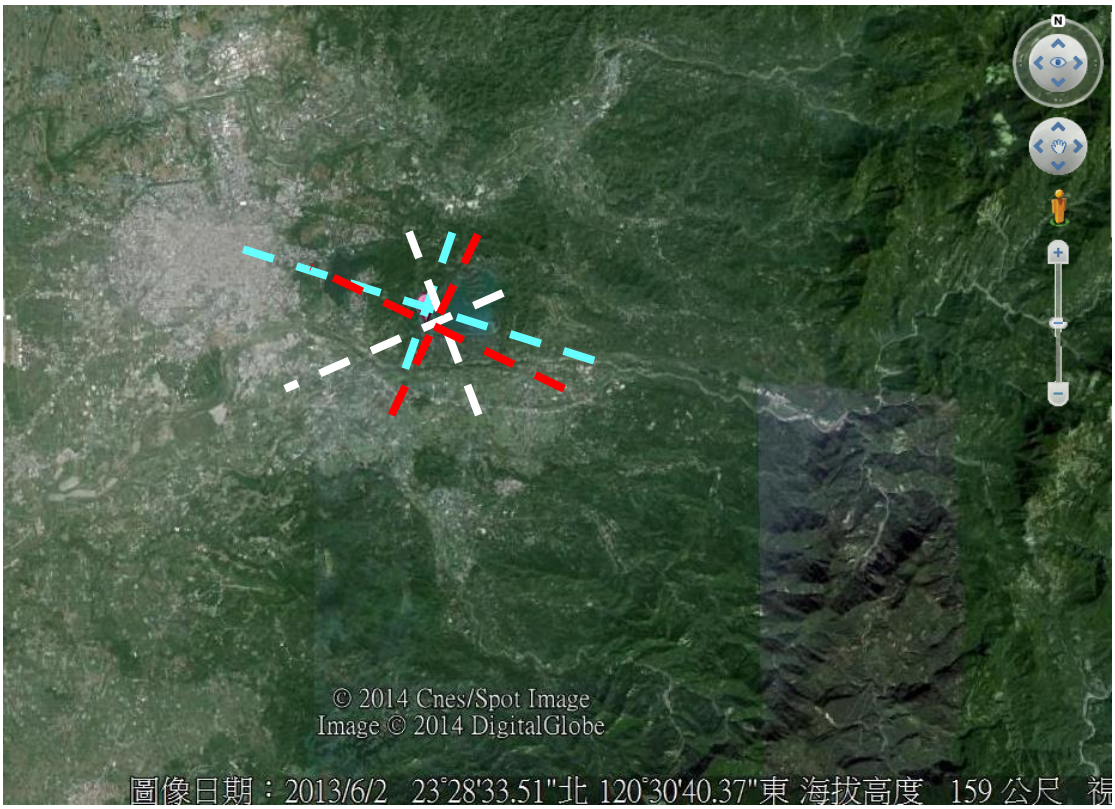

Figure 3.52. Satellite image of the adjacent area of Renyitan Reservoir (background map from Google Earth, 2017)

Secondly it also can be identified through the aerial image in Figure 3.53 that the below shear bands exist in the overall shear band in the adjacent area of Renyitan Reservoir spillway: the principal displacement shear D (red) on N25°E, the thrust shear P (white) on N66°E, the riedel shear R (blue) on N20°E, the conjugated Riedel shear R' (grey) on N21°W, and the compression texture S (pink) on N64°W.

Figure 3.53. Aerial image of the adjacent area of Renyitan Reservoir (background map from Taiwan Waterworks Fifth District Management Office, 2013)

3.4.2 The Theoretical Basis of Piping Failure

It is understood from Section 3.2.5 and Section 3.2.6 that in the past scholars and experts have used the method related to groundwater seepage in the analysis of reservoir safety assessment to analyze or monitor the downstream slope leakage of dams that may cause piping failure, and the control equation used to analyze the groundwater seepage is the Laplace equation. The theoretical basis of the Laplace equation includes: (1) steady state groundwater flow conditions; (2) the overall soil structure maintains stability in the seepage flow due to the ellipticity.

However, in piping failure torrent flows in the pipe-shaped discharge tunnel (Terzaghi and Peck, 1967), the seepage flow of groundwater originates from the slow flow of water in the soil pore space; hence the theoretical basis are completely different from each other.

When water flows out of the leakage path in the downstream slope of the dam, the velocity of the water in the pipe-shaped discharge tunnel is much greater than the average velocity of the seepage, so that the soil particles after rupture in the pipe-shaped discharge tunnel will be lost after floating, and the width and height of the tunnel will also be increased. Therefore, the theoretical basis of the formulas used to analyze the leakage problems in the downstream slope of the dam includes: (1) unsteady state groundwater flow conditions; (2) the overall soil structure in the leakage process tends to be unstable due to the gradual loss of ellipticity.

Because the theoretical basis of seepage analysis or leakage analysis is not the same in the stable and unstable state of the whole soil structure, the seepage analysis and leakage analysis of the downstream slope of the dam can only be carried out in the stable and unstable state of the whole soil structure, respectively.

Therefore, it can be seen that in terms of the leakage issue of Hsin-shan Reservoir and A-kung-tien Reservoir as described in Chapter 2 of this dissertation, since the relevant research methods to analyze the seepage used in the past were all based on the assumption that the whole soil structure was stable, the leakage issue when the whole soil structure was in the unstable state could not be correctly analyzed.

3.4.3 The Shear Band Model in the Adjacent Area of Renyitan Reservoir Spillway

The pipe-shaped discharge tunnel proposed by Terzaghi and Peck are located in the intersection area of shear bands on different strikes, therefore in order to understand the cause of the pipe-shaped discharge tunnel, we must first understand the cause of the shear bands. Shear bands are only present in the tectonic earthquake. When the tectonic plate is subjected to continuous lateral compression (or laterally extension), once the shear strain penetrates sufficiently far into the plastic range, the tectonic plate is locally deformed due to the loss of ellipticity, and further forms the shear band (Drucker, 1950; Hill, 1962; Mandel, 1966; Rice, 1976; Rudnicki and Rice, 1975; Valanis, 1989).

In actual piping failure problems, the theoretical analysis and numerical simulation analysis of the shear band are both very complicated and time-consuming. For the sake of simplicity, the following two-stage operation is carried out to do the assessment of piping failure:

Stage 1: construct the shear band model, in order to identify the location of the pipe-shaped discharge tunnel.

Stage 2: calculate the bottom critical velocity v_{bc} of the piping failure corresponding to particles of different sizes in the pipe-shaped discharge tunnel (to be discussed in Chapter 5).

Taking the piping failure of Renyitan Reservoir spillway as an example, Figure 3.54 shows that Renyitan Reservoir spillway is located on the west ridge of the northwest side of the dam. Figure 3.55 shows the sectional view of the west ridge. Figure 3.56 shows the local image of Renyitan Reservoir spillway before the 1022 Chiayi earthquake.

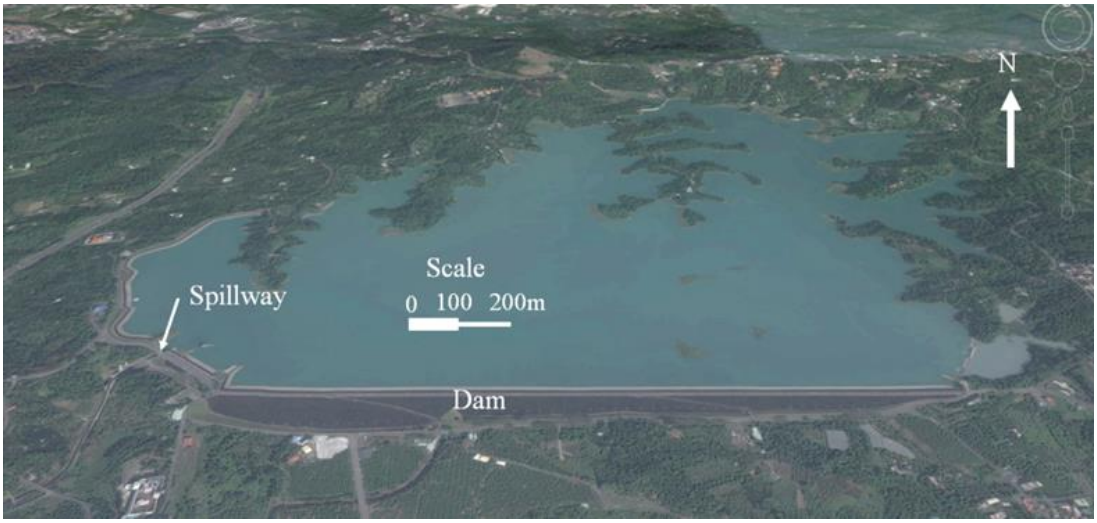

Figure 3.54. The spillway and dam body of Renyitan Reservoir (background map from Google Earth, 2017)

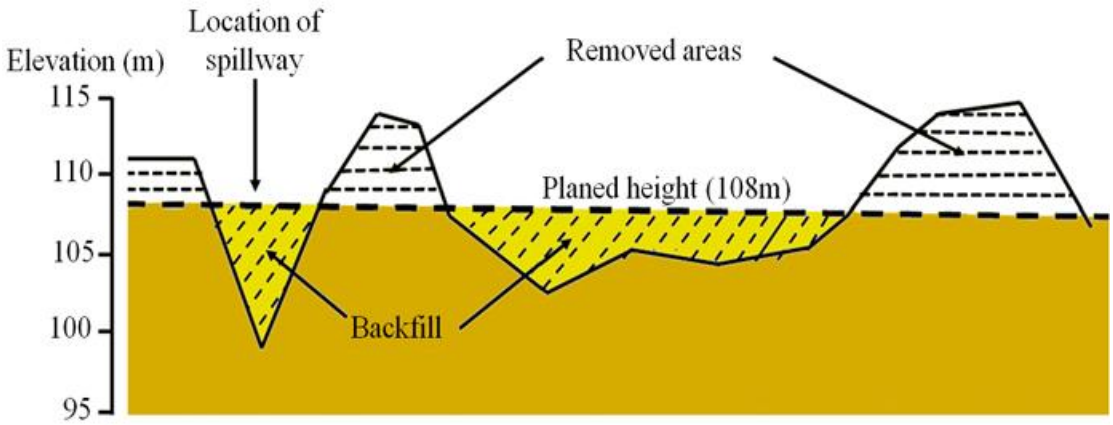

Figure 3.55. Sectional view of the original west ridge of Renyitan Dam (redraw from ZTE Engineering Consultants Co. Ltd., 2008)

Figure 3.56. Local image for the spillway of Renyitan Reservoir before the 1022 Chiaya earthquake

Shear banding will cause the site to rise, so for the adjacent area of spillway of Renyitan Reservoir, the author developed the shear band model as shown in Figure 3.57.

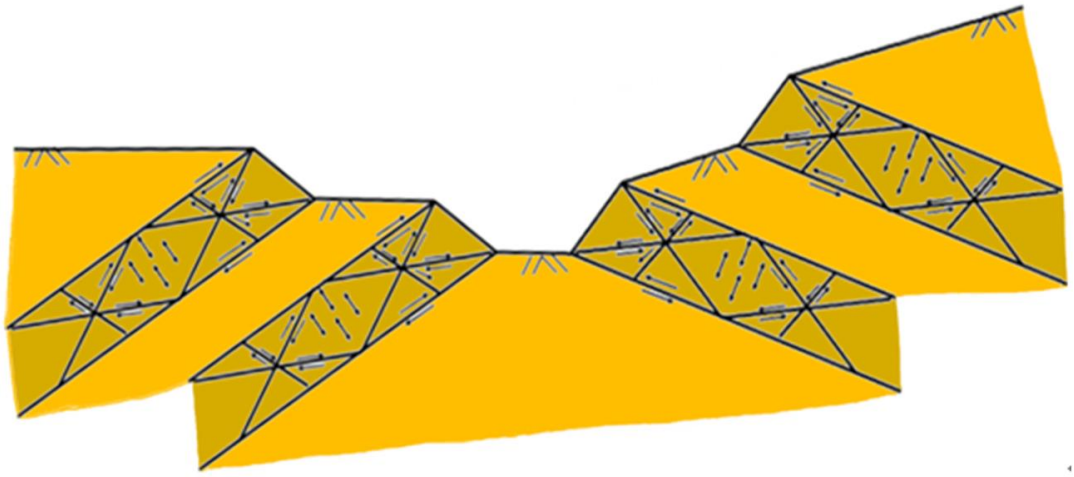

(a) Prior to the construction of the spillway

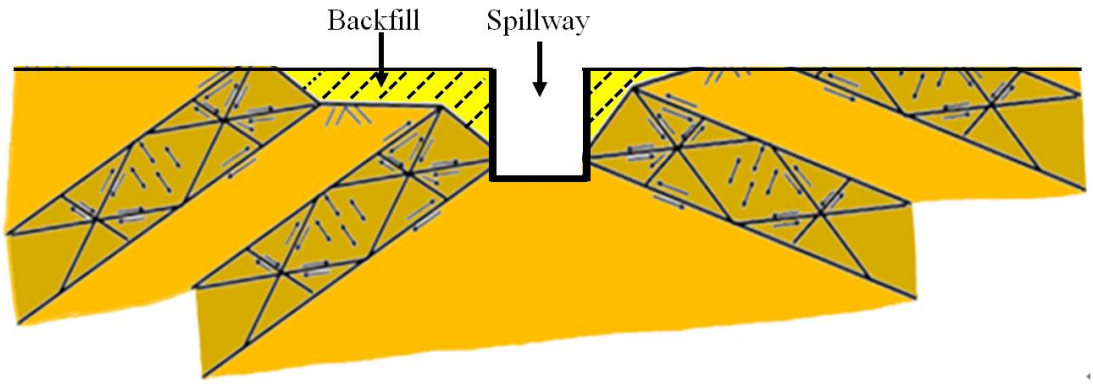

(b) After the completion of spillway construction

Figure 3.57. The shear Band Model in the Area Adjacent to Renyitan Reservoir Spillway

3.4.4 The Related Data of the Piping Failure for Renyitan Reservoir Spillway

Shear bands will be extended due to earthquake or the periodic increase-decrease of the reservoir water, and the rupture degree of shear band soils will continue to increase. However, most engineers ignored the existence of shear zones in the design stage or operation stage after the completion of the project, and thus paid a painful price after piping failure occurred. Take Gouhou Dam in China as an example, it was only after the piping failure that dozens of shear bands were found at the bottom of the dam, some of which extended to the dam body after the dislocation, and the pipe-shaped discharge tunnel was formed in the intersection area of shear bands on different strikes (see Figure 3.58).

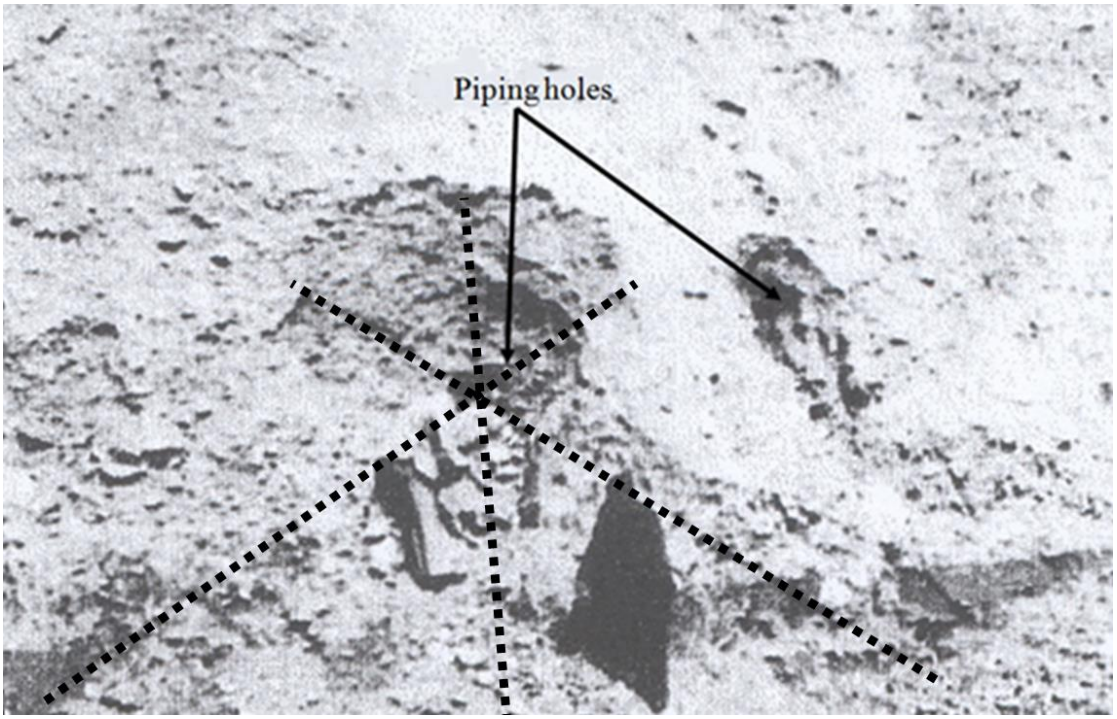

Figure 3.58 The pipe-shaped discharge tunnel formed in the intersection area of shear bands in Gouhou Dam (background map from Sinotech Foundation for Research and Development of Engineering Sciences and Technologies, 2008)

Figure 3.59 is the sectional view of Renyitan Reservoir spillway. It is known from Figure 4.9 that, the height of the overflow weir is 102.5m, the spillway width is 9m, the slope is 25°, the design discharge is 75cms, and the maximum flow rate is continuously increased from 6m/sec at the end of the overflow weir to 22m/sec at the bottom of the spillway.

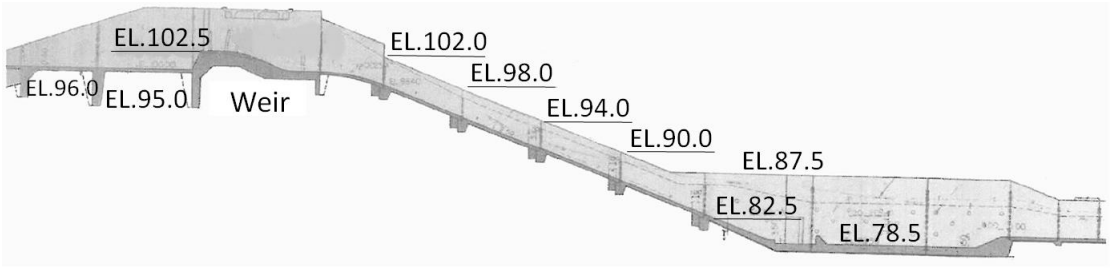

Figure 3.59 Sectional view for the spillway of Renyitan Reservoir (ZTE Engineering Consultants Co. Ltd., 2008)

The 1022 Chiayi earthquake occurred in 1999. The local magnitude of the earthquake M_L was 6.4, and the focal depth was 16.5km. In the earthquake, the peak ground acceleration at the junction of the right bank and the southwest ridge at the top of the dam, as shown in Figure 3.44, was about 993 gal (ZTE Engineering Consultants Co. Ltd., 2008) .

Figure 3.44 shows the six shear bands on different strikes identified by the horizontal displacement velocity vector map. Due to the fact that other shear bands on the same strike will appear in groups, it may have an impact on Renyitan Reservoir spillway, causing bottom plate rupture (Figure 3.60), bending deformation of side walls (Figure 3.60), dislocation of side walls (Figure 3.61), and particles of different sizes deposited in the stilling basin (Figure 3.62), thus there was a big pit on the back of the wall (see Figure 3.50)

Figure 3.60 Bottom plate rupture and bending deformation of the side wall of the spillway for Renyitan Reservoir

Figure 3.61 Dislocation of the side wall of Renyitan Reservoir spillway

Figure 3.62 Soils of different sizes flowed out due to piping failure of Renyitan Reservoir spillway

After the piping failure of the spillway, the seepage water through the southwest ridge continued to flow in the rupture zone under the bottom plate and side wall foundations (see Figure 3.48) but the flowing speed of this seepage was not high enough to cause cobble or boulder piping failure, thus proving that the seepage through the ridge was not the main cause of the piping failure of the spillway.

In the process of repairing the spillway bottom plates, when the 3rd bottom plate to the 6th bottom plate were removed, it was first found that there was a large loss of soils under the 3rd to 6th bottom plate (see Figure 3.63), and there was also a large loss of soils under the 2nd and 3rd sidewall foundations on the left bank (see Figure 3.64). Secondly, during the repair, when the spillway gate was closed, Figures 3.63 and 3.64 show that the soils around the pipe-shaped discharge tunnel were gradually air-dried. This phenomenon proves that the water source causing piping failure came from the flood and discharged to downstream through the spillway after the gate was open.

Figure 3.63. The space after the soil loss of the spillway bottom plate

Figure 3.64. The space after the soil loss of the spillway sidewall foundation

For the shear band soils that remained in the field after the piping failure, although the degree of rupture was relatively low, it can still be identified through Figure 3.63 and Figure 3.64 that there were principal deformation shear D, thrust shear P, Riedel shear R, conjugated Riedel shear R', and compression texture S existing in the overall shear band (see Figure 3.65 and Figure 3.66).

Figure 3.65. Shear textures existing in the bottom plate soils

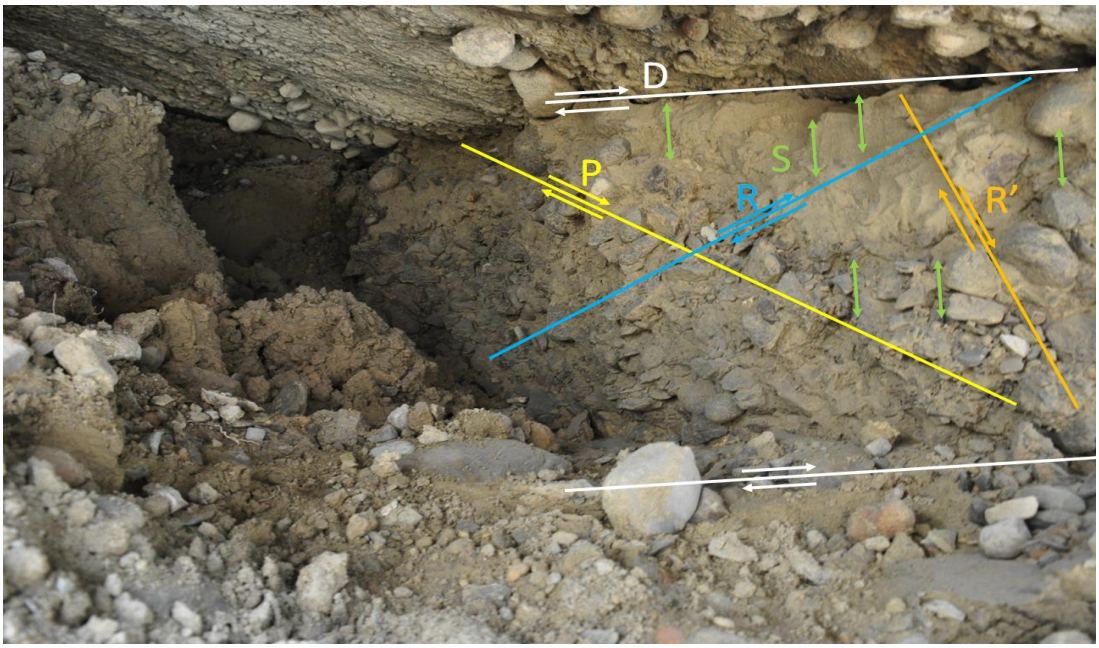

Figure 3.66. Shear textures existing in the sidewall foundation soils

For the warped and damaged soils beneath the bottom plate of the spillway, due to the existence of a shear texture similar to the one shown in Figure 3.65, and the axis in the intersection area of the shear texture extending to the slope below the upper stream water surface of the reservoir, some pipe-shaped discharge tunnels remained below the bottom plate of the spillway after the piping failure of Renyitan Reservoir spillway (see Figure 3.67).

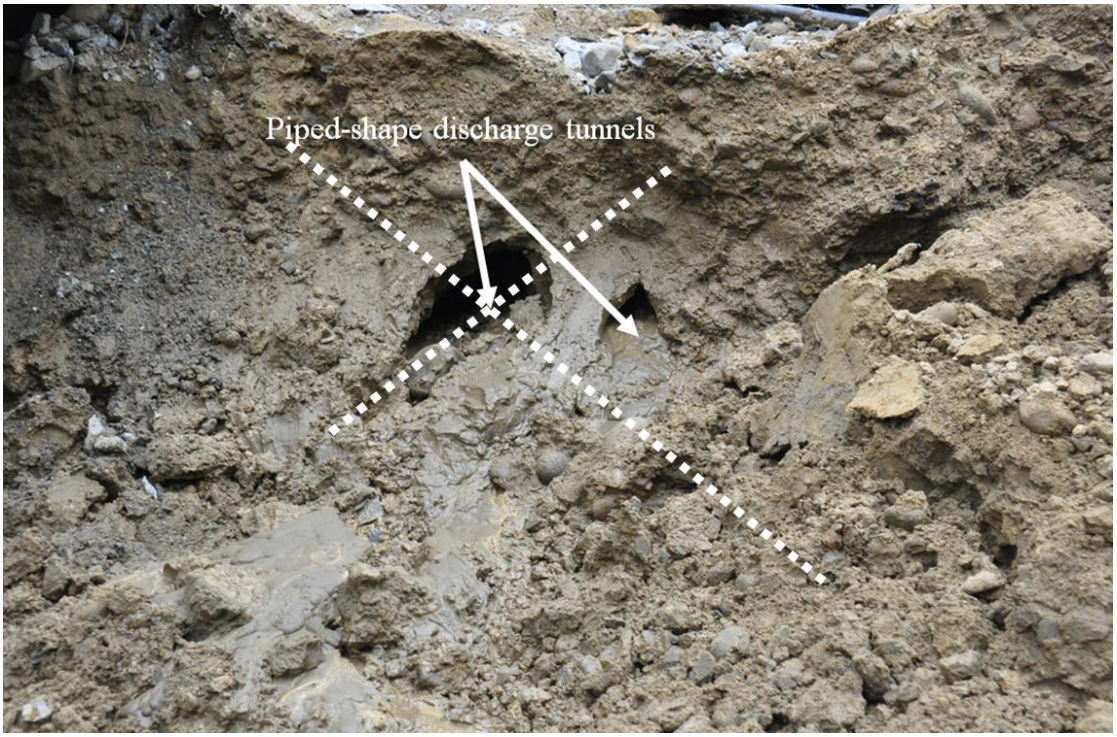

Figure 3.67. Pipe-shaped tunnel formed in the intersection area of shear textures of Renyitan Reservoir spillway

3.5 The Bottom Critical Velocity of the Particles Causing Piping Failure

The slopes of the bottom plate and side wall foundation of Renyitan Reservoir spillway are both 25°. During the spillway repair process, after the spillway bottom plates No. 3 to No. 6 were removed, it was found that there was no anti-slip steel bars provided to the anti-slip block prior to the repair project (see Figure 3.68a). Therefore, anti-slip steel bars were immediately added into the repair project (see Figure 3.68b).

(a) Anti-slip block without anti-slip steel bars prior to the repair project

(b) Anti-slip steel bars were added into the repair project

Figure 3.68. Anti-slip block with or without anti-slip steel bars for the bottom plate of Renyitan Reservoir spillway

As the anti-slip steel bars were not provided, the anti-slip function could not play. Therefore, whether in normal times, in heavy rains, or in earthquake, both the spillway bottom plate and side wall foundation will slide. Once the spillway bottom plate slid (see Figure 3.69), the shear textures in the soil below the bottom of the spillway were induced (see Figure 3.66). Especially after the warping and rupture of the 6th bottom plate and side wall foundation, the various bottom plates and side wall foundations above it will all slide due to the loss of sliding resistance below, thus increasing the rupture degree of the spillway bottom plates, side wall foundations, and the soil underneath. The discharged flood flows easier into the soil in the shear bands below the spillway bottom plates and side wall foundations, and the pipe-shaped discharge tunnel is also formed. After that the width and height of the pipe-shaped tunnel are continuously increasing, and finally the cobbles and boulders in the pipe-shaped discharge tunnel can also be carried away by the torrent.

Figure 3.69. Dislocation of the center line and expansion joint of the bottom plate of Renyitan Reservoir spillway

The Formula Used to Calculate the Bottom Critical Velocity of Particles Causing the Piping Failure . When the soil below the spillway bottom plate and the side wall foundation forms a pipe-shaped discharge tunnel, the soil in the tunnel will be broken into pieces due to the intersection of shear bands. These broken soil pieces, when the pore space is greatly expanded, will be lost due to the bottom speed v_b greater than bottom critical velocity v_{bc}.

The above problem is a piping problem rather than a seepage problem. However currently when doing reservoir safety assessment, the consultants continue to consider the “leakage” occurring in the downstream slope of the dam as "seepage loss", and to monitor the “leakage” by using the groundwater table or water pressure monitoring methods related to “seepage”, and then assess the piping failure potential closely related to “leakage” by "seepage analysis results".

The installed monitoring wells or water pressure gauges have difficulties in passing through the pipe-shaped discharge tunnel, and "seepage analysis results" cannot display the pipe-shaped discharge tunnel either. Therefore, although the safety assessment report is very illustrative, and in line with the current Water Conservancy Construction Inspection and Safety Assessment Methods (Water Resources Bureau of Ministry of Economic Affairs, 2003) and Water Conservancy Construction Inspection and Safety Assessment Technical Requirements (Water Resources Bureau of Ministry of Economic Affairs, 2008), the occurrence of piping failure cannot be prevented by using the reservoir safety assessment report. This is why in the past, before piping failure occurred in different dams around the world, there was always a group of scholars and experts doing group consultation onsite, but piping failure still occurred since these scholars and experts could not come to a resolution. It can be seen that the "leakage" in the downstream slope of the dam cannot be regarded as "seepage loss", nor can the reservoir safety assessment be carried out by using the analysis method or monitoring method related to "seepage".

Since the loss of particles in the pipe-shaped discharge tunnel starts from small-size to large-size particles, after the small-size particles are lost, the pore space volume, the bottom velocity of the particles, and the width and height of the pipe-shaped discharge tunnel are also increased. Therefore, in the assessment of piping failure, in addition to assessing the location of the pipe-shaped discharge tunnel based on the monitoring results of the leakage path exits and shear bands, it is also necessary to calculate the bottom critical velocity v_{bc} of the particles required to cause the piping failure based on the diameters of the flowed particles.

In this dissertation, in order to break through the traditional dam piping failure assessment method, the author uses Equation 3.1 to calculate the bottom critical velocity v_{bc} of the particles required for the occurrence of piping failure.

The Bottom Critical Velocity of Particles Causing the Piping Failure of Renyitan Reservoir Spillway. Taking Renyitan Reservoir spillway as an example, for the particles of different diameters that remained in the stilling basin after the piping failure as shown in Figure 4.13, when the void ratio *e* in the pipe-shaped discharge tunnel increased from 0.5 to 1.0 with the loss of small particles, the specific gravity G_s is 2.65, and the particle diameter *D* increased from 0.0001m to 0.35m. Table 5.1 shows the relationship between the bottom critical velocity v_{bc}, the particle diameter *D* and the void ratio *e*, of the particles required to cause the piping failure based on analysis results.

Table 5.1 The relationship between v_{bc}, *D*, and *e* of the particles required for the occurrence of piping failure

Particle size *D*(m)	v_{bc} (m/sec)		
	e= 0.5	e= 0.75	e= 1.0
0.0001	0.042	0.039	0.037
0.0005	0.095	0.087	0.081
0.001	0.133	0.123	0.115
0.005	0.297	0.276	0.258
0.01	0.421	0.389	0.365
0.05	0.942	0.871	0.816
0.10	1.331	1.233	1.153
0.35	2.491	2.306	2.157

The Cause of the Piping Failure of Renyitan Reservoir Spillway. In the above sections, it is found that shear banding not only caused the bottom plate rupture of Renyitan Reservoir spillway, but also caused the dislocation of the expansion joints and the center line (Figure 5.2) as well as the side wall foundation rupture (Figure 5.3).

Figure 5.3 Side Wall Foundation Rupture

For the spillway bottom plate with thickness of 20cm and unit weight of 23.54kN/m^3, when the water flows through the rupture area of the spillway bottom plate and side wall foundation to the pipe-shaped discharge tunnel underneath, when the water head of the lifting force is greater than 0.48m for the 6th bottom plate and side wall foundation, the lift failure phenomenon will appear, and in the case of excessive lifting force the warped rupture as shown in Figure 3.11 will be induced.

For the shear band soil under the spillway bottom plate or side wall foundation of Renyitan Reservoir spillway with a slope of 25°, it is known from Table 5.1 that with the increase in the rupture degree and the loss of smaller particles, the void ratio increased from 0.5 to 1.0, at this time the v_{bc} required for the piping failure is reduced by 13.4%; while when the void ratio is equal to 0.5, and the v_{bc} required for the piping failure increased from 0.042m/sec corresponding to D=0.0001m to 2.491m/sec corresponding to D=0.35m.

When the degree of soil rupture in the pipe-shaped discharge tunnel increases, and the flooding velocity in the soil of the shear band reaches 0.042m/sec, the pipe-shaped discharge tunnel will be clearly formed after the loss of smaller soil particles with $D \leq 0.0001m$. This phenomenon can be proved by the hole distribution map obtained through the ground penetrating radar test as shown in Figure 3.14. Then the width and height of the pipe-shaped discharge tunnel are also increased with the increase of v_b. For the largest particle (D=0.35m) flowing out due to piping, Table 5.1 shows that the v_{bc} required for the piping failure is 2.491m/sec. In general, such a large v_b may exist after the continuous increase in the cross section area of the pipe-shaped discharge tunnel.

Based on the above results, it is concluded that the causes of the piping failure of Renyitan Reservoir spillway include the following four procedures:

1. In the 1022 earthquake the shear bands around the spillway extended into the spillway, accompanied by the rupture of the spillway bottom plate, the side wall dislocation and the bending deformation of the side wall, etc.

2. Part of the discharged flood flowed along the rupture area of the spillway bottom plate and side wall foundation into the soil of the shear bands underneath.

3. Because the spillway bottom plate was not provided with anti-slip steel bars, after the warped rupture of the 6th bottom plate and the side wall foundation, the various bottom plates above the 6th bottom plate and the side wall foundation caused a higher degree of rupture in the shear bands underneath due to further sliding. And the velocity of the water flow in the soil of the shear bands was also increased, thus the pipe-shaped discharge tunnel was formed after the loss of smaller particles.

4. With the increase in the diameter of the lost particles, the width and height of the pipe-shaped discharge tunnel increased rapidly, and the particles with a diameter of 35cm were able to be taken away by torrents in the discharge path.

5. When the space of the pipe-shaped discharge tunnel below the side wall foundation was getting bigger and bigger, the soil on the back of the wall gradually slipped down, and the particles that slid into the pipe-shaped discharge tunnel also continued to be taken away by the torrent, thus forming a large hole in the back of the wall.

3.5 The Relevant Laws and Regulations on Reservoir Safety Assessment

The Basis of the Traditional Dam Safety Assessment. The current safety and maintenance related to reservoirs is mainly based on Water Conservancy Construction Inspection and Safety Assessment Method (Water Resources Bureau of Ministry of Economic Affairs, 2003), as well as Water Conservancy Construction Inspection and Safety Assessment Technical Specifications (Water Resources Bureau of Ministry of Economic Affairs, 2008); where the water storage and drainage sections specified the below reservoir safety assessment contents:

Chapter 1: General Provisions;

Chapter 2: Safety Data Collection;

Chapter 3: Safety Data Filing;

Chapter 4: Review and Evaluation of Safety Data;

Chapter 5: On-site Inspection and Evaluation;

Chapter 6: Supplementary Surveys and Tests;

Chapter 7: Audit Analysis;

Chapter 8: Dam Break Calculations and Disaster Lost Assessment;

Chapter 9: Comprehensive Assessment and Conclusions and Recommendations;

Chapter 10: Safety Assessment Report Writing.

For the above-mentioned Chapter 10 – safety assessment report writing, the specified format is as follows:

1. Introduction

The contents include:

(1) Name and location of water storage and diversion works;

(2) Water storage, water diversion construction owner (name of organization);

(3) Water storage, water diversion construction planning, design, construction unit, start and completion date;

(4) Overview of water storage and diversion construction;

(5) The importance of water storage and diversion construction (based on the classification and size of the disaster);

(6) Date of previous and this safety assessment;

(7) The level of this safety assessment;

(8) The scope and project of this safety assessment.

2. Main body of the report

The contents include:

(1) Discovery and assessment of safety data review;

(2) The process, discovery, and evaluation of on-site inspection;

(3) Necessary audit analysis, process, results, assessment and improvement recommendations.

3. Appendix

The contents include:

(1) Important reference list and storage unit relating to the project;

(2) Memorandum of review, on-site inspection or inspection checklist;

(3) Photos;

(4) Analysis and calculation data;

(5) Important instrumental observations;

(6) Relevant references.

4. Conclusions and recommendations

In the end conclusions and recommendations are made from the safety assessment of water storage and water diversion construction, after safety data review, on-site inspection, and audit analysis, etc. The items includes:

(1) Geology and earthquakes;

(2) Hydrological analysis and drainage safety;

(3) Safety monitoring data analysis and main structure safety;

(4) Operation and alarm system;

(5) Surrounding stability of the construction or water storage area;

(6) Recommendations to improve the work;

(7) Dam break and disaster lost assessment;

(8) Dam break emergency response plan;

(9) Safety of other important facilities.

The Relevant Laws and Regulations on Reservoir Safety Assessment. Although the reservoir safety assessment has a clear basis, and the report content and writing format are also clearly defined, the reservoir safety maintenance and management personnel do not need a beautiful report, but a report that can ensure the long-term safety of the reservoir.

Therefore, if the fatal factors that harm the safety of the reservoir cannot be included in the specification, the reservoir safety assessment report cannot ensure the safety of the reservoir even if it looks beautiful.

Take the US Teton Dam and Taiwan’s Renyitan Dam as examples, the reservoir safety assessment is carried out every five years, and the reports are also in line with the regulations; yet, why can the emergencies not be controlled, and why has piping failure occurred?

Considering the 2014 Taiwan gutter oil scandal, before the outbreak of the incident, all the gutter oil went through various tests according to the regulations, so as to be legally sold. When the legally sold oil turned out to be gutter oil, the actual cause was that the fatal factors were not included in the specification by the food law. Similarly, the actual cause of the above mentioned piping failure was that the fatal factors were not included in the specification by "Water Conservancy Construction Inspection and Safety Assessment Methods" and "Water Conservancy Construction Inspection and Safety Assessment Technical Specifications".

As for which factor is the fatal factor of piping failure of the dam body? The answer to this question can be obtained from the Chapter 4 and Chapter 5 of this dissertation – the fatal factor of dam piping failure is the intersection area of shear textures on different strikes, becoming a pipe-shaped discharge tunnel, due to the high degree of brittle fracture and the loss of some smaller particles.

At present, the Internet is very developed and the images of earthquake disasters all over the world can be shared. Therefore, it is known that all dam piping failures are caused by tectonic earthquakes, and the main effect of a tectonic earthquake is tectonic plate fault, followed by tectonic plate vibration.

For the reservoir safety assessment, the work related to earthquakes includes: (1) basic data collection, supplement, review, and assessment; (2) audit analysis and the design of earthquake assessment (including tectonic structure, seismic activities, fault activity evaluation, seismic hazard assessment, and acceleration time history curve, etc.); (3) the dam body material parameters, pseudo-static stability analysis, and dynamic analysis of the dam body structure safety assessment; (4) assessment on safety monitoring system observation items and frequency (including water pressure gauge, inclinometer, settlement ring, horizontal displacement meter, earth pressure meter, flow meter, quantity of seepage flow, surface subsidence measurement point, and seismograph, etc.).

It can be seen that the current reservoir safety assessment only contains the secondary effect of tectonic earthquakes (tectonic plate vibration), while ignoring the main effect of tectonic earthquakes (tectonic plate faulting). Therefore, although before the piping failure a reservoir safety assessment was carried out every five years, the content of the report: (1) is mostly

irrelevant to tectonic plate faulting; (2) only contains the dam dynamic analysis of tectonic plate vibration; (3) only contains the safety monitoring system, items, and frequency relevant to tectonic plate vibration.

Based on the above, it is known the current Water Conservancy Construction Inspection and Safety Assessment Methods and Water Conservancy Construction Inspection and Safety Assessment Technical Specifications both do not contain the impact of the fatal factor (tectonic plate faulting). Therefore, for Hsin-shan Dam and A-kung-tien Reservoir, the reservoir management unit could continue to do seepage analysis and seepage monitoring when there was local leakage in the downstream slope of the dam. In this way, they were unable to grasp the leakage path, and the implemented leakage prevention project was also completely unable to function.

3.6 Summary of the Main Points

1. After the piping failure of Renyitan Reservoir spillway, although the seepage analysis, the in-situ tests, and the monitoring plan in the traditional reservoir safety assessment have been continuously carried out, the actual cause of the piping failure is still unable to be effectively grasped.

2. In the traditional reservoir safety assessment, the formula used in the seepage analysis of the dam is the Laplace equation. Since this formula is always under steady state conditions and conserving of ellipticity, it can only show structure analysis results of dam body under stable conditions. However in the analysis of the leakage in the downstream slope of the dam body, as the particles are lost during the leaking process, the formula adopted is not under steady state conditions. In addition, because the ellipticity will be lost with the loss of particles, the analysis results of an unstable dam body structure can be shown. This is the main reason why the leakage path and piping failure cause cannot be grasped by seepage analysis methods.

3. For the leakage on the downstream slope of the dam body, the analysis of an unstable dam body structure is very complex and time and energy consuming. For the sake of simplicity, this dissertation takes Renyitan Reservoir spillway as an example. Firstly, the shear band model around the spillway was built in order to illustrate the cause of the spillway

bottom plate rupture, side wall dislocation and bending deformation of the side wall in the 1022 Chiayi earthquake, and to assist in identifying the location of the pipe-shaped discharge tunnel. Secondly, based on the slope conditions, particle properties, and diameter evaluation, the bottom critical velocity required to cause a piping failure was evaluated, so as to further grasp the causes of piping failure.

4. The cause of the piping failure of Renyitan Reservoir spillway is as follows: in the 1022 Chiayi earthquake, the shear bands around the spillway extended to the spillway bottom plate and the side wall foundation, and the pipe-shaped discharge tunnel required for piping failure was gradually formed during the flooding period after Typhoon Kong-Rey. The width and height of the pipe-shaped discharge tunnel were rapidly increasing after the continuous loss of the particles. When the bottom velocity was increased to the bottom critical velocity corresponding to the particles of 35cm diameter, which is required for piping failure, the piping failure of maximum particle size of 35cm was then induced.

5. Since the vast majority of earthquakes in the world are tectonic earthquakes and the most destructive earthquakes are also tectonic earthquakes, four recommendations with regard to piping failure caused by shear bandings are made as follows:

   (1) The "Water Conservancy Construction Inspection and Safety Assessment Methods" and "Water Conservancy Construction Inspection and Safety Assessment Technical Specifications" of seismic zones should include tectonic plate faulting effect into the specification.

   (2) The construction of the shear banding monitoring network the monitoring frequency should be clearly regulated.

   (3) The test result of “the dam body material strength parameter decreasing with the increase of the cumulative shear banding” should be regulated to be provided, in order to avoid carrying out the static and dynamic analysis using the same dam body material strength parameter in the reservoir safety assessment once every five years.

   (4) The warning value of the dam body material strength parameter after weakening should be clearly defined, in order to further ensure that piping failure does not happen in the tectonic plate faulting.

Chapter 4

Null Construction-Induced Neighbor Damage Methods

T.-S. Hsu, K.-T. Shen and Y.-M. Huang

4.1 Introduction

For two neighboring buildings built in different eras, if the new building induces leaning on the old building (Figure 4.1) or cracking (Figure 4.2) during construction, which then results in disputes, according to different laws or regulations, these disputes shall be judged as construction neighboring damage disputes.

Figure 4.1. The leaning phenomena in neighboring buildings caused by construction in Luzhou District of New Taipei City (background picture is from Wang, 2012)

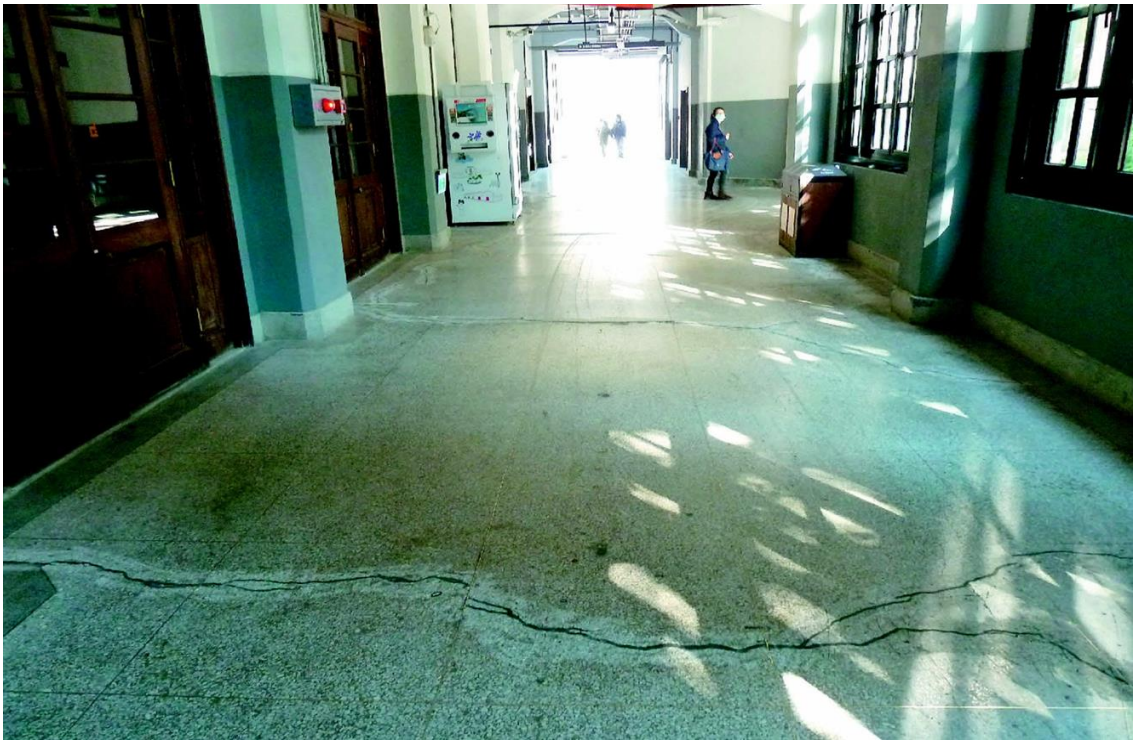

Figure 4.2. The cracking phenomena in neighboring buildings caused by construction of the Taipei Dome project in Songshan District of Taipei City (Zhou, 2017)

Current laws, regulations, rules, and authentication manuals that exist to deal with any leaning or cracking problems in neighboring buildings induced by construction include: Article 69 of the Building Law (Ministry of Interior, 1995), Article 6 of the Environmental Impact Assessment Law (Department of Environmental Protection Administration Institute, 1999), Article 8.6 of the Structural Design Standard for the Foundation of Buildings (Ministry of Interior, 2001), Article 25 of the Taipei Building Management Rules (Government of Taipei City, 1974), and the Taipei Building Construction Neighboring Damage Authentication Manual (Government of Taipei City, 2006), etc.

It can be seen that the government has simplified complicated leaning or cracking issues in neighboring buildings induced by construction into neighboring damage problems, and the elements of neighboring damage, the authentication methods, and the compensation are regulated by rules, regulations, and authentication manuals.

The purpose of good laws, regulations, rules, and authentication manuals is to prevent the problems from happening again, however, for construction neighboring damage problems, reoccurrence is almost

inevitable according to previous construction and excavation experience in metropolitan areas. It can also be proven by the fact that in Kaohsiung, every construction site has to set aside 500 million New Taiwan dollars for neighboring damage compensation before the start of construction.

Secondly, it is not rare to see neighboring damage disputes induced by construction in metropolitan areas. Take Kaohsiung as an example, there were 295 construction neighboring damage disputes in 1.5 years between January 1991 and July 1993, in which 2024 households were affected and the compensation amount was up to billions of New Taiwan dollars (Central News Service, 2013).

For large-scale development cases, both the range of neighboring damage and the number of households affected are enormous. In addition, as the compensation is too high, aside from security of living problems after building damage, the victims also need to contend with tediously-long contentious procedures, which often lead to a lose-lose situation for both sides of neighboring damage disputes.

As the existing laws, regulations, rules, and authentication manuals cannot effectively prevent construction neighboring damage problems from occurring, there is obvious room for these laws to be improved.

In the past, the government of Kaohsiung once authorized the Civil Engineering School of National Kaohsiung University of Applied Sciences to establish the “Talents Training & Authentication Center of Retaining Wall Excavation & Neighboring Household Protection”, in the hope of cultivating talents to deal with construction neighboring damage problems, in order to protect people’s security of living and properties. In July 1993, the construction management department of Kaohsiung government claimed that any buildings more than 50 meters high or with more than two floors at basement level must pass the inspections of construction-planning consulting organizations.

Under the active training and management of the Kaohsiung government, between July 1993 and June 2004, the number of construction neighboring damage disputes declined dramatically however, these disputes could still not be eliminated (Figure 4.3). The essential reason is that the specialists and scholars who draft the laws, regulations, rules, and authentication manuals concentrate on the techniques of excavating retaining walls but they neglect other reasons that induce neighboring damage. In this case, the construction-planning consulting organization can only advise the construction sites where neighboring damage is likely to occur with technical

advice such as ground modification or retaining walls enhancement. However, ground modification or retaining walls enhancement can only resolve part of the neighboring damage problems rather than completely solve the problems.

In this regard, based on ultimate foundation bearing capacity contours, stress contours, decline of ground water table, and ground water table in the pressure aquifer of shear banding tilted slopes, this chapter will discuss neighboring buildings of different eras from the point of view of who was responsible for the infringing behaviors, the new builder or the old builder?

After revealing the essence of the infringement issues of neighboring damage, this chapter will propose null-neighbor-damage methods based on ultimate foundation bearing capacity contours, stress contours, decline of ground water table, and ground water table in the pressure aquifer of shear banding tilted slopes.

(a) Cracking on neighboring roads

(b) Depression and cracking on neighboring buildings

Figure 4.3. The neighboring damage problems induced by consistent excavation on slurry wall trenches in the building construction site at the cross road of Ziqiang Road and Qingnian Road in Kaohsiung (Huang, 2016)

Finally, the chapter takes Cathay Pacific Tienmu Shopping Mall as an example, exploring the reasons for the occurrence of neighboring damage in the range of 9.2~12.6 times the excavated depth. This chapter also discusses, after construction neighboring damage occurs, why there are some problems that still cannot be settled effectively even after authorized national scholars and specialists investigate and research the cases.

The neighboring area of this construction site consists of shear banding tilted slopes, and the tilted slopes contain a high-permeable pyroclastic deposit layer. The pyroclastic deposit layer is a kind of pressure aquifer, so it is beneficial for comprehending the reasons for special neighboring damage problems and producing effective solutions by deeply understanding the behaviors of shear banding tilted slopes.

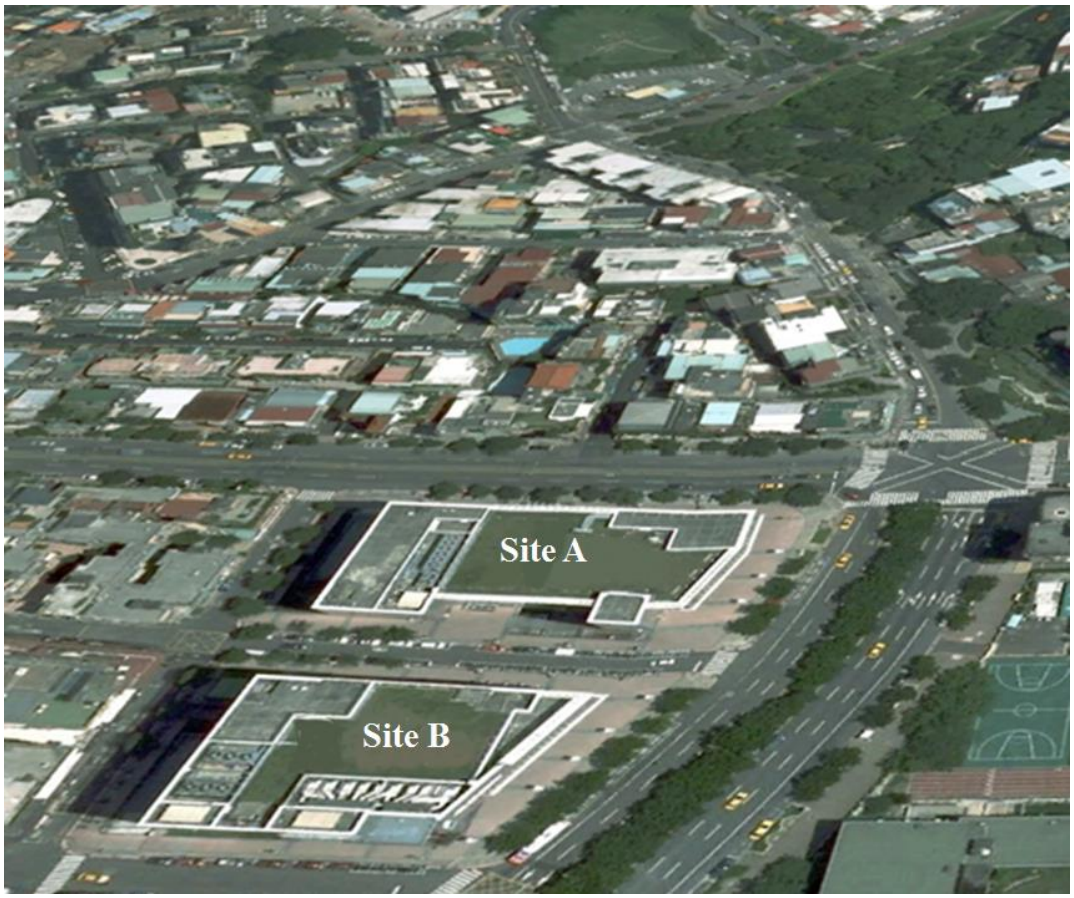

(a) Site A and Site B

(b) Site A, Site B, and shear banding tilted slopes.

Figure 4.4. Cathay Pacific Tienmu Shopping Mall and neighboring territories (Google Earth, 2017)

4.2 Literature Review

4.2.1 Foundation Ddisplacement Induced by Slurry Wall Construction

Foundation displacement induced by groove excavation. Although stabilizing liquid exists in the trenches of slurry walls, the unit weight of stabilizing liquid is smaller than the soil thus, groove excavation could still lead to ground settlement if the pressure is released laterally.

With regard to groove excavation on slurry walls, Cowland and Thorley (1985) stated that the displacement of a slurry wall when excavation is just completed can be up to 40%~50% of the total displacement during the whole excavation; Clough and O'Rourke (1990) analyzed cases and demonstrated that during slurry wall construction, the ratio of the maximum ground settlement δ_{vm} and groove depth H_t (δ_{vm}/H_t) is 0.15%. Ou and Yang (2000) also claimed that for slurry wall excavation, the δ_{vm}/H_t is 0.05% in a single unit excavation, while it is 0.07% in a multi-unit excavation.

The maximum ground settlement usually occurs within a range of 0.3 H_t from a unit of slurry wall groove, among which within the range of 0.5 H_t from slurry wall trenches is the most sensitive section. However, for sections 1.0 H_t from a slurry wall, effects are unremarkable. Figure 4.5 shows that δ_{vm}/H_t is approximately 0.13% after the entire slurry wall construction is completed, and ground settlement amounts in the range of 1.5~2.0 H_t are nearly negligible.

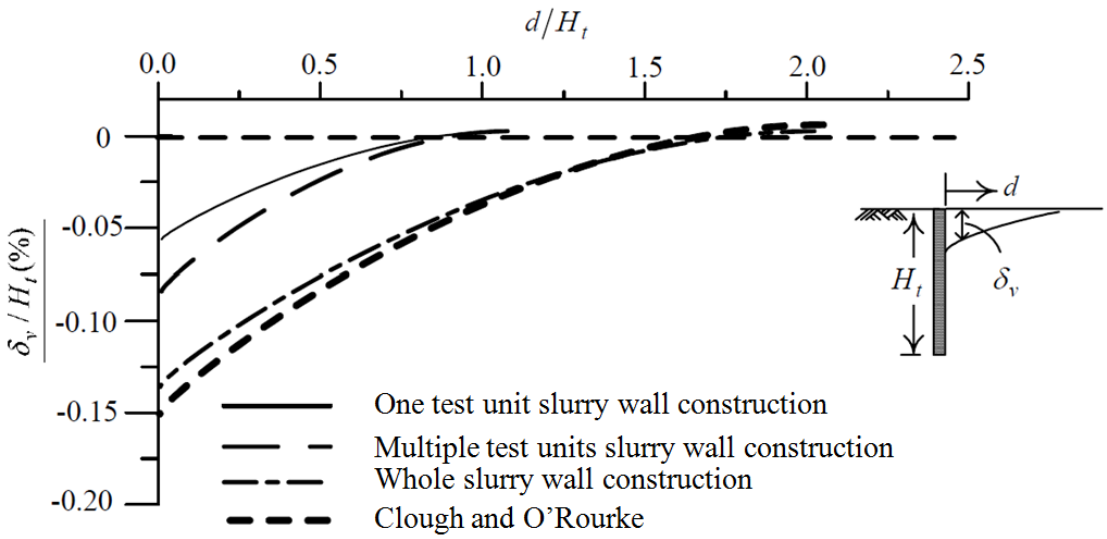

Figure 4.5. Comparisons of envelope curves of ground settlement in slurry wall construction (Ou and Yang, 2000)

4.2.2 The Characteristics of Retaining Walls Displacement Induced by Excavation

Clough and O'Rourke (1990) indicated that excavation can deform retaining walls, the deformed retaining walls are shown in Figure 4.6:

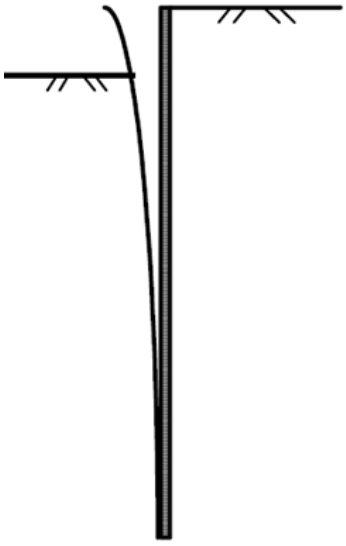

(a) Cantilever type in earlier stage

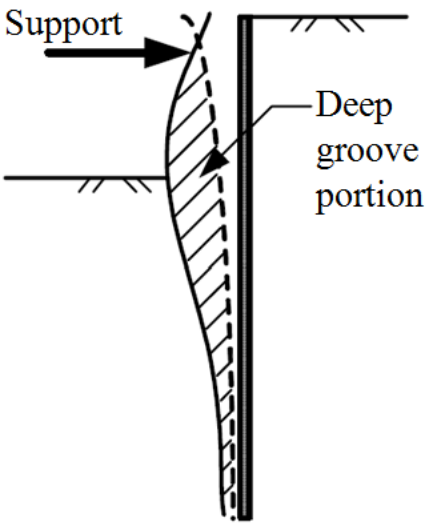

(b) Big-belly type in later stage

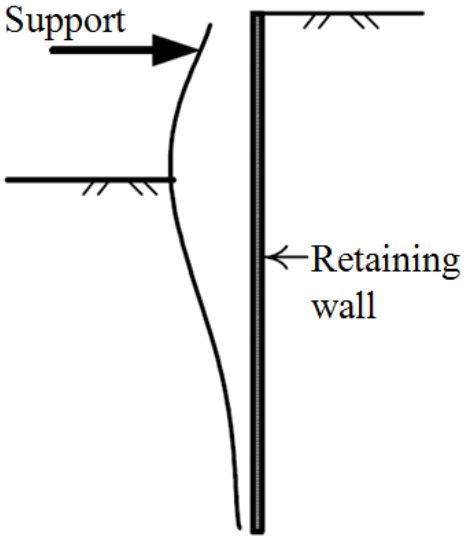

(c) Combination of earlier and later stage deformation

Figure 4.6. The shapes of deformed retaining walls induced by excavation (Ou, Hsieh and Chiou, 1993)

4.2.3 The Maximum Lateral Displacement of Retaining Walls Induced by Excavation

For excavation in a clay layer, when steel sheet piles and horizontal slats are used as supports, the ratio of the maximum lateral displacement of steel sheet piles and the depth of excavation, δ_{hm}/H_e, changes with FS, the safety coefficient of hump resistance. When FS is smaller than 1.5, δ_{hm}/H_e will dramatically increase (Mana and Clough, 1981; Hsieh, 2001).

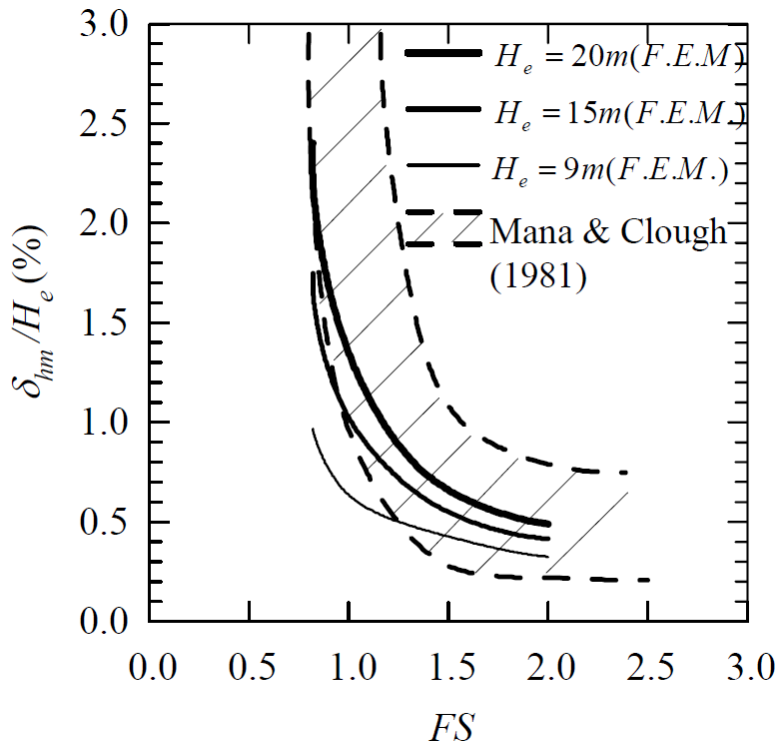

Figure 4.7. Curves showing how δ_{hm}/H_e changes with the increase of safety coefficient (Hsieh, 2001)

For excavations in a stiff clay layer, residual soil layers, and sandy soil layer, Clough and O'Rourke (1990) indicated that the average value of δ_{hm}/H_e is 0.2%~0.3%, and only when constructions have flaws or the penetration depth of the retaining walls is insufficient can δ_{hm}/H_e be larger than 0.5%.

For excavation in a soft clay layer, δ_{hm} correlates with *FS*. When considering FS, retaining walls strength *EI*, and average distance of support h_{avg} together, Clough and O'Rourke (1990) demonstrated in Figure 4.8: (1) when FS=3.0, δ_{hm}/H_e < 0.5% ; (2) when $FS \leqq 1.4$, δ_{hm}/H_e increase dramatically and in this case retaining walls strength EI has a great influence on δ_{hm}/H_e; (3) When $FS \leqq 1.1$, although the construction quality is good, δ_{hm}/H_e can still be larger than 2.0%.

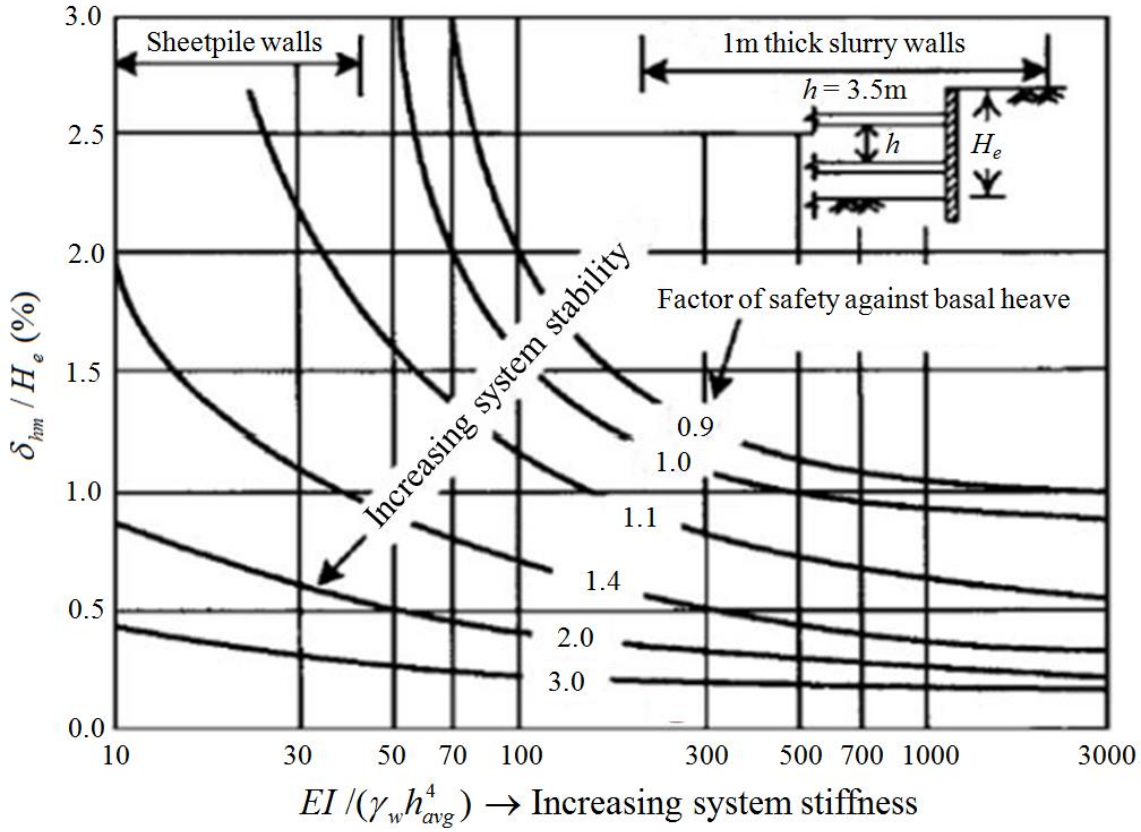

Figure 4.8. Correlating curves of $\delta_{hm}/H_{e,}$ strength of support system EI and FS (Clough and O'Rourke, 1990)

Ou et al. (1993) drafted a figure (Figure 4.9) indicating a correlation between δ_{hm} and H_e based on construction cases using high-stiffness prepakt mortar piles or a slurry wall.

$$\delta_{hm} = (0.2\% \sim 0.5\%)H_e \qquad \text{(Eq. 4.1)}$$

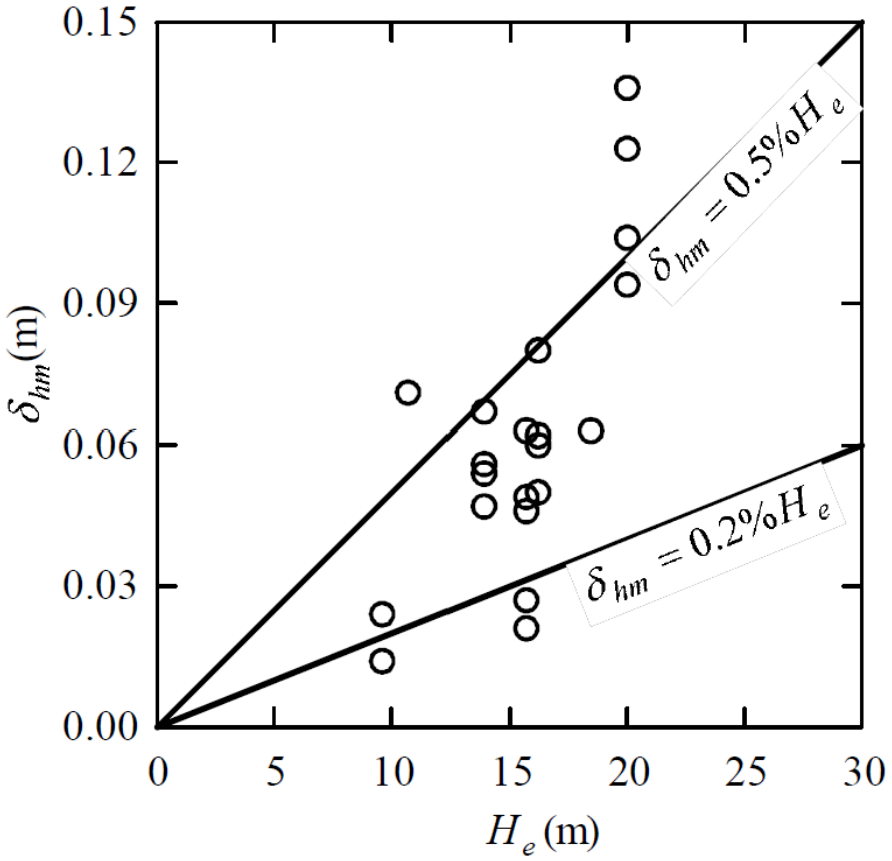

Figure 4.9. Correlation figure between retaining walls δ_{hm} and excavation depth H_e (Ou et al., 1993)

4.2.4 Ground Settlement Caused by Excavation

Generally speaking, excavation can lead to earth pressure disequilibrium inside and outside the construction site, which can result in lateral displacement of the retaining walls and ground settlement on the back of the retaining walls.

Hsieh and Ou (1998) indicated that the types of ground settlement on the back of the retaining walls induced by excavation are concave type and spandrel type, as shown in Figure 4.10.

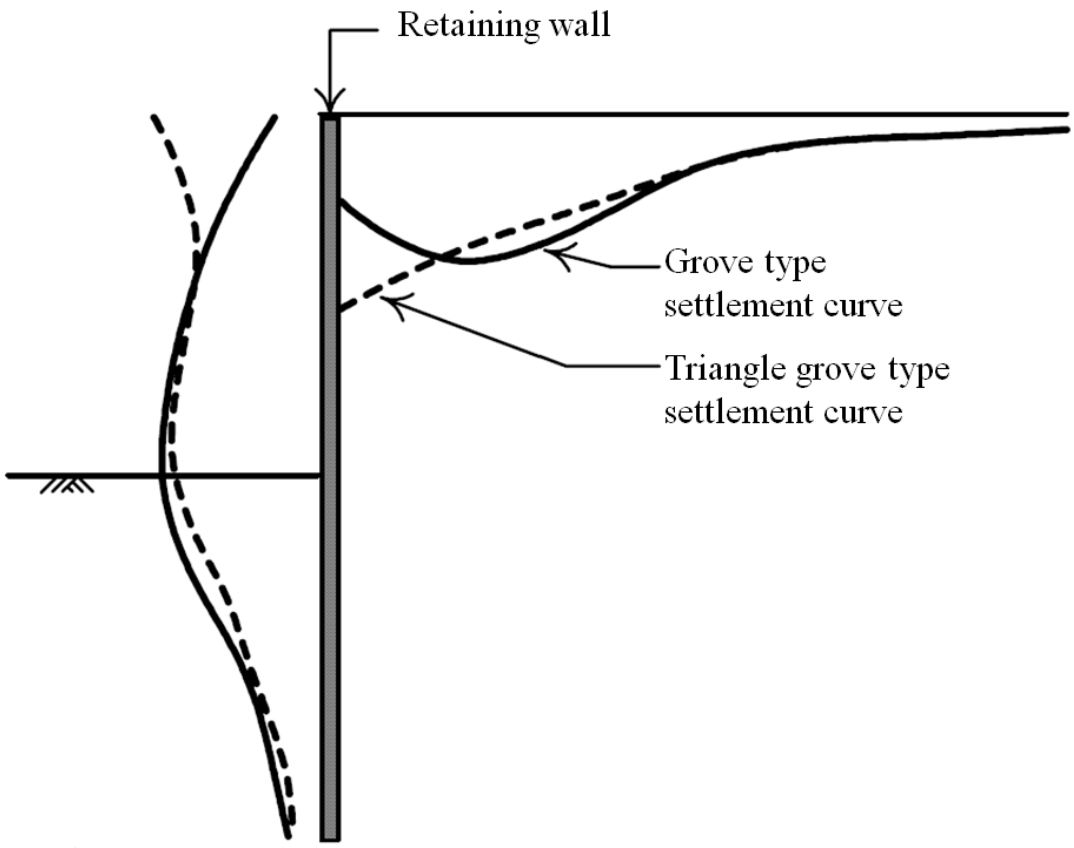

Figure 4.10. The types of ground settlement caused by excavation (Clough and O'Rourke, 1990)

Spandrel Type. If a moderately big lateral displacement occurs on the retaining walls when the excavation depth is just 1~2 meter in the first stage, but in the later excavations, the lateral displacement on the retaining walls is small, then the type of ground settlement on the back of retaining walls is spandrel type.

Concave Type. If the displacement of the retaining walls is small in the first stage when the excavation depth is 1~2 meters, but the lateral displacement of retaining walls consistently increases in the later excavations, and the maximum lateral displacement of the retaining walls occurs on the excavated surface, then the type of ground settlement on the back of retaining walls is concave type.

Hsieh and Ou (1998) defined the area of the cantilever component A_c and area of the deep inward components A_s using a formula of lateral displacement of the retaining walls as shown in Figure 4.11.

$$A_C = Max(A_{C1}, A_{C2}) \quad \text{(Eq. 4.2)}$$

In Equation 4.2 where

A_{c1}: area of the cantilever at the completion of first stage.

A_{c2}: area of the cantilever at the completion of final stage.

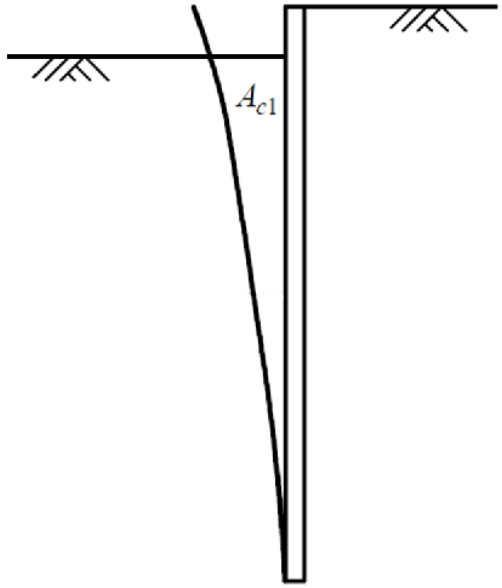

(a) Excavation of first stage

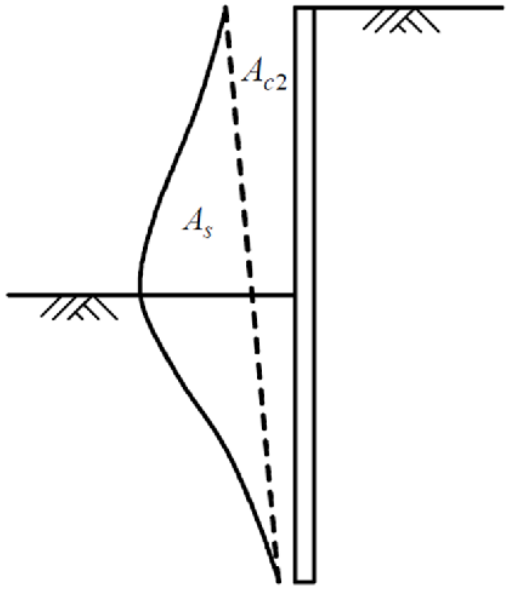

(b) Completion of excavation

Figure 4.11. Definition of the area of cantilever component and area of the deep inward components in lateral deflection of retaining walls (Hsieh and Ou, 1998)

Figure 4.12 shows the relationship between the retaining walls lateral displacement and ground settlement based on A_c and A_s from 16 excavation cases according to Hsieh and Ou (1998). From Figure 4.12, it can be seen that when $A_s > 1.6A_c$, the type of ground settlement is concave; when $A_s < 1.6A_c$, the type of ground settlement is spandrel; Therefore, the relationship above can be used to determine the type of ground settlement.

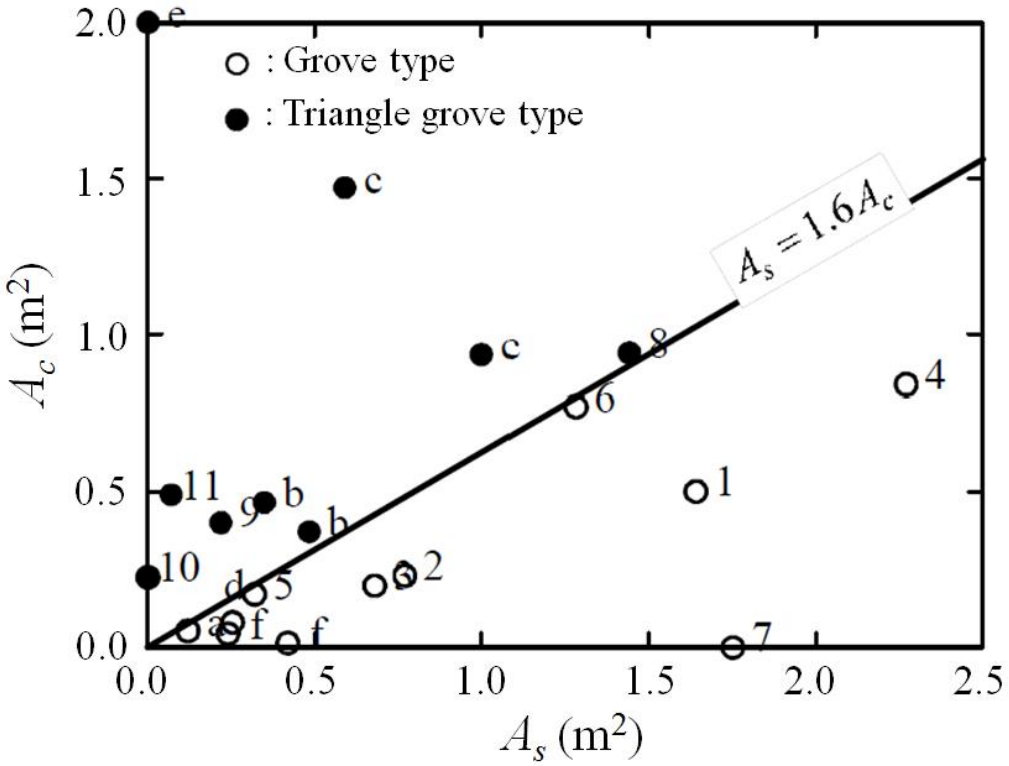

Figure 4.12. Relationship of ground settlement and retaining walls lateral displacement (Hsieh and Ou, 1998)

4.2.5 The Range of Ground Settlement Induced by Excavation

Milligan (1983) and Nicholson (1987). In undrained cases, when excavating a clay layer and super soft sandy layer, the range of ground settlement at the back of the retaining walls is the potential depth of retaining walls lateral displacement, H_0.

Clough and O'Rourke (1990). When excavating a sandy layer and medium stiff clay layer, the range of ground settlement at the back of the retaining walls is $2H_e$; when excavating stiff or super stiff clay layers, the range of ground settlement at the back of the retaining walls is $3H_e$.

Woo and Moh (1990). When excavating the Taipei basin, the range of ground settlement at the back of the retaining walls is up to4 H_e ~5H_e.

Hsieh and Ou (1998) and Ou and Hsieh (1999). They suggested the concepts of primary influence zone, *PIZ*, and secondary influence zone, *SIZ*. The slope of ground settlement in the *PIZ* is steep, which has greater impact on buildings. The slope of ground settlement in the *SIZ* is gentle which has less impact on buildings.

In Equations 4.4 and 4.5, H_g is the depth of stiff soil layer, B is the width of excavation surface, H_f is depth of bottom of soft clay layer; the range of *SIZ* is almost same as the range of *PIZ*.

$$PIZ = \text{Max}(PIZ_1,\ PIZ_2) \qquad \text{(Eq. 4.3)}$$

$$PIZ_1 = \text{Min}(2H_e\ ,\ H_g) \qquad \text{(Eq. 4.4)}$$

$$PIZ_2 = \text{Min}(H_f\ ,\ B) \qquad \text{(Eq. 4.5)}$$

4.2.6 The Position of Maximum Ground Settlement Induced by Excavation

1. Spandrel type

The position of maximum ground settlement is tightly close to the retaining walls.

2. Concave type

Nicholson (1987) suggested:

The distance between the position of maximum ground settlement and the retaining walls $D_m = 0.5H_1$, where H_1 is the depth of maximum retaining walls lateral displacement.

Ou and Hsieh suggested(1998):

D_m does not change with excavation depth H_e, D_m=0.3PIZ。

4.2.7 The Maximum Ground Settlement Induced by Excavation

1. Milligan (1983) suggested:

When excavating soft and saturated soil under undrained conditions, the volume covered by the lateral displacement of the retaining walls is similar to the volume covered by the ground settlement.

2. Mana and Clough (1981), Ou etc (1993), Hsieh and Ou (1998) suggested:

$$\delta_{vm} = (0.5 \sim 0.75)\delta_{hm} \qquad \text{(Eq. 4.6)}$$

In Equation 4.6, sandy soil adopts the lower limit, clay soil adopts the upper limit, but δ_{vm} of soft clay may be larger than $1.0\delta_{hm}$

3. Hsieh (2001) suggested according to Figure 4.13:

$$\delta_{vm}/H_e(\%) = 0.24[\delta_{hm}/H_e(\%)]^2 + 0.52[\delta_{hm}/H_e(\%)] \qquad (4.7)$$

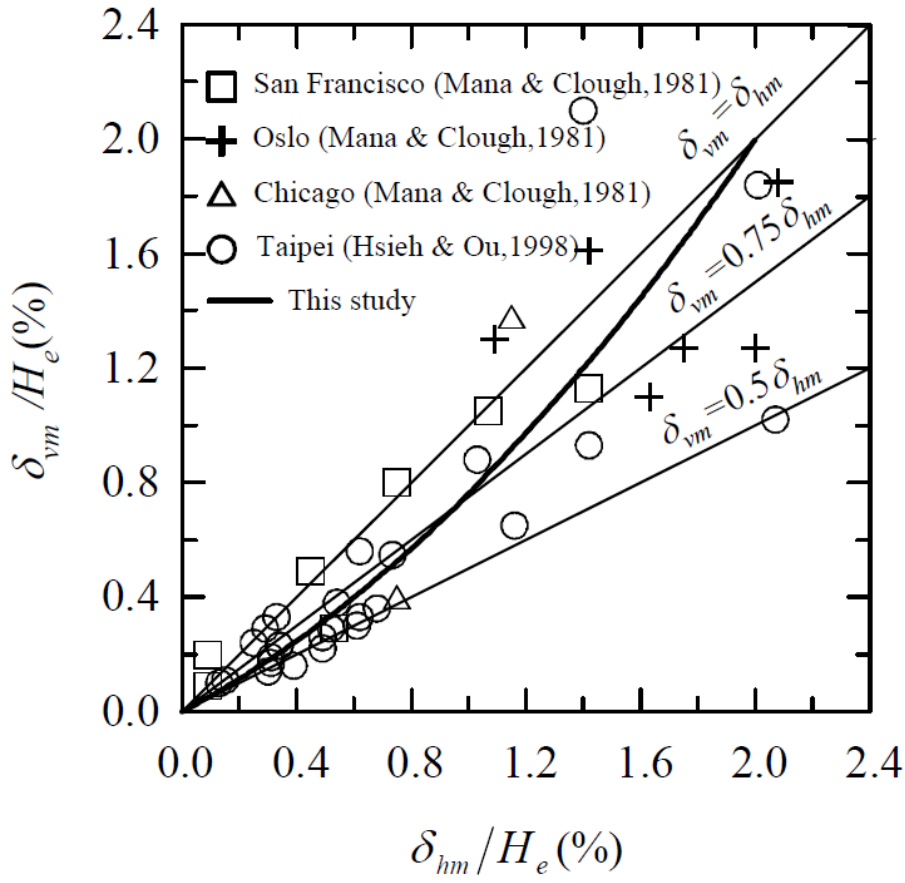

Figure 4.13. The predicted and actual measured curves of relationships ofδ_{vm}/H_e *and* δ_{hm}/H_e (Hsieh, 2001)

4.2.8 Assessment of Foundation Displacement Induced by Construction

1. Method of elastic foundation beams

The method of elastic foundation beams uses springs to simulate the interactions between soils and foundations, in which Winkler (1867) model is most widely used.

In Figure 4.14a, retaining walls are considered as elastic foundation beams, where the soil on both sides of the retaining walls is simulated as a series of springs.

Before excavation, the soil on both sides of the retaining walls is at rest earth pressure (see Figure 4.14b); after excavation, the soil at the back of the retaining walls is at pressure release status. Figure 4.14c shows that under the lateral disequilibrium pressure $p_{02}-p_{01}$, some displacement occurs on

beams on the elastic foundation; whereas under this displacement, the earth pressure outside the retaining wall is reduced to $p_0 - k_h\delta$, where k_h is the coefficient of horizontal subgrade reaction, δ is lateral displacement of the retaining walls. If the soil is hypothesized to not bear any tension, then the minimum of the lateral earth pressure is the lateral earth pressure under the active failure state.

The soil below the excavation surface is under lateral squeezing pressure from the retaining walls, which increase the earth pressure to $p_0 + k_h\delta$. However, Figure 4.14d shows, under lateral squeezing of the retaining walls, the lateral earth pressure can only increase to the lateral earth pressure under passive failure state.

For soil next to the retaining walls, the state of soil, either the active failure state or the passive failure state, is regarded as plastic state. Under the plastic state, Mohr's circle is tangential to the Mohr-Coulomb failure envelope.

When the lateral earth pressure is larger than the active earth pressure (or smaller than the passive earth pressure), since Mohr's circle is below the Mohr-Coulomb failure envelope, the soil state is regarded as elastic state.

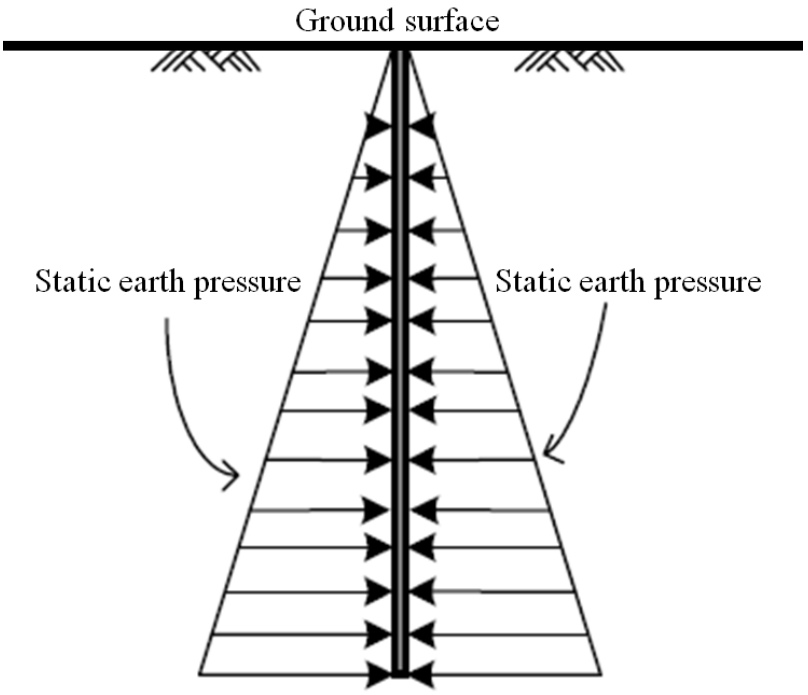

(a) Retaining walls at rest conditions before excavation

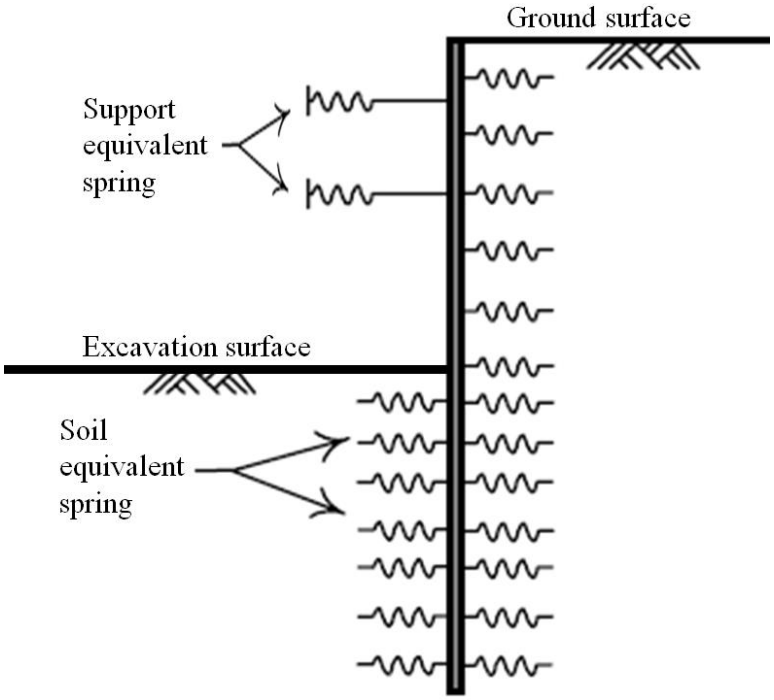

(b) Springs are installed at both sides of continuous beam after excavation

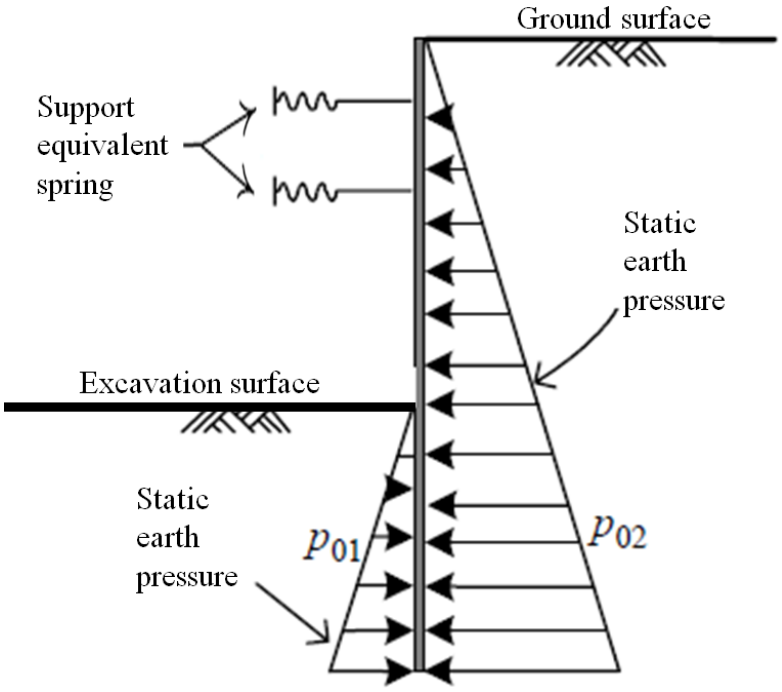

(c) The earth pressure profile on both sides of continuous beam before the displacement of retaining walls after excavation

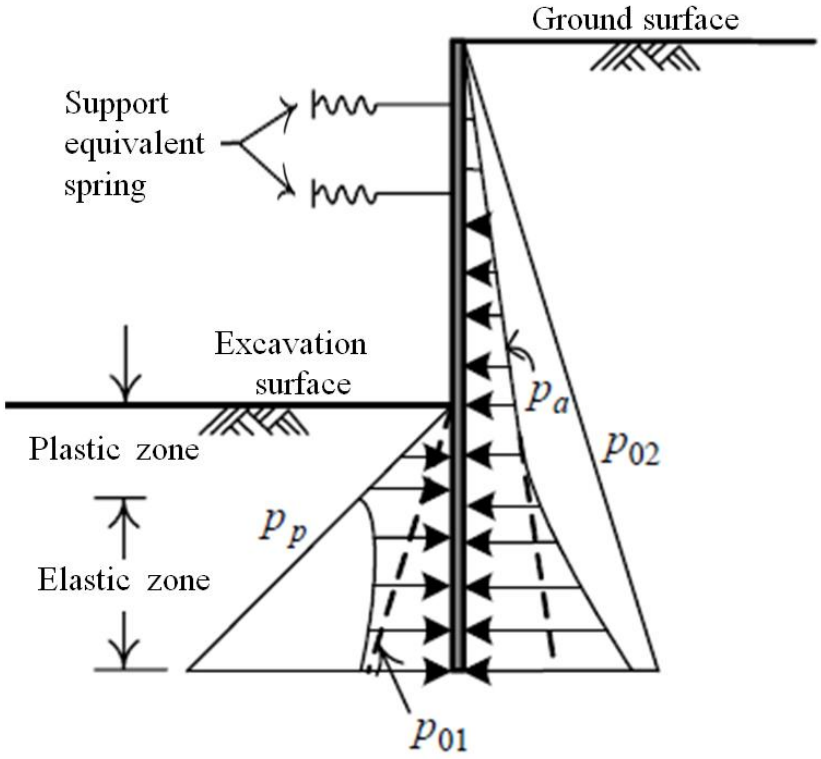

(d) The earth pressure profile on both sides of continuous beam after the displacement of retaining wall after excavation

Figure 4.14. The double-side elastic foundation beams method on foundation displacement induced by excavation (Winkler, 1867)

Figure 4.15 demonstrates another analysis mode for elastic foundation beams, where the lateral support system of the retaining walls after excavation is replaced by equivalent springs in the simulation, and the lateral support system from soil under the excavation surface is simulated by series of springs. Lateral pressure exerting on the retaining walls, when above excavation surface, is considered active earth pressure, when it is below the excavation surface, it is considered the pressure difference between the active earth pressure and passive earth pressure.

At each stage of excavation, the active earth pressure on the back of the retaining walls must be equivalent to the lateral support forces of the retaining walls and all spring forces. When the spring force somewhere is smaller than the passive earth force, soil in this place is in an elastic state (see Figure 4.15b); when the spring force somewhere is greater than the passive earth force, then the spring force at this place is made equal to passive earth force, and soil in this place is in the plastic state.

In this analysis mode, when considering the impact of excavation width, the active earth pressure below the excavation surface is hypothesized to increase with the depth and converge to a point of convergence, where the depth of the point of convergence is equal to the width of the excavation surface, but in principle does not exceed the depth of hard soil (see Figure 4.15).

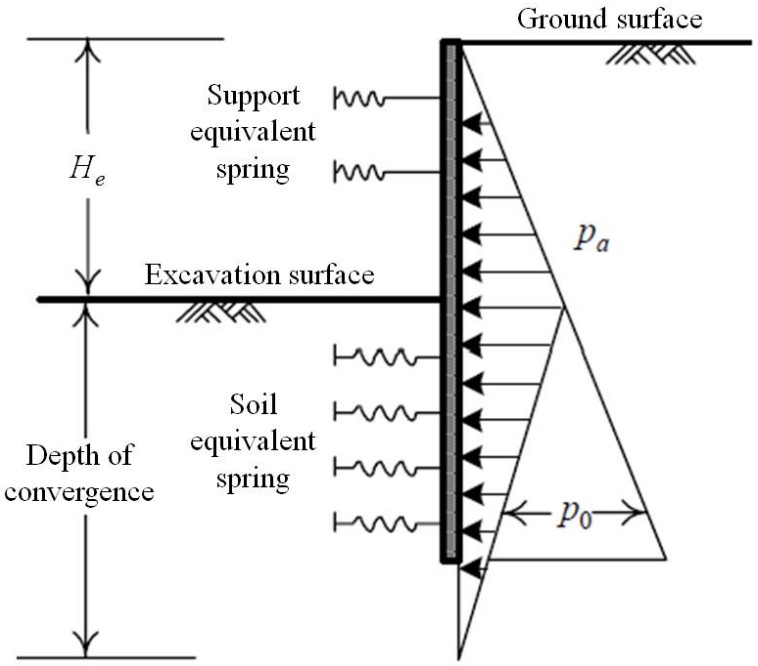

(a) Install springs on only one side of continuous beams

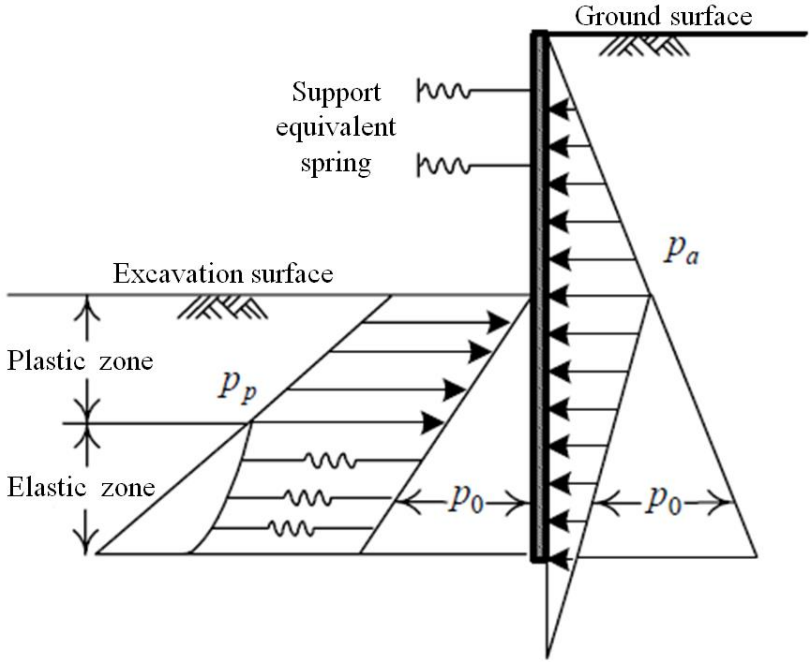

(b) Earth pressure profiles on both sides of continuous beams

Figure 4.15. One-side elastic foundation beams method on foundation displacement induced by excavation (Miyoshi, 1977)

Since the analysis mode of the elastic foundation beam method is simple and the parameters are easy to obtain, it is broadly used in construction. However, the elastic foundation beam method can only assess retaining walls displacement.

2. Finite element analysis or finite difference analysis

When using finite element analysis or finite difference analysis to conduct engineering analysis of excavations, the retaining walls and soil must be meshed first, and then the element types and the constitutive models will be defined on each element according to material properties; finally, the deformation, deflection, and stress induced by excavation on each element can be solved.

Finno and Harahap (1991), White etc. (1993), and Wang (1999) used finite element analysis or finite difference analysis to simulate excavations; the lateral displacement of the retaining walls in the result is in accordance with the monitoring displacement, however the ground settlement is different to the monitoring data.

Hsieh et al. (2003) proposed a stress-strain model where the undrained and the strain softening behaviors of clay can be simulated by using a small strain model; Figures 4.6 and 4.17 show that such a model can improve the inconsistency of ground settlement between simulation and monitoring data mentioned above.

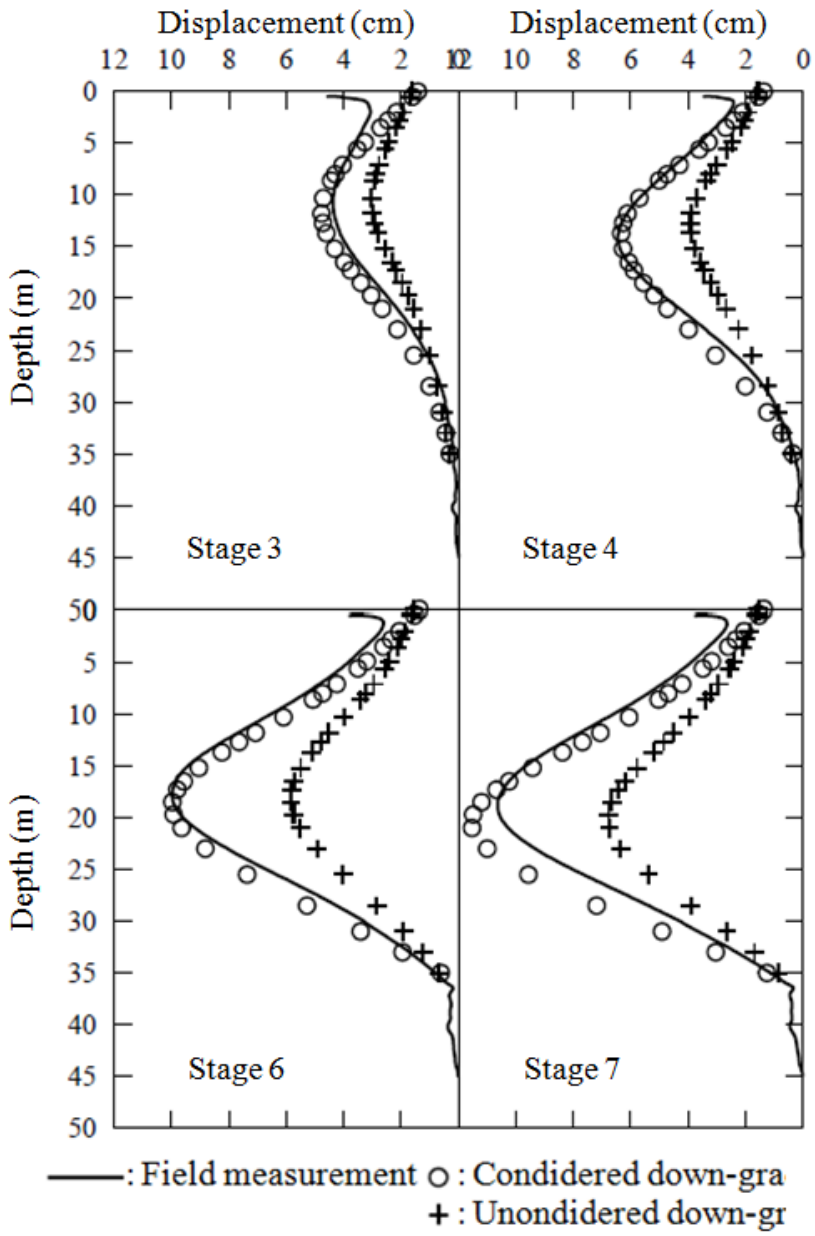

Figure 4.16. Comparison of simulation and monitoring results of lateral displacement of retaining walls induced by excavation (Hsieh et al., 2003)

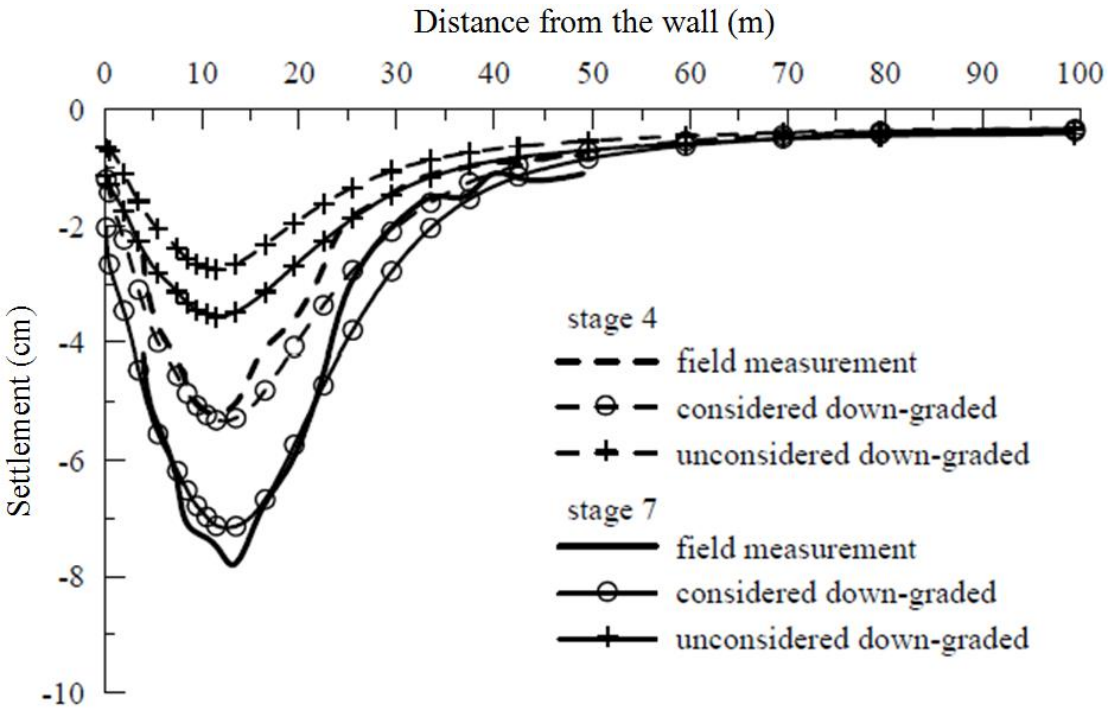

Figure 4.17. Comparison of simulation and monitoring results of ground settlement induced by excavation (Hsieh et al., 2003)

3. Empirical methods

Analysis of Lateral Displacement of Retaining Walls. Besides soil, the factors that influence the lateral displacement of the retaining walls also include excavation depth, excavation width, penetration depth of retaining walls, stiffness of retaining walls, stiffness of support, support configuration, prestress, etc., so it is difficult to describe the influence of all factors with one formula, one figure, or one table.

Analysis of Ground Settlement.

(1) Peck method

In 1969, based on materials in Chicago and Oslo, Peck (1969) compiled methods of predicting ground settlement induced by excavation. For soil layers with different properties, when *d* is the distance between the retaining walls and some point on the back of retaining walls, Figure 4.18 illustrates the relationship curve of ground settlement δ_v and *d*, where soil with different properties will be divided into three zones by retaining walls.

Zone I: Under general construction quality, suits sand or soft to stiff clay.

Zone II: a. suits very soft to soft clay

(a) The depth of the clay layer beneath the excavation surface is finite.

(b) The depth of the clay layer beneath the excavation surface is very thick, but $N_b < N_{cb}$.

b. settlement is influenced by the difficulties of construction

Zone III: suits very soft to soft clay

The depth of the clay layer beneath the excavation surface is very thick and $N_b < N_{cb}$.

Where N_b: stability coefficient of soil ($\gamma H_e / S_u$)

γ: unit weight of soil

H_e: depth of excavation surface

S_u: undrained shear strength of soil

N_{cb}: critical stability coefficient corresponding to heaving on excavation surface

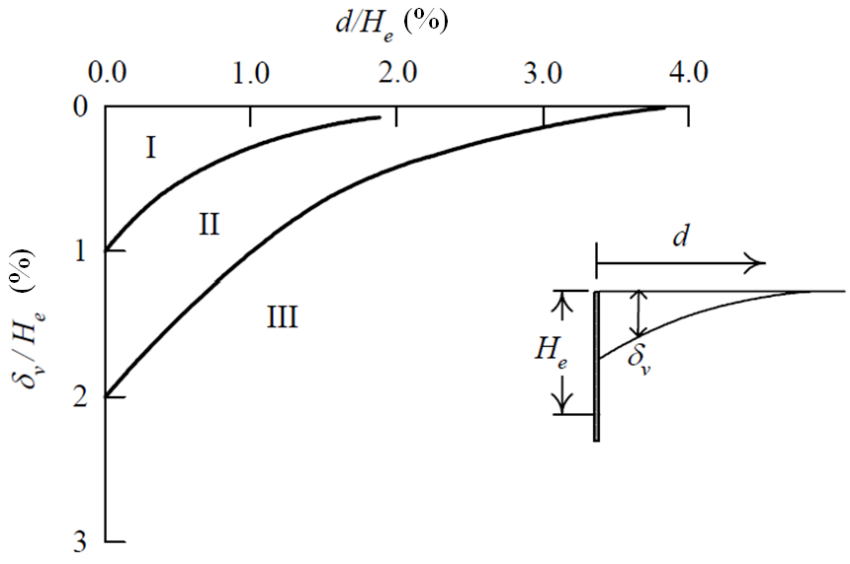

Figure 4.18. Ground settlement predicted by Peck method (Peck, 1969)

The Peck method shown in Figure 4.18 suits excavations between sheet piles and horizontal laths, it is not suitable for excavating a slurry wall.

As the Peck method is too conservative, Clough and Schmidt suggested that when excavating clay layers, the maximum lateral displacement of the retaining walls $\delta_{h\max}$ can be analyzed by the two relationships presented in Figure 4.19.

When lateral displacement of retaining walls is small, $\delta_{h\max} = 1.4\delta_{v\max}$.

When lateral displacement of retaining walls is large, $\delta_{h\max} = \delta_{v\max}$.

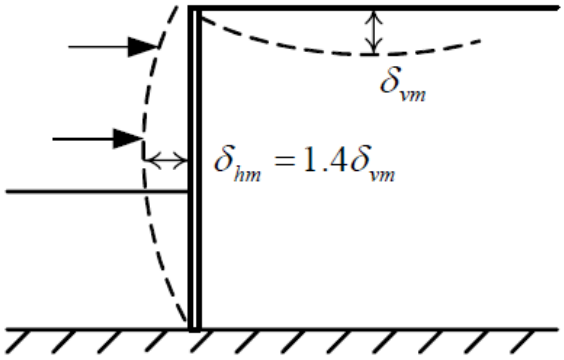

(a) When retaining walls deflection is small

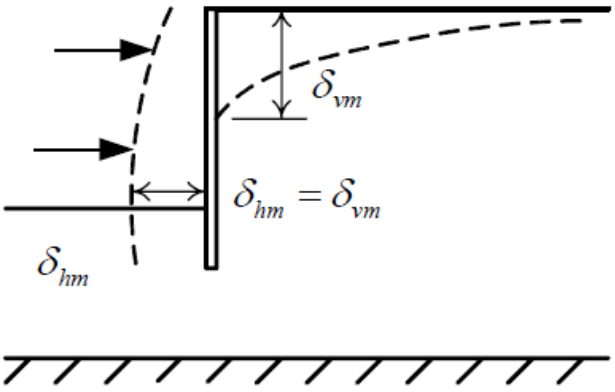

(b) When retaining walls deflection is large

Figure 4.19. Two deflected shapes of retaining walls in clay layer (Peck, 1969)

(2) Finno and Harahap method

When excavating soft clay layers, the retaining walls stiffness EI and clay cohesion are two influential factors of the amount and range of ground settlement. Finno and Harahap (1991), after monitoring material in 10 sites, considered: (1) the relationship between settlement distribution and; (2) the relationship among maximum ground settlement, excavating depth, and clay cohesion (Figure 4.20, 4.21).

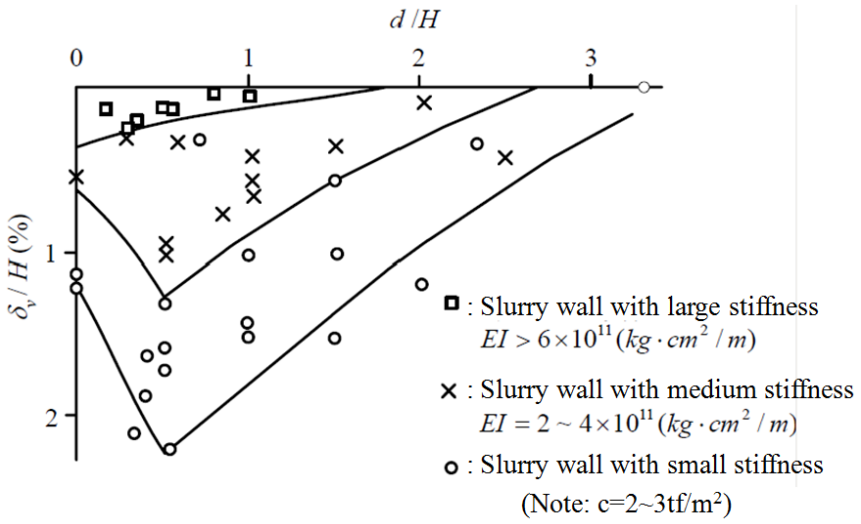

Figure 4.20. Relationship between maximum ground settlement and retaining walls stiffness (Finno and Harahap, 1991)

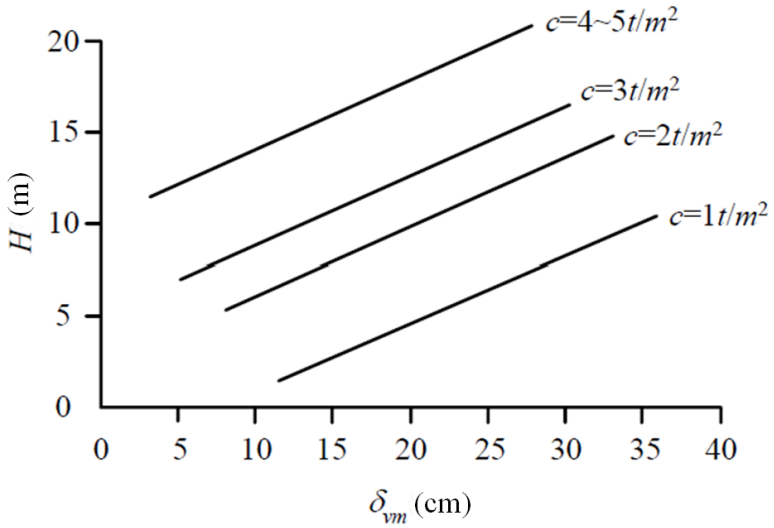

Figure 4.21. Relationship between maximum ground settlement and excavating depth (Finno and Harahap, 1991)

(3) Mana and Clough method

Mana and Clough (1981), under planar deflection conditions, used the elastic-plastic model based on Von-Mises yielding function to simulate the excavation of a clay layer, and they built the relation of δ_{hm}/H and δ_{vm}/H in Figure 4.22 according to monitoring data.

$$\delta_{vm} / H = (0.5 \sim 1.0)\ \delta_{hm} / H \qquad \text{(Eq. 4.8)}$$

After δ_{vm} is derived, Figure 4.23 is then used to estimate the distribution of ground settlement.

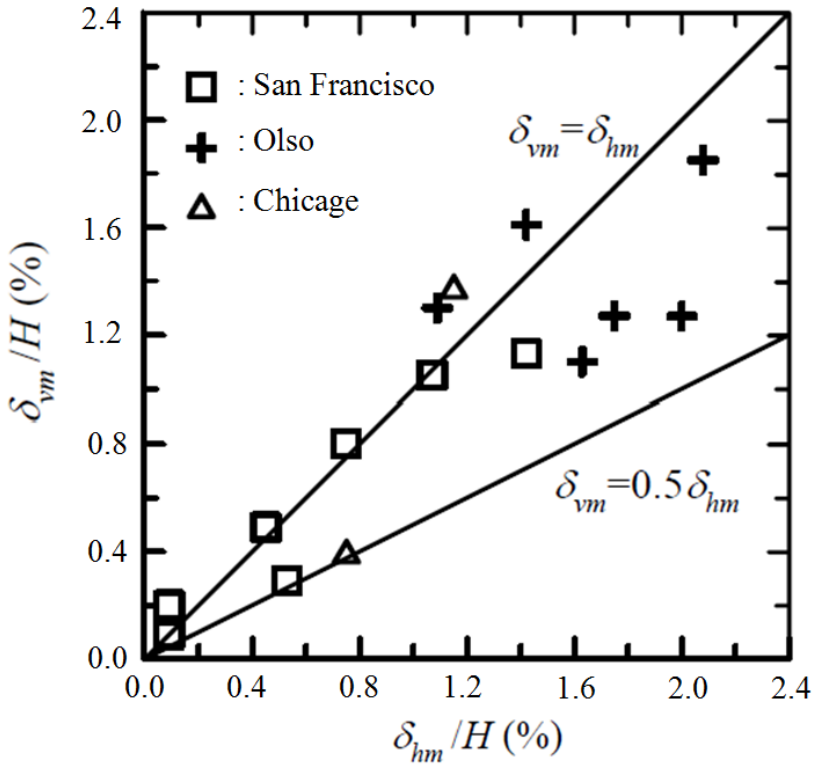

Figure 4.22. The relationship between maximum ground settlement and maximum lateral displacement (Mana and Clough, 1981)

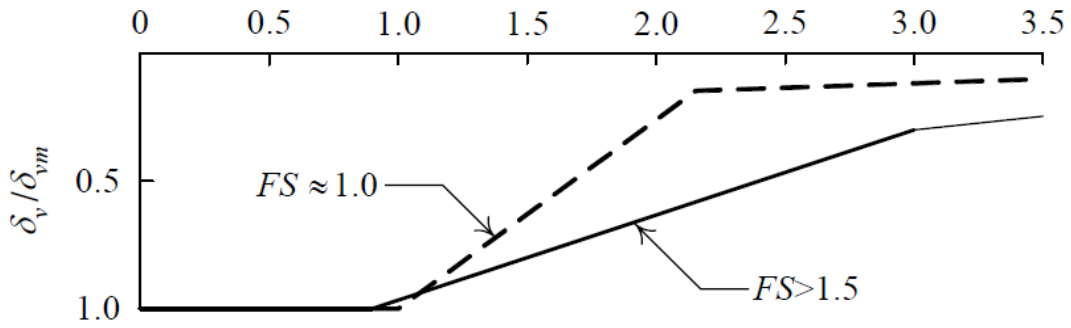

Figure 4.23. Curves of ground settlement (Mana and Clough, 1981)

(4) Matsuo and Kawamura method

Matsuo and Kawamura (1977) monitored the settlement status in eight sites and derived the minimum safety coefficient FS_{min} on the potential glide surface by conducting circular slope stabilization analysis on soil properties of the sites. They then summarized the relationship between maximum ground settlement and minimum safety coefficient in Figure 4.24. Figure 4.25 presents the relationship between minimum safety coefficient FS_{min} and the range influenced by settlement.

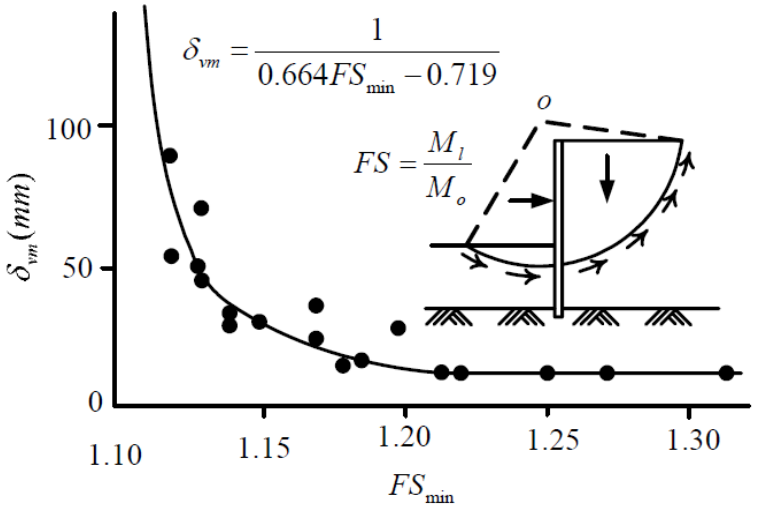

Figure 4.24. Relationship between maximum ground settlement and minimum safety coefficient (Matsuo and Kawamura, 1977)

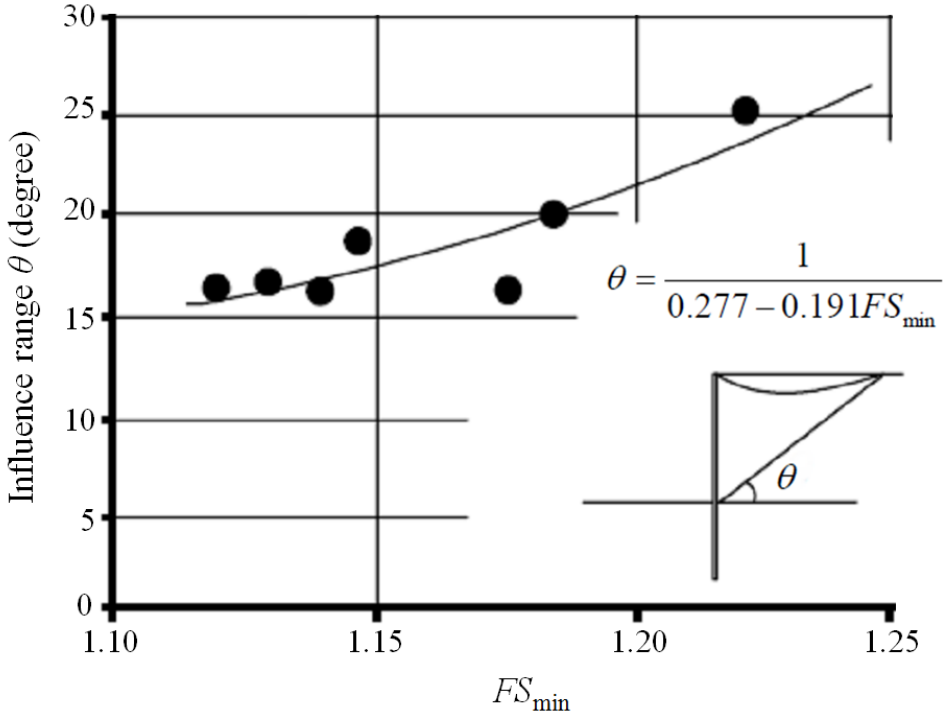

Figure 4.25. Relationship between minimum safety coefficient FS_{min} and the range influenced by settlement (Matsuo and Kawamura, 1977)

Figure 4.24 shows that when FS_{min}<1.15, the maximum settlement tends to increase dramatically. The monitoring materials used in this method are mostly from sites where the retaining walls are mostly made of steel sheet piles or slurry walls and the soil strata are mostly clay layers, the average excavation depth is 14 meters and the depths of retaining walls all reach the bearing layer.

(5) Bauer method

The method proposed by Bauer (1984) is a half-empirical method, which can be used to estimate ground settlement induced by excavation on sand layers (Figure 4.26). Factors include relative density D_r, friction angle ϕ', construction quality, and construction difficulties. The procedures are demonstrated as follows:

a. According to relative density D_r, the settlement ratio r_0 can be defined by the following equation or Figure 4.26b:

$$r_0 = \frac{2-(2D_r)^{1/2}}{100} \tag{4.9}$$

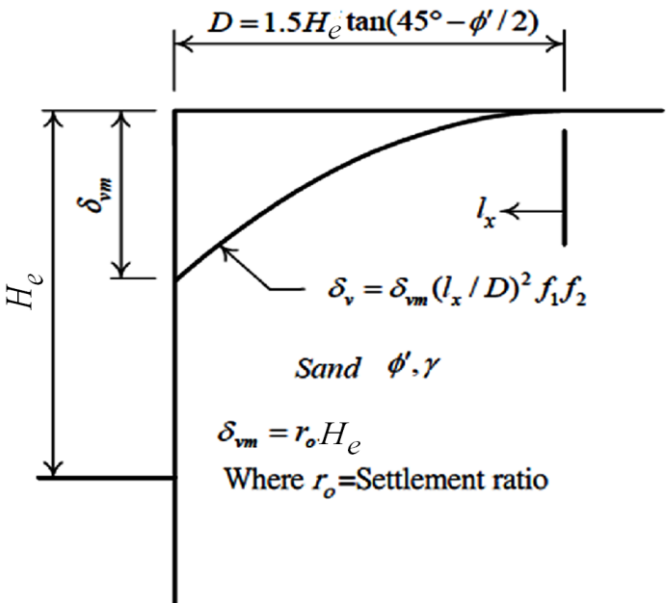

(a) Curves of settlement

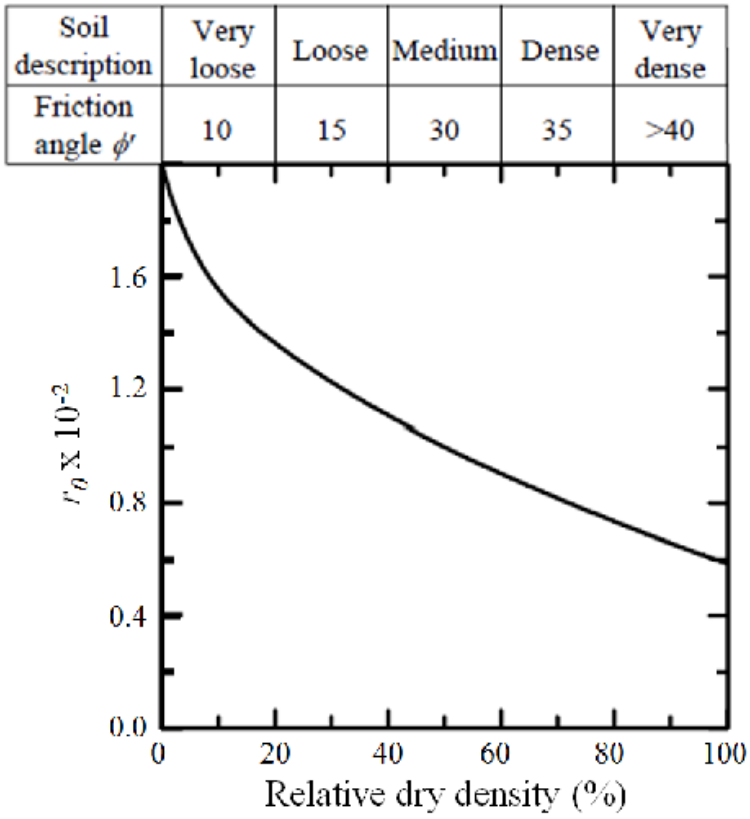

(b) Curves of settlement ratio

Factor	Workmanship				Factor	Construction difficulty		
	Excellent	Good	Average	Poor		None	Average	Severe
f_1	0.8	0.9	1.0	1.1	f_2	1.0	1.02	1.05

(c) f_1 and f_2

Figure 4.26. Half-empirical method of estimating ground settlement on sandy layers (Bauer, 1984)

b. According to the width of the excavation surface H_e, the maximum ground settlement δ_{vm} can be calculated by the following equation:

$$\delta_{vm} = r_0 H_e \tag{4.10}$$

c. According to the friction angle ϕ' in sandy soil, the range influenced by settlement D can be calculated by the following formula:

$$D = 1.5 H_e \tan\left(45^\circ - \phi'/2\right) \tag{4.11}$$

d. Calculate the settlement δ_v at the corresponding position on l_x presented in Figure 4.26a:

$$\delta_v = \delta_{vm}\left(\frac{l_x}{D}\right)^2 f_1 f_2 \tag{4.12}$$

Where f_1 is the correction factor relevant to construction quality;

f_2 is the correction factor relevant to construction difficulties.

Detailed numbers are shown in Figure 4.26c.

(6) Bowles method

Bowles (1986) estimated the amount and the range of settlement induced by excavation according to Figure 4.27, and the procedures are as follows:

a. Calculate the lateral displacement of the retaining walls induced by excavation using finite element analysis or the elastic foundation beam method.

b. When the distribution of lateral displacement of the retaining walls is known, calculate the area of lateral soil displacement a_d

c. Use the method suggested by Caspe (1966) to calculate the range influenced by ground settlement D:

$$D = H_{t1} \tan(45^\circ - \phi/2) \tag{4.13}$$

$$H_{t1} = H_e + H_d \tag{4.14}$$

In equation 4.14，H_e is excavation depth, when the excavation width is B, for cohesive soil ($\phi = 0$), $H_d = B$; for non-cohesive soil, $H_d = 0.5B\tan(45^\circ + \phi/2)$.

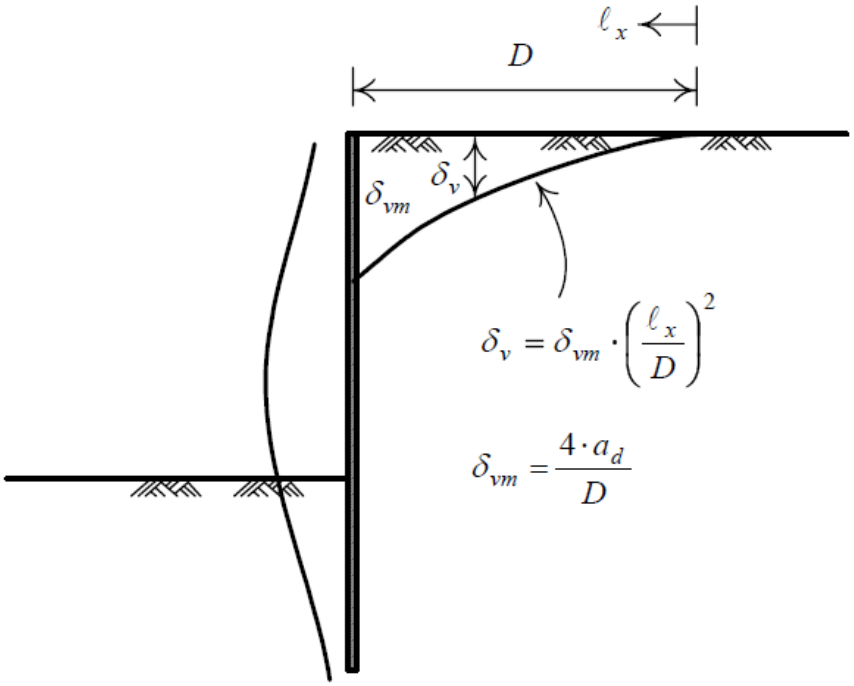

Figure 4.27. Estimate ground settlement using Bowles method (Bowles, 1986)

d. If the maximum ground settlement is hypothesized on the location of the retaining walls, then the maximum ground settlement at the location of the retaining walls δ_{vm} is estimated by:

$$\delta_{vm} = \frac{4a_d}{D} \tag{4.15}$$

e. Settlement δ_v at corresponding positions on l_x is estimated by following formula

$$\delta_v = \delta_{vm}(\frac{l_x}{D})^2 \tag{4.16}$$

(7) Nicholson method

Nicholson (1987), based on experience of excavating soft clay layers in Singapore, believed that in soft clay, the range D influenced by excavation equals the depth that lateral displacement H_0 occurs on slurry walls, the maximum settlement occurs in the location which is $H_1/2$ from slurry wall, where H_1 is the maximum depth of lateral displacement of retaining walls.

(8) Wang and Li method

Wang and Li (1993), based on the research results of the Nicholson Method, suggested that settlement on the retaining walls should be estimated by the lateral displacement of the top of retaining walls (Figure 4.28); the settlement S_1 curve from the location of maximum settlement to the retaining walls is estimated by $y = a + bx^2$; the settlement S_2 curve from the location of maximum settlement to the influenced range D is estimated by $y = e + fx^2$; and the maximum ground settlement is suggested to be estimated at $0.75\delta_{hm}$.

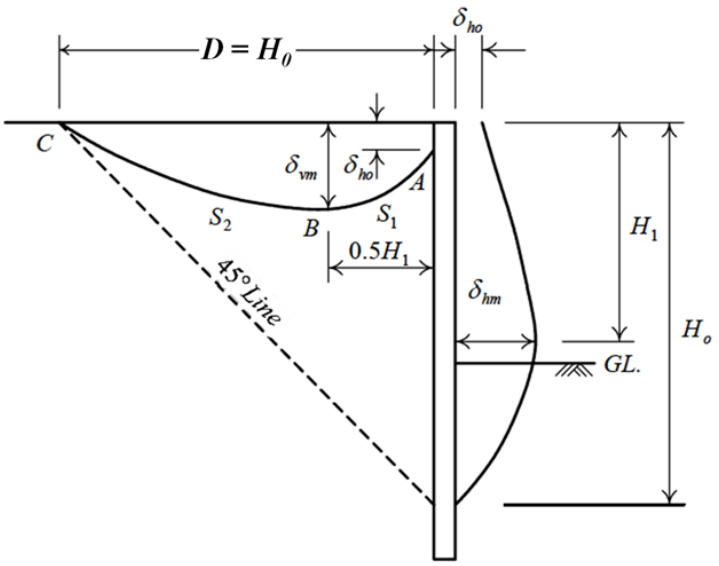

Figure 4.28. Ground settlement induced by excavation
(Wang and Li, 1993)

(9) Clough and O'Rourke method

Clough and O'Rourke (1990), based on analysis results of cases, suggested the envelopes of ground settlement for different soil properties during excavation:

a. Sandy soil layer and stiff clay layer

Ground settlement occurring in excavation and support stages tend to be constrained by a triangle, Figure 4.29a and 4.29b show that the positions of maximum settlement of sandy soil layer and stiff clay layer are the positions of retaining walls, and the influenced ranges are $2H_e$ and $3H_e$ respectively.

b. Soft to medium stiff clay

The envelope of ground settlement induced by excavation is a trapezium (Figure 4.29c)

zone of maximum settlement: $0 \le d / H_e \le 0.75$

transition zone: $0.75 \le d / H_e \le 2.0$

where settlement decreases from maximum to a negligible amount.

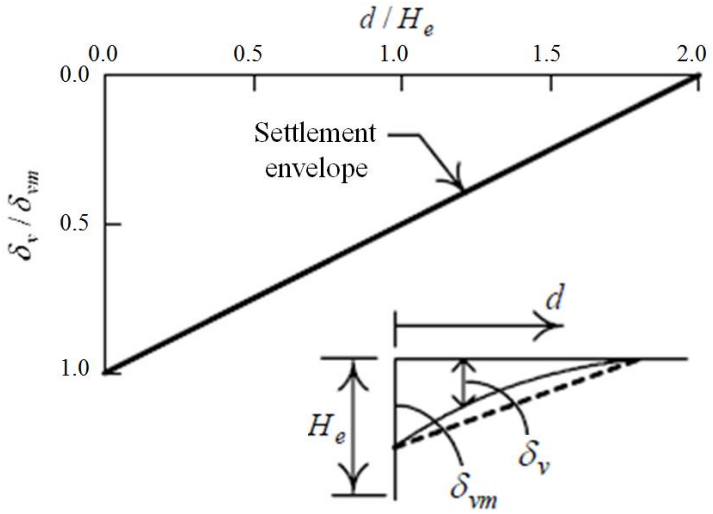

(a) Sandy soil layer

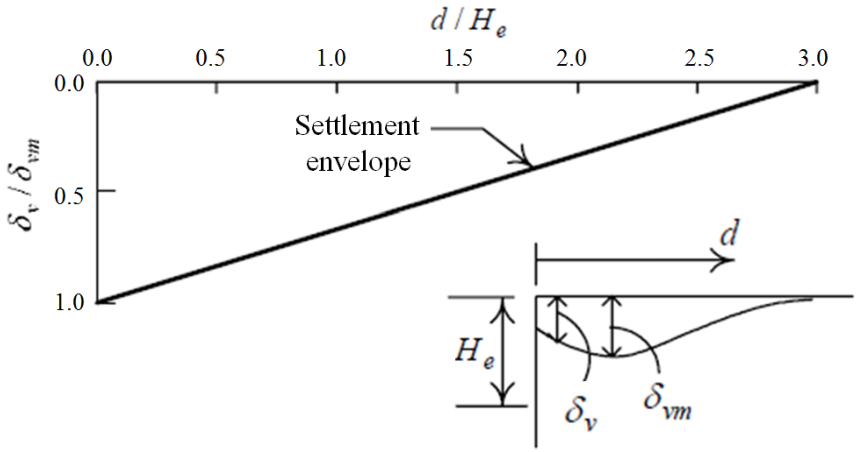

(b) Stiff clay layer

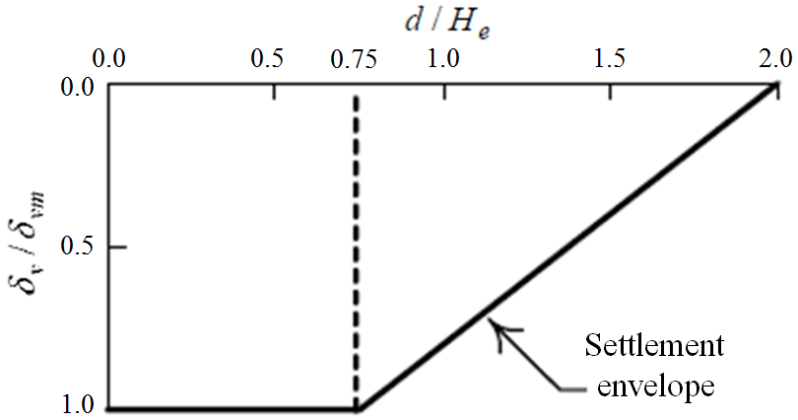

(c) Soft to medium stiff clay layer

Figure 4.29. Assessment of ground settlement curves induced by excavation (Clough and O'Rourke, 1990)

(10) Woo and Moh method

Woo and Moh (1990) suggested the maximum ground settlement to be $\delta_{vm} = (0.25 \sim 1.0)\delta_{hm}$ or $\delta_{vm} = (0.0002 \sim 0.0005)H_e^2$ according to the monitoring results of excavations in the Taipei basin. In addition, an envelope of settlement curves was built based on the monitoring results of excavation settlement in the K1 Site And T2 Zone (Figure 4.30). In the early stage of assessment, the envelope of ground settlement induced by excavation in the K1 Zone is:

$$\frac{\delta_v}{H_e}(\%) = 0.8 - 0.2d / H_e$$

And the envelope of ground settlement induced by excavation in the T2 Zone is

$$\frac{\delta_v}{H_e}(\%) = 0.4 - 0.08d / H_e$$

Where δ_v: value of ground settlement

H_e: depth of excavation surface

d: distance to retaining walls

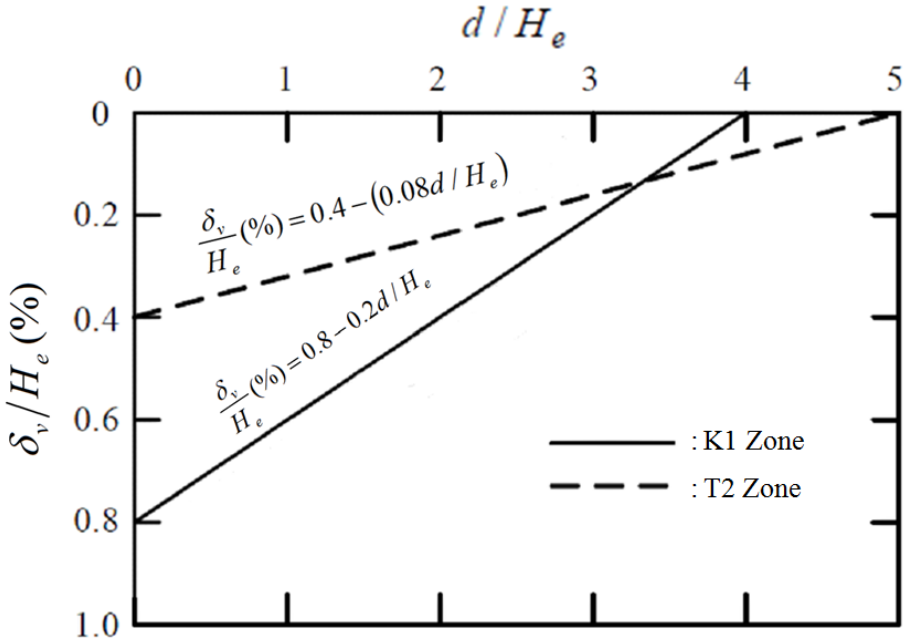

Figure 4.30. Envelope curves of round surface settlement in the K1 and T2 Zone of the Taipei basin (Woo and Moh, 1990).

(11) He and Li method

He and Li (1990) proposed assessment methods for three factors that lead to ground settlement in excavation respectively.

a. According to analysis results of monitoring materials in London, they suggested, for ground settlement curves induced by slurry wall construction, the maximum settlement is 0.04%H_t, and the influenced range is:

$$D = H_t \tan(45° - \frac{\phi'}{2})$$

Where H_t : depth of slurry wall

ϕ' : friction angle in the soil

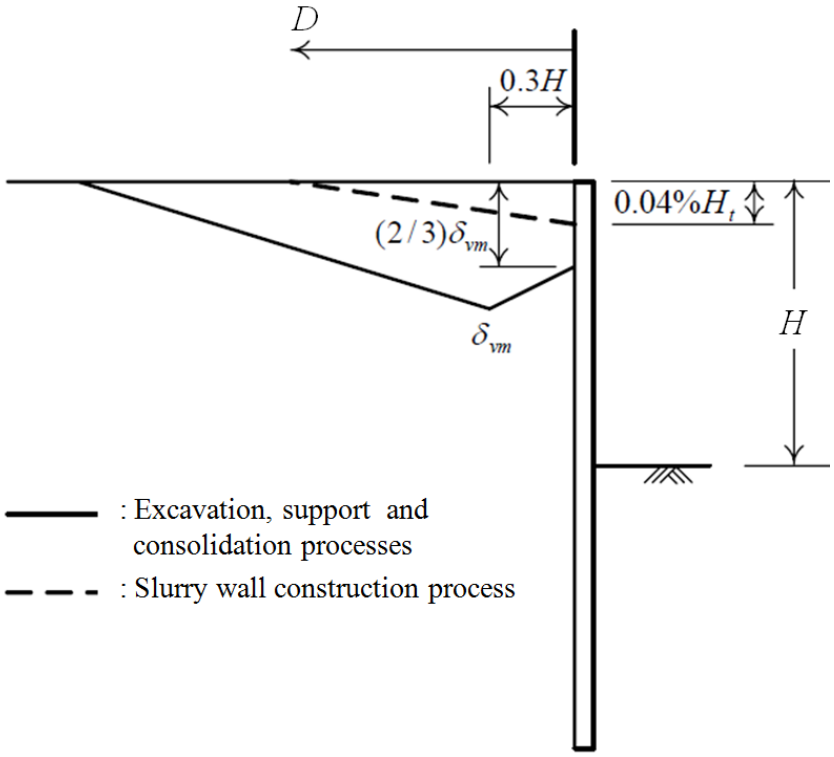

Figure 4.31. Distribution of ground settlement induced by excavation (He and Li, 1990)

b. The maximum settlement is $\delta_{vm} = (0.5 \sim 1.0)\delta_{hm}$. For clay layers, the value 1.0 in the bracket is selected; for sandy soil, usually the value 0.6 in the bracket can be selected. The influenced range of settlement:

$$D = 2H_t \tan(45° - \frac{\phi'}{2})$$

Where $H_t = H + H_p$

$H =$ depth of excavation

$\phi' =$ friction angle in the soil

$H_p = 0.5B\tan(45^\circ - \phi'/2)$

$B =$ width of excavation

c. Settlement curves induced by compression and other factors are shown in Figure 4.31, δ_{vm} is estimated at $0.15\delta_{hm}$, the influenced range is:

$$D = 4H_t \tan(45° - \frac{\phi'}{2}) \quad (4.22)$$

(12) Hsieh and Ou method

a. Spandrel settlement

Hsieh and Ou (1998) used Figure 4.32a to show that the distribution of ground settlement comprises two lines:

When: $d/PIZ \leq 1.0$

$$\delta_v = \left(-0.9\sqrt{\frac{d}{PIZ}} + 1.0\right)\delta_{vm} \quad (4.23)$$

When $1.0 < d/PIZ \leq 2.0$:

$$\delta_v = \left(-0.242\sqrt{\frac{d}{PIZ}} + 0.342\right)\delta_{vm} \quad (4.24)$$

Where *PIZ* is the primary influence zone, *d* is the distance to retaining walls.

In Figure 4.32a, line *ab* represents the *PIZ* with a steep slope; line *bc* represents the *SIZ* with a gentle slope

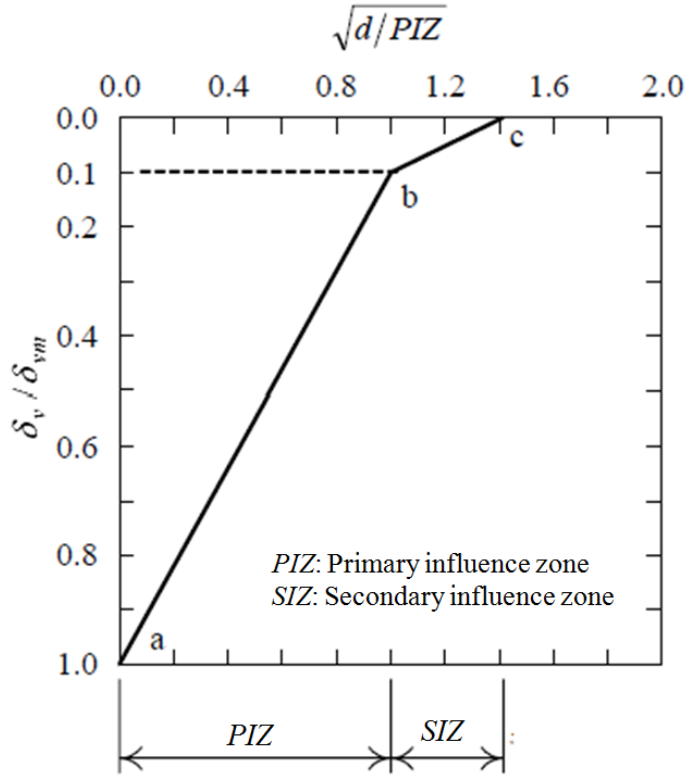

(a) Spandrel type

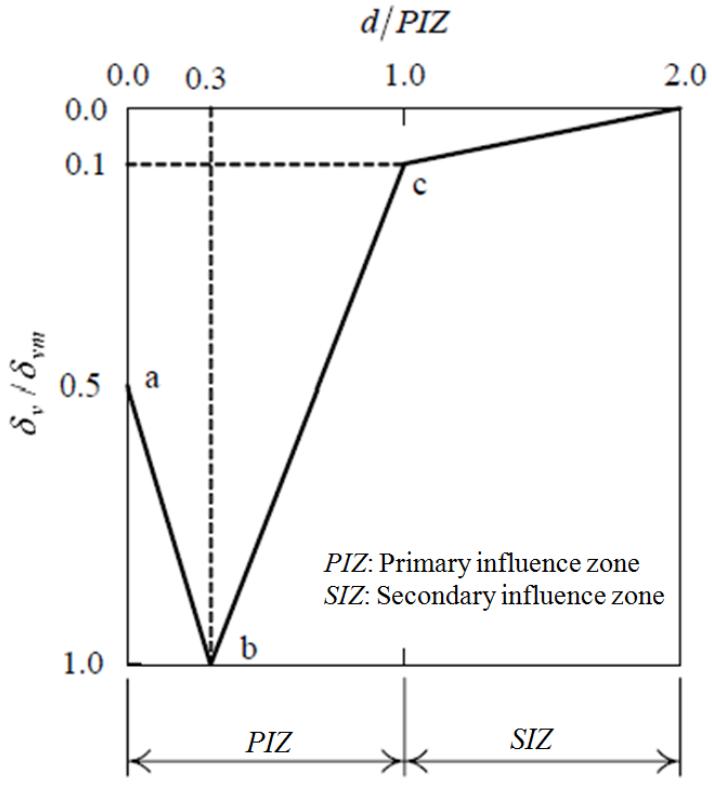

(b) Concave type

Figure 4.32. Assessment of ground settlement (Hsieh and Ou, 1998)

b. Concave settlement:

Hsieh and Ou (1998) used Figure 4.32b to show the distribution of ground settlement induced by excavation with three lines, where line *abc* represents the *PIZ* and line *cd* represents the *SIZ*:

When $d / H_e \le 0.3$:

$$\delta_v = \left(1.667\frac{d}{PIZ} + 0.5\right)\delta_{vm} \tag{4.25}$$

When $0.3 < d / H_e \le 1.0$:

$$\delta_v = \left(-1.286\frac{d}{PIZ} + 1.386\right)\delta_{vm} \tag{4.26}$$

When $1.0 < d / H_e \le 2.0$:

$$\delta_v = \left(-0.1\frac{d}{PIZ} + 0.2\right)\delta_{vm} \tag{4.27}$$

4.2.9 Causes and Mechanism of Conventional Neighboring Damage Induced by Construction

Li (1991) claimed that the reasons for neighboring damage in construction include inappropriate design, construction flaws, natural factors, and other factors.

1. Neighboring damages induced by inappropriate construction

(1) Quoting inappropriate excavation materials and design.
(2) Incorrect structural calculations.
(3) Inappropriate material selection.
(4) Incorrect selection of construction methods.

2. Neighboring damages induced by construction flaws

(1) Soil disturbance induced by foundation excavation.
(2) Ground settlement induced by draining ground water.
(3) Insufficient retaining walls measures.
(4) A retaining walls failure due to excessive basement excavation.
(5) Vibration of construction tools.

(6) Weight of heavy machinery exceeds the bearing capacity of the soil.
(7) Construction machines crashing into neighboring buildings.
(8) Leaning and collapse of scaffolds.
(9) Damage to neighboring buildings during demolition.

3. Neighboring damage induced by natural factors

(1) Excessive water content in soil due to long-term rainfall.
(2) Earthquake or hurricane.
(3) Inhomogeneous settlement.
(4) Other reasons
a. Neighboring building itself has failures in structure and foundations.
b. Owners of neighboring buildings try to extort due to greed.
c. Incorrect construction or monitoring of construction staff.
d. Disputes of infringement and boundary crossing.

According to Section 2.2 of this chapter, under conventional mechanisms, the causes of neighboring damage disputes are due to the ground settlement on the back of retaining walls. Thus, as long as ground settlement on the back of retaining walls is induced in a construction site, then relevant laws or regulations all unilaterally judge the ground settlement on the back of retaining walls as a type of infringement behavior. However, the inappropriate design, construction flaws, natural factors, and other neighboring damage reasons, although they are written in a different way, still unilaterally hold the excavation side responsible for neighboring damage.

4.2.10 Conventional Ways to Reduce Neighbor Damage in Construction

1. Reduce displacement of retaining walls

(1) Reinforcing techniques of retaining walls

Retaining wall deflection can be reduced by increasing the stiffness of the retaining walls, which can further reduce the displacement of nearby foundations. For example, the steel sheet pile can be replaced with steel rail pile, slurry walls can be replaced with steel sheet pile, or a larger size of steel sheet pile or slurry wall can be used, etc.

(2) Reinforcing the support of excavation zone

The layers of excavation support can be increased, the thickness of the cross-section of the support can be increased, or prestress can be deployed.

(3) Diaphragm Walls

The same techniques can be used to build a steel reinforced concrete wall in the excavation zone, slurry walls can be cascaded in different orientations, and then the displacement of slurry walls during excavation can be reduced.

(4) Buttress

The use of buttresses is not limited to the excavation zone. A buttress should not penetrate the excavation zone. A buttress must be used with slurry walls.

(5) Grouting techniques in excavation zone

These techniques are usually used to improve soil quality and strength by being deployed homogenously. There are many different grouting methods and different grouting techniques need to be used for different soil properties.

(6) Bearing plate method

In the excavation zone, a grouting method can be used to improve soil quality at a depth interval, then a layer of bearing plates with high strength and low compressibility is formed, which is used to support the retaining walls.

(7) Soil replacement

High-strength columnar bodies are homogeneously installed by using mixing piles, wall piles, or prepakt mortar piles to form a composite soil layer with high strength in the excavation zone.

2. Enhance foundation or structure of neighbor building

(1) Foundation grouting method

This method is usually deployed below the foundations of neighboring buildings when construction space is limited. Grouting methods include low pressure grouting, chemical grouting, high pressure grouting, and displacement-compaction grouting etc.

(2) Underpinning construction

Underpinning can be directly applied under foundations of buildings, the cost is high, the construction period is long, yet it is effective.

(3) Temporary timbering method

This method can be directly applied to buildings, relevant methods include building side bracing, building an open structure, or temporary timbering under beams etc. This method is economical and fast, the only disadvantage is that it influences the available space within the building, and whether demolishing the timbering after construction needs more discussion.

(4) Repairing method

This method apply direct repair to damaged beams, piles, plates, walls, and other structural components in the building.

(5) Structural enhancement method

For example, structural cracks in the building can be enhanced, in order to improve the building’s vibration resistance ability and extend the lifespan.

(6) Righting method

This method has a high cost and long construction period, such as the healing righting method.

(7) Demolish and reconstruction method

This method can reconstruct a building based on existing rules, although it is not a protective method, it is a comparatively good method to protect a building from being damaged again.

3. Isolating the influence of construction on neighboring buildings

Installing micro piles, prepakt mortal piles, or soldier piles on the neighboring building side of the excavation zone can isolate the influence of construction on the neighboring building.

4. Grouting Techniques

Stratified grouting can be conducted in the excavation zone, which can change the soil of the foundation excavation zone to a composite soil with high strength, low compression and low permeability, and further reach the goal of protecting neighboring properties.

4.2.11 Basic Norm of Laws for Neighboring Damage in Construction

Building Law. Article 69 stipulates that in building construction, when conducting excavation near other buildings, necessary measures of protecting the neighboring building from leaning or collapse shall be compulsory. For any excavation depth over 1.5 meters, the design drafts and instruction of protective measures should be submitted together with applications for a building license or miscellaneous license.

Environmental Impact Assessment Law. Article 6 of this law stipulates that if the development behaviors comply with those that are required to conduct an environmental impact assessment of Article 5, then the developer must follow the construction rules of Environmental Impact law in the layout stage, and conduct the first stage of an Environmental Impact Assessment.

Building Technical Regulations.

1. Article 150 of Chapter 8 of the Building Design and Construction Section stipulates that for any company who engage in the construction, expansion, reconstruction, and demolishment etc., that company is required to conduct appropriate security measures such as installing protective enclosures, retaining walls machines, scaffolds, to prevent accidental casualties, ground settlement, building collapse etc. from damaging public security.

2. Article 154, Chapter 8 of the Building Design and Construction Section stipulates that when conducting excavation, well drilling, and caisson etc., the following necessary security measures must be taken according to laws below:

(1) Prevent damaging underground burials such as natural gas pipes, electricity cables, water pipes, and sewer pipes etc.
(2) The construction blueprints need to be calculated according to the soil layer distributions and ground water table.
(3) When excavation depth is deeper than the foundations of neighboring buildings, the relevant instructions in the building structure passage of this law should be followed.
(4) For excavation depths over 1.5 meters, except for those in good soil, which will not lead to collapse or those with no security concerns in the neighboring area, all companies are required to have soil retaining machines and set up the machines following the relevant rules of building construction of this law.
(5) Soil retaining machines should be checked at any time during construction, to observe the change in nearby foundations and enhance methods whenever necessary, and appropriate water draining methods should be adopted to stabilize the states.
(6) When removing plate piles, appropriate measures should be taken to prevent nearby foundations from settling.

3. Article 62, Chapter 2 of the Building Structure Section stipulates that:
   (1) Foundation design and construction should protect the security of neighboring buildings.
   (2) Before design and construction, the company should investigate the status of neighboring buildings including foundations, underground building, locations, and structure type of infrastructures, in order to provide a reference for design of protective facilities.

4. Article 122, Chapter 2 of the Building Structure Section stipulates that when using soil retaining excavation as a foundation excavation method, companies should base designs on standards of foundation structure design, conduct analysis of wall deflection and timbering design, and discuss the possibility and security of soil humps, soil boil, and soil uplift on the bottom surface of excavation.

5. Article 123, Chapter 2 of the Building Structure Section stipulates that when the excavation depth of foundations is below ground water table, companies should discuss a way of controlling the ground water table, to avoid damage to nearby facilities and neighboring households.

6. Article 124, Chapter 2 of the Building Structure Section stipulates that the design of soil retaining facilities should follow the standards of foundation structural design to guarantee the strength, stiffness, penetration depth, and stabilization of soil layers in excavation surfaces and nearby zones.

7. Item 1, Article 127, Chapter 2 of the Building Structure Section stipulates that foundation excavation should make use of a proper monitoring system when necessary, in order to monitor the change in soil retaining facilities, timbering facilities, soil quality, and neighboring buildings before and after the excavation, and companies should make a timely judgment and take appropriate measures to maintain the security of excavation and neighboring buildings.

8. Article 130, Chapter 2 of the Building Structure Section stipulates that the underground structure of buildings and the underground walls in contact with nearby soil layers should be able to handle the weight load coming from upper buildings and the lateral pressure from nearby soil layers; its structural design should comply with the rules in this passage.

Design standard of building foundation's structure.

1. Article 8.6 stipulates:
   (1) Geological characteristics of foundation and type of soil retaining facilities.
   (2) Types of beams of the underground structure.
   (3) Material strength of soil retaining facilities.
   (4) Water-proof ability of soil retaining facilities.
   (5) Strength and displacement of soil retaining structure system and the impact on neighboring environment.
   (6) Stability of excavation surface at different stages of foundation excavation.
   (7) Construction procedures, timing, and pre-stressing of soil retaining facilities and timbering system.

2. Article 8.7 stipulates:
   Timbering facilities should be strong enough to handle the load conveyed by soil retaining facilities, in order to restrain or reduce its displacement where the load taken into consideration includes:
   (1) Lateral soil pressure.
   (2) Ground water pressures.

(3) Loads on the land surface.
(4) Temporary loads during construction.
(5) Impacts of earthquake.

Taipei Building Construction Neighboring Damage Authentication Manual.

1. Definition and purpose

Neighboring damage issues induced by construction is a type of infringement. Authentication of neighboring damage occurs after neighboring damage occurs and according to the degree of damage. Some institutions authenticate the reason of damage, then judge the party responsible, and assess how the construction influences the structural safety of the subject matter (neighboring households). They also estimate the repair cost according to the damage and provide reference for both sides in negotiations, third party mediation, or judgment about the compensation for the damage.

2. Items to be authenticated

(1) Preliminary prospecting and conjunction prospecting.

(2) Structure, usage, and status of subject matter.

(3) Checking surveying of subject matter.

(4) Photos and illustrations of damaged sections of subject matter.

(5) Estimations of amount and fees of repairing the damaged subject matter.

a. Compare with authentication results on spot.

b. Checking surveying of subject matter.

c. The assessment principles of structural bodies.

The fees for structural cracks on reinforced concrete need to be estimated from the point of view of repairing with epoxy grouting or repairing enhancement.

d. The assessment principles of compensation for subject matter's leaning.

(a) Engineering compensation.

(b) Non-engineering compensation.

(i) level l ($\Delta / H \leq 1/200$)

(ii) level 2 ($1/200 < \Delta / H \leq 1/100$)

(iii) level 3 ($1/100 < \Delta / H \leq 1/50$)

(iv) level 4 ($1/50 < \Delta / H \leq 1/40$)

(v) level 5 ($1/40 < \Delta / H$)

(6) Drafting the report.

4.3 Professional Speculations on Engineering Ethics of Neighboring Damage

4.3.1 Investigation of Construction Disputes of Neighboring Damage

Survey Results of Neighboring Damage Disputes. From 1985 to 1990, the investigation results presented by Li (1991) show that there were 2349 cases of neighboring damage disputes, and the disputes processed by all institutions are listed below:

1. Taipei Architects Associations: 1885
2. Taipei Structural Engineering Association: 196
3. Taiwan Professional Civil Engineers Association: 67
4. Taipei Professional Civil Engineers Association: 74
5. Taiwan Regional Engineering Contractors Association: 96
6. Taiwan Architecture & Building Center: 31

Discussion of Neighboring Damage Issues Induced by Construction.

1. Completed preliminary inspections: 688, accounting for 29.30%
2. Completed entire authentication procedures: 774, accounting for 33.00%
3. Authenticated the types of subject matter's structure:

Buildings made of RC and reinforced bricks account for the majority of heavily-damaged buildings, among which more than 50% of buildings are made of RC.

4. Heights of damaged buildings:

   Most damaged buildings are 2~5 floors high

5. Types of building failures:

   Cracking is the most common type of building failure, followed by settlement failure and leaning failure.

6. Reason for building failure:

   Excavation disturbance induce most building failures, followed by inhomogeneous settlement and drainage of ground water.

Summary. According to the survey results in this chapter:

1. Most neighboring damage disputes induced by excavation occurred in 2~5 floor buildings made of RC and reinforced bricks. These types of building did not usually have a basement, and their foundation type was spread footing, which is vulnerable to the impacts of neighboring excavation and construction. Once a building is higher than 5 floors, due to the existence of a basement and mat-type foundations or pile foundations, it is less influenced by excavation and construction.

2. Cracking failure was the most common type of failure; when the failure type was cracking failure, since enhancement of cracks is comparatively easier, the rate of neighboring damage disputes that have finished the entire authentication procedure is pretty low and only accounts for 33% of the total neighboring damage disputes.

3. For large neighboring damage disputes, due to the massive compensation amounts and verbose legal proceedings involved, even if the excavation and construction company is willing to pay full compensation after the judgment of the court, the process can be slow. For the victims of building failure, even though they can receive compensation, they still need to bear the living inconvenience brought by building damage, which results in a lose-lose situation.

4.3.2 Professional Definition of the Technical Causes of Neighboring Damage Induced by Construction

Necessity of a Professional Definition for Neighboring Damage. Although the government follows the laws, regulations, and authentication manuals released in the past, today's consistent neighboring damage disputes have become one of the primary reasons of neighbor disharmony. Based on the results of the oriented feedback and continuous improvement process, it can be known that a professional definition of the technical causes for neighboring damage is very important. Only by referring to a professional definition of technical causes for neighboring damage, can existing laws, regulations, and authentication manuals comply with the needs in reality.

Professional Definition of Technical Causes for Neighboring Damage. Professional technical causes of neighboring damage must comply with following three elements; causes for neighboring damage complying with only one or two elements can only be defined as unprofessional technical causes of neighboring damage.

Engineers of excavation and construction only need to be responsible for the professional technical causes of neighboring damage, rather than the unprofessional technical causes of neighboring damage. The elements of professional technical causes of neighboring damage are:

1. Uniqueness: during excavation and construction, only when this cause exists can neighboring damage happen.
2. Entirety: as long as this cause exists in some sites of the country, then neighboring damage should occur in all neighboring zones of these sites.
3. Comprehensiveness: as long as this cause exists in some sites all over the world, then neighboring damage should occur in all neighboring zones of these sites.

4.3.3 Whether Current Laws or Regulations Comply with the Inspection of the Professional Definition of Technical Cause

Inspections of Article 69 of the Building Law. The main idea of Article 69 of the Building Law is to request excavation and construction companies to provide appropriate protection methods to prevent neighboring buildings from leaning or collapse failure.

The main idea of Article 69 of Building Law above means as long as the protection methods are appropriate, no leaning or collapse failure would occur on neighboring buildings during excavation and construction. According to this main idea, it can be extrapolated that the cause of leaning or collapse failure of the neighboring building is the inappropriate protection methods.

1. Whether inappropriate protection methods comply with the inspections of the first elements

According to Article 69 of the Building Law above, the main idea of the first element is "during excavation and construction, only the existence of inappropriate protection methods can lead to neighboring damage".

However, facts show that during excavation and construction, neighboring damage could still occur even with today's best protection techniques (see the cases of Chapter 4.1) and appropriate protection methods. Therefore, it can be known that inappropriate protection methods do not comply with the first elements, which further proves that the content regulated in Article 69 of the Building Law is not a technical cause of neighboring damage.

2. Whether inappropriate protection methods comply with the inspections of the second elements

According to Article 69 of the Building Law above, the main idea of the second element is "as long as this reason exists somewhere in a site of the country, then neighboring damage should occur in all neighboring zones of this site."

Facts show that in a certain excavation and construction site in this country, even if neighboring damage occurs due to inappropriate protection methods, neighboring damage would hardly occur in all

neighbor zones. Therefore, it can be known that inappropriate protection methods do not comply with the second element, which further proves that the content regulated in Article 69 of the Building Law is not a technical cause of neighboring damage.

3. Whether inappropriate protection methods comply the inspections of the third elements

According to Article 69 of the Building Law above, the main idea of the third element is "as long as this reason exists somewhere in a site of the world, then neighboring damage should happen in all neighboring zones of this site."

Facts show that in excavation and construction sites all around the world, even if neighboring damage occurs due to inappropriate protection methods, neighboring damage would hardly occur in all neighboring zones. Therefore, it can be known that inappropriate protection methods do not comply with the third element, which further proves that the content regulated in Article 69 of the Building Law is not a technical cause of neighboring damage.

Inspections of Article 6 of the Environmental Impact Assessment Law. The main idea of Article 6 of the Environmental Impact Assessment Law is that excavation and construction companies much conduct environmental impact assessment and predict the potential environmental impacts induced by excavation and developing behaviors, and then provide plans of environmental protection and substitute plans.

The main idea of Article 6 of the Environmental Impact Assessment Law above shows that as long as plans of environmental protection and substitute plans are appropriate, excavation and construction would not influence the environment; in other words, as long as plans of environmental protection and substitute plans are appropriate, excavation and construction would not induce leaning or collapse failures to neighboring buildings. According to this main idea, it can be extrapolated that the cause of leaning or collapse failure of neighboring buildings is the inappropriate plans of environmental protection and substitute plans.

1. Whether inappropriate plans of environmental protection and substitute plans comply with the inspections of the first elements

According to Article 6 of the Environmental Impact Assessment Law

above, the main idea of the first element is “during excavation and construction, only the existence of inappropriate plans of environmental protection and substitute plans can lead to neighboring damage”.

However, facts show that during excavation and construction, neighboring damage could still occur even with today’s best protection techniques (see the cases of Chapter 4.1) and appropriate plans of environmental protection and substitute plans. Therefore, it can be known that inappropriate plans of environmental protection and substitute plans do not comply with the first elements, which further proves that the content regulated in Article 6 of the Environmental Impact Assessment Law is not the technical cause of neighboring damage.

2. Whether inappropriate plans of environmental protection and substitute plans comply the inspections of the second elements

According to Article 6 of the Environmental Impact Assessment Law above, the main idea of the second element is “as long as somewhere in a site of the country there exists inappropriate plans of environmental protection and substitute plans, then neighboring damage should occur in all neighboring zones of this site.”

Facts show that in a certain excavation and construction site in this country, even if neighboring damage occurs due to inappropriate plans of environmental protection and substitute plans, hardly would neighboring damage occur in all neighboring zones. Therefore, it can be known that inappropriate plans of environmental protection and substitute plans do not comply with the second element, which further proves that the content regulated in Article 6 of Environmental Impact Assessment Law is not a technical cause of neighboring damage.

3. Whether inappropriate plans of environmental protection and substitute plans comply the inspections of the third elements

According to Article 6 of Environmental Impact Assessment Law above, the main idea of the third element is “as long as inappropriate environmental protection and substitute plans exist in a site somewhere in the world, then neighboring damage should occur in all neighboring zones of this site.”

Facts show that in excavation and construction sites all around the world, even if neighboring damage occurs due to inappropriate plans of environment protection and substitute plans, neighboring damage would

hardly occur in all neighboring zones. Therefore, it can be known that inappropriate plans of environmental protection and substitute plans do not comply with the third element, which further proves that the content regulated in Article 6 of the Environmental Impact Assessment Law is not a technical cause of neighboring damage.

Inspections on Article 8.6 of the Design Code and Specifications of Building Foundations. The main idea of Article 8.6 of the Design Code and Specifications of Building Foundations is that the excavation design company must provide a retaining structure system of adequate strength in order to reduce the impacts on the neighboring environment by reducing dislocations.

The main idea of Article 8.6 of the Design Code and Specifications of Building Foundations above shows that as long as the strength of the retaining structure system is large enough, no leaning or collapse failures due to the excessively large dislocations of the retaining structure system would happen to buildings during excavation and construction. According to this main idea, it can be extrapolated that the reason for leaning or collapse failure of neighboring buildings is the excessively large dislocations of the retaining structure system.

1. Whether excessively large dislocations of the retaining structure system comply with the inspections of the first elements

According to Article 8.6 of the Design Code and Specifications of Building Foundations Law above, the main idea of the first element is “during excavation and construction, only the existence of excessively large dislocations of the retaining structure system can lead to neighboring damage”.

However, facts show that during excavation and construction, neighboring damage could still occur even with today’s best protection techniques (see the cases of Chapter 4.1) and appropriate plans of environmental protection and substitute plans. Therefore, it can be known that excessively large dislocations of retaining structure system do not comply with the first elements, which further proves that the content regulated in Article 8.6 of the Design Code and Specifications of the Building Foundations Law is not a technical cause of neighboring damage.

2. Whether excessively large dislocations of the retaining structure system comply the inspections of the second elements

According to Article 8.6 of the Design Code and Specifications of the Building Foundations Law above, the main idea of the second element is "if a site somewhere in the country with excessively large dislocations of retaining structure system exists, then neighboring damage should occur in all neighboring zones of this site."

Facts show that in a certain excavation and construction site in this country, even if neighboring damage occurs due to excessively large dislocations of the retaining structure system, neighboring damage would hardly occur in all neighboring zones. Therefore, it can be known that excessively large dislocations of the retaining structure system do not comply with the second element, which further proves the content regulated in Article 8.6 of the Design Code and Specifications of Building Foundations Law is not a technical cause of neighboring damage.

3. Whether excessively large dislocations of the retaining structure system comply the inspections of the third elements

According to Article 8.6 of the Design Code and Specifications of Building Foundations Law above, the main idea of the third element is "as long as excessively large dislocations of the retaining structure system exist in a site somewhere in the world, then neighboring damage should occur in all neighboring zones of this site."

Facts show that in excavation and construction sites all around the world, even if neighboring damage occurs due to excessively large dislocations of the retaining structure system, neighboring damage would hardly occur in all neighbor zones. Therefore, it can be known that excessively large dislocations of the retaining structure system do not comply with the third element, which further proves that the content regulated in Article 8.6 of the Design Code and Specifications of Building Foundations Law is not a technical cause of neighboring damage.

Inspections on Article 25 of Taipei City Construction Management Rules. The main idea of Article 25 of the Taipei City Construction Management Rules is excavation and construction companies must conduct detailed investigation of the situations around the foundations, the existing neighboring buildings' foundations, and other potential factors, following which companies should provide appropriate safety measures to prevent

neighboring buildings from foundation settlement, cracking failure, or collapse.

The main idea of Article 25 of the Taipei City Construction Management Rules above shows that as long as protection measures are appropriate, no leaning or collapse failures would happen to buildings during excavation and construction. According to this main idea, it can be extrapolated that the reason for leaning or collapse failure of neighbor building is inappropriate safety measures.

1. Whether inappropriate safety measures comply with the inspections of the first elements

According to Article 25 of the Taipei City Construction Management Rules above, the main idea of the first element is "during excavation and construction, only the existence of inappropriate safety measures can lead to neighboring damage".

But facts show that during excavation and construction, neighboring damage could still occur even with today's best protection techniques (see the cases of Chapter 4.1) and appropriate plans of environmental protection and substitute plans. Therefore, it can be known that inappropriate safety measures do not comply with the first elements, which further proves that the content regulated in Article 25 of the Taipei City Construction Management Rules is not a technical cause of neighboring damage.

2. Whether inappropriate safety measures comply the inspections of the second elements

According to Article 25 of the Taipei City Construction Management Rules above, the main idea of the second element is "as long inappropriate safety measures exist somewhere in a site of the country, then neighboring damage should occur in all neighboring zones of this site."

Facts show that in a certain excavation and construction sites in this country, even if neighboring damage occurs due to inappropriate safety measures, neighboring damage would hardly occur in all neighboring zones. Therefore, it can be known that inappropriate safety measures do not comply with the second element, which further proves that the content regulated in Article 25 of the Taipei City Construction Management Rules is not a technical cause of neighboring damage.

3. Whether inappropriate safety measures comply the inspections of the third elements

According to Article 25 of Taipei City Construction Management Rules above, the main idea of the third element is “as long as inappropriate safety measures exist somewhere in a site of the world, then neighboring damage should happen in all neighboring zones of this site.”

Facts show that in excavation and construction sides all around the world, even if neighboring damage occurs due to inappropriate safety measures, neighboring damage would hardly occur in all neighbor zones. Therefore, it can be known that inappropriate safety measures do not comply with the third element, which further proves that the content regulated in Article 25 of the Taipei City Construction Management Rules is not a technical cause of neighboring damage.

4.4 Investigation of Cases for Neighboring Damage Induced by Construction

4.4.1 Instructions for the Neighboring Damage Case

Ou and Hsieh (2004) investigated the neighboring damage case of Cathay Pacific Tienmu Shopping Mall, their main conclusions are summarized below:

Project Overview. Cathay Pacific Tienmu Shopping Mall is located at the crossroads of Tienmu East Road and Chung Cheng Road, the plan view of its base is shown in Figure 4.37. Figure 4.37 shows that its base zone is divided into Site A and Site B, Site A has an area of 4419 square meters, with 9 over-ground floors and 4 under-ground floors; Site B has an area of 3810 square meters, with 10 over-ground floors and 4 under-ground floors.

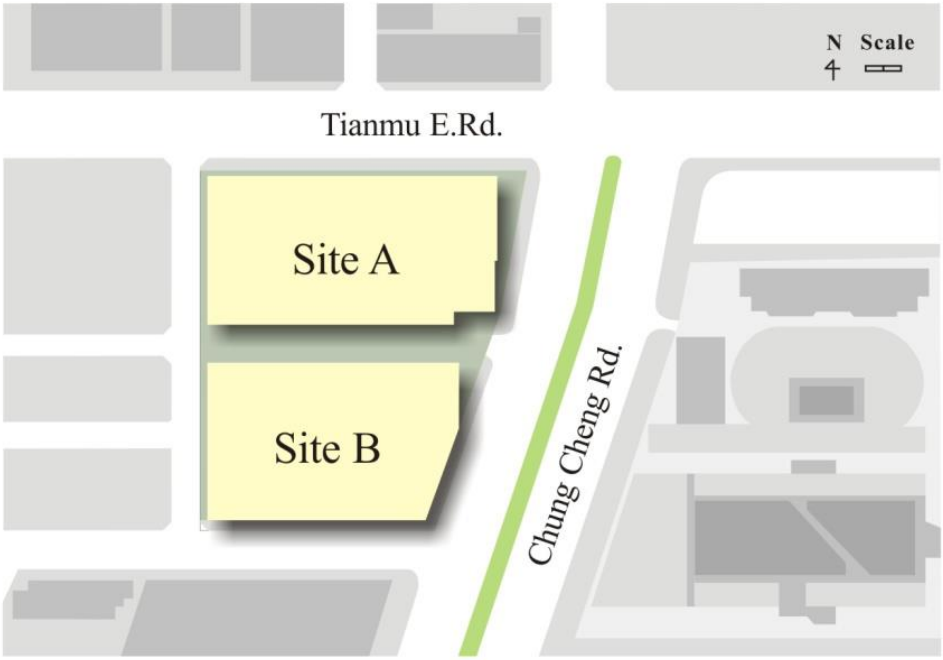

Figure 4.37. Plan view of base (Ou and Hsieh, 2004)

The section of underground buildings is shown in detail in Figure 4.38, where the depth of the slurry wall H_t = 30m and thickness is 1.2m; The basement zone is built through 6 stages, the estimated excavation depth is GL. -19.05m, and excavation started in November, 2000.

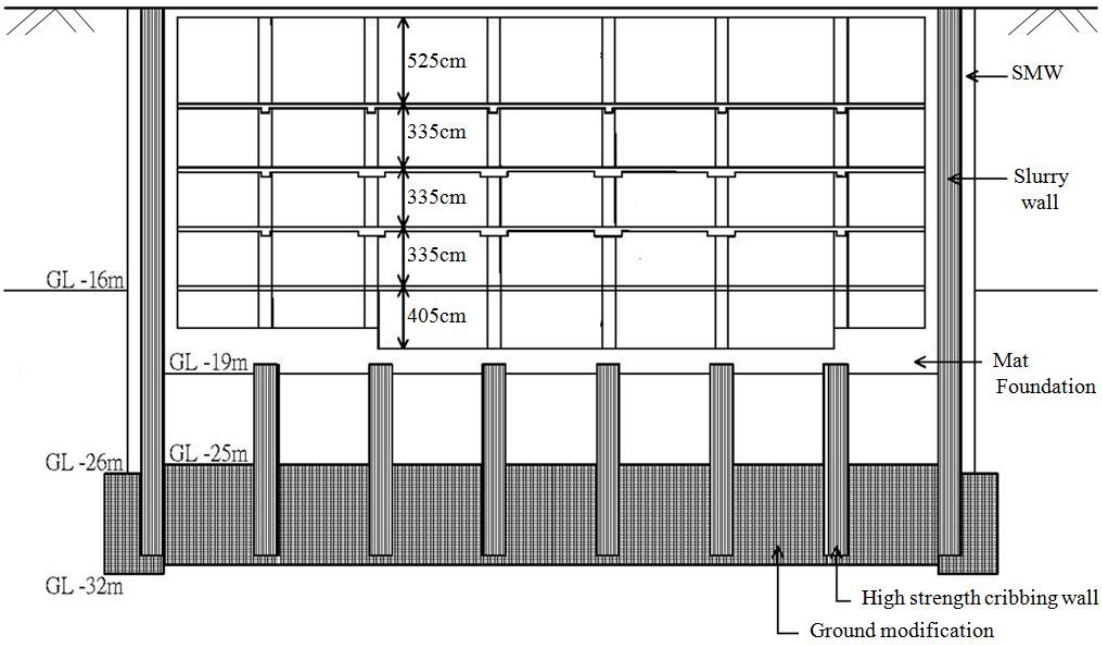

Figure 4.38. Section of underground buildings (Ou and Hsieh, 2004)

Geological Survey. Before construction, eight holes were drilled in Site A while six holes were drilled in Site B. Afterwards, since the construction method was changed to the top-down construction method, additional holes were drilled. The drilled holes in Site A increased from eight holes to twelve holes, while the drilled holes increased from six to ten in Site B, the planar configuration graph of drilled holes is shown in Figure 4.39.

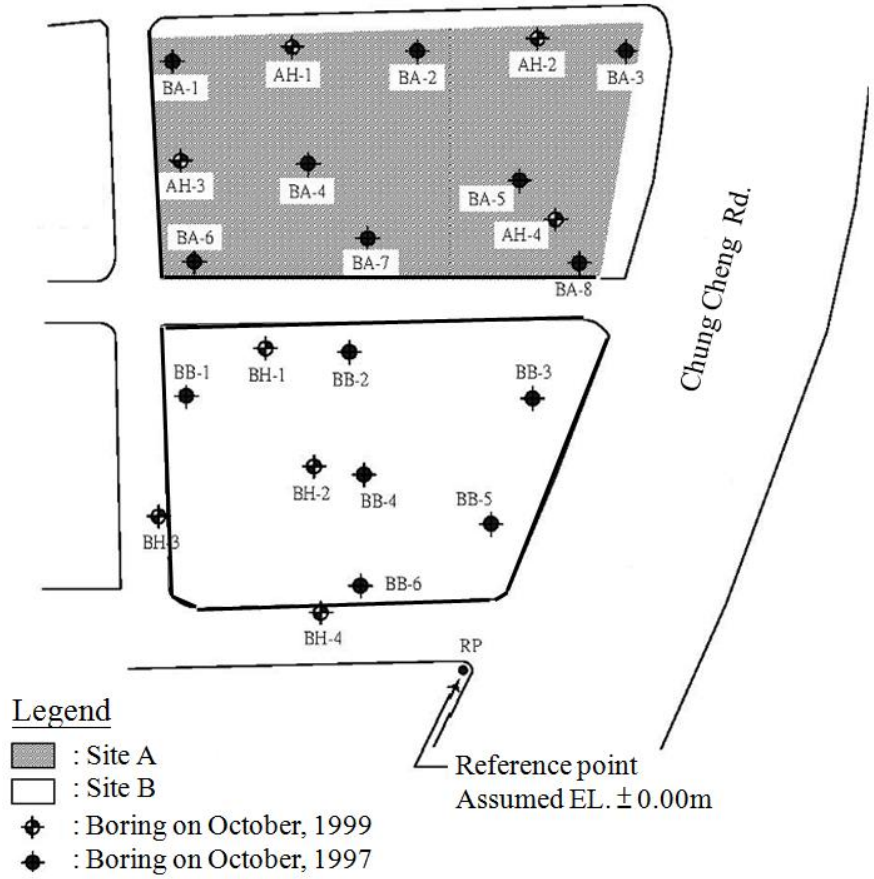

Figure 4.39. Planar configuration graph of drilled holes (Ou and Hsieh, 2004)

1. Results of geological survey in Site A

Figure 4.40 shows the boring logs in Site A. Within the range of GL. 0.0m~GL. -45m, the soil layers of Site A were divided into five floors, and the soil layer distributions as well as soil description are listed in detail in Table 4.1.

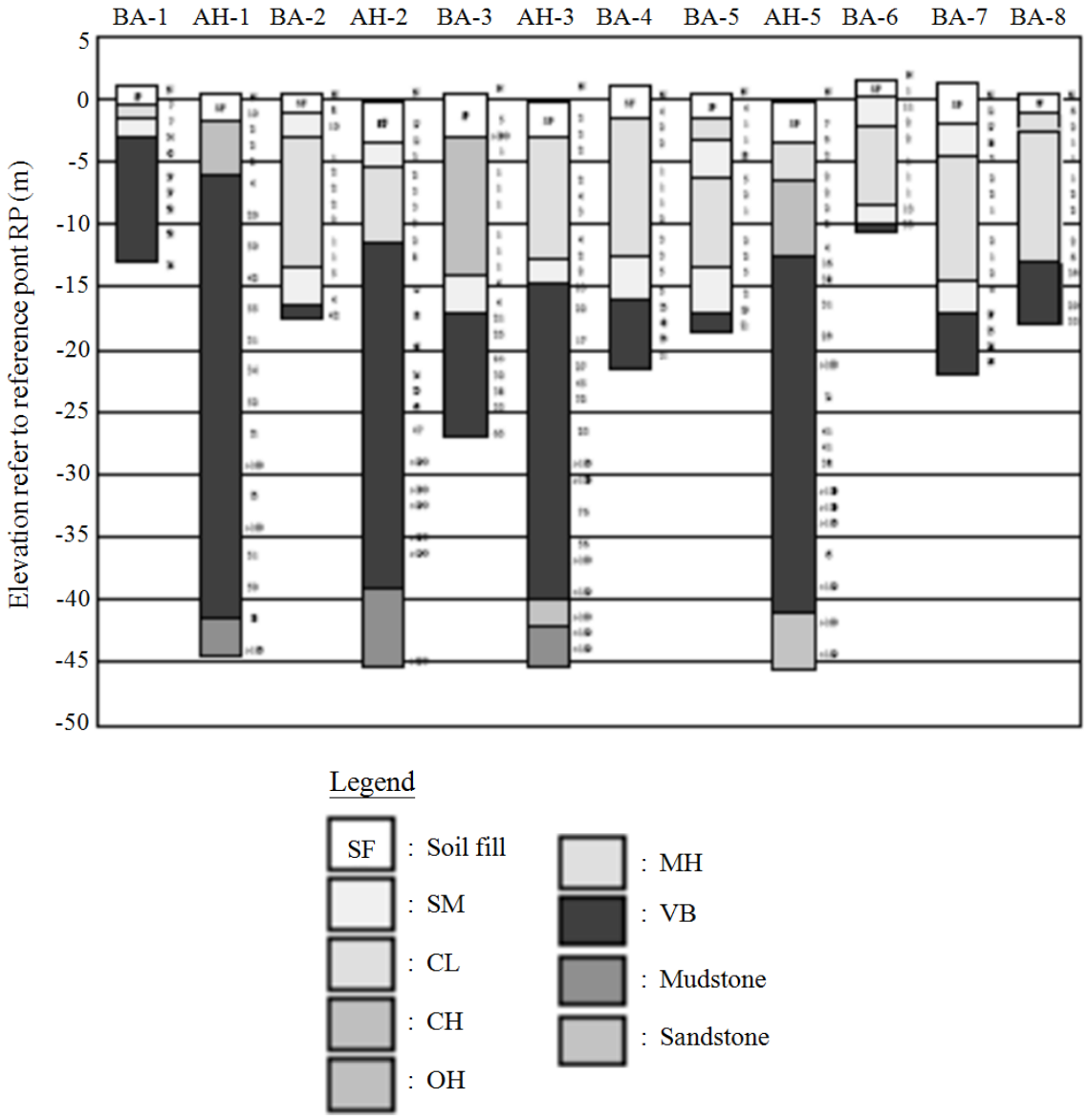

Figure 4.40. Boring logs in Site A (Ou and Hsieh, 2004)

Table 4.1. Distributions of soil layers and soil description in Site A (Ou and Hsieh, 2004)

Soil Layer No.	Types of soil	Distributions	Soil description
1	SM	0~6.3m, average thickness is around 3.5m	Yellow brown or dark brown silty fine sand, occasionally mixed with silty clay, loose to medium compactness, including fillers such as gravel stones and bricks
2	CL CH	1.5m~15.8m, soil thickness on the west side of base is around 1.0m thinner, thickness of the other places is around 10m	Brown silty clay, low to high plasticity, mixed with trace fine sand, gravels and grass roots, depth of 4.5~9.9m
			Grey or yellow grey silty clay, low to high plasticity, very soft consistency, including tiny to a large amount of fine sand, occasionally including gravels or yellow brown weathering gravels.
3	SM	10.2~17.7m, thicker in the middle of the base, tending to be thinner towards the northwest and southeast, average thickness is around 2.7m.	Yellow brown silty medium-fine sand, loose to medium compactness, including a small amount of small gravels and andesite.
4	VB	Depth of middle part of the base is 17.5m; depths of the north side and southeast side are 4m and 13.5m.	Yellow brown pyroclastic deposits, main body is silty medium sand and silty fine sand, medium to high compactness, including many andesites, the maximum particle diameter is around 9.0cm.
5	MS	Average depth is 41m beneath ground surface.	Yellow brown weathering mudstone, soft to medium hard, good degree of cementation

2. Results of geological survey in Site B

The boring logs in Site B is shown in detail in Figure 4.41, within the range of GL. 0m to GL. -45m, soil in Site B is divided into four layers, the distribution of soil layers and soil descriptions are listed in detail in Table 4.2.

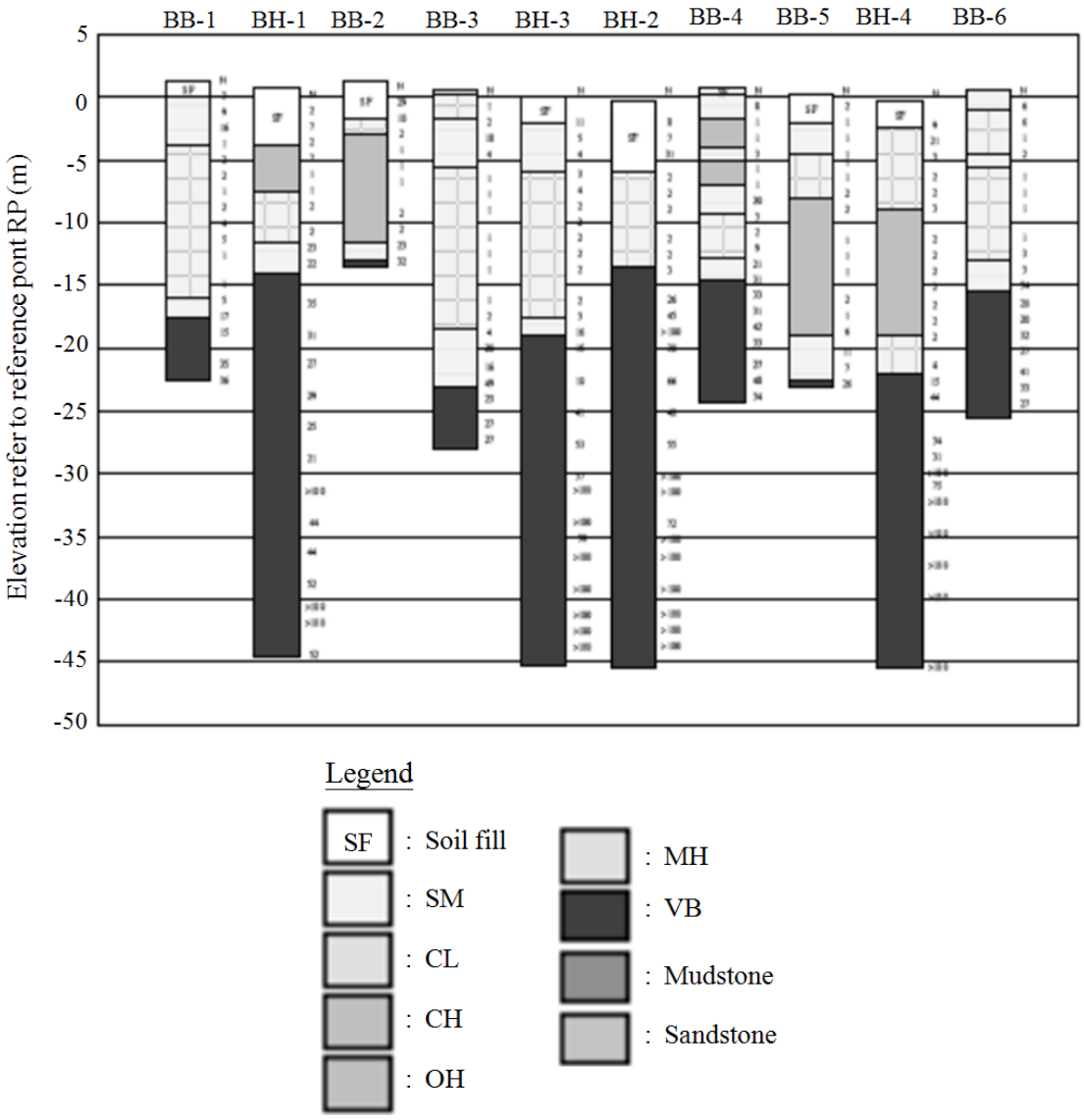

Figure 4.41. Boring logs in Site B (Ou and Hsieh, 2004)

Table 4.2. Distributions of soil layers and soil description in Site B (Ou and Hsieh, 2004)

Soil layer No.	Types of soil	Distributions	Soil descriptions
1	SM	0~6.0m, average thickness is around 5.2m, thicker at east and west side	Yellow brown or deep brown silty fine sand, mixed with silty clay occasionally, super-loose to medium compactness, including gravels, bricks and concrete blocks etc.
2	CL CH	4.7m~19.4m, average thickness is around 10.6m, thicker at east and west side.	Brown silty clay, high plasticity, super-soft consistency, including rotten woods and trace fine sand.
			Grey or yellow grey silty clay, low to high plasticity, including trace fine sand and gravel occasionally.
3	SM	12.5~23.5m, average thickness is 2.7m, thicker at east and west side.	Yellow brown silty medium and fine sand, medium to high compactness, including large amount of small gravels and small amount of andesite.
4	VB	Below 15.0~23.5m, depth in the middle part of base is shallower, thickness increases towards east side and west side.	Yellow brown pyroclastic deposits, main body is silty medium sand and silty fine sand, medium to high compactness, including many andesites, the maximum particle diameter is around 8.0cm.

Distributions of Ground Water Table and Water Pressure. In this case, the ground water table beneath the construction site is around GL. -1.5m. The water pressure of the first soil layer of silty sand presents a static water pressure distribution; the ground water pressure distribution of silty sand and pyroclastic deposits below the second soil layer of silty clay is larger than the static water pressure distribution, if the trend of ground water pressure distribution of pyroclastic deposits is raised to the ground surface, the water head of the pressure aquifer is estimated at around 2 meters above the ground surface.

Protection Methods for Neighboring Properties. Due to the existence of a soft clay layer at the construction depth of 4~16m, to prevent large displacement of the slurry wall during construction, the installation of SMW improved piles inside and outside the foundation was decided before construction. Secondly, since a pressure aquifer with high permeability

exists in pyroclastic deposits, in order to avoid piping phenomenon in construction, it was decided to conduct ground modification on four soil layers, the two layers on the top adopted partial improvement, the third floor adopted bottom-sealing improvement, and the fourth layer adopted the improvement of chemical grouting on bottom sealing.

However, in the course of grouting operations, due to gallons of ground water spilling out, the original ground modification plan was changed in order to prevent the liquid from the chemical grouting on the bottom sealing from bursting upwards. Figure 4.42 shows the ground modification plan after the change; according to Figure 4.42, the altered part of the ground modification includes:

1. Timbering to the slurry wall:

The SMW improved piles are changed to JSP improved piles within the distance of GL.0m~ GL.-5m to the inside of slurry walls.

2 .Bottom-sealing of foundation:

The original improvement zones of the third floor and fourth floor were changed to 100% JSG improved piles.

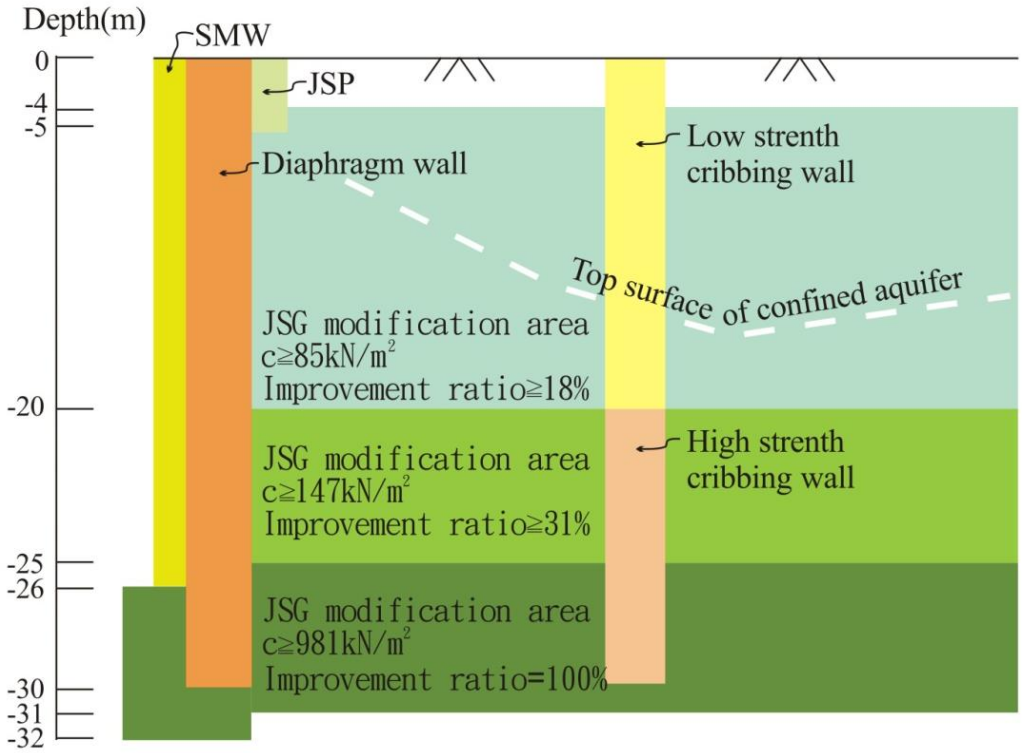

Figure 4.42. Section of ground modification after plan alterations (Ou and Hsieh, 2004)

After the plan alterations, JSG improved piles were deployed in three layers:

(1) GL.-4m~GL.-20m: partial improvement, $c > 85kN/m^2$, improvement proportion >18%.

(2) GL.-20m~GL.-25m: partial improvement, $c > 147kN/m^2$, improvement proportion > 31%.

(3) GL.-25m~GL.-32m: complete improvement, improvement proportion =100%, $q_u > 981kN/m^2$.

Troubleshooting. After the occurrence of neighboring damage disputes in August, 2001, the contractor conducted the following emergency plan:

1. Waterlogging grouting

Figure 4.43 is the section graph of waterlogging grouting on a side of the cribbing wall; according to Figure 4.43, both high-pressure grouting and low-pressure grouting exist in the waterlogging grouting zone, where high-pressure waterlogging grouting is deployed next to the cribbing wall while low-pressure waterlogging grouting is deployed in the division zones between cribbing walls. The range of high-pressure grouting is from GL.-20m to GL.-26.5m, while the range of low pressure grouting is from GL.-20m to GL.-27m.

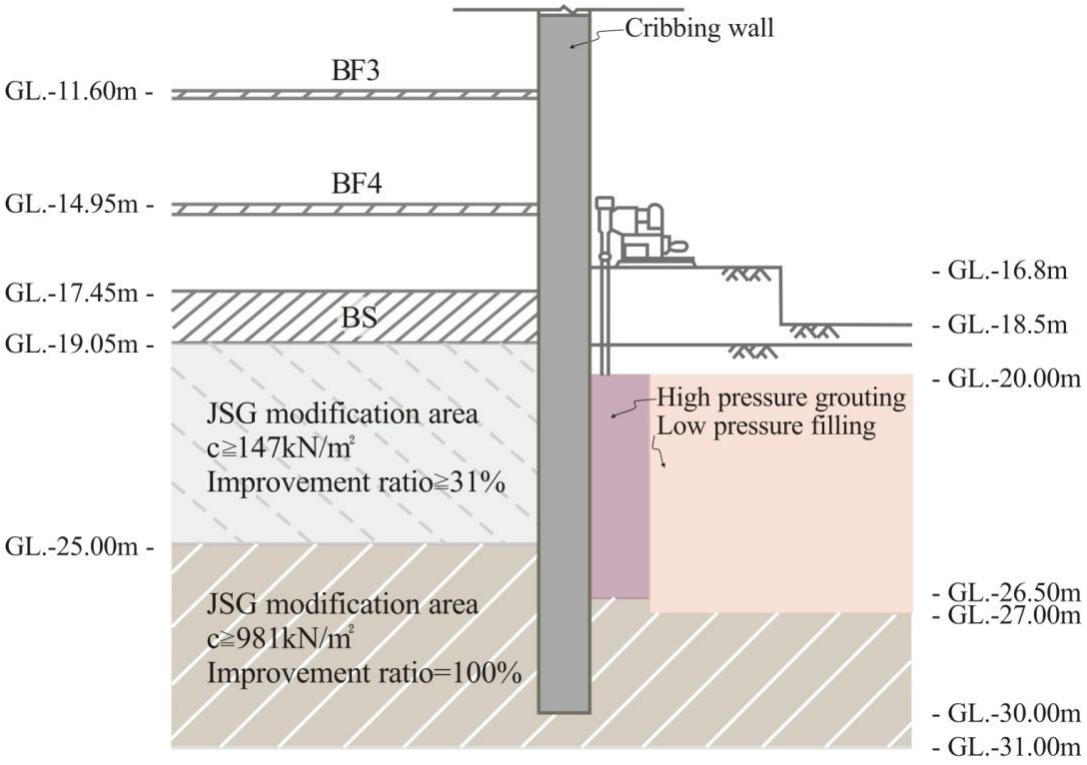

Figure 4.43. Section of waterlogging grouting on a side of igeta (Ou and Hsieh, 2004)

2. Deploying recharging wells and observation wells

In the foundations, recharging wells are drilled along the outside of slurry walls, the depth of drilled holes changes from 25m to 33m, after that water is injected into the recharging wells by gravity or pressure.

For gravity-driven recharging wells, six holes were drilled in Site A and twenty one holes were drilled in Site B, water heads were all 5m; however, for pressure-driven wells, fifteen holes were drilled in Site A and three holes were drilled in Site B, pressures were all 686.57kPa (Ou and Hsieh, 2004).

In addition, six water table observation wells were deployed on the north side of Tienmu East Road. If the decline of water pressure reached the operation value in the follow-up construction, ground water could be recharged through observation wells to alleviate the decline of ground water on the north side of Tienmu East Road (Ou and Hsieh, 2004).

3. The change of water pressure and ground settlement

After the accomplishment of waterlogging grouting and ground water recharging, Figure 4.44 shows that water pressure could still decline because of the piping phenomenon, which could also lead to the consistent increase of ground settlement.

Note: black line is ground water pressure, green line is ground settlement.

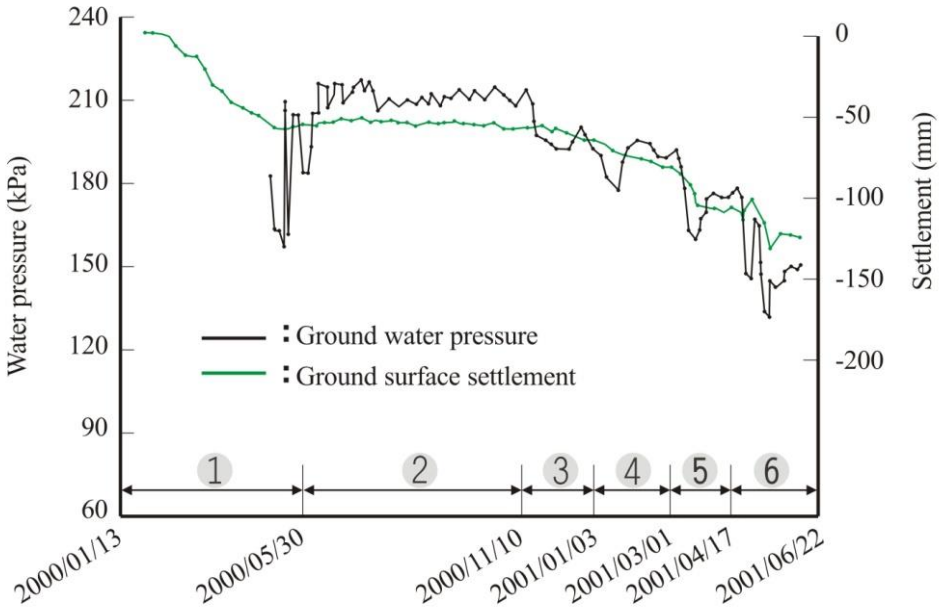

Figure 4.44. The graph of water pressure and ground settlement change over time (Ou and Hsieh, 2004)

4. Enhancement of neighboring households

When excavating to GL.-16.8m, Figure 4.45 shows the neighboring damage disputes that include Qiao-Tzu Building and San-Feng Building. The maximum distance from Qiao-Tzu Building to slurry walls on the north of Site A is measured at 212m, while the maximum distance from San-Feng Building to slurry walls on the north of Site A is measured at 155m. Since the foundation excavation depth is 16.8m, when neighboring damage disputes occurred the maximum distance from Qiao-Tzu Building to slurry walls on the north of Site A was taken as 12.6 times the excavated depth, while the maximum distance from San-Feng Building to slurry walls on the north of Site A was taken as 9.2 times the excavated depth.

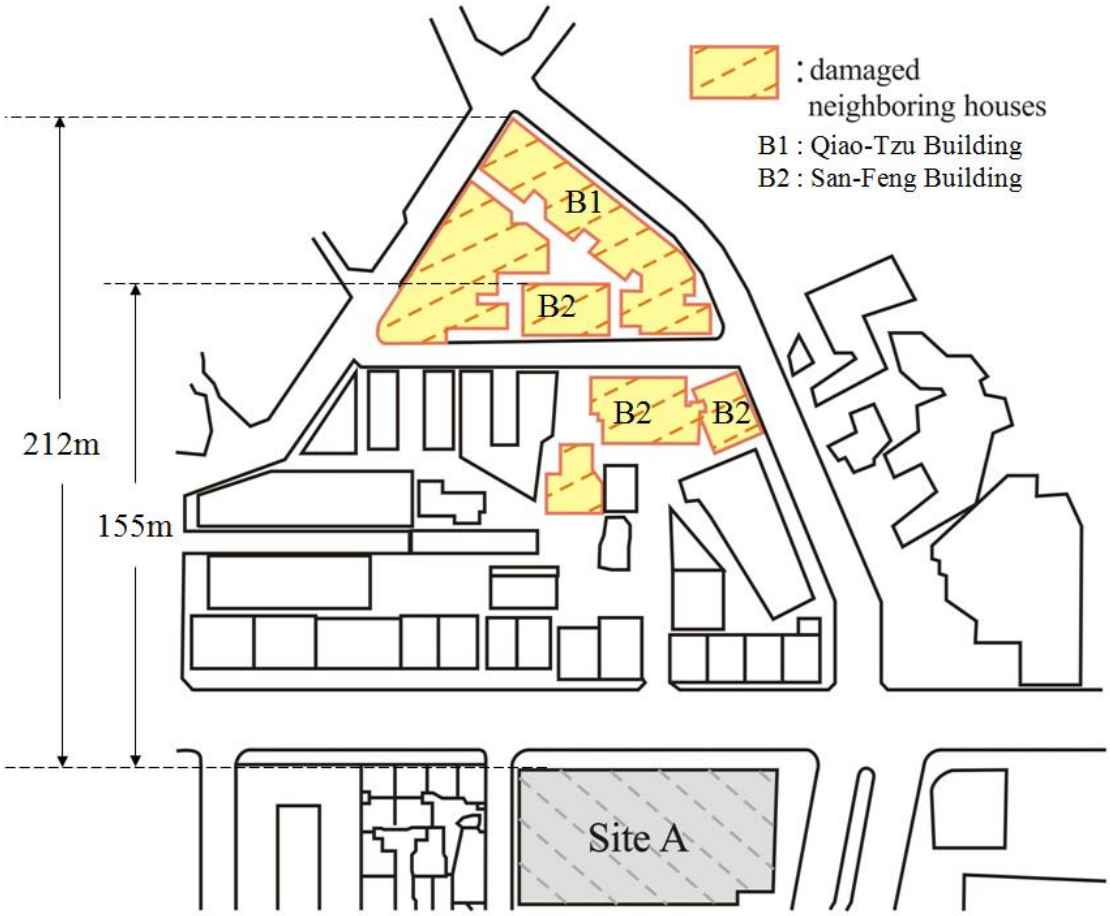

Figure 4.45. Zones of neighboring damage and the range of neighboring household settlement (Ou and Hsieh, 2004)

5 . Inspection operation

In this case, inspection operation is continuously conducted in the follow-up construction, and security patrols are deployed according to the reactions of neighboring residents. If the decline of ground water pressure reaches the warning value, or new cracks occur on neighboring buildings, the frequency of measuring and inspection should be increased (Ou and Hsieh, 2004).

4.4.2 Analysis of Neighboring Damage Cases

For the neighboring damage case of Cathay Pacific Tienmu Shopping Mall discussed in Chapter 4.1 of this chapter, some difficult problems or unsettled problems, which require further research include:

1. For Cathay Pacific Tienmu Shopping Mall, the amount of ground modification is huge, and the ground modification project must change depending on the circumstance. The purpose of the ground modification t project is to decrease the lateral deformation of slurry walls and the permeability of bottom-sealing grouting. Further the slurry walls around the excavation site and the bottom-sealing grouting are expected to be the block body to block ground water.

2. The excavation depth of slurry walls on the north side of Site A is 30m, and the geological survey results of BA-1, AH-1, BA-2, AH-2, and BA-3 in the north side of Site A show that the soil beneath GL.-3m, GL.-6m, GL.-17m, GL.-12m, GL.-18m are all in the pyroclastic deposits layer. The pyroclastic deposits layer is pressure aquifer, and the head of ground water of the pressure aquifer is 2m above the ground surface.

3. Figure 4.42 shows that the excavation depth of slurry wall trenches is GL.-30m, it is known that most slurry walls are next to pyroclastic deposits, thus the pressure aquifer can have significant impacts on stabilizing liquid in trenches. When stabilizing liquid is boiling, particle separation and incomplete cementing could occur on the concrete slurry poured through tremie pipes, which can lead to loss of water tightness of slurry walls.

4. The JST jet grouting method, uses a high pressure pump to inject hardener into soil layers at a very high speed through pipes and injection devices, which can cut and destroy the original soil issues and make a soil tightly mixed with hardener. With the rotation or lifting of grouting rods, a hard and impermeable improved soil pile is formed. However, the JSR jet grouting method is not suitable for the modification of pyroclastic deposits .

5. According to the second point of this section, the soil of the bottom-sealing grouting layer in Site A is composed of pyroclastic deposits, which contain a pressure aquifer. However, in this case, the grouting methods selected by the construction company, either the bottom-sealing grouting or waterlogging grouting, are not suitable for pyroclastic deposits with a pressure aquifer, so the quality of bottom-sealing grouting or waterlogging grouting cannot be guaranteed.

6. After the occurrence of neighboring damage disputes, an outsourced research report claims that the water gushing paths are the primary reason for neighboring damage disputes, but the actual-existing water gushing paths could not be found.

7. For the locations of neighboring damage disputes, such as Qiao-Tzu Building and San-Feng Building etc., the maximum distance from Qiao-Tzu Building to slurry walls on the north of Site A is 12.6 times the excavated depth, while the maximum distance from San-Feng Building to slurry walls on the north of Site A is 9.2 times the excavated depth. These locations of neighboring damage disputes are much larger than the range influenced by ground settlement induced by lateral displacement of the retaining walls discussed in Section 4.2.8; and the reason why the locations are so special have not been discussed by scholars and specialists before.

The Existing Shear Bands or Shear Textures.

1. Use the features of dislocation terrain to identify shear bands or shear textures

Figure 4.46 shows that according to satellite images of the features of dislocation terrain, the existing shear textures in a total shear band width can be identified in the neighboring area of the construction site of Cathay Pacific Tienmu Shopping Mall. The content includes principal deformation shear D (strike N64^{o}E), thrust shear P (strike N82^{o}W), Riedel shear R (strike N20^{o}E), conjugated Riedel Shear R’ (strike N12^{o}W), and compression texture S (strike N48^{o}W).

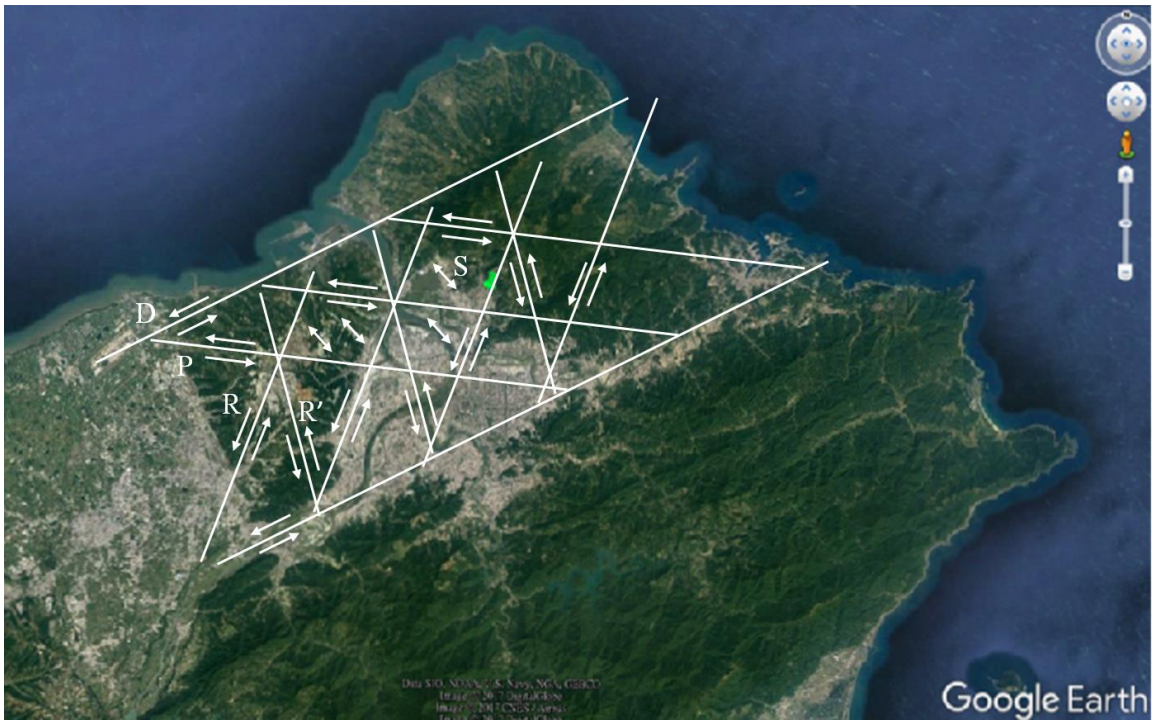

Figure 4.46. Shear textures in a total shear band width exists in the neighboring zone of construction site of Cathay Pacific Tienmu Shopping Mall (background picture is from Google Earth, 2017)

2. Use epicenter distribution to identify shear bands

Figure 4.47 shows the graph of earthquake epicenter distribution (the yellow pins) in the neighboring area of Cathay Pacific Tienmu Shopping Mall after 2006. According to Figure 4.47, there are two groups of shear bands with different strikes, and they are very close to the shear textures of the neighboring damage site of Cathay Pacific Tienmu Shopping Mall. Its strikes are the same as the strikes of primary deformation shear D (direction N64^{o}E) and Riedel shear R (direction N20^{o}E).

On further inspection of Figure 4.47, it can be seen that the neighboring damage location of Cathay Pacific Tienmu Shopping Mall is exactly the intersection zone of primary deformation shear D and Riedel shear R according to Figure 4.47.

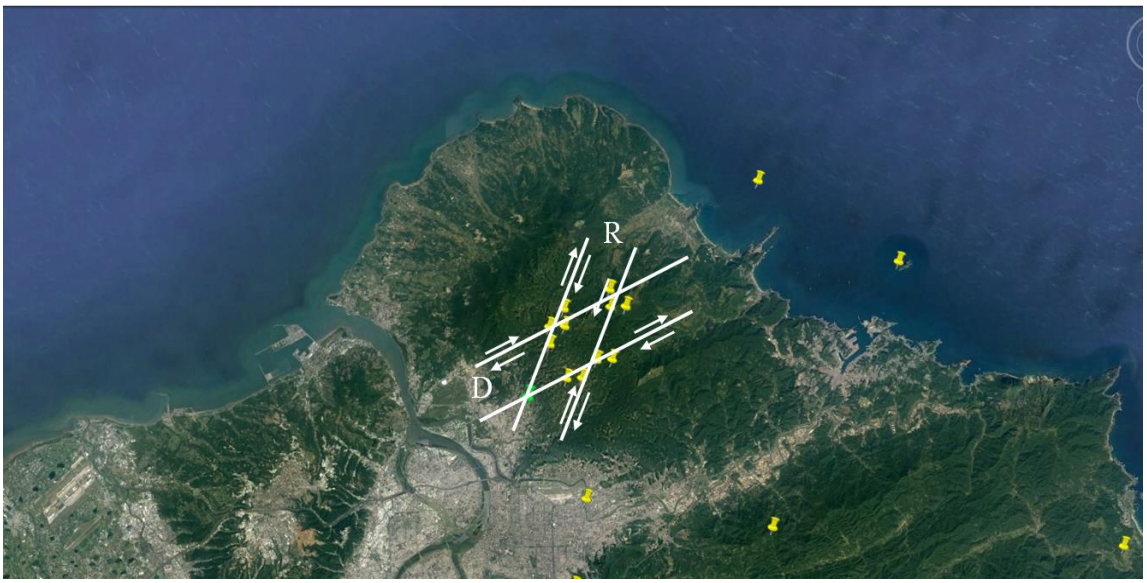

Figure 4.47. Taipei tectonic earthquake epicenter and corresponding shear bands after 2006
(background picture is from Google Earth, 2017)

Secondly, Taipei experienced destructive tectonic earthquakes 7~8 times in the twentieth century, where a tectonic earthquake epicenter is located near the corner of Danshui River, Chongyang Bridge, which is close to the neighboring damage site of Cathay Pacific Tienmu Shopping Mall. In addition, Figure 4.48 shows that the neighboring area of this epicenter contains two groups of shear bands with strikes of N64^{o}E and N20^{o}E respectively, their strikes are close to the strikes of principal deformation shear D and Riedel shear R, respectively. If the neighboring damage site of Cathay Pacific Tienmu Shopping Mall is linked to the epicenter, then the strike of this line is same as the strike of Riedel shear R shown in Figure 4.46.

Therefore, it can be known that if the tectonic earthquake epicenter is close to the principal deformation shear D and Riedel shear R shown in Figure 4.46, the amount of shear banding and the degree of fracture at of site of neighboring damage near Cathay Pacific Tienmu Shopping Mall can be consistently increased, which can increase the neighboring damage.

Note: 1. Green circle pin is the location of neighboring damage in Cathay Pacific Tienmu Shopping Mall

2. Center of the black star is the epicenter of earthquake

Figure 4.48. Epicenter of 7~8 destructive earthquakes that occurred in Taipei in the twentieth century (Chang, 2004)

3. Use fault distribution to identify shear textures

If the two groups of shear bands in Figure 4.49 are overlaid on the active fault distribution of north Taiwan, it can be seen that there are two groups of shear bands near the neighboring damage site of Cathay Pacific Tienmu Shopping Mall, which are highly related to the active faults such as Jinshan Fault, Kanjiao Fault, and Shanchiao Fault. Faults such as the Taipei fault and Chuchih fault etc., which are parallel to the Kanjiao fault, although they are quite far away, when the magnitude of tectonic earthquake is large enough, they may also have some relationship to the existence of two groups of shear textures shown in Figure 4.49.

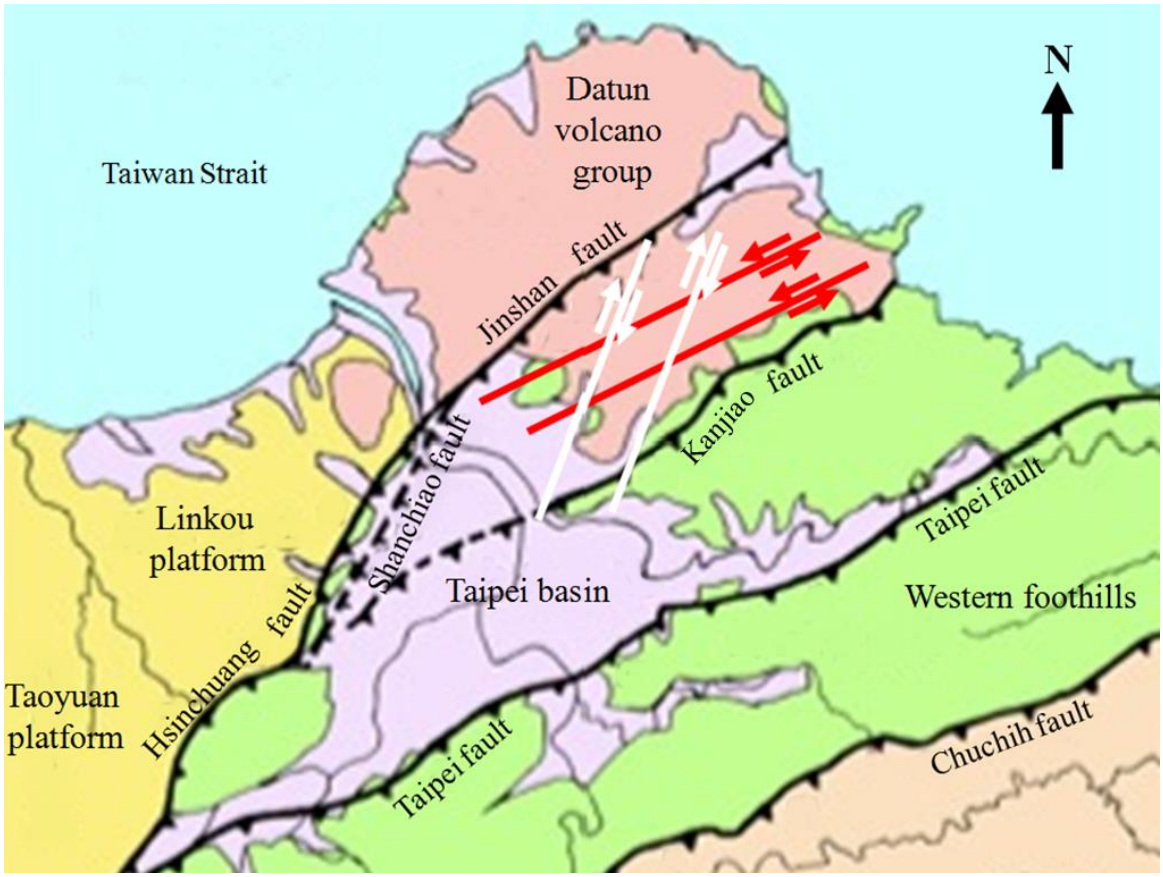

Figure 4.49. The relationships between active faults in north Taiwan and the shear bands corresponding to the epicenters of north Taiwan

(Digital Education Portal of Education Department, 2017)

4. Shear banding tilted slopes

Shear textures with different strikes within a total shear band width can facilitate the formation of a shear banding tilted slope in a mountainous area, for example, the three slope sections of po, oi, and ie shown in Figure 4.50.

Since a shear texture dislocates easily in a felt tectonic earthquake, the degree of fracture consistently increases, which causes the shear band rocks to be subject to weathering and softening after submerged in water. Therefore, sliding failure phenomenon can happen again on shear banding tilted slopes an appropriate long period of time after the first sliding, as shown in Figure 4.51, the three slope sections of pm, mh, and hc. This sliding failure used to be called retreating sliding failure; and the actual

retreating sliding failure that occurs in the shear banding tilted slope is shown in Figure 4.52, where ABE blocks slide first, followed by BCFE blocks, and CDGF blocks are the last to slide. The actual shear banding tilted slope consisting of sliding surface GF, FE, and EA is similar to that made by three sliding surfaces ch, hm, and mp in Figure 4.51. This result also validates the mechanism of sliding failure in the shear banding tilted slopes presented in Figures 4.50 and 4.51, and the potential of sliding failure in the shear banding tilted slope is considerable.

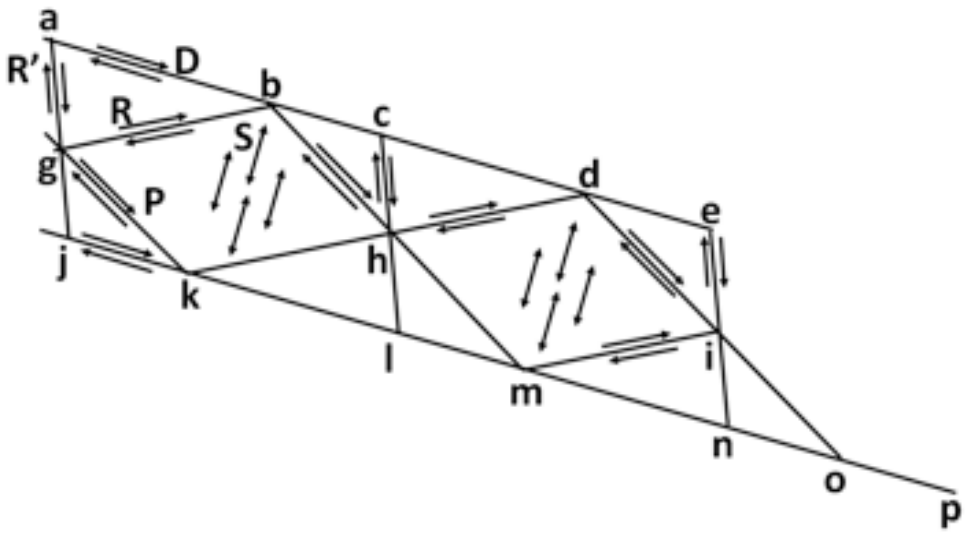

Figure 4.50. First sliding failure on shear banding tilted slope

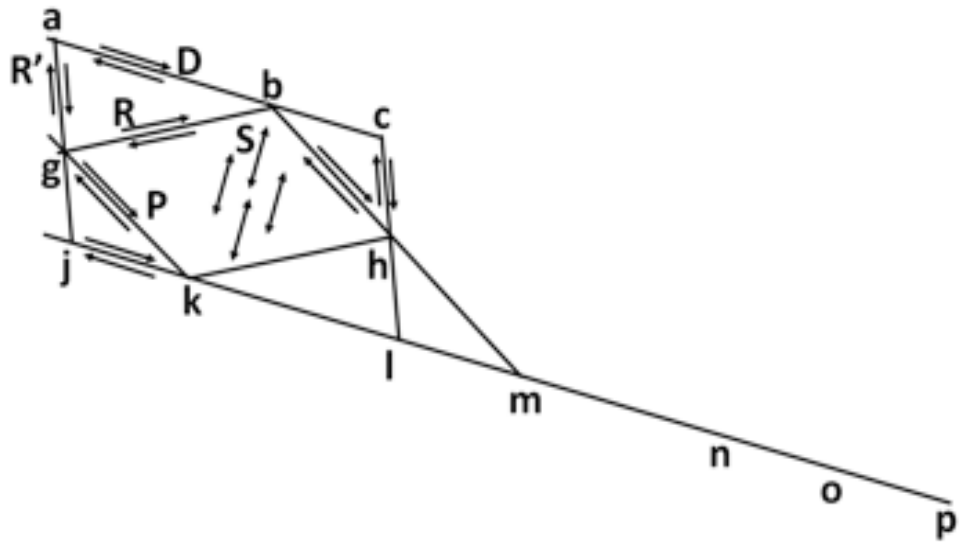

Figure 4.51. Second sliding failure on shear banding tilted slope

(a) After sliding failure

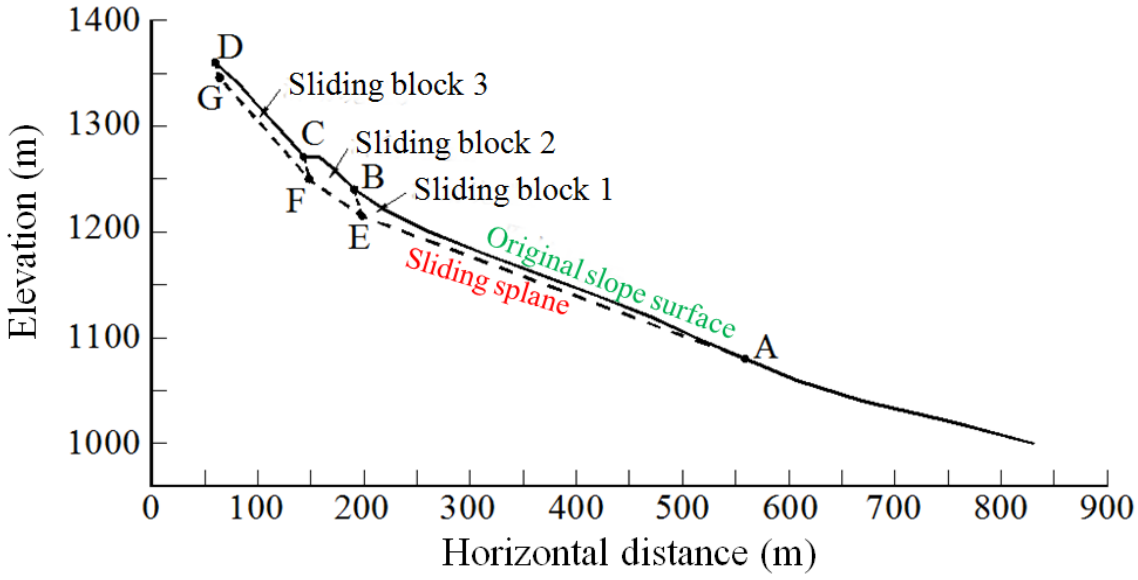

(b) Section of sliding

Figure 4.52. Retreating sliding failure on tilted slopes of shear band

5. The impacts of the change of ground water table in the pressure aquifer of shear banding tilted slopes

After the formation of the three slope sections pm, mh, and hc (Figure 4.51), pyroclastic ashes, silty sand, high plasticity clay, and low plasticity clay accumulate on mh and hc slope sections, and this is how the geological features of Site A and Site B of the Cathay Pacific Tienmu project (Figure 4.37 and Figure 4.38) form.

The permeability of pyroclastic deposits is high while the permeability of silty sand, high plasticity clay, and low plasticity clay is low, and the pyroclastic deposit is a pressure aquifer. Figure 4.48 shows that when the construction site is located on a gentle slope, if the ground water table is expected to be lowered to 1m below the excavated surface by draining water before excavation, then the decline of the ground water table on the right and left side of building B is quite similar according to Figure 4.53, and the settlement on the right and left side of building B is quite similar too, so the cracking issues on building B are slight. However, the decline of the ground water table on the right and left side of building A is quite different, so the settlement on the right and left side of building A is quite different too and the cracking issues on building A are more serious.

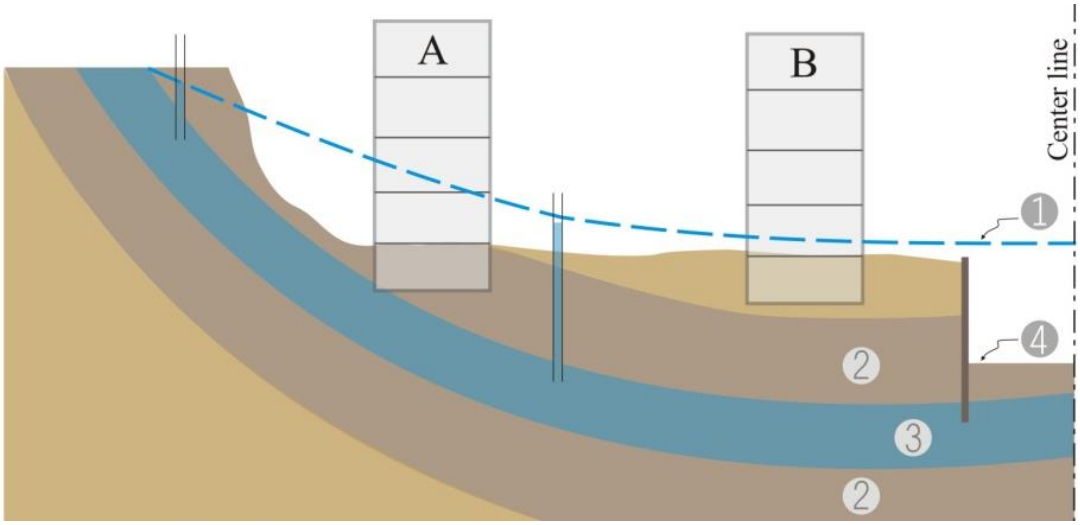

(a) Before draining the water

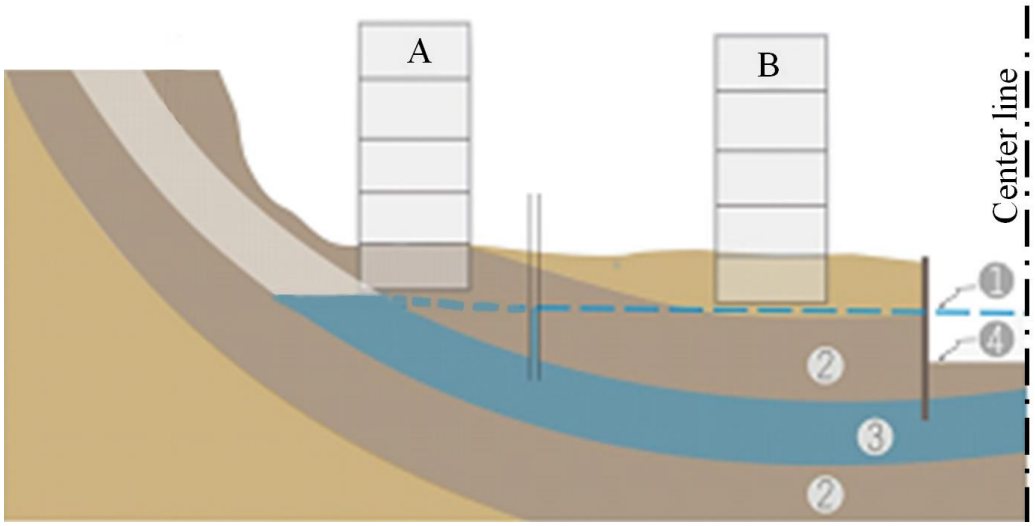

(b) After draining the water

Legend: ① pressure water table，② impermeable layer，③ permeable layer，④ excavation surface

Figure 4.53. Model of water table change due to drainage in a pressure aquifer

6. Effects of shear banding

When a tectonic earthquake of large magnitude occurs, shear bandings can dramatically increase the degree of rock fracture in the shear banding zone (Figure 4.54).

Figure 4.54. Leaning failure of buildings induced by shear banding in 921 Earthquake

When a shear band is located on a river bed, the rock fragments in the shear banding zone are going to flow with flood, which can lead to deep channelization of the riverbed (Figure 4.55), river bank erosion (Figure 4.56), and wash-out (Figure 4.57).

Figure 4.55. Deep channelization phenomenon on a shear banding zone of riverbed

Figure 4.56. Erosion phenomenon of a shear banding river bank

Figure 4.57. Wash-out phenomenon of a shear banding river bank

For the shear banding tilted slope shown in Figure 4.58, in a tectonic earthquake with a large magnitude, the large shear banding can lift the hanging wall and increase the degree of rock fracture. While in a lot of small tectonic earthquakes, the degree of rock fracture in the shear band will consistently accumulate.

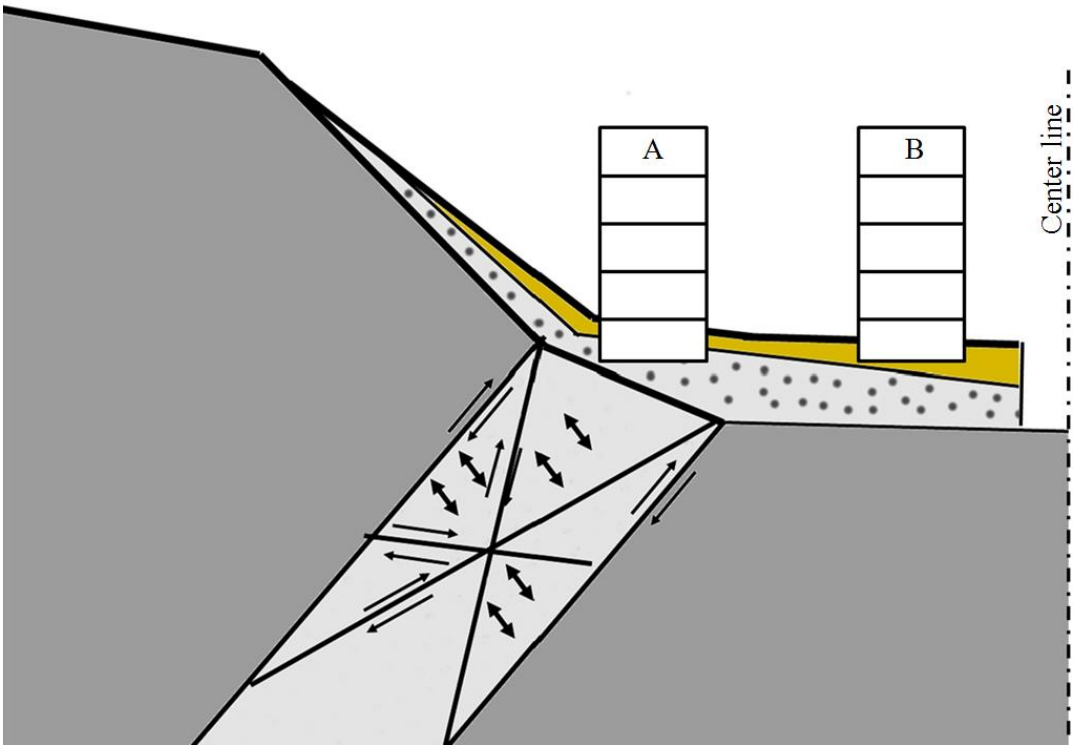

Figure 4.58. Alluvial layers on shear banding tilted slope

After the formation of a shear banding tilted slope, after pyroclastic ashes and low-permeable soil accumulate on the tilted slope, and after pyroclastic deposits become a pressure aquifer, if draining water in a gentle slope section, then the rock fragments of the shear band at the steep side can be washed away at a velocity from slow to fast by the flow of the pressure water, so the building on this section will suffer differential settlement. This phenomenon is similar to the deep channelization of riverbed, river bank erosion, and wash-out phenomena mentioned above, and it is similar to the piping failure of a rock dam.

For Cathay Pacific Tienmu Shopping Mall, when constructing slurry walls, the slurry trench deeps into the pressure aquifer of pyroclastic deposits. Since pyroclastic deposits locate in pressure aquifer, in a case where the head of the pressure aquifer is 2m higher than the ground surface and ground water of the excavation zone continuously bursts upwards, stabilizing liquid in the slurry trench cannot fulfill its functions. When the initial-set environment of concrete in the water is not ideal, it is very difficult to control the quality and strength of slurry walls.

For ground modification project in Site A, due to the impacts of the pressure aquifer, the quality of JSG modification in the first layer, JSG

modification on the second layer, and JSG bottom-sealing grouting on the third layer might be influenced because the cement paste (hardener) is influenced by the pressure aquifer, and the grouting quality of pyroclastic deposits cannot be guaranteed.

In a situation where the quality of slurry walls, JSG modification in the first layer, JSG modification on the second layer, and JSG bottom-sealing grouting on the third layer cannot be guaranteed, during construction, the phenomenon of recharging ground water from one side and ground water flow out on the other side might occur.

Based on the discussion above, it can be known that the out-flowing paths of ground water are obvious, these ground water paths are from the pressure aquifer of the shear banding tilted slope, which flow to the excavation zone due to consistent water drainage in the construction site. Then the water, starting from pyroclastic deposits, flows upwards though cracks, or through slurry walls modification by low-quality JSG, or JSP, or other ground modification methods.

Discussion of Why the Range of Neighboring Damage is Extremely Large. According to the distribution of permeable layers and impermeable layers on the shear banding tilted slope, for excavations on the gentle side of tilted slope, when slurry walls deeps into the high-permeable pressure aquifer and ground water table is lowered by drainage before or during excavation (Figure 4.53), it is easy for leaning failure or severe cracking phenomenon to occur to buildings on a steep side of shear banding tilted slopes (building A), whose foundation is supported by shear band rocks, due to differential settlement induced by consistent water drainage and inhomogeneous change of ground water table.

For buildings on the gentle section of the shear banding tilted slope, since its foundation soil does not have a shear band and the change of ground water table induced by consistent drainage is quite homogeneous, the settlement of building B is quite even and cracking phenomenon is very slight.

In this regard, the degree of leaning or cracking failure of buildings on shear banding tilted slopes, depends on the location of localized shear bands and the change of water table, which is irrelevant to the multiples of excavation depth. In other words, in the neighboring damage case of Cathay Pacific Tienmu Shopping Mall, when excavation depth reaches 16.8m, although the maximum range of neighboring damage disputes is 12.6 times

the excavated depths, the location of neighboring damage disputes is exactly the location of maximum slope variation of shear banding tilted slopes, which is also the locations of localized shear band (Figure 4.58).

4.5 Null-neighbor-damage Construction Methods

4.5.1 Null-neighbor-damage methods Relevant to Foundation Bearing Capacity

Extending Range of Shear Failure Surface of Foundation Soil Before Construction. As shown in Figure 4.59, when the foundation of a building is next to property line, under the ultimate bearing force q_u, the left sliding failure surface $\overline{abcd}$ has exceeded the property line, marked by red broken line, before the shear stress of foundation soil reaches the shear resistance strength. In other words, the stabilization of the building's foundation in Figure 4.59 is maintained by other land bases outside the property line, this phenomenon, either according to the reality or law, belongs to infringement behaviors.

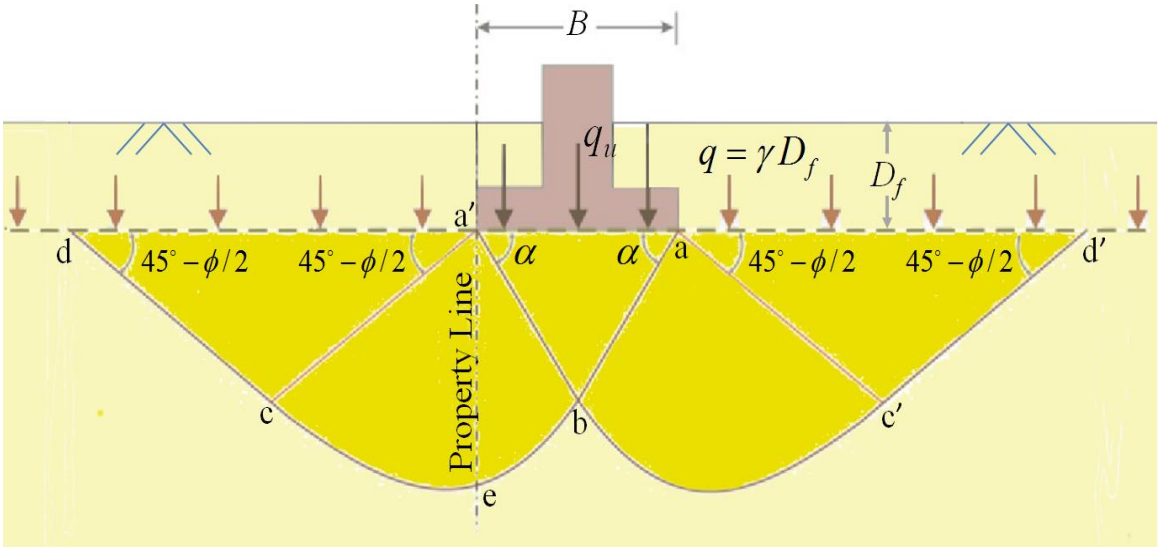

Figure 4.59. The range of shear failure surface of ultimate bearing capacity before construction (redrawn from Terzaghi, 1943)

The Range of Shear Failure of Foundation Soil after Excavation. When the excavation of new building is carried out, the old building's range of shear failure of ultimate bearing capacity is changed from the total range of abecd and a'bc'd' in Figure 4.59 to the range of abea' in Figure 4.60.

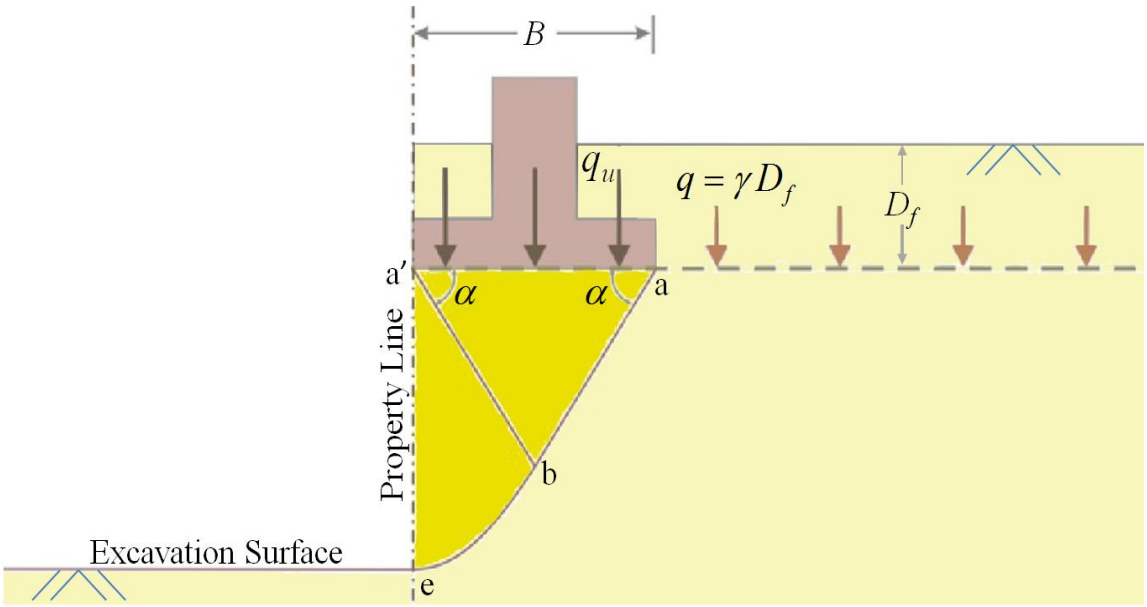

Figure 4.60. The range of shear failure surface of ultimate bearing capacity after construction

Figure 4.60 shows that after the excavation of new building, the old building's range of shear failure of ultimate bearing capacity has dramatically decreased. And during the excavation of a new building, the reason why the foundation bearing capacity decreases so much is due to the loss of symmetry. The second reason is that part of the range of shear failure , which exceeds the property line, is demolished in the construction of the new building.

The Null-neighbor-damage Method one Relevant to Foundation Bearing Capacity. Figure 4.61 shows when the property line at one side of the old building's foundation, then the range of shear failure of ultimate bearing capacity shall cross the property line a distance of W_b. If the foundation retreat a distance of W_b from the property line, all the range of shear failure of ultimate bearing capacity can be guaranteed within the property line. Thus no neighboring damage problems relevant to foundation bearing capability can occur during construction.

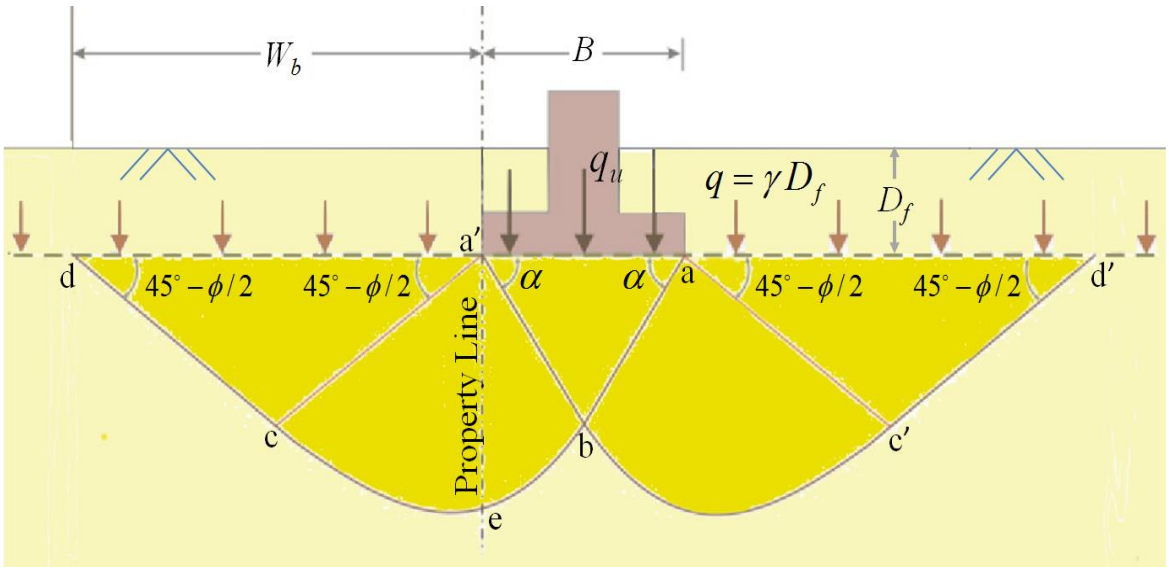

Figure 4.61. The retreat distance of null-neighbor-damage building relevant to foundation bearing capacity

The null-neighbor-damage Method Two Rrelevant to Foundation Bearing Capacity. When the foundation of the old building is a pile-group type foundation, if the excavation of the new building does not induce differential settlement in the foundation of the old building, excavation would not induce neighboring damage issues relevant to foundation bearing capacity. On the contrary, excavation would induce neighboring damage issues relevant to foundation bearing capacity if differential settlement is induced in the foundation of the old building.

Above all, when calculating the settlement of pile groups, if all piles are located in homogeneous soil, the total load can be hypothesized as loading on the surface of two thirds of the pile length. If the tips of the pile group are located in the soil, which is more compact or harder than the overburden layer, then the total load can be hypothesized as loading on the surface of pile tips.

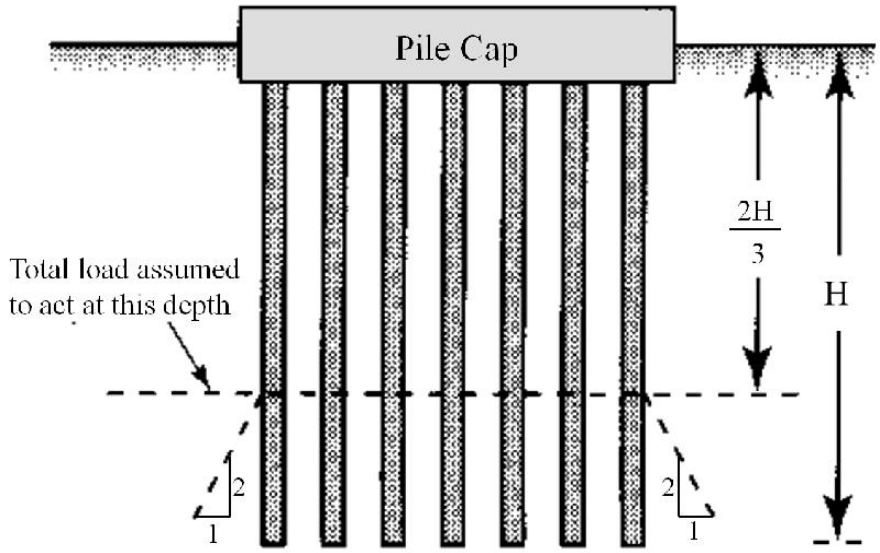

(a) Homogeneous soil

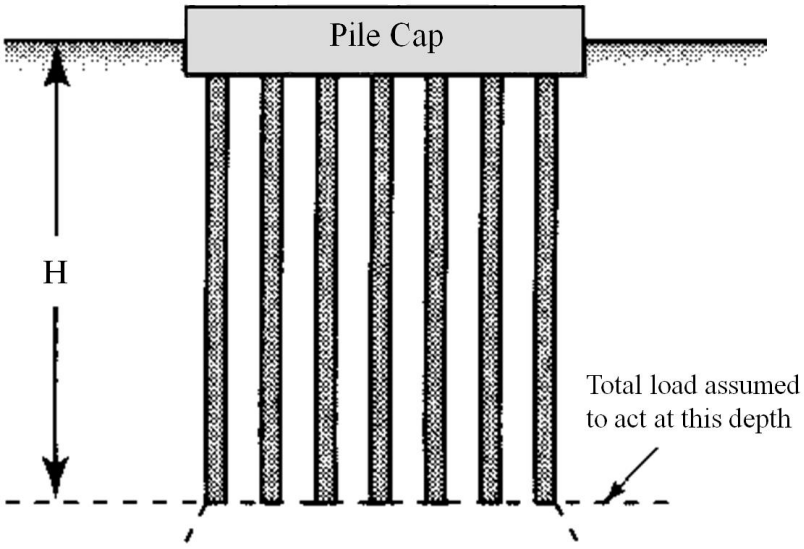

(b) Hard clay or compact sand on the pile tips

Figure 4.62. The hypothesized conditions of calculating settlement of pile group (McCarthy, 2007)

When the old building's pile groups (pile length H) are located in homogeneous soil, according to Figure 4.62a, as long as the building's excavation depth is no more than 2H/3, then it can be guaranteed that excavation would not induce any neighboring damage issues relevant to foundation bearing capacity or differential settlement.

When the old building's pile groups (pile length H) are located in hard clay or compact sand soil, according to Figure 4.62b, as long as the building's excavation depth is no more than H, then it can be guaranteed that excavation would not induce any neighboring damage issues relevant to foundation bearing capacity or inhomogeneous settlement.

4.5.2 Null-neighbor-damage Methods Relevant to Vertical Stress Contour

Vertical Stress Contour before Construction. As shown in Figure 4.63, if a building's foundation is next to the property line, regardless of whether the foundation is a square foundation or strip foundation, when the foundation bears a vertical stress q_s, the vertical stress contours σ_v in the foundation soils will be distributed outside the property line marked by broken lines. In other words, the stabilization of a building's foundation in Figure 4.63 is maintained by other land bases outside the property line, this phenomenon, either according to the reality or law, belongs to infringement behaviors.

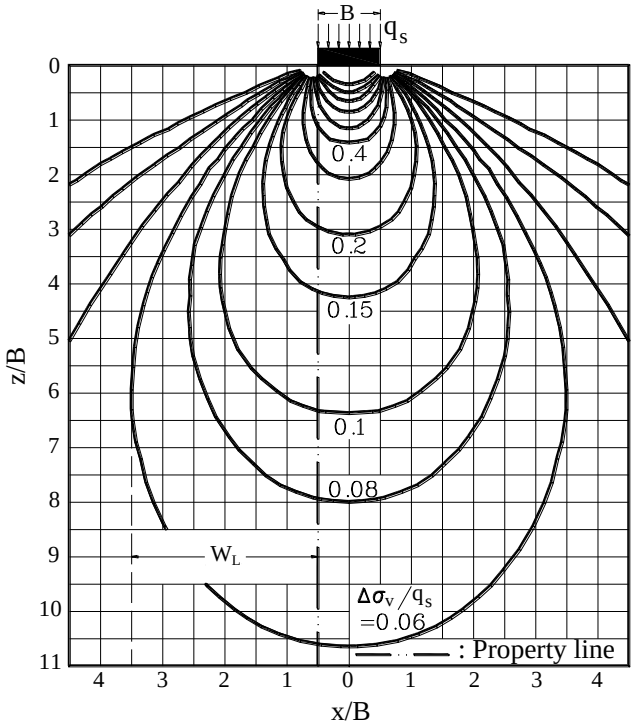

(a) Strip foundation

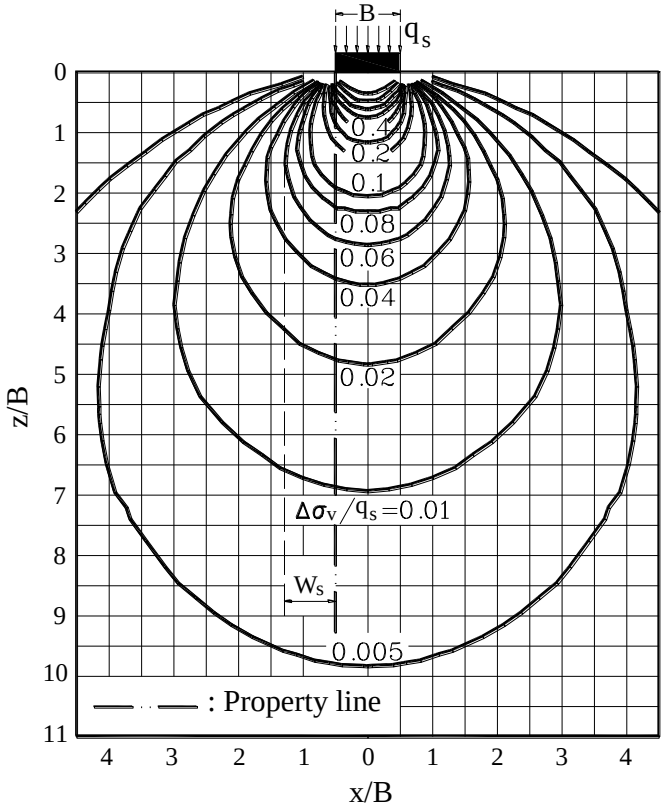

(b) Square foundation

Figure 4.63. Vertical stress contours in foundation soils (Lambe and Whitman, 1972)

Null-neighbor-damage Methods Relevant to Vertical Stress Contours of Foundation Soil. Firstly, hypothesize that the vertical stress contours σ_v of the foundation soil are smaller than $0.06q_s$, excavation would not induce neighboring damage disputes or the infringement problem. Under such a hypothesis, according to Figure 4.63a, moving the strip foundation of an old building backwards, keeping a distance of W_L from the property line, can guarantee that the vertical stress contours larger than $0.06q_s$ would all locate in the property line, and neighboring damage issues relevant to vertical stress contours induced by excavation would not occur. Secondly, according to Figure 4.63b, moving the square foundation of an old building backwards, keeping a distance of W_S from the property line, can guarantee that the vertical stress contours larger than $0.06q_s$ would all locate in the property line, and neighboring damage issues relevant to vertical stress contours induced by excavation would not happen.

4.5.3 Null-neighbor-damage Methods Relevant to Ground Settlement

1. According to Rankine's Theory of Active Earth Pressure

Before the excavation of a new building, if the stresses of the old building's foundation soil are under K_o conditions such that the corresponding Mohr circle marked in blue line is presented in Figure 4.64a, then during the excavation of the new building, if the vertical stress σ_v of soil on one side of excavation zone remains unchanged, and the lateral stress σ_h continues to decrease, then Mohr's circle of soil failure is shown by the red line of Figure 4.64a, where σ_{hf} is the lateral stress when a Rankine active failure surface occurs in the foundation soil, while the red broken line represents the angle $45^\circ - \phi/2$ between Rankine active failure surface and the vertical line .

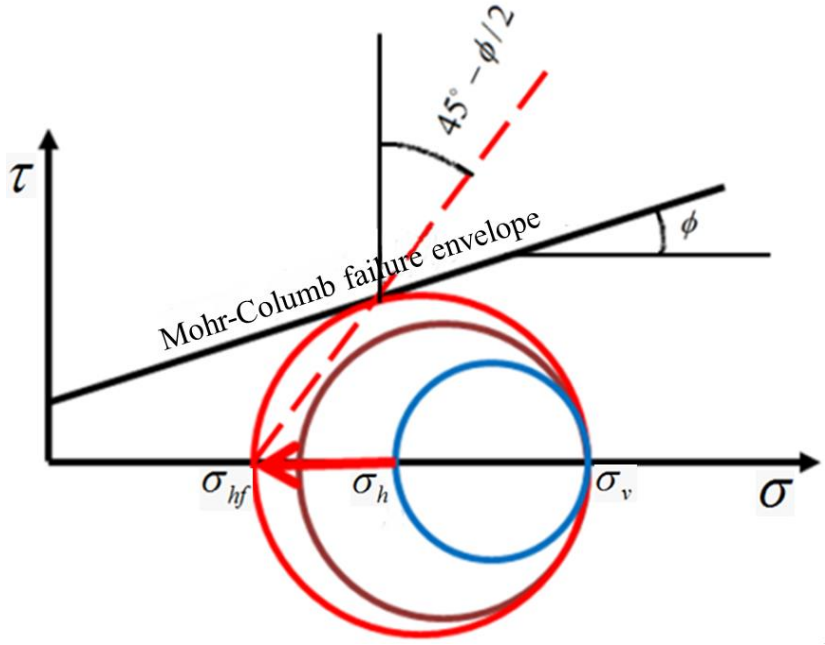

(a) Lateral decompression failure presented by Mohr's circle

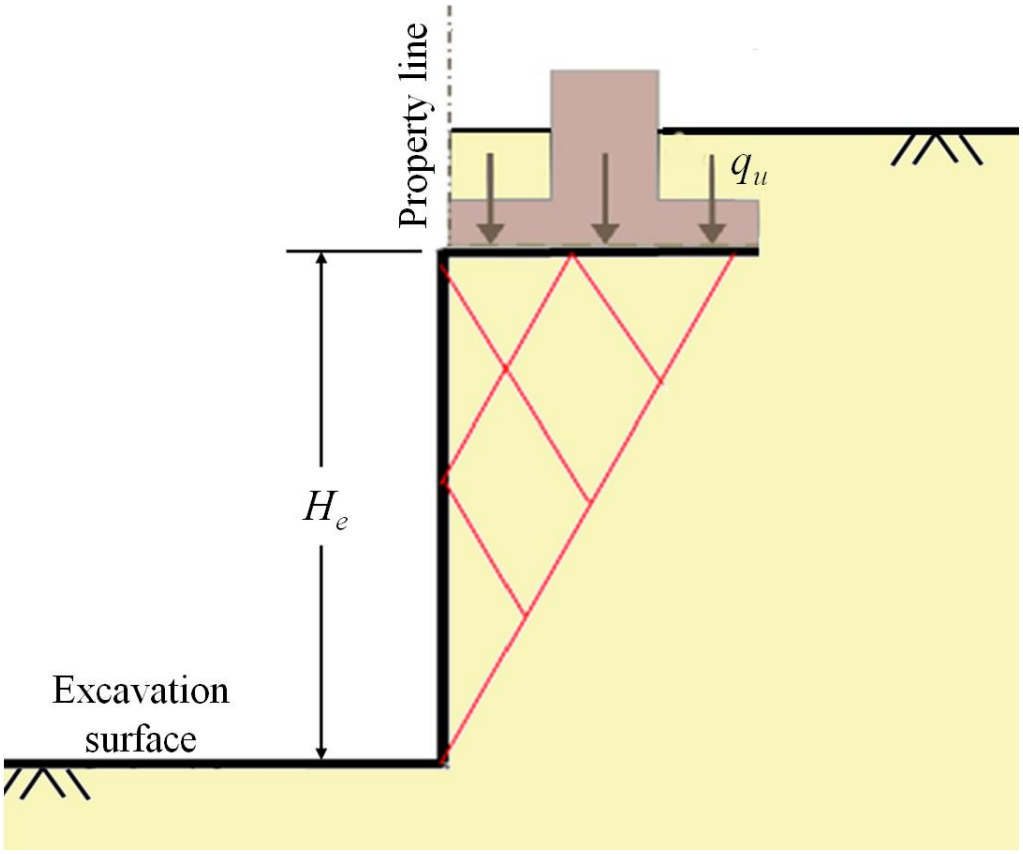

(b) Rankine active failure surfaces

Figure 4.64. Rankine active failure surfaces induced by lateral decompression of soil on one side of excavation

Above all, during the construction of a new building, to prevent the old building from Rankine active sliding failure induced by lateral decompression of the foundation soil as well as the neighboring damage disputes, then the location of foundation in Figure 4.64 must move backwards by at least $H_e \tan(45^\circ - \phi/2)$ from the property line (Figure 4.65).

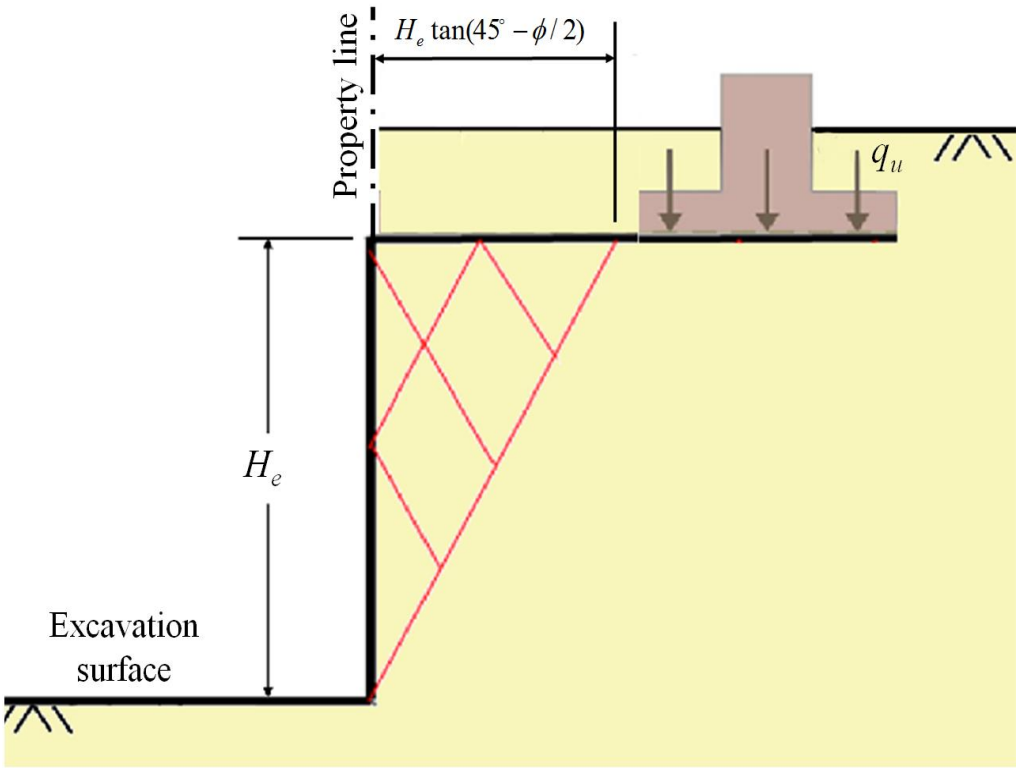

Figure 4.65. Null-neighbor-damage method to lateral depression on one side of soil in excavation zone

2. According to the influenced area of ground settlement

(1) Milligan and Nicholson:

Applicable condition:

Very loose sand layer and clay layer under undrained conditions

Foundation's retreat distance:

Lateral displacement depth of retaining walls H_o

(2) Clough and O'Rourke:

Foundation's retreat distance:

$2H_e$ (sand and soft to medium stiff clay)

3 H_e (hard to very hard clay)

(3) Woo and Moh:

Foundation's retreat distance: 4~5H_e (Taipei Basin)

(4) Ou and Hsieh

Foundation's retreat distance: *PIZ*, PIZ_1, or PIZ_2

(5) Bauer Method:

Foundation's retreat distance: $1.5H_e \tan(45^\circ - \phi'/2)$

(6) Caspe Method

Foundation's retreat distance:

$H_{t1} \tan\left(45^\circ - \phi/2\right)$

Where $H_{t1} = H_e + H_d$

When excavation width is B

$H_d = B$ (Cohesive soil, $\phi = 0$)

$H_d = 0.5B \tan(45° + \phi/2)$ (non-cohesive soil)

(7) Clough and O'Rourke Method:

Foundation's retreat distance:

$2H_e$ (sand layer)

$3H_e$ (hard clay layer)

(8) Taiyuan He and Kuishi Li method

Foundation's retreat distance:

$H_t \tan\left(45^\circ - \phi'/2\right)$ (sand layer)

Where H_t = depth of slurry wall

= $H_e + H_p$

$$H_p = 0.5B\tan\left(45^\circ - \phi'/2\right)$$

B = excavation width

(9) Rules of local government

Foundation's retreat distance:

$2H_e$：Miaoli County, Nantou County, Kaohsiung City, Hualien County, Penghu County

$3H_e$：Taipei City, Hsinchu City, Hsinchu County, Taichung City, Tainan City

$4H_e$：New Taipei City, Yilan County, Yunlin County, Changhua County, Chiayi County, Pingtung County

$5H_e$：Keelung City

4.5.4 Null-neighbor-damage Methods Relevant to Gground Water Table Decline

Descent curves of ground water table. In general, in order to avoid construction under water, ground water tables need to be lowered to 1.0m below the excavated surface by drainage before excavation.

Figure 4.66 shows that declining ground water table within the range of the property line can also result in a decline of ground water table outside the range of the property line. Therefore, regardless of new or old building, as long as the decline of ground water table outside the property line exceeds the maximum allowable value, then this type of drainage behavior is a type of infringement behavior.

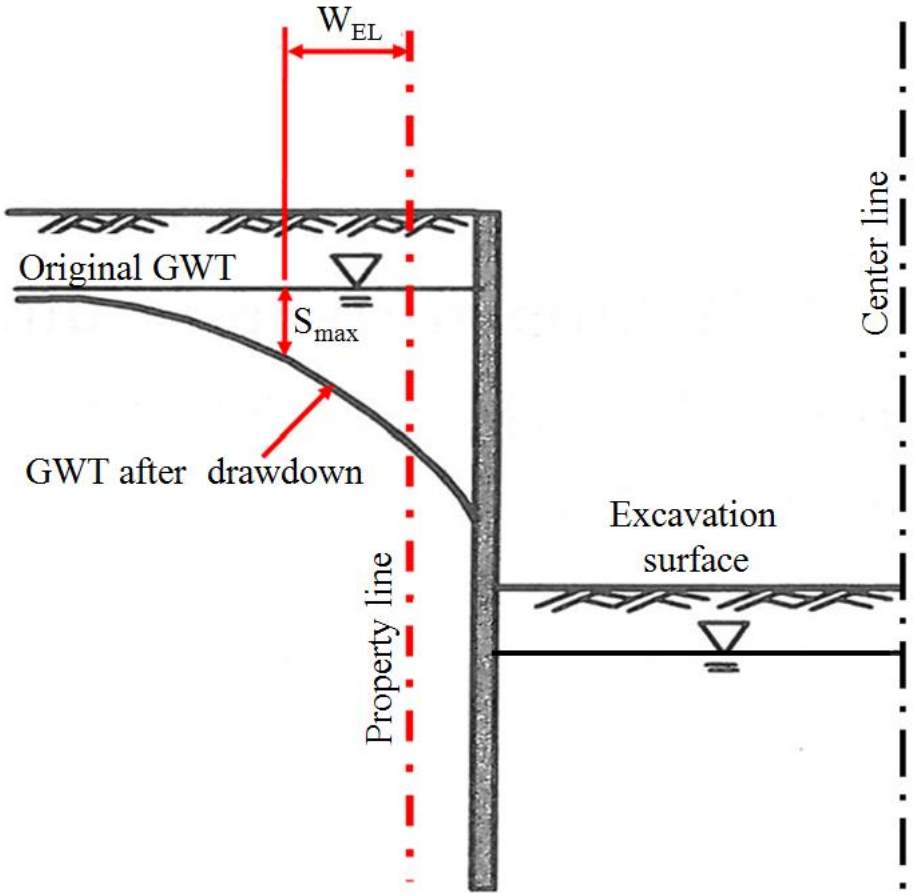

Figure 4.66. Descent curve of ground water table induced by water drainage

Null-neighbor-damage Method Rrelevant to Ground Water Table Decline. For the descent curve of ground water table induced by drainage shown in Figure 4.66, if the maximum allowable value of ground water table decline is hypothesized as S_{max}, then the construction site in Figure 4.66 must retreat a distance of W_{EL} from property line, in order to guarantee that no neighboring damage disputes would be induced by excessive ground water table decline.

Null-neighbor-damage method Relevant to Ground Water Decline in Pressure Aquifer. Figure 4.53 shows that pressure aquifers usually exist in shear banding tilted slopes, so when draining water from a gentle slope section on shear banding tilted slope, the ground water table of pressure aquifer would consistently decrease, which can easily lead to the leaning or cracking of a building on the steep slope change section. Therefore, when a pressure aquifer exists in a shear banding tilted slope, the construction of buildings on the steep slope section should be limited by regulations.

4.5.5 Combinations of All Types of Retreat Distances for Null-neighbor-damage Methods

Based on the distribution of ultimate foundation bearing capacity, stress contours, distribution of ground water table decline, ground water table distribution of a pressure aquifer in shear banding tilted slopes, and settlement distribution induced by lateral retaining walls displacement, the foundation or construction site must maintain a distance from the property line. To avoid infringements, the retreat distance of null-neighbor-damage must be selected as the maximum from all the types of retreat distances. Only when agreement on types, size, and depth of building foundation is drawn between people on both sides of the property line and on the premise of mutual reciprocity, can people analyze and sum up the retreat distances of both sides, which can be used as a retreat distance for both sides after multiplying 0.5~0.7.

4.6 Summary of the Main Points

1. Buildings in metropolitan areas are mostly constructed next to property lines and regardless of the construction order, the area of ultimate foundation bearing capacity or stress contours all exceed property lines, which is an obvious infringement but not regulated by laws in the past.

2. For old buildings, once the range covered by the property line-exceeding area of ultimate foundation bearing capacity or stress contours is excavated, the ultimate foundation bearing capacity can dramatically decline due to the loss of symmetry and lateral decompression of foundation soils, which induce neighboring damage disputes.

3. Although today’s government regulates the elements, authentication methods, and compensation of neighboring damage by laws, regulations, rules, and authentication manuals, there is a lack of understanding that the cause of neighboring damage is due to both sides having infringement behaviors. Therefore, in a case where the infringement behaviors of old buildings are not controlled, neighboring damage disputes can happen consistently.

4. On the premise of no infringement behaviors of both sides and based on the area of ultimate foundation bearing capacity, stress contours, descent curves of ground water table, ground water table of pressure aquifer in shear banding tilted slopes, and ground settlements induced by lateral retaining wall displacements, this chapter proposes null-neighbor-damage methods using retreat distance as the main parameter. When designers wish to reduce the retreat distance, they can install a nonyield cutoff wall next to the property line to prevent the ultimate bearing area, stress contours, and descent curves of ground water table from exceeding the property line.

5. Findings of the case of Cathay Pacific Tienmu Shopping Mall:

   (1) The adopted slurry wall pouring techniques and grouting techniques in ground modification are not compatible with pyroclastic deposits with features of a pressure aquifer.

   (2) Since the adopted construction techniques and geological techniques are not compatible with pyroclastic deposits, after construction the quality of slurry walls and grouting is not adequate, the slurry walls and bottom-sealing grouting cannot effectively prevent ground water in the pressure aquifer from flowing upwards. Therefore, although ground water can be resupplied by recharging wells, the ground settlement is still increasing with the decline of ground water pressure.

   (3) If water drainage is consistently conducted on a gentle section of shear banding tilted slopes, since inhomogeneous ground water table decline occurs on the steep slope change section of the shear banding tilted slope, and the degree of fracturing of shear band rock beneath the section increases with the frequency of earthquakes, so when the fractured rock fragments of the shear band continuously vanish, leaning or cracking failures may occur on Qiao-Tzu Building and San-Feng Building, that are above the shear band.

   (4) The maximum distance between Qiao-Tzu Building and the slurry walls on the north of Cathay Pacific Tienmu Shopping Mall is 12.6 times the excavated depth, while the maximum distance between San-Feng Building and the slurry walls on the north of Cathay Pacific Tienmu Shopping Mall is 9.2 times the excavated depth. Therefore, according to the research of this chapter, during the construction of Cathay Pacific Tienmu Shopping Mall, the cause of neighboring

damage on Qiao-Tzu Building and San-Feng Building is the inhomogeneous ground water table decline in pressure aquifer of shear banding tilted slopes and the vanishing of rock fragments of the shear band induced by consistent water drainage in the excavation zone.

6. To eliminate neighboring damage disputes, three suggestions are made as follows:

   (1) The government should refer to this chapter, and revise laws relevant to elements of neighboring damage infringements. Only by matching the elements of infringements to the actual cases, can the neighboring damage disputes be eliminated.
   (2) After revision of infringement elements, neither the old building nor the new building's area of ultimate foundation bearing capacity or stress contours can exceed property lines. The ground water table decline due to drainage in areas outside the property line shall not be excessive. Under these foregoing conditions, the designer has to build nonyield cutoff walls if they want to keep the foundation as close to the property line as possible.
   (3) Today, most people do understand the concept of a shear banding tilted slope, so buildings could be built on shear banding tilted slopes. However, the degree of fracture for shear band rocks can increase with the occurrence of an earthquake, and the rock fragments of a shear band can vanish during water drainage. Thus, it is suggested that the government adopt relevant regulations to limit construction on shear banding tilted slopes.

Chapter 5
Lishan Landslides Caused by Shear Bandings

T.-S. Hsu, H.-C. Chang, Y.-T. Liu, G.-L. Huang and S.-H. Huang

5.1 Introduction

Taiwan is a mountainous country with frequent earthquakes, typhoons, and rainstorms, which lead to frequent landslides. In this case, every year the government spends a lot of money on monitoring, performing slope stability analyses and designing remediation projects. However, landslides are persistently happening even after the deployment of remediation works. This fact proves that the monitoring methods, landslide mechanism, and remediation works might not meet the actual needs and that the slope stability analysis methods do not completely comply with the conditions such as terrain, geology, geological structure, geometric conditions, boundary conditions, load conditions, and water pressure distribution, etc. Therefore, since the deployed landslide mechanism, monitoring methods, and remediation works do not satisfy the needs in reality, a suspected trend of "more remediation works, larger disaster damage" could exist.

With such a trend, scholars, or consulting companies, who persistently benefit from the disaster prevention budget, never reflect on the reason that causes "more remediation works, larger disaster damage", and they even blame innocent nature and people after the occurrence of a large landslide disaster.

This chapter takes Lishan landslide as an example, discusses the landslide mechanism, shear resistance strength required for slope stability analysis, monitoring methods, and remediation works, etc. adopted by scholars and consulting companies in the past, and investigates the reasons why the landslide mechanism, monitoring methods, and remediation works adopted by scholars and consulting companies in the past did not work, as well as providing effective improvement methods with the purpose of ensuring that the projects of future delegations with regard to landslide mechanism, monitoring methods, and remediation works comply with the

needs in reality. Furthermore, on the premise of a well-spent budget, the authors of this chapter hope to help realize the designated goals of the projects. In addition, this chapter also indicates the human reasons, objective reasons, incident reasons of “more remediation works, larger disaster damage”, in order to distinguish the scholars or consulting companies who possess real ability in disaster prevention and protect people in the disaster areas from the threat of persistent landslide failures.

5.2 Literature Review

5.2.1 Remediation Works on Lishan Landslide

According to the Soil and Water Conservation Bureau, Council of Agriculture, Executive Yuan (2017), Lishan landslide area is an ancient landslide area, where massive landslides occurred in April 1990. The total area of the landslide region is around 230 acres according to the research, and it is characterized as a landslide area in deep rock layers with a large sliding area (Figure 5.1).

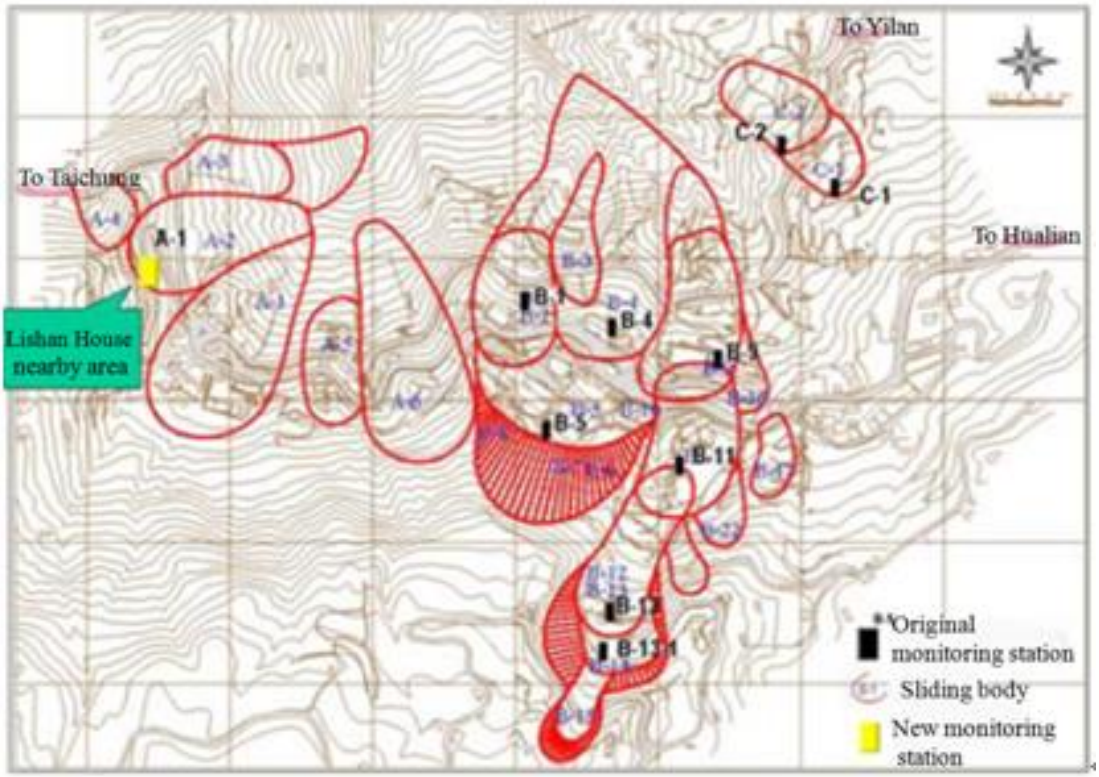

Figure 5.1. Distribution of Lishan landslide
(Su et al., 1990)

The remediation projects for landslides in the Lishan area have been conducted since 1995. The total budget is more than that for any other landslide areas in Taiwan, and mainly includes following remediation works:

a. Sand collection engineering: includes a check dam, submerged dam, and hydraulic drop structure etc.

b. Water drainage project on ground surface: includes wrinkled steel sheet piles and RC drainage ditch etc.

c. Underground water drainage system: includes horizontal collection wells, collection wells, and drainage corridors, etc.

For the Lishan landslide area, most scholars and consulting companies involved in the projects attribute the Lishan landslide to agricultural development in a mountainous area, road construction, and lifting of the underground water table. To limit the expansion of the landslide area, at that time, the state government entrusted the Energy and Resources Institute of the Industrial Technology Research Institute to design the landslide investigation and remediation project for the Lishan area, and the first phase of the project started in 1995 and ended in 2002.

5.2.2 Monitoring Lishan Landslide

In 1999, four years after remediation project started, landslides continued to happen. Since Lishan is the transportation hub of the Central Cross-Island Highway, a landslide occurrence can not only harm people’s lives and properties, but also harm people’s livelihood, economy, and sightseeing.

In order to understand the stratigraphic change, underground water change, and remediation effects of landslide area, automatic monitoring systems were deployed in stages on the landslide bodies that were sensitive to landslides in Lishan area. In addition, human monitoring stations were built in New Jiayang Community, Old Tribe, Songmao Tribe, and Lishan Village. The purpose of the monitoring was addressed to use monitoring data to evaluate the security status of landslide areas, provide alerts of landslides, provide immediate observation results to predict potential hazards of landslide, and provide relevant information via websites.

The current monitoring system in Lishan landslide area includes a human, an automatic and a semi-automatic monitoring systems, the whole system includes three components: (1) monitoring stations on site; (2) control station of Lishan Public Works Office; (3) management centers in the Soil and Water Conservation Bureau of Zhongxing New Village and Second Works Office in Fengyuan. The monitoring devices include surface inclinometers, tube inclinometers, surface telescopes, underground water table meters, and rain gauges, etc., and nine monitoring stations are built including B1, B4, B5, B9, B11, B13, B13-1, C1, and C2.

5.2.3 Investigation and Research Results of Lishan Landslide

According to domestic literature, the investigation or research results of Lishan landslides are summarized below:

1. Xie (1984) proposes that in the slope slide failures from Deji section to Lishan section of Central Cross-Island Highway, the sliding surface extends to the rock, which has been ultimately weathered and fractured, so they belong to deep seated circular sliding failures.

2. Cai et al. (1987) speculate that the potential for irregular slide in the shallow land layer is the highest among all slope collapse layers at 80.5K of Tai-7a Route, and the contact area between the bottom of the collapse layer and weathering fracture slates or newly-formed slates comprises a water permeable layer, which can facilitate the weathering effects.

3. Su et al. (1990) propose that at 72.5K of Tai-7a Route, the slopes slip along sand with clay interlayer beneath the collapse layer, its failure type is similar to planar sliding.

4. Liu et al. (1991) indicate that on the west line of the Central Cross-Island Highway, the soil layers from outside to inside are hillside deposits, weathering disturbed slate layer, and weathering fractured slate layer, which are easily infiltrated by water and thus rise the underground water table and pose threats to the stability of slopes. The fractured slate with clay interlayer inside have a severe degree of weathering.

5. Lin (1991) indicate that the local area is divided into 3 layers, from top to bottom: (1) poorly-cemented topsoil and fractured slate collapse layer; (2) silty clay layer; (3) newly-formed slate layer. The types of slope failure are mainly debris flow, shallow soil layer sliding, and deep seated sliding.

6. Lin et al. (2000) consider the landslide from the east section of Central Cross-Island Highway to Deji section, and use landslide susceptibility analysis to research the weight of evaluation factors. Further, they use the all-area satellite images of Sept. 27th, 1999 to classify the landslide susceptibility into 5 grades: stable, low, low-to-medium, medium-to-high, and high, where 84.92% of landslides belong to medium-to-high susceptibility or higher.

7. The research report of China Engineering Consultants Incorporated (1996) indicates that the rock layer in the landslide area is mainly made of grey black slate, covered by thick collapse soil. Due to the violent impact of geological change, the rock layer has an ultimate degree of weathering and fracture, so the division of the rock layer is only based on the weathering degree. According to the investigation results from drilling, geotechnical testing, and ground surface terrains, the layers of the Lishan landslide area are divided into collapse soil, weathering fractured slate, and newly-formed slate, the general physical properties, mechanical properties and strength parameters of each layer are summarized below:

   Collapse Soil. This layer is made of brown silty sand mixed with fractured slate blocks and ashes of slate, where the thickness is between 2.5cm to 16cm, the value N of the standard penetration test is from 9 to 100; the gravel content is between 14.6% and 82.3%, sand content is between 17.7% and 47.9%, clay content is between 0.0% and 37.5%, water content is between 4.0% and 20.5%, the specific gravity is between 2.66 and 2.78, unit weight is between 1.51tf/m^3 and 2.36t/m^3, and void ratio is between 0.26 and 1.10.

   Weathering Fractured Slate. This layer is grey and black and the majority of the rock core has been fractured into blocks or slices. Its water content is between 0.2% to 1.3%, specific gravity is between 2.73 and 2.79, unit weight is between 2.60 tf/m^3 and 2.73 tf/m^3, and void ratio is between 0.01 and 0.07.

   Newly-formed Slate. This layer is grey and black, with uniaxial compressive strength of between 164.68kgf/cm^2 and 609.54kgf/cm^2, the friction angle of the weak plane is between 28.5^o and 31.8^o, and cohesion is between 0.03 kgf/cm^2 and 0.18 kgf/cm^2.

Secondly, according to the classification method of Tengyuan-Mingmin (1979) , geological formation in this area can be divided as: upper layer is collapse soil layer, middle layer is rock layer from ultimate weathering to slight weathering, bottom layer is rock layer from slight weathering to newly-formed. Most sliding surfaces go along the clayey interlayer, and the physical properties of this clay interlayer are shown in Table 1, and according to universal classification method, this soil is clayey sand (SC).

Table 5.1. Physical properties of clayey interlayer
(Su et al., 1990)

D_{10}	D_{60}	C_u	LL	PI
0.003mm	0.22mm	73.3	30.3%	15.5%
Water content	Specific gravity	Unit weight of wet soil	Unit weight of dry soil	Void ratio
12.72%	2.77	2.25tf/m^3	1.996tf/m^3	0.39

5.3 Discussions

5.3.1 The Cause of the Lishan Landslides

In the past, the Soil and Water Conservation Bureau, Council of Agriculture, Executive Yuan (2017) thought Lishan landslide area was an ancient collapse area and blamed Lishan landslide on agricultural development in the mountainous area and road construction. However, Figure 5.2 shows that in Lishan area, there are many roads such as Tai-8 Route, Tai-7a Route, Central 131 County Road (Fushou Road), and agricultural roads, etc. Most roads going across mountainous agricultural development zones do not induce significant landslides. Only when the roads or mountainous agricultural development zones intersect with shear banding zones, can the landslide phenomenon occur. Figure 5.2 conversely shows that a large number of landslides occur on the shear banding tilted slopes where no roads or mountainous agriculture development zones exist.

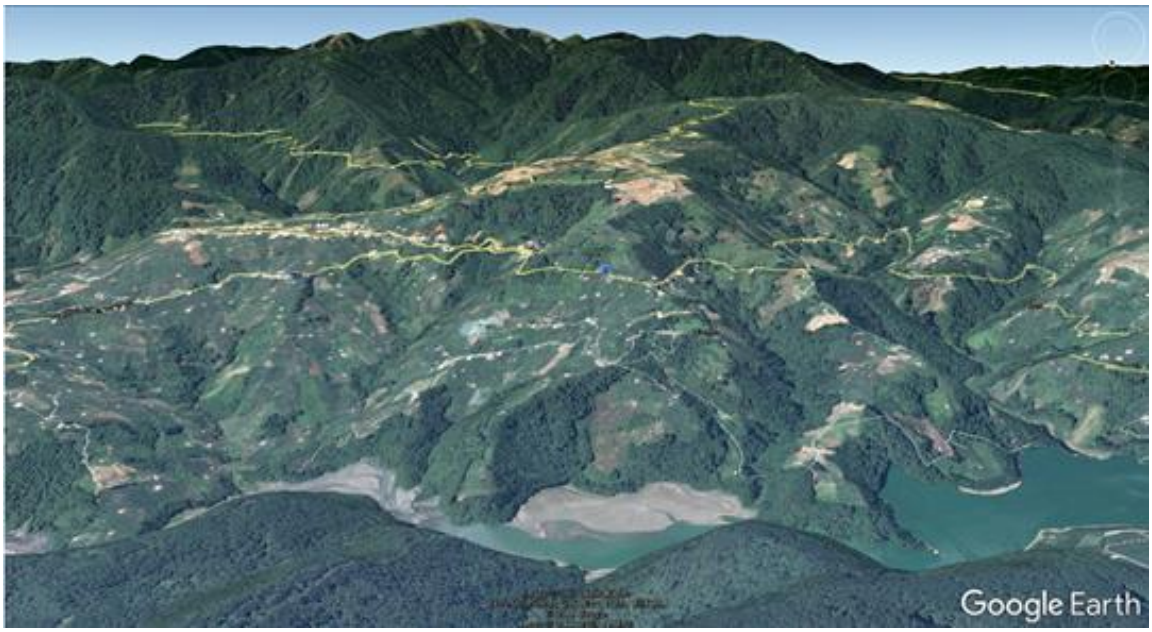

Figure 5.2. Mountainous agriculture development zones, roads, and landslide areas in Lishan (Google Earth, 2017)

In order to understand the actual cause of Lishan landslides, firstly Figure 5.3 shows that the Lishan landslide area is exactly at the intersection of three shear bandings, whose strikes are N32^{o}E (white line), N74^{o}W (blue line), and N83^{o}E (orange line) respectively.

Figure 5.3. Lishan landslide area is the intersection zone of three shear bandings (background picture is from Google Earth, 2017)

Secondly, Figure 5.4 shows the historical satellite images of persistent partial-delamination landslide failures in this area during the period from Dec. 31st 1989 to Dec. 31st 2016. Therefore, the discussion mentioned above that Lishan landslide area is an ancient collapse area does not comply with the facts.

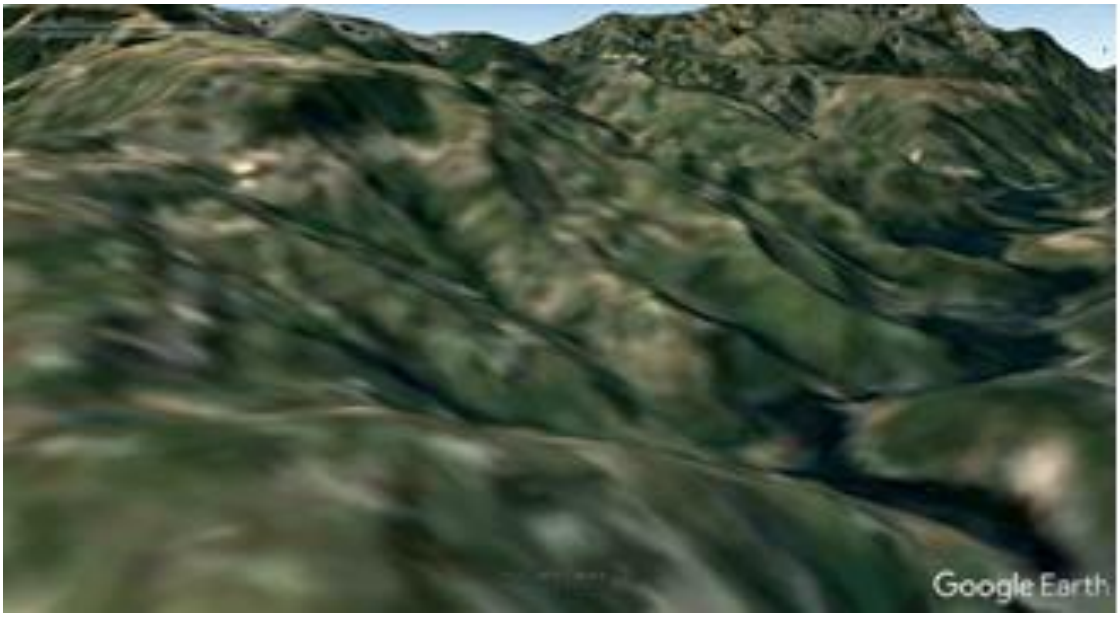

(a) 1989, Dec. 31st

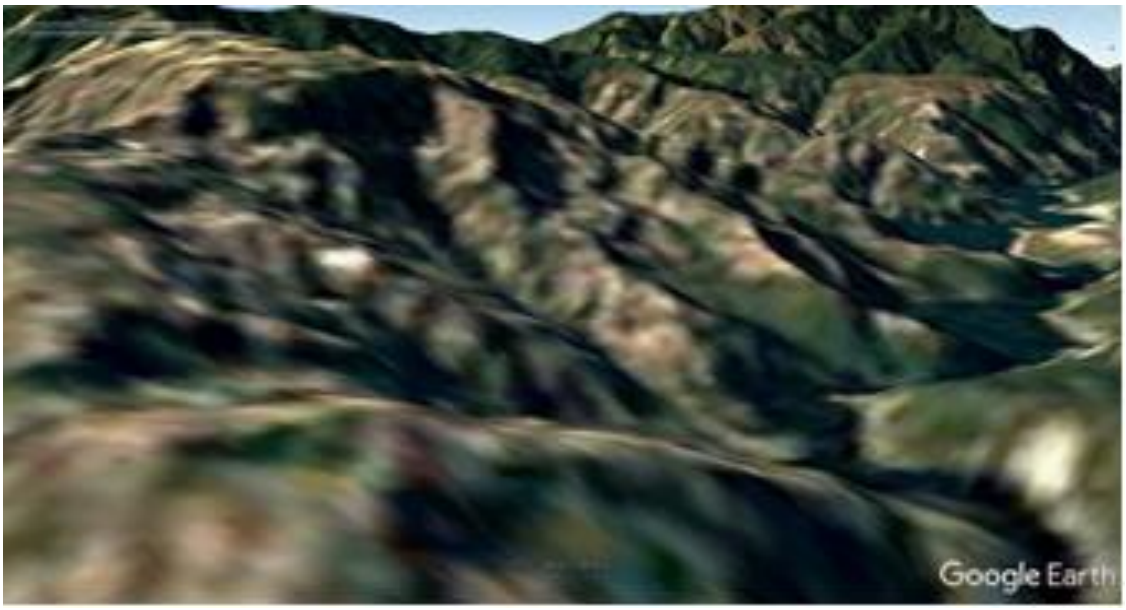

(b) 1991, Dec. 31st

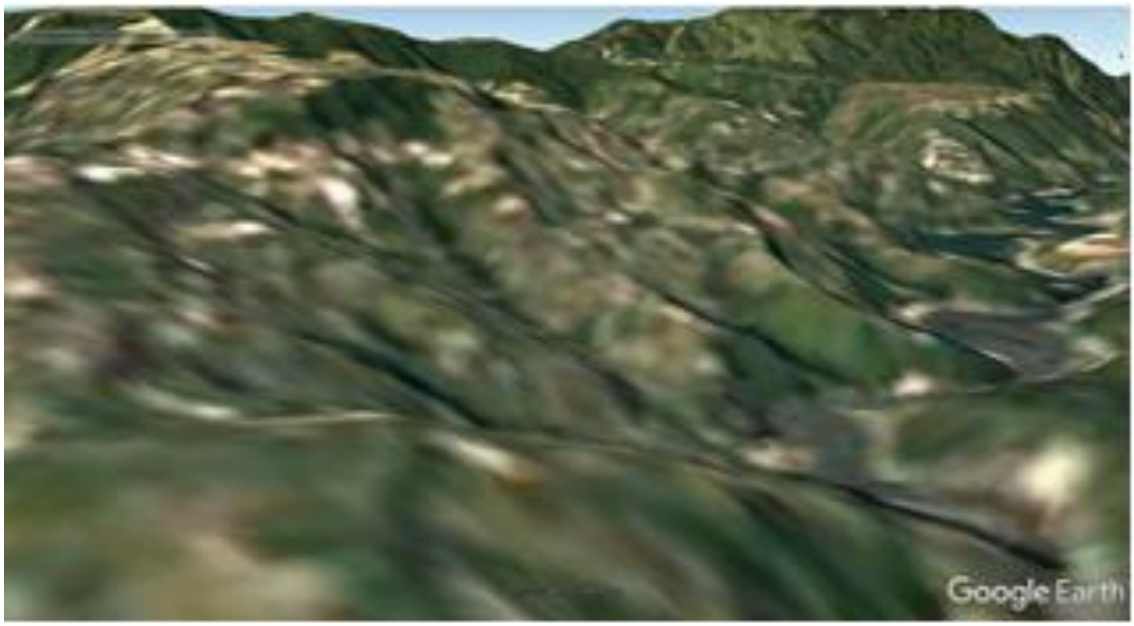

(c) 1993, Dec. 31st

(d) 2006, Feb 1st

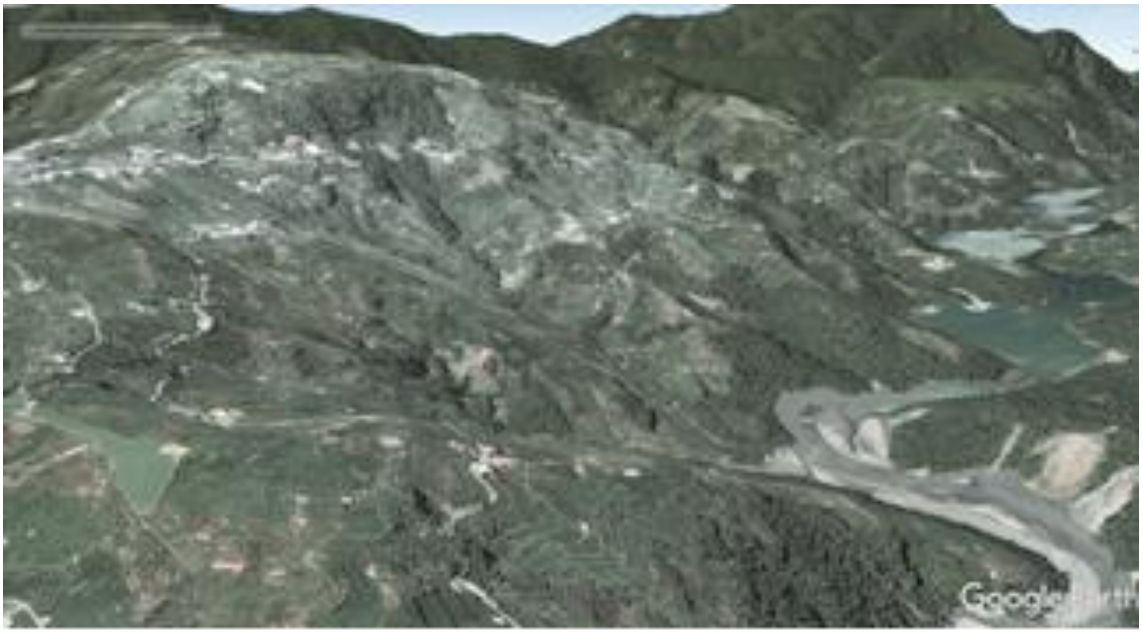

(e) 2013, Oct. 22nd

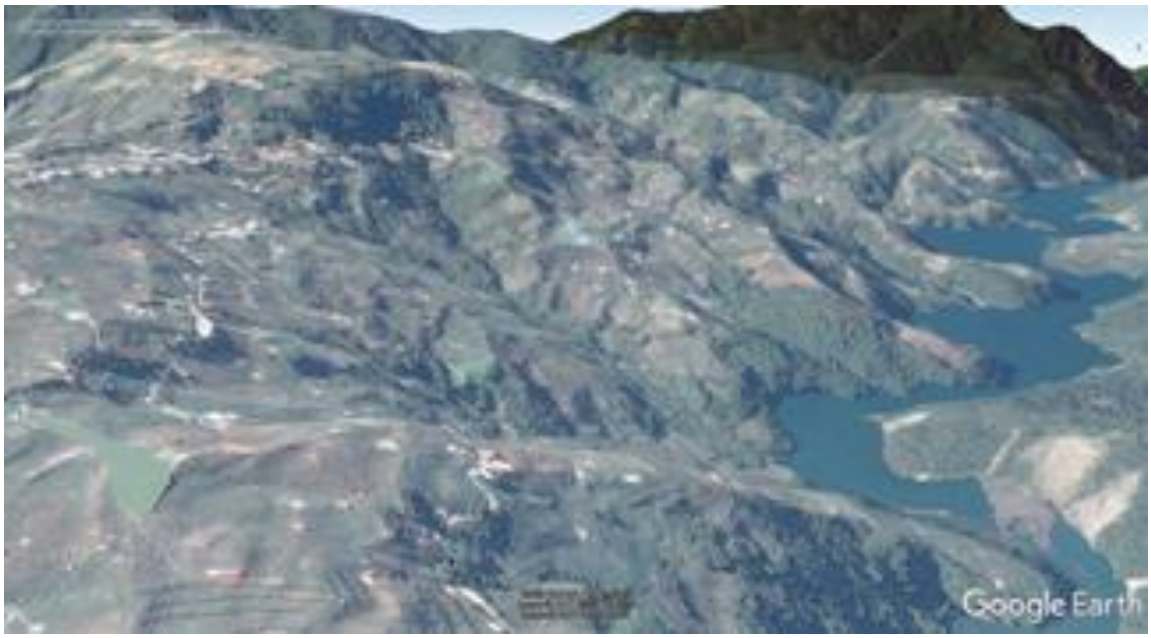

(f) 2015, Apr. 15th

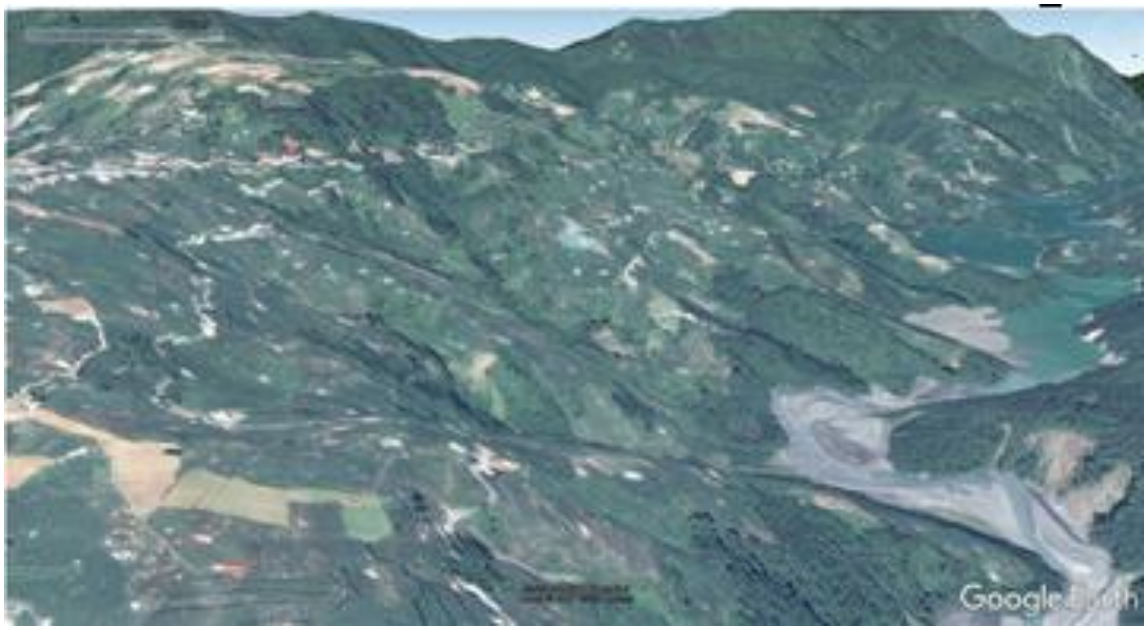

(g) 2016, Dec. 31st

Figure 5.4. Historic satellite images of Lishan landslide area (Google Earth, 2017)

When lateral compression persistently acts on a tectonic plate and shear strain goes deep into the plasticity range, localizations of deformations of plates occur due to the loss of ellipticity, which further induce the shear band. Within the total shear band width, the shear textures include principal displacement shear, thrust shear, Riedel shear, conjugate Riedel shear, and compression texture. According to microscopic fractography mechanics, the propagation of the shear band is accompanied with the interlacing river patterns and curved surfaces.

Based on these results, shear banding is accompanied by shear textures that have different strikes. Therefore, the three shear bandings shown in Figure 3 would induce the up-and-down ridge line and twisty river valleys in the Lishan area shown in Figure 5.5.

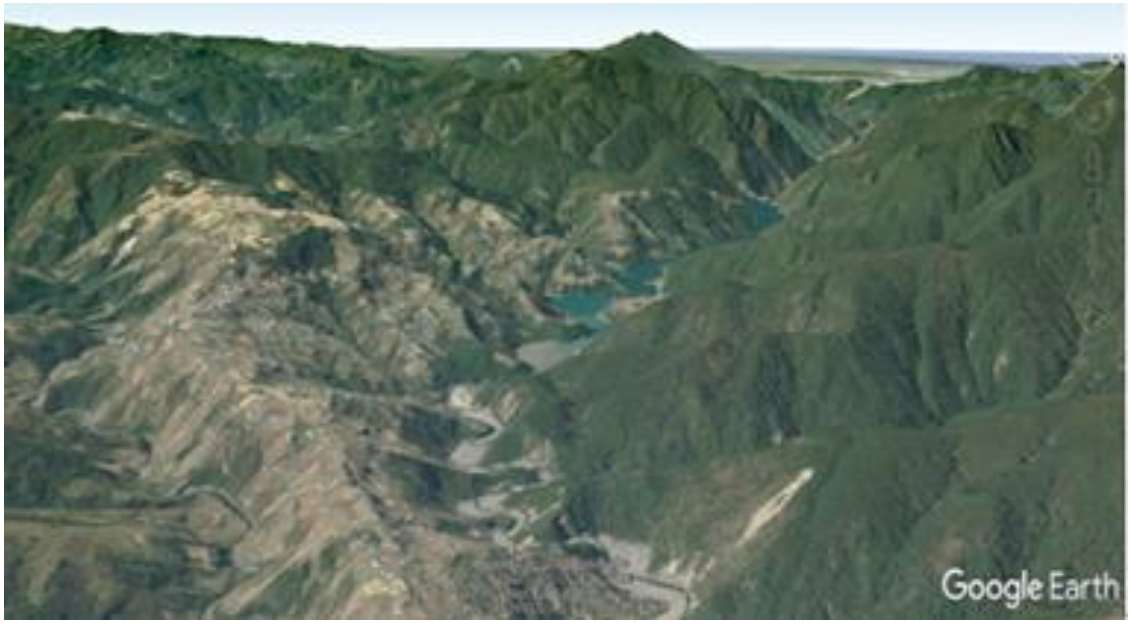

Figure 5.5. The up-and-down ridge line of Lishan and twisty river valley (Google Earth, 2017)

The special reason why Lishan area has become a landslide area is that Yilan, northeast to Lishan, and Hualian, east to Lishan are located at the edge of Eurasian continental plate, where irregular "C-shaped" and "ε -shaped" deformation occurs under irregular lateral compression from the Pacific plate. The irregular deformation continues to propagate to the northwest or west, inducing the up-and-down ridge line, the dislocation, and highly-twisty river valleys of Lishan area.

When the ridge line is up-and-down or dislocated, and the river valley is highly-twisty, it indicates that multiple shear bands or shear textures with different strikes exist in this area.

According to the satellite image of areas near Lishan and the displaced topographic features of the shear band, the strikes can be identified from Figure 5.6a that principal deformation shear D (red) is N21°W, thrust shear P (blue) is N3°W, Riedel shear R (yellow) is N38°W, conjugate Riedel R' (green) is N88°W, and compression texture S (white) is N67°E. Besides, from Figure 5.6b, another five groups of shear textures can be identified, their strikes are: principal deformation shear D (red) is E0°, thrust shear P (blue) is N72°W, Riedel shear R (yellow) is N74°E, conjugate Riedel R' (green) is N24°E, and compression texture S (white) is N0°. Finally, from Figure 5.6c, another five groups of shear textures can be identified, their strikes are: principal deformation shear D (red) is N42°E, thrust shear P (blue) is N61°E, Riedel shear R (yellow) is N26°E, conjugate Riedel R' (green) is N24°W, and compression texture S (white) is N48°W.

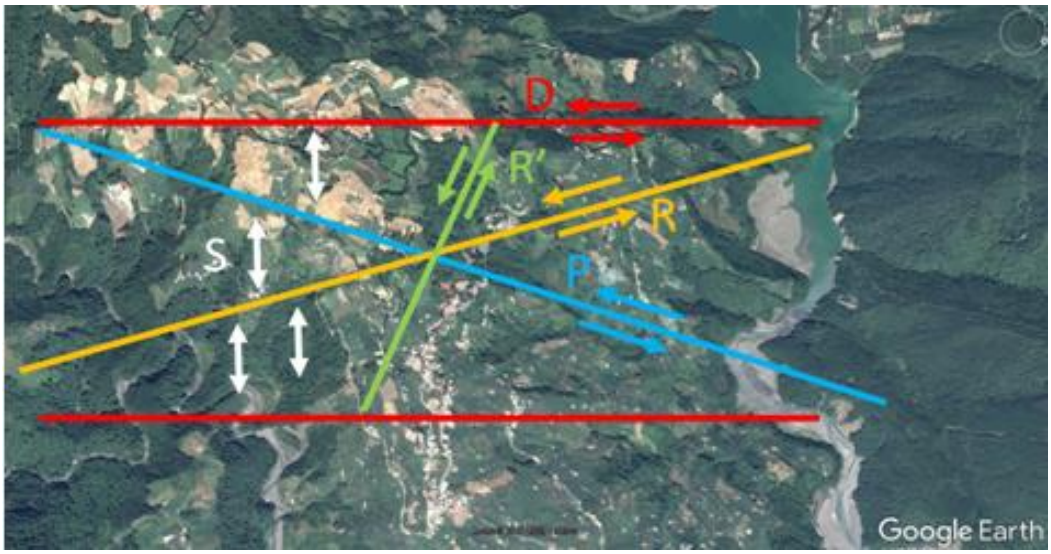

(a) First shear band and its shear textures

(b) Second shear band and its shear textures

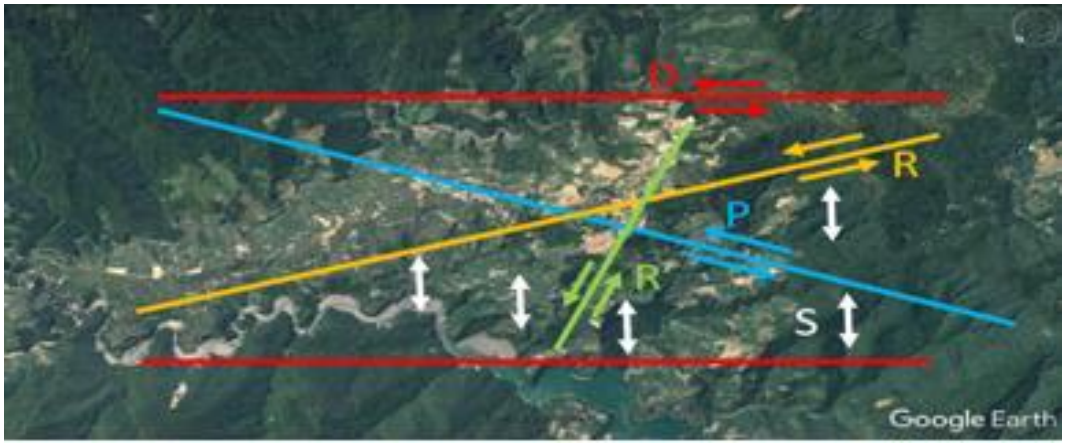

(c) Third shear band and its shear textures

Figure 5.6. Shear bands and shear textures identified by satellite images (background picture is from Google Earth, 2017)

5.3.2 Mechanism of Lishan Landslide

The Mechanism Adopted by Scholars or Consulting Companies of Lishan Landslide Remediation Project. In the past, when the scholars or consulting companies of Lishan landslide remediation project conducted slope stability analysis, they usually adopted a circular or noncircular landslide mechanism (details in Figure 5.7). Taking the cross section of B3, B4, B5, and B8, four sliding blocks in Lishan landslide area, as an example analysis (details in Figure 5.8) was carried out with a circular or noncircular landslide mechanism by Su et al. (1990).

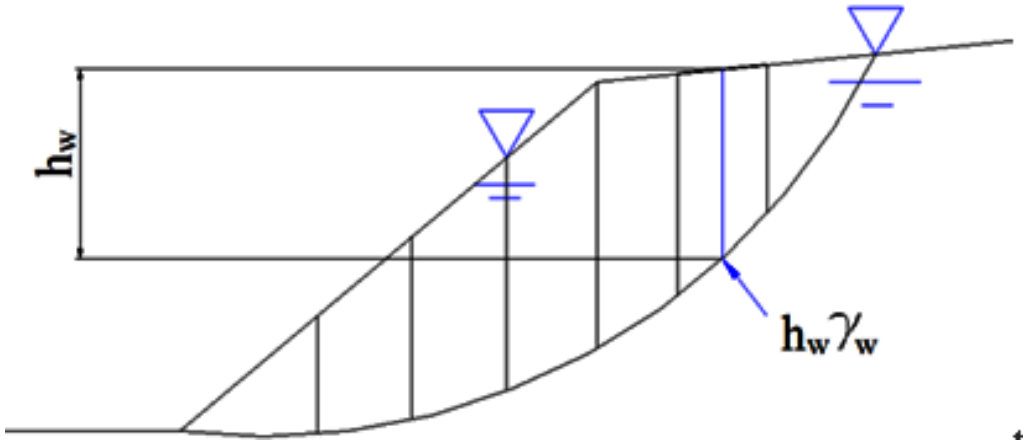

Figure 5.7. Circular or noncircular landslide mechanism

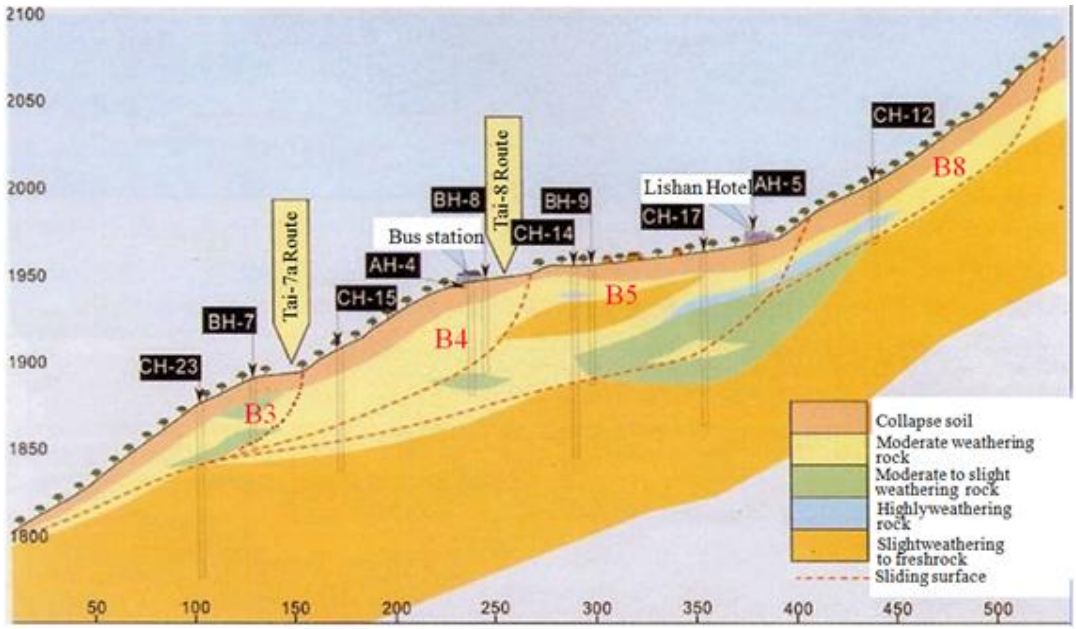

Figure 5.8. B3, B4, B5, and B8 sliding blocks on the cross section of Lishan landslide area (Su et al., 1990)

The mechanism adopted by authors. The authors conducted landslide analysis on the location of the Guest Hotel during a persistent slide (Figure 5.9). In this analysis, a wedge landslide mechanism comprising five surfaces (sliding surface 1, sliding surface 2, gentle slope, steep slope, and tension crack) was adopted, as shown in Figure 5.10.

Figure 5.9. Landslide of wedge type on the location of Guest Hotel

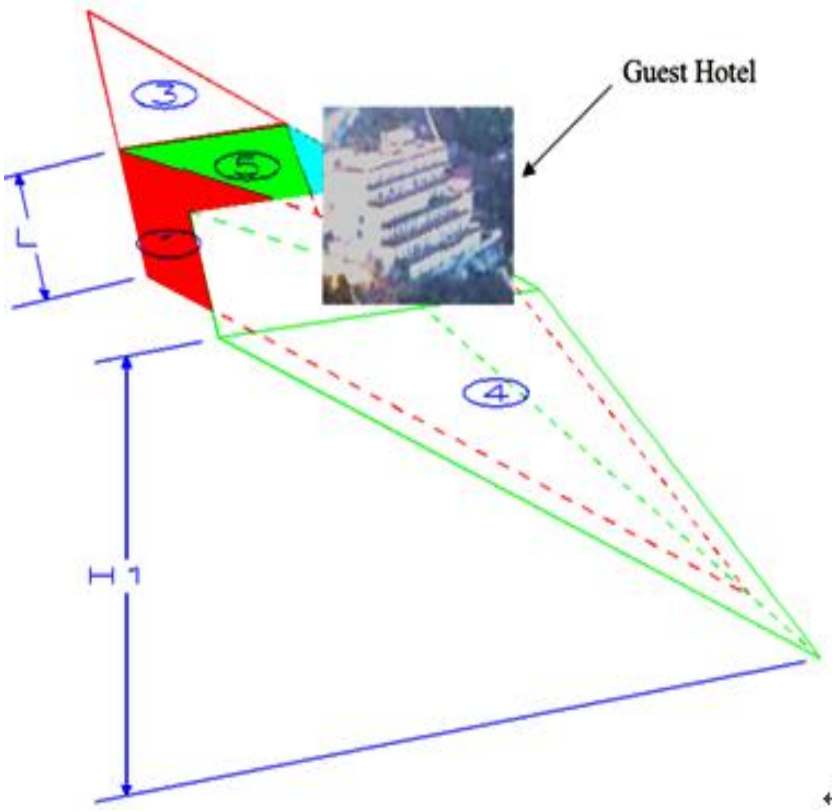

Figure 5.10. A wedge landslide mechanism on the location of Guest Hotel

In addition to the slope stability analysis (Figure 5.9) with a wedge landslide mechanism, the authors also conducted slope stability analysis on four sliding blocks B3, B4, B5, and B8 shown in Figure 5.8. Before the analysis, the potential sliding failure planes of four sliding blocks B3, B4, B5, and B8 of Figure 5.8 were found based on the exploration on the site. However, failure surfaces were not circular or non-circular, but were wedge-type consisting of five planes, which had a steeper slope at lower elevation. Therefore, the four sliding blocks B3, B4, B5, and B8 in Figure 5.8 can be redrawn to be four wedge-type sliding blocks as shown in Figures 5.11 and 5.12, where only after the sliding failure of wedge-type block B3, can sliding failures occur to the other three wedge-type blocks in order.

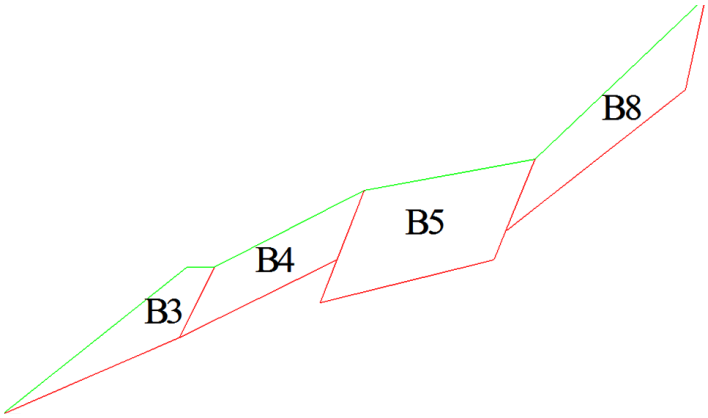

Figure 5.11 2-D diagrams for the four potential sliding failure blocks shown in Figure 8

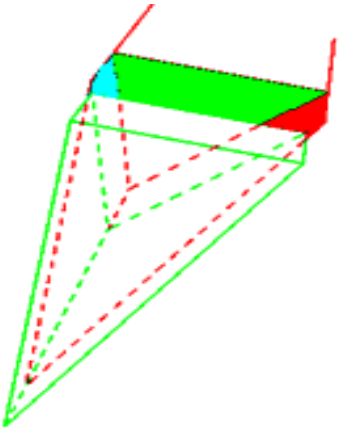

(a) B3

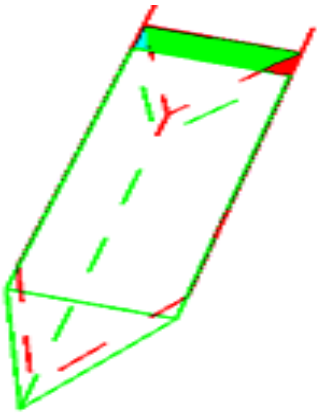

(b) B4

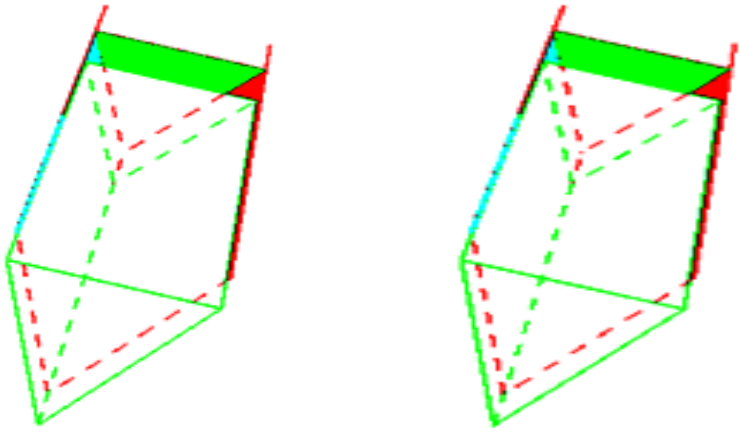

(c) B5 (d)B8

Figure 5.12. 3-D diagrams for the wedge-type sliding failure blocks shown in Figure 11

5.3.3 Shear Strength Parameters of Soils

The mechanism adopted by scholars or consulting companies of Lishan landslide remediation project. When a circular or non-circular sliding failure plane penetrates collapsed soil, medium to high weathered slate, or non-weathered to slight-weathered slate, the cohesion *c* and angle of internal friction ϕ adopted or suggested by the scholars or consulting companies of Lishan landslide remediation project are shown in Table 2.

The method adopted by the author. For the landslide area at the location of the Guest Hotel in Figure 5.7, based on the wedge landslide mechanism, the author adopts the adhesive force c_α of the interfaces between layers and friction angle δ as the parameters of shear resistance strength of the sliding surfaces, where

Sliding surface 1: c_α =19.5kPa、δ =24.6^o

Sliding surface 2: c_α =18.7kPa、δ =32.1^o

Table5. 2a. Shear resistance strength parameters adopted in slope stability analysis (Zhan and Su, 2002)

		Collapse soil	1*	2*
Miaobin Su	c (kPa)	0	---	---
	ϕ	35^o	---	---
MAA Consulting	c (kPa)	0	---	---
	ϕ	29^o~34.5^o	---	---
Bingseng Lin	c (kPa)	2~16	---	---
	ϕ	33^o-38^o	---	---
Guangrong Cai	c (kPa)	19~38	---	---
	ϕ	33.5^o~35^o	---	---
Industrial Technology Research Institute	c (kPa)	1~22	20~59	294
	ϕ	15^o~45^o	36^o~39^o	40^o
China Engineering Consul. Inc.	c (kPa)	---	---	---
	ϕ	---	---	---
Reverse calculation of China engineering Consul. Inc.	c (kPa)	---	---	---
	ϕ	---	---	---
Suggested by China Engineering Consul. Inc.	c (kPa)	5~10	29	294
	ϕ	28^o~32^o	28^o	33^o

1*: Medium to high weathering slate

2*: No weathering to slight weathering slate

Table 5.2b. Parameters of shear resistance strength adopted in slope stability analysis (Zhan and Su, 2002)

		Sliding surfaces		
		Collapse soil	1*	2*
Miaobin Su	c (kPa)	---	21~37	21~37
	ϕ	---	9^o ~16^o	9^o ~16^o
MAA Consulting	c (kPa)	---	---	---
	ϕ	---	---	---
Bingseng Lin	c (kPa)	---	13~28	13~28
	ϕ	---	18.2^o ~18.5^o	18.2^o~18.5^o
Guangrong Cai	c (kPa)	---	18~39	18~39
	ϕ	---	25^o ~45^o	25^o~45^o
Industrial Technology Research Institute	c (kPa)	---	0~196	0~196
	ϕ	---	20^o~23^o	20^o~23^o
China Engg Consul. Inc.	c (kPa)	---	5~11	3~18
	ϕ	---	28.7^o~30.9^o	28.5^o~31.3^o
Reverse calculation of China ngg Consul. Inc.	c (kPa)	5	0~49	29
	ϕ	28^o	15^o~31^o	33^o
Suggested by China Engg Consul. Inc.	c (kPa)	5~10	20^o	29^o
	ϕ	28^o~32^o	20^o	33^o

For the four wedge-type sliding blocks B3, B4, B5, and B8 on the cross-section of Lishan landslide areas in Figure 9 and 10, the author adopts the following parameters of shear resistance strength:

Sliding surface 1: c_α =19.5kPa、δ =24.6^o

Sliding surface 2: c_α =18.7kPa、δ =32.1^o

Comprehensive Discussion. Figure 5.12 is the classification graph of rock uniaxial compressive strength suggested by the International Society for Rock Mechanics, ISRM, according to Figure 5.12:

1. weak rock: uniaxial compressive strength is between 5~25Mpa;

2. very weak rock: uniaxial compressive strength is between 1~5Mpa;

3. super weak rock: uniaxial compressive strength is between 0.5~1Mpa.

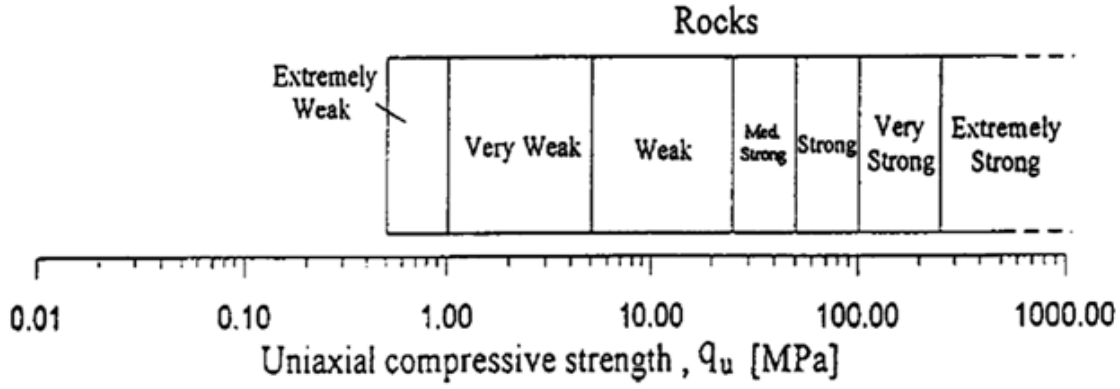

Figure 5.12. Classification graph of rock uniaxial compressive strength suggested by ISRM (Johnston, 1993)

For clayey weak rock, clayey very-weak rock, and clayey extremely-weak rock, under the conditions of saturation and no water drainage, the angle of internal friction $\phi = 0^o$, and the cohesions c of clayey weak rock, clayey very-weak rock, and clayey extremely-weak rock are 2.5~12.5MPa, 0.5~2.5MPa, and 0.25~0.5MPa (or 250~500kPa), respectively.

For sandy weak rock, sandy very-weak rock, and sandy super-weak rock, if the angle of internal friction is hypothesized as $\phi = 30^o$, then the cohesions c are 1.44~7.22MPa, 0.29~1.44MPa, and 0.144~0.29MPa (or 144~290kPa), respectively.

When the potential sliding failure faces of a slope penetrate very stiff clay, whose angle of internal friction $\phi = 0^o$ and cohesion c is between 96~192kPa, or hard clay, whose angle of internal friction $\phi = 0^\circ$ and cohesion c is larger than 192kPa, the factors of safety of slope stability analyses are all larger than 1.5. Therefore, these kinds of potential sliding

failure planes would not induce slope slide failure. Based on this, it can be extrapolated that：

1. When the potential failure surfaces of a slope penetrate clayey weak rock, or clayey very-weak rock, or clayey extremely-weak rock, whose angle of internal friction is $\phi = 0^\circ$ and cohesion c is 2.5~12.5MPa, or 0.5~2.5MPa, or 0.25~0.5MPa, respectively, these kinds of potential failure surfaces would not induce landslide.

2. When the potential failure surfaces of a slope penetrate sandy weak rock, or sandy very-weak rock, or sandy extremely-weak rock, whose angle of internal friction is $\phi = 0^\circ$ and cohesion c is 1.44~7.22MPa, or 0.29~1.44MPa, or 0.144~0.29MPa, respectively, these kinds of potential failure surfaces would not induce landslide.

According to these results, when the potential failure surfaces of a slope penetrate weak rock, very-weak rock, and extremely-weak rock, potential failure faces would not induce landslide.

To this regard, the cohesion c and angle of internal friction ϕ adopted, reverse-calculated, or suggested by scholars or consulting companies of Lishan landslide remediation project in slope stability analysis shown in Tables 5.2a and 5.2b are not the shear strength parameters that the rocks possibly possess.

In order to ensure that the landslide mechanism and the shear strength parameters comply with the actual needs of landslides happening in Lishan, the authors provides the following procedures to decide the shear strength parameters of sliding failure planes:

1. Use the distribution of the displacement velocity vectors, satellite images, and on-site images to identify shear bands existing in Lishan landslide area.

2. Determine the accumulated length of shear banding tilted slopes

3. Decide the potential sliding failure planes with the gentlest slope derived from primary deformation shear in shear banding tilted slopes, after that decide one section or two sections of potential sliding failure planes with

a slightly steep slope, the potential sliding failure planes with slightly steep slope might be the shear textures within the total shear band width (Figure 14).

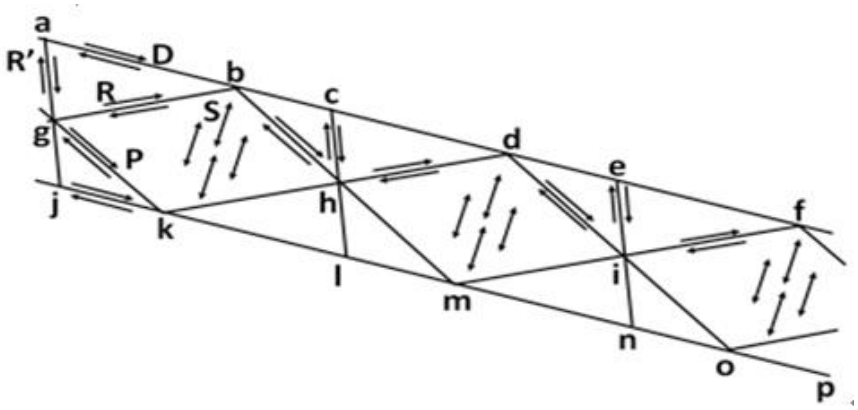

(a) The shear banding tilted slope

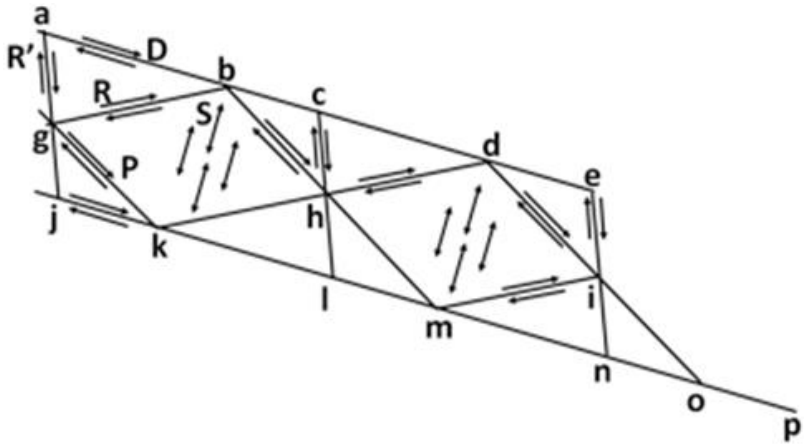

(b) The first landslide

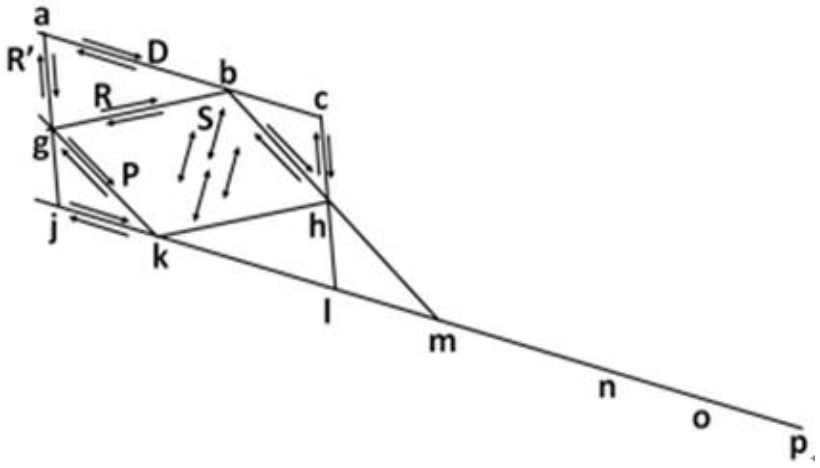

(c) The follow-up landslide

Figure 14. The landslide mechanism of shear banding tilted slopes (Hsu et al., 2015)

4. The degree of fracture increases with the increase of accumulated length of shear banding. Therefore, the shear strength parameters required in slope stability analysis would decrease rapidly with the increase of accumulated length.

5. The cohesion *c* and adhesion c_α corresponding to rock fracture surfaces and layer interfaces respectively will vanish during sliding, so only friction resistant force left, and the friction coefficient would decrease with the increase of sliding velocity.

6. For layering rock slopes, only after the cohesion c of rocks or adhesion c_α of layer interface vanishes, can the slope stability be significantly influenced by water pressure. The reason is the remaining friction resistance force $F_{friction} = (N - U)\, f$, where *N* is the normal force generated by the weight of sliding blocks on the potential sliding surfaces, *U* is the force of water pressure exerted on the potential sliding surfaces, *f* is the friction coefficient when sliding blocks slide on the potential sliding surfaces. When *f* decreases with the increase of sliding velocity or *U* increases with the rising of water table, and the only friction resistance force is smaller than the driving force generated by sliding blocks or water in the fracture zone, then can sliding failure occur on this sliding block.

7. For shallower delamination sliding failure planes, since the underground water table of layering rock slopes cannot actually rise to the range of shallow delamination slide failure, the underground water table monitored by drill holes on layering rock slopes are actually not relevant to shallow delamination slide surfailure. The real cause relevant to water pressure of Lishan landslide is the rainfall flowing into the shear band through cracks, and it does not require a heavy rain to fill all cracks in the shear band. This is the reason why landslide of shear banding tilted slopes can still occur under no wind, no rain, no earthquake conditions.

8. When scholars or consulting companies of Lishan landslide remediation project conducted slope stability analysis, they usually adopted a circular or non-circular potential failure plane, so they derived some conclusions about deep seated failure surface. However, it is inevitable that a circular or non-circular potential failure plane penetrates layering rocks, and in cases where the shear strength parameters of rock are comparatively high,

the factor of safety FS obtained from slope stability analysis can be very high, which prevents the possibility of slide failure. However, in the situations where Lishan landslides persistently happen on layering rock layers, in order to get the analysis result of factor of safety FS=1.0 from slope stability analysis, based on the circular or non-circular slide failure mechanism and its reverse-calculation method, they calculated the cohesion c and the angle of internal friction angle φ corresponding to the cases of potential sliding surfaces penetrating the layering rocks under the factor of safety FS=1.0. However, according to Table 2b, the reverse-calculated cohesion c and angle of internal friction φ are all very small, so the reverse-calculated cohesion c and angle of internal friction φ can never be the shear strength parameters of layering rocks in reality.

9. Lishan landslide remediation requires a new sliding failure mechanism and the results of slope stability analysis that comply with reality. In addition, newly proposed monitoring methods based on remediating delamination slide failure on shear banding tilted slopes are also needed. Furthermore, the monitoring data should be used to identify the shear bands and evaluate the shear strength parameters by the accumulated slide length. Only in this way can people conduct slope stability analysis based on the actual needs and further implement effective remediation works, otherwise it will be inevitable that slide failures continue to happen on slopes after remediation works are implemented.

5.4 Summary of the Main Points

1. In the past, scholars or consulting companies of remediation projects did not know shearing band tilted slopes, and did not consider shear banding tilted slopes as the cause of Lishan landslide. Therefore, Lishan landslides continue to happen even after a big budget had been spent on remediation works.
2. The cause of landslides proposed by scholars or consulting companies of remediation projects did not comply with the facts, that was how the dilemma of “say one thing and do another” happened.
3. The reverse-calculated shear strength parameters (including cohesion c and angle of internal friction φ) on the potential failure plane according to the factor of safety FS=1.0, which do not comply with those of real rocks.

4. Since delamination slide failure that occurs in shallow layers is the only type of landslide for shear banding tilted slopes. Therefore, neither the underground water table monitoring system nor the underground water drainage project, which are based on deep seated sliding failure plane, can work effectively. The main reason is after rainfall fills the layer interfaces and the shear textures of the shear bands in the shallow layers of rocks, the shear banding tilted slope has already experienced the critical state of slide failure, and the formation of this critical state is irrelevant to the underground water table monitored by currently installed monitoring holes. Therefore, the effects of the large underground water drainage project derived from the monitoring data of the drilled holes are very limited.
5. Therefore it is suggested that Lishan landslide remediation must be based on the delamination slide failure mechanism of shear banding tilted slopes, the investigation, analysis, monitoring, and remediation methods relevant to delamination slide failure of shear banding tilted slopes must be restudied and redrawn. Only in this way can the budget be spent wisely and the effects of remediation be improved, which can also avoid the dilemma situation of “more remediation works, larger disaster damage”.

Chapter 6

A World-shocked Landslide Disaster Caused by Shear Bandings

T.-S. Hsu, Z.-L. Wu, E.-C. Su, J.-H. Yang and C.-H. Lin

6.1 Introduction

Taiwan is situated at the edge of the Eurasian tectonic plate. Under continuing pressure from the Philippine Sea Plate, once the shear strains go deep into the plastic range, localizations of deformations can occur in a tectonic plate due to the loss of ellipticity, which can further result in shear banding (Drucker, 1950; Hill, 1962; Mandel, 1966; Rudnicki and Rice, 1975; Rice, 1976; Valanis, 1989).

Figure 6.1 shows that during the shear bandings that formed the mountains in the area around 3.1K of National Freeway No. 3, the rock layer interface is at a small angle of approximately 16°–19° from the horizontal. This section of the road is constructed as a cut road. The upper slope lost lateral support once excavation was completed, and the slope experienced creeping, very slow slipping, slow slipping, fast slipping, and very fast slipping under frequent felt earthquakes. This eventually caused slip failures of the slope even if there was no wind, no rain, and no earthquake (refer to Figure 6.2).

(a) Landslide area

(b) Adjacent areas

Figure 6.1. Shear banding features of National Freeway No. 3 3.1K (Google Earth, 2017).

Figure 6.2. National Freeway No. 3 3.1K landslide (Taiwan Geotechnical Society, 2011).

The design of the national freeways is of the highest standard and carried out by the most prestigious design consultants in Taiwan. However, the upper slope at 3.1K of the National Freeway No. 3 experienced slip failure and caused four fatalities. Is the real reason for this type of slope failure the corrosion of ground anchors, as stated in the investigation report (Taiwan Geotechnical Society, 2011)? If it is, then ground anchors in freeway slopes should all be changed to high-quality anchors with double corrosion protection, which should in theory ensure slope stability; otherwise,

there is no point in changing the anchors. Therefore, it is necessary to identify the real reason behind the failure of the anchored slope at 3.1K of National Freeway No. 3.

6.2 Stability Analysis for Anchored Slopes

This section first compares the slip failure mechanism in the design and in the investigation report of Taiwan Geotechnical Society with the actual failure mechanism. The results of the slope stability analysis in the design and in the investigation report of Taiwan Geotechnical Society (2011) are then investigated regarding where they deviate from the actual situations. Finally, overall slope stability analysis is conducted based on the actual slope failure mechanism.

6.2.1 Slope Stability Analysis in the Original Design

Analysis Profiles. The analysis profiles in the original design are presented in Figure 6.3.

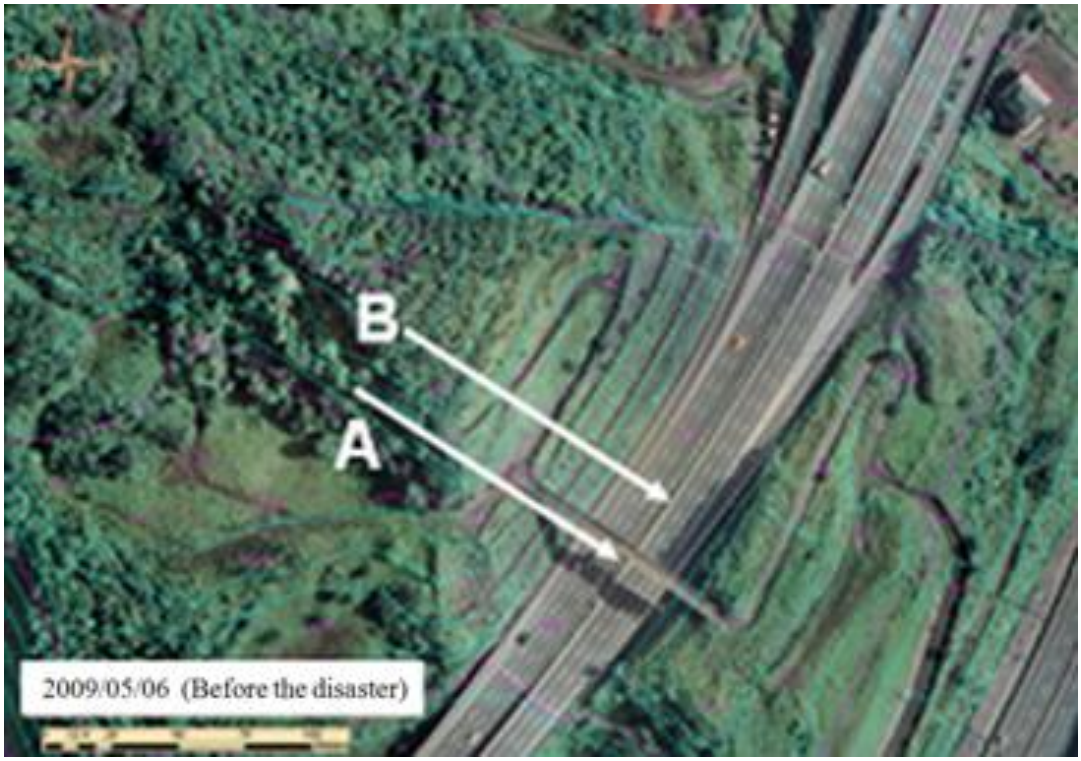

(a) Locations of the profiles A and B

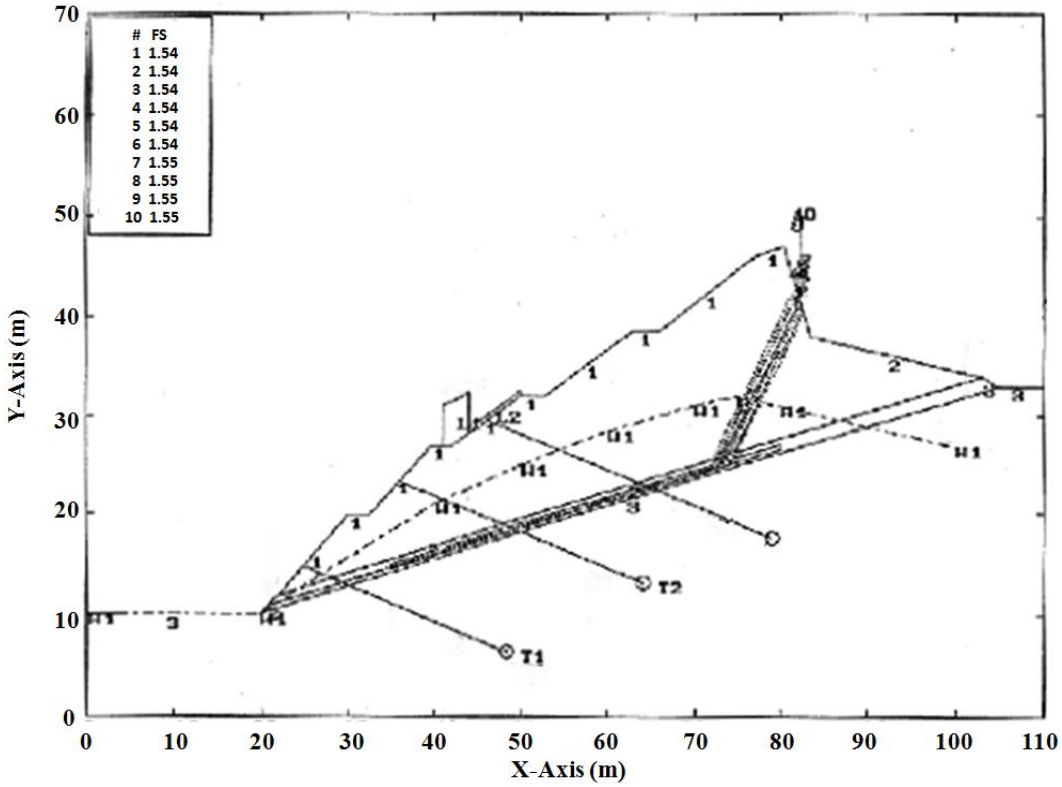

(b) Profile A

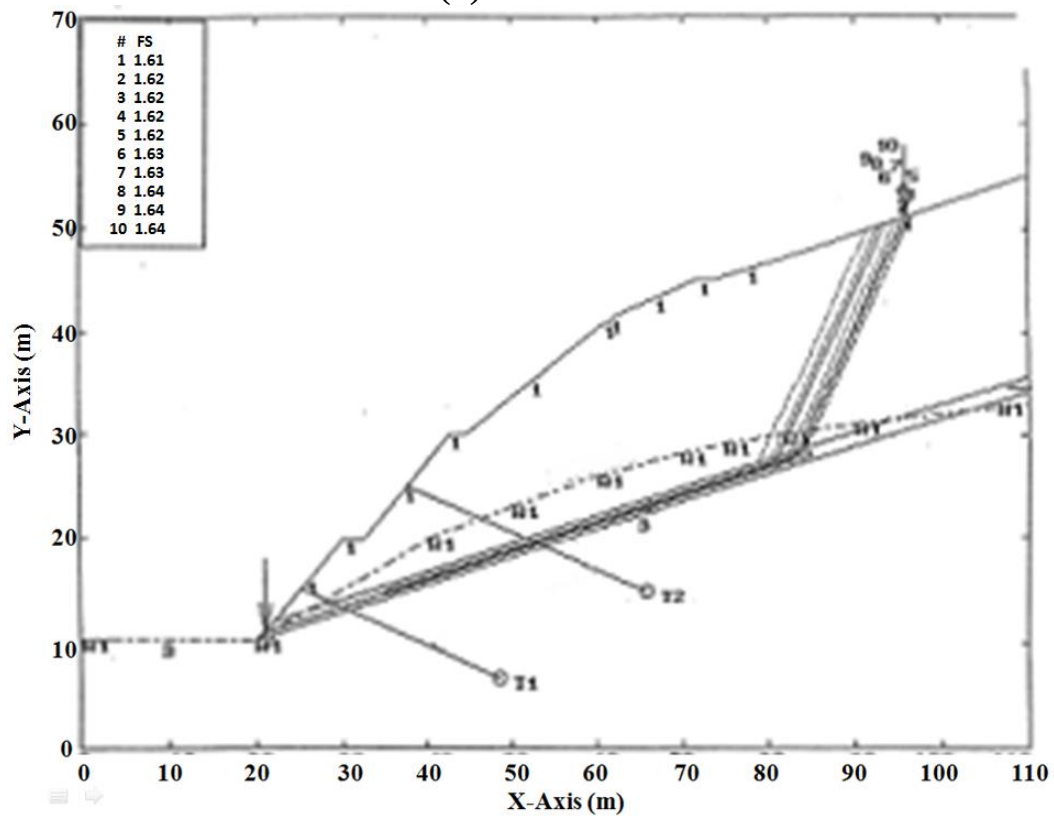

(c) Profile B

Figure 6.3. The analysis profiles in the original design (Taiwan Geotechnical Society, 2011).

Shear Strength Parameters Adopted and Results of Slope Stability Analysis.

1. Profile A:
   Sandstone:
   $c = 3Tf/m^2$ and $\phi = 32^\circ$;
   Sandstone and shale interbeds:
   $c = 3Tf/m^2$ and $\phi = 32^\circ$;
   Slip layer:
   $c = 1Tf/m^2$ and $\phi = 20^\circ$.
2. Profile B:
   Sandstone:
   $c = 3Tf/m^2$ and $\phi = 32^\circ$;
   Sandstone and shale interbeds:
   $c = 3Tf/m^2$ and $\phi = 28^\circ$;
   Slip layer:
   $c = 1Tf/m^2$ and $\phi = 20^\circ$.
3. Results of slope stability analysis
   (a) Profile A: Factor of safety: *FS* = 1.54.
   (b) Profile B: Factor of safety: *FS* = 1.61.

6.2.2 Slope Stability Analysis in the Investigation Report

Analysis Profiles. Figure 6.4 presents the analysis profiles adopted in the investigation report (Taiwan Geotechnical Society, 2011). Profiles A and B are those in the original design, and profiles E and F are additional sections used in the investigation.

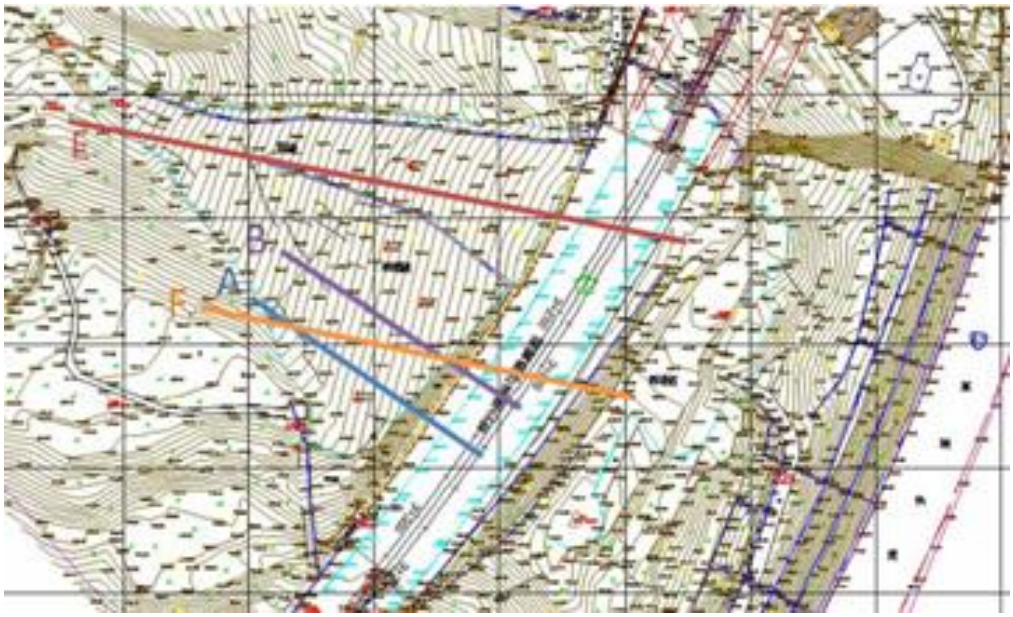

Figure 6.4. Analysis profiles in the investigation report (Taiwan Geotechnical Society, 2011).

Shear Strength Parameters Adopted and Results of Slope Stability Analysis. The cohesions and angles of internal friction for the sandstone, the sandstone and shale interbeds, and the sliding layer in profiles A and B are the same as those adopted in the original design.

Profiles E and F adopt c = 0 and ϕ=14.7. These shear strength parameters are obtained from the results of direct shear tests conducted on the thin silt seams at 19.9-m-deep holes drilled in the affected area.

Results of slope stability analysis**:**

(a) Profile A: Factor of safety: FS = 1.54.

(b) Profile B: Factor of safety: FS = 1.60.

(c) Profile E: Factor of safety: FS = 1.55.

(d) Profile F: Factor of safety: FS = 3.47.

6.2.3 The Proposed Slope Stability Analysis

Slip Failure Mechanism in the Shear Banding Tilted Slope. When the slope slips very slowly along the layer interface, Figure 6.5 shows that a shear band and various shear textures will develop. The first slip failure may follow a path connecting the “eiop” dots (or the “einop” dots) shown in Figure 6.5(b). The second slip failure may follow the path connecting the “chmno” dots (or the “chimno” dots) shown in Figure 6.5(c). This type of slip failure originates from shear banding, and the higher up the slope it is, the steeper it is. Therefore, it is named a shear banding tilted slope.

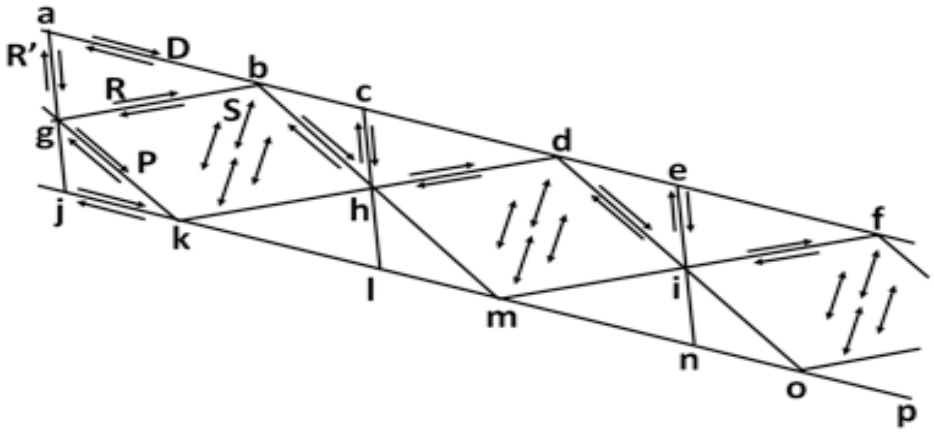

(a) Shear band and shear textures

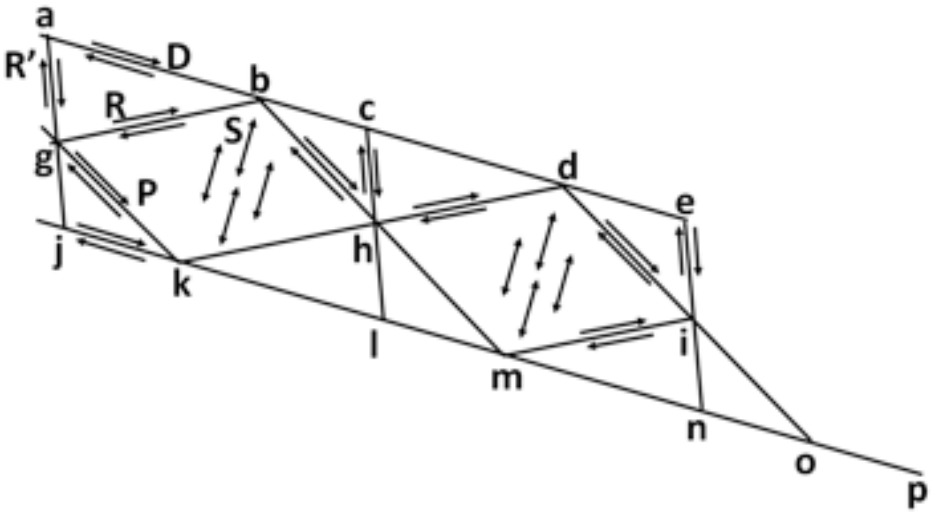

(b) First slip failure

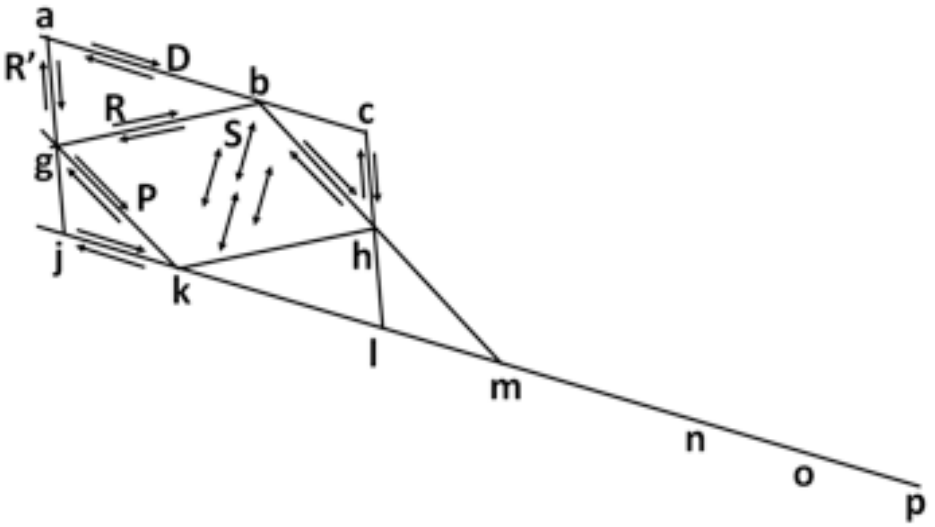

(c) Second slip failure

Figure 6.5. Slip failure path in the shear banding tilted slope (Hsu, et al., 2015).

It can be seen from Figure 6.5 that, prior to the first slip failure, due to shear banding, sliding blocks connecting the “feiop” points (or the “feinop” points) continue to slip very slowly along the o-p path (or the n-o-p path). Therefore, before the slip accelerates, the e–i and i–o paths (or the e–i and i–n paths) will show cracking and these cracks may be filled with water.

Analysis Profiles. Figure 6.6 presents the landslide areas adopted by the authors. They are the primary and secondly landslide areas.

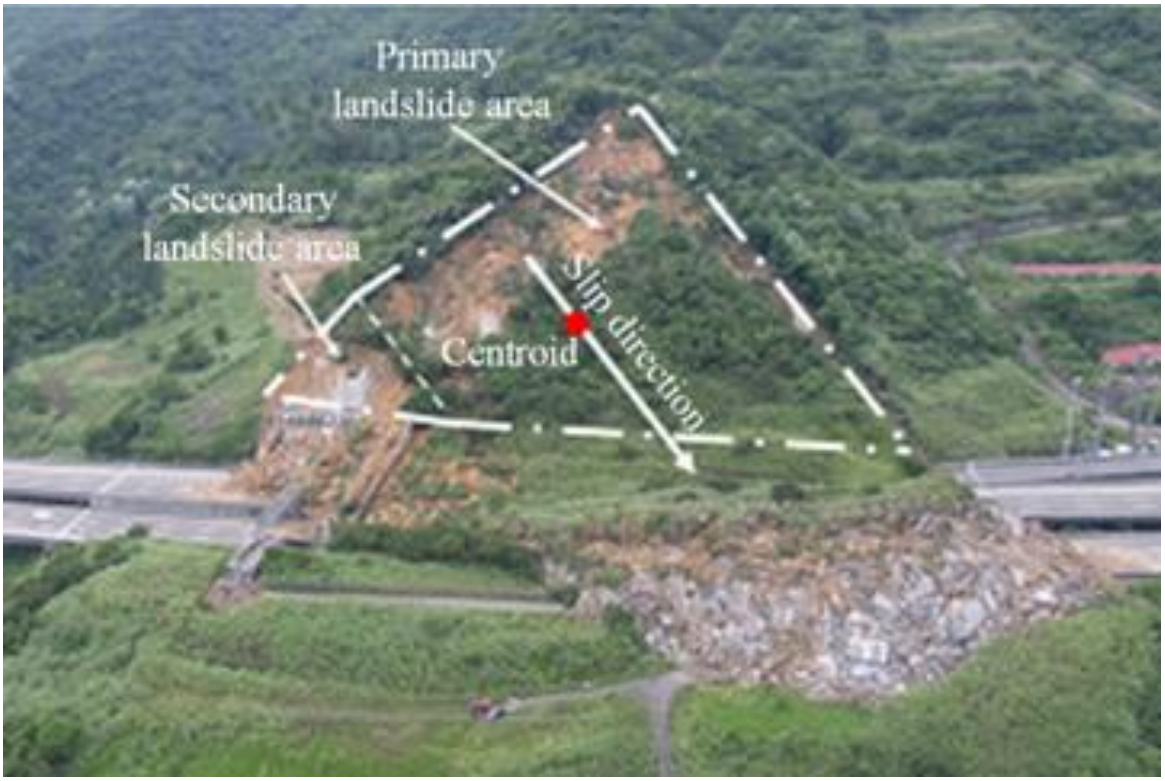

Figure 6.6. The slip areas adopted by the authors (background image from Taiwan Geotechnical Society, 2011).

Shear Strength Parameters Adopted. The slip failure occurs as a result of sliding of the yellow silty sandstone on the surface of grey to black shale. The shear strength parameters adopted in slope stability analysis for the sandstone and shale interface are as follows:

1. Static state:
   interface adhesion $c_\alpha = 0.374 Tf / m^2$;
   friction angle $\delta = 29.8^\circ$
   (i.e. friction coefficient f =0.57).
2. Slip at a very slow velocity:
   interface adhesion $c_\alpha = 0$
   friction angle $\delta = 17^\circ$ (i.e. f =0.30).
3. Slip at a slow velocity:
   interface adhesion $c_\alpha = 0$
   friction angle $\delta = 14^\circ$ (i.e. f =0.25).

Other Relevant Information.

1. The total number of ground anchors at completion of construction was 534, and after the landslide this number came down to 58. The remaining ground anchors are below the failure plane and, as a result, they did not take any reactions from the landslide. The total number of anchors resisting the slip deformation is 476. The design tensile strength of the anchors is 60Tf, and the total design tensile strength from the sum of the 476 anchors amounts to 28,560Tf.
2. The total landslide area in the upper slope is 12,400m^2, which consists of the primary landslide area of 11,550m^2 and the secondary landslide area of 850m^2. The volume of sliding blocks in the landslide area is 200,000m^3, which consists of 186,290m^3 blocks in the primary landslide area and 13,710m^3 blocks in the secondary landslide area. The total weight of blocks in the landslide area is 500,000Tf, which consists of 465,725Tf of blocks in the primary landslide area and 34,275Tf in the secondary landslide area.
3. The inclination angle of the slip surface is 16°–19°, with an average of 17.5°. The angle between the anchor tensile force and the slip plane is 36°.

Analysis Results.

1. The potential block driving force, F_D, is calculated as:

$$F_D = 500{,}000 \times \sin 17.5^\circ = 150{,}353\ Tf$$

2. Calculation of the resisting forces is as follows:

Static State. Prior to the commencement of excavation, assume zero slippage of yellow silty sandstone blocks on the grey to black shale surface. The interface is in full contact. At the stationary state, $P_f / P_{f0} = 100\%$, where P_f is the tensile strength of the ground anchors during shear banding, and P_{f0} is the tensile strength prior to shear banding.

Resisting force from ground anchor A_R:

$$A_R = 28560 \times (\cos 36^\circ + \sin 36^\circ \times f) = 32675\ Tf$$

where $f = 0.57$.

Resisting force from interface adhesion F_{R,c_α}:

$$F_{R,c_\alpha} = c_\alpha \times Area = 0.374 \times 12400 = 46376\ Tf$$

Resisting force from interface friction $F_{R,f}$:

$$F_{R,f} = 500000 \times \cos 17.5^\circ \times f = 271809\ Tf$$

Total resisting force, $F_{R,total}$:

$$F_{R,total} = 32675 + 46376 + 271809 = 350860\ Tf$$

Percentage of anchor resisting force in the total force $A_{R,\%}$:

$$A_{R,\%} = 32675 / 350860 \times 100\% = 9.3\%$$

Factor of safety FS:

FS = 350,860Tf/150,353Tf = 2.33 ≧ 1.5 (O.K.)

Slip at a Very Slow Velocity. When the block slips at a very slow velocity, *i.e.*, the yellow silty sandstone slips very slowly on the grey to black shale surface, the interface has transformed from full contact to partial contact as shown in Figure 6.7.

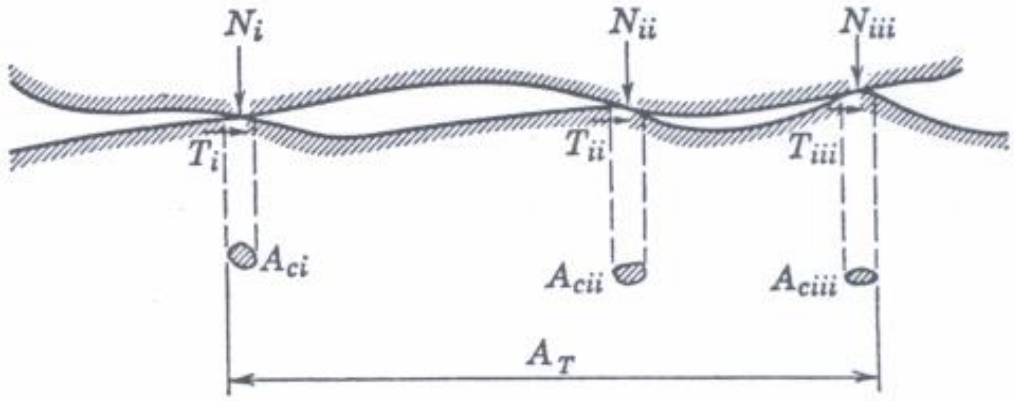

(a) Schematic drawing (Lambe and Whitman, 1972)

(b) Field condition

Figure 6.7. Partial contact between two adjacent blocks.

As the weight of the sliding block remains the same, the normal force on the contact surface, *N*, increases with reduced contact area, and the area around the contact of the sandstone and shale will exhibit softening behavior after yielding. According to the Hertzian theory of contact, partial contact area A_c increases with $N^{2/3}$, and friction coefficient f reduces with increasing *N*.

As the block continues to slip at a very slow velocity, the interface adhesion c_α approaches zero and the friction coefficient *f* decreases with increasing *N*.

For blocks sliding on the shale surface at a very slow velocity, the actual contact area is very difficult to assess. For the sake of convenience, the slip resisting force is calculated as the product of the normal force *N* on the sliding block and the overall average friction coefficient *f*. From the assessment of partial contact area in Figure 7(b), a friction coefficient $f = 0.30$ is adopted for very slow velocity.

For anchored slopes, if the cumulative amount of slip is *e*, the tensile strength of the anchors can be calculated using the formula derived by the authors: $P_f = P_{f0}/(1+8e/D)$, where *D* is the nominal diameter of the anchor.

The ground anchor's shear resistance A_R is computed as follows:

When D = 9cm, e = 1.125cm, e/D = 1/8, $P_f / P_{f0} = 0.5$:

$$A_R = 28560 \times (\cos 36^\circ + \sin 36^* \times f) \times 0.5 = 14071\,Tf \text{ ; and}$$

When D=9cm, e=9cm, e/D=1, $P_f / P_{f0} = 0.111$:

$$A_R = 28560 \times (\cos 36^\circ + \sin 36^* \times f) \times 0.111 = 3124\,Tf$$

The resisting force from the adhesion of the slip interface F_{R,c_α} is calculated as:

$$F_{R,c_\alpha} = c_\alpha \times Area = 0.0 \times 12400 = 0.0\,Tf$$

The resisting force from interface friction $F_{R,f}$ is:

$$F_{R,f} = 500000 \times \cos 17.5^\circ \times 0.30 = 143058\ Tf$$

The total slip resistance $F_{R,total}$ is:

When the cumulative amount of slip reaches 1.125cm,

$$F_{R,total} = 14071 + 143058 = 157129\ Tf \text{ ; and}$$

When the cumulative amount of slip reaches 9cm,

$$F_{R,total} = 3124 + 143058 = 146182\ Tf$$

The percentage of the resisting force provided by the anchors $A_{R,\%}$ is:

When the cumulative amount of slip reaches 1.125 cm,

$$A_{R,\%} = 14071 / 157129 \times 100\% = 9.0\%; \text{ and}$$

When the cumulative amount of slip reaches 9 cm,

$$A_{R,\%} = 3124 / 146182 \times 100\% = 2.1\%$$

The slope stability factor of safety FS is computed as follows:

When the cumulative amount of slip reaches 1.125cm,

$$FS = 157129 / 150353 = 1.05 < 1.5 \quad \text{(NG); and}$$

When the cumulative amount of slip reaches 9cm,

$$FS = 146182 / 150353 = 0.97 < 1.0 \quad \text{(NG).}$$

Slip at a Slow Velocity. The ground anchor's slip resistance A_R is computed as follows:

When D = 9cm, e = 16.875cm, e/D =15/8, $P_f / P_{f0} = 0.0625$:

$$A_R = 28560 \times (\cos 36^\circ + \sin 36^\circ \times f) \times 0.0625 = 1706\ Tf$$

where f is further reduced to 0.25.

The resisting force from the adhesion of the slip interface F_{R,c_α} is calculated as:

$$F_{R,c_\alpha} = c_\alpha \times Area = 0.0 \times 12400 = 0.0 Tf$$

The resisting force from interface friction $F_{R,f}$ is:

$$F_{R,f} = 500000 \times \cos 17.5^\circ \times 0.25 = 119215\ Tf$$

The total slip resistance $F_{R,total}$ is:

When the cumulative amount of slip reaches 16.875 cm,

$$F_{R,total} = 1706 + 119215 = 120921\ Tf$$

The percentage of the resisting force provided by the anchors $A_{R,\%}$ is:

When the cumulative amount of slip reaches 16.875 cm,

$$A_{R,\%} = 1706 / 120921 \times 100\% = 8.2\%$$

The factor of safety FS for the slope is:

When the cumulative amount of slip reaches 16.875 cm,

$$FS = 120921 / 150353 = 0.80 < 1.0 \quad \text{(NG).}$$

6.3 Comparison of Results and Discussion

Comparison and Discussion of Results From the Original Design and the Incident Investigation Report. Given that the landslide at 3.1K of National Freeway No. 3 took place under no wind, no rain, and no earthquake conditions, the occurrence of the landslide demonstrates the instability of the slope, *i.e.*, its factor of safety *FS* from slope stability analysis should be less than 1.0. Based on this, the following is derived by comparing the results of the slope stability analysis in the original design and in the incident investigation of Taiwan Geotechnical Society (2011):

1. With regard to profiles A and B, the slope stability analysis in the original design shows that the factor of safety of this anchored slope was greater than 1.5 (satisfying the requirement of the design standard). Therefore, the designers believe that, after completion, this anchored slope is stable under normal conditions, *i.e.*, no wind, no rain, and no earthquake. However, such a slope experienced shear failure under normal conditions, which means the original stability analysis results do not reflect the reality.
2. For profiles A and B that are under normal conditions, the analysis results in the investigation report (Taiwan Geotechnical Society, 2011) also show that the factor of safety was greater than 1.5. Therefore, this set of analyses do not reflect the reality either.
3. For profiles E and F under normal conditions, the factor of safety should be less than 1.0 since the anchored slope has already experienced shear failure prior to the investigation. However, the reported factors of safety are as high as 1.55 and 3.47, respectively (Taiwan Geotechnical Society, 2011). This result significantly contradicts the reality.
4. For profiles A and B, the shear strength parameters should adopt the adhesion c_α and friction angle δ of the sandstone and shale interface since the slip plane is known to pass through this interface. However, in the investigation report (Taiwan Geotechnical Society, 2011), the adopted parameters are cohesion *c* and angle of internal friction ϕ for the rock materials, *i.e.*, assuming the failure surface directly cuts through the sandstone or shale.
5. For profiles E and F, the shear strength parameters adopted in the report (Taiwan Geotechnical Society, 2011) are not the experimental results of the interface plane between the sandstone and shale (adhesion c_α and friction angle δ). The adopted parameters are the direct shear test results of thin silt seams (i.e. cohesion *c* and angle of internal friction ϕ) at a depth of 19.9m in the B-6 drill hole, below the slip plane. One cannot understand the meaning of the experimental results and whether they are sufficiently representative.

Comparison of Slope Stability Analysis Results and Discussion. The results of the slope stability analysis obtained by the authors for the failed anchored slope at 3.1K of National Freeway No. 3 are summarized in Table 6.1.

Table 6.1. Summary of results of the overall stability analysis of the anchored slope at 3.1K of National Freeway No. 3.

State	e (cm)	Anchor performance (%)	FS	$F_{R,f}$ (%)	$A_{R,\%}$ (%)
Static	0.000	100	2.33	77.5	9.3
Slip at a very slow velocity	1.125	50	1.05	91.0	9.0
	9.000	11	**0.97**	97.9	2.1

Static State.

1. Table 6.1 shows that the factor of safety for the anchored slope in the static state is FS = 2.33. Since it is greater than 1.5, the analysis results agree with the stable condition of the anchored slope when construction was completed.
2. The percentage of anchor resistance against slipping is only 9.3% of the total resisting force. Therefore, even if the ground anchors are not installed, the factor of safety for the slope would still satisfy the design requirement. The percentage of block friction resistance is 77.5% of the total resisting force. When the slope in the landslide area is stable, the main component of slip resistance is the friction force, not that mobilized from the anchors.

Slip at a Very Slow Velocity.

1. Table 6.1 shows that, when the cumulative amount of slip reaches 1.125 cm, the factor of safety FS drops significantly to 1.05. In this state, the anchored slope is already on the verge of shear failure.
2. When the cumulative amount of slip reaches 9.0 cm, the factor of safety FS = 0.97 < 1.0. In this state, the anchored slope is already experiencing shear failure.
3. When slipping at a very slow velocity, the mobilized resisting force from the anchors is less than 10% of the total resistance while the resisting force from friction accounts for more than 90% of the total. Therefore, the main component of the slip resistance is the friction force, not the anchors.
4. Given that the contribution of the anchors to the total shear resistance is quite low, the significant reduction in the slope's factor of safety is mainly due to the disappearance of adhesion c_α during shear banding.

5. When slip initiates, sandstone blocks slide on the interface with shale, which results in diminishing contact area, stress concentration, strain softening, and brittle failure. Cumulative amount of slip during very slow velocity can also lead to slip failure of the slope. Therefore, it is recommended that long-term monitoring of the cumulative amount of slip be implemented so that the slope's factor of safety can be correctly evaluated and slope stability be ensured.
6. At present, the National Expressway Bureau has renewed all ground anchors to have double corrosion protection. However, the effectiveness of corrosion protection is limited to the segments not affected by shear banding. For anchor segments through the shear band, as shown in Figure 6.8, no matter how many layers of corrosion protection it has, the protection will be ruptured during shear banding and cannot effectively protect the anchor.

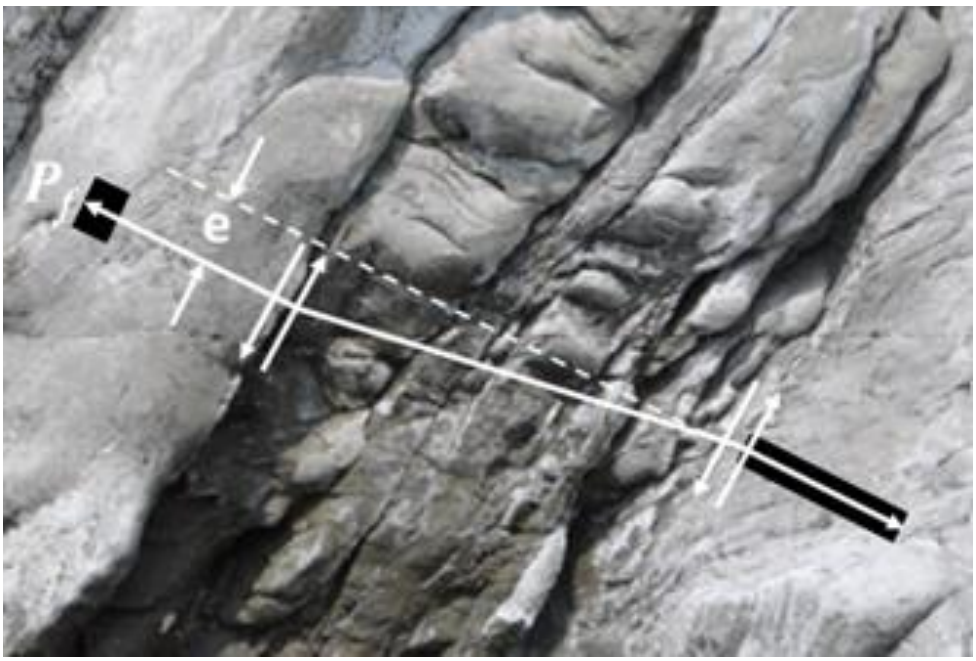

Figure 6.8. Anchor through the shear band.

7. The tensile strength of the corroded anchors is not necessarily greatly reduced at failure. However, for anchors passing through shear bands, as long as shear banding occurs, the tensile strength at failure will reduce significantly. Therefore, the key factor affecting the anchor's maximum tensile strength at failure is shear banding, not corrosion.
8. As the slip resistance provided by the anchors is not the main component in the total resisting force, even if they are changed to double-corrosion-protection anchors, slope stability cannot be ensured.

6.4 Summary of the Main Points

1. For the slope failure at 3.1K of National Freeway No. 3, the landslide failure mechanisms used in the original design and in the investigation report are completely different from that of shear banding tilted slopes in reality. The resulting factors of safety are all greater than 1.5, even when the slope had already experienced slip failure.
2. When adopting the whole area in the slope stability analyses, the simulated failure mechanism is the same as the actual one. Therefore, the resulting factor of safety from the analysis matches with field observations in the static state shortly after the completion of construction and in the state sometime after construction when shear banding occurred at a very slow to slow velocity.
3. It is known from the authors' slope stability analysis results that when the slope starts shear banding in a very slow velocity, the factor of safety continues to drop with increasing cumulative amount of shear banding. When the cumulative amount of slip reaches 9cm, the factory of safety is less than 1.0, *i.e.*, the slope is unstable.
4. For the anchored slope at 3.1K of National Freeway No. 3, more than 77.5% of the slip resistance is from the friction between the bottom of the sliding blocks and the shale surface, and the resistance by the anchors accounts for less than 9.3%. Under this circumstance, anchor corrosion is not in fact the main reason for the slope failure. The main reason is that, as the cumulative amount of shear banding increases, the adhesion of the slip plane c_α reduces to zero, the friction coefficient reduces and the tensile strength of the anchors reduces significant as well.
5. After the investigation report was issued by Taiwan Geotechnical Society in 2011, the host organization immediately re-constructed the existing anchored slope with a grid pattern at 3.2K of the National Freeway No. 3 to anchored retaining walls. However, only five years after the reconstruction, the retaining wall has shown severe deformation (see Figure 6.9). This resembles the instability of the retaining wall on the left bank of the southbound lane at 3.1K of National Freeway No. 3 prior to the landslide (see Figure 6.10). The host organization should have the proper understanding with regard to the design and safety maintenance of anchored slopes. It should not treat the secondary factor as the primary factor of the landslide and ignore the primary factor, thus undermining the stability of freeway slopes.

(a) Severe leaking out of the cemented substances

(b) Cracking of the retaining wall

(c) Warping of the retaining wall

Figure 6.9. Current slope instabilities at 3.2K of National Freeway No. 3.

(a) Severe leaking out of the cemented substances

(b) Cracking of the bridge abutment

(c) Bending of the bridge

Figure 6.10. Slope instabilities at 3.1K of National Freeway No. 3 prior to the landslide (Google Earth, 2017).

Chapter 7

An Effective Method for Repairing a Damaged Earth Dam Caused by Shear Bandings

T.-S. Hsu, C.-M. Yen, J.-D. Lai , Y.-C. Lin
Z.-X. Lin, Z. Wang and S.-E. Chiu

7.1 Introduction

Hutoupi Reservoir is an old dam. It was often destroyed by floodwaters during the period from 1841 to 1867 and it was also destroyed in the earthquake of 1906. After the 1935 Guan-Dao-Shan Earthquake, the embankment of the Hutoupi Reservoir dam collapsed following heavy rainfall and gushing due to piping damage emerged at the corner between dam body section 1 and section 2, as illustrated in Figure 7.1.

Figure 7.1. The dam for the Hutoupi Reservoir

(Taiwan Chia-Nan Irrigation Association, 2010).

In addition to the historical catastrophe mentioned above, the corner of the Hutoupi Reservoir dam also exhibited earthquake damage after the 2010 Jiaxian Earthquake. Afterwards, scholars from a well-known national university and engineering consultants established an emergency response plan. After using results from different tests to detect crack position, extent, and depth, an emergency repair project was designed and reconstruction was carried out accordingly. It was originally believed that, with the results of the

detection using modern precision instruments, no further earthquake damage could occur after the completion of the emergency repair project. However, unexpectedly, three years after the completion of work, the downstream-side of the slope where the emergency repair work was carried out exhibited leakage (see Figure 7.2).

Figure 7.2. Leakage occurring at the downstream-side slope of the dam body in 2013 (Google Earth, 2017).

Then, during the 2016 Meinong Earthquake, the original emergency repair site once again exhibited earthquake damage. As shown in Figure 7.3, the extent of earthquake damage after the 2016 Meinong Earthquake was higher than that after the 2010 Jiaxian Earthquake. Shocked and not wanting further earthquake damage to occur in the future, the organizing body requested the authors to provide a high-quality and effective emergency repair method, as required for homogeneous dams, thereby ensuring that the dam body will not exhibit earthquake damage again after an earthquake of similar magnitude in the future.

(a) After the 2010 Jiaxian Earthquake

(b) After the 2016 Meinong Earthquake

Figure 7.3. Comparison of degrees of earthquake damage for the two earthquakes in succession.

7.2 Basic Data

Geographic Location. Figure 7.4 shows the geographic location of Hutoupi Reservoir. Hutoupi Reservoir is located near the intersection of the highways Nan 168 and Nan 175. The section indicated by the brown strip in Figure 4 is the location of the earthquake damage to the dam after the two earthquakes.

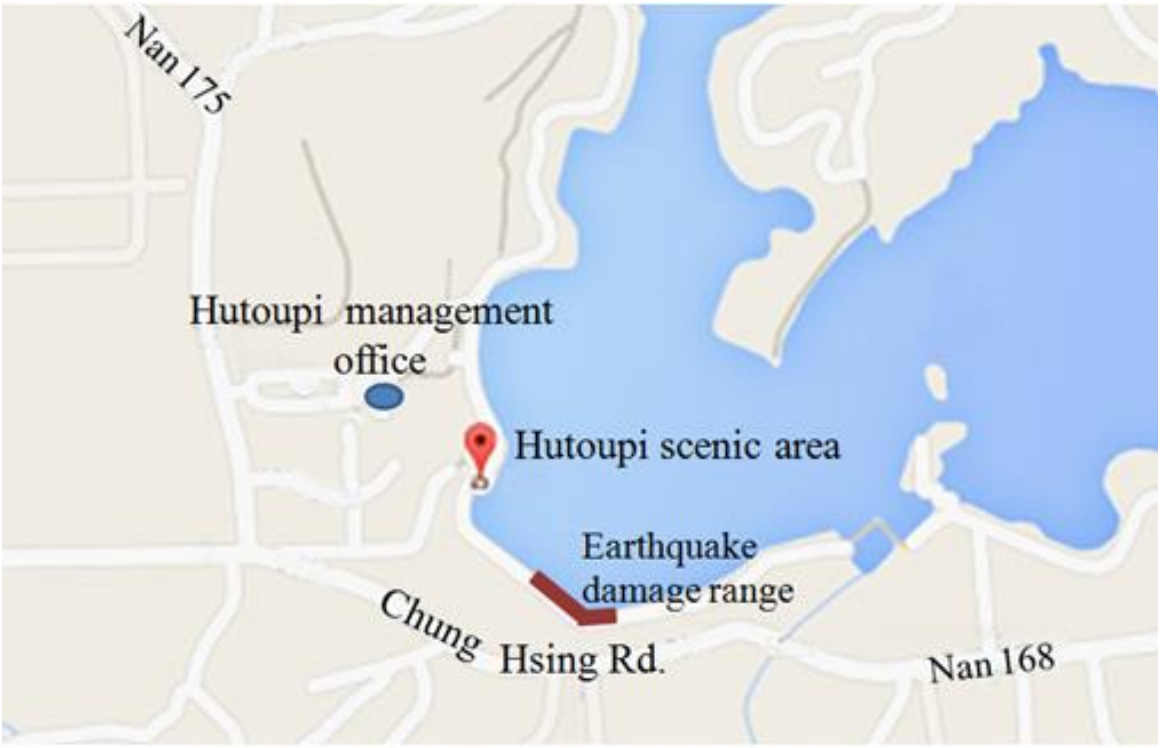

Figure 7.4. Map of the nearby area of the Hutoupi Reservoir (Google Map, 2017).

Geology and Geological Structure. Figure 7.5 shows the geology and geological structure in the vicinity of the Hutoupi Reservoir. The strata of this area can be divided into the Chiting formations of the Pleistocene and terrazzo and an alluvial layer of the Holocene.

Seismic Data. Figure 7.6 shows a histogram of the number of earthquakes each year with Tainan City as the epicenter (Central Weather Bureau Global Information, 2017). The top three values are 32 times in the year 2015, 28 times in the year 2008, and 25 times in the year 2000.

Figure 7.7 shows a histogram of the annual maximum magnitude of earthquakes in Tainan City. The top three values are 5.4 in the year 2000 and 5.2 in the years 1995 and 2010.

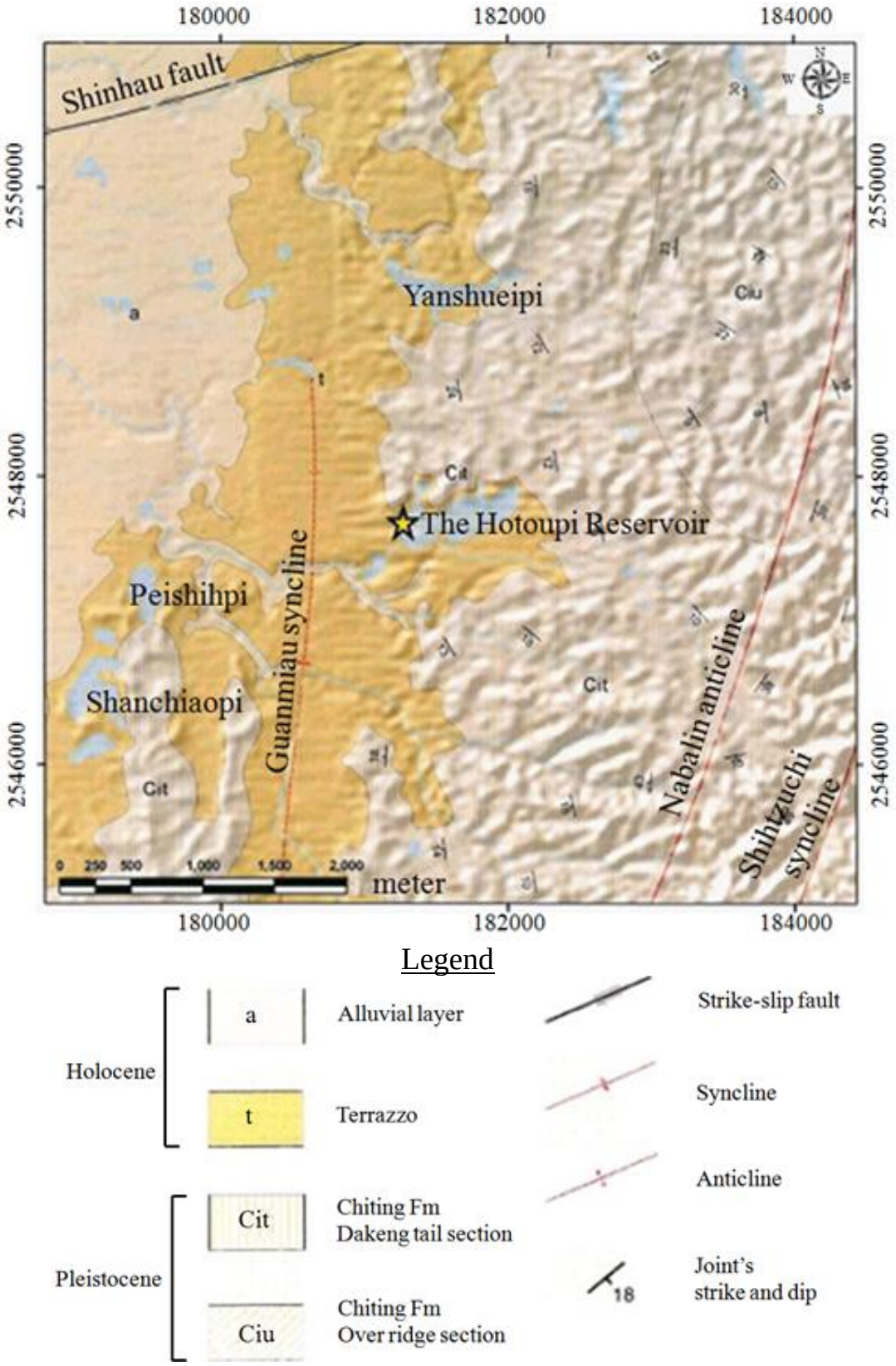

Figure 7.5. Geology and geological structure map for the area around the Hutoupi Reservoir (Central Geological Survey, Ministry of Economic Affairs, 2017).

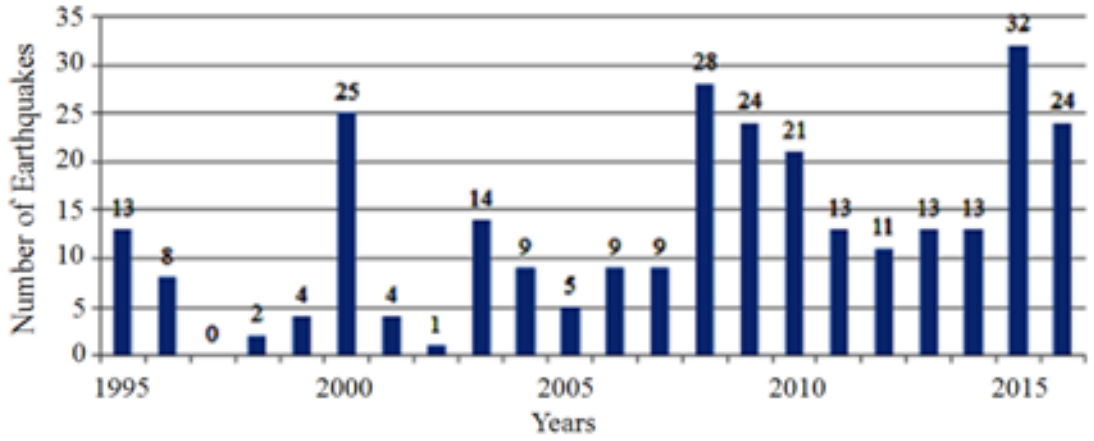

Figure 7.6. Distribution of the number of earthquakes in Tainan City (Central Weather Bureau Global Information, 2017).

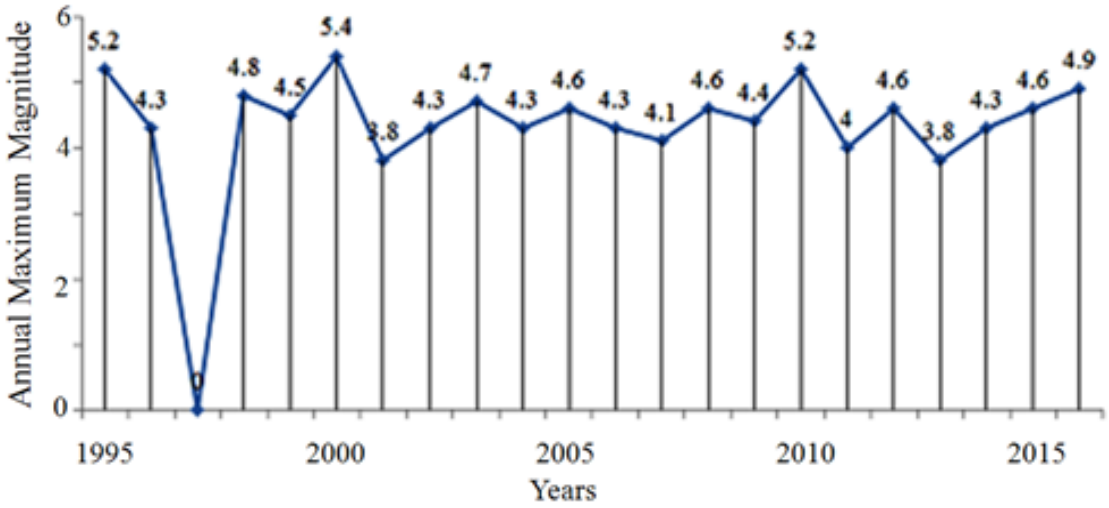

Figure 7.7. Annual maximum magnitude in Tainan City (Central Weather Bureau Global Information, 2017).

7.3 High-Quality and Effective Dam Body Emergency Repair Project

7.3.1 Causes of Earthquake Damage on a Dam Body in a Tectonic Earthquake

The China Earthquake Disaster Prevention Center (2017) states that earthquakes can be divided into five types: tectonic earthquake, volcanic earthquake, collapse earthquakes, induced earthquakes, and artificial earthquakes. Of these, the number of tectonic earthquakes is the greatest, accounting for approximately 90% of the total number of earthquakes around the world. Its destructive power is also the strongest and all the earthquakes that cause major disasters are tectonic earthquakes. Therefore, when investigating earthquake damage, it is necessary to focus on tectonic

earthquakes. However, the major effect of tectonic earthquakes is shear banding of the tectonic plate, which accounts for more than 90% of the total seismic energy; the secondary effect of tectonic earthquakes is the vibration of the tectonic plate, which accounts for less than 10% of the total seismic energy. Because the Jiaxian Earthquake and the Meinong Earthquake are both classified as tectonic earthquakes, when exploring the causes of earthquake damage in a dam body, it is necessary to first identify the locally existing shear bands.

Identifying Shear Bands From a Map of the Distribution of Displacement Velocity Vectors. From a map of the distribution of displacement velocity vectors shown in Figure 7.8, the mechanism of shear band formation can be identified. There are four groups of shear bands with different strikes in the vicinity of Hutoupi Reservoir: (1) a twinning-type shear band indicated by the white solid line with a strike of N26°W; (2) a conjugate twinning-type shear band denoted by the red dotted line with a strike of N54°E; (3) a slip-type shear band indicated by the yellow solid line with a strike of N56°W; and (4) a conjugate slip-type shear band indicated by the orange dotted line with a direction of N34°E.

Identifying the Shear Bands and Shear Textures From a Satellite Image. From the satellite image in Figure 7.9, the displaced topographic features can be used to identify shear textures. There are five groups of shear textures with different strikes within the total shear band width in the vicinity of Hutoupi Reservoir: (1) a principal displacement shear D with a strike of N56°W; (2) a thrust shear P with a strike of N26°W; (3) a Riedel shear R with a strike of N85°W; (4) a conjugate Riedel shear R′ with a strike of N54°E; and (5) a compression texture S with a strike of N34°E.

Identifying the Shear Bands and Shear Textures From a Cross-sectional View of the Dam. Figure 7.10(a) shows a cross-section of the Hutoupi Reservoir dam. The Hutoupi Reservoir dam zone is divided into an upper dam body and a lower dam body. Since the cross-section of the upper dam body is aberrant, it will exhibit shear banding relative to the lower dam body in all previous tectonic earthquakes. The aforementioned shear banding will induce various shear textures within the total shear band width (see Figures 7.10(b) and 7.10(c) for detail).

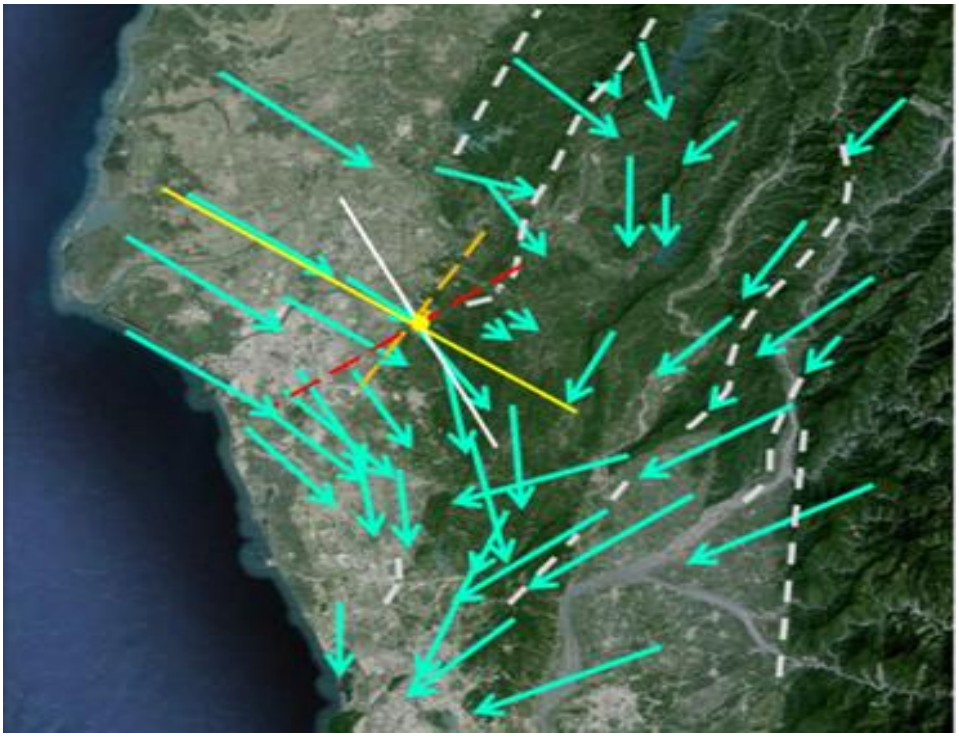

Figure 7.8. Shear bands identified from the distribution of displacement velocity vectors (background figure and vectors taken from Google Earth (2017) and GPS LAB (2017), respectively).

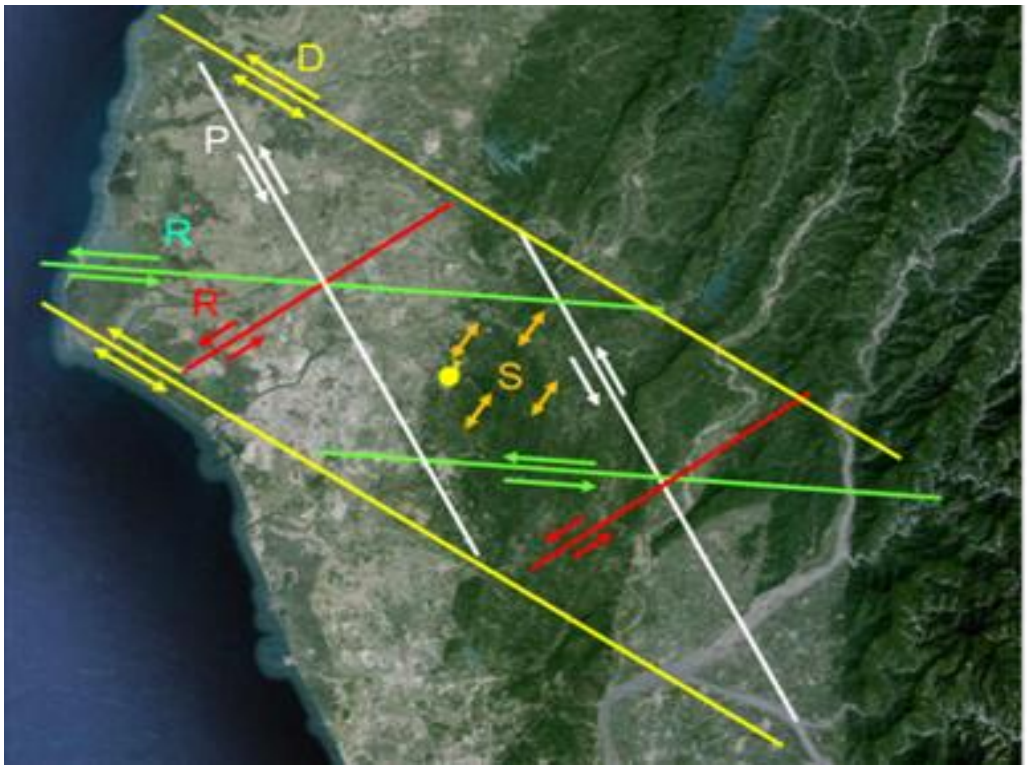

Figure 7.9. Shear bands identified from satellite imagery (background figure taken from Google Earth, 2017).

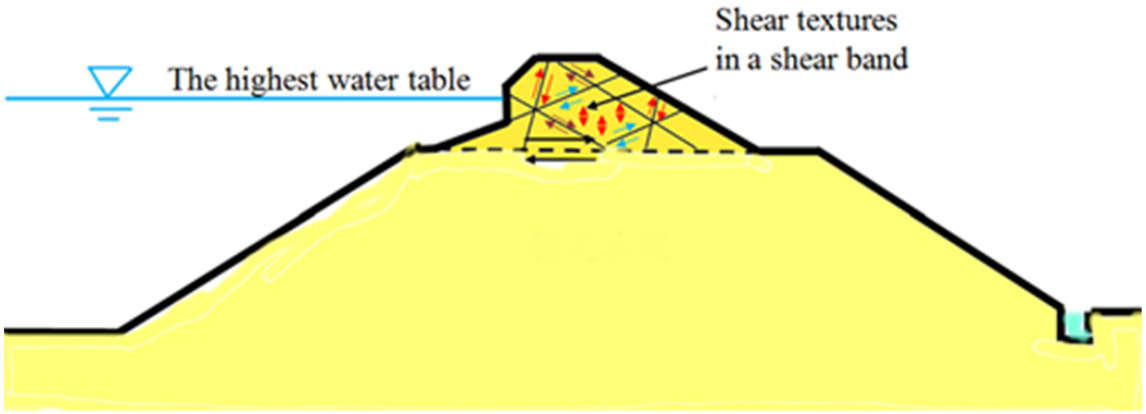

(a) Schematic diagram for the shear band occurring in the upper dam body.

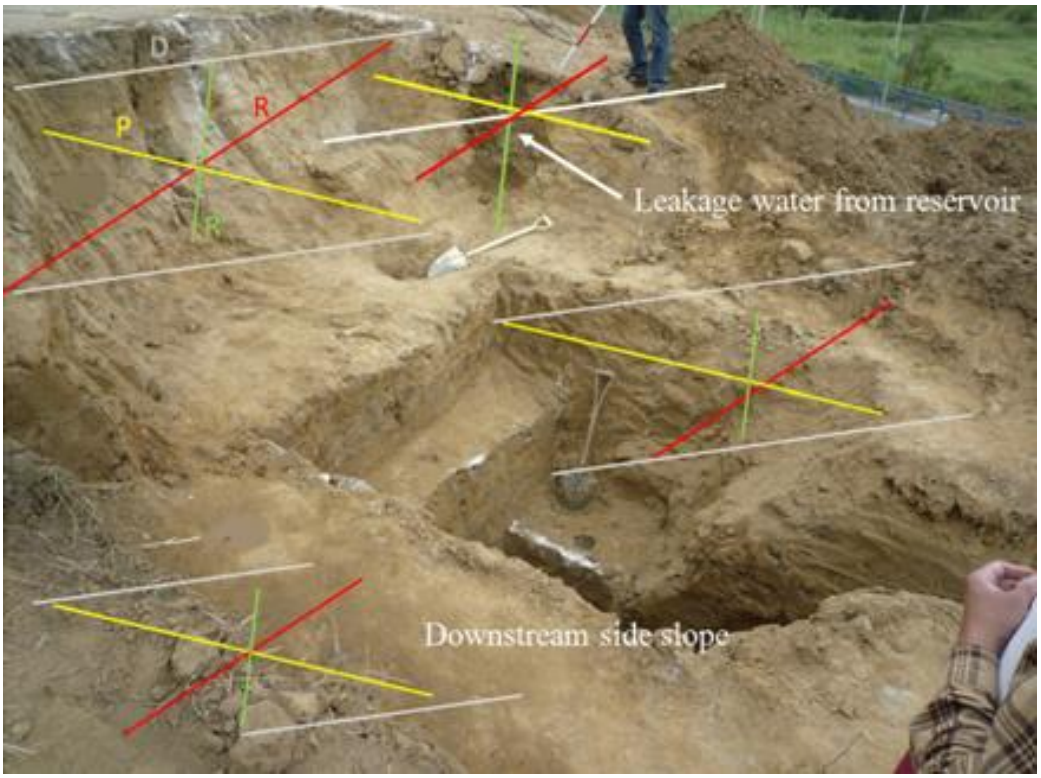

(b) In-situ shear bands caused by the 2010 Jiaxian Earthquake.

(c) In-situ shear bands caused by the 2016 Meinong Earthquake.

Figure 7.10. Identified shear bands and shear textures occurring in the dam body of Hutoupi Reservoir.

7.3.2 Decision-making on the Extent of Repairs Needed for the Dam Body

With the shear bands and shear textures clearly identified, the cross-section of the dam that requires repair is the whole upper dam body above the red line depicted in Figure 7.11(a), while the dam perimeter that requires repair is the extent of shear banding illustrated in Figure 7.11(b).

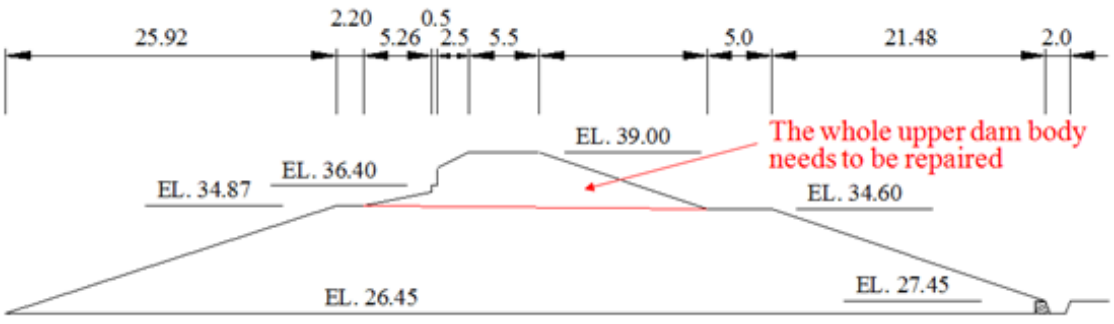

(a) Cross-section of the area that needs to be repaired.

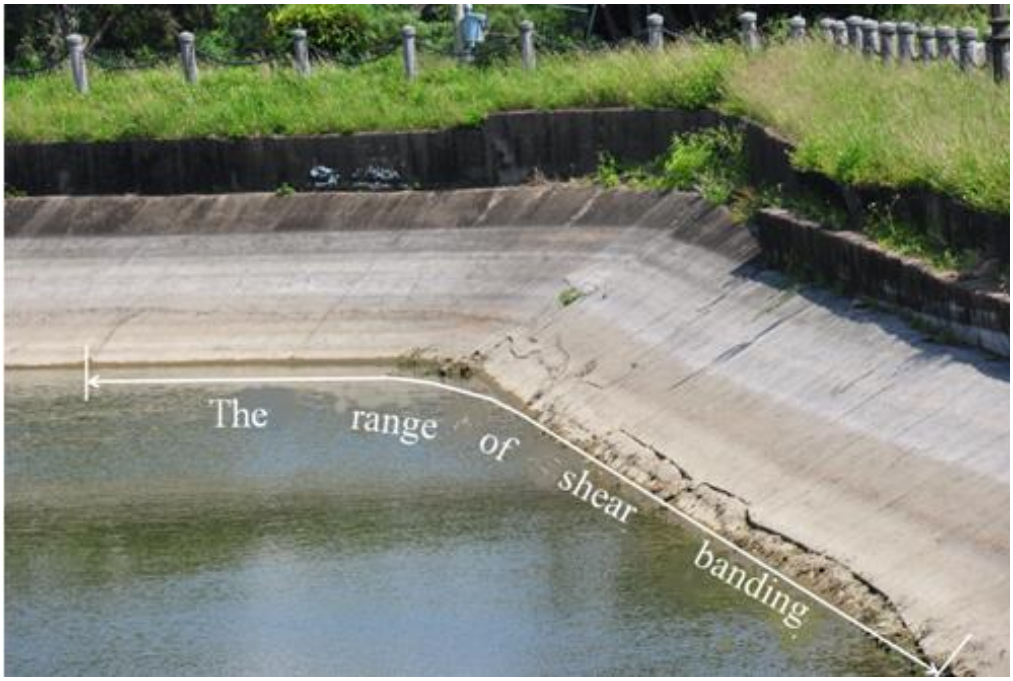

(b) The dam perimeter needs to be repaired.

Figure 7.11. The area of shear banding that needs to be repaired after the 2016 Meinong Earthquake.

7.3.3 High-quality and Effective Repair Materials

Before developing high-quality and effective repair materials, the authors first went to the repair zone for sampling, in order to conduct the Atterberg limit test and a compaction test. The test results showed that the original dam material in the repair zone had a plasticity index PI = 3.1~4.1, and the soil classification results as ML, while the compaction test results showed that the optimum water content is 12.5% and the maximum dry unit weight is 1.892Tf/m^3. Subsequently, an on-site density test using the sand-cone method showed the dry unit weight from the test to be 1.594Tf/m^3, thereby confirming that the relative compaction of the repair zone to the original dam zone is only 84.2%.

For a homogeneous dam, an index of relative desirability of 1 is the best and an index of 14 is the worst. According to Wagner (1957), the relative desirability of silt with low plasticity (ML) is 6, which is classified as moderate. The contract stipulates that the minimum value of relative compaction must be greater than 95%, and the average value must not be less than 98%, so after using silt with low plasticity (ML) for emergency repair, the relative compaction of the compacted soil (84.2%) in fact does not meet the contracted requirements. Finally, according to Hsu *et al*. (2015), silt with low plasticity (ML) is the least earthquake-resistant material. Under the combined effects of the three factors mentioned above, more severe earthquake damage occurred during the Meinong Earthquake following the

completion of the Hutoupi Reservoir dam emergency repair project after the 2010 Jiaxian Earthquake (see Figure 3 for details).

Based on the study results above, the authors consider that the Hutoupi Reservoir dam emergency repair project for the 2016 Meinong Earthquake must excavate the area indicated in Figure 11 and then conduct stratified backfilling with more earthquake-resistant clayey gravels (GC), which has a relative desirability index of 1 (Wagner, 1957). During the backfilling process, systematic compaction quality counseling and management are introduced in anticipation that the compacted soil quality of the whole repair zone will comply with the contracted requirements.

When the dam repair material is changed from low-plasticity clay (ML) to clayey gravels (GC), then, according to Wagner (1957), the permeability of the dam body will be enhanced from being semi-permeable to being non-permeable; the shear strength will be enhanced from general to good-to-general; the compressibility will be enhanced from moderate to very low; the workability will be enhanced from general to good; and the relative compaction will be increased from 84.2% to over 98%. According to Hsu *et al*. (2015), the earthquake resistance will also be improved from being the least earthquake resistant to being the most earthquake resistant. Therefore, after the Meinong Earthquake emergency repair project for the Hutoupi Reservoir dam is completed, theoretically it should be able to survive a similar magnitude earthquake and no longer exhibit earthquake damage.

In order to formulate the clayey gravels (GC), the proportions of the repair materials are detailed in Table 7.1. Here, the gravel content is 35%, the sand content is 30%, and the mudstone soil content is 35%.

Table 7.1. Proportion of GC in emergency repair project materials.

	Percentage by weight (%)
Gravel	35% (11.666% each for particle diameters 7.5cm, 3.75cm, and 1.9cm)
Sand	30% (10% each for particle diameters 2mm, 0.85mm, and 0.25mm)
Mudstone Soil	35% (including fine sand 0.23%, silt and clay 34.77%)

For the gradation of the gravels shown in Table 1, the construction manufacturer can purchase three gravels of specified weights with particle diameters of 7.5 cm, 3.75 cm, and 1.9 cm for addition to satisfy the requirements. Figure 7.12 shows that the gradation of the mixed sand provided by the construction manufacturer is in compliance with contract requirements.

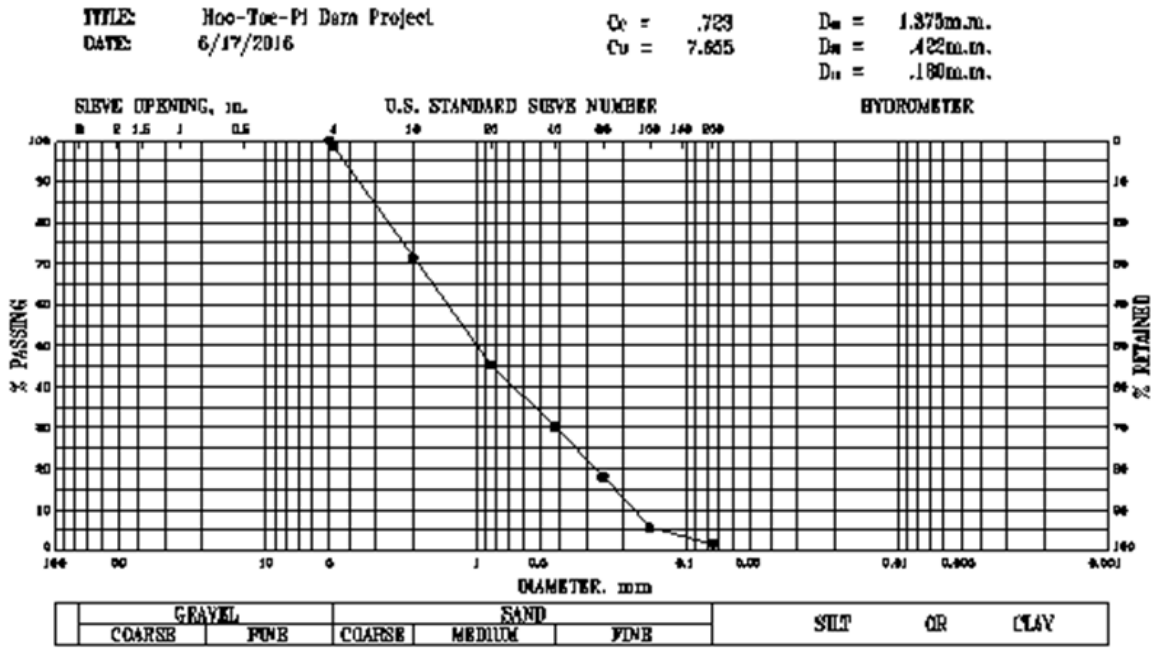

Figure 7.12. Sieve analysis results of the mixed sand materials.

For the gradation of the mudstone soils, the test results for a wet-washing method and sieve analysis of the Pingtung mudstone soils provided by the construction manufacturer show that almost all pass through the US standard sieve No. 200. Next, as indicated by the Atterberg limits test results (Figure 7.13), the liquid limit of this mudstone soil is LL = 34.7, the plastic limit is PL = 23.4, and the plasticity index is PI = 11.3. It is clear that this Pingtung mudstone soil conforms to the standard defined by the Bureau of Reclamation in the USA that the PI value of a homogeneous dam be between 7 and 25.

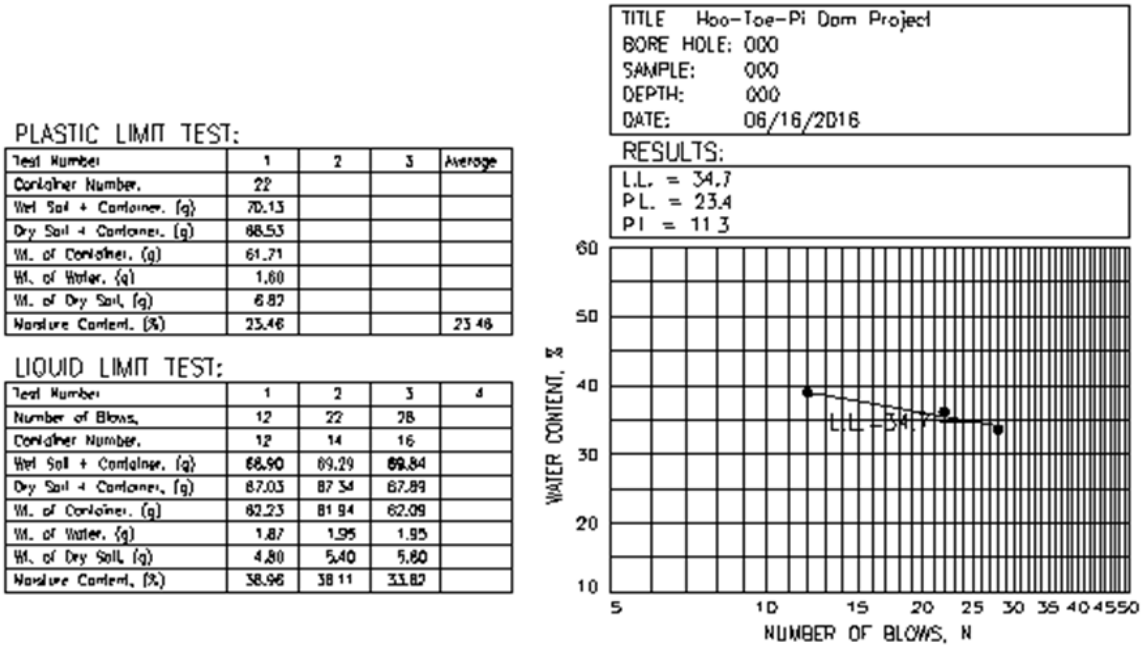

PLASTIC LIMIT TEST:

Test Number	1	2	3	Average
Container Number.	22			
Wet Soil + Container. (g)	70.13			
Dry Soil + Container. (g)	68.53			
Wt. of Container. (g)	61.71			
Wt. of Water. (g)	1.60			
Wt. of Dry Soil. (g)	6.82			
Moisture Content. (%)	23.46			23.46

LIQUID LIMIT TEST:

Test Number	1	2	3	4
Number of Blows.	12	22	28	
Container Number.	12	14	16	
Wet Soil + Container. (g)	68.90	69.29	69.84	
Dry Soil + Container. (g)	67.03	67.34	67.89	
Wt. of Container. (g)	62.23	61.94	62.09	
Wt. of Water. (g)	1.87	1.95	1.95	
Wt. of Dry Soil. (g)	4.80	5.40	5.80	
Moisture Content. (%)	38.96	38.11	33.62	

Figure 7.13. Atterberg limit test results for the repair material.

Finally, based on the Unified Soil Classification Method (SA), the Pingtung mudstone soil is classified as CL, and the whole repair material is classified as GC. Therefore, it is clear that all the repair material provided by the construction manufacturer is in compliance with the contract requirements.

7.3.4 Construction Quality Counseling and Management of Compacted Soil

The first step of construction quality counseling and management for compacted soil is to ensure the maximum dry unit weight of the soil and the optimum water content of the whole material containing gravels with a maximum particle size of 7.5cm.

Since the gravel content is greater than 30%, it is necessary to conduct a large-scale compaction test according to the provisions of the specifications (*ASTM Book of Standards*, 2017). Since the large-scale compaction test for a specimen diameter of 75cm (*Earth Manual*, 1972) is time-consuming and laborious, as well as not being in line with the requirements of an emergency repair project, it is necessary to modify the standard Proctor compaction test result for a gravel content of P = 0% via a modified formula into a large-scale compaction test result for a gravel content of P = 35%. Hsu and Saxena (1991) conducted large-scale compaction tests for similar soil in the past and compiled the results into a modified formula.

Before using the modified formula, it is necessary to first conduct a test of the soil sample passing through the US standard sieve #4. It shows that, for a soil sample with a gravel content of P=0%, the resulting specific gravity is G_s=2.672, the maximum dry unit weight is $\gamma_{d,\max}$ = 1.848Tf/m^3, and the optimum moisture content is OMC_0 = 14.3% (see Figure 7.14 for details).

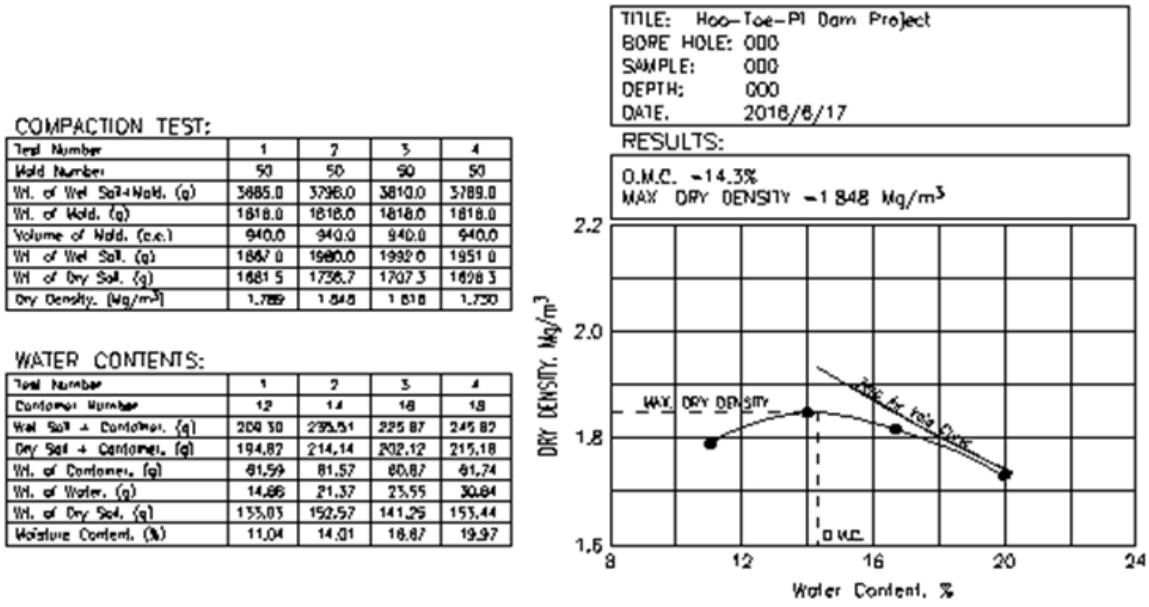

COMPACTION TEST:

Test Number	1	2	3	4
Mold Number	50	50	50	50
Wt. of Wet Soil+Mold. (g)	3685.0	3796.0	3810.0	3789.0
Wt. of Mold. (g)	1818.0	1818.0	1818.0	1818.0
Volume of Mold. (c.c.)	940.0	940.0	940.0	940.0
Wt of Wet Soil. (g)	1867.0	1980.0	1992.0	1951.0
Wt of Dry Soil. (g)	1681.5	1736.7	1707.3	1698.3
Dry Density. (Mg/m³)	1.789	1.848	1.818	1.750

WATER CONTENTS:

Test Number	1	2	3	4
Container Number	12	14	18	18
Wet Soil + Container. (g)	209.30	235.51	225.87	245.82
Dry Soil + Container. (g)	194.87	214.14	202.12	215.18
Wt. of Container. (g)	81.59	81.57	80.87	81.74
Wt. of Water. (g)	14.66	21.37	23.55	30.64
Wt. of Dry Soil. (g)	133.03	152.57	141.25	153.44
Moisture Content. (%)	11.04	14.01	16.67	19.97

Figure 7.14. Results of the standard Proctor compaction test for a gravel content of P=0%.

Next, for a gravel content of P=0%, it is necessary to calculate the void ratio corresponding to $\gamma_{d,\max}$ = 1.848Tf/m^3 to be $e_0 = 0.4459$, and use Equation 7.1 to modify e_0 to be the void ratio of the full soil with a gravel content of P=35% to be $e = 0.314$.

$$e = e_0 + A \cdot P + B \cdot P^2 + C \cdot P^3 + D \cdot P^4 . \tag{7.1}$$

For the material formed by mixing the gravels, sand, and mudstone soils, using the standard Proctor compaction method, the coefficients of A, B, C, and D in Equation 7.1 are found to be −0.442861167, −0.088452600, 0.979631467, and −0.519465600, respectively.

The maximum dry unit weight of the soil without gravel, that is, with a gravel content of P=0%, is $\gamma_{d,\max}$ =1.848Tf/m^3. After obtaining $e = 0.314$ from the above calculation and using the specific gravity of the gravels obtained from the test, G_g=2.640, this dry unit weight can be modified to the maximum dry unit weight of the total soil with a gravel content, $\gamma_T = 2.024T/m^3$, via Equation 7.2:

$$\gamma_T = \frac{1}{(1+e)[P/(G_g\gamma_w) + (1-P)/(G_s\gamma_w)]} . \tag{7.2}$$

The validity of adopting Equation 7.2 for gravel content modification can be explained by Figure 7.15. In Figure 7.15, the solid dots are derived from the large-scale compaction test results; the solid line is derived from the modified formula proposed by Hsu and Saxena (1991), in which the

applicable range is for a gravel content of P=0~100%; the dashed line is derived from the modified formula proposed in the *Earth Manual* (1972), in which the applicable range is for a gravel content of P≤30%; and the solid triangles are derived from the D method of the American Society for Testing Materials (ASTM)'s compaction methods (2017). It shows that the applicable range for the modified formula proposed by Hsu and Saxena (1991) is much larger than those for the modified curve proposed in the *Earth Manual* (1972) and for the D method of the ASTM compaction methods.

When further comparing the results obtained from a variety of oversized particle modification methods with the large-scale compaction test result, it is seen that the modified formula proposed in the *Earth Manual* has a tendency to be higher; the D method of the ASTM compaction methods has a tendency to be lower; and only the modified formula proposed by Hsu and Saxena (1991) has a tendency to be consistent with the large-scale compaction test results.

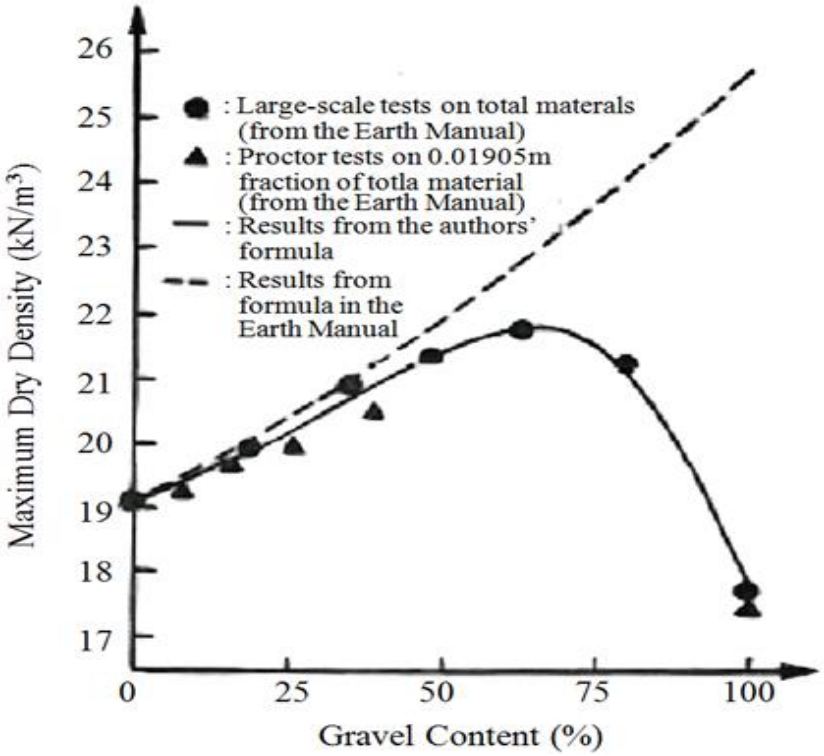

Figure 7.15. The correction equation proposed by Hsu and Saxena (1991) and the test results addressed in the *Earth Manual* (9172).

Finally, the optimum moisture content obtained from the test with a gravel content of P=0%, OMC_0 = 14.3%, is modified to the optimum moisture content of the total soil with a gravel content of P=35%, OMC_T =9.3%, using Equation 7.3:

$$OMC_T = (1-P)OMC_0 . \tag{7.3}$$

After learning that the maximum dry unit weight of the total compacted soil is γ_T=2.024T/m^3 and its optimum moisture content is OMC_T = 9.3%, the compaction quality can be controlled with systematic management. First, it is necessary to plan the range and height of each compacted soil stratum, the total dry unit weight of the total soil, the total weight of the wet soil under OMC_T, the gravel weight under a variety of different particle sizes, the total dry unit weight of mixed sand, and the total dry unit weight of mudstone soil for the area of emergency repair zone. Afterwards, the moisture content test is conducted in an oven provided by the authors on the site, thereby controlling the moisture content in each batch of feed material by calculating the amount of added water required to increase the on-site moisture content to OMC_T.

After the total soil is fully stirred, the stirring uniformity is inspected via a sieve analysis test. After passing inspection, soil is transported by truck in batches to the repair zone marked with construction measurement control points for even spreading. The rolling compaction is carried out using a 10-Tf steel road roller until all elevations marked by the construction measurement control points reached the designated elevation. This is followed by random sampling for site density, and after the compaction quality is found to be in compliance with the contract requirements, the next stratum of soil can then be spread.

Throughout the progress of the emergency repair project, four sets of on-site density tests are conducted at random in accordance with contract regulations. The compacted soil quality must meet the following contract regulations:

a. The minimum values of relative compaction for the four sets of tests must be ≥95%.
b. The average relative compaction for the four sets of tests must be ≥98%.
c. The moisture content for the four sets of tests must be between −1% OMC_T and +3% OMC_T, *i.e.*, the moisture content must be between 8.3% and 12.3%.

For this emergency repair project, the stirring uniformities of each stratum of compacted soil are all demonstrated through the sieve analysis test to be in compliance with the contract regulations and the results of the four sets of on-site density tests conducted randomly show that the relative compactions are 98.81%, 101.78%, 98.02%, and 101.48% with an average value of 100.02%. Therefore, it is found that the relative compaction of the compacted soil is in compliance with Articles 1 and 2 of the contract regulations. Next, the results of tests of moisture content of the four sets of compacted soils are 9.6%, 8.7%, 10.9%, and 9.7%, respectively. Therefore, it

is found that the moisture content of the compacted soil is in compliance with Article 3 of the above-mentioned contract regulations.

In addition to the random sampling tests mentioned above, high compacted soil construction quality depends on systematic quality counseling and management, so that the random sampling results can fully represent the total compacted soils. An expert who has teaching, research, and practical experiences should be appointed as the quality assurer. The main quality counseling work is to conduct theoretical analysis and implement the proposed method on compacted soils throughout the progress of construction in the area, so that construction manufacturers will accept the quality counseling, convinced not only that the compacted soils pass the sampling tests, but also that the finished products can pass withstand an earthquake after completion of work, such that the Hutoupi Reservoir dam will no longer suffer earthquake damage.

7.3.5 Slope Stability Analysis of the Dam Body

In the emergency repair project for the Hutoupi Reservoir dam after the Meinong Earthquake, the earthquake resistance of the dam is indicated by the result of the slope stability analysis. In order to have mutual comparison, the slope stability analysis zone is divided into two sets, one of which is the emergency repair project after the Jiaxian Earthquake, and the other set is the emergency repair project after the Meinong Earthquake.

In the slope stability analysis after the Jiaxian Earthquake, the dam body materials for both the original dam body and the repair zone are silts with low plasticity (ML), where the cohesion of the compacted soil is c=5kPa with an angle of internal friction of $\phi = 26^\circ$ (details in McCarthy, 1977).

In the slope stability analysis after the Meinong Earthquake, the original dam body material is silt with low plasticity (ML), where the cohesion of the compacted soil is c=5kPa and the angle of internal friction is $\phi = 26^\circ$ (details in McCarthy, 1977). The material for the repair zone is clayey gravel (GC), where the cohesion of the compacted soil is c=70kPa with an angle of internal friction of $\phi = 36^\circ$ (details in McCarthy, 1977).

The seismic coefficient chosen in the slope stability analysis is based on the value of the horizontal peak ground acceleration (PGA_h) at 0.42g, as recorded by stations in the vicinity of Hutoupi Reservoir during the Meinong Earthquake, with data provided by the National Center for Earthquake Engineering. Then, according to Table 7.2, the horizontal seismic coefficient is $k_h = 0.15$ and the vertical seismic coefficient is $k_v = 0.15 \times 0.5 \quad = 0.075$.

Table 7.2. Relationship between seismic coefficients and design peak ground acceleration (Water Resources Agency, 2008).

Horizontal design peak ground acceleration, PGA_h	Horizontal coefficient of earthquake, k_h
<0.12 g	0.10
0.12–0.18 g	0.10–0.12
0.18–0.50 g	0.12–0.16
0.50–0.80 g	0.16–0.24
>0.80 g	0.24
Note: The vertical seismic coefficient, k_v, should be directly reduced by the horizontal seismic coefficient, k_h; the reduction ratio shall not be less than 1/2.	

For a homogeneous dam, based on the arc-shaped sliding failure mechanism, the five potential sliding failure surfaces corresponding to the minimum safety factor obtained from the slope stability analysis are shown in Figure 7.16.

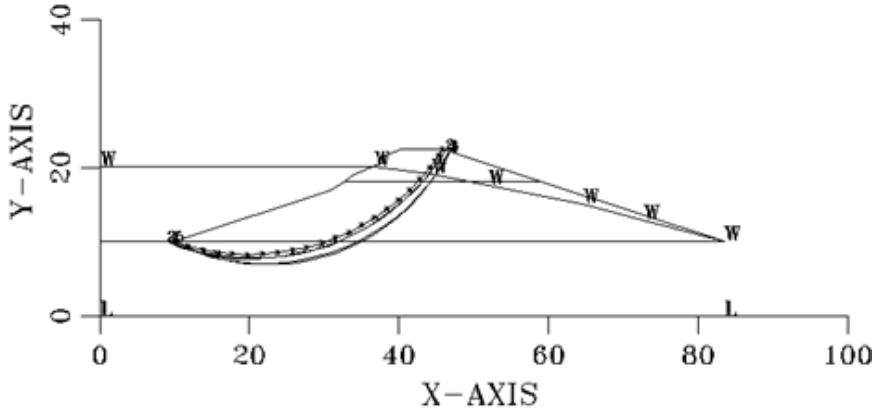

(a) Materials of both the original dam body and repair zone are ML.

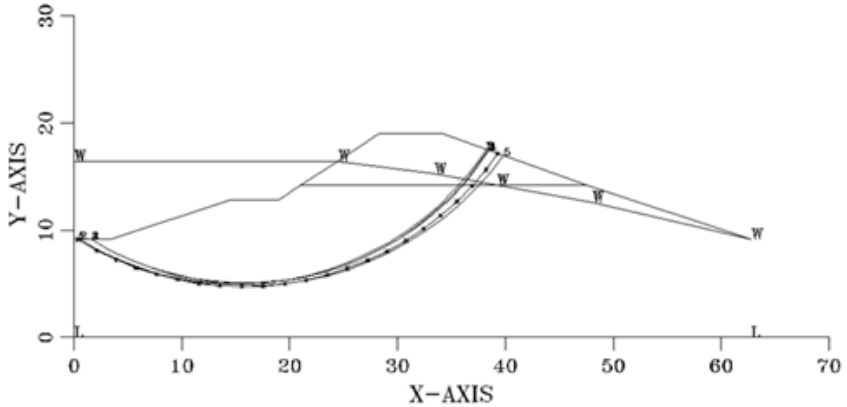

(b) Material of the original dam body is ML; material of the repair zone is GC.

Figure 7.16. Typical slope stability analysis results for the Hutoupi Reservoir dam.

In the Jiaxian Earthquake emergency repair project, the minimum safety factor obtained from the slope stability analysis during calm periods is 1.606, indicating that this type of dam body is stable. During an earthquake, the minimum safety factor obtained from the slope stability analysis is 0.998, indicating that this type of dam body tends to be unstable during earthquakes.

In the Meinong Earthquake emergency repair project, the minimum safety factor obtained from the slope stability analysis during calm periods is 2.252, indicating that this type of dam body is stable. During an earthquake, the minimum safety factor obtained from the slope stability analysis is 1.309, indicating that this type of dam body is also stable during an earthquake.

7.3.6 In-situ Entity Test Results After the Completion of Work

After the completion of work on the Jiaxian Earthquake emergency repair project, the dam body exhibited water leakage on the downstream slope in 2013, as shown in Figure 2. During the 2016 Meinong Earthquake, the dam body exhibited more severe earthquake damage, as shown in Figure 3(b). The in-situ entity test results after the completion of these works directly shows that the quality of the Jiaxian Earthquake emergency repair project was poor.

After the completion of work on the Meinong Earthquake emergency repair project, the dam body and the AC road surface on the crest of dam, as illustrated in Figure 7.17, both did not display any earthquake damage after the 2017 Tainan Earthquake. This shows that the quality of the Meinong Earthquake emergency repair project is excellent. The in-situ entity test results also demonstrate that earthquake damage to a homogenous dam or gushing due to piping damage can be eliminated by using the high-quality and effective emergency repair method proposed in this work.

(a) Dam body after emergency repair

(b) AC road surface on the crest of the dam after emergency repair

Figure 7.17. Entity test results for the emergency repair project of the Hutoupi Reservoir dam after the 2017 Tainan Earthquake.

7.6 Summary of the Main Points

1. The earthquake damage and the gushing due to piping failure exhibited after tectonic earthquakes on the Hutoupi Reservoir dam occurred because shear bandings generated in the upper dam body and then exhibited various shear textures that are much more harmful to the dam body than cracks induced by the vibration of the earthquake.
2. After the authors have prudently evaluated the relative desirability and earthquake resistance of repair materials, in order to avoid the re-occurrence of earthquake damage or gushing due to piping failure, the most desirable and the most earthquake-resistant clayey gravel (GC) was chosen for the Meinong Earthquake emergency repair project for the Hutoupi Reservoir dam to replace the moderately desirable yet least earthquake-resistant silts with low plasticity (ML).
3. During the Meinong Earthquake emergency repair project for the Hutoupi Reservoir dam, not only have the authors conducted systematic quality counseling and management throughout the whole progress, for a maximum particle size of 7.5cm and a gravel content of 35%, the author has chosen the modified formula proposed by Hsu and Saxena to modify the standard Proctor compaction test result with a gravel content of P=0% to a compaction test result with a gravel content of P=35%. This modified result is shown to be consistent with the large-scale compaction test results.
4. Not only did studies directly show that silt with low plasticity (ML) is the least earthquake-resistant and clayey gravel (GC) is the most earthquake-resistant, the slope stability analysis results also showed that silt of low plasticity (ML) must be replaced with clayey gravel (GC) as a repair material, so that the slope of the dam body can go from being unstable to being stable during an earthquake.
5. For the Hutoupi Reservoir dam, the in-situ entity test results show that the Jiaxian Earthquake emergency repair project is the least earthquake-resistant, so more severe earthquake damage occurred during the 2016 Meinong Earthquake. The Meinong Earthquake emergency repair project was the most earthquake-resistant, so earthquake damage did not re-occur in the 2017 Tainan Earthquake. The in-situ entity test results also show that the high-quality emergency repair method for a homogeneous dam proposed in this paper can effectively turn a non-earthquake-resistant dam body into an earthquake-resistant dam body.

Chapter 8

Localizations of Soil Liquefactions Caused by Shear Bandings

T.-S. Hsu, C.-C. Tsao, **C. T. Lin,** Z. Wang and C.-C. Fan

8.1 Introduction

It has been revealed that the conventional cause of soil liquefaction is "With sufficiently high horizontal seismic coefficient k_h and sufficiently long earthquake duration while the ground water table is near ground surface, loose saturated sand strata within 20m of underground depth tend to compress and decrease in volume such that the induced excessive pore water pressure is greater than or equal to effective confining stress of soils thus inducing soil liquefaction."

Based on conventional cause, soil liquefactions can be divided into two different types: (1) the flow liquefaction which takes place when static shear stress is greater than liquefaction shear strength, where the major deformation is induced by static shear stress, and the cyclic shear stress only reduced shear strength of the soil; (2) the cyclic mobility takes place when the static shear stress is less than liquefaction shear strength, where the flowing deformation is induced by both static and cyclic shear stresses (Kramer, 1996).

Soil liquefaction will result in building damage during earthquake, thus design engineers must carry out evaluation of soil liquefaction potential as stipulated in Seismic Design Specifications and Commentary of Buildings (2006).

The conventional methods for evaluation of soil liquefaction potential include using simple criteria and simplified procedures. Simple criteria can be used for initial evaluation of liquefaction potential in large area; simplified procedures are empirical methods based on onsite test result,

where the onsite tests include standard penetration test, cone penetration test, and shear wave velocity test. Currently the frequently used calculation analysis methods include Japan Road Association Method (1996), Seed Method (1987; 1990), and Tokimatsu and Yoshimi Method (1983). Among them, Japan Road Association Method (1996) is the soil liquefaction potential evaluation method adopted by Seismic Design Specifications and Commentary of Buildings (2006).

For a certain position, when depth z falls within the range of 0~20m, the safety factor against liquefaction $F_L(z)$ is defined as the ratio of the computed cyclic resistance ratio (R_z) for the soil at this depth to cyclic stress ratio (L_z) generated by the design earthquake (Ishihara 1985; 1993; Seed 1987; Seed and Harder 1990); and then the liquefaction potential of this position P_L can be calculated by the equation proposed by Iwasaki, Tokida and Tatsuoka (1981) (as shown in Equation 8.1).

$$P_L = \sum_{i=1}^{n} F_i(z) \cdot W_i(z) \cdot \Delta z_i \tag{8.1}$$

In the equation above, $F_i(z)$=1-$(F_L)_i$, $W_i(z)$=10-0.5 z_i, Δz_i is the thickness of the i^{th} layer counting from the ground surface. As for the calculated P_L, when P_L=0, there is no liquefaction potential; when 0<$P_L \leqq$5, there is minor liquefaction potential; when 5<$P_L \leqq$15, there is moderate liquefaction potential; when 15<P_L, there is high liquefaction potential.

For different positions with identical horizontal seismic coefficient k_h, geological condition, and ground water table, the results of liquefaction potential evaluations will all be the same. Take Tainan City of Taiwan as an example, with k_h=0.33 and the ground water table close to ground surface, the soil liquefaction potential diagram published by Central Geological Survey, MOEA based on conventional soil liquefaction potential evaluation method is as shown in Figure 8.1; in Figure 1 the evaluation revealed that all areas covered by alluvial soil layer in Tainan City are equipped with high, moderate, or low soil liquefaction potential.

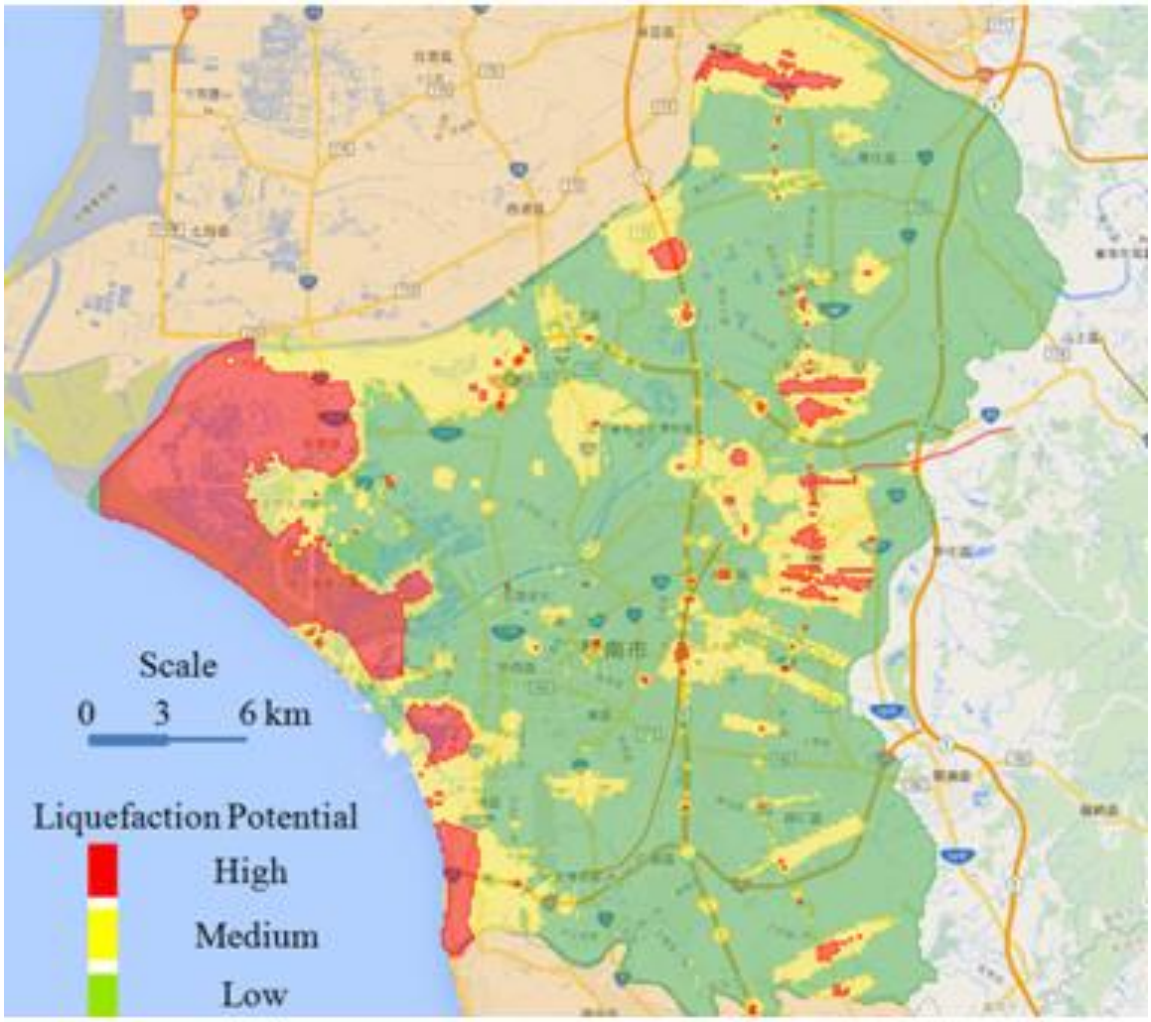

Figure 1. Distribution of soil liquefaction potentials in Tainan City of Taiwan (Central Geological Survey, MOEA, 2016)

The actual location of soil liquefaction in Tainan City took place during Meinong Earthquake on February 6th, 2016 is as shown in Figure 8.2; it has been revealed in Figure 8.2 that: (1) soil liquefaction was merely a kind of localized phenomenon; (2) the actual area of soil liquefaction is far less than the area of soil liquefaction potential announced by Central Geological Survey, MOEA; (3) the actual locations of soil liquefaction were mostly outside the areas with high liquefaction potentials. Thus we know that the conventional cause of soil liquefaction is different from the cause of localizations of soil liquefactions. The result of soil liquefaction potential evaluation obtained from conventional cause of soil liquefaction cannot fully reflect the actual localizations of soil liquefactions behavior.

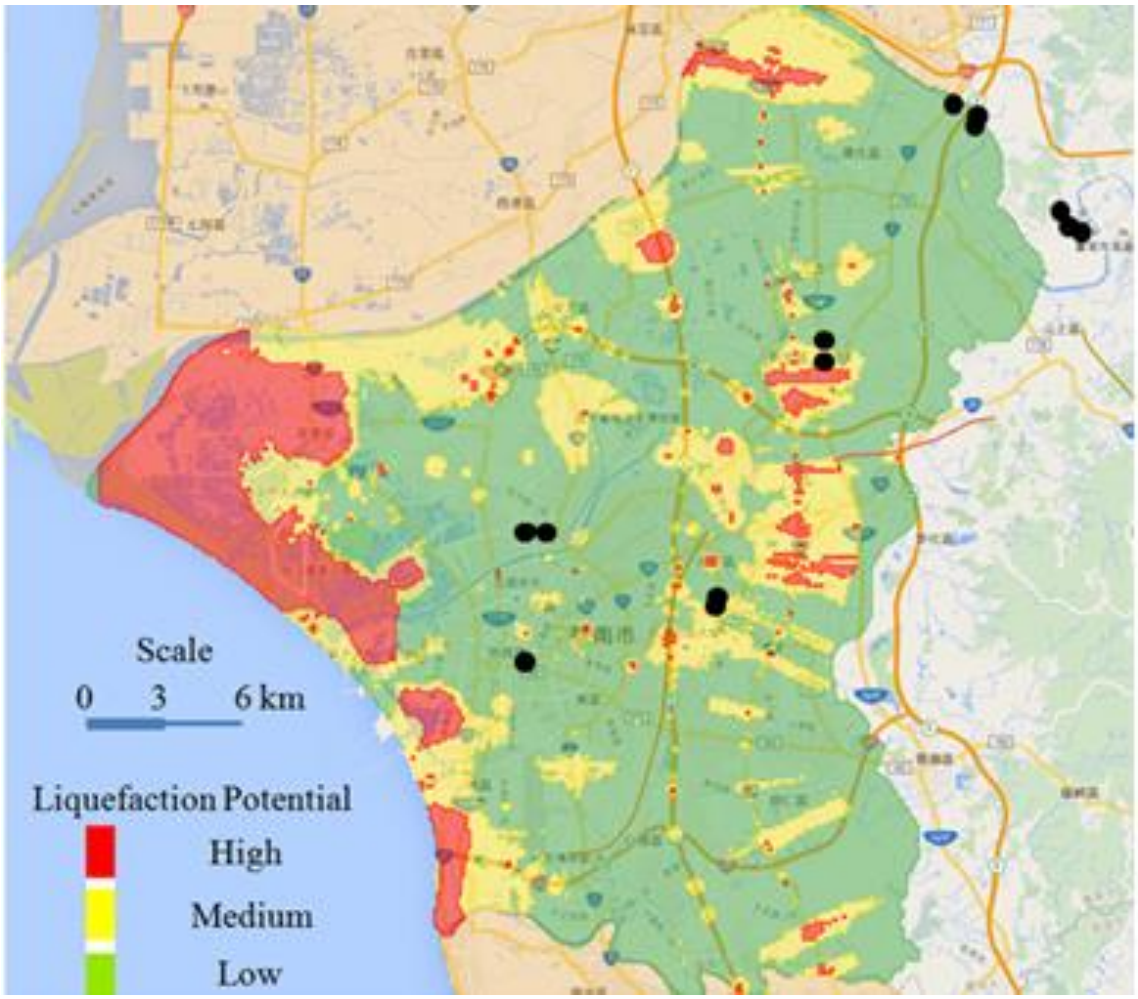

Figure 8.2. Comparison between the locations of soil liquefactions induced by Meinong Earthquake and the distribution of liquefaction potentials (Central Geological Survey, MOEA, 2016)

To capture the localizations of soil liquefactions, it is known that localizations of deformations have to be induced during tectonic earthquakes before obtaining the highly concentrated excessive pore water pressure in the shear bands. Thus it is necessary to investigate the cause of localizations of soil liquefactions via simulation and analysis of tectonic earthquakes.

8.2 Numerical Simulation and Analysis of Tectonic Earthquakes

For a 5.08cm x 2.54cm plate shown in Figure 8.3 under plane strain conditions loaded at both ends, where the movement in the direction perpendicular to the loading is constrained, the uniform 50 x 25 mesh is used to analyze the behavior of the plate under uniformly prescribed loading conditions. Material properties used are: (1) the initial size of yield surface, κ, equal to 24kPa, (2) the Young's modulus, *E*, equal to 1200kPa, (3) Poisson's ratio, ν, equal to 0.3, (4) the shear modulus, *G*, equal to 462kPa, (5) the bulk modulus of water, B_w, equal to 2140MPa, and (6) the strain softening parameter, *H*/2*G*, equal to -0.05 (for modeling strain softening behavior).

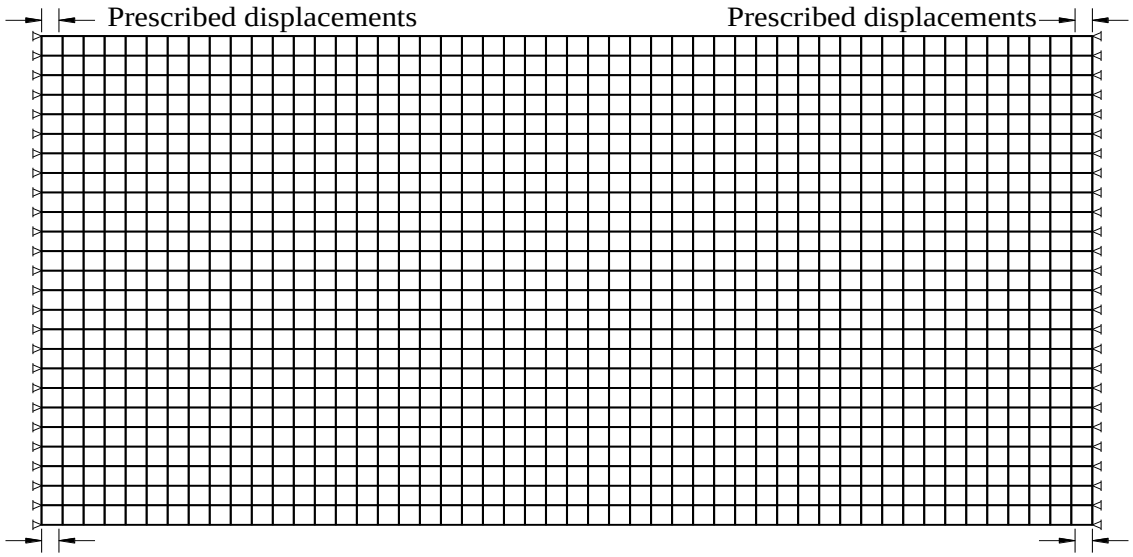

Figure 8.3. Finite element mesh, boundary conditions and prescribed lateral displacements

Results And Discussion. The behavior of localizations of deformations and the excessive pore water pressure contours under loading conditions are shown in Figures 8.4 and 8.5, respectively. Figure 8.4 shows when shear strains are deep into plastic range, shear bandings induced by localizations of deformations are captured due to the loss of symmetry and ellipticity. Figure 5 indicates that the distribution of the excess pore water pressure can be highly concentrated in each shear band. Such a phenomenon can be the cause of the localizations of soil liquefactions.

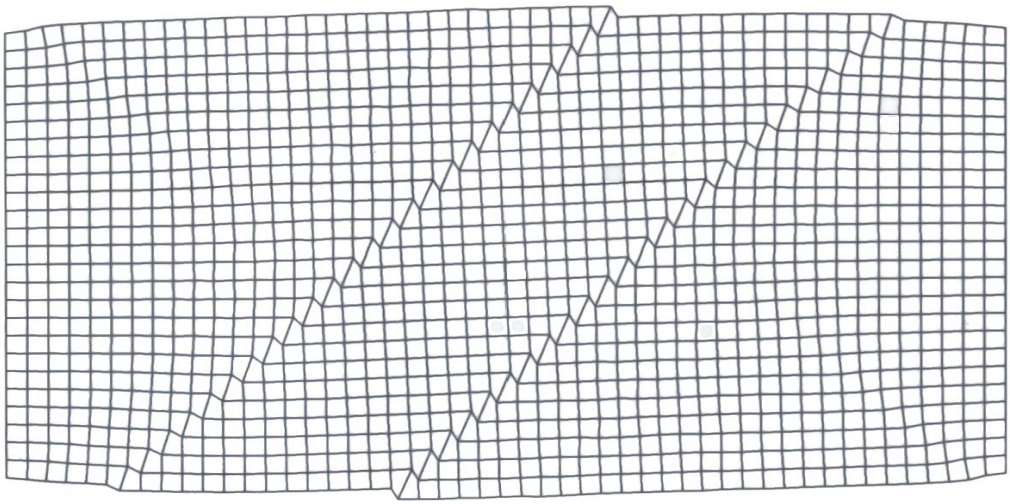

Figure 8.4. Deformed finite element mesh

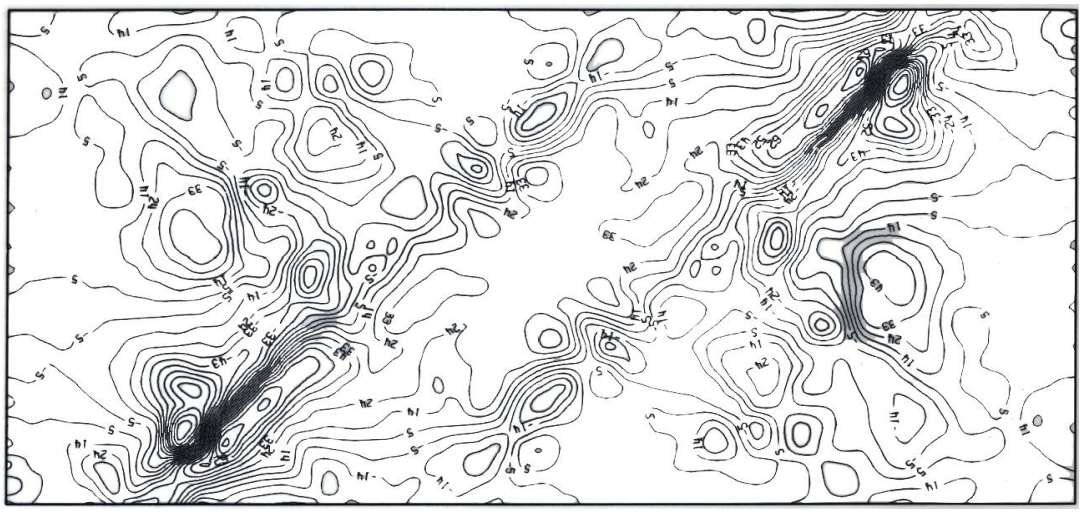

Figure 8.5. Contours of excess pore water pressures

It is well known that there are five different types of earthquakes and most of the mass destruction caused by an earthquake over the history is due to tectonic earthquakes (The China Earthquake Disaster Prevention Center, 2017; Hubpages, 2011).

The localizations of soil liquefactions can only take place in tectonic earthquakes because they are the only earthquakes with shear bandings resulted from localizations of deformations.

Even though the conditions before the force is applied to the soil are uniform, homogeneous, and isotropic, once the shear strain of the plate gets deep into plastic range under lateral compression during a tectonic earthquake, localizations of deformations will take place in the plate due to the loss of ellipticity (Drucker, 1950; Hill, 1962; Mandel, 1966; Rudnicki and Rice, 1975; Rice, 1976; Valanis, 1989), thus leading to highly concentrated excess pore water pressure in shear bands. The brittle fractures of the soils in shear bands have led to greatly increased pore space thus forming the channel for upward ground water flow with sediment entrainment.

Even though the seismic vibration will induce excess pore water pressure, there is neither highly concentrated excessive pore water pressure nor channel for upward ground water flow with fragment entrainment in the tectonic plate.

Localizations of soil liquefactions can be divided into tubular soil liquefaction (as shown in Figure 8.6) and striped soil liquefaction (as shown in Figure 8.7). The tubular soil liquefaction is resulted from the tectonic plate equipped with tubular water channel similar to piping (Terzaghi and Peck, 1967). Hsu and Chiu (2016) believed that this tubular water channel is formed by intersection of shear textures of different strikes; the striped soil liquefaction is resulted from the tectonic plate equipped with striped water channel, which is the shear band under plane strain conditions (as shown in Figure 8.4).

As for areas adjacent to soil liquefaction area, even though they are equipped with identical conditions, the localizations of soil liquefactions do not exist because highly concentrated excess pore water pressure and ground water channel were not induced during the earthquake.

Causes of localizations of soil liquefactions include: (1) high shear resistance of foundation soil has led to strain softening behavior; (2) shear banding has led to tectonic local uplift of the Earth surface; (3) loosening of the shear band soil due to brittle fractures; (4) the expanded pore-space of the shear band soil becomes the channel for upward ground water flow with fragment entrainment; (5) the upward flowing water with fragment entrainment will further loosen the shear band soil.

Figure 8.6. Tubular soil liquefaction took place during Chi Chi Earthquake (EOU Education Market, 2014)

Figure 8.7. Striped soil liquefaction took place during Meinong Earthquake (Liberty Time Net, 2016)

Comparison among various causes of conventional and localizations of soil liquefactions is as shown in Table 8.1. It appears that the cause of conventional soil liquefaction is totally different from the cause of localizations of soil liquefactions. Obviously the cause of localizations of soil liquefactions can better meet the requirement of actual soil liquefaction as shown in Figure 8.6 and Figure 8.7.

The building damage pattern induced by localizations of soil liquefactions during a tectonic earthquake is as shown in Figure 8.8. This kind of damage pattern is totally different from the damage pattern described by Hsu and Ho (2016) where the building was collapsed due to punching shear failure or tilted due to local shear failure.

Different damage patterns will require different disaster mitigation methods related to earthquake, so the building damage induced by foundation punching shear failure (as shown in Figure 8.9a) or local shear failure (as shown in Figure 8.9b) must not be misidentified as to be induced by soil liquefaction.

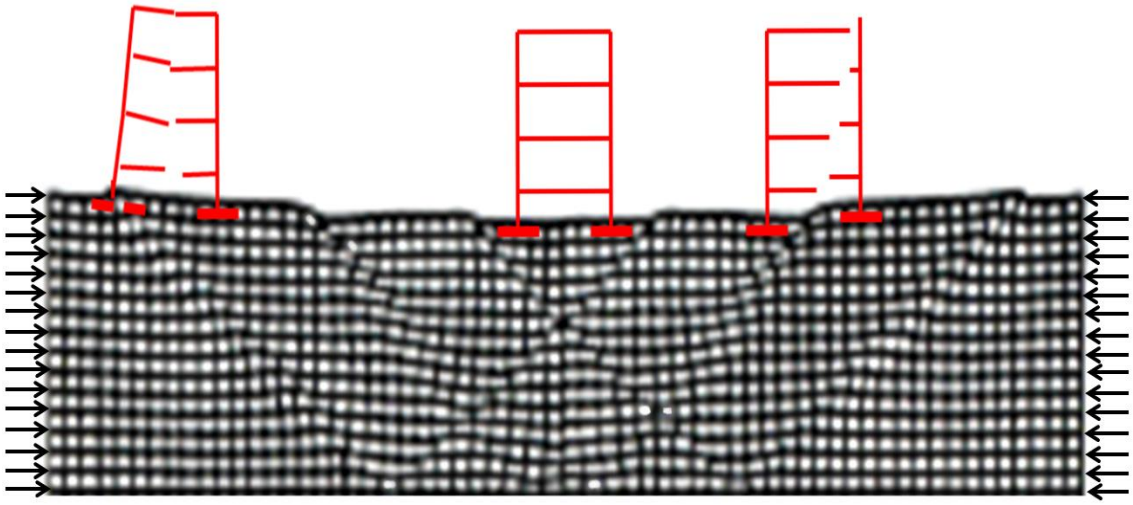

(a) Illustration of building damage pattern

(b) Actual building damage pattern (Pixnet, 2010)

Figure 8.8. Building damage induced by localizations of soil liquefactions during a tectonic earthquake

(a) The case of misidentifying the punching shear failure of foundation as soil liquefaction (Lee, Der-Ho, 2016)

(b) The case of misidentifying the local shear failure of foundation as soil liquefaction (Moh et al., 2000)

Figure 8.9. Cases of building damages during earthquake misidentified as to be induced by soil liquefaction

In the past there were soil liquefactions took place in The Lin Family Mansion and Garden in Taichung, Taiwan during the two tectonic earthquakes in 1906 and 1999, respectively. The conventional cause of soil liquefaction fails to explain why soil liquefaction took place at the same location in two consecutive earthquakes. This is because loose sands will be densified after soil liquefaction, and the densified soil will no longer suffer liquefaction theoretically. However, the aforementioned problem can easily be explained by the cause of localizations of soil liquefactions, because the localizations of soil liquefactions only take place in shear bands with highly concentrated distribution of excess pore water pressure. As long as shear banding takes place at the same location during two consecutive tectonic earthquakes, the soil liquefaction will occur consecutively.

8.3 Comparison of Different Causes for Soil Liquefaction

Table 8.1 is a comparison of various causes of conventional soil liquefactions and localizations of soil liquefactions. According to Figure 8.1, the causes of conventional soil liquefactions and localizations of soil liquefactions are totally different, where the causes of the localizations correspond more with the needs of actual soil liquefactions.

Table 8.1. Comparison among various causes of conventional soil liquefaction and localization of soil liquefaction (Hsu et al., 2017)

	Conventional soil liquefactions	**Localizations of soil liquefactions**
Soil conditions	Loose or perfectly plastic	Dense or strain softening
Type of earthquake causing soil liquefactions	Not specified	Tectonic earthquake
Inducing factor for the major excess pore water pressure	All-around vibrations	Localizations of deformations
Change of soil conditions	All soils are changed from loose state to dense state	Only the shear band soil is changed from dense state to loose state
Highly concentrated excess pore water pressure	Not exist	Exist in shear bands
Discharge water path for ground water to flow upward	Not exist	The expanded pore-space in the shear band soil

8.4 Comparison of Prevention Methods of Conventional Soil Liquefactions and the Localizations of Soil Liquefactions

8.4.1 Prevention Methods of Conventional Soil Liquefactions

In the past, scholars and specialists focused on the conventional constituting elements of soil liquefactions. They believed the cause of soil liquefaction was all-around vibrations, so the lecturing mould of soil liquefaction was as simple as a box of saturated loose sand and different models of buildings. When consistent horizontal vibration was applied, the building model settled down gradually (Figure 8.10); the ultimate cause of this kind of settlement was the punching shear failure induced by the lack of foundation bearing capacity (McCarthy, 2014). However, this kind of lecturing mould misled students to believe that the punching shear failure of the foundation was soil liquefaction. Under the guidance of such lecturing moulds, for people who became scholars or specialists in the future, it would be very natural for them to misidentify that, during tectonic plate vibration, building settlement (Figure 8.9a) induced by punching shear failure was instead induced by soil liquefaction**.**

Seismic Vibration Effect. In tectonic earthquakes, when the land is affected by the seismic vibration only, accompanied with an increase in the acceleration coefficients, k_h and k_v, there is a shallowing trend in the bearing area of the ultimate foundation bearing capability (details in Figure 2.33). This shallowing trend is decreasing as the friction angle is increasing, so granular soil with a larger friction angle has better earthquake resistance abilities.

For strip foundations, the ultimate bearing capability of the foundation under earthquake conditions, $q_{ult,E}$, can be calculated using Equation 2.1

When only seismic vibration exists on land in a tectonic earthquake, to prevent a building leaning failure from occurring, Equation 2.5 can be used to calculate *H*. The soft soil in the depth range of $H\text{-}D_f$ can then be replaced with gravels, which have a high vibration resistance capability.

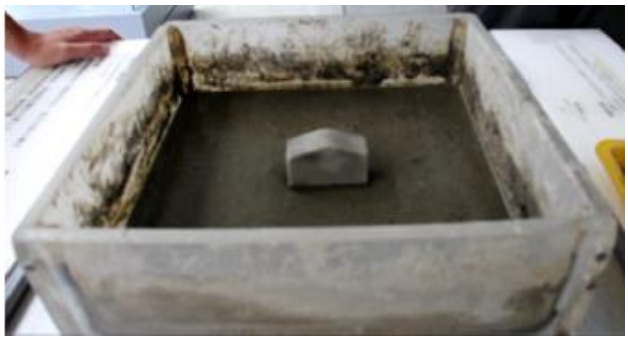

(a) No punching shear failure before vibrating

(b) Only punching shear failure produced after vibrating

(c) No shear banding and no ground water flow upward with sediment entrainment after vibrating

Figure 8.10. The lecturing mould used in teaching soil liquefaction today

The Self Checklist for Soil Liquefaction (Chen, 2016) provided by the Ministry of the Interior lists five conditions that are invulnerable to soil liquefaction. They believe soil liquefaction is not a significant threat to buildings as long as the building meets one of the following five conditions:

1. The building's design follows the revised standards of building earthquake resistance, designed on December 29, 1999.

2. The building foundation is located in a non-liquefaction soil layer, such as a clay layer, a gravel layer, bedrocks, etc.
3. The building has more than 3 floors of basement.
4. The building foundation is pile foundation.
5. The building foundation is mat foundation and the building is not higher than three floors.

Shear Banding Effect. In tectonic earthquakes, when the land is affected by the shear bandings, any buildings complying with any one of the above-mentioned five conditions, designers should still worry about the threat of soil liquefaction to the buildings according to the following three reasons, regarding tectonic earthquakes:

1. The revised standards of building vibration resistance design on December 29, 1999 only considers the secondary effect of a tectonic earthquake (seismic vibration), not the primary one (shear banding).
2. Clay layers, gravel layers, and bedrocks are non-liquefaction layers, in relation to the secondary effect of a tectonic earthquake. When a building founded on these non-liquefaction layers are subjected to seismic vibrations, building leaning failure could still occur.
3. For buildings with more than three floors of basement and lower than three floors, or buildings with pile foundations, raft foundations, or pile foundations: foundation or foundation soil may maintain stability during seismic vibrations because they maintain a comparatively large bearing capability or bear a comparatively small shearing stress, however they may not be able to maintain stability under the effect of shear banding, where shear textures in the foundation soils and highly concentrated excess pore water pressure exist.

8.4.2 Prevention Methods of Localizations of Soil Liquefactions

Localizations of soil liquefactions can only appear in shear bands of a tectonic plate. When foundations in the hanging-wall are lifted and the foundations in the footwall are not lifted, buildings cannot avoid falling apart no matter the designed vibration isolation, vibration damping, or vibration resistance. In order to alleviate buildings' failures induced by shear bandings,

the Ministry of the Interior should promulgate shear banding liquefaction areas and non-shear banding liquefaction areas based on the map of the GPS velocity vectors in each city in the future (Figure 8.11). A standard of building's seismic resistance design should also be provided based on the vital factor of shear bandings, to replace the existing standards based on the factors of seismic vibration only. The Minister should further confirm that the standards of building earthquake resistance design can guarantee no building failures during a tectonic earthquake.

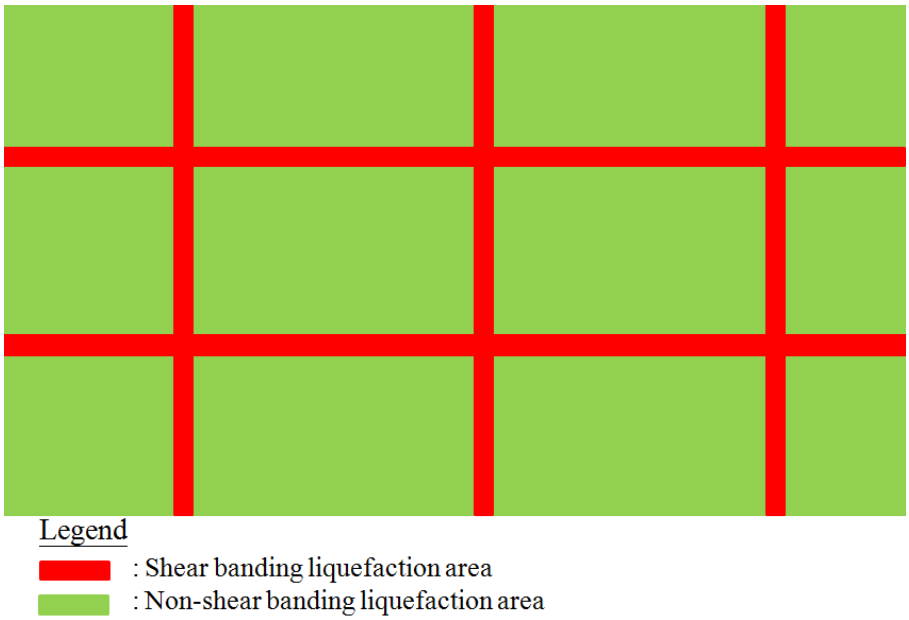

Figure 8.11. Schematic diagram of shear banding liquefaction areas and non-shear banding liquefaction areas which should be provided by Minister of Interior

Prevention Methods in the Shear Banding Liquefaction Zones. For liquefaction zones in the shear band, except in cases of special need, buildings should avoid passing through the shear band. In case where a building must pass through the shear banding liquefaction zones, it must penetrate the ground with special ground modification at first. Then to confirm that the shear band would not reach the range of the bearing area of the ultimate foundation bearing capacity. This is a priority of tectonic earthquake alleviation.

In order to alleviate the shear banding, verification tests of a shear banding table can be conducted (Figure 8.12). As shown in Figure 8.12a, the shear banding compensated on each layer of synthetic blocks need to be confirmed. Then, all shear bandings must be compensated by design to guarantee that all foundations are free from the impacts of shear banding of a tectonic plate.

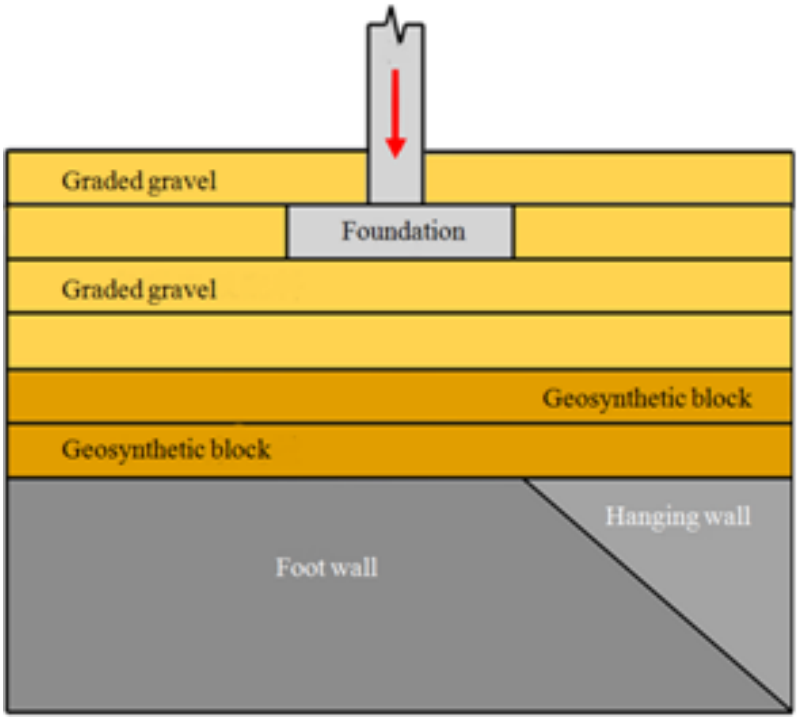

(a) before shear banding

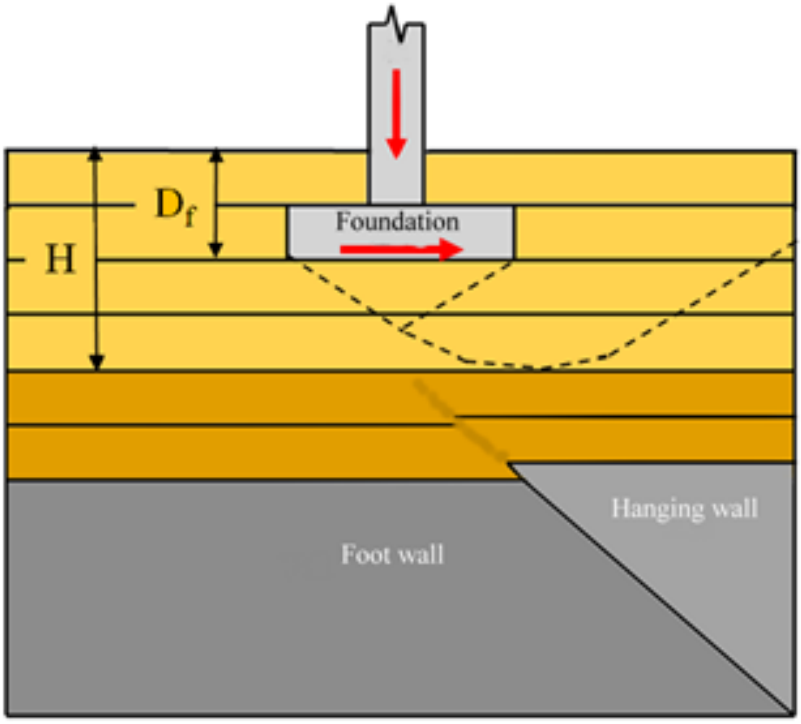

(b) after shear banding

Figure 8.12. Illustrations of verification tests on faulting table

Prevention Methods in the Non-shear Banding Liquefaction Zones. Next, after all foundations are free from the impacts of shear banding for the tectonic earthquake, the foundation bearing capacity under seismic vibrations should be calculated by using Equation 2.1. Finally, the safety factor, $FS_E \geqq 1.2$, must be verified to make sure the safety factor of the foundation bearing capacity under seismic vibrations meets the specification requirements.

8.3.3 Comparison of Prevention Methods of Conventional Soil Liquefactions and Localizations of Soil Liquefactions

The prevention methods of conventional soil liquefactions and those of localizations of soil liquefactions are summarized in Table 8.2. Comparing the prevention methods of conventional soil liquefactions and those of localizations of soil liquefactions, it is apparent that the Self-checklist of Soil Liquefaction provided by the Minister of Interior only considers the secondary effect of a tectonic earthquake, and not the primary one. Therefore, to remove the threat of soil liquefaction to buildings, it is necessary to separate shear banding soil liquefaction areas and non-shear banding liquefaction areas, and to provide necessary prevention methods for these two areas individually.

Table 2. Comparison of prevention methods of conventional soil liquefactions and localizations of soil liquefactions

	Layering or Area-dividing	**Prevention Methods**
Conventional Soil Liquefaction	The identified liquefaction stratum or non-liquefaction stratum based on types of soils	Method 1: Building's design follows the revised standard of building earthquake resistance design, created on Dec. 29 1999 Method 2. Foundation of the building located in non-liquefaction stratum (such as a clay layer, a gravel layer, or a bedrock, etc.) Method 3. Buildings with more than 3 floors of basement Method 4. The building foundation is pile Method 5. Buildings with mat foundation, or Buildings no higher than 3 floors
Localizations of Soil Liquefactions	The identified shear banding liquefaction area	Step 1: To ensure that shear banding does not reach the ultimate bearing capacity area. Verification tests can be conducted on a faulting table to confirm the shear banding is compensated in each layer of synthetic blocks. After that all shear banding should be compensated by design. Step 2: Calculate the bearing capability of foundation under the designed tectonic plate vibration conditions during an earthquake, and make sure the safety factor of the foundation bearing capability under earthquake conditions is $FS_E \geqq 1.2$.
	The identified non-shear banding liquefaction area	Step 1: Calculate the bearing capability of the foundation under the designed tectonic plate vibration conditions during an earthquake, and make sure the safety factor of the bearing capability under earthquake conditions is $FS_E \geqq 1.2$.

8.6 Summary of the Main Points

1. All-around seismic vibrations can be found in tectonic earthquakes, volcanic earthquakes, collapse earthquakes, and explosion earthquakes. However, localizations of deformations induced shear bandings can only be found in tectonic earthquakes.

2. In the simulation analysis of tectonic earthquakes where a tectonic plate is under lateral compression, when localizations of deformations are captured in a deformed finite element mesh, a highly concentrated excess pore water pressure distribution can be found in each shear band. Such phenomenon is the main cause of localizations of soil liquefactions induced in tectonic earthquakes.

3. Localizations of soil liquefactions include tubular and striped soil liquefactions. Among all localizations of soil liquefactions, the intersection area of shear textures of different strikes and the shear band under plane strain condition will provide water channel for tubular and striped soil liquefactions respectively.

4. The soil liquefaction potential evaluation method currently adopted by Seismic Design Specifications and Commentary of Buildings (2006) is based on conventional cause of soil liquefaction, such that all areas formed by alluvial soils will be evaluated as with liquefaction potentials. Such result of evaluation is totally inconsistent with the actual situation of soil liquefaction.

5. The conventional cause of soil liquefaction cannot explain the occurrence of soil liquefactions at the same location in two consecutive earthquakes; however, this can be explained by the cause based on localizations of soil liquefactions.

6. Based on conventional cause of soil liquefaction, building damage induced by either punching shear failure or local shear failure of a foundation during an earthquake can be easily misidentified as to be caused by soil liquefaction.

7. Today’s soil liquefaction lecturing moulds are mainly based on vibration. Thus, they can only demonstrate the punching shear failure of a foundation due to the substantial reducing of bearing capacity under applying vibration, but not the phenomenon of the localizations of soil liquefactions caused by highly concentrated excess pore water pressure while shear banding. In this case, scholars and specialists, based on their formative education as students, misidentify the punching shear failures of a building foundation as soil liquefaction, after which it is natural for them to make incorrect judgments when they become scholars or specialists. Therefore, the prevention methods of soil liquefaction proposed by them do not comply with actual needs.

8. A new lecturing mould for localizations of soil liquefactions is presented in Figure 8.13. It can be seen from Figure 8.13 that shear banding between hanging wall and foot wall has led to highly concentrated excess pore water pressure and forming the channel for upward ground water flow with sediment entrainment.

(a) Before ground water flow upward with sediment entrainment

(b) After ground water flow upward with sediment entrainment

Figure 8.13. A lecturing mould for localizations of soil liquefactions

9. Prevention methods of soil liquefaction provided by the Ministry of the Interior, only include enhancing the bearing capability for a building foundation under seismic vibration. However, building falling apart failures caused by the localizations of soil liquefactions under shear bandings are not avoided.

10. Besides the secondary effect of a tectonic earthquake, the standards of building earthquake resistance design should also include the primary one. Only in this way can the buildings be prevented from falling apart due to localizations of soil liquefactions.

Bibliography

1. Anand, L., and Spitzig, W. A., “Initiation of Localized Shear Bands in Plane Strain,” *Journal of the Mechanics and Physics of Solids*, Vol. 28, pp.113-128, 1980.
2. Apple Daily, "Schematic diagram on the deep submersion of block A during the collapse of Weiguan building,” Website: http://apple. nextmedia.tw/news/local /20160213/34846087/privacy, 2016.
3. Architecture and Building Research Institute, Ministry of the Interior, “A comparative study on the seismic design practice of buildings among Taiwan, USA and Japan,” Website: www.abri.gov.tw/tw/research/dl/ 392/1.
4. Asaro, R. J., and Rice, J. R., “Strain Localization in Ductile Single Crystals,” *Journal of the Mechanics and Physics of Solids*. Vol. 25, pp. 309-338. 1977.
5. *ASTM Book of Standards, Designation: D 698, Standard Test Methods for Laboratory Compaction Characteristics of Soil Using Standard Effo*rt, Website: http://www.dres.ir/fanni/khak/DocLib4/D%20698%20%E2%80%93%2000%20%20;RDY5OA__.pdf, 2017.
6. Atkinson, J. H., “Anisotropic Elastic Deformation in Laboratory Tests on Undisturbed London Clay,” *Geotechnique*, Vol. 25, No. 2, pp. 357-374, 1975.
7. Bardet, J. P. and Mortazari, S. M., “Simulation of Shear Band Formulation in Overconsolidated Clay,” *Proceedings of the Second International Conference on Constitutive Laws for Engineering Materials: Theory and Applications*, Tucson, Arizona, Vol. 2, pp. 805-812, January 1987.
8. Bathe, K., *Finite Element Procedures in Engineering Analysis*, Prentice-Hall, Inc., Englewood Cliffs, New Jersey, 1982.
9. Bauer, G. E., “Movements Associated with the Construction of a Deep Excavation,” *Proceeding of the 3rd International Conference on Ground Movements and Structures*, Cardiff, pp. 694-706, 1984.
10. Bazant, Z. P., “Imbricate Continuum and Its Variational Derivation,” *Journal of Engineering Mechanics,* ASCE, Vol. 110, pp. 1693-1712, 1984.
11. Bazant, Z. P., Belytschko, T. B., and Chang, T-P, “Continuum Theory for Strain-Softening,” *Journal of Engineering Mechanics*. ASCE. Vol. 110. pp. 1666-1692. 1984.
12. Beene, R. R. W., “Waco Dam Slide,” *Journal of the Soil Mechanics and Foundations Division, Proceedings ASCE, SM4,* pp. 35-44, 1967.

13. Berg, C. A., "Plastic Dilation and Void Interaction," in *Inelastic Behavior of Solids*, ed. Kanninen et al., McGraw-Hill, Inc., New York. pp. 171-209. 1970.
14. Bhasjaran, R., A Discussion of "Some Deviation from Isotropy in a Lightly Overconsolidated Clay," (by Hitchell, R. J., *Geotechnique*, Vol. 22, No. 3, pp. 459-467, 1972), *Geotechnique*, Vol. 23, No. 2, pp. 292-294, 1973.
15. Bishop, A. W., Webb, D. W., and Lewin, P. 1., "Undisturbed Samples of London Clay from the Ashford Common Shaft: Strength-effective Stress Relationships," *Geotechnique*, Vol. 10, pp. 129-150, 1965.
16. Bjerrum, L., "Mechanics of Progressive Failure in Slopes of Overconsolidated Plastic Clays and Clay Shales," *Journal of Soil Mechanics and Foundation Division*, ASCE, Vol. 93, SM5, pp. 1-49,1967.
17. Blair-Fish P. M., and Bransby, P. L., "Flow Patterns and Wall Stresses in a Mass-Flow Bunker," *Journal of Engineering for Industry*, pp. 17-26, 1973.
18. Bowles, J. E., *Foundation Analysis and Design*, 4th Ed, Mcgraw-Hill Book Company, New York, U. S. A., 1986.
19. Brooker, E. W., "Strain Energy and Behavior of Overconsolidated Soils," *Canadian Geotechnical Journal*, Vol. 2, pp. 1-15, 1965.
20. Budhu, M. and Al-Karni, A., "Seismic Bearing Capacity of Soils," *Geotechnique*, Vol. 43, No. 1, pp. 181-187, 1993.
21. Bureau of Standards, Metrology & Inspection, Ministry of Economic Affairs, "CNS 560, Steel deformed and plain bars for concrete reinforcement."
22. Cai, Heng and Yang, Jianfu, Taiwan's Fault and Earthquake, Teacher Hou Culture Co. Ltd., 2004.
23. Cai, Guangrong, Chen, Wangzhi, Yang, Yanshan and Lin, Jinbing, "Slope Stability Investigation and Mechanical Properties Testing of Central Cross-Island Highway III", National Science Council Disaster Prevention Science and Technology Research Report, No. 75-36, 1987.
24. Caspe,M.S. "Surface Settlement Adjacent to Braced Open Cuts" JSMFD,ASCE, 92 (SM4):51-59,1966.
25. Central Geological Survey, Ministry of Economic Affairs, Integrated Geological Data Inquiry System, Website: http://gis. moeacgs.gov.tw/gwh/gsb97-1/sys8 /index.cfm, 2017.
26. Central News Service, "Talents Training for Retaining Walls Excavation and Neighbor Household Protection: Responsible for Residents' Living Security," website: http://www.cna.com.tw/postwrite/Detail/128476. aspx#.WSD755Bf270, June 19th, 2013.

27. Central Research Institute of the Ministry of Economic Affairs, “Potential Soil Liquefaction Query System,” Website: http://www.liquid.net.tw/CGSSL/Public /process/Tainan.aspx, 2017.
28. Central Weather Bureau Global Information Web Site, Seismic Activity Archive, Website: http://www. cwb. gov.tw/V7/earthquake/rtd_eq.htm, 2017.
29. Central Weather Bureau, Ministry of Transportation and Commu- nications, Disastrous earthquakes, Website: http://www.cwb. gov.tw/ V7/ earthquake /damage_eq.htm, 2017.
30. Chandler, R. J. , “Shallow Slab Slide in the Lias Clay near Uppingham,” Rutland, Geotechnique, Vol. 20, pp. 253-260, 1970.
31. Chang, Jianxing, “Applications of a Dense Seismic Network Data on the Study of Seismogenic Structures of Central and Eastern Taiwan,” Institute of Geophysics, National Central University, 2004.
32. Chang, Y. W., and Asaro, R. J., “Lattice Rotations and Localized Shearing in Single Crystals,” *Journal of the Mechanics and Physics of Solids*, Vol. 32, pp. 369-388, 1980.
33. Chen, Cheng-Ping, “Study on the reinforcement bar arrangement details,” *Engineers Times*, Website: http://www. twce.org.tw/modules/free content/include.php?fname=twce/paper/991/2-1.htm, 2015.
34. Chen, Yu-Jhen, “Self-checklist of Soil Liquefaction: if building meets one of these five conditions, it is fine”, China Times, Website: http://www.chinatimes. com/newspapers/20160314000332-260102, March 14th, 2016.
35. China Earthquake Disaster Prevention Center, "How do earthquakes happen? — Types of earthquakes", China Digital Science and Technology Museum: Earthquake, Website: http://amuseum.cdstm.cn/AMuseum/earthquak/1/2j-1-2. html, 2017.
36. China Engineering Consultants Incorporated, *Year 85 Slope Disaster Remediation Project & Monitoring System Technical Service - Work Execution Project Book*, Commissioned by Soil and Water Conservation Bureau of Agriculture and Forestry Department of Taiwan Provincial Government Second Engineering Office, 1996.
37. Christoffersen, J., and Hutchinson, J. W., “A Class of Phenomenological Corner Theories of Plasticity,” *Journal of the Mechanics and Physics of Solids*, Vol. 27, pp. 465-487, 1979.
38. Chung, Lap-Loi, Ku, Ting-Yu, Huang, Chun-Ting, Yang, Yao-Sheng, Lai, Yong-An, Wu, Lai-Yun," Simplified pushover analysis for in-situ test of existing school buildings", *Structural Engineering*, Vol. 28, No.2, pp. 3-29, 2013.

39. Chung, Lap-Loi, Yeh, Yeong-Kae, Chien, Wen-Yu, Hsiao, Fu-Pei, Shen, Wen-Cheng, Chiou, Tsung-Chih, Chow, Te-Kuang, Chao, Yi-Feng, Yang, Yao-Sheng, Tu, Yaw-Shen, Chai, Juin-Fu, Hwang, Shyh-Jiann, Sun, Chi-Hsiang, Technical Manual Technology handbook for seismic evaluation and reinforcement of school buildings, 2nd Edition, Report No: NCREE-09-023 National Center for Research on Earthquake Engineering, 2009.
40. Clough, G. W. and Duncan, J. M., "Finite Element Analyses of Port Alien and Old River Locks," University of California, Department of Civil Engineering, Geotechnical Engineering, Report TE-69-3, Berkeley, California. September 1969; also U. S. Army Engineer Waterways Experiment Station, Contract Report S-69-3, Vicksburg, Mississippi.
41. Clough, G.W. and O'Rourke, T. D., "Construction-induced Movements of In-situ Walls," *Design and Performance of Earth Retaining Structures, ASCE Special Publication*, No. 25, pp. 439-470, 1990.
42. Collection of Seismic Activities, Central Meteorological Bureau Glo- bal Information Network, Website: http://www.cwb. gov.tw/V7/ earthquake/rtd_eq.htm, 2017.
43. Construction and Planning Agency, Ministry of the Interior, "Building Technical Regulations," 2015.
44. Construction and Planning Agency, Ministry of the Interior, "Design specifications of building foundations," Website: http://www.cpami. gov.tw/chinese/index.php?option=com_content&view=article&id=10423&Itemid=57, 2001.
45. Construction and Planning Agency, Ministry of the Interior, "Scheme on Implementing seismic capacity evaluation and reinforcement for buildings," 2008.
46. Construction and Planning Agency, Ministry of the Interior, "Seismic isolation design specification of buildings and commentary", 2002.
47. Construction and Planning Agency, Ministry of the Interior, "Seismic design specification of buildings and commentary", 2005.
48. Construction and Planning Agency, Ministry of the Interior, "Seismic design specifications of buildings and commentary," 2011.
49. Construction and Planning Agency, Ministry of the Interior, "The five major conditions not easy generating soil liquefaction: Self-checklist on soil liquefaction," Website: http://www.chinatimes. com/newspapers/ 20160314000332-260102, 2016.
50. Construction Department of the Interior Ministry, "921 Jiji earthquake – Seismic zoning adjustment in Taiwan," 2000.

51. Cowland, J. W. and Thorley, C. B. B., "Ground and Building Settlement Associated with Adjacent Slurry Trench Excavation," *Ground Movements and structures*, Pentech Press, London, U.K., pp.723-738, 1985.
52. Davis G. H., Bump A. P., Garca P. E., Ahlgren S. G., ''Conjugate Riedel Deformation Band Shear Zones,'' *Journal of Structural Geology*, Vol. 22, No. 2, pp. 169-190, 2000.
53. De Borst R., and Vermeer P. A., "Possibilities and Limitations of Finite Elements for Limit Analysis," *Gectechnique*, Vol. 34. No. 2. pp. 199-210. 1984.
54. Department of Environmental Protection Administration Institute, R.O.C., "Environmental Impact Assessment Law," Dec. 22nd, 1999.
55. Desai, C. S., and Abel, J. F., *Introduction to the Finite Element Method*, Van Nostrand Reinhold Company, New York, 1972.
56. Digital Education Portal of Education Department, "Legend of Taipei Basin," website: http://content.edu.tw/senior/earth/tp_ml/taipei/, 2017.
57. Drescher, A., "Photoelastic Verification of a Mechanical Model for the Flow of a Granular Material," *Journal of the Mechanics and Physics of Solids*, Vol. 20, pp. 337-351, 1972.
58. Drecher, A., "An Experimental Investigation of Flow Rules for Granular Materials Using Optically Sensitive Glass Particles," *Geotechnique*, Vol. 26. No. 4, pp. 591-601, 1976.
59. Drucker, D. C., "Some implications of work hardening and ideal plasticity," *Quarterly of Applied Mathematics*, Vol. 7, No. 4, pp. 411-418, 1950.
60. Earle, S., "A Simple Paper Model of a Transform Fault at a Spreading-Ridge," *Journal of Geoscience Education*, Vol.52,No.4, September, pp. 391-392, 2004.
61. *Earth Manual: A Water Resources Technical Publication*, Bureau of Reclamation, United States Department of the Interior, 1st Edition-Revised, Second Printing, pp. 1-69, 1972.
62. Enquiry on live fault, Central University Institute of Geophysics and Central University Applied Geology Institute, Chiayi County, website: http://gis.geo.ncu.edu.tw/921/acfaults/images/ chiayi.jpg, 2017.
63. Finno, R. J. and Harahap, I. S., "Finite element analyses of HDR-4 excavation," *Journal of Geotechnical Engineering, ASCE*, Vol. 117, No. 10, pp. 1590-1609, 1991.
64. Fleming, R. W. , Spencer, G. S. , and Banks, D. G., "Empirical Study of Behavior of Clay Shale Slopes," N. G. G., Technical Report No. 15 (2 Volumes), U. S. Army Engineer Nuclear Crater in a Group, Livermore, California, 1970.
65. Frac Focus, Chemical Disclosure Registry, "Hydraulic Fracture & How It Works," Website: https://fracfocus.org/hydraulic-fracturing- process, 2017.

66. Fukuhei Takaneya, "Vibration control seismic structure", Patent No. 136411, 1940; reprinted from *Seismic isolation, shock prevention and vibration control of buildings*, edited by Takeda Juichi, translated by Zhenyuan Wang, Publishing Department of Ding Da Industrial Co., Ltd., 2000.
67. Geological information enquiry, Central Geological Survey of the Ministry of Economic Affairs, Website: http://gis.moeacgs. gov.tw/ gwh/gsb97-1/sys8/index.cfm, 2017.
68. Gilman, J. J., *Micromechanics of Flow in Solids*, McGraw-Hill, Inc., New York, pp. 47-51, 1969.
69. Google Earth, Website: http://www.google.com/ earth/index.html, 2017.
70. Google Map, Website: https://www.google.com. tw/maps/, 2017.
71. Government of Taipei City, "Taipei Building Construction Neighboring Damage Authentication Manual," Revised by Taipei Architects Associations, Taipei Structure Engineering Association and Taipei Professional Civil Engineers Association, 2006.
72. Government of Taipei City, "Taipei City Building Management Rules," 1974.
73. GPS LAB, Website: http://gps.earth.sinica.edu.tw, 2017.
74. Graham, J. R., Creegan, P. J., Hamilton, W. S., Hendrickson, J. G. Jr., Kaden, R. A., McDonald, J. E., Noble, G. E., Schrader, E. K., "Erosion of Concrete in Hydraulic Structures," ACI 210R-93, Reported by ACI Committee 210, 1998.
75. Hadamard, J., "Lecons sur la Propagation des Ondes et les Equations de l'Hydrodvnamique," Paris, 1903, (Cited from Reference [62]).
76. Hallbauer, D. K., Wagner, H., and Cook, C. W., "Some Observations Concerning the Microscopic and Mechanical Behavior of Quartzite Specimens in Stiff, Triaxial Compression Tests," *International Journal of Rock Mechanics, Mineralogy Science, and Geomechanics Abstract*, Vol. 10, pp. 265-302. 1973.
77. Hansen, J. B., "A Revised and Extended Formula for Bearing Capacity," *Danish Geotechnical Institute Bulletin*, No. 28, Copenhagen, pp. 5-11, 1970.
78. He, Taiyuan, Li, Kuishi, "Ground Surface Settlement Induced by Deep Excavation and Building Protection (I)," *Modern Management*, pp. 41~53, 1990.
79. Henkel, D. J., "The Relevance of Laboratory Measured Parameters in Field Studies," *Proceedings of Roscoe Memorial Symposium*, Cambridge, pp. 669-675, 1971.
80. Hertzberg, R. W., *Deformation and Fracture Mechanics of Engineering Materials*, John Wiley & Sons Canada Limited, Canada, 1983.
81. Hill, R., "Acceleration waves in solids," *Journal of the Mechanics and Physics of Solids*, Vol. 10, pp. 1-6, 1962.

82. Hill, R., “A General Theory of Uniqueness and Stability in Elastic-Plastic Solids,” *Journal of the Mechanics and Physics of Solids*, Vol. 6, PP. 236-249, 1958.
83. Hill, R., “Aspects of Invariance in Solid Mechanics,” *Advanced Applied Mechanics*, Vol. 13, pp.1-75, 1978.
84. Hill, R., “Some Basic Principles in the Mechanics of Solids without a Natural Time,” *Journal of the Mechanics and Physics of Solids*, Vol. 7, pp. 209-225, 1959.
85. Hill, R., *The Mechanical Theory of Plasticity*, Oxford University Press, London, 1950.
86. Hill, R., and Hutchinson, J. W., “Bifurcation Phenomena in the Plane Tensile Test,” *Journal of the Mechanics and Physics of Solids*, Vol. 23, pp. 239-264. 1975.
87. Hsiao, Fu-Pei, Chung, Lap-Loi, Yeh, Yeong-Kae, Chien, Wen-Yu, Shen, Wen-Cheng, Chiou, Tsung-Chih, Chow, Te-Kuang, Chao, Yi-Feng, Weng, Pu-Wen, Yang, Yao-Sheng, Tu, Yaw-Shen, Chai, Juin-Fu, Hwang, Shyh-Jiann, "Technology handbook for seismic evaluation and reinforcement of school buildings”, 3rd Edition, National Center for Research on Earthquake Engineering, Website: http://conf.ncree.org.tw/download%5C0-A1030425-%E6%A0%A1%E8%88%8D%E7%B5%90%E6%A7%8B%E8%80%90%E9%9C%87%E8%A9%95%E4%BC%B0%E8%88%87%E8%A3%9C%E5%BC%B7%E6%8A%80%E8%A1%93%E6%89%8B%E5%86%8A%E7%AC%AC%E4%B8%89%E7%89%88(%E8%8D%89%E6%A1%88).pdf, 2009.
88. Hsieh, P. G., “Prediction of Ground Movements Caused by Deep Excavation in Clay,” *Journal of the Chinese Institute of Civil and Hydraulic Engineering*, Vol. 13, No. 3, pp. 489-498, 2001.
89. Hsieh, P. G., Kung, T. C., Ou, C. Y. and Tang, Y. G., “Deep Excavation Analysis with Consideration of Small Strain Modulus and Its Degradation Behavior of Clay,” *Proceeding of 12th Asian Regional Conference on Soil Mechanics and Geotechnical Engineering*, Singapore, Vol. 1, pp. 785-733, 2003.
90. Hsieh, P. G. and Ou, C. Y., “Shape of ground surface settlement profiles caused by excavation,” *Canadian Geotechnical Journal*, Vol. 35, No.6, pp. 1004-1017, 1998.
91. Hsu, Tse-Shan, *Capturing Localizations in Geotechnical Failures*, Ph.D. Dissertation, Civil Engineering in the school of Advanced Studies of Illinois Institute of Technology, 1987.
92. Hsu, Tse-Shan and Chiu, Shey-En, “Piping Failure Induced By Shear Bandings: Take The Renyitan Reservoir Spillway As An Example,” *The International Journal of Organizational Innovation*, Vol. 9 No. 2, pp. 239-259, 2017.

93. Hsu, Tse-Shan and Saxena, Suren K., “A General Formula for Determining Density of Compacted Soils with Oversize Particles,” *Soils and Foundations*, Vol. 31, No. 3, pp. 91-96, 1991.
94. Hsu, Tse-Shan, Cao, Chang-Qi, Ho, Cheng-Chieh, Shen, Kuan-Tang, Su, Chun-Yi, Su, Ying-Cheng, Huang, Shih-Hsuan, "Critical cause of inclining destruction of buildings in the earthquake," *The 40th National Conference on Theoretical and Applied Mechanics by STAM*, Taiwan, 2016.
95. Hsu, Tse-Shan, Chiu, Shey-En, Hong, Shao-En, Chao, Tzu-Tse, “Investigation on the Failure in Remediation of Shear Banding Tilted River Embankment Slope”, *Proceedings of Environment Technology Management and Hazard Prevention Conference*, Taoyuan Innovation Institute of Technology, pp. 71-83, 2015.
96. Hsu , Tse-Shan, Chiu, S.-E., Hsu, S., Ho, C-C, “A Particle Floating Model for the Initiation of Debris Flows,” *37th National Conference on Theoretical and Applied Mechanics & The 1st International Conference on Mechanics, Procedia Engineering*, Elsevier, Vol. 79, pp. 606-611, 2014.
97. Hsu, Tse-Shan, Luo, Jian-Hua, Xiong, Qiang-Zhi and Chiu, Shey-En "Re-exploration of the causes of water leakage in the downstream of Hsin-shan Reservoir", *the Annual Meeting of ROC Society of Mechanics and the 35th Symposium on Mechanics*, No. B1-003, pp. 355-359, 2011.
98. Hsu, Tse-Shan, Qiu, Shi-En, Hong, Shao-En, and Zhao, Zize, “An Investigation of Failure Renovation Cases of River Bank on Shear Band Tilted Slopes,” *2015 Symposium on Environmental Science and Technology Management and Disaster Prevention and Rescue*, Taoyuan Innovation Technology Institute, 2015.
99. Hsu, Tse-shan, Shen, Kuan-Tang, Ko, Ming-Chao, Su, Chun-Yi, Ho, Cheng-Chieh, “Influence of shear banding on the destruction of school classroom buildings”, *Proceedings on the 39th National Conference on Theoretical and Applied Mechanics by the Society of Theoretical and Applied Mechanics in the Republic of China*, CTAM2015-1127, National Taiwan University of Science and Technology, 2015.
100. Hsu, Tse-Shan, Tsao, Chang-Chi and Lin, Chihsen T., " Localizations of Soil Liquefactions Induced by Tectonic Earthquakes", *The International Journal of Organizational Innovation*, Vol .9, No. 3, pp. 110-131, 2017.
101. Huang, Jialin, “Neighboring Damage Cases in Gaoxiong, Liberty Times,” website: http://news.ltn.com.tw/news/society/breakingnews /1714296, 2016.
102. Hull, D., *Introduction to Dislocation,* Pergarnon Press, New pp. 21-23, 1965.

103. Hull, Derek, *Fractography: Observing, Measuring and Interpre- ting Fracture Surface Topography*, Cambridge University Press, 1999.
104. Hutchinson, J. W., and Tvergaard, V., "Shear Band Formation in Plane Strain," *International Journal of Solids and Structures*, Vol. 17. pp. 451-470. 1981.
105. Hvorslev, M. J., "Physical Properties of Remolded Cohesive Soils," Translation No. 69-5, U. S. Army Engineer Waterways Experiment Station, Vicksburg, Mississippi, (Translation Published in 1969).
106. Hvorslev, M. J., "Physical Components of the Shear Strength of Saturated Clays," *Research Conference on Shear Strength of Cohesive Soils, ASCE*. pp. 169-273. 1961.
107. Hwang, Shyh-Jiann, *E-paper of seismic evaluation and reinforcement for school buildings*, No. 17, National Center for Research on Earthquake Engineering, 2014.
108. Hwang, Shyh-Jiann, *E-paper of reinforcement project office for school buildings*, No. 2, National Center for Research on Earthquake Engineering, 2009.
109. Johnson, S. J., "Engineering Properties and Behavior of Clay Shales," Specialty Session 10, *Proceedings of the seventh International Conference on Soil Mechanics, and. Foundation Engineering*, Mexico City, Vol. 3, pp. 483-438, 1969.
110. Johnston, I. W., "Soft Rock Engineering," *Comprehensive Rock Engineering*, Ed. J. A. Hudson, 1, 367-393, 1993.
111. Kenzaburo Kito, "Building seismic device", Patent No. 131135, 1924; reprinted from *Seismic isolation, shock prevention and vibration control of buildings*, edited by Takeda Juichi, translated by Zhenyuan Wang, Publishing Department of Ding Da Industrial Co., Ltd., 2000.
112. King, I. P., "Finite Element Analysis of Two-dimensional Time-dependent Stress Problems," University of California, Department of Civil engineering, Structural Material Research Report 65-1, Berkley, California, .January 1965.
113. Kramer, S. L., Geotechnical Earthquake Engineering, *Prentice-Hall*, pp. 366-367, 1996.
114. Kulhawy, F. H.. Duncan. J. M., and Seed, H. B., "Finite Element Analyses of Stresses and Movements in Embankments during Construction," University of California, Department of Civil Engineering, Geotechnical Engineering, Report TE-69-4, Berkeley, California, November 1969; Also U. S. Army Engineer Waterways Experiment Station, Contract Report S-69-8, Vicksburg, Mississippi.

115. Kyouzo Yamashita, "Building Seismic Device", Patent No. 63867, 1924; reprinted from *Seismic isolation, shock prevention and vibration control of buildings*, edited by Takeda Juichi, translated by Zhenyuan Wang, Publishing Department of Ding Da Industrial Co., Ltd., 2000.
116. Lambe, T. W., *Soil Testing for Engineers*, Prentice-Hall, Inc., Englewood Cliffs, New Jersey, 1951.
117. Lambe, T. W., and Whitman, R. V., *Soil Mechanics*, John Wylie and Sons, Inc.. New York. 1972.
118. Larsson, M., Needleman, A., Tvergaard, V., and Storakers, B., "Instability and Failure of Internally Pressurized Ductile Metal Cylinders," Report NSF-ENG76-16421/9, Division of Engineering, Brown University, 1981.
119. Leawel, D. A., Peters, J. F., and Townsend. F. C., "Engineering Properties of Clay Shales, Report 4; Laboratory and Computational Predictions of Pore Pressures in Clay Shale Foundations," Report S-71-6, U. S. Army Engineer Waterways Experiment Station, Vicksburg, Mississippi, September, 1982.
120. Lee, Der-Ho, "Characteristic Investigation of the Geotechnical Environment for Tainan Seismic Disaster Area," Special Conference of 0206 Meinong Earthquake , Department of Civil Engineering, National Cheng-Kung University, 2016.
121. Liberty Times Net, "Weiguan building after collapse and destruction," Website: http://m.ltn. com.tw/topic/%E6%B0%B8%E5%BA%B7%E7 %B6%AD%E5% 86%A0%E5%A4%A7%E6%A8%93, 2016.
122. Li, Dezhang, "A Study of Disaster Alleviation and the Compensation System," Report of Architectural Research Institute, Construction Department, Ministry of interior, 1991.
123. Lin, Bingseng, *Mechanical Properties and Stability Research on Collapse Soil Slopes II*, National Science Council Disaster Prevention Science and Technology Research Report, No. 79-64, 1991.
124. Lin, Chaozong, Application of Remote Sensing Image on the Tectonic Geology Research," *Chinese Culture University Press*, 1988.
125. Lin, Qiwen, Zhang, Huizheng, Lu, Shiding, and Shi, Tongsheng, An Introduction to Taiwan' Active Faults, Central Geological Survey Bureau of Ministry of Economic Affairs, 2000.
126. Lin, Weixiong, Lin, Minglang, Chen, Kairong, Li, Xidi, and Zheng, Fushu, "Landslide Potential Research From East Section of Central Cross-Island Highway to Diji Section Sensitive to Landslide", *Proceedings of the Conference on Rock Engineering*, 2000.

127. Lin, Zhiping, Pan, Yiwen, Liao, Zhizhong, Wu, Weijin, Huang, Zhenfeng and Pan, Mingsong, "Investigation and Mechanism of Leakage in Hsin-shan Reservoir", *Geotechnical Engineering*, Vol. 126, pp. 39-50, 2010.
128. Little, A. L., A Discussion of "Waco Dam Slide," (Beene, [4]), *Journal of Soil Mechanics and Foundations Division*, Proceedings ASCE, SM2, pp. 588-590, 1968. *Journal of Soil Mechanics and Foundations Division*, Proceedings ASCE, SM2, pp. 586-590, 1968.
129. Liu, Changling, Yu, Jinli and Chen, Yiquan, "Central Cross-Island Highway Underground Water Investigation II", National Science Council Disaster Prevention Science and Technology Research Report, 1991.
130. Liu, Gee-Yu, "Seismic damage evaluation and countermeasure study of people's livelihood system", *Conference Proceedings of the Chinese Taipei Earthquake Loss Estimation System (TELES)*, National Center for Research on Earthquake Engineering Research Report; NCREE-07-057, Taipei, 2007.
131. Mana, A. I. and Clough G.W., "Prediction of movements for braced cut in clay," *Journal of Geotechnical Engineering Division, ASCE*, Vol. 107, No. 6, pp. 759-777, 1981.
132. Mandel, J., "Conditions de Stabilite et Postulat de Drucker," In *Rheologie et Mechanique des Sols* (Edited by J. Kravtchenko and P. M. Sirieys), Springer, 1966.
133. Mandel, J., "Stability Conditions and Drucker s Postulate," Paper Translated from "Conditions de stabilite et Postulat de Drucker," *Rheology and Soil Mechanics*, ed. Krautchenko J. and Sirieys, P. M., Springer-Verlag Company, Berlin, 1966.
134. Matsuo, M and Kawamura, K "Diagram for Construction Control of Embankment on Soft Ground" *Soils and Foundations*, Vol. 17, No. 3, pp:37-52,1977.
135. McCarthy, David F., *Essentials of Soil Mechanics and Foundations: Basic Geotechnics*, 7th Ed., Pearson Education Limited, p. 413. 1977.
136. Melosh R. J., and Marcal, P. V., "An Energy Basis for Mesh Refinement of Structure Continuua," *International Journal of Numerical Methods in Engineering*, Vol. 11, No. 7, pp. 1013-1092, 1977.
137. Meyerhof, G. G. "The Ultimate Bearing Capacity of Foundations," *Geotechnique*, Vol. 2, No. 4, pp. 301-331, 1951.
138. Milligan, G. W. E., Soil Deformation Near Anchored Sheet-pile Walla, *Geotechnique*, Vol. 33, No.1, pp. 41-55, 1983.

139. Ministry of Economic Affairs, *Derivation of Seismic Coefficient, Technical directions for hydraulic structures inspection and safety evaluation* (*Reservoir and water-conveying structures*), 2008.
140. Ministry of Interior, R.O.C., "Building Law," Aug. 2nd, 1995.
141. Ministry of Interior,R.O.C., "Design Code and Specifications of Building Foundations," 2001.
142. Miyoshi, M. "Mechanical Behavior of Temporary Braced Wall," *Proceedings of the 9th International Conference on Soil Mechanics and Foundation Engineering*, Tokyo, Vol. 2, No. 2/60, pp.655-658, 1977.
143. Molemkamp, F., "Comparison of Frictional Material Models respect to Shear Band Initiation," *Geotechnique*, Vol. 35, No. 2, pp. 127-143, 1985.
144. Nagtegaal, J. C., Parks, D. M., and Rice, J. R., "On Numerical Accurate Finite Element Solution in the Fully Plastic Range," *Computational Methods of. Applied Mechanical. Engineering*, Vol. 4, pp. 153-177, 1974.
145. National Center for Research on Earthquake Engineering NCREE, *E-paper of reinforcement project office for school buildings*, No. 17, 2014.
146. National Center for Research on Earthquake Engineering NCREE, "Important history on seismic design specifications of buildings," Website: http://www.ncree.org/SafeHome/ncr05/pc5_3.htm, 2017.
147. National Center for Research on Earthquake Engineering NCREE, "Structural Analysis Model," Website: http://www.tsea.com.tw/mod ules/tad_uploader /index.php?op=dlfile&cfsn=38, 2017.
148. Nayak, G. C., and Zienkiewicz, 0. C., "Elasto-Plastic Stress Analysis. A Generalization for Various Constitutive Relations Including Strain Softening," *International Journal for Numerical Methods in Engineering*, Vol. 5, pp. 133-135, 1972.
149. Needleman, A., and Rice, J. R., "Limits to Ductility Set by Plastic Flow Localization," in *Mechanics of Sheet Metal Forming*, ed. Koistinen, D. P., and Wang, N.-M., Plenum, Inc., New York. p. 237, 1978.
150. Needleman, A., and Tvergaard, V., "Crack Tip Stress and Deformation Fields in a Solid with a Vertex on Its Yield Surface," *Elastic-Plastic Fracture: Second Symposium*, ed. Shih C. F., and Gudas, J. P., ASTM STP 803, 1983.
151. Needleman. A., and Tvergaard, V., "Finite Element Analysis of Localization in Plasticity," in *Finite Elements: Special Problems in Solid Mechanics*, Vol. 5, ed. Oden, J. T., and Carey, G. F., Prentice-Hall. Inc.. Englewood Cliffs, New Jersey, pp. 94-157, 1983.

152. New Tang Dynasty, "Local inclining destruction of civil houses along Taizi 1st Street in Tainan," Website: http://www.ntdtv.com/xtr/b5/ 2016/02/06/a1251366.html, 2016.
153. Nicholson, D. P., “The Design and Performance of the Retaining Wall at Newton Station,” *Proceedings of Singapore Mass Rapid Transit Conference*, Singapore, pp. 147-154, 1987.
154. Oda, M., and Konishi, J., “Microscopic Deformation Mechanism Granular Material in Simple Shear,” *Soils and Foundations*, Japanese Society of Soil Mechanics and Foundation Engineering, Vol. 14, No. 4, pp. 25-37, December 1974.
155. Oliveria, E. R. A., “Optimization of Finite Element Solutions,” *Proceedings of the third. Conference on Matrix Methods in Structural Mechanics*, Wright-Patterson Air Force Base, Ohio, October 1973.
156. Oka Ryuichi, "Inspection on the foundation of seismic isolation," *Journal of Architecture and Building Science*, 1928; reprinted from *Seismic isolation, shock prevention and vibration control of buildings*, edited by Takeda Juichi, translated by Zhenyuan Wang, Publishing Department of Ding Da Industrial Co., Ltd., 2000.
157. Ou, C. Y., Hsieh, P. G., “Neighboring Properties Protection of Deep Excavation,” Report of Architectural Research Institute of the Ministry of the Interior, website: http://www.abri.gov.tw/tw/research/ show/670 /p/print, 2004.
158. Ou, C. Y., Hsieh, P. G., “Prediction of Ground Surface Settlement Induced by Deep Excavation,” *Deep Excavation Design and Service*, Edited by Lin, Honda, Science and Technology Book Company, Taipei, 1999.
159. Ou, C. Y., Hsieh, P. G. and Chiou, D. C., “Characteristics of ground surface settlement during excavation,” *Canadian Geotechnical Journal*, Vol. 30, pp. 758-767, 1993.
160. Ou, C. Y., Yang, L. L., “A Study of Ground Movements due to Construction of Diaphragm Wall,” National Taiwan University of Science and Technology, GT200005, Taipei, 2000.
161. Parry, R. H. G., and Wroth, C. P., “Shear Stress Strain Properties of Soft Clays,” in *Soft Clay Engineering*, ed. Brand, E. W., and Brenner, R. P., Elsevier Scientific Publishing Company, New York, pp. 311-364, 1981.
162. Peck, R. B., “ Deep Excavation and Tunneling in Soft Ground, ” Proceedings, 7th International Conference on Soil Mechanics and Foundation Engineering, State-of-the-Art-Volume, Mexico City, pp. 225-290, 1969.
163. Peggy, "921 Earthquake Education Park," Website: http://peggy900316. blogspot.tw /2013/04/blog-post_25.html, 2013.

164. Peirce, D., Asaro, R. J, and Needleman, A., “An Analysis of Nonuniform and Localized Deformation in Ductile Single Crystals,” *Acta Metall.*, 1981.
165. Peters, J. F., personal communications, July 1985-April 1986
166. Peterson, R., “Rebond in the Bearpaw Shale, Weatern Canada,” *Bulletin of Geological Society of American*, Vol. 69, pp. 1113-1124, 1958.
167. Petryk, H., and Thermann, K., “Second-order Bifurcation in Elastic-Plastic Solids,” *Journal of the Mechanics and Physics of Solids*, Vol. 33. No. 6, pp. 577-593, 1985.
168. Prevost, J. H., “Soil Stress-Strain-Strength Models Based on Plasticity Theory,” Dissertation submitted to the Department of Civil Engineering of Stanford University in partial fulfillment of the requirements for the Degree of Doctor of Philosophy, 1974.
169. Prevost, J. H., and Hughes, T. J. R., “Finite-Element Solution of Elastic-Plactic Boundary-Value Problems,” *Journal of Applied Mechanics*, Vol. 48, pp. 69-74, 1981.
170. Prevost, J. H., “Short Communication: Localization of Deformations in Elastic-Plastic Solids,” *International Journal for_Numerical and_Analytical Methods in Geomechanics*, Vol. 3, pp. 187-196, 1984.
171. Raniecki.B., and Bruhns, O. T., “Bounds to Bifurcation Stresses in Solids with Non-associated Plastic Flow Rule at Finite Strains,” *Journal of the Mechanics and Physics of Solids*, Vol. 29. pp. 153-172, 1981.
172. Ren-Mei General Affairs Office, "2015 Seismic capacity reinforcement project for west side of the school building," Website: https://sites. google.com/a/zmjhs. tyc.edu.tw/510/xun-yu-zu/gong-cheng-xiang-pian/104nian-du-xi-ce-lou-xiao-she-nai-zhen-neng-li-bu-qiang-gong-cheng, 2015.
173. Rice, J. R., “The Localization of Plastic Deformation," in *Theoretical and Applied Mechanics* (*Proceedings of the 14th International Congress on Theoretical and Applied Mechanics*, Delft, 1976, ed. W.T. Koiter), NorthHolland, Amsterdam, Vol. 1, pp. 207-220, 1976.
174. Rudnicki, J. W., and Rice, J. R., “Conditions for the Localization of Deformation in Pressure-Sensitive Dilatant Materials,” *Journal of the Mechanics and Physics of Solids*, Vol. 23. pp. 371-394. 1975.
175. Saje, M., Pan, J., and Needleman, A., “Void Nucleation Effects on Shear Localization in Porous Plastic Solids,” *International Journal of Fracture*, 1980.
176. Sanlih E-Television News (SETN), "Exposure on the moment of collapse of Weiguan building by the 6.4 magnitude strong earthquake in Southern Taiwan,” Website: https://www.youtube.com/watch?v= TVhz2SP1ytk, 2016.

177. Scott, J. S., and Brooker, E. W., “Geotechnical and Engineering Aspects of Upper Cretaceous Shales in Western Canada,” Paper 66-37, Geological Survey of Canada, Department of Energy, Mines and Resources, Ottawa. 1968.
178. Sengupta, A., and Saxena, S. K., “An Alternative Approach to Capture Localization of Shear Band,” accepted for publication in NUMETA, *International Conference on Numerical Methods in Engineering Analyses*, Swansea, U. K., 1987.
179. Shephard, M. S., “Finite Element Grid Optimization-A Review,” in: M.S. Shephard and R.H. Gallagher, eds., Finite Element Grid Optimization, ASME Special Publication PVP-38, pp. 1-14, 1979.
180. Shephard, M. S., Gallagher, R. H., and Abel, J. F., “Experiences with Interactive Computer Graphics for the Synthesis of Optimal Finite Element Meshes,” in *Finite Element Grid Optimization*, ASME Special Publication PVP-38, ed. Shephard, M. S., and Gallagher, R. H., New York, 1979.
181. Shih, Chung-Hsien, "Preliminary inspection on structural problems of Weiguan building based on numerical simulation", Academic Seminar on Meinong Earthquake, Department of Civil Engineering, National Cheng Kung University, 2016.
182. Sibson, R. H., Moore, J. and Rankin, A. H., “Seismic Pumping---a Hydrothermal Fluid Transport Mecha- nism,” *Journal of Geological Society*, Vol. 131, pp. 653-659, 1975.
183. Sinotech Foundation for Research and Development of Engineering Sciences and Technologies, “Summary of the Gouhou Dam Accident in Qinghai Province China – the case album of the dam accident”, 2008.
184. Sinotech Foundation for Research and Development of Engineering Sciences and Technologies, “Summary of the US Teton Dam Accident – the case album of the dam accident”, 2008.
185. Skempton, A. W., “Horizontal Stresses in an Over-consolidated Eocene Clay,” *Proceedings of the Fifth International Conference on Soil Mechanics and Foundation Engineering*, Paris, Vol. 1, pp. 351-387, 1961.
186. Soil and Water Conservation Bureau, Council of Agriculture, Executive Yuan, website: http://eng2. swcb.gov.tw/content.asp?Aid=1194, 2017.
187. Southern District Water Resources Bureau, Ministry of Water Re- sources, Final Work Achievement of Safety Inspection and Monitoring Analysis of A-kung-tien Reservoir of R.O.C.105, 2016.

188. Stroman, W. R., Beene, R. R. W., and Hull, A. M., “Clay Shale Foundation Slide at Waco Dam, Texas,” *International Conference on Case History in Geotechnical Engineering*, ed. Shamsher Prakash, University of Missouri", Rolla, Vol. 2, pp. 579-586. May 6-11, 1984.
189. Stroman, W. R., and Feese, A. H., “Engineering Properties of Clay Shales, Report 5: Strength and Deformation Properties of Pepper and Del Rio Clay Shales from Waco Dam,” April 1984.
190. Su, Miaobing, Liu, Qifeng and Su, Jianlong, “Investigation of Slope Stability Remediation on Central Cross-Island Highway”, National Science Council Disaster Prevention Science and Technology Research Report, No. 79-10, 1990.
191. Taiwan Chia-Nan Irrigation Association, “Review Report on the Safety of First Water Storage and Water-Conveying Structures in Hutoupi for the Year 2010,” 2010.
192. Taiwan Geotechnical Society, *Summary Report of Investigation into the Landslide at 3.1K of National Freeway No. 3*, Investigation Project Commissioned by Ministry of Transportation and Communications, 2011.
193. Taiwan Waterworks Fifth District Management Office, "Meeting Briefing of the Discussion on Cause Investigation and Repair Project of Renyitan Reservoir Spillway", 2013.
194. Takuji Kobori, Riyoichiro Minami, "Analysis of earthquake control mechanism” No. 102, *Transactions of Architectural Institute of Japan*, 1954; reprinted from *Seismic isolation, shock prevention and vibration control of buildings*, edited by Takeda Juichi, translated by Zhenyuan Wang, Publishing Department of Ding Da Industrial Co., Ltd., 2000.
195. Tainan Civil Engineering Technician Association (TNCE), “Identification report of cause identification on the collapse of Weiguan building in Yongkang District, Tainan, Taiwan,” 2016.
196. Taro Nakamura, "Let’s talking about the seismic energy absorption equipment device", *Journal of Architecture and Building Science*, 1934; reprinted from *Seismic isolation, shock prevention and vibration control of buildings*, edited by Takeda Juichi, translated by Zhenyuan Wang, Publishing Department of Ding Da Industrial Co., Ltd., 2000.
197. Taylor, G. E., and Elam, C. F., “Bakerian Lecture: The Distortion of an Aluminum Crystal during a Tensile Test,” *Proceedings of the Royal Society*, London, A102, pp. 643-667, 1923.
198. Taylor, G. E., and Elam, C. F., “The Plastic Extension and Fracture of Aluminum Crystals,” *Proceedings of the Royal Society*, London, A108. pp. 28-51, 1925.

199. Tchalenko, J. S., "The evolution of kink-bands and the development of compression textures in sheared clays," *Tectonophysics*, Vol. 6, pp. 159-174, 1968.
200. Tengyuan-Mingmin, *Analysis and Prevention of Landslide*, Science and Technology Book Co., Ltd., 1979.
201. Terzaghi, K., "Stability of Slopes in Natural Clay," Proceedings of the. First *International Conference on Soil Mechanics and Foundation Engineering*, Vol. 1, pp. 161-165, 1936.
202. Terzaghi, K., *Theoretical Soil Mechanics*, John Wiley and Sons, New York, 1943.
203. Terzaghi, K. and Peck, R. B., *Soil Mechanics in Engineering practice*, 2nd ed., John Wiley & Sons, Inc., pp. 169-173, 1967.
204. Thomas, T. Y., *Plastic Flow and Fracture in Solids*, Academic Press. New York. 1961.
205. Ting-Wei Hsu, "RC wing wall method," Reinforced concrete building and repair reference illustration and commentary seminar, 2011.
206. Toshio Ikeda (Superviser); co-compiled by Katsuya Okada, Kenyichi Ikeda and Tatsuya Hasegawa, Investigation from the Active Fault to Seismic Design, Japan Kashima Publishing, 2000.
207. Triantafyllidis, N., Needleman, A., and Tvergaard, V., "On the Development of Shear Bands in Pure Bending," *Internationa1 Journal of Solids and Structures*, Vol. 13, pp. 121-138, 1982.
208. Tsai, Heng and Yang, Jian-Fu, *Taiwan's Faults and Earthquakes*, Teacher Hou's Culture Ltd. Company, Taipei, 2004.
209. Turcke, D. J., "Optimum Mesh Configuration in the Finite Element Method," Dissertation submitted to the Department of Civil Engineering of University of Waterloo in partial fulfillment of the requirements for the Degree of Doctor of Philosophy, Canada, July 1974.
210. Turcke, D. J., "Characteristics of Piecewise Approximations in Numerical Analysis," in *Finite Element Grid Optimization*, ASME Special Publication PVP-38, ed. Shephard, M. S., and Gallaaher, R, H., 1979.
211. Turcke, D. J., and McNeice, G. M., "Guidelines for Selecting Finite Element Grids Based on an Optimization Study," *Computer and Structures*, Vol. 4. pp. 499-519. 1974.
212. Tvergaard, V., Needleman, A., and Lo, K. K., "Flow Localization in the Plane Strain Tensile Test," *Journal of the Mechanics and Physics of Solids*, Vol. 29, pp. 115-142, 1981.

213. Underwood, L. B., “Classification and Identification of Shales,” *Journa1 of. Soil Mechanics and Foundation Division,* ASCE, Vol. 93. SM6, pp. 97-116. 1967.
214. Uriel, A. 0., and de Caminos, A Discussion of “Prediction of Undrained Deformations and Pore Pressures in Weak Clav under Two Embankments,” (by Raymond, G. P., *Geotechnque*, Vol. 22, No. 3, pp. 381-401, 1972), Geotechnique, Vol. 23, No. 2, pp. 294-298. 1973.
215. Valanis, K. C., “Banding and stability in plastic materials,” *Acta Mech.* Vol. 79, pp. 113-141, 1989.
216. Vermeer P. A., and De Borst, R., “Non-associated Plasticity for Soils, Concrete and Rock,” *Heron*, Vol. 29, No. 3, pp. 1-64, 1984.
217. Wagner, A. A., “The Use of Unified Soil Classification System by the Bureau of Reclamation,” *Proceedings of the 4th International Conference of Soil Mechanics and Foundation Engineering (London)*, Vol. 1, P. 125, 1957.
218. Wang, Jisheng, Li, Yaoming, “Building protection in deep excavation projects,” Sino-Geotechnology, Vol. 41, pp. 62-71, 1993.
219. Wang, Jianzhi, Lin, Hongda, Wu, Mingfeng, “Ground Surface Settlement Induced by Deep Excavation on Clay Strata,” *Sino-Geotechnology*, Vol. 76, pp. 51-62, 1999.
220. Wang, Yanqiang, Deformation Mechanism of the Southern Section of the Fault in Jiji Earthquake of 1999, the master's thesis of the National Chung Cheng University, Chiayi, Taiwan, 2007.
221. Wang, Yuchun, “Ground Settlement Due to Construction Flaws: Neighboring Building is Also Leaning,” HouseFun News, Website: https://news.housefun. com.tw/news/article/6046563387. html, 2012.
222. Ward, W. H., Marsland, A., and Samuels, S. G., Properties of the London Clay at the Ashford Common Shaft: Undrained Strength Tests,” *Gentechnique*, Vol. pp. 321-344, December, 1965.
223. Water Resources Agency, Ministry of Economic Affairs, *Technical Directions for Hydraulic Structures Inspection and Safety Evaluation* (*Reservoir and Water-Conveying Structures*), 2008.
224. Water Resources Bureau of Ministry of Economic Affairs, “Water Conservancy Construction Inspection and Safety Assessment Methods”, 2003.
225. Water Resources Bureau of Ministry of Economic Affairs, “Water Conservancy Construction Inspection and Safety Assessment Technical Specification”, 2008.
226. Whittle, A. J., Hashash, Y. M. and Whitman, R. V., “Analyses of Deep Excavation in Boston,” *Journal of Geotechnical Engineering, ASCE*, Vol. 119, No. 1, pp. 69-90, 1993.

227. Wikipedia, “1964 Niigata earthquake,” Website: https://en.wikipedia.org/wiki/1964_Niigata_earthquake, 2017.
228. Wikipedia, "Construction of the World Trade Center," Website: https://zh.wikipedia.org/wiki/ %E4%B8%96%E8%B4%B8%E4%B8% AD%E5%BF%83%E7%9A%84%E5%BB%BA%E9%80%A0, 2017.
229. Wikipedia, “Teton Dam,” Website: https://en.wikipedia.org/wiki/ Teton_Dam, 2016.
230. Winkler, E., *Die Lehre Von Elasticitaet Und Festigkeit*, Pray (H. Dominicus), pp. 182-184, 1867.
231. Woo, S. M. and Z. C. Moh, “ Geotechnical Characteristics of Soils in Taipei Basin, ” *Proceedings of the 10th Southeast Asian Geotechnical Conference, Special Taiwan Session*, Taipei, Vol. 2, pp. 51-65, 1990.
232. Wright, S. G., “A Study of Slope Stability and the Undrained Shear Strength of Clay Shales,” Dissertation presented to the University of California, Berkeley, in partial fulfillment of the requirements for the Degree of Doctor of Philosophy, 1969.
233. Wu, Min-fu, "An investigation of the relations between building damages and shear bands occurred in the 921 Jiji Earthquake,” Master’s thesis from Department of Civil Engineering, Feng-Chia University, 2010.
234. Wright, S. G., and Duncan, J. M., “Analyses of Waco Dam Slide,” *Journal of the Soil Mechanics and Foundation Division*, ASCE, SM9, pp. 369-877, September, 1972.
235. Xiang-hai Ye, Tai-kuang Lee, "Drafting history of seismic design specifications of building", Taiwan Architecture & Building Center, 2005.
236. Xie, Jingyi, “Slope Failure Investigation and Remediation on Deji Section of Central Cross-Island Highway”, *Sino-Geotechnology*, Vol. 7, pp. 50-61(1984).
237. Yamada, Y., Yoshimura, N., and Sakurai, T., “Plastic Stress-Strain Matrix and Its Application for Solution of Elastic-Plastic Problems by the Finite Element Method,” *International Journal of Mechanical Sciences*, Vol. 10, No.5, pp. 343-354, 1968.
238. Yamamoto, H., “Conditions for Shear Localization in the Ductile Fracture of Void-Containing Materials,” *International Journal of Fracture*, Vol. 14, pp. 347-365. 1978.
239. Young, N. J. B., "Bifurcation Phenomena in the Plane Compression Test,” *Journal of the Mechanics and Physics of Solids*, Vol. 24, pp. 77-91. 1976.

240. Zhan, Lianchang and Su, Miaobin, “Stratigraphic Sliding Remediation Project in Lishan Area V: Effectiveness Evaluation and Follow-up Processing”, *Proceedings of the Conference on Lishan Stratigraphic Sliding Remediation Project & Effectiveness Evaluation*, pp. 199-244, 2002.
241. Zhang, Huizheng, Lin, Qiwen, Chen, Mianming, and Lu, Shidin, Taiwan Active Fault Distribution Chart, Central Geological Survey Bureau of Ministry of Economic Affairs, 1998.
242. Zhou, Zhihao, Dome Project: Cracks on Songyi Monuments,” *HouseFun News*, Website: https://news.housefun.com.tw/news/ article/20047154772. html, 2017.
243. Zienkiewicz, O. C., *The Finite Element Method*, 3rd edition, McGraw-Hill, New York, 1977.
244. ZTE Engineering Consultants Co. Ltd., the Second Safety Assessment Report of Renyitan Reservoir–a research plan authorized by Water Resources Commission of the Ministry of Economic Affairs, 2008.